Acta GEODAETICA, GEOPHYSICA *et* MONTANISTICA

ACADEMIAE SCIENTIARUM HUNGARICAE

Editor-in-chief
A. TÁRCZY-HORNOCH

Editor
J. VERŐ

Editorial board
GY. BARTA
B. BÉLL
L. HOMORÓDI
L. KAPOLYI
F. MARTOS
J. SOMOGYI
J. ZAMBÓ

VOLUME 17
NUMBER 1
1982

AKADÉMIAI KIADÓ, BUDAPEST

ACTA GEODAETICA, GEOPHYSICA et MONTANISTICA

A Quarterly Journal of the Hungarian Academy of Sciences

Acta Geodaetica, Geophysica et Montanistica (AGGM) publishes original reports on geodesy, geophysics and minings in English.

AGGM is published in yearly volumes of four numbers by

AKADÉMIAI KIADÓ
Publishing House of the Hungarian Academy of Sciences
H-1054 Budapest, Alkotmány u. 21.

Manuscripts and editorial correspondence should be addressed to

AGGM Editorial Office
H-9401 Sopron P.O. Box 5

Subscription information

Orders should be addressed to

KULTURA Foreign Trading Company
H-1389 Budapest P.O. Box 149

INSTRUCTIONS TO AUTHORS

Manuscripts should be sent to the editors (MTA Geodéziai és Geofizikai Kutató Intézete, Sopron, Pf. 5., H-9401, HUNGARY). Only articles not submitted for publication elsewhere are accepted.

Manuscripts should be typewritten in duplicate, double-spaced, 25 lines with 50 letters each. The papers generally include the following components, which should be presented in the order listed.

1. Title, name of author(s), affiliation, dateline, keywords, abstract
2. Text, acknowledgements
3. References
4. Footnotes
5. Legends
6. Tables and illustrations

1. The *affiliation* should be as concise as possible and should include the complete mailing address of the authors. The *date of receipt* of the manuscript will be supplied by the editors. 5—10 significant expressions describing the content are used as *keywords*. Authors may recommend these keywords. The *abstract* should not exceed 250 words and should clearly and simply summarize the most important methods and results.

2. The *text* should be generally in English and as short and clear as possible. From Hungarian authors papers are also accepted in Hungarian.

The section heading should *not* be underlined or in capitals.

Please note that underlining denotes special types:

— single underlining: italics
— double underlining: bold-face roman

ACTA GEODAETICA, GEOPHYSICA et MONTANISTICA

ACADEMIAE SCIENTIARUM HUNGARICAE

EDITORIAL BOARD

GY. BARTA, B. BÉLL, L. HOMORÓDI,
L. KAPOLYI, F. MARTOS, J. SOMOGYI,
J. ZAMBÓ

EDITOR

J. VERŐ

EDITOR-IN-CHIEF

A. TÁRCZY-HORNOCH

VOLUME 17

AKADÉMIAI KIADÓ, BUDAPEST
1982

CONTENTS

Somosvári, Zs.: Investigation of the zone in front of road heads in order to determine the cause of rocks and gas outbursts 1
Somosvári, Zs.: Mechanism of rock and gas outbursts 29
Somosvári, Zs.: Main parameters of the rock and gas outburst danger 51
Somosvári, Zs.: Mechanism of action of provoking explosions 67
Balla, L.: Mathematical formalism of the 2^{n-p} type first-power factorial test planning ... 81
Pethő, Sz.—Tompos, E.: Über die Erzeugung von Dolomit-Mahlgut für Edelverzputz 99
Patvaros, J.: Die Synthese bergbaulicher Technologie-systeme 117
Ádám, J.—Halmos, F.—Varga, M.: On the concepts of combination of satellite and terrestrial geodetic networks 147
Ádám, J.—Tarcsai, Gy.: Doppler location equations for platform localization using satellites 171
Csernyák, L.—Steiner, F.: Amplifying residual filters 181
Csernyák, L.—Steiner, F.—Zilahi-Sebess, L.: A short note to prescribed w-properties 205
Abdelhamid Kamal Hassan: Comparison between results of the gyro-azimuths determined with old and new gyrotheodolites 209
Kardos, I.—Borza, T.—Vass, T.: Laser ranging observations at the Satellite Geodetic Observatory (SGO) 237
Krasnobaeva, A. G.—Diakonov, B. P.—Astafiev, P. F.—Batalova, O. V.—Vishnev, V. S.—Gavrilova, I. E.—Zhuravlyova, R. B.—Kirillov, Magnetotelluric data on the geoelectric structure in the North-Eastern part of the Baltic Shield 255
Raspopov, O. M.—Afanasyeva, L. T.: Localization of the Pc5-source and of the auroral oval 267
Rösler, R.—Lindner, H.: Ableitung von Feldtransformationen für Profile von Potential-feldanomalien 277
Немеши Л. — Богнар Е. Лавбанзурен-Ховбан-Майкут, Т. Том, Ч.: Комплексная геофизическая разведка в пустине Гоби 291
Gasco, J. C.—Febrer, J. M.—Demicheli, J.—Fournier, J. G.: Zarate MT sounding and upper mantle resistivity 307
Tóth, J.: 25 years of the Petroleum Engineering Research Laboratory of the Hungarian Academy of Sciences 311
Balla, L.: Modelling of flow phenomena in porous media 317
Bauer, K.: Determination of the diffusion mass transport coefficient of a $CO_2—CH_4$ gas mixture in porous media at reservoir temperature and pressure 329
Lakatos, I.—Mrs. Lakatos, Szabó, J.: Stability of polyacrylamide solutions in presence of carbon dioxide 345
Lakatos, I.—Mrs. Lakatos, Szabó, J.—Mrs. Kiss, Gáspár, M.: A comparative laboratory study of well-treatment techniques based on in situ cross-linking and polymerization 363
Milley, Gy.—Wagner, O.: A new method of modelling capillary pressure curves 383
Munka, M.: Application of mathematical simulation to polymer flood design 391
Heinemann, Z.—Milley, Gy.—Wagner, O.: Modification of pore structure by inorganic gels to increase displacement efficiency 401
Milley, Gy.—Wagner, O.—Jónap, K.—Bukta, B.—Lövei, J.: Long core model apparatus for the laboratory investigation of oil recovery processes 415
Tóth, J.—Mrs. Milley, Tóth, J.—Mrs. Lakatos, Szabó, J.: Determination of the degree of crude oil metamorphism with application to prospecting purposes 437
Tóth, J.—Mrs. Milley, Tóth, J.: Possible role of mechanical effects in crude oil generation and geochemical investigations of hydrocarbons 447
Zoltán, Gy.: Energy consumption of underground gas storage (Independence of specific storage energy on reservoir structure) 455

Acta Geodaet., Geophys. et Montanist. Acad. Sci. Hung. Volume 17 (1), pp. 1—27 (1982)

INVESTIGATION OF THE ZONE IN FRONT OF ROAD HEADS IN ORDER TO DETERMINE THE CAUSE OF ROCK AND GAS OUTBURSTS

ZS. SOMOSVÁRI

TECHNICAL UNIVERSITY OF HEAVY INDUSTRY, MISKOLC

[Manuscript received February 23, 1979]

Based on an analysis of the interactions of the rock–gas system, it will be proved that the reason for outbursts occurring more frequently at road heads than in workings is that the basic condition of outbursts, *viz.* the reduction of rock volume, is always satisfied. In workings, this condition is not valid in case of small Poisson's ratios, $m \leq 2.33$.

The values of layer strength (uniaxial compressive strength) required to prevent outbursts will be derived as a function of the initial pore gas pressure, vertical primary stress, Poisson's ratio and the angle of internal friction of the layer. This relationship explains, among others, why the frequency of outbursts increases with the increasing depths and drift cross sections and why could outbursts ensue in certain cases at very low pore gas pressure values (0.2—0.4 MPa) while in other cases they do not occur at even much higher pressures. The relationship derived will also imply that outbursts should generally occur in layers of low strength, even though in certain cases they can set in in layers of greater compressive strength as well.

In course of the analysis of the intensity of outbursts, it will be investigated why their intensity increases with the dirft cross section and why do we have outbursts of greater intensity in drifts that cross the layer than in those driven within the boundaries of a given layer. The calculations will furnish orders of magnitudes for the intensities comparable with those experienced in actual cases.

Finally, connections between outburst danger and the effectiveness of supports and drifting speed will be analysed.

Symbols

$\bar{\sigma}_r$	primary radial stress
$\bar{\sigma}_\varphi$	primary tangential stress
$\bar{\sigma}_a$	primary axial stress
$\tau_{r,\varphi}$	primary shear stress
σ_r	secondary radial stress
σ_φ	secondary tangential stress
σ_a	secondary axial stress
$\tau_{r,\varphi}$	secondary shear stress
$\Delta\sigma$, $\Delta\tau$	deformation stresses
σ', τ'	effective stresses
τ	shear limit stress
m	Poisson's ratio
E	Young's modulus of the surrounding rock
E_s	Young's modulus of the support ring
γ	average bulk weight
ϱ	radius of the plastic zone
H	depth beneath the surface
v	thickness of support ring
R	radius of excavation
η	coefficient of viscosity
ϑ	relaxation time
r, φ	polar co-ordinates
t	time
x	distance from the face

ε_r, ε_φ, ε_a	deformations
u_r, u_φ, u_a	displacements
u^*	radial displacement of the drift surface far away from the road head
σ_Y	yield stress
B	Brinke's number
Φ	angle of internal friction
σ_C	uniaxial compressive strength
σ'_C	uniaxial compressive strength in the presence of pore gas pressure
σ_t	total stress
p	pore gas pressure
p_0	initial pore gas pressure
e_0	initial void ratio
$\Delta V/V$	specific volume change
k'	coefficient of loosening
V	volume of deteriorated rock
G	weight of deteriorated rock
α, β, α', β', A, C, D, F	constants

A great number of unexpected rock and gas outbursts occurs even today all over the world in spite of the great efforts and expenses paid to protection methods. This is but a consequence of our poor understanding of the causes of outbursts. We do not always know in advance in which seam do we have to expect outbursts, while even in those layers regarded as dangerous the outbursts can occur quite unexpectedly.

In a similar way as in our previous studies [10], [11], [12], the interactions of the rock–gas system will be investigated in order to determine the causes of outbursts. Main results of our previous investigations can be summed up as follows.

The outburst is a sudden, explosion-like deterioration process of the rock–gas system. The basic cause of outbursts is the strength-reducing effect of the pore gas pressure. The basic condition of outbursts is a load that reduces rock volume. No outbursts can occur if the rock volume increases during deterioration. On the surface of shafts and drifts far away from the road head, no outbursts have ever set in because, here volume increase takes place during rock deterioration. Outbursts always occur at rock faces, road heads, shaft soles and workings because the load in front of the face of excavations causes a volume reduction. In workings within coal layers of extremely low strength, it is possible to have a volume increase even in front of the face [12]. In such cases, according to experience, no outburst occurs in the workings.

If the rock volume decreases in front of the rock face, its pore volume also decreases so that the pore gas pressure becomes greater. In front of the face, the load on the solid structure of the rock becomes greater due to the transferred rock pressure, while the strength decreases because of the increased pore gas pressure. Thus the condition of deterioration is easily met. With advancing deterioration the load is gradually transferred from the solid structure of the rock on the pore gas, increasing the gas pressure. With the increase of the pore gas pressure the strength further decreases, the condition of deterioration will also be met at stronger rock points and the process of deteriora-

tion proceeds further. Consequently, a chain reaction commences during which rock deterioration is greatly accelerated, spreads over a great zone and takes up an explosion-like shape while the pore gas pressure increases to many times its initial value. The resulting state can be characterized by a great pore gas pressure and the presence of a rock mass possessing hardly any internal resistance. Thus an intensive, explosion-like gas flow starts towards the open space throwing out a great amount of solid material. During this out-throw the adsorbed gas phase gets free and a great amount of gas enters the surrounding mining excavations. The above description of the phenomenon of rock and gas outburst was derived in our previous works [10, 11, 12].

Experience shows that the vast majority of outbursts occur at road heads. Outbursts are rather rare in workings because in coals of extremely low strength and small Poisson's ratio the basic condition of outbursts requiring a volume reduction during deterioration is not satisfied. In the Pécs region, Hungary, practically no outbursts have ever occurred in workings because of extremely low coal strength and Poisson's ratio, 99 per cent of them have taken place at road heads. It is, therefore, an actual task, indeed, to thoroughly analyse the mechanical state of the rock zone in front of the road head.

The mechanical behaviour of the zone *in front of* rock faces is hardly dealt with in rock mechanics, the few available results cannot be used but for qualitative conclusions. In order to obtain quantitative results, we have to investigate the mechanical behaviour of the rock zone in front of road heads. Since the mechanical state around drifts far away from the road head is well known [1, 2, 3], it is advantageous to start out from this knowledge for the analysis of the rock zone in front of the road head.

1. Mechanical state around a drift of circular cross section far away from the road head

The elastic secondary stresses around a horizontal drift of circular cross section without supports after excavation can be described in the polar co-ordinate system of Fig. 1 as follows:

$$\begin{aligned}
\sigma_r &= \frac{H\gamma}{2(m-1)}\left[m\left(1-\frac{R^2}{r^2}\right)+(m-2)\left(1-4\frac{R^2}{r^2}+3\frac{R^4}{r^4}\right)\cos 2\varphi\right] \\
\sigma_\varphi &= \frac{H\gamma}{2(m-1)}\left[m\left(1+\frac{R^2}{r^2}\right)-(m-2)\left(1+3\frac{R^4}{r^4}\right)\cos 2\varphi\right] \\
\sigma_a &= \frac{H\gamma}{2(m-1)}\left(2-\frac{m-2}{m}4\frac{R^2}{r^2}\cos 2\varphi\right) \\
\tau_{r,\varphi} &= \frac{H\gamma}{2(m-1)}(m-2)\left(3\frac{R^4}{r^4}-2\frac{R^2}{r^2}-1\right)\sin 2\varphi\,.
\end{aligned} \tag{1}$$

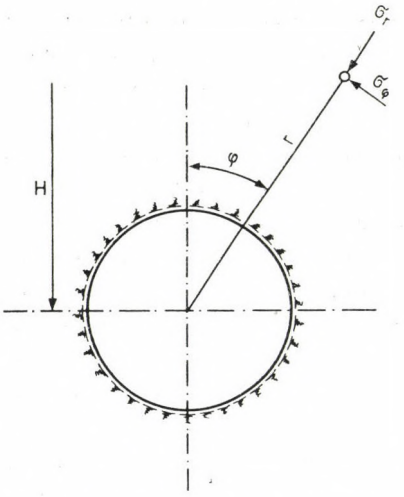

Fig. 1. Co-ordinate system schematics

The primary stresses before excavation are, at the same place and in the same polar co-ordinates:

$$\bar{\sigma}_r = \frac{H\gamma}{m-1}[1-(m-2)\cos 2\varphi]$$

$$\bar{\sigma}_\varphi = \frac{H\gamma}{m-1}[1+(m-2)\sin 2\varphi]$$

$$\bar{\sigma}_a = \frac{H\gamma}{m-1} \tag{2}$$

$$\bar{\tau}_{r,\varphi} = -\frac{H\gamma}{m-1}\frac{m-2}{2}\sin 2\varphi\,.$$

The stress changes due to excavation, i.e. the differences between secondary and primary stresses, the so-called deformation stresses, are:

$$\Delta\sigma_r = -\frac{H\gamma}{2(m-1)}\left[m\frac{R^2}{r^2}+(m-2)\left(4\frac{R^2}{r^2}-3\frac{R^4}{r^4}\right)\cos 2\varphi\right]$$

$$\Delta\sigma_\varphi = \frac{H\gamma}{2(m-1)}\left[m\frac{R^2}{r^2}-(m-2)\,3\frac{R^4}{r^4}\cos 2\varphi\right]$$

$$\Delta\sigma_a = -\frac{H\gamma}{2(m-1)}\frac{(m-2)}{m}4\frac{R^2}{r^2}\cos 2\varphi \tag{3}$$

$$\Delta\tau_{r,\varphi} = -\frac{H\gamma}{2(m-1)}(m-2)\left(2\frac{R^2}{r^2}-3\frac{R^4}{r^4}\right)\sin 2\varphi$$

where H depth of the excavation,

γ average bulk weight of the overburden,

m Poisson's ratio,

R radius of excavation.

For $m = 2$ the above formulae become much straightforward. When analysing the rock zone in front of the road head one can take $m = 2$ for places far away from the road head. Throughout the investigation this value will be used.

For supported drifts, and taking the time factor into account, the above stresses can be expressed as follows [2].

Secondary stresses:

$$\sigma_r = H\gamma\left\{1 - \left(\frac{R}{r}\right)^2 [1 - \alpha'(1 - e^{-\beta' t})]\right\}$$

$$\sigma_\varphi = H\gamma\left\{1 + \left(\frac{R}{r}\right)^2 [1 - \alpha'(1 - e^{-\beta' t})]\right\}$$

$$\sigma_a = H\gamma \tag{4}$$

$$\alpha' = \frac{\frac{E_s}{E} v}{\frac{E_s}{E} v + \frac{4}{5} R}$$

$$\beta' = \frac{\frac{E_s}{E} v + \frac{4}{5} R}{2R\frac{\eta}{E} + \frac{E_s}{E} v\vartheta}$$

here t time,

E Young's modulus of the surrounding rock,

E_s Young's modulus of the support ring,

v wall thickness of the support ring,

η viscosity,

ϑ relaxation time.

These equations can be derived from the Poyinting—Thomson (standard) model.

Deformational stresses:

$$\Delta\sigma_r = -H\gamma\left(\frac{R}{r}\right)^2 [1 - \alpha'(1 - e^{-\beta' t})]$$

$$\Delta\sigma_\varphi = H\gamma\left(\frac{R}{r}\right)^2 [1 + \alpha'(1 - e^{-\beta' t})] \tag{5}$$

$$\Delta\sigma_a = 0.$$

Deformations:

$$\varepsilon_r = -H\gamma \frac{\alpha' R}{E_s v} \left(\frac{R}{r}\right)^2 (1 - e^{-\beta' t})$$

$$\varepsilon_\varphi = H\gamma \frac{\alpha' R}{E_s v} \left(\frac{R}{r}\right)^2 (1 - e^{-\beta' t}) \tag{6}$$

$$\varepsilon_a = 0$$

where ε_r radial deformation,
ε_φ tangential deformation,
ε_a axial deformation.

Displacements:

$$u_r = H\gamma \frac{\alpha' R^2}{E_s v} \frac{R}{r} (1 - e^{-\beta' t})$$

$$u_\varphi = 0 \tag{7}$$

$$u_a = 0$$

where u_r radial displacement,
u_φ tangential displacement,
u_a axial displacement.

If the secondary stresses are expressed in terms of the radial discplacement, the following equations are obtained:

$$\sigma_r = H\gamma \left[1 - \left(\frac{R}{r}\right)^2 \left(1 - u_r \frac{rvE_s}{R^3 H\gamma}\right)\right]$$

$$\Delta\sigma_r = -H\gamma \left(\frac{R}{r}\right)^2 \left(1 - u_r \frac{rvE_s}{R^3 H\gamma}\right)$$

$$\sigma_\varphi = H\gamma \left[1 + \left(\frac{R}{r}\right)^2 \left(1 - u_r \frac{rvE_s}{R^3 H\gamma}\right)\right] \tag{8}$$

$$\Delta\sigma_\varphi = H\gamma \left(\frac{R}{r}\right)^2 \left(1 - u_r \frac{rvE_s}{R^3 H\gamma}\right)$$

$$\sigma_a = H\gamma$$

$$\Delta\sigma_a = 0.$$

Thus the displacement—stress relationship is independent of time.

The radial stress on the surface of the excavation at $r = R$ can be written as

$$\sigma_R = v \frac{u_R v E_s}{R^2}. \tag{9}$$

This gives, at the same time, the load on the support which, in consequence, is linearly proportional to the radial displacement.

Around the drift, the elastic state of stress does not always exist. If the secondary elastic state of stress satisfies the condition of plasticity, a zone in plastic state is formed around the drift. Since the properties of the plastic zone have been much less studied than in the elastic state, the plastic zone deserves a closer scrutiny.

The plastic rock zone around a drift of circular cross section far away from the road head can be characterized as follows. A plastic state is created if Coulomb's condition of plasticity

$$\sigma_\varphi = B\sigma_r + \sigma_Y \tag{10}$$

is satisfied, where

σ_Y denotes the yield stress of uniaxial compression, and
B is Brinke's number,

$$B = \tan^2\left(45° + \frac{\Phi}{2}\right) \tag{11}$$

with Φ being the angle of internal friction.

The equation of equilibrium becomes for planar deformation:

$$\frac{\partial \sigma_r}{\partial r} + \frac{\sigma_r - \sigma_\varphi}{r} = 0 \tag{12}$$

or, by Eq. (10)

$$\frac{\partial \sigma_r}{\partial r} = \frac{1}{r}\left[\sigma_r(B-1) + \sigma_Y\right]. \tag{13}$$

The solution to this linear differential equation at $r = R$, subject to the condition $\sigma_r = \sigma_R$, is

$$\sigma_r = \left(\frac{\sigma_Y}{B-1} + \sigma_R\right)\left(\frac{r}{R}\right)^{B-1} - \frac{\sigma_R}{B-1} \tag{14}$$

and

$$\begin{aligned} \sigma_\varphi &= \left(\frac{\sigma_Y}{B-1} + \sigma_R\right)\left(\frac{r}{R}\right)^{B-1} B - \frac{\sigma_Y}{B-1} \\ \sigma_a &= \frac{\sigma_r + \sigma_\varphi}{2}. \end{aligned} \tag{15}$$

If the radius $r = \varrho$ denotes the limit of the plastic zone, the above equations are valid for the zone $r \leq \varrho$.

The elastic zone around the plastic one can be regarded as a zone surrounding an excavation of radius ϱ supported by a homogeneous load of the intensity σ_ϱ. At $r = \varrho$ the stresses can be calculated both from the equations of the elastic zone and from those of the plastic one. The axial stress at $r = \varrho$ becomes

$$\sigma_a = \frac{\sigma_r + \sigma_\varphi}{2} = H\gamma = \frac{\sigma_\varrho + \sigma_\varrho B + \sigma_Y}{2} = \frac{\sigma_\varrho (1 + B) + \sigma_Y}{2}. \tag{16}$$

Hence

$$\sigma_\varrho = \frac{2H\gamma - \sigma_Y}{B + 1} = \left(\frac{\sigma_Y}{B - 1} + \sigma_R\right)\left(\frac{\varrho}{R}\right)^{B-1} - \frac{\sigma_Y}{B - 1}. \tag{17}$$

From this equation the radius of the plastic rock zone is

$$\varrho = R\left[2\,\frac{H\gamma\,(B - 1) + \sigma_Y}{\sigma_R\,(B^2 - 1) + (B + 1)\,\sigma_Y}\right]^{\frac{1}{B-1}}. \tag{18}$$

If we have for the reaction of support $\sigma_R = 0$, the radius becomes

$$\varrho = R\left[2\,\frac{H\gamma\,(B - 1) + \sigma_Y}{(B + 1)\,\sigma_Y}\right]^{\frac{1}{B-1}}. \tag{19}$$

No plastic zone is formed if $\varrho = R$, i.e. if the value of the reaction of support is

$$\sigma_R = 2\,\frac{H\gamma\,(B - 1) + \sigma_Y}{B^2 - 1} - \frac{\sigma_Y}{B - 1}. \tag{20}$$

The elastic stresses beyond the plastic zone, i.e. for $(r \geq \varrho)$ become

$$\begin{aligned} \sigma_r &= H\gamma\left[1 - \left(\frac{\varrho}{r}\right)^2\right] + \frac{2H\gamma - \sigma_Y}{B + 1}\left(\frac{\varrho}{r}\right)^2 \\ \sigma_\varphi &= H\gamma\left[1 + \left(\frac{\varrho}{r}\right)^2\right] - \frac{2H\gamma - \sigma_Y}{B + 1}\left(\frac{\varrho}{r}\right)^2 \\ \sigma_a &= H\gamma. \end{aligned} \tag{21}$$

In rocks of small strength, i.e. a small yield point and small angle of internal friction, a very large reaction of support is required to prevent the formation of the plastic zone. Taking, e.g. $\sigma_Y = 2$ MN/m² and $B = 2$ we obtain $\varrho_R = 0.67\,H\gamma - 66.7$. If $H\gamma = 10$ MN/m² which approximately corresponds to

a depth of $H = 400$ m, a reaction of support $\sigma_R = 6$ MN/m² would have been required to avoid the formation of the plastic zone. Since the supports of the drifts are generally able to exert a reaction of support around $\sigma_R \cong 0.5 - 1$ MN/m² at most, the plastic rock zone is almost always present in rocks of small strength. It should be emphasized, however, that even if there were a plastic zone around the drift far away from the road head this does not necessarily imply that the rock zone in front of the road head is in a plastic state as well, since this zone is in a more favourable state of stress.

The knowledge of these relationships is of utmost importance in order to characterize the mechanical behaviour of the rock zone in front of the road head, since the mechanical fields (stress, deformation and displacement) in this zone are not independent of the fields around the drift.

2. Mechanical state in the rock zone in front of the road head

The rock zone in front of the road head can be considered as composed of two parts (Fig. 2). The first is the rock support of a drift of circular cross

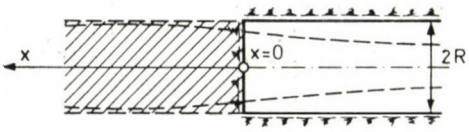

Fig. 2. Rock cylinder in front of the road head

section if $r \leq R$, the second is the rock around a supported drift of circular cross section at $r \geq R$. The thickness of the support is $v = R$, its Young's modulus being $E_s = E$. The radial stress on the mantle of the rock cylinder is

$$\sigma_R(x) = \frac{u_R(x)\,E}{R}. \tag{22}$$

The radial displacement u_R of the mantle diminishes with the distance x from the face.

The radial deformation of the rock cylinder in front of the road head can be written as

$$\varepsilon_r = \frac{u_R}{R}. \tag{23}$$

The tangential deformation is

$$\varepsilon_\varphi = \frac{2R\pi - 2(R - u_R)\pi}{2R\pi} = \frac{u_R}{R} = \varepsilon_r. \tag{24}$$

The deformations can also be calculated by means of the generalized Hook's law, from the deformation stresses:

$$\varepsilon_r = \frac{1}{E}\left(\Delta\sigma_r - \frac{\Delta\sigma_\varphi + \Delta\sigma_a}{m}\right)$$
$$\varepsilon_\varphi = \frac{1}{E}\left(\Delta\sigma_\varphi - \frac{\Delta\sigma_r + \Delta\sigma_a}{m}\right) \tag{25}$$
$$\varepsilon_a = \frac{1}{E}\left(\Delta\sigma_a - \frac{\Delta\sigma_r + \Delta\sigma_\varphi}{m}\right).$$

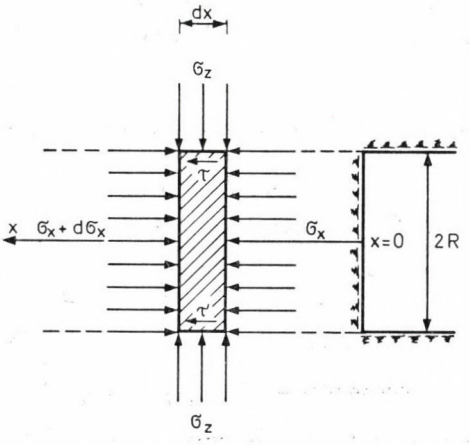

Fig. 3. Stresses acting on a volume element in front of the road head

Because of $\varepsilon_r = \varepsilon_\varphi$, $\Delta\sigma_r = \Delta\sigma_\varphi$ must hold, thus

$$\Delta\sigma_a = E\varepsilon_a + \frac{2\Delta\sigma_r}{m}. \tag{26}$$

The equilibrium of a volume element of thickness dx, as illustrated in Fig. 3, implies that the following equation holds:

$$\sigma_a R^2\pi - (\sigma_a + \mathrm{d}\sigma_a)\, R^2\pi - \tau_{a,r}\, 2R\pi\, \mathrm{d}x = 0\,. \tag{27}$$

Hence

$$\frac{\mathrm{d}\sigma_a}{\mathrm{d}x} = \frac{2\tau_{a,r}}{R}. \tag{28}$$

The shear stress can be written as $\tau_{a,r} = -A\Delta\sigma_a$ thus we obtain the linear differential equation

$$\frac{\mathrm{d}\sigma_a}{\mathrm{d}x} + \frac{2A}{R}\sigma_a = \frac{2AH\gamma}{R} \tag{29}$$

whose solution is

$$\sigma_a = H\gamma\left(1 - e^{-\frac{2A}{R}x}\right) \tag{30}$$

subject to the initial conditions $x = 0$ and $\sigma_a = 0$. Using this solution, we obtain for the rock cylinder in front of the face that

$$\Delta\sigma_a = -H\gamma\, e^{-\frac{2A}{R}x}\,; \quad \tau_{a,r} = AH\gamma\, e^{-\frac{2A}{R}x}\,. \tag{31}$$

In order to achieve better approximations in the following discussion we shall drop the assumption $m = 2$ and will make use of the relationships

$$\begin{aligned} \sigma_a &= \frac{H\gamma}{m-1}\left(1 - e^{-\frac{2A}{R}x}\right) \\ \Delta\sigma_a &= -\frac{H\gamma}{m-1}\, e^{-\frac{2A}{R}x} \\ \tau_{a,r} &= A\,\frac{H\gamma}{m-1}\, e^{-\frac{2A}{R}x}\,. \end{aligned} \tag{32}$$

Let us turn now to the radial stress. According to our previous results

$$\Delta\sigma_r = \frac{mE\varepsilon_r + \Delta\sigma_a}{m-1} = \frac{1}{m-1}\left[\frac{mEu_R(x)}{R} + \Delta\sigma_a\right]. \tag{33}$$

The radial displacement $u_R(x)$ of the mantle of the rock cylinder in front of the road head proceeds under very similar conditions as the subsidences of the overburden layers above worked areas.

For this reason we can write (by making use of [13]) that

$$\begin{aligned} u_R(x) &= u_R^*\left(0.362\, e^{-3.1\frac{\sqrt{m-1}}{h}x} + 0.138\, e^{-8.1\frac{\sqrt{m-1}}{h}x}\right) \\ u_R(x) &= u_R^* U(x);\ x \geq 0 \end{aligned} \tag{34}$$

with h being the height of the rock zone above the road head still under deformation and displacement,

u_R^* the radial displacement of the surface of the drift far away from the road head.

According to Section 1, this displacement is of the form $u_R^* = H\gamma\, CR^2/E$, thus

$$\Delta\sigma_r = \frac{1}{m-1}\left[mH\gamma\, CRU(x) + \Delta\sigma_a\right]. \tag{35}$$

The parameter C characterizes the effectiveness of the support. A support of smaller effectiveness exerts such an effect on the transferred stress as if the drift radius were greater. Consequently, in case of a great drift radius and a support of small effectiveness, the transferred stress is especially high. According to the previous considerations, the parameter C depends on time, i.e., implicitly, on the speed of drifting as well. In case of a quicker advance C becomes smaller.

The dimensions of the moving rock zone above the drift far away from the road head strongly depends on whether or not there has developed a plastic zone around the drift. Nearer to the road head the condition of plasticity becomes ever more difficult to satisfy. Inside the rock cylinder, in front of the road head but far away from it, this condition is only exceptionally met because of the triaxial state of stress. Therefore, $h = 4\,R$ holds for the rock cylinder in front of the road head.

Consequently,

$$U(x) = 0.362\, e^{-0.8\frac{\sqrt{m-1}}{R}x} + 0.138\, e^{-2.0\frac{\sqrt{m-1}}{R}x}\,. \tag{36}$$

In Eq. (36) the second term on the right-hand side diminishes much more apidly than the first one for increasing values of x, thus, approximately

$$U(x) = 0.5\, e^{-\frac{\sqrt{m-1}}{R}x} \tag{37}$$

i.e.

$$\Delta\sigma_r = \frac{H\gamma}{m-1}\left(0.5mCR\, e^{-\frac{\sqrt{m-1}}{R}x} - \frac{e^{-\frac{2A}{R}x}}{m-1}\right). \tag{38}$$

Since $\Delta\sigma_r \geq 0$ must hold,

$$A = 0.5\sqrt{m-1} \tag{39}$$

yielding

$$\begin{aligned} \Delta\sigma_r &= \frac{H\gamma}{m-1}\, e^{-\frac{\sqrt{m-1}}{R}x}\left(0.5mCR - \frac{1}{m-1}\right) > 0 \\ \sigma_r &= H\gamma\left\{1 + \left[\frac{0.5mCR}{m-1} - \frac{1}{(m-1)^2}\right] e^{-\frac{\sqrt{m-1}}{R}x}\right\} \geq H\gamma\,. \end{aligned} \tag{40}$$

The condition $\sigma_r \geq H\gamma$ has to be satisfied in case of $m = 2$, too, from which $CR > 1$ follows.

All the equations derived above relate to the elastic state. Let us now investigate the conditions bringing about plastic state. The axis of the drift

where $\tau_{a,r} = 0$ holds is in a plastic state if the condition

$$\sigma_r - B\sigma_a \geq \sigma_Y \tag{41}$$

is valid, i.e. if

$$\frac{e^{-\frac{\sqrt{m-1}}{R}x}}{\sqrt{m-1}}\left[0.5mCR + B - \frac{1}{m-1}\right] - \frac{B}{m-1} + 1 \geq \frac{\sigma_Y}{H\gamma}. \tag{42}$$

If the plastic state has already developed at the face, it will extend up to a distance

$$x_0 = \frac{R}{\sqrt{m-1}} \ln \frac{0.5mCR + B - \frac{B}{m-1}}{(m-1)\left(\frac{\sigma_Y}{H\gamma} + \frac{B}{m-1} - 1\right)}. \tag{43}$$

In the plastic rock zone in front of the road head the stresses can be expressed as follows ($x \geq x_0$)

$$\begin{aligned} \sigma_a &= \frac{H\gamma}{m-1}\left(1 - e^{-\frac{\sqrt{m-1}}{R}x}\right) \\ \sigma_r &= H\gamma\left[\frac{\sigma_Y}{H\gamma} + \frac{B}{m-1}\left(1 - e^{-\frac{m-1}{R}x}\right)\right]. \end{aligned} \tag{44}$$

The depth of the plastic rock zone in front of the face is illustrated in Figs 4—7 for various parameters. As illustrated by the Figures, the depth

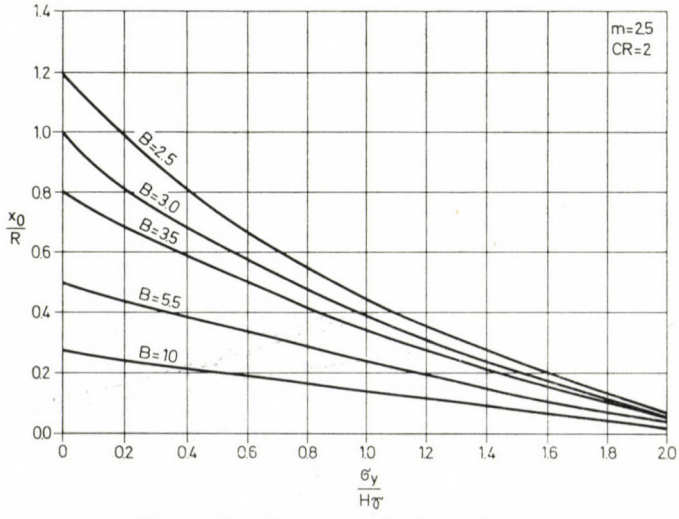

Fig. 4. Depth of the plastic rock zone

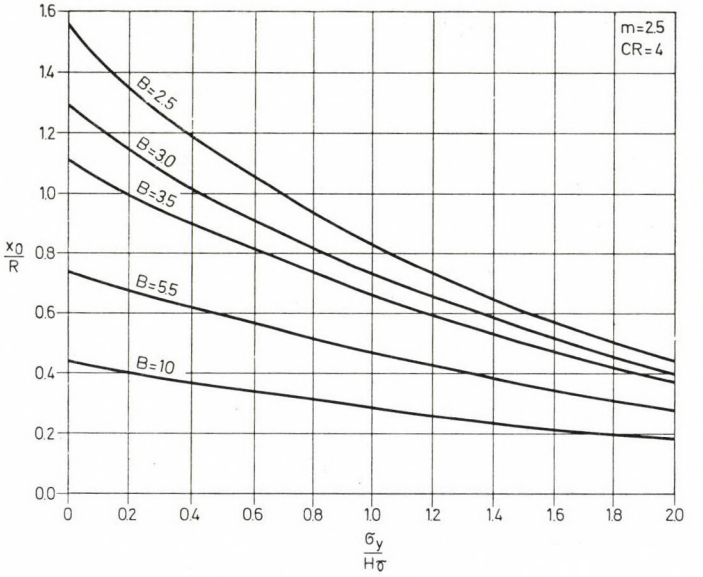

Fig. 5. Depth of the plastic rock zone

of the plastic rock zone sharply decreases with increasing strength. This is due to the fact that the yield strength and Brinke's number of rocks of greater strength are also greater. It is further seen from the Figures that the depth of the plastic zone at the face of the drift increases with the value of *CR*. This means that the greater the radius of the drift or the smaller the effectiveness of the built in support, the greater load will act on the rock cylinder n front of the road head.

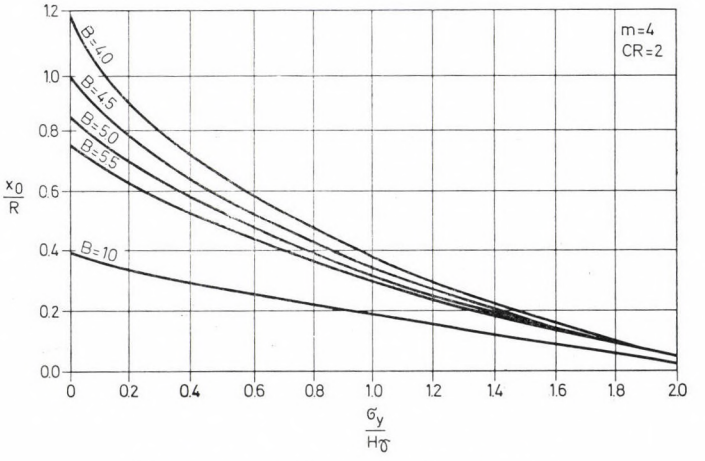

Fig. 6. Depth of the plastic rock zone

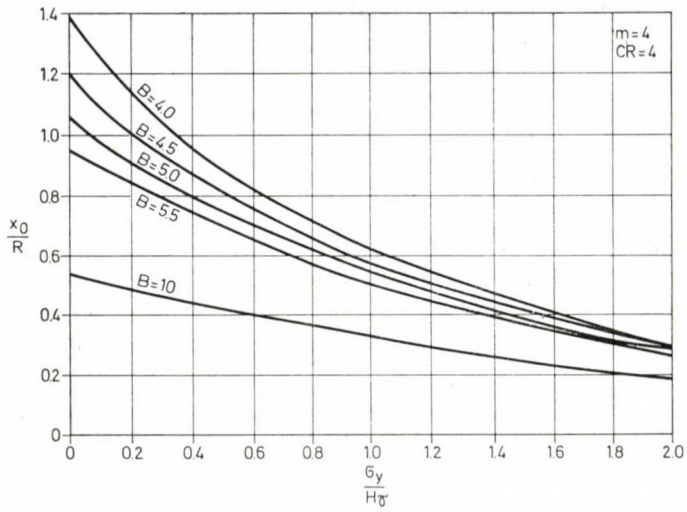

Fig. 7. Depth of the plastic rock zone

3. Volume change in the rock zone in front of the drift face

In the first part of our study we emphasized the importance of the sign of the volumetric change in front of the rock face from the standpoint of outburst danger, i.e. whether the volume of the rock decreases or increases.

The specific volume change along the axis of the drift is

$$\frac{\Delta V}{V} = \varepsilon_r + \varepsilon_\varphi + \varepsilon_a \,. \tag{45}$$

Here, $\Delta V/V > 0$ means a volume reduction, $\Delta V/V < 0$ a volume increase. Using the equations of Section 2

$$\frac{\Delta V}{V} = 2\varepsilon_r + \varepsilon_a = \frac{m-2}{mE}\,(2\Delta\sigma_r + \Delta\sigma_a)\,. \tag{46}$$

Making use of

$$\Delta\sigma_r = -\left(0.5mCR - \frac{1}{m-1}\right)\Delta\sigma_a \tag{47}$$

we obtain

$$\frac{\Delta V}{V} = \Delta\sigma_r \frac{m-2}{mE}\left[2 - \frac{m-1}{0.5m(m-1)CR - 1}\right]. \tag{48}$$

Since $CR > 1$ and $\Delta\sigma_r > 0$ hold in real cases (for $m > 2$), we have $\Delta V/V > 0$, i.e. there is always a volume reduction in front of the road head. The smaller

the Young's modulus and the effectiveness of the support built in or the greater the radius of the drift and the Poisson's ratio, the greater will be the volume increase.

It is a common experience that the frequency of outbursts increases with the cross section of the drift [5], [6]. This is in accordance with our result that the specific volume reduction, i.e. the danger of outburst as well, increases with the radius of the dirft.

In the plastic rock zone in front of the face ($x \leqq x_0$) the specific volume change is zero. At the place of the plastic rock zone, however, the rocks had already been in the elastic state (up to the time the drift reached there) and the corresponding volume change has already taken place. Consequently, the plastic rock zone does not play any role as regards the sign of volume change (increase or decrease).

4. Stresses in the rock zone in front of the road head in the presence of pore gas pressure

In the presence of pore gas pressure, the so-called effective stress σ' in the solid structure has to be distinguished from the pore gas pressure or neutral stress p. The resultant of these two stresses is the total stress σ_t.

The equilibrium of a volume element of thickness dx in the investigated rock zone can be expressed as (Fig. 8):

$$\Delta\sigma'_a R^2\pi - [\Delta\sigma'_a + \mathrm{d}(\Delta\sigma'_t)]\, R^2\pi + [\Delta p + \mathrm{d}(\Delta p)]\, R^2\pi - \Delta p R^2\pi + \tau'_{a,r} 2R\pi\, \mathrm{d}x = 0. \tag{49}$$

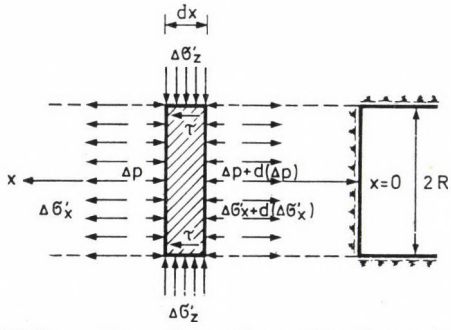

Fig. 8. Equilibrium of a volume element in front of the road head

Hence

$$\frac{\mathrm{d}(\Delta\sigma'_t)}{\mathrm{d}x} - \frac{\mathrm{d}(\Delta p)}{\mathrm{d}x} = \frac{2\tau'_{a,r}}{R}\,. \tag{50}$$

The change of the pore gas pressure Δp due to excavation is approximately proportional to the specific volume change of the rock. The specific volume

change, however, is linearly proportional to the axial deformational stress $\Delta\sigma'_a$, i.e. the change of pore gas pressure can be written as $\Delta p = -D\Delta\sigma'_a$. This yields the differential equation

$$(D+1)\frac{\mathrm{d}(\Delta\sigma'_a)}{\mathrm{d}x} = \frac{2\tau'_{a,r}}{R} = -\frac{2A\Delta\sigma'_a}{R} \tag{51}$$

having the general solution

$$\Delta\sigma'_a = F \cdot e^{-\frac{2A}{R(D+1)}x}. \tag{52}$$

Since for $x = 0$

$$\Delta\sigma'_a = -\frac{H\gamma + p_0}{m-1} \tag{53}$$

must hold, we have

$$F = -\frac{H\gamma - p_0}{m-1} \tag{54}$$

i.e.

$$\Delta\sigma'_a = -\frac{H\gamma - p_0}{m-1} e^{-\frac{\sqrt{m-1}}{R(D+1)}x} \tag{55}$$

with p_0 being pore gas pressure before the excavation. By Eq. (55) the stresses in the solid structure of the rock can be expressed in the secondary state as:

$$\begin{aligned}
\sigma'_a &= \frac{H\gamma - p_0}{m-1}\left(1 - e^{-\frac{\sqrt{m-1}}{R(D+1)}x}\right) \\
\tau'_{a,r} &= 0.5\,\frac{\sqrt{m-1}}{m-1}(H\gamma - p_0)\,e^{-\frac{\sqrt{m-1}}{R(D+1)}x} \\
\sigma'_r &= (H\gamma - p_0)\left\{1 + \left[\frac{0.5mCR}{m-1} - \frac{1}{(m-1)^2}\right] e^{-\frac{\sqrt{m-1}}{R(D+1)}x}\right.
\end{aligned} \tag{56}$$

Of course, we still have to determine the parameter D. For a small specific volume change the pore gas pressure of methane is, according to [12],

$$p = 1.26\,p_0 \frac{1+e_0}{e_0}\frac{\Delta V}{V}; \quad \frac{\Delta V}{V} < \frac{e_0}{1+e_0} \tag{57}$$

e_0 being the initial void ratio of the rock (belonging to pore gas pressure p_0).

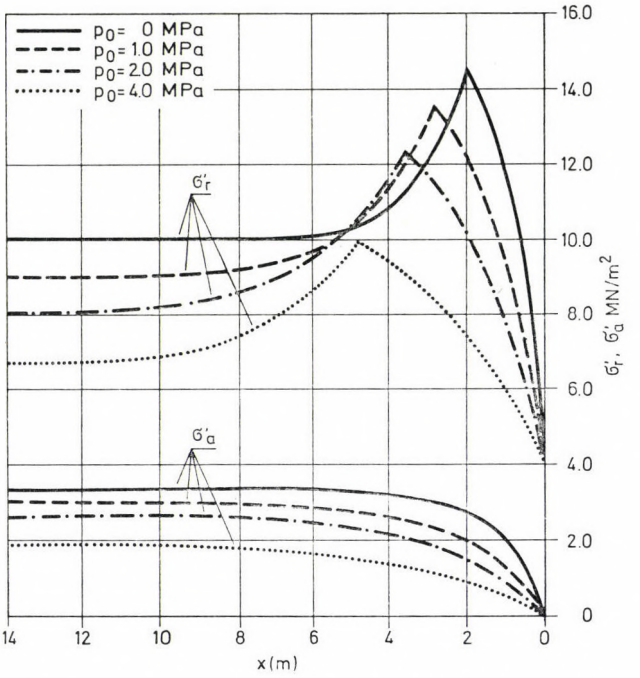

Fig. 9. Elastic and plastic stresses in front of the drift face

Further,

$$\frac{\Delta V}{V} = -\Delta\sigma'_a \frac{m-2}{mE}\left[2\left(0.5\,mCR - \frac{1}{m-1}\right) - 1\right] \tag{58}$$

yielding

$$D = 1.26 p_0 \frac{1+e_0}{e_0}\frac{m-2}{mE}\left[2\left(0.5\,mCR - \frac{1}{m-1}\right) - 1\right]. \tag{59}$$

Consider now the variation of stresses, for the values $m = 4$, $B = 4$, $E = 400$ MN/m², $e_0 = 0.05$, $H = 400$ m, $\gamma = 25$ kN/m³, $R = 2\,m$ and $CR = 4$. With these values, we obtain $D = 0.047\,p_0$.

Using these values, the elastic stresses become

$$\sigma'_a = \frac{100 - p_0}{3}\left(1 - e^{-\frac{0.866}{0.05p_0+1}x}\right)$$

$$\sigma'_r = (H\gamma - p_0)(1 + 2.556e^{-\frac{0.866}{0.05p_0+1}x}) \tag{60}$$

$$p = p_0 - D\Delta\sigma'_a = p_0\left[1 + 0.016\,(100 - p_0)\,e^{-\frac{0.866}{0.05p_0+1}x}\right]. \tag{61}$$

The stresses as a function of distance x are plotted in Fig. 9 for the parameter values $p_0 = 0, 1, 2$ and 4 MPa. As seen from the Figure, the greater the pore gas pressure, the greater the zone of stress changes in front of the drift face.

The stresses in the elastic rock zone are

$$\sigma'_a = \frac{H\gamma - p_0}{m-1}\left(1 - e^{-\frac{\sqrt{m-1}}{R(D+1)}x}\right)$$
$$\sigma'_r = (H\gamma - p_0)\left[\frac{\sigma_Y}{H\gamma - p_0} + \frac{B}{m-1}\left(1 - e^{-\frac{\sqrt{m-1}}{R(D+1)}x}\right)\right]. \tag{62}$$

The depth of the plastic rock zone is

$$x_0 = \frac{R(D+1)}{\sqrt{m-1}} \ln \frac{0.5mCR + B - \frac{1}{m-1}}{(m-1)\left(\frac{\sigma_Y}{H - p_0} + \frac{B}{m-1} - 1\right)}. \tag{63}$$

With our previous data, and $\sigma_Y = 4$ MN/m^2, the stresses of the plastic rock zone can be expressed as

$$\sigma'_a = \frac{100 - p_0}{3}\left(1 - e^{-\frac{0.866}{0.05p_0+1}x}\right) \tag{64}$$

$$\sigma'_r = (100 - p_0)\left[\frac{40}{100 - p_0} + 1.33\left(1 - e^{-\frac{0.866}{0.05p_0+1}x}\right)\right] \tag{65}$$
$$p = p_0 + D\Delta\sigma'_a(x_0).$$

These stresses are also illustrated in Fig. 9.

5. Deterioration of the rock zone in front of the road head in the presence of pore gas pressure

Pore gas pressure decreases the strength of the rock. The equation of the fracture limit line can be written [10] as

$$\tau = \frac{\sigma_C}{2\sqrt{B}}\left[1 + \frac{B-1}{\sigma_C}(\sigma_t - p)\right] \tag{66}$$

where σ_C is the uniaxial compressive strength without pore gas pressure, and p is pore gas pressure.

The uniaxial compressive strength becomes, in the presence of pore gas pressure [10]:

$$\sigma'_C = \sigma_C - (B - 1)\, p\,. \tag{67}$$

In the drift axis, accepting the linear fracture limit curve deterioration comes about if the equality

$$\sigma'_r = \sigma_C - (B - 1)\, p + B\sigma'_a \tag{68}$$

holds. From this equation the uniaxial compressive strength required to prevent deterioration can be expressed as:

$$\sigma_{C_{\text{req.}}} = \sigma'_r - B\sigma'_a + (B - 1)\, p$$

$$\sigma_{C_{\text{req.}}} = (H\gamma - p_0)\left[\frac{e^{-\frac{\sqrt{m-1}}{R(D+1)}x}}{m-1}\left(0.5mCR - \frac{1}{m-1} + B\right) + 1 - \frac{B}{m-1}\right] + \\ + (B-1)p_0\,. \tag{69}$$

This relationship shows that the greater $H\gamma$, the greater the compressive strength required to prevent rock deterioration. This explains why does the frequency of outbursts increase with depth, for the greater the compressive strength required to prevent deterioration, the more frequently would it occur that the strength is less than this limit.

A further lesson from the above equation is that the greater the drift radius, the greater compressive strength is required to prevent rock deterioration. This explains the observation that the frequency of outbursts increases with increasing drift cross sections.

The compressive strength required to prevent deterioration is plotted against a dimensionless distance measured from the road head, for various parameters, in Figs 10—13. The compressive strength required to prevent deterioration quickly falls to zero with the distance from the face if the pore gas pressure is small. When zero compressive strength is required this means the internal friction of the rock alone is sufficient to prevent deterioration. For greater pore gas pressures the compressive strength required to prevent deterioration does not tend to zero with the distance from the face. These cases are very unfavourable from the point of outburst danger. If the layer strength does not change considerably and is smaller at the face than the compressive strength required to prevent deterioration, rock deterioration comes about at the face. This, however, does not indicate an outburst, for the pore gas and the evaporating adsorbed gas can easily leave the face thus the pore gas pressure cannot increase. If, however, the deterioration has penetrated to a greater depth behind the face, there is a possibility for the pore gas

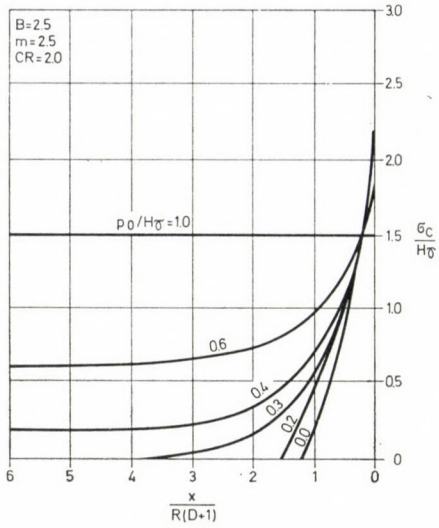

Fig. 10. Compressive strength required to prevent deterioration

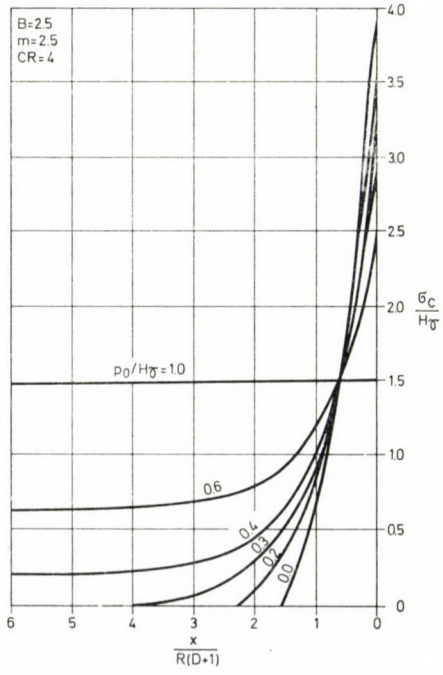

Fig. 11. Compressive strength required to prevent deterioration

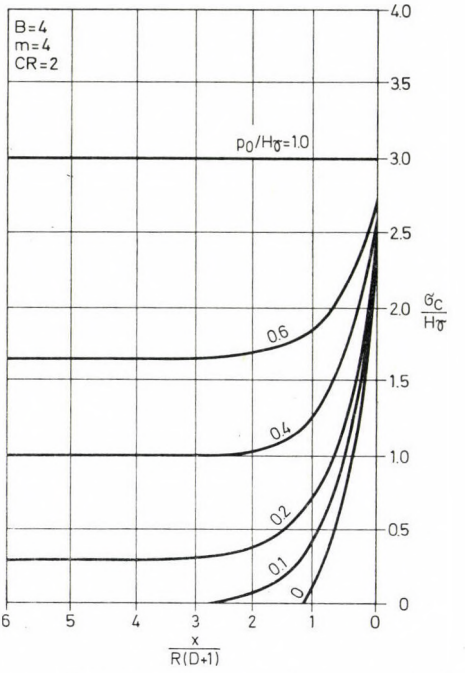

Fig. 12. Compressive strength required to prevent deterioration

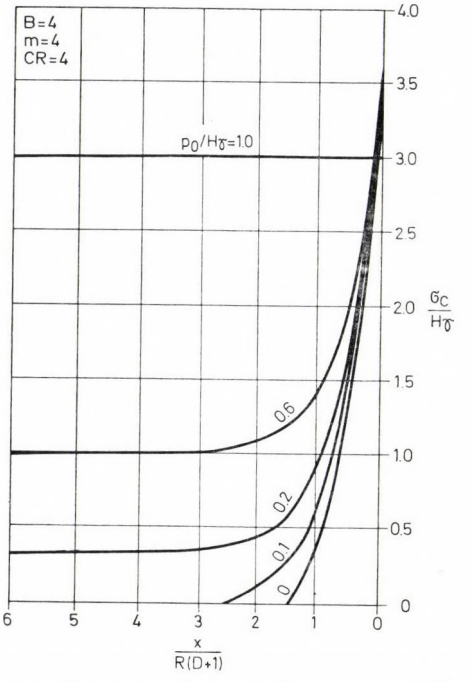

Fig. 13. Compressive strength required to prevent deterioration

pressure to increase, the deterioration process gets accelerated and an outburst ensues. The situation is especially dangerous if the coal strength more quickly decreases with the distance from the face than the compressive strength required to prevent deterioration. In such cases, deterioration comes about farther from the face. Here, the pore gas pressure increases but the intact rock mass of the face does not allow the gas to escape so that at a certain point of the process the gas pressure will suddenly throw out the face from its original place. This situation can be observed near geological distrubances (fault zones, foldings etc.).

It should be noted that the pore gas pressures greater than $p_0 = (0.4 - 0.5)\, H\gamma$ from among the values $(0 - 1.0)\, H\gamma$ in Figs 10—13 have no practical importance. Experience shows, namely, that pore gas pressure ranges within 0—5 MPa, in many cases only between 0.5—1 MPa, while values around $H\gamma \simeq 10$ MPa should be regarded as general.

6. Intensity of outbursts

The intensity of outbursts is characterized by the weight of the loose rock thrown out. The most frequent intensity value, from among the more than ten thousand outbursts having been recorded up to now all over the world, was between 1 and 20 MN [6]. The intensity of the greatest known outburst (Donets basin, July 1969) was 140 MN coal. As a check of our previous results, let us try to explain how is it possible that vast amount of solid material being thrown out.

The outburst starts with the deterioration of the rock cylinder in front of the road head. Deterioration penetrates in front of the road head into a depth αR, with a maximum of $\alpha = 4$. The volume of the deteriorated rock cylinder

$$V_1 = \alpha R^3 \pi . \tag{70}$$

With $\alpha = 4$ and $R = 2$ m the volume becomes $V_1 = 100$ m^3. This gives the weight $G_1 = 1.3$ MN for coal and $G_1 = 2.5$ MN for waste. This order of magnitude is characteristic for outbursts of smaller intensity. In some cases the outburst ends with the deterioration of the rock cylinder in front of the road head. However, it is only the beginning in some other cases. With the outthrow of the rock cylinder in front of road head, a new, unsupported free surface and road head are created in the rock. The unsupported rock mantle falls in and heaves while the rock mass is thrown out, and the outstreaming gas forces this debris into the drift. Deterioration penetrates radially up to the distance βR. Thus the volume of the deteriorated and thrown out material becomes

$$V = \alpha \beta^2 R^3 \pi . \tag{71}$$

Table I

Amount of material thrown out by outbursts

β	V m^3	G_{coal} MN	G_{waste} MN	$G_{average}$ MN
1	100	1.3	2.5	1.9
2	400	5.2	10.0	7.6
3	900	11.7	22.5	17.1
4	1600	20.8	40.0	30.4
7	4900	63.7	122.5	93.1

With $\alpha = 4$ and $R = 2$ m the amounts of the thrown-out material are shown in Table I for various values of β. The values in Table I indicate only orders of magnitude since the values of α, β and R may be different. To find β, recall that the attrition of the unsupported rock cylinder proceeds radially until the excavation is filled up by the rock due to the effect of loosening, i.e.

$$k'[(\beta R)^2 - R^2]\,\pi = (\beta R)^2\,\pi\,. \tag{72}$$

Hence

$$\beta = \sqrt{\frac{k'}{k'-1}} \tag{73}$$

where k' is the coefficient of loosening.

The value of k' varies within wide boundaries for rocks of different quality. It is generally 1.02—1.7 for gas-rich coals. For rocks of small strength it is smaller, for rocks of greater strength greater. Using the extreme values of the coefficient of loosening we obtain $\beta = 1.6 - 7.1$.

The values of intensity obtained by calculation coincide with the order of magnitudes found by experience. According to the above calculation the intensity of outbursts increases with the third power of the drift radius. Also, since experience proves that the intensity rapidly increases with the cross section of the drift, we have a further check of our theory.

In reality, of course, irregular vents are formed in various directions around the face because of the heterogeneity of the surrounding rock body. It is worth while to sketch the greatest outburst over the world. On the 710 m level of the Gagarin mine (Donets basin) a provoking explosion was carried out while drifting the main cross-cut in front of the 1 m thick Mazurka layer inclined at 68°. The provoking explosion triggered the outburst of 140 MN coal and 250,000 m³ methane. After the outburst the vent of outburst was investigated and it was found that the vent ascended almost to the upper

level (Fig. 14). The explanation is that the deterioration and the out-throw of the rock cylinder in front of the road head produced an unsupported free surface. Because of the transferred pressure perpendicular to the plane of the layer, the condition of deterioration was satisfied in front of the free surface while volume reduction took place. Th chain-reaction-like deterioration process quickly spread upwards and sidewards in the layer. Deterioration did not proceed downwards since because of the self-weight a more favourable state of stress developed near the free surface. The deterioration abruptly stopped near the cross-cut at the upper level. This was due to the fact that in the rock zone around the upper cross-cut a volume increase took place and the gas had been drained.

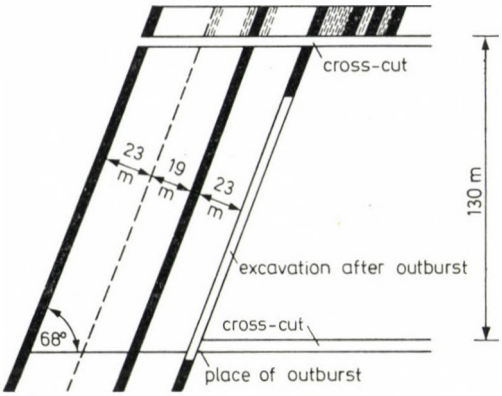

Fig. 14. Display of an outburst (Gagarin mine, 1969)

7. General conclusions

The results reported in this study form a sequel to our previous investigations [10, 11, 12]. Some of the further conclusions about the outbursts, again in agreement with experience, can be summarized as follows:

— Outbursts occur more frequently at road heads than in workings because the basic condition of outbursts is always satisfied in front of the road head. This condition requires that rock volume should decrease. This condition is not met in workings if the Poisson's ratio is small, $m < 2.33$, i.e. if the rock strength is too small. Therefore, no outbursts come about in workings in such cases.

— The frequency of outbursts increases with depth because a steadily increasing rock strength would have been required to prevent outbursts at greater depths. Thus, the rock fails more frequently to produce such a strength.

— The frequency of outbursts increases with drift cross section because an increasing rock strength would have been required to prevent outbursts for greater drift radii. Therefore, the rock generally does not have this strength.

— The intensity of outbursts increases with drift cross section because the volume of the rock zone exposed to the transferred pressure in front of the face increases with the drift radius.

— The outburst intensity is greatly influenced by the actual state of the surrounding rock at the moment of the outburst. If the layer is penetrated, the intensity of outburst is generally much higher than in drifts within the boundaries of the layer, because a much greater rock zone is radially deteriorated.

— The outburst danger is greater if there is a mixed section consisting of coal and stronger rocks of greater Young's moduli in front of the road head. In this case, the coal suffers a stronger compression due to the interactions. In consequence, pore gas pressure increases more sharply and this reduces strength at an increased rate. This is the case near intrusions.

— The outburst danger is also affected by the effectiveness of the support applied in the drift. The smaller the effectiveness of the support (i.e. the greater the contraction of the cross section allowed), the greater load will act on the rock zone in front of the face. Thus, the condition of deterioration is more easily met, the danger of outburst becomes greater. Experience also shows that considerably fewer outbursts occur if closed-arch supports are used than in case of open-arch supports.

— The time factor, or the drifting speed also influence the outburst danger. The slower the drifting, the longer the time available for deformations and volume reduction in the rock zone in front of the face and, similarly, for the pore gas pressure to increase and for the rock strength to decrease. A slow drifting is a factor increasing outburst danger. A face staying untouched for several days is especially dangerous, as proved by the experience that quite a few outbursts have occurred after holidays or after the waiting time of provoking explosions.

REFERENCES

1. Richter, R.: Körszelvények deformációi (Deformations of circular sections). *Műszaki Élet Tatabányán*, 1963, No. 2. 1—40.
2. Asszonyi, Cs.—Richter, R.: Bevezetés a kőzetmechanika reológiai elméletébe (Introduction into the Rheological Theory of Rock Mechanics). NIMTK (Postgraduate Centre of the Ministry of Heavy Industry), 1974.
3. Richter, R.: Képlékeny alapjelenségek a kőzetmechanikában (Plastic Phenomena in Rock Mechanics). University Text-Book. Miskolc, 1968.

4. Hodot, V. V.: Unexpected Coal and Gas Outbursts. (In Russian) Moscow, 1961.
5. Biró, J.—Pusztafalvai, J.—Szirtes, A.: Bányaterek méreteinek befolyása a gázkitörések intenzitására a mecseki szénbányászatban (The effect of mining excavations on the intensity of gas outbursts in the Mecsek Coal Mines). *Bányászati és Kohászati Lapok, Bányászat*, 1980, No. 6. 402—405.
6. Szirtes, L.: Szén- és gázkitörések leküzdése (Combat Against Coal and Gas Outbursts). Műszaki Könyvkiadó, Budapest, 1971.
7. Kovács, F.: A gázkitörések gyakoriságának változása a művelési mélység függvényében (Frequency of outbursts as a function of working depth). *Bányászati és Kohászati Lapok, Bányászat*, 1973, No. 5, 318—324.
8. Kovács, F.: A gázkitörések intenzitásával kapcsolatos néhány törvényszerűség (Some characteristics concerning the intensity of gas outbursts). *Bányászati és Kohászati Lapok, Bányászat*, 1974, No. 2, 96—106.
9. Kovács, F.: A gázkitörésveszély várható mértékének meghatározása és gazdasági kihatásainak értékelése (Determination of the Degree of the Gas Outburst Danger and Evaluation of its Economic Effect). Doctor's Thesis. Hungarian Academy of Sciences. Budapest, 1975.
10. Somosvári, Zs.: Investigation of the deterioration of the rock-gas system to clarify the cause of rock and gas outbursts. *Acta Geod., Geoph. Mont. Hung.*, 15 (1980), 257—269.
11. Somosvári, Zs.: Investigation of the load assumption of rock-gas systems, aiming at the detection of the causes of rock and gas outbursts. *Acta Geod., Geoph. Mont. Hung.*, 15 (1980), 271—294.
12. Somosvári, Zs.: Investigation of the zone in front of the face of rock-gas systems to determine the origin of rock and gas outbursts. *Acta Geod., Geoph. Mont. Hung.* (in press)
13. Somosvári, Zs.: Aláfejtett (közel szintes településű) fedőkőzetek mozgásmezejének meghatározása (Determination of the Displacement Field of (Pseudohorizontal) Overburden Layers Above Workings). Ph. D. Thesis. Miskolc, 1973.

ИССЛЕДОВАНИЯ ОБЛАСТИ ПЕРЕД ТОРЦА ВЫРАБОТКИ В СИСТЕМЕ ПОРОДА-ГАЗ ДЛЯ ВЫЯСНЕНИЯ ПРИЧИН ВЫБРОСОВ ГАЗА И ПОРОД

Ж. ШОМОШВАРИ

РЕЗЮМЕ

На основе исследований взаимодействий системы порода-газ нами устанавливается, что выбросы на торце выработки происходят намного чаще чем на забоях потому, что в области перед забоем всегда выполняется основное условие выброса — уменьшение объема породы. На забоях это условие при небольших чисел Пуассона ($M < 2{,}33$) не выполняется.

Выводим значения прочности залежи (сопротивление давлению в одном назправлении), необходимые во избежание выброса, в зависимости от первоначального давления газа пор, вертикального первичного натяжения, числа Пуассона и угла внутреннего трения залежи. Этим соотношением объясняется в частности тот опыт, почему увеличивается частота выбросов с увеличением глубины и поперечного сечения выработки, а также тот факт, что в отдельных случаях выбросы происходят при совсем малых значениях давления газапор (2—4 кп/см^2), а в других случаях не происходят и при давении, значительно превышающем этого значения. Упомянутым выше соотношением объясняется и тот опыт, что выбросы происходят как правило в залежах с маленькой прочностью, а в отдельных случаях взрывы происходят и в залежах с большей прочностью на сжатие.

При исследовании интенсивности выбросов получаем ответ на вопросы: почему повышается интенсивность с увеличением поперечного сечения выработки, почему интенсивность выбросов в сбойсках обычно больше, чем интенсивность выбросов в выработках, проведенных в залежах. При помощи исчислений получаются такие же порядки величин интенсивности, которые были установлены эмпирическим путем.

Указывается связь между выбросоопасностью и эффективностью предохранения а также взывоопасностью и скоростью проходки выработки.

Acta Geodaet., Geophys. et Montanist. Acad. Sci. Hung. Volume 17 (1), pp. 29—49 (1982)

MECHANISM OF ROCK AND GAS OUTBURSTS

ZS. SOMOSVÁRI

TECHNICAL UNIVERSITY OF HEAVY INDUSTRY, MISKOLC

[Manuscript received March 28, 1979]

Based on the investigation of the physicochemical, thermodynamical and mechanical interactions of the rock–gas system, the mechanism of the rise of rock and gas outbursts is described and basic causes, conditions and main parameters of outbursts are determined. It is pointed out that in the rise of outbursts an active role is played by the mechanical interactions of the rock–gas system while thermodynamical and physicochemical interactions have but a passive effect.

It is emphasized that there cannot be such a difference in the structure of the coal that would explain the danger of outburst in some places and the lack of it elsewhere. Outbursts can occur in any rock (coal, sandstone, salt etc.) containing gas under certain circumstances, such as a sufficiently high pore gas pressure, small strength, small Young's modulus, etc. The rise, or the danger, of outburst is not a matter of liability. Rather, the outburst is a process that commences with the deterioration of the load-bearing rock–gas system under certain circumstances, and results in an explosion-like throw-out of a great amount of rock and gas.

In outburst processes the main effect is exerted by the free gas in the pores, in spite of its very small amount compared with the adsorbed gas. The adsorbed gas does not exert any effect until the beginning of the outburst when the decrease of the pore gas pressure initiates a desorption process, replacing the free gas on the one hand and preventing pressure reduction on the other.

Symbols

v_t	total gas amount
v_a	adsorbed gas
v_f	free gas
v_m	maximum amount of adsorbed gas
b_0, b, α, β	constants
R	gas constant, radius of drift
T	absolute temperature
Q	potential of adsorption
p	pore gas pressure
p_0'	atmospheric pressure
f	specific surface
n	porosity (volume of voids)
e	void ratio
ϱ	bulk density of the rock
$\varkappa$	adiabatic exponent
$\bar{\varkappa}$	polytropic exponent
$\Delta V/V$	specific volume change of the rock
ε	deformation of the rock
E	Young's modulus
m	Poisson's ratio
$\Delta\sigma_x'$	axial effective stress
$\Delta\sigma_z'$	vertical effective stress
τ'	shear limit stress
σ_t	total normal stress
c	cohesion of the rock
Φ	angle of internal friction of the rock

B	Brinke's number of the rock
σ_C	uniaxial compressive strength of the rock
σ_T	tensile strength of the rock
σ_C'	uniaxial compressive strength in the presence of pore gas
σ_{Ct}'	triaxial compressive strength in the presence of pore gas
σ_3'	lateral effective stress
x	distance from the face
H	depth beneath the surface

Research work carried out all over the world, involving high expenses and great efforts, has failed up to now to determine exactly the basic causes and conditions of rock and gas outbursts. The very complex problem to be solved involves the following details: geological–geochemical questions concerning the rise of gases; chemical and physicochemical problems of the place and equilibrium of gases in pores and on pore surfaces; the thermodynamics of the changes of state of gases; rock-physical questions about the structure of gas-rich rocks; we also need rock mechanics to describe the stresses and deformations around mining excavations and mining technology to evaluate the respective situations of mining excavations in space and time, etc. All these questions form an enormous field of research both in the vertical and horizontal senses, where great efforts have been lavished on minor issues. May be, this is why we still do not have an adequate theory of the basic causes of outbursts.

Sure, a lot of questions have already been settled and much is known today about the various factors influencing the phenomenon. The basic causes of outburst, however, have not been determined up to now, and a great number of practical observations have remained to be answered. A basic question of this kind why do not we have outbursts in many layers with high gas content while they do occur, rather frequently in the presence of much less gas; or, why no outbursts occur in certain workings while they do both in workings and drifts elsewhere. And there are a legion of similar questions that still have not got a proper answer.

As some of the factors affecting outbursts had become known, a distinct improvement took place in the field of preventive measures. Of course, without knowing the basic causes of outbursts no really effective protection can be worked out. Even nowadays outbursts occur in various places of the world, in this country as well, some of them demanding human lives.

1. Review of previous research work

Many theories have been proposed concerning the rise of outbursts. Since some of them show similar features, all these theories will be grouped and considered as various research trends. Three main research trends should be pointed out which followed each other also historically in more or less the

same sequence as they will be discussed now. One of the research trends looked for the cause of outbursts in gas accumulation, the other attributed great importance to rock pressure in bringing about outbursts, while the third one regarded gas and rock as equally important and analysed gas content, gas pressure and rock pressure as well. There is no doubt that the latter approach is the most up-to-date and successful. It was first of all the energy centered approach of Professor Hodot that made an important contribution to this field.

There are, of course, lines of thoughts that do not fit to any of the aforementioned categories. One of them attributes the cause of outbursts to the structure of the coal.

We think that even the most up-to-date and successful trend has at least two major deficiencies. The first is that even though both rock and gas are analysed, they are not regarded as a system, i.e. their interactions are not investigated. The second deficiency, that it has been only tried to explain experiences of outbursts and it has never been challanged to understand the conditions of prevention, let alone to answer some other basic questions. The basic question, e.g. why the outbursts always occur at the rock face and never on the surface of drifts and shafts has never been raised. In scientific research it is, however, of utmost importance that the method of analysis should suit the character of the problem and, also, that all relevant questions should be asked and answered.

With the realization in mind a research project was launched in 1976 at the Technical University of Heavy Industry to investigate the mechanical interactions of the rock–gas system in order to determine the causes of unexpected rock and gas outbursts. The gas and solid phases are simultaneously analysed, a due attention being paid to their interactions. In our investigations we tried to answer basic questions in the first place. The interactions can be analysed, of course, in many ways. At the beginning of our investigations we assumed that the processes leading to outbursts are essentially mechanical phenomena. This hypothesis has been extensively verified by the results obtained. The first reports of our investigations were submitted to the Mecsek Coal Mines in 1977 [6].

The investigation based on the interactions of the rock–gas system represents a new research trend in the theory of outbursts. This research policy has been in accordance with the general trend in Hungarian rock-mechanical research, where it has lately come into the focus of attention to investigate complex continua (Richter) in the frame-work of natural systems (Kapolyi).

2. Connection between the two elements of the rock–gas system

The smallest structural parts of coal are the macromolecules which group into crystallites. The partly ordered bundles of crystallites create disordered micelles. Within this structure the pore size can range from macromolecular pores to macropores. Pores below 10^{-5} mm are called *micropores*, between 10^{-5}—10^{-4} mm *transition pores*, those in the range 10^{-4}—10^{-3} mm *submacropores* and pores of a diameter 10^{-3}—10^{-1} mm *macropores*. Pores above 0.1 mm are already visible. Beside pores, the coal also contains networks of cracks of smaller or greater size.

From among the various gases (CH_4, CO_2 etc.) in the earth's crust, the connection between methane and coal (or other rocks) will be dealt with. Methane develops in the process of coalification through various chemical and biological reactions. The development of methane goes on for as long as allowed by the specific thermodynamic conditions at the given temperature and pressure.

The developed methane is partly adsorbed on the walls of the pores and cracks, partly fills the pores and cracks in the form of a free gas. The majority of methane is physically adsorbed in the coal on the surface of the micropores, for the micropores have a very great specific surface: 100—400 m^2/g. The volume of micropores is independent of the elastic deformations of the rock, its effect on gas permeability is also negligible. The specific surface of the macropores (1—2 m^2/g) is considerably smaller than that of the micropores so that they are mostly filled with free gas. The macropores and the cracks across the coal determine the gas permeability and are especially susceptible to deformations. The deformations of the coal due to changes of load proceed mainly at the expense of macropores and crack systems, containing free gas.

A part of the free gas in the macropores and crack networks can escape from their place of origin and invade the pores of the side rocks.

The equilibrium of the gas adsorbed on the walls of the pores and of the free gas in the pores is unambiguously determined by the pore gas pressure p and temperature t. Physical adsorption is brought about by the free surface energy of the rocks. The adsorption process is fairly well described by means of Langmuir's monomolecular adsorption theory. According to this theory, adsorption continues as long as a full monomolecular saturation is achieved on the surface. Langmuir's theory could not explain all aspects of the phenomenon of adsorption but the equation given for the amount of the adsorbed gas coincide quite well with experience. The amount of the adsorbed gas is, according to Langmuir's theory [4]:

$$v_a = v_m \frac{b(t)p}{1 + b(t)p} \tag{1}$$

where p is pore gas pressure (Pa),

v_m maximum amount of adsorbed gas corresponding to a fully covered surface (cm^3/g),

$b(t)$ constant, depending on temperature but independent of pressure (Pa^{-1}).

The maximum amount of gas v_m to be adsorbed is independent of temperature. It is determined, first of all, by the specific surface and the free surface energy of the solid phase with respect to the gas.

Physical adsorption is accompanied by an energy release, i.e. the adsorption process is exotherm. Measurements have shown that the so-called differential adsorption heat, referring to a unit amount of adsorbed gas, decreases with the increased amounts of the adsorbed gas. This can be explained by two reasons [4]:

— Owing to heterogeneities in the adsorbent there are points of various potentials (activities) and the gas molecules get adsorbed in the order of the potentials. Thus, as the adsorption proceeds, less and less energy is released.

— A polymolecular adsorption layer is formed, hence the adsorption of gas layers farther away from the solid phase is combined with less energy development.

The polymolecular adsorption theory of Brunauer, Emett and Teller was based on this latter idea. Experience shows, that the amount of adsorbed gas can always be arranged into a monomolecular layer on the surface of the adsorbant. Thus the monomolecular theory meets the demands of practice.

Williams, using a kinetic approach, determined the amount of adsorbed gas in terms of the adsorption potential and temperature. His solution was improved by Mückel who expressed this relationship in the form of Langmuir's equation as:

$$v_a = v_m \frac{b_0 e^{\frac{Q}{RT}} \cdot p}{1 + b_0 e^{\frac{Q}{RT}} \cdot p}. \tag{2}$$

That is, in Langmuir's equation

$$b(t) = b_0 e^{\frac{Q}{RT}} \tag{3}$$

where T absolute temperature,

R gas constant,

Q adsorption potential (heat),

b_0 a constant factor.

The equation expresses the amount of adsorbed gas as function of pressure and temperature in a way that satisfies all requirements of practice. For $T =$ const. we get the equation of the adsorption isotherm, for $p =$ const. the adsorption isobar.

Of course, quite a few empirical formulae have been proposed for the adsorption isotherm, as e.g. the Boedecker—Ostwald quation:

$$v_a = \alpha p^{\frac{1}{\beta}} \tag{4}$$

where α and β are constants. Measurements on coal–methane systems have yielded the values $\alpha = 2.69$ cm^3/g and $1/\beta = 0.56$ [4]. For theoretical research purposes, however, it is best to avoid any kind of empirical equations.

In the following discussions the Langmuir—Hückel's equation will be used; its parameters v_m, Q/R and b_0 will be determined from the measured results as follows. We start out from published values [5] of the maximum amount v_m of adsorbed gas as a function of temperature t for various coal layers given as tables based on the adsorptional isotherms at different temperatures. The values are plotted in a diagram in Fig. 1. The curves show a rather irregular shape. This can be attributed first of all to an inaccurate evaluation of the adsorptional isotherms. Nevertheless, they are suitable for

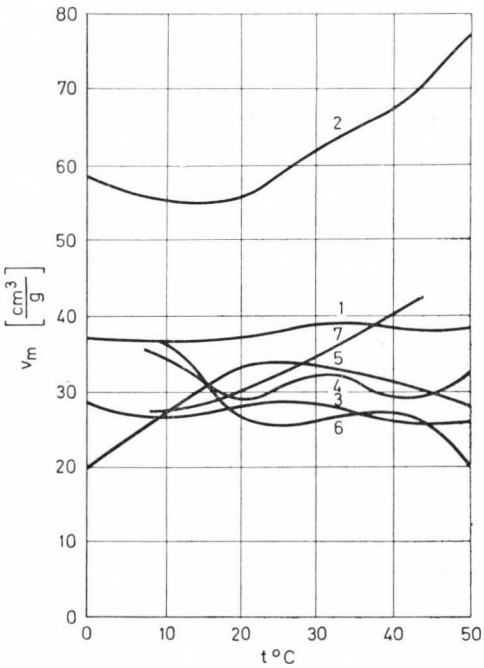

Fig. 1. Maximum amount of absorbed methane as function of temperature

our purposes since they show that v_m is independent of temperature. Its variation ranges from 20 to 74 cm³/g. In [5] values of $1/b$ are also compiled as a function of temperature, for various coal layers, in tables based on the adsorption isotherms at different temperatures. These values are illustrated in Fig. 2. At $t = 20$ °C $1/b$ varies within 0.3 and 1.7 MPa, at $t = 30$ °C within 0.4 and 2.5 MPa and at $t = 40$ °C within the range 0.5 and 5.0 MPa.

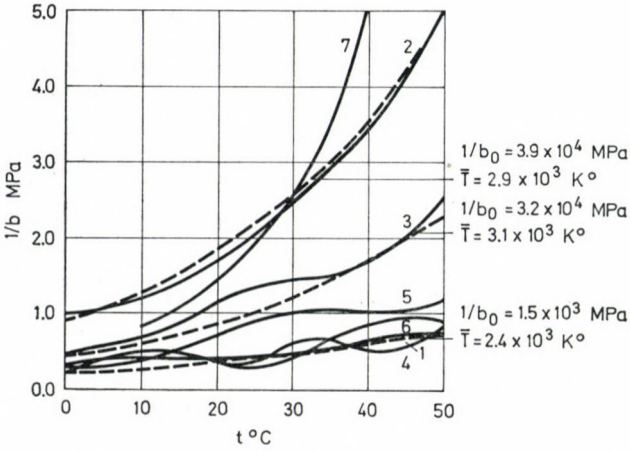

Fig. 2. Parameter $1/b$ as function of temperature

Figure 2 also shows the values computed according to the functions

$$\frac{1}{b} = \frac{e^{-\frac{Q}{RT}}}{b_0} \frac{e^{-\frac{\bar{T}}{T}}}{b_0}; \quad \bar{T} = \frac{Q}{R}. \tag{5}$$

We have $1/b_0 = 3.9 \cdot 10^4$ MPa and $\bar{T} = 2.9 \cdot 10^3$ °K for curve 2, $1/b_0 = 3.2 \cdot 10^4$ MPa and $\bar{T} = 3.1 \cdot 10^3$ °K for curve 3 and $1/b_0 = 1.5 \cdot 10^3$ MPa and $\bar{T} = 2.4 \cdot 10^3$ °K for curves 1, 4, 5 and 6. The gas constant of methane is 520 J/kg K. Using this value, we obtain for the heat of adsorption,

$$Q = 0.85 - 1.09 \text{ J/cm}^3.$$

The values published in [5] for various kinds of coal fall in the range

$$Q = 0.75 - 2.26 \text{ J/cm}^3.$$

Correspondingly,

$$\bar{T} = 2.1 \cdot 10^3 - 6.4 \cdot 10^3 \text{ °K}.$$

The adsorption isotherms for coal samples from seams 3 and 7 of István Mine, from seam 23 of Széchenyi Mine and from the Mány area, respectively, are illustrated in Fig. 3. The equation of the adsorption isotherm for the coal sample from seam 23 of Széchenyi Mine is

$$v_a = 14 \frac{1.07\,p}{1 + 1.07\,p}\ \mathrm{cm^3/g},\ p\ [\mathrm{MPa}],\quad t = 20\ ^\circ\mathrm{C}. \tag{6}$$

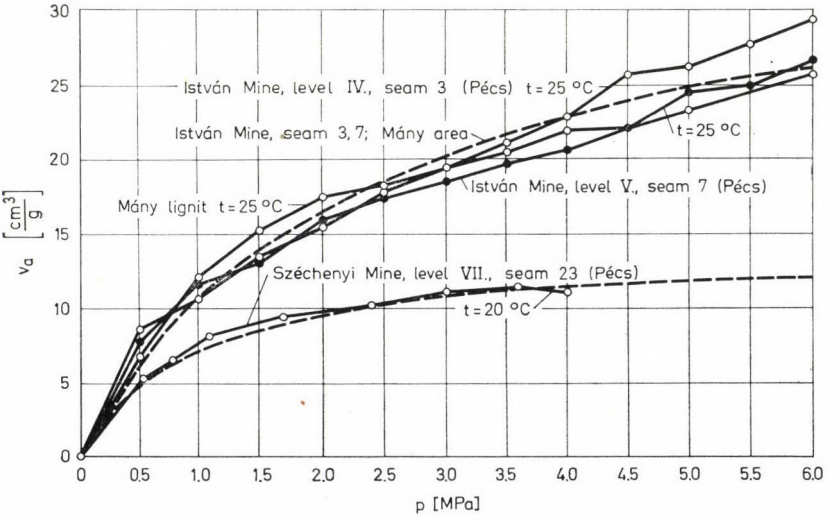

Fig. 3. Adsorption isotherms

For the coal samples from seams 3 and 7 of the István Mine and from the Mány area, the adsorption isotherm is, approximately

$$v_a = 37 \frac{0.41\,p}{1 + 0.41\,p}\ \mathrm{cm^3/g},\ p\,[MPa],\quad t = 25\ ^\circ\mathrm{C}. \tag{7}$$

It should be pointed out that while outbursts are rather frequent in seam 23 of the Széchenyi Mine and seam 7 of the István Mine, they have never occurred in seam 3 of the István Mine so far. Nevertheless, their adsorption isotherms show hardly any difference. The adsorption isotherm of the coal sample from the Mány area under development is practically identical with that of the coal samples from the István Mine.

Using the adsorption isotherm, the specific surface of the coal can be calculated since the number of gas molecules can be determined from Avogadro's law at a given volume, pressure and temperature and the size of the methane molecules are also known. From these data and the specific surface

we can calculate the amount of adsorbed gas ensuring a full coverage or, alternately, the specific surface can be determined from v_m [2] as

$$f = 5.0\, v_m \ \mathrm{m^2/g}, \quad v_m \quad [\mathrm{cm^3/g}]\,. \tag{8}$$

The amount of free gas in the pores is determined by the pore volume, pressure and temperature:

$$v_f = \frac{273\, np}{\varrho g T p_0'} = \frac{273\, ep}{\varrho g T (1+e) p_0'} \ \mathrm{cm^3/g} \tag{9}$$

where T is absolute temperature, °K,
p pore gas pressure, Pa,
n volume of voids (porosity),
e void ratio,
ϱ bulk density of the rock, g/cm³,
p_0' atmospheric pressure, Pa.

The total amount of gas in the rock is

$$v_t = v_a + v_f\,.$$

With $v_m = 30$ cm³/g, $n = 5\%$, $\varrho = 1.5$ g/cm³, $\overline{T} = 3 \cdot 10^3$ °K and $1/b_0 = 3 \cdot 10^5$, the equilibrium of the adsorbed and free gas phases is illustrated in Fig. 4. The equations of the curves in the Figure are

$$v_a = \frac{v_m}{\dfrac{e^{-\frac{\overline{T}}{T}}}{b_0 p} + 1} = \frac{30}{\dfrac{3 \cdot 10^5 \cdot e^{-\frac{3 \cdot 10^3}{T}}}{p} + 1} \tag{10}$$

$$v_f = \frac{273\, np}{\varrho g T p_0'} = \frac{10.5\, p}{T}\,. \tag{11}$$

It can be seen from Fig. 4 that if the pore gas pressure p ranges between 0 and 7 MPa, the free gas is but a small fraction of the total amount of gas. Further, while the amount of adsorbed gas strongly changes with temperature, the free gas content is practically independent of temperature in the interval investigated.

The above summary of the main features of the connection between rock and gas should suffice for our present purposes. Even though the question has been dealt with somewhat lengthily, this should not imply that it were considered as of basic importance in the theory of outbursts. On the contrary:

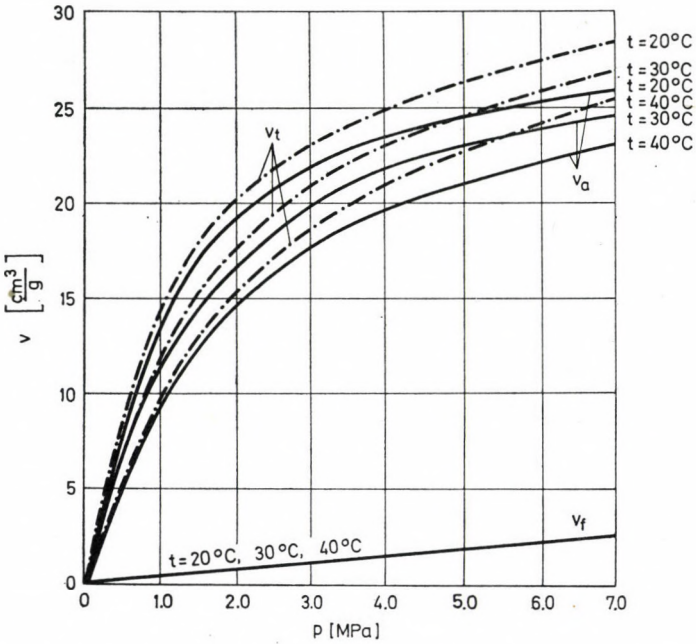

Fig. 4. Amounts of the free, adsorbed and total gas plotted against pressure, for various temperatures

with this analysis we tried to prove that gas adsorption capabilities do not differ that much between coals of various structures as to explain why certain kinds of coal are outburst dangerous while others not. This circumstance is further emphasized by the frequently neglected fact that outbursts do not only occur in coal layers but in the side rocks as well.

3. Effect of deformation on the state of the rock–gas system

The equilibrium of the free and adsorbed gases in the rock is unambiguously determined by the available volume, pore gas pressure and temperature. The change of any of these parameters involves a change of state of the free gas phase and also a change in the equilibrium of the adsorbed and free gas phases. This means that simultaneous thermodynamic and physicochemical changes take place.

In the surroundings of underground excavations the mining activity causes displacements and deformations. Since rocks are rheological media and the excavation proceeds in time, the displacements and deformations are also time-dependent processes. The deformation of the surrounding rock mainly proceeds at the expense of the pores and the crack system of the rock.

Consequently, the deformation of the surrounding rock implies a volume change of the free gas. This means, a mechanical change (deformation) triggers thermodynamic and physicochemical changes.

If the pore volume of the gas-bearing rock changes due to deformation so that its void ratio becomes e instead of the original e_0, the amount of free gas becomes

$$v_f = \frac{273\, pn_0}{\varrho_0 g T p_0'} \frac{e}{e_0}. \tag{12}$$

In case of negligible temperature change

$$v_f = \frac{273\, pn_0}{\varrho_0 g T_0 p_0'} \frac{e}{e_0}. \tag{13}$$

In the general case the gas undergoes a polytropic change, i.e.

$$\frac{p}{p_0} = \left(\frac{T}{T_0}\right)^{\frac{\bar{\varkappa}}{\bar{\varkappa}-1}} \qquad 1 \leq \bar{\varkappa} \leq \varkappa \tag{14}$$

with $\bar{\varkappa}$ being the polytropic exponent,
$\varkappa$ the adiabatic exponent.

The two extreme cases will also be regarded as polytropic with $\bar{\varkappa} = 1$ for the isothermal change of state and $\bar{\varkappa} = \varkappa$ for the adiabatic change.

During the change of state the amounts of free and adsorbed gas also change while the total amount of gas remains constant. Before deformation

$$v_t = \frac{b_0 p_0 v_m}{e^{-\frac{\bar{T}}{T}} + b_0 p_0} + \frac{273\, p_0 n_0}{\varrho_0 g T_0 p_0'} = \text{const.} \tag{15}$$

while after deformation the pressure and temperature are determined by the simultaneous equations:

$$\left.\begin{aligned} v_t = \text{const.} &= \frac{b_0 p v_m}{e^{-\frac{\bar{T}}{T}} + b_0 p} + \frac{273\, n_0 e p}{\varrho_0 g T_0 e_0 p_0'} \\ \frac{p}{p_0} &= \left(\frac{T}{T_0}\right)^{\frac{\bar{\varkappa}}{\bar{\varkappa}-1}} \end{aligned}\right\}. \tag{16}$$

The change of void ratio is determined by the specific volume change of the surrounding rock

$$\frac{e}{e_0} = 1 - \frac{\Delta V}{V} \frac{1 + e_0}{e_0} \tag{17}$$

where $\Delta V/V$ is the specific volume change of the rock determined by the deformations:

$$\frac{\Delta V}{V} = \varepsilon_1 + \varepsilon_2 + \varepsilon_3 . \tag{18}$$

By means of these equations, the pore gas pressure and temperature after the deformation become

$$\left.\begin{aligned} v_t = \text{const.} &= \frac{b_0 p v_m}{e^{-\frac{\bar{T}}{T}} + b_0 p} + \frac{273\, n_0 p}{\varrho_0 g T_0 p_0'} \left(1 - \frac{\Delta V}{V} \frac{1 + e_0}{e_0}\right) \\ \frac{p}{p_0} &= \left(\frac{T}{T_0}\right)^{\frac{\bar{\varkappa}}{\bar{\varkappa}-1}} \end{aligned}\right\} \tag{19}$$

with

$$v_t = \frac{v_m b_0 p_0}{e^{-\frac{T}{T_0}} + b_0 p_0} + \frac{273\, n_0 p_0}{\varrho_0 g T_0 p_0'} . \tag{20}$$

The solution of the simultaneous equations can be explicitly given as

$$\begin{aligned} \frac{\Delta V}{V} = \frac{e_0}{1 + e_0} \Bigg\{ 1 - \frac{g \varrho_0 T_0 (1 + e_0) p_0'}{273\, e_0 p} \Bigg[& \frac{v_m b_0 p_0}{e^{-\frac{T}{T_0}} + b_0 p_0} + \\ & + \frac{273\, e_0 p_0}{(1 + e_0) g \varrho_0 T_0 p_0'} - \frac{v_m b_0 p}{e^{-\frac{\bar{T}}{T_0}\left(\frac{p_0}{p}\right)^{\frac{\bar{\varkappa}-1}{\bar{\varkappa}}}} + b_0 p} \Bigg] \Bigg\} \end{aligned} \tag{21}$$

$$\begin{aligned} \frac{\Delta V}{V} = \frac{e_0}{1 + e_0} \Bigg\{ 1 - \frac{g \varrho_0 T_0 p_0'}{273 n_0} \Bigg[& \frac{v_m b_0^{\left(\frac{T}{T_0}\right)^{\frac{\bar{\varkappa}}{\bar{\varkappa}-1}}}}{e^{-\frac{\bar{T}}{T}} + b_0 p_0} + \\ & + \frac{273\, n_0 p_0'}{g \varrho_0 T_0} \left(\frac{T_0}{T}\right)^{\frac{\bar{\varkappa}}{\bar{\varkappa}-1}} - \frac{v_m b_0}{e^{-\frac{\bar{T}}{T}\left(\frac{T_0}{T}\right)} + b_0 p_0 \left(\frac{T}{T_0}\right)^{\frac{\bar{\varkappa}}{\bar{\varkappa}-1}}} \Bigg] \Bigg\} . \end{aligned} \tag{22}$$

Using the exact solution to the simultaneous Eqs (19)—(20) we computed the function

$$\frac{p-p_0}{p_0}=\frac{\Delta p}{p_0}=f\left(\frac{\Delta V}{V}\right)$$

by a Hewlett—Packard 9825 A type desk-top calculator, for the parameters $\varrho_0 = 1300$ kg/m³, $T = 303$ °K, $\bar{T} = 4000$ °K, $1/b_0 = 10^4$ MPa, $\bar{\varkappa} = 1$ and 1.3, $p_0 = 0.5$; 1; 3; 5 MPa and $e_0 = 0.05$; 0.10; 0.15. The results are displayed in Fig. 5. The Figure shows that the pore gas pressure sharply changes with void

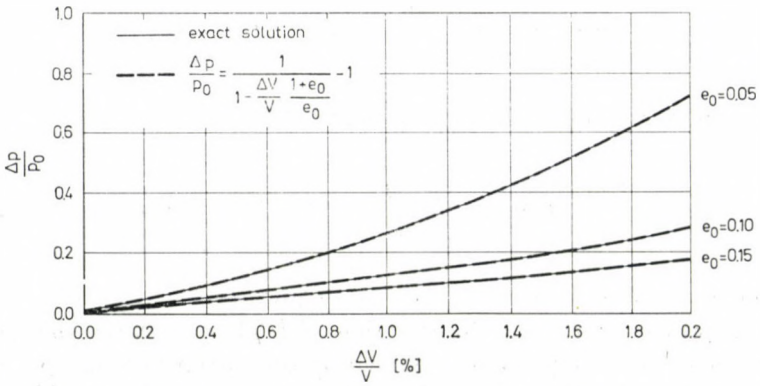

Fig. 5. Change of the pore gas pressure as function of the specific volume change of the rock for elastic deformations

ratio while it is independent of $\bar{\varkappa}$. This latter result proves that it is of no importance whether the pore gas pressure suffers an isothermal or adiabatic change of state, or some kind of polytropic change between these extremes, in course of the deformation.

In order to get an explicit expression for pore gas pressure, we have to simplify expression (21). Since in practical cases

$$e^{-\frac{\bar{T}}{T_0}} \simeq 0$$

holds, we obtain

$$\frac{\Delta V}{V}=\frac{e_0}{1+e_0}\left(1-\frac{p_0}{p}\right) \tag{23}$$

i.e.

$$p=\frac{p_0}{1-\frac{\Delta V}{V}\frac{1+e_0}{e_0}} \tag{24}$$

$$\frac{p-p_0}{p_0}=\frac{\Delta p}{p_0}=\frac{1}{1-\frac{1+e_0}{e_0}\frac{\Delta V}{V}}-1\,. \tag{25}$$

The same result is obtained if one assumes a change of state where the amount of free gas is unchanged, i.e. $v_f(T, p, e) = v_f(T_0, p_0, e_0)$. Thus, the solution obtained by neglecting the exponential term corresponds to this case. Further, the exact solution can be fairly well approximated by the tangent of the above function at the initial point $\Delta V/V = 0$. The equation of the tangent is

$$\frac{\Delta p}{p_0}=\frac{1+e_0}{e_0}\frac{\Delta V}{V}\qquad(\varkappa=1.0-1.3)\,. \tag{26}$$

A somewhat better approximation is provided by the equation

$$\frac{\Delta p}{p_0}=1.3\,\frac{1+e_0}{e_0}\frac{\Delta V}{V}\qquad(\varkappa=1.0-1.3)\,. \tag{27}$$

This simple formula satisfies all practical requirements.

In the range of elastic deformations ($\Delta V/V < \sim 0.02$) the pore gas pressure change Δp is uniquely determined by the initial pore gas pressure p_0, the initial void ratio e_0 and the specific volume change of the rock. The smaller the initial void ratio, the greater will be the change of the pore gas pressure with the change of the specific volume.

For elastic deformations the change of the pore gas pressure is practically independent on whether the free gas suffers an isothermal or an adiabatic change of state. Just before deterioration sets in, when the pore volume had

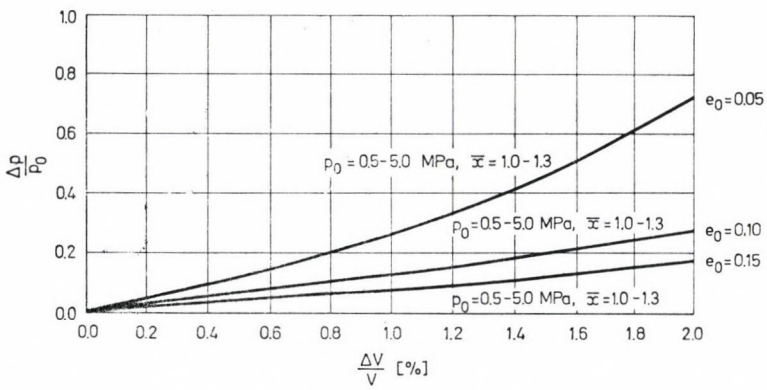

Fig. 6. Change of pore gas pressure as a function of specific volume change for an elastic deformation. Exact and approximate solutions

already decreased to such an extent that the deformation can not proceed further at the expense of pore volume, the pore gas pressure becomes several times of its original value and depends on the change of state of the free gas, as well (Fig. 7). The difference is, however, still negligible, because $\varkappa$ is 1.3 at an adiabatic change of state of the methane, i.e. only slightly deviates from unity. What is much more important, the increase of pore gas pressure accelerates with increasing specific surface,

$$\frac{\mathrm{d}(\Delta p)}{\mathrm{d}\left(\frac{\Delta V}{V}\right)} \gg \left.\frac{\mathrm{d}(\Delta p)}{\mathrm{d}\left(\frac{\Delta V}{V}\right)}\right|_{\frac{\Delta V}{V}=0} . \tag{28}$$

This change has a great significance for rock deterioration.

The relationships and diagrams obtained show that a decrease in rock volume ($\Delta V/V > 0$) makes the pore gas pressure increase while an increase of rock volume ($\Delta V/V < 0$) reduces pore gas pressure. A deformational process can lead to rock and gas outbursts only if the pore gas pressure increases, i.e. if the deformation reduces rock volume [6, 7, 8].

Deformations reducing rock volume occur in front of road heads, beneath shaft soles and, frequently, also in front of working faces [6—10]. This is in accordance with experience that outbursts always occur at rock faces (road heads, shaft soles, working faces) but never on the side walls of shafts or drifts where the rock volume increases during deformation. No outbursts occur in such workings where the strength of the coal layer is low (as e.g. in the Pécs region, S. Hungary). As proved in [9], a low coal strength is always combined with a Poisson's ratio around 2, so that in such a case the rock volume will

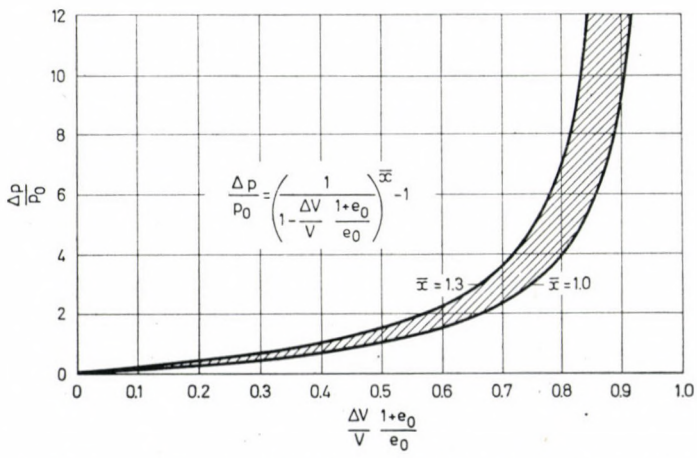

Fig. 7. **Change of pore gas pressure as a function of specific volumetric change according to the approximate solution**

increase in front of the working face during the deformation and no outbursts will set in.

Thus, the specific volume change of the rock plays a determinative role in the outbursts. The volumetric change of positive sign (i.e. volume reduction) is one of the basic conditions of outbursts. No outburst can set in if this condition is not met.

4. Load assumption and deterioration of the rock–gas system

The pressure of the free gas in the pores and crack systems of the rock causes contradictory effects:

— on the one hand, it reduces the stresses in the solid structure of the rock
— and, on the other, it decreases the strength of the rock.

When investigating rock–gas systems we have to distinguish between the *effective stresses* in the solid rock matrix and the pore gas pressure or *neutral stresses*. The sum of these two stresses is the total stress determined by the external load.

Before excavation the following stresses arise in the rock–gas system in the earth's crust [6, 7, 8]:

$$\sigma'_z = H\varrho g - p_0; \; \sigma'_x = \frac{\sigma'_z}{m-1} = \frac{H\varrho g - p_0}{m-1} \tag{29}$$

where H is depth beneath the surface,
ϱ average bulk density of the overburden,
m Poisson's ratio,
p_0 pore gas pressure,
σ'_z vertical effective stress,
σ'_x horizontal effective stress.

In the rocks surrounding the excavations, deformations and volumetric changes take place affecting both the effective stress and the pore gas pressure.

Experience shows that the outbursts most frequently occur on faces of drifts. Let us consider the state of stress in front of the face of the drift (for further details see our study [10]). Since a volume reduction takes place in front of the road head due to the transferred stresses, the pore gas pressure increases:

$$p = p_0 + \Delta p = p_0 \frac{1+e_0}{e_0} f(m, 1/E, R)\, \Delta\sigma'(x) \tag{30}$$

with p_0 being the initial pore gas pressure,
e_0 initial void ratio,
E Young's modulus,
$\Delta\sigma'_x$ axial effective deformational stress,
R drift radius,
x distance from the face.

With the increase of the Young's modulus the pore gas pressure change decreases.

The vertical effective stress in front of the road head is

$$\sigma'_z = (H\varrho g - p_0) + \Delta\sigma'_z; \qquad \sigma'_z > H\varrho g - p_0 \tag{31}$$

the horizontal effective stress being

$$\sigma'_x = \frac{H\varrho g - p_0}{m-1} - \Delta\sigma_x \qquad \sigma'_x = \frac{H\varrho g - p_0}{m-1}. \tag{32}$$

The increased vertical stress and the decrease of the horizontal one make the mechanical state to approach towards deterioration.

The strength-reducing effect of the pore gas pressure plays a substantial role in the deterioration process. In the presence of pore gas or water pressure the equation of the linear fracture limit curve of the rock can be written as:

$$\tau' = c + (\sigma_t - p)\tan\Phi = (c - p\tan\Phi) + \sigma_t \tan\Phi \tag{33}$$

with τ' the shear limit stress,
σ_t total normal stress,
c cohesion of the rock,
Φ angle of internal friction of the rock.

The above relationship expressing deterioration of rock–water systems is a generally accepted equation in soil mechanics. Since the relationship is valid no matter whether water or gas exerts its effect in the pores, Eq. (33) applies for the deterioration of rock–gas systems as well.

In reality, it is only the solid phase i.e. the rock matrix that suffers deterioration. Nevertheless, the expression "deterioration of the rock–gas system" is correct, because with the deteriorating solid phase also the rock–gas system as a whole ceases to exist in its previous form. After deterioration a completely new kind of rock–gas system comes into being, where the solid phase does not carry a load any more but, rather, the solid particles will be suspended in the gas phase.

A more convenient form of the fracture limit curve can be written as [6, 7]:

$$\tau' = \frac{\sigma_C}{2\sqrt{B}}\left[1 + \frac{B-1}{\sigma_C}(\sigma_t - p)\right] \tag{34}$$

where σ_C is the uniaxial compressive strength without pore gas pressure,

$B = \frac{\sigma_C}{\sigma_T} = \tan^2\left(45 + \frac{\Phi}{2}\right)$ is Brinke's number,

σ_T is the tensile strength.

The uniaxial compressive strength becomes, in the presence of pore gas pressure [6, 7]

$$\sigma'_C = \sigma_C\left[1 - \frac{p}{\sigma_C}(B-1)\right] = \sigma_C - (B-1)\,p\,. \tag{35}$$

The greater the angle of internal friction or the Brinke's number of the rock, the greater will be the decrease of the uniaxial compressive strength with increasing pore gas pressure.

In the absence of pore gas pressure, the strength is independent of the magnitude of deformation at slow deformation rates and a quasistatic load; it is determined by the internal resistance of the rock. However, in case of pore gas pressure, the strength is affected by the magnitude of the deformation, since the pore gas pressure reduces the internal resistance of the rock. The uniaxial compressive strength in the elastic deformation zone is

$$\sigma'_C = \sigma_C - 1.3\,(B-1)p_0\left(1 + \frac{1+e_0}{e_0}\frac{\Delta V}{V}\right). \tag{36}$$

The triaxial compressive strength is

$$\sigma'_{Ct} = \sigma'_C + B\sigma'_3 = \sigma_C - 1.3\,(B-1)\,p_0\left(1 + \frac{1+e_0}{e_0}\frac{\Delta V}{V}\right) + B\sigma'_3 \tag{37}$$

with σ'_3 being the lateral effective principal stress.

The greater the specific volume reduction of the rock the greater the strength reduction, i.e. the condition of deterioration will be more easier met. Near the deterioration, if the deformation exceeds the elastic limit, we can write

$$\sigma'_{Ct} = \sigma'_C - (B-1)\frac{p_0}{1 - \frac{\Delta V}{V}\frac{1+e_0}{e_0}} + B\sigma'_3\,. \tag{38}$$

If

$$\frac{\Delta V}{V}\frac{1+e_0}{e_0} \to 1 \tag{39}$$

it is seen from Fig. 7 that the pore gas pressure increases quickly and greatly, thus also the strength decreases the similar way. Under such circumstances the condition of deterioration is easily fulfilled.

Apart from its strength reducing effect, pore gas pressure also affects the process of deterioration. In the absence of pore gas pressure and for a quasistatic load, the deterioration process of low-strength rocks ($\sigma_C < 20$ MN/m^2) is slow and does not result in explosion. It starts in the weakest points of the planes of the most unfavourable state of stress, then gradually extends over a wider area. If the rock volume decreases during the deformation, the pore gas pressure accelerates the process of deterioration, thus rock points are suddenly deteriorated over a large area. At the beginning of deterioration, pore gas pressure increases greatly and this rather sharply reduces strength. Consequently, pore gas pressure increases still further, strength becomes even less, etc. So, in the presence of pore gas pressure, a chain reaction-like process ensues at the beginning of deterioration. As a result of this process the solid rock structure suddenly deteriorates over a wide area, gets unable to bear any load and the total load will be transferred to the pore gas so that its pressure would approach the geostatic ($H\varrho g = 5 - 20$ MPa). The process produces a great gas pressure and a solid phase suspended in the gas that is unable to bear load. The gas pressure acts on the rock in front of the face where it is usually in a plastic state and has a low gas permeability, and throws it out from its original place. Thus, a flow of rock and gas will start towards the open space, i.e. an outburst sets in.

5. Basic causes and conditions of outbursts

The basic cause of rock and gas outbursts is the strength-reducing and deterioration-accelerating effect of the pore gas pressure. The basic condition of outburst that the rock volume should decrease during deformation. There is no outburst without a reduction in rock volume, similarly, no outburst is possible without pore gas pressure. However, rock deterioration is quite possible without pore gas pressure and rock volume reduction. An explosion-like deterioration, however, can only ensue if rock volume reduction takes place in the presence of pore gas.

Thus, the free gas in the pores plays a major role in bringing about outbursts in spite of its small proportion to the total amount of gas. The

adsorbed gas becomes activated during the outburst. A desorption process begins due to the pressure reduction of the pore gas which streams towards the open space, replacing free gas, thus preventing pressure reduction. This shows that the phenomenon of outburst cannot be compared to the model of a gas-outflow from a reservoir, rather, it is similar to the drainage of a gas reservoir with a steady replacement.

Our theoretical investigations have also called attention to the important role of the strength parameters σ_C, B and Φ. The greater the pore gas pressure, the angle of internal friction and Brinke's number or the smaller the compressive strength, the greater will be the danger of outburst. Porosity and Young's modulus are also important factors. The smaller the porosity or Young's modulus, the greater the danger of outburst. Compressive strength, Young's modulus and porosity are, however, not independent parameters. In general, the strength and Young's modulus are smaller for rocks of greater porosity and *vice versa*. The effect of a low porosity in increasing the outburst danger will only be realized if the Young's modulus of the rock (coal) is small. The effect of Young's modulus is stronger for rocks of great Young's moduli (sandstones), i.e. the outburst danger is greater for sandstones of small Young's modulus and high porosity.

It has also been proved that the structure, microstructure and adsorption parameters b_0, $\overline{T}$ and v_m have no important effect upon provoking outbursts.

Practice has justified the results of our theoretical investigations. Observations show that if we have mining activity below or above some layer, this layer will be stronger if it is affected by gas drainage (resulting in a smaller pore gas pressure) [1, 3]. A properly ventilated and drained coal face is rather difficult to win, i.e. it is stronger [1, 3]. Seam 4 of the István Mine I—II in Pécsbánya of 9—10% porosity shows no outburst danger while seam 11 of 3—4 per cent porosity is affected by a serious danger of outburst [1, 8]. It has also been observed that the porosity of sandstones affected by outburst danger in the Donets basin or the Ruhr district (10—14 per cent) is twice as great, while their strength is only half that measured in sandstones without outburst danger [3]. A further experience is that the greater the strength of the coal, the greater the ratio of the specific gas amount released by outbursts and to that released during production. This means that a greater gas content or pore gas pressure is necessary to cause outbursts if the coal strength is high [3].

It has also been shown in the study that the mechanical interaction is the decisive one among the possible interactions between the solid and gas phases. Although, necessarily, thermodynamic and physicochemical interactions also take part in the process, their effect is negligible and is limited to the increase of pore gas pressure while pore volume decreases.

REFERENCES

1. Szirtes, L.: Szén- és gázkitörések leküzdése (Combat Against Coal and Gas Outbursts). Műszaki Könyvkiadó, Budapest, 1971.
2. Fejér, L.—Radnainé: A mecseki alsó liász kőszenek gázfelvevő és gázleadó képessége (Gas sorption and gas desorption capability of Lower Liassic bituminuous coals in the Mecsek area). *Bányászati és Kohászati Lapok, Bányászat*, 1978. No. 8.
3. Kovács, F.: Connection between the gas content and strength of rocks exposed to gas outburst danger. *Acta Geod., Geoph., Mont. Hung.*, 16 (1981), 115—130.
4. ХОДОТ, В. В.: Внезапные выбросы угля и газа. Государственное научно-техническое издательство литературы по горному дели. Москва, 1961.
5. Buzágh, A.: Kolloidika (Colloidics). Part I. Akadémiai Kiadó. Budapest, 1951.
6. Somosvári, Zs.: Zobák bányán a pillér hatásnak kitett területek kőzetfeszültségének feloldása a bányaművelés irányításával (Relief of rock pressure in areas of the Zobák Mine exposed to pillar effect by the control of mining operations). Research Rept. 1977.
7. Somosvári, Zs.: Investigation of the deterioration of the rock-gas system to clarify the cause of rock and gas outbursts. *Acta Geod., Geoph. Mont. Hung.*, 15 (1980), 257—269.
8. Somosvári, Zs.: Investigation of the load assumption of rock-gas systems, aiming at the detection of the causes of rock and gas outbursts. *Acta Geod., Geoph. Mont. Hung.*, 15 (1980), 271—294.
9. Somosvári, Zs.: Investigation of the rock-gas system in front of the face of workings in order to determine the cause of rock and gas outbursts. *Acta Geod., Geoph. Mont. Hung.*, 16 (1981), 131—149.
10. Somosvári, Zs.: Investigation of the zone in front of road heads in order to determine the cause of rock and gas outbursts. *Acta Geod., Geoph. Mont. Hung.*, 17 (1982), 1—27.

МЕХАНИЗМ ВОЗНИКНОВЕНИЯ ВЫБРОСОВ ГАЗА И ПОРОД

Ж. ШОМОШВАРИ

РЕЗЮМЕ

В статье на основе исследования физико-химических, термодинамических и механических взаимодействий описывается механизм возникновения выбросов газа и пород, излагаются основные причины и условия выбросов, а также основные параметры возникновения выбросов. Подчеркивается, что активную, главную роль в возникновении выбросов играют механические взаимодействия системы порода-газ, а термодинамические и физико-химические взаимодействия играют пассивную роль.

В статье указывается и на то, что в структуре угля не могут быть такие качественные различия, которые могли бы объяснить опасность или безопасность выбросов. В любой газоносной породе (уголь, песчаник, соль и т. д.) при определенном большом давлении поровых газов, небольшой прочности, небольшом динамическом модуле упругости и т. д., т. е. при определенных условиях выброс может произойти. Возникновение выброса и выбросоопасность не зависят от природы пород, а от разрушения несущей системы порода-газ, что происходит в определенных условиях и ведет к выбросам.

В возникновении выброса главную роль играет свободный газ, содержащийся в порах, несмотря на то, что его количество составляет только незначительную часть адсорбционно связанного газа. Связанный газ играет роль только после начала выброса, когда из-за уменьшения давления газа пор начинается десорбционный процесс, который одной стороны дополняет количество свободного газа, а с другой стороны препятствует уменьшению давления.

Acta Geodaet., Geophys. et Montanist. Acad. Sci. Hung. Volume 17 (1), pp. 51–66 (1982)

MAIN PARAMETERS OF THE ROCK AND GAS OUTBURST DANGER

ZS. SOMOSVÁRI

TECHNICAL UNIVERSITY OF HEAVY INDUSTRY, MISKOLC

[Manuscript received September 22, 1979]

The most important, universal parameters of the danger of rock and gas outbursts will be determined and their interrelationships analysed. The starting point is that the outburst mechanism is brought about by the mechanic and thermal interactions of the two phases of the load-bearing rock–gas system. The following are the main parameters characterizing the outburst danger: pore gas pressure, compressive strength and angle of internal friction of the gas-bearing rock, and the yield point-to-compressive strength ratio expressing the brittleness (toughness) of the rock.

Using the interrelationship between the main parameters determining outburst danger the study explains some basic observations according to which coal layers containing a small amount of gas are frequently rather dangerous, while those with a higher gas content not at all, from the point of view of gas outburst. In certain areas a very small pore gas pressure is sufficient to initiate outbursts; in other regions, however, the same pore gas pressure does not involve an outburst danger.

The study emphasizes that the relationship between the main parameters determining outburst danger can be applied in almost all fields of the struggle against unexpected rock and gas outbursts, that is they are of utmost practical importance.

Symbols

σ_T	tensile strength
σ_C	uniaxial compressive strength
c	cohesion
Φ	angle of internal friction
σ_{Ct}	triaxial compressive strength
f	Protodiakonoff's number
σ_Y	yield point
σ_C'	uniaxial compressive strength in the presence of pore gas pressure
m	Poisson's ratio
γ	average volume weight of the overburden
p	pore gas pressure
p_0	initial pore gas pressure
H	layer depth
h_0	depth of the upper boundary of the gas-bearing zone
x	horizontal distance from the drift face
x_0	thickness of the plastic rock zone
R	drift radius
$\Delta V/V$	specific volume change
σ_r'	effective radial stress
σ_a'	effective axial stress
e_0	void ratio
E	Young's modulus
C	factor depending on the effectiveness of drift support
B	Brinke's number
$\overline{\sigma}_{Ct}$	measured triaxial compressive strength
σ_3	surface pressure applied at triaxial investigations
$\overline{\sigma}_C$	measured uniaxial compressive strength
$\overline{E}$	measured Young's modulus
$\overline{m}$	measured Poisson's ratio

The technical literature dealing with the main parameters of the rock and gas outburst danger relies first of all upon experience, determines the basic influencing factors from observations and establishes empirical relationships between the various parameters. Although observations and statistical analyses of outbursts can inform us about the most obvious parameters, they cannot determine all parameters of importance, or reveal all possible relationships between the important parameters; the most we can expect is to get some rules of approximative and local validity.

The universally valid relationships between the main parameters of the outburst danger can only be determined by theoretical investigations based on empirical data.

Previous investigations [10, 11, 12, 13, 14] on the mechanical and thermal interactions of the load-bearing dual rock–gas system, i.e. on the basic causes and conditions of rock and gas outbursts, have revealed the interconnections of the basic parameters characterizing outburst danger.

These theoretical findings greatly enhance the effectiveness of the struggle against outbursts, in two broad fields:

— in forecasting outbursts and
— in the development of protective methods against outbursts.

The interrelationship of the main parameters can be used to develop new and more reliable forecasting methods, to increase the effectiveness of the protective means and to introduce new and more effective ones.

Due attention should be paid to the empirical data published in technical literature, since these enable us to check the results obtained by theoretical analyses.

1. Experimental findings on the main parameters of the outburst danger

According to observations, the basic parameter of outburst danger is the strength of the gas-bearing rock [1, 3, 4, 5]. The less this strength, the greater the outburst danger.

In the Soviet literature types I—V coal are distinguished from the point of view of structure. Coals with intact structure belong to type I, strongly shattered ones to type V. Experience shows that coals of higher types are more common at places affected by frequent outbursts [1, 3].

Strength data of various coal types of the Donets basin are summarized in Table I [3]. Notations used are as follows:

σ_T tensile strength,
σ_C compressive strength,
c cohesion,
σ_{Ct} triaxial compressive strength.

Table I

Strength data MN/m²	Type of structure		
	I—II	III	IV—V
σ_T	0.13—0.38	0.14—0.21	0.05—0.09
c	0.46—0.152	0.47—0.93	0.13—0.3
σ_C	3.6—7.6	3.5—3.9	0.9—1.55
σ_{Ci} (if $\sigma_3 = 2$ MN/m²)	4.4—15.5		

Table II shows strength data for the various types of coals of Vorkuta resources.

According to the Tables, the experience that coals belonging to higher types are more frequent at places affected by outbursts, means that coals of less compressive and tensile strength and less cohesion are more dangerous from the point of view of outbursts.

It has also been experienced that pore gas pressure is a further basic parameter of outburst danger. The greater the pore gas pressure, the greater the danger of outburst. According to experience, pore gas pressure increases with depth. For the Donets basin the correlation between pore gas pressure p and depth H is given by the empirical equation.

$$p = 0.01\,(H - h_0) \quad \text{MN/m}^2, \qquad H\ [\text{m}] \quad h_0\ [\text{m}]$$

with h_0 being the upper limit of the gas-bearing zone [8, 9]. For the Prokopievsk region of the Kuznetsk basin [7]

$$p = 0.061\,(H - h_0)^{0.6} + 0.25 \qquad \text{MN/m}^2,\ H\ [\text{m}] \quad h_0\ [\text{m}]$$

and for the Kamerovo area [6]:

$$p = 0.12\,H - 22 \ \text{kp/cm}^2, \qquad H\ [\text{m}].$$

Table II

Strength data MN/m²	Type of structure		
	I—II	III	IV—V
σ_T	0.16—0.22	0.08—0.09	0.015—0.02
c	0.79—0.85	0.43—0.53	0.15—0.23
σ_C	4.6—5.4	3.4—3.5	0.5—1.2

Experience also shows that rock strength and pore gas pressure do not influence the danger of outburst independently, but in strong connection with each other. In case of a great rock strength even a high pore gas pressure does not indicate serious outburst danger and *vice versa*, for a small strength rock even a small pore gas pressure can initiate outbursts.

The danger of outburst is expressed by the inequality

$$p > 19 f^2$$

for the Kamerovo area of the Kuznetsk basin [1, 6]. If the above inequality holds, there is outburst danger. In this inequality strength is characterized by Protodiakonoff's number f which approximately corresponds to one hundredth of the compressive strength. The above rule is not universally valid, for it has been established for the Kuznetsk conditions on the one hand, and, on the other, Protodiakonoff's number is not an adequate parameter to characterize rock strength. Therefore, the above correlation between rock strength and pore gas pressure can only be considered as strongly approximate.

The depth of the layer is also a basic parameter for the determination of outburst danger according to technical literature [2]. This view is corroborated by the experience that the frequency and intensity of outbursts increase with depth. According to previous considerations, one of the reasons of this tendency is the inevitable increase with depth of the pore gas pressure. Therefore, the depth of the layer should not be considered as a decisive parameter if pore gas pressure has already been taken into account.

In various areas of the world a great variety of parameters, some of them rather artificial, have been introduced to characterize the outburst danger. These parameters, however, do not have a general validity in all areas.

All in all, based on experience, we are left with two universally valid parameters of outburst danger: rock strength and pore gas pressure. No universal correlation between the two parameters and the danger of outburst has, however, been ever established.

Obviously, the complicated mechanism of rock and gas outbursts must depend on more than two parameters. Were this not the case, the observations would have furnished much more reliable results in the struggle against outbursts.

The main parameters of outburst danger and their mutual dependence can only be determined if the mechanism of the development of outbursts is well known. This mechanism will be discussed in the next section.

2. Development of rock and gas outbursts

The mechanism of the development of rock and gas outbursts has been investigated [10, 11, 12, 13, 14], here only the main features will be summarized in order to make the following discussions self-contained.

Rock and gas outbursts are brought about by a special mechanical–thermal interaction of the load-bearing rock–gas system. Strictly speaking, it is only the solid phase that deteriorates, it is still correct to call the phenomenon the *deterioration of the load-bearing rock–gas system*, since after deterioration a rock–gas system of a totally different character will be produced containing solid particles suspended in gas.

The deterioration of the load-bearing rock–gas system ensues suddenly, explosion-like, if the deformation causes a decrease in rock volume. If rock volume increases during deformation, the deterioration proceeds slowly and no outburst sets in.

The basic condition of outbursts that the specific volume change of the rock should be a reduction, i.e.

$$\frac{\Delta V}{V} > 0 . \tag{1}$$

The basic cause of outbursts is the rock strength reducing effect of pore gas pressure. The uniaxial compressive strength can be written, using e.g. the linear fracture limit curve

$$\sigma_C' = \sigma_C - \left[\tan^2\left(45 + \frac{\Phi}{2}\right) - 1\right] p \tag{2}$$

with σ_C being the uniaxial compressive strength of the rock without pore gas pressure,

Φ angle of internal friction,

p pore gas pressure.

If the rock strength is reduced by pore gas pressure if a rock volume reduction takes place, and the load is quasistatic, the rock deterioration proceeds as follows. With increasing load pore gas pressure increases, rock strength decreases, thus the state of the rock tends towards deterioration because of two reasons: load increase and strength reduction. When deterioration begins, some load-bearing points drop out which causes further volume reduction and the load gets transferred even more on the pore gas. Consequently, pore gas pressure increases, strength is further reduced, some more rock points drop out from the load-bearing system, etc. This way a self-accelerating chain reaction process commences which makes the deterioration

explosion-like. After the end of deterioration the rock is comminuted, becomes unable to carry load and at the same time the pore gas pressure greatly increases. As a result of all this a rock phase suspended in the gas comes into being, together with a high gas pressure. This usually throws the generally plastic and low permeability front zone of the rock into the open space. An outburst sets in: a great amount of gas and rock flows into the mining excavation.

The described mechanism of the development of outbursts explains all experiences concerning outbursts.

As regards the fact that outbursts occur most frequently at drift faces, the main parameters of the outburst danger will be determined from the analysis of stresses at drift faces. Of course, we have to obtain the same result no matter the analysis refers to a shaft sole or a working.

3. Rock deterioration in front of drift faces

Stresses in front of the face of a horizontal drift of circular cross section have been described in greater detail in [13]. The results are illustrated in Fig. 2, using the co-ordinate system of Fig. 1, and the notations:

σ_r' effective radial stress in the rock structure,
σ_a' effective axial stress,
p_0 initial pore gas pressure,
x horizontal distance from the drift face.

The radial stress increases towards the interior, attains a maximum at some $x = x_0$, then decreases. For $x_0 > x > 0$ the rock is in the plastic state, for $x > x_0$ in the elastic state.

The stresses are, by [13]:

$$x \geqq x_0$$

$$\sigma_r' = (H\gamma - p_0)\left\{1 + \left[\frac{0.5\, mCR}{m-1} + \frac{1}{(m-1)^2}\right] e^{-\frac{\sqrt{m-1}}{R(Dp_0+1)}x}\right\} \tag{3}$$

$$\sigma_a' = \frac{H\gamma - p_0}{m-1}\left[1 - e^{-\frac{\sqrt{m-1}}{R(Dp_0+1)}x}\right] \tag{4}$$

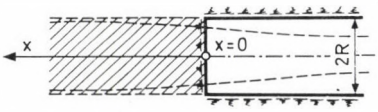

Fig. 1. Rock zone and coordinate system around the drift face

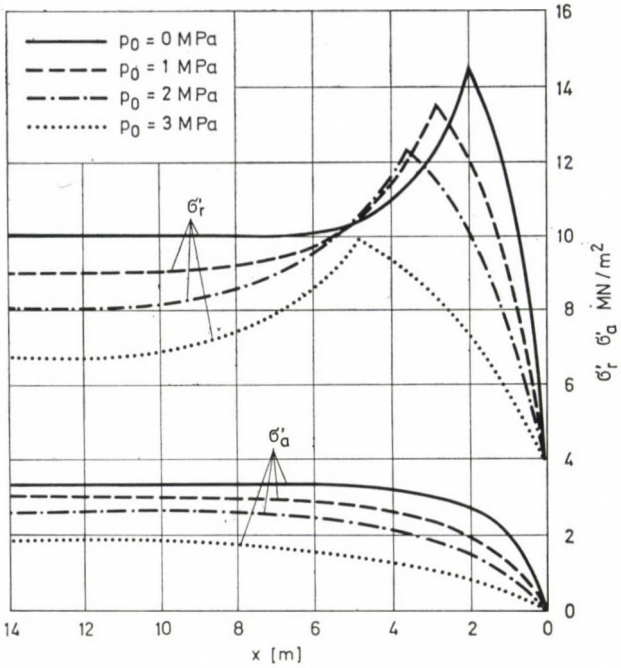

Fig. 2. Effective stresses in front of the drift face

$$x \leq x_0$$

$$\sigma'_r = (H\gamma - p_0)\left\{\frac{\sigma_Y}{H\gamma - p_0} + \frac{B}{m-1}\left[1 - e^{-\frac{\sqrt{m-1}}{R(Dp_0+1)}x}\right]\right\} \tag{5}$$

$$\sigma'_a = \frac{H\gamma - p_0}{m-1}\left[1 - e^{-\frac{\sqrt{m-1}}{R(Dp_0+1)}x}\right] \tag{6}$$

where H is depth,

γ average volume weight of the overburden,
σ_Y yield point of the rock,
m Poisson's ratio of the rock,
R drift radius,

and

$$B = \tan^2\left(45 + \frac{\Phi}{2}\right) \tag{7}$$

$$D = 1.3\,\frac{1+e_0}{e_0}\,\frac{m-2}{mE}\left[2\left(0.5\,mCR - \frac{1}{m-1}\right) - 1\right] \tag{8}$$

with e_0 void ratio of the rock,
E Young's modulus of the rock,
C factor depending on the effectiveness of the drift support,

$$x_0 = \frac{R(Dp_0 + 1)}{\sqrt{m-1}} \ln \frac{0.5\, mCR + B - \dfrac{1}{m-1}}{(m-1)\left(\dfrac{\sigma_Y}{H\gamma - p_0} + \dfrac{B}{m-1} - 1\right)} . \tag{9}$$

Figure 2 illustrates the stresses for the following choice of the parameters: $m = 4$, $B = 4$, $E = 400$ MN/m^2, $e_0 = 0.05$, $H = 400$ m, $\gamma = 25$ kN/m^3, $R = 2$ m, $CR = 4$, $\sigma_Y = 4$ MN/m^2.

Rock deterioration commences at quasistatic load if the equality

$$\sigma_r' = \sigma_C' + B\sigma_a' = \sigma_C - (B - 1)\, p + B\sigma_a' \tag{10}$$

holds. Since the stress in the rock is maximum at $x = x_0$, the condition of deterioration has to be expressed for this place. By substituting this value into the deterioration condition

$$\sigma_C = \sigma_Y - (B - 1)\, p \tag{11}$$

with p being maximum gas pressure in front of the rock face. Introducing

$$q \equiv \frac{\sigma_Y}{\sigma_C} < 1 \tag{12}$$

the condition of deterioration becomes

$$\frac{\sigma_C}{p} = \frac{B-1}{1-q} . \tag{13}$$

The same result is obtained both for the working and the shaft meaning that the relationship is of universal validity.

4. Main parameters of the outburst danger

According to our previous considerations, the condition of outbursts is that the inequality

$$\frac{\sigma_C}{p} < \frac{B-1}{1-q} \tag{14}$$

should hold.

The inequality is satisfied if the compressive strength of the rock is small, its angle of internal friction and the pore gas pressure are great, and the yield point is as near the compressive strength as possible. The compressive strength and the angle of internal friction are not independent quantities since

$$\sigma_C = 2c \tan\left(45 + \frac{\Phi}{2}\right) \tag{15}$$

where c is cohesion.

It would be more appropriate to express the outburst danger in terms of independent parameters, i.e. by

$$\frac{c}{p} < \frac{\tan^2\left(45 + \frac{\Phi}{2}\right) - 1}{2\tan\left(45 + \frac{\Phi}{2}\right)} \frac{1}{1-q}\,. \tag{16}$$

The compressive strength, however, is a more easily available parameter than cohesion, therefore we shall use the formula of outburst danger as expressed in terms of compressive strength. We should not forget, however, that it is not indifferent from the standpoint of outburst danger whether the same compressive strength resulted from a greater cohesion and a smaller angle of internal friction, or *vice versa*. A compressive strength value made up of a greater internal friction and smaller cohesion is especially disadvantageous concerning outburst danger.

Equation (14) contains the main parameters characterizing the outburst danger. One of the main parameters is the compressive strength of the rock σ_C. Concerning the compressive strength, it should be noted that the crackedness of the rock changes strength parameters. Because of the separation surfaces, the tensile strength decreases first of all, then cohesion, and least of all the compressive strength. Under compression, namely, the separation surfaces mostly get in contact with each other and the internal resistance due to friction exerts its effect on all possible surfaces. Thus, we have almost the same case as in the absence of cracks. A tension, however, separates crack surfaces so that the friction cannot exert its effect along them. Therefore, the strength against this type of stress is considerably reduced as compared with the case of no cracks.

A further main parameter affecting outburst danger is the angle of internal friction, Φ, of the rock. For rocks without cracks the angle of internal friction, and the compressive and tensile strengths, respectively are in the following relationship with each other. Brinke's number of the rock:

$$\bar{B} = \frac{\sigma_C}{\sigma_T} \tag{17}$$

$$\bar{B} = \frac{\sigma_C}{\sigma_T} = B = \tan^2\left(45 + \frac{\Phi}{2}\right). \tag{18}$$

For cracked rocks

$$\bar{B} \neq B \quad \text{but} \quad \bar{B} > B.$$

The value of B and the angle of internal friction of cracked rocks can be determined from uni- and triaxial compression measurements by the following way:

$$B = \frac{\bar{\sigma}_{Ct} - \bar{\sigma}_C}{\sigma_3} \tag{19}$$

where $\bar{\sigma}_{Ct}$ is measured triaxial compressive strength,
σ_3 surface pressure applied,
$\bar{\sigma}_C$ measured uniaxial compressive strength.

For example for the coal layers of the Donets basin $\bar{\sigma}_{Ct} = 4.4 - 15.5$ MN/m² has been obtained from $\bar{\sigma}_T = 0.05 - 0.38$ MN/m², $\bar{\sigma}_C = 0.9 - 7.6$ MN/m² and $\sigma_3 = 2$ MN/m² [3]. Thus $\bar{B} = 18 - 20$ and $B = 2 - 4$. For coals we generally have $B \simeq 2 - 4$, i.e. $\Phi = 11 - 37$.

It always has to be taken into account that the laboratory specimens usually origin from more or less intact, only slightly cracked parts of the rock. Consequently, the compressive strength determined in the laboratory is always greater than *in situ*. On the other hand, the tensile strength obtained by laboratory measurements is always smaller than its *in situ* value because of the damage caused when preparing the specimens. Cohesion, as determined in the laboratory is a parameter whose value can properly characterize the *in situ* state. Based on this observation, the compressive strength characterizing the *in situ* state is:

$$\sigma_C = \bar{\sigma}_C \sqrt{\frac{B}{\bar{B}}}. \tag{20}$$

A further decisive parameter of outburst danger is the factor q that characterizes the toughness or brittleness of the rock: the more this q factor approaches unity, the more brittle is the rock, the less q, the tougher the rock. Rocks of great strength ($\sigma_C > 50$ MN/m²) usually have a q value around 0.6, i.e. rocks of great strength are tough, rather than brittle. Coals are generally small strength rocks ($\sigma_C < 20$ MN/m²) but at the same time they are brittle for their q factors are around 0.80—0.95. Since the value of the quotient q as determined on laboratory specimens are also characteristic to the *in situ* state, this factor is a sensitive indicator of the danger of outburst.

Last but not least, pore gas pressure p should also be considered as a main parameter of the outburst danger. The maximum pore gas pressure in front

of the rock face depends on many variables. While opening excavations, the initial pore gas pressure changes, it usually increases because of the changed rock volume in front of the rock face. At the same time, the evaporation through the free rock surface reduces pore gas pressure. Therefore, the maximum pore gas pressure observed in front of the rock face of low strength coals, does not exceeds some 0.1—0.5 MPa. The permeability of hard, tough and less cracked coals is small, thus evaporation also is small, and it reduces pore gas pressure only to a small extent. Strong and tough coals allow a much higher maximum pore gas pressure of 2—5 MPa. As already mentioned, pore gas pressure increases with the depth of the layer.

In the following discussions some basic observations will be explained with the help of the main parameters of outburst danger, based on laboratory measurements.

5. Explanation of some basic observations of the outburst danger

Experience shows that in many cases there is no danger of outburst in some types of coal containing large quantities of gas, while other coal types with much less gas can be rather dangerous. It is well known, e.g. that the mining activity in the highly gaseous coal layers of the Mecsek region, Hungary, has to face the danger of outburst while in the Tatabánya region there is no outburst danger even though the coal contains much gas. To explain this observation, parallel rock mechanical investigations have been carried out on Mecsek and Tatabánya coal samples. Figures 3—5 illustrate the stress deformation diagrams of uniaxial compression experiments on some Mecsek coal samples. The three $\sigma-\varepsilon$ curves in Fig. 3 are results of experiments on coal samples

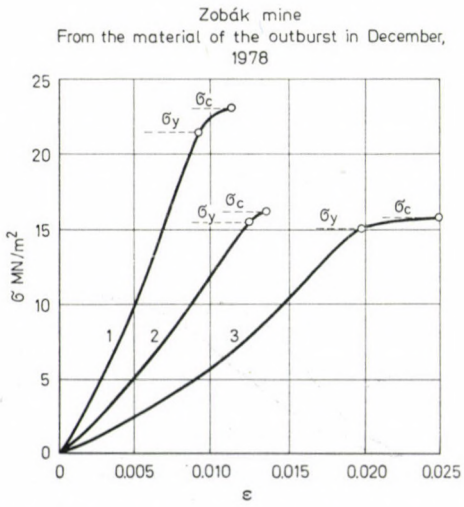

Fig. 3. Stress deformation curves of uniaxial compression experiments

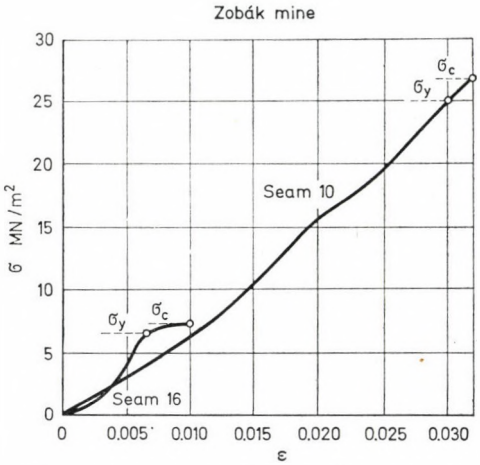

Fig. 4. Stress deformation curves of uniaxial compression experiments

taken from places of unexpected outbursts in the Zobák mine, in December 1978. According to the Figures, $q = 0.93 - 0.95$. The curves in Fig. 4 characterize the samples taken from seams 10 and 16 of level I in Zobák mine. According to the Figure, $q = 0.93$. Figure 5 illustrates curves obtained from measurements on samples from seams 3, 4 and 11 of the István mine. The quotient q is in this case 0.91—0.95. The values of 8 coal samples taken from the Mecsek region show hardly any scatter, they vary between 0.91 and 0.95. These values indicate a coal type that is definitely brittle. At the same time, the values of other rock parameters determined for the same samples show a much higher scatter. The compressive strength is $\overline{\sigma}_C = 1.2 - 23$ MN/m²,

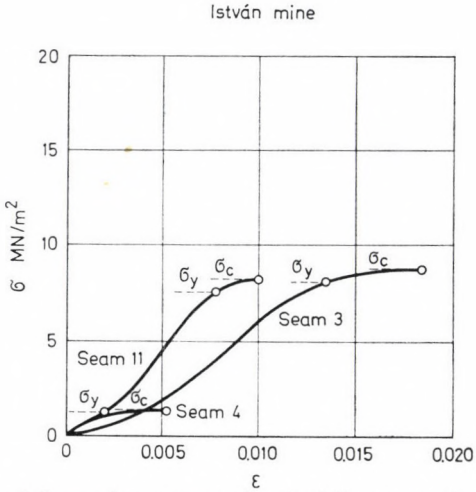

Fig. 5. Stress deformation curves of uniaxial compression experiments

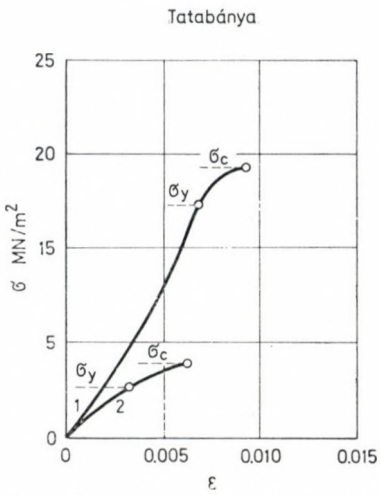

Fig. 6. Stress deformation curves of uniaxial compression experiments

the tensile strength $\overline{\sigma}_T = 0.1 - 2$ MN/m², Young's modulus $\overline{E} = 350 - 2500$ MN/m², Brinke's number $\overline{B} = 12 - 24$ and Poisson's ratio $\overline{m} = 2.1 - 2.5$. The water content of the coal samples varied between 1.0 and 1.5%.

The $\sigma - \varepsilon$ curves of coal samples from shaft XII in Tatabánya are illustrated in Fig. 6. The corresponding parameters are: $q = 0.58 - 0.84$, $\overline{\sigma}_C = 4 - 25$ MN/m² and $\overline{E} = 2100$ MN/m². The water content of the samples was around 15%. Figure 7 illustrates the $\sigma - \varepsilon$ curves of dried coal samples from Tatabánya. In this case $q = 0.91 - 0.93$, $\overline{\sigma}_C = 7 - 12$ MN/m² and $\overline{E} = 1200 - 2400$ MN/m².

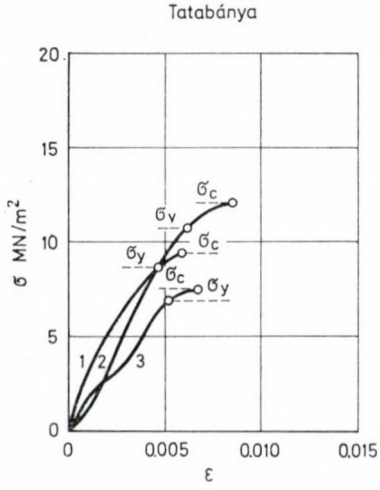

Fig. 7. Stress deformation curves of uniaxial compression experiments

The results show that the brittleness or toughness of the coal types are in correlation with natural water content. Coal types with higher natural water content are less brittle, those with lower water content are very brittle. The natural water content of the coal layers in Mecsek is between 2 and 5%, in Tatabánya it is around 15%. On the basis of the available data it can be stated that values of $q_1 = 0.90 - 0.95$ characterize the Mecsek coal layers and $q_2 = 0.60 - 0.85$ the Tatabánya ones. It follows from Eq. (14) that a pore gas pressure higher by a factor of

$$\frac{1 - q_2}{1 - q_1} = \frac{0.15 - 0.40}{0.05 - 0.10} = 3 - 4$$

would be required to initiate an outburst under the Tatabánya circumstances. This is the main reason why no outburst danger has ever occurred in the gas-rich coal layers of Tatabánya.

It can also be generally stated that tough, less brittle, gas-rich coals are not affected by the danger of outburst while brittle, less tough, gas-rich coals show a great outburst danger. The tough character of the coal is usually accompanied by a great *in situ* strength while brittle coals have a lower *in situ* strength. This fact also contributes to the difference in outburst danger.

A common experience, that in some coal basins (e.g. Mecsek) a very low pore gas pressure, $p = 0.2 - 0.3$ MPa is sufficient to cause outbursts, while in other places such a pore gas pressure should not be considered outburst dangerous. Equation (14) clearly shows that if the coal is brittle and its *in situ* strength is low then a very low pore gas pressure is sufficient to initiate the chain-reaction-like outburst mechanism.

Laboratory measurements performed on coal samples taken from the material of a sudden outburst in the Zobák mine, 1978, gave the following average values:

$$\bar{\sigma}_C = 23 \text{ MN/m}^2$$

$$\bar{\sigma}_T = 0.4 \text{ MN/m}^2$$

$$q = 0.94$$

$$\bar{B} = 57$$

$$B = 2.5 \text{ (estimated)}.$$

Using Eq. (20), the *in situ* compressive strength of a highly cokified, cracked coal can be calculated as $\sigma_C = 4.8$ MN/m². The pore gas pressure required to provoke an outburst can be written as

$$p > \sigma_C \frac{1 - q}{B - 1} = 4.8 \frac{1 - 0.94}{2.5 - 1} = 0.19 \text{ MPa}.$$

Thus, in the given case, a slightly higher pore gas pressure than 0.19 MPa is sufficient to cause outbursts. As a matter of fact, measurements established the same magnitude of pore gas pressure at the place of outburst.

This example also suggests the conclusion that in the surrounding of intrusions there is a great outburst danger, first of all because of the extreme brittleness of cokified coal.

Using the interdependence of the parameters determining the danger of outburst, several observations about outbursts can be explained. Equation (14) can be used in almost all fields of the struggle against outbursts, therefore this relationship is of a great practical importance.

REFERENCES

1. SZIRTES, L.: Szén és gázkitörések leküzdése (Struggle Against Coal and Gas Outbursts). Műszaki Könyvkiadó, Budapest. 1971.
2. KOVÁCS, F.: A gázkitörésveszély várható mértékének meghatározása és gazdasági hatásának értékelése (Determination of the Expected Measure of Gas Outburst Danger and Evaluation of its Economic Effects). Doctor's Thesis. Hungarian Academy of Sciences. Miskolc. 1975.
3. ХОДОТ, В. В. и др.: Физико-химия газодинамических явлений в шахтах. Издательство «Наука», Москва, 1973.
4. ХОДОТ, В. В.– ШЕВЬЯКОВ, Ф. Д.: Итоги работы института им. А. А. Скочинского в области борьбы с газодинамическими явлениями в угольных шахтах. Внезапные выбросы в угольных шахтах. Издательство «Недра», Москва, 1970.
5. ЧЕРНОВ, В. И.– ПУЗЫРЁВ, В. Н.: Работы Вост. НИИ по совершенствованию разработки угольных пластов восточных бассейнов, опасных по внезапным выбросам угля и газа. Внезапные выбросы в угольных шахтах. Издательство «Недра», Москва, 1970.
6. ЧЕРНОВ, В. И.: О прогнозе внезапных выбросов угля и газа в Кузбассе на больших глубинах. Физико-технические проблемы разработки полезных ископаемых. АН СССР, Сибирское отделение, 1966. 3.
7. ХАШИН, Б. Н.– ЛУДЗИШ, В. С.: Некоторые особенности проявления внезапных выбросов на шахтах прокопьевского месторождения Кузбасса. Физико-технические проблемы разработки полезных ископаемых. АН СССР, Сибирское отделение, 1974. 2.
8. ФЕЙТ, Г. Н.: Вероятность внезапных выбросов угля и газа в различных горногеологических условиях. Внезапные выбросы в угольных шахтах. Издательство «Недра», Москва, 1970.
9. ФЕЙТ, Г. Н.: Метод прогноза выбросоопасности угольных пластов по физико-химическим показателям. Физико-технические проблемы разработки полезных ископаемых. АН СССР, Сибирское отбеление, 1968. 2.
10. SOMOSVÁRI, Zs.: Investigation of the deterioration of the rock-gas system to clarify the cause of rock and gas outbursts. *Acta Geod. Geoph. Mont. Hung.*, 15 (1980), 257—269.
11. SOMOSVÁRI, Zs.: Investigation of the load assumption of rock-gas systems, aiming at the detection of the causes of rock and gas outbursts. *Acta Geod. Geoph. Mont. Hung.*, 15 (1980), 271—294.
12. SOMOSVÁRI, Zs.: Investigation of the rock-gas system in front of the face of working in order to determine the cause of rock and gas outbursts. *Acta Geod. Geoph. Mont. Hung.*, 16 (1981), 131—150.
13. SOMOSVÁRI, Zs.: Investigation of the zone in front of road heads in order to determine the cause of rock and gas outbursts. *Acta Geod. Geoph. Mont. Hung.*, 17 (1982), 1—28.
14. SOMOSVÁRI, Zs.: Mechanism of rock and gas outbursts. *Acta Geod. Geoph. Mont. Hung.*, 17 (1982), 29—49.

ОСНОВНЫЕ ПАРАМЕТРЫ ВЫБРОСООПАСНОСТИ ПОРОД И ГАЗОВ

Ж. ШОМОШВАРИ

РЕЗЮМЕ

В статье на основе механизма выброса вызванного механическими и термическими взаимодействиями двух фаз несущей системы порода-газ определяются общепринятые основные параметры выбросоопасности и функциональная зависимость выбросоопасности от основных параметров. Основными параметрами выбросоопасности являются: давление поровых газов, сопротивление давлению и угол внутреннего трения газообильной породы и отношение условного предела текучести к сопротивлению давлению, выражающее хрупкость и цепкость породы.

На основе функциональной зависимости выбросоопасности от основных параметров в статье дается объяснение такого основополагающего опыта, соответственно которому менее газообильный уголь часто является выбросоопасным, а более газообильный уголь не характеризуется выбросоопасностью. В отдельных областях совсем малое давление поровых газов достаточно для наступления выброса, а в других областях такое давление поровых не ведет к выбросоопасности.

Статья обращает внимание на то, что зависимость, определяющую выбросоопасность от главных параметров можно использовать почти во всех областях в борьбе с внезапными выбросами газов, поэтому она имеет исключительно большое практическое значение.

Acta Geodaet., Geophys. et Montanist. Acad. Sci. Hung. Volume 17 (1), pp. 67—79 (1982)

MECHANISM OF ACTION OF PROVOKING EXPLOSIONS

ZS. SOMOSVÁRI

TECHNICAL UNIVERSITY OF HEAVY INDUSTRY, MISKOLC

[Manuscript received January 30, 1980]

The study summarizes the causes and conditions of rock and gas outbursts and some new results explaining the action mechanism of outbursts, by analysing the interactions of the two phases of the load-bearing rock–gas system. It is pointed out that outbursts triggered by provoking explosions come about in exactly the same way as outbursts generally do. The action mechanism of provoking explosions is described and the causes of outbursts occurring with a delay after provoking explosions are analysed. The study proves that seismic vibrations caused by explosions are not direct causes of the outbursts. They can only be considered as indirect causes as far as they bring about changes in the affected rock zone that satisfy the conditions of outbursts.

Symbole

σ	total normal stress
$\bar{\sigma}_z$	primary vertical total stress
$\bar{\sigma}_z'$	primary vertical effective stress
τ'	effective shear limit stress
p_0	initial pore gas pressure
p	pore gas pressure
Δp	change of pore gas pressure
p_{max}	maximum pore gas pressure
ϱ	average bulk density of overburden layers over the gas-bearing layer
g	acceleration due to gravity
c	cohesion of the rock
c'	cohesion of the rock under the effect of pore gas pressure
Φ	angle of internal friction of the rock
σ_Y	yield point of the rock
B	Brinke's number
σ_C	uniaxial compressive strength
σ_C'	uniaxial compressive strength of the rock
q	coefficient characterizing the brittleness of the rock
σ_{Ct}'	triaxial compressive strength of the rock under the effect of pore gas pressure
σ_3'	lateral effective principal stress
$\Delta V/V$	specific volume change of the rock
e_0	initial void ratio of the rock
E	Young's modulus of the rock
m	Poisson's ratio of the rock

On of the most widely used preventive methods against unexpected rock and gas outbursts is the *provoking explosion*. The aim of this method is to cause a controlled outburst in a particular place and time thus preventing other sudden outbursts. The advantage of provoking outbursts is, as compared with other local protective methods, that they can be applied in every case (if explosions are permitted) even if the use of other local protective methods would be accompanied with the danger of sudden outburst. The only disadvan-

tage of provoking explosions is that they greatly hinder the normal working procedure [10].

Two versions of provoking explosions have been developed: the French and the Belgian methods [10]. The French method, apart from shaking the solid rock body, also ensures winnings. In the Belgian method the only effect of the explosion is the vibration of the coal layers of low strength. The technologies of provoking explosions adapted at the Mecsek Coal Mines are similar to the Belgian method.

Outbursts triggered by provoking explosions set in, in certain cases, with a delay and unexpectedly. Experience has shown that delayed outbursts occur in the majority of cases when coal layers of low strength are provoked. In coal layers of great strength, e.g. in Lower Silesia, the provoking explosion either causes immediately an outburst or no outburst sets in even after a delay [10]. Under such circumstances, the provoking explosion gives a 100 per cent protection against outbursts.

Under the circumstances of the Mecsek Coal Mines, in coal layers of extremely low strength, outbursts with a certain delay after provoking explosions occur rather frequently: their proportion is about 20% [10]. In order to decrease the frequency of delayed outbursts we have to understand the action mechanism of provoking explosions, a task that has not yet been solved by the research workers. Most theories try to attribute the cause of outbursts to the seismic vibrations of sufficient energy evoked by the explosion and they derive the mechanism of action starting from this point. Experience, however, shows that earthquakes have never caused any outbursts. This fact casts a strong doubt on seismic vibrations as a direct cause of outbursts [1].

The action mechanism of provoking explosions cannot be expected to be fully understood until the basic causes and conditions of outbursts are satisfactorily explained, even though this might seem an unusually hard task. However, this problem has to be solved first if we aim to achieve any further progress in the protection against outbursts and in planning the protection technologies.

Outbursts are determined by many parameters. Obviously, some of them determine basically the conditions of outbursts while some others only influence the danger of outburst. The many variables and the great amount of accumulated experience indicate the need of a research based on systems theory. An investigation with such a point of view can reveal the parameters affecting the rise of outbursts but first of all the correlation or correlations that determine the conditions of outbursts.

The main feature of our research is that unlike the most of modern research trends, it does not analyse the individual behaviour of the rock and gas phases but emphasizes their interactions [3, 4, 5, 6, 7, 8, 9]. Thus the subject of the analysis is the complicated interactions between the phases

of the load-bearing rock–gas system. The two phases of the load-bearing rock–gas system are in

chemical,
thermal, and
mechanical

interactions. These interactions can be analysed by means of the laws of continuum mechanics and irreversible thermodynamics. At the beginning of our investigations, based on experience, outbursts have been assumed as essentially mechanical phenomena. Consequently, first of all the mechanical interactions of the two phases have been thoroughly investigated. Of course, the thermodynamical changes of state of the gas have not been neglected. Various observations of outbursts proved the results obtained from the analyses.

Another feature of our research method is that it seeks the causes of outbursts independently of the material or quality of the rock, only common characteristics of the various rocks are taken into consideration. The most important of these is that rocks are considered as porous media where pores and cracks form a more or less communicating system. Thus the analysis of the rise of outbursts is not bound to the structure of the coal unlikely to the other — to our mind incorrect — methods of investigation. The theoretical analyses in our research have always been carried out so as to take into consideration the real rock–gas system. Essentially, the effect of opening excavations on the gas-bearing rock (rock–gas system) has been investigate. Thus, our investigations form a part of the research of natural systems based on systems theory suggested by L. Kapolyi.

1. Requirements towards a new theory of outbursts

A universally valid theory of the rise of outbursts has to explain all observations regarding rock and gas outbursts irrespective of the fact whether the outburst is a coal–gas, salt–gas or sandstone–gas one, the outstreaming gas is CH_4, CO_2 or N_2 and the outburst happens in a drift, working, room or shaft [6].

The requirements can be summarized as follows:

a) Any universally valid theory should give an equally valid explanation for the basic causes, conditions and mechanism of coal–gas, salt–gas, sandstone–gas or, in general, rock–gas outbursts.

b) The theory should enable us to derive numerically, and to determine in form of formulae, the main parameters and all essential factors affecting the danger of outburst. These main parameters and factors have to characterize the danger of coal–gas, salt–gas and sandstone–gas outbursts as well.

c) The theory has to answer the principal question: why does no outburst occur in certain layers in spite of their great gas content while at other places, rocks with a much lower gas content show a great danger of outburst.

d) The theory must explain the outbursts in drifts, workings, rooms and at shaft soles, and the experience why outbursts occur most frequently in drifts, while they are extremely rare at shaft soles.

e) The theory should explain the experience that outbursts never set in when the layers affected by outburst danger are penetrated by boreholes from the surface.

f) The theory has to explain the experience that no outburst occurs in the workings of coal layers of low strength while they do occur in coal layers of great strength.

g) The theory has to explain the experience that outburst may occur at some places with extremely low initial pore gas pressure of 0.2—0.3 MPa, while in certain cases a much greater initial pore gas pressure, 4—5 MPa is necessary to cause an outburst.

h) The theory has to answer the quantitative questions of the intensity of outbursts: why does the intensity increase with increasing working depth.

2. Basic causes, conditions and the mechanism of the outbursts based on the new theory of outburst

The results of our investigations can be summarized as follows [3, 4, 5, 6, 7, 8, 9]. When load, load assumption and stresses of the load-bearing rock–gas system are dealt with, stresses in the solid structure of the rock and in the pore gas have to be clearly distinguished. The stresses in the solid structure of the rock are called *effective stresses* — keeping with the terminology of soil mechanics — while those in the free gas in the pores are called *pore gas pressure*. The sum of these two stresses is the so-called *total* or *whole* stress.

The external load on the system determines the total stress. For example a horizontal gas-bearing rock layer in the earth's crust is loaded by a vertical total principal stress

$$\bar{\sigma}_z = H\varrho g \tag{1}$$

with ϱ the average bulk density of the overburden layers above the gas-bearing layer,
g acceleration due to gravity,
H depth.

If the pressure of the free gas in the pores of the gas-bearing rock is p_0 then:

$$\bar{\sigma}_z = H\varrho g = \bar{\sigma}'_z + p_0 . \tag{2}$$

This means that the effective vertical stress in the solid structure of the rock becomes

$$\overline{\sigma}'_z = H\varrho g - p_0 . \tag{3}$$

Consequently, the load on the gas-bearing rock layer is divided between the solid structure of the rock and the pore gas. The latter relieves a part of the load from the solid structure of the rock to the extent of the pore gas pressure.

The deterioration process of the load-bearing rock–gas system plays a decisive role in the rise of outbursts. In reality, it is only the solid phase which can suffer deterioration. Nevertheless, it is suitable to call the phenomenon *the deterioration of the load-bearing rock–gas system* since due to the deterioration of the solid phase the rock–gas system ceases to exist in its previous state and with its properties, i.e. it deteriorates. After deterioration a rock–gas system with a wholly new character comes into being. Here the solid phase hardly bears any load, the system is rather a mass of solid particles suspended in gas. By calling the phenomenon deterioration of the rock–gas system, we would emphasize that the two phases are regarded as to be in a close interaction with each other, even when analysing the deterioration of the solid structure of the rock.

The equation of the linear fracture limit curve of the rock, taking into account the pore pressure (water or gas), can be written:

$$\tau' = c + (\sigma - p) \tan \Phi = (c - p \tan \Phi) + \sigma \tan \Phi = c' + \sigma \tan \Phi, \tag{4}$$

with τ' effective shear limit stress,
σ total normal stress,
c cohesion of the rock,
Φ angle of internal friction of the rock.

This is the basic equation of the deterioration of rocks saturated with water, generally accepted in soil mechanics. Since the equation is independent of what kind of medium (water or gas) exerts its effect in the pores, it is the basic equation of the deterioration of the load-bearing rock–gas system as well.

The equation expresses that the pore gas pressure reduces the shear limit stress of the solid structure of the rock. The greater the pore gas pressure and the angle of internal friction of the rock, the greater this reduction. The pore gas pressure exerts its effect in such a way that it reduces cohesion to the value of $c' = c - p \tan \Phi$.

The equation of the fracture limit line can be written in the following more practical form:

$$\tau' = \frac{\sigma_C}{2\sqrt{B}} \left[1 + \frac{B-1}{\sigma_C} (\sigma - p) \right] \tag{5}$$

with σ_C uniaxial compressive strength in the rock without the effect of pore gas ($p = 0$),

$$B = \tan^2\left(45 + \frac{\Phi}{2}\right). \tag{6}$$

The uniaxial compressive strength of the rock becomes in the presence of pore gas

$$\sigma'_C = \sigma_C - (B - 1)\, p \tag{7}$$

cohesion being given by

$$c' = c - p\frac{B - 1}{2\sqrt{B}}. \tag{8}$$

The triaxial compressive strength of the gas-bearing rock can be written as

$$\sigma'_{Ct} = \sigma'_C + B\sigma'_3 = \sigma_C - (B - 1)\, p + B\sigma'_3 \tag{9}$$

where σ'_3 is the lateral effective principal stress.

The deterioration process of rocks with no pore gas under the effect of quasistatic load can be schematically described as follows. With the increase of the load on the rock, in the weakest point or points of surfaces with the most unfavourable stress, suddenly deterioration ensues. This transfers a certain excess load on the surrounding rock points. Therefore, deterioration sets in at points of greater strength, too, which transfers much higher load on the still intact and strong rock points in the neighbourhood. Thus, deterioration also comes about in these points. Finally, when even the strongest points of the rock deteriorate the process of deterioration comes to an end. The excess load, caused by the deterioration of rock particles, reaches the surrounding stronger rock points in impulses. The speed of the process depends, for this reason, also on Young's modulus. The greater the Young's modulus, the greater the speed of deterioration, similarly to the velocity of elastic waves. This explains the observations gained in laboratory compression experiments that rock specimens of great strength, great Young's modulus and less degree of non-homogeneity, deteriorate in many cases in an explosion-like fashion.

In the presence of pore gas, the deterioration process becomes more complex. Essentially, two processes have to be distinguished in the deterioration of the load-bearing rock–gas system, depending on whether the specific volume change of the rock during deterioration is a reduction ($\Delta V/V > 0$) or an increase ($\Delta V/V < 0$).

Type A. The load on the rock causes a specific reduction of volume ($\Delta V/V > 0$). If the deterioration of the solid structure starts under such circumstances then while the solid structure gradually ceases to carry load, the volume reduction gets more intensive, load is transferred to the pore gas,

consequently, pore gas pressure increases. The increase of the pore gas pressure reduces the strength of the rock thus the deterioration process becomes greatly accelerated. Under such circumstances, deterioration of the solid structure of the rock ensues in a very short time, in the form of an explosion, while pore gas pressure further increases.

Type B. The load on the rock causes a specific increase of volume ($\Delta V/V < 0$). If the deterioration of the solid structure starts under such circumstances, then while the solid structure gradually ceases to carry load, the volume increase gets more intensive, in consequence, pore gas pressure decreases. A reduction in the pore gas pressure results in a strength increase thus the deterioration process is slowed down. Under such circumstances, the deterioration of the solid structure of the rock proceeds slowly, not like an explosion and the pore gas pressure gradually decreases.

In mining practice, there are examples of rock deterioration with a specific volume reduction or a specific volume increase as well. Rock deterioration at rock faces (drift face, shaft sole and very frequently at faces of working, too) is accompanied by a specific volume reduction. On the contrary, rock deterioration at the mantles of drifts of circular cross section and shafts is accompanied by a specific volume increase. Recalling that outbursts always occur at rock face (drift face, shaft sole or working) while they never do at mantles of drifts of circular cross section and shafts, it becomes obvious that an indispensable condition of outbursts is the specific volume reduction of the rock, i.e.

$$\frac{\Delta V}{V} > 0 \tag{10}$$

or a load producing this volume change because in this case $\Delta p > 0$. Considering the type A deterioration of the load-bearing rock–gas system, the basic causes of outbursts can be summed up as:

— the effect of the pore gas pressure reducing rock strength, and
— its effect accelerating the deterioration process.

The outburst itself is nothing else but a deterioration process of the load-bearing rock–gas system that proceeds explosion-like if $\Delta V/V > 0$. The deterioration of the load-bearing rock–gas system does not always cause an outburst. If $\Delta V/V < 0$ is valid during deterioration (type B) then no outburst ensues.

All in all, the basic condition of outbursts is that the load should exceed the strength of the gas-bearing rock face: this will bring about deterioration. This is the necessary, but not sufficient condition of the outburst. Besides this another condition that has to be satisfied is that the volume change of the rock be a volume reduction.

The necessity of this latter condition becomes obvious if we take into account the experience that in the Pécs region in S. Hungary, where cracked coal layers of low strength are mined, no outburst occurs in the workings while they are rather frequent in workings of stronger coal layers in other places of the world [2, 10]. It can be proved [5, 9] that the real explanation for this observation is that the displacement of the face towards the mining excavation is so great in these cracked coal layers of small strength and small Poisson's ratio that the volume change of the rock at and in front of the face is an increase. In such cases the deterioration of the rock at the faces of workings does not cause outbursts.

According to these considerations, the mechanism of outbursts can be explained as follows. The face, and the rock zone in front of the face driven, is loaded with an excess load transferred from the zone above the excavation. Therefore, the stresses in the zone in front of the face are greater than in other zones farther away and they are also less favourable because the free side of the face has no support. Due to the excess load, the rock zone in front of the face suffers volume reduction and the initial pore gas pressure increases to a value $p > p_0$. The increase of the pore gas pressure reduces the initial strength of the rock. If the stress in the solid structure of the rock exceeds the strength of the rock zone in front of the face, deterioration starts in this zone. At the beginning of the deterioration the rock volume decreases, the pore gas pressure increases, consequently, the strength of the rock decreases further. The deterioration then goes on with an increased speed, rock volume further decreases, pore gas pressure increases, strength reduces and so on. Thus, the self-strengthening chain reaction-like process starts, resulting at the end in a high gas pressure and a rock structure that is hardly able to carry any further load and can only exert some internal resistance by means of friction. The high gas pressure removes the front rock zone that is usually in a plastic state and of low gas permeability, thus an outburst ensues throwing a great amount of gas and rock into the open mine space. During outburst the pressure of the free gas is drastically reduced, in consequence of this a great amount of desorbed gas gets into the mine air.

It can be seen that the adsorbed gas plays a passive role in the process as compared with the free gas, even though its amount exceeds that of the free gas.

The mechanism of outbursts should be considered as a deterioration process of the load-bearing rock–gas system automatically enforcing and accelerating itself, in a chain reaction-like manner. Similar kinds of chain reactions can be recognized in most dynamic phenomena of nature.

3. Main parameters of the danger of outburst

The main characteristics of outburst danger should be parameters that characterize the danger independently of the local circumstances, they should be equally valid for coal–gas, salt–gas, and sandstone–gas outbursts in shafts, drifts or workings as well. A set of such parameters is contained in the inequality describing the basic condition of outbursts [6, 9].

The condition of deterioration of the gas-bearing rock can be written as

$$\frac{\sigma_C}{p_{\max}} \leq \frac{\tan^2\left(45 + \frac{\Phi}{2}\right) - 1}{1 - q}; \quad q = \frac{\sigma_Y}{\sigma_C} \tag{11}$$

for the case of a drift face, working face or a shaft sole as well [6, 9], with $p_{\max}$ being the maximum pore gas pressure in front of the rock face and σ_Y the yield point of the rock. This inequality expresses the most important necessary, although not sufficient, condition of outbursts. An outburst can occur only if the condition

$$\Delta V/V > 0 \quad \text{or} \quad \Delta p > 0$$

is also satisfied.

The inequality expressing the basic condition of outbursts is satisfied if the compressive strength of the rock is low, the pore gas pressure in front of the rock face and the angle of internal friction are great and the yield point of the rock approaches the compressive strength as close as possible.

The inequality expressing the basic condition of outbursts enables us to answer many essential questions, as e.g. why a very low pore gas pressure is sufficient to initiate outbursts in certain cases while in other cases no outburst ensues but for very great pore gas pressures. Inequality (11) shows that if the strength of the rock is low, i.e. $\sigma_C \to 0$ and it is very brittle, i.e. $q \to 1$, then a very low pore gas pressure $p_{\max} \to 0$ is sufficient to cause deterioration of the load-bearing rock–gas system, i.e. to initiate an outbursts. If rock strength is great and the rock is tough, i.e. q is small, a high pore gas pressure is needed to cause outburst.

If the above inequality is not satisfied, no outburst can ensue, even in gas-rich coal layers. This explains the observation that many mines with great gas outputs are not dangerous for outburst.

There are some further parameters that cannot be considered as main factors, but are still important for the characterization of the danger of outburst:

— void ratio of the gas-bearing rock e_0,
— Young's modulus of the gas-bearing rock E,
— Poisson's ratio of the gas-bearing rock m.

These parameters characterize the outburst danger independently of the quality of material (coal, salt or sandstone). Furthermore, if the maximum pore gas pressure p_{max} in front of the rock face is expressed as a function of the initial pore gas pressure p_0, the inequality expressing the condition of deterioration of the load-bearing rock–gas system will also contain the parameters e_0, E and m [9]. However, the condition of deterioration expressed this way gives different inequalities for drifts, workings and shafts. Therefore, according to our view concerning the main parameters, the parameters e_0, E and m should not be considered as main parameters of the outbursts.

If the Young's modulus of the rock is smaller, the change of volume of the rock — i.e. the change of the pore gas pressure as well — becomes greater at the same stress, foı this reason the danger of outburst is greater. If the void ratio of the rock is small, the pore gas pressure varies more intensively with the volume change of the rock, therefore the danger of outburst is greater. If the Poisson's ratio is great, the rock at the face moves only slightly towards the open space: the volume reduction and the increase of the pore gas pressure are greater and, consequently, also the danger of outburst is greater.

The void ratio, Young's modulus, Poisson's ratio and the strength of the rock are not independent quantities. Generally, rocks that are more compact and have a smaller porosity and void ratio, possess greater strength, Young's modulus and Poisson's ratio. Since the compressive strength of the rock *determines* the deterioration of the load-bearing rock–gas system while the parameters E, m and e_0 only *influence* it, it might occur that the danger of outburst is greater in gas-bearing rocks of greater void ratio, or in those of smaller Young's modulus and smaller Poisson's ratio, because the strength of the rock is smaller. The porosity of sandstones of the Donets and Ruhr area, e.g. where outbursts have occurred is twice as large while their strength is only half that found in sandstones without outbursts [2, 9, 10].

The equations obtained above have not included the *gas permeability* of the gas-bearing rock. This is due to the fact that the gas permeability of rocks is usually extremely small, and small values of gas permeability do not have any essential effect on the results. This does not mean, however, that the role of gas permeability could be totally neglected. In certain investigations, as e.g. in the analysis of the mechanism of outbursts following with some delay the provoking explosions, it is just the gas permeability that plays an essential role [7].

Experience has shown that gas permeability of the coal affected by an outburst is in some cases five times smaller than otherwise [10]. Since gas permeability is determined first of all by the porosity — the smaller the porosity, the smaller is the gas permeability — this experience indicates that the danger of outburst increases with the decrease of the porosity or void ratio.

4. Mechanism of action of provoking explosions

The causes and conditions of outbursts triggered by provoking explosions must be the very same as the causes and conditions of outbursts in general. Seismic vibrations of sufficient energy content cannot be direct causes of outbursts, for no earthquakes have ever caused an outburst [1]. There is also another reason, why seismic vibrations cannot be direct causes of outbursts: if the outbursts were initiated by a seismic vibration of sufficient energy content, then its delay after the provoking explosion could have been avoided by generating seismic vibrations of greater energy content. Experience, however, proves that this is not the case.

It follows from the previous considerations that seismic vibrations raised by provoking explosions cannot bring about outbursts in a direct way, only indirectly, as far as they cause changes in the surrounding rock, altering the main and influencing parameters of outbursts until they satisfy the discussed conditions of outbursts.

The force impulses generated by the provoking (shaking) explosions make the affected rock zone cracked by brittle fracture, leading to the following changes:

— the cohesion of the rock decreases while the internal friction hardly changes,
— the uniaxial compressive strength of the rock decreases,
— the Young's modulus of the rock decreases, and
— the gas permeability of the rock increases.

Only a part of these changes act so as to encourage outbursts, the other part of them act the opposite way. The decrease of the cohesion, compressive strength and Young's modulus of the rock are factors promoting outbursts while the increase of gas permeability acts against it. Therefore it is by no means sure, even when applying an otherwise adequate technology, that a provoking explosion would always bring about outbursts.

Indeed, experience shows that part of the provoking explosions bring about outbursts, another part do not, while some of them cause outbursts but with a delay.

In case of rocks of great strength, there is a danger of outburst if the pore gas pressure is great. A provoking explosion in a rock of great strength causes great reduction in the vugularity, cohesion, compressive strength and Young's modulus. At the same time, gas permeability greatly increases. Provoking explosions usually cause an outburst because of the reduction of the compressive strength if the pore gas pressure is great, i.e. if the state before the explosion was near the outburst. If pore gas pressure is small, i.e. if the state before the explosion had been far from outburst, provoking explosions

do not cause outburst, only an intensive gas evaporation due to a considerable increase in gas permeability. Thus provoking explosion is a reliable tool in such cases in the struggle against unexpected outbursts.

For a cracked coal with extremely small strength even a small pore gas pressure indicates an outburst danger. In this case, provoking explosions only slightly increase the vugularity of coal and the gas permeability, as compared with the original state, and only slightly decrease the cohesion, strength and Young's modulus. In such cases outbursts can only ensue if the state before the explosion had been very near to the outburst. If the provoking explosion does not cause an immediate outburst, a delayed outburst can be expected because the danger of outburst is increased due to reductions in strength and Young's modulus. This increase is not counterbalanced by the effect of the increased gas permeability. Consequently, in such cases, conventionally performed provoking explosions do not yield a reliable protection against unexpected outbursts.

The mechanism of delayed outbursts can be described as follows. Provoking explosions suddenly reduce rock strength and the Young's modulus and increase gas permeability in the zone before the rock face. The decrease of the Young's modulus allows for the rock volume to decrease. Since the rock is a rheological medium, this volume reduction may take a long time. The volume reduction increases pore gas pressure and the outburst suddenly sets in, according to the described mechanism.

The chance of delayed outbursts approaches zero in case of a strong rock face because, if gas pressure is high, the provoking explosion greatly increases gas permeability enabling an intensive gas flow towards the open space. Thus, the reduction of rock volume is not accompanied with an increase of pore gas pressure and the chain reaction-like rise of the outburst cannot start.

Consequently, with the help of theoretical investigations, it could be proved that provoking explosions of conventional technology can not furnish a total protection against unexpected outbursts in strongly cracked coal layers of extremely low strength. Both theory and practice indicate unequivocally that the effectiveness of provoking explosions is necessarily limited in coal layers of extremely low strength. This does not mean, of course, that no explosion technology could be planned that would be more effective than those in current use. It should be stressed, however, that in coal layers of extremely low strength, provoking explosions of special technology are required to improve the effectiveness of the protection methods.

REFERENCES

1. Hodot, V. V.: Sudden Coal and Gas Outbursts. (In Russian) *Ugletechizdat*, Moscow. 1961.
2. Kovács, F.: Connection between the gas content and strength of rocks exposed to gas outburst danger. *Acta Geod., Geoph. Mont. Hung.*, 16 (1981), 115—130.
3. Somosvári, Zs.: Investigation of the deterioration of the rock-gas system to clarify the cause of rock and gas outbursts. *Acta Geod., Geoph. Mont. Hung.*, 15 (1980), 257—269.
4. Somosvári, Zs.: Investigation of the load assumption of rock-gas systems, aiming at the detection of the causes of rock and gas outbursts. *Acta Geod., Geoph. Mont. Hung.*, 15 (1980), 271—294.
5. Somosvári, Zs.: Investigation of the zone in front of road heads to determine the cause of rock and gas outbursts. *Acta Geod., Geoph. Mont. Hung.*, 17 (1982), 1—28.
6. Somosvári, Zs.: Kőzet- és gázkitörések új elmélete I—II—III (A new theory of rock and gas outbursts. Parts I, II and III). *Bányászati és Kohászati Lapok, Bányászat*, 1980. No. 8. 505—515; No. 9. 610—616; No. 10. 681—687.
7. Somosvári, Zs.: On rock-mechanical investigations of provoking explosions. Paper presented at the Seminar on Explosion Techniques. Miskolc, 1979.
8. Somosvári, Zs.: Conditions of rise of rock and gas outbursts. Paper presented at the Xth International Conference on Rock and Gas Outbursts. Pécs, 1979.
9. Kovács, F.—Somosvári, Zs.: A new method of forecast based on the determination of the basic causes and conditions of rock and gas outbursts. Competition on safety of mines. Miskolc, 1979.
10. Szirtes, L.: Szén- és gázkitörések leküzdése (Struggle Against Coal and Gas Outbursts). Műszaki Könyvkiadó, Budapest 1971.

ПРИНЦИП ДЕЙСТВИЯ ПРОВОКАЦИОННЫХ ВЗРЫВОВ

Ж. ШОМОШВАРИ

РЕЗЮМЕ

Одним из наиболее распространенных методов предохранения от неожиданных выбросов газов и пород является провокационный взрыв, цель которого на данном месте и в данном моменте вызывать выброс для предохранения возникновения неожиданного выброса. Преимущество провокационных взрывов по сравнению с другими локальными методами предохранения заключается в том, что их можно применять в каждом случае (если взрыв разрешается), даже в том случае, когда применение другого способа предохранения могло бы вызвать неожиданный взрыв. Недостаток провокационных взрывов заключается в том, что они мешают нормальный режим работы [10].

Существуют два метода провокационных взрывов: французский и бельгийский методы [10]. Французским методом кроме сотрясения твердой среды пород обеспечивается и отбойка. Бельгийский метод не стремится к отбойке, его влияние проявляется только через сотрясения в залежах угля малой твердости. Технологии провокационных взрывов, использованных в Объединении угольных шахт Мечек похожи на бельгийский метод.

Acta Geodaet., Geophys. et Montanist. Acad. Sci. Hung. Volume 17 (1), pp. 81—98 (1982)

MATHEMATICAL FORMALISM OF THE 2^{n-p} TYPE FIRST-POWER FACTORIAL TEST PLANNING

L. BALLA

CHEMICAL RESEARCH LABORATORY FOR MINING OF THE HUNGARIAN ACADEMY OF SCIENCES, MISKOLC

[Manuscript received October 5, 1979]

The paper deals with the mathematical formalism of the 2^{n-p} type first-power factorial test planning whereby it is supposed that the intuitive decisions needed for planning are already made on the basis of à priori informations. Mathematical formalism is given to the methods applied so far and a mathematical method is worked out for the retransformation of the transformed function. Thus, the calculations getting complicated in case of several factors can be computerized by means of algorithms developed for general cases.

Symbols

a	coefficient
D^2	square of scatter
f	function component
k	value of defining contrast
m	number of coefficients
n	number of factors
p	number of fractional factors
r, p	exponents
x	independent variable (factor)
y	dependent variable
a mod b	remain after division a/b

Indices

g	gradient
h, i, j, k, l, r	index of serial number
H	high
L	low
T	matrix transformation
-1	matrix inversion
*	transformed form

In the followings under the concept of "system" an arbitrarily limited part of the world is understood which is examined from given points of view. The effect of the environment on the system is called input signal (or signals), the response of the system to the input signal output signal (or signals). Here the case will be investigated where the number of input signals is greater than one and they are independent from each other, further the output signals depend only on the input signals.

The aim is to determine how the variation of the output signals depends on the variation of the input signals within a given range. Further on we restrict ourselves to the investigation of one output signal, since the investigation of the others is similar. This means mathematically that we look for the

function $y = \psi(\mathbf{x})$ in the range

$$x_{jL} \leqq x_j \leqq x_{jH} \qquad (j = 1, 2 \ldots n),$$

where $\mathbf{x} = \{x_j\}$.

In the majority of practical cases the mathematical model of the system is not properly known or for other reasons it is advisable to approximate the function ψ on the basis of tests with a function of the following form:

$$\psi \cong \hat{\psi} = \sum_{k=1}^{m} a_k \cdot f_k$$

where

$$f_k = \prod_{j=1}^{n} x_j r_{kj}, \quad r_{kj} \in V, \quad \mathbf{R} = \{r_{kj}\} \tag{1}$$

V is the set of the real, not-negative numbers.

We call "test" the process, when for a given combination of input signals, i.e. for $\mathbf{x}_i$ the response y_i is determined.

In the majority of cases it is sufficient to determine the first-power function, i.e., when $\hat{\psi}$ is in $r_{kj} \in \{0, 1\}$. One of the simplest and most effective method to determine a function of this type on the basis of tests is the 2^{n-p} type factorial test planning method of Box—Wilson [1], the theoretical and practical problems of which are dealt with by several authors [2, 3, 4]. The method can be easily understood, but in case of more factors the calculation becomes complicated, there are many factors to be taken into account, the possibility of mistakes increases. Therefore, it is necessary to give a mathematical form to the algorithms generally developed.

In this paper we deal only with the mathematical description of the first-power Box—Wilsonian test planning. We suppose that the intuitive decisions necessary for the planning are already made (by using à priori informations). Our task is to develop the planning matrix and to determine the coefficients a_k.

The extension of matrix operations

For the mathematical description of the test planning besides the known matrix operations the following matrix operations must also be defined:

1. — direct multiplication

$$\mathbf{A} \bigcirc \mathbf{B} = \mathbf{C} \quad \text{where} \quad c_{ij} = a_{ij} \cdot b_{ij} \tag{2}$$

2. — direct raise to power

$$\mathbf{A} \square \mathbf{B} = \mathbf{C} \quad \text{where} \quad c_{ij} = \prod_{s=1}^{n} a_{is}^{b_{sj}}. \tag{3}$$

Matrices **A** and **B** are congruous, i.e. **A** $(m \times n)$ and **B** $(n \times r)$ is fulfilled. For the multiplication and the raise to powers, the conditions and connections known for the complex numbers are valid, and let be $0^0 = 1$.

The priority order of the matrix operations is:

1) $\square$ (direct raise to power),
2) $\cdot$ (multiplication),
3) $\bigcirc, +, -$ (direct multiplication, addition, subtraction).

The following connections are valid:

ad. 1.
$$(\mathbf{A} \bigcirc \mathbf{B}) \square \mathbf{C} = \mathbf{A} \square \mathbf{C} \bigcirc \mathbf{B} \square \mathbf{C}. \tag{4}$$

The (i, j) element of the matrix on the left side of (4) is $\prod_s (a_{is} \cdot b_{is})^{c_{sj}}$, the element of the right side matrix is $\prod_s a_{is}^{c_{sj}} . \prod_s b_{is}^{c_{sj}}$ on the basis of definitions 2 and 3. The (i, j) elements of the left side and of the right side matrix are the same, as it can be easily seen after carrying out the operations for $\prod$ and for the raise to power. Since (i, j) is an arbitrary element of the matrix, the matrix on the left sight is equal to that on the right side, i.e. condition (4) is fulfilled.

ad. 2.
$$(\mathbf{a} \bigcirc \mathbf{b}) \cdot \mathbf{c}^T = \mathbf{a} \cdot (\mathbf{b}^T \bigcirc \mathbf{c}^T). \tag{5}$$

The number on the left side is $\sum_s (a_s b_s)\, c_s$, that on the right side $\sum_s a_s (b_s c_s)$. When using the formulas of multiplication and addition it can be seen that Eq. (5) is fulfilled.

ad. 3.
$$\big(\mathbf{A} \square (-\mathbf{E})\big) \square \mathbf{B} = \mathbf{A} \square (-\mathbf{B}). \tag{6}$$

The (i, j) element of the left side matrix is $\prod_s (a_{is}^{-1})^{b_{sj}}$ the (i, j) element of the right side matrix $\prod_s a_{is}^{-b_{sj}}$, which are equal on the basis of the formulas concerning the raise to power and the multiplication, consequently Eq. (6) is fulfilled.

The following identity is worth mentioning, too:

$$\mathbf{A} \square (\mathbf{B} + \mathbf{C}) = \mathbf{A} \square \mathbf{B} \bigcirc \mathbf{A} \square \mathbf{C}.$$

It is not the aim of this paper to find further connections, since they are not needed for the understanding of the followings.

The method of the determination of coefficients

In order to fulfil certain statistical requirements, the Box—Wilsonian method of test planning approximates the function ψ with a function of the following form:

$$\psi \simeq \hat{\psi}^* = \sum_{l=1}^{m^*} a_l^* \cdot f_l^* \tag{7}$$

where

$$f_l^* = \sum_{j=1}^{n} x_j^* r_{lj}^* , \quad r_{lj}^* \in V, \quad \mathbf{R}^* = \{r_{lj}^*\}$$

and

$$x_j^* = \frac{x_j - \alpha_j}{\beta_j} \tag{8}$$

where

$$\alpha_j = \frac{x_{jH} + x_{jL}}{2}, \quad \alpha = \{\alpha_j\}, \quad \beta_j = \frac{x_{jH} - x_{jL}}{2}, \quad \beta = \{\beta_j\} .$$

That means that instead of the variables x_j the variables x_j^* described by the transformation formula 8 appear in the the function to be looked for. Equation 7 can be transformed into the form of Eq. (1) by the inverse transformation 8, this problem will be dealt with later.

The function $\hat{\psi}^*$ can be described with matrix operations as follows:

$$\hat{\psi}^* = \mathbf{x}^* \square \mathbf{R}^{*T} \cdot \mathbf{a}^{*T} \tag{9}$$

where

$$\mathbf{x}^* = \{x_j^*\}, \quad \mathbf{a}^* = \{a_l^*\}$$

will be determined so that $N \geq m^*$ tests will be carried out and the measured results will be adjusted on the basis of $\hat{\psi}^*$ according to the principle of the least squares, i.e.:

$$\sum_{i=1}^{N} (y_i - \hat{\psi}_i^*)^2 \to \min .$$

With matrix operations:

$$(\mathbf{y}^T - \mathbf{X}^* \square \mathbf{R}^{*T} \cdot \mathbf{a}^{*T})^T \cdot (\mathbf{y}^T - \mathbf{X}^* \square \mathbf{R}^{*T} \cdot \mathbf{a}^{*T}) \to \min$$

where

$$\mathbf{X}^* = \{\mathbf{x}_i^*\}, \ \mathbf{y} = \{y_i\} .$$

$\mathbf{X}^*$ is the planning matrix, its i-th row gives the value of $\mathbf{x}^*$ in the i-th test.

The result of the adjustment is:

$$\mathbf{a}^{*T} = [(\mathbf{X}^* \square \mathbf{R}^{*T})^T \cdot (\mathbf{X}^* \square \mathbf{R}^{*T})]^{-1} \cdot (\mathbf{X}^* \square \mathbf{R}^{*T})^T \cdot \mathbf{y}^T . \qquad (10)$$

The Box—Wilson method determines — due to the fulfilment of the statistical requirements — in case $r_{lj}^* \in \{0, 1\}$ the generally valid planning matrix that depends on the number of factors so that matrix $(\mathbf{X}^* \square \mathbf{R}^{*T})^T \cdot (\mathbf{X}^* \square \mathbf{R}^{*T})$ be a diagonal matrix, which ensures the orthogonality of the plan, further that $D^2(\hat{\psi}_g^*)$ should depend only on $|\mathbf{x}^*|$, ensuring the acceptability of the plan.

$\hat{\psi}_g^* \subseteq \hat{\psi}^*$ and contains only the main effects, i.e.:

$$\hat{\psi}_g^* = a_0^* + a_1^* x_1^* + a_2^* x_2^* + \ldots + a_n^* x_n^* .$$

$\hat{\psi}_g^*$ is used for the estimation of gradients.

The composition of the matrix R*

The element r_{lj}^* of the matrix $\mathbf{R}^*$ can be determined as follows:

$$r_{lj}^* = \begin{cases} 0 & \text{if} \quad x_j^* \not\subseteq f_l^* \\ 1 & \text{if} \quad x_j^* \subseteq f_l^* \end{cases} .$$

Let us e.g., compose the matrix $\mathbf{R}^*$ belonging to the function

$$\hat{\psi}^* = a_1^* + a_2^* x_1^* + a_3^* x_2^* + a_4^* x_3^* + a_5^* x_1^* x_2^* + a_6^* x_1^* x_2^* x_3^* .$$

As result we receive the following matrix:

$$\mathbf{R}^* = \begin{bmatrix} 0 & 0 & 0 \\ 1 & 0 & 0 \\ 0 & 1 & 0 \\ 0 & 0 & 1 \\ 1 & 1 & 0 \\ 1 & 1 & 1 \end{bmatrix} .$$

In the majority of the practical cases is of the type $\hat{\psi}^*$ containing only the individual effect of the different variables, further the effect of the product of any two variables and a constant term. In case of such type functions:

$$m^* = 1 + \binom{n}{1} + \binom{n}{2} = \frac{n(n+1)}{2} + 1 .$$

E.g., in case of three variables:

$$\hat{\psi}_3^* = a_1^* + a_2^* x_1^* + a_3^* x_2^* + a_4^* x_3^* + a_5^* x_1^* x_2^* + a_6^* x_1^* x_3^* + a_7^* x_2^* x_3^* .$$

The matrix $\mathbf{R}_3^*$ can be written in the form of the following hypermatrix:

$$\mathbf{R}_3^* = \begin{bmatrix} \mathbf{0}_3 \\ \overset{o}{\mathbf{R}}_3^* \end{bmatrix} \quad m^* = 7$$

where

$$\overset{o}{\mathbf{R}}_3^* = \begin{bmatrix} 1 & 0 & 0 \\ 0 & 1 & 0 \\ 0 & 0 & 1 \\ 1 & 1 & 0 \\ 1 & 0 & 1 \\ 0 & 1 & 1 \end{bmatrix} .$$

Number 3 in the index means the number of variables, its presence means that the function is of the above $\hat{\psi}_3^*$ type. On the basis of the groups denoted with broken lines in matrix $\overset{o}{\mathbf{R}}_3^*$ it can be easily seen that in case of n variables it will be:

$$\overset{o}{\mathbf{R}}_n^* = \begin{bmatrix} \mathbf{E}_n \\ \mathbf{s}_{n-1}^T \quad \overset{o}{\mathbf{R}}_{n-1}^* \end{bmatrix}$$

where

$$\mathbf{s}_{n-1} = \{\underbrace{1,1 \ \ldots \ 1}_{n-1}, \underbrace{0, 0, \ldots\ldots\ldots 0}_{\frac{(n-1)\cdot(n-2)}{2}}\}$$

i.e.:

$$\mathbf{R}_n^* = \begin{bmatrix} \mathbf{0}_n \\ \overset{o}{\mathbf{R}}_n^* \end{bmatrix} . \tag{11}$$

Composition of the planning matrix

The main point of the 2^{n-p} type factorial test planning is that the factors are varied on two levels, on an upper and on a lower level. The upper level is denoted by +, the lower by —, in matrix notation by 1 and —1. That means, if:

$$x_j^* = 1 \quad \text{then} \quad x_j = x_{jH}, \quad \text{if} \quad x_j^* = -1 \quad \text{then} \quad x_j = x_{jL}\,.$$

Each variation of the factors corresponds to a test setting. For an effective test it is necessary to compose the variations and the test settings according to some system.

Total factorial test

A test where all possible level combinations of the factors are realized is called a total factorial test. One method of the composition of the planning matrix $\mathbf{X}_n^*$ is that the signs change in the first column in each row, in the second column in every second rows, in the third column in every fourth rows, in the fourth column in every eighth rows, in the j-th column in every 2^{j-1} rows. For the mathematical description of this method we propose the following:

$$\mathbf{X}^*(i,j) = \begin{cases} 1 & \text{if} \quad 0 < i \mod 2^j \leq 2^{j-1} \\ -1 & \text{if} \quad \mathbf{X}^*(i,j) \neq 1 \end{cases} \tag{12}$$

or

$$\mathbf{X}^*(i,j) = \begin{cases} -1 & \text{if} \quad 0 < i \mod 2^j \leq 2^{j-1} \\ 1 & \text{if} \quad \mathbf{X}^*(i,j) \neq -1 \end{cases} \tag{13}$$

which are —1 times the other, but this is of no importance due to symmetry conditions. The correctness of the compositions (12) and (13) can be easily seen,

Table I

Serial number of test settings \ factors	x_1	x_2	x_3
1.	+	+	+
2.	—	+	+
3.	+	—	+
4.	—	—	+
5.	+	+	—
6.	—	+	—
7.	+	—	—
8.	—	—	—

e.g. let us consider the 2^3 total factorial test composed on the basis of Eq. (12) (Table I). Corresponding by the planning matrix will be

$$\mathbf{X}_3^* = \begin{bmatrix} 1 & 1 & 1 \\ -1 & 1 & 1 \\ 1 & -1 & 1 \\ -1 & -1 & 1 \\ 1 & 1 & -1 \\ -1 & 1 & -1 \\ 1 & -1 & -1 \\ -1 & -1 & -1 \end{bmatrix}.$$

If we compose $\mathbf{X}_3^*$ according to the rule of the change of signs (by starting with $+1$ in the first column) we will receive the values of Table I. An identical result can be received, too, if $\mathbf{X}_3^*$ is composed according to Eq. (13) or the rule of change is started with -1. The planning matrix which corresponds to latter is:

$$\mathbf{X}_3^* = \begin{bmatrix} -1 & -1 & -1 \\ 1 & -1 & -1 \\ -1 & 1 & -1 \\ 1 & 1 & -1 \\ -1 & -1 & 1 \\ 1 & -1 & 1 \\ -1 & 1 & 1 \\ 1 & 1 & 1 \end{bmatrix}$$

and it can be seen that this is -1 times the former.

For the planning matrix $\mathbf{X}_n^*$ the following properties are valid:

— property of symmetry

$$\sum_{i=1}^{N} \mathbf{X}_n^*(i, j) = 0 \tag{14}$$

— property of norming

$$\sum_{i=1}^{N} [\mathbf{X}_n^*(i, j)]^2 = N \tag{15}$$

— property of orthogonality

$$\sum_{i=1}^{N} \prod_{j=1}^{n} [\mathbf{X}_n^*(i, j)] r_j = \begin{cases} 0 & \text{if} \quad \max\limits_{j} \quad r_j = 1 \\ N & \text{if} \quad \max\limits_{j} \quad r_j = 0 \end{cases} \qquad r_j \in \{0, 1\} \tag{16}$$

— property of possibility of rotation

$$D^2(\hat{\psi}_g^*) = D^2(y) \cdot \frac{1 + |\mathbf{x}^*|^2}{N} \qquad |\mathbf{x}^*|^2 = \sum_{j=1}^{n} x_j^{*2} \tag{17}$$

where $N = 2^n$ is the number of the test settings.

Fractional factorial test

In case of the total factorial test the difference between the number of test settings and the number of coefficients can be great, i.e.: $N \gg m^*$. This raises the problem of redundant tests, which, can be solved by the fractional factorial test, where the number of test settings is decreased so that the planning does not loose its characteristics of symmetry, norming, orthogonality and possibility of rotation.

The main point of the method is that among the n factors, p factors are set equal to the product of factors selected from the remaining $n - p$ factors according to certain aspects. E.g.: in the 2^{3-1} fractional test be $x_3^* = x_1^* \cdot x_2^*$, correspondingly the defining contrast will be $1 = x_1^* \cdot x_2^* \cdot x_3^*$. (The defining contrast is the product of columns all elements of which are either 1 or —1.)

The general formula of the method is:

$$\begin{gathered} x_h^* = k_h \prod_{j=1}^{n-p} x_j^* p_{hj} \\ h = n - p + 1, \ \ldots n, \ k_h \in \{-1, 1\}, \ p_{hj} = \{0, 1\} \ \ \mathbf{P} = \{p_{hj}\} \end{gathered} \tag{18}$$

where

$$p_{hj} = \begin{cases} 1, \text{ if } x_j^* \text{ is taken into account in the } h\text{-th factor} \\ 0, \text{ if } x_j^* \text{ is not taken into account in the } h\text{-th factor.} \end{cases}$$

Thus, the planning matrix of the 2^{n-p} fractional factorial test is a hypermatrix composed of the planning matrix of the 2^{n-p} total factorial test and of the matrix determined on the basis of Eq. (18):

$$\mathbf{X}_{n,p}^* = [\mathbf{X}_{n-p}^* \quad \mathbf{X}_{n-p}^* \,\square\, \mathbf{P}^T \,\bigcirc\, \mathbf{K}^T]\,. \tag{19}$$

K can be easily obtained as the following hypermatrix:

$$\mathbf{K} = [\underbrace{\mathbf{k}^T \mathbf{k}^T \ldots \mathbf{k}^T}_{N}]$$

where

$$\mathbf{k} = \{k_h\}\,.$$

The characteristics (14), (15), (16), (17) are also valid for the planning matrix $\mathbf{X}^*_{n,p}$, $N = 2^{n-p}$ is the number of test settings.

E.g., let us compose the planning matrix of the 2^{6-3} fractional factorial test, where $x_4^* = x_1^* \cdot x_2^*$, $x_5^* = -x_2^* \cdot x_3^*$, $x_6^* = x_1^* \cdot x_2^* \cdot x_3^*$.

$\mathbf{X}_3^*$ has been already composed earlier according to Eq. (12):

$$\mathbf{P} = \begin{bmatrix} 1 & 1 & 0 \\ 0 & 1 & 1 \\ 1 & 1 & 1 \end{bmatrix}.$$

The matrix $\mathbf{K}$ is:

$$\mathbf{K} = \begin{bmatrix} 1 & 1 & 1 & 1 & 1 & 1 \\ -1 & -1 & -1 & -1 & -1 & -1 \\ 1 & 1 & 1 & 1 & 1 & 1 \end{bmatrix}.$$

By using these, the planning matrix $\mathbf{X}^*_{6,3}$ will be on the basis of Eq. (19):

$$\mathbf{X}^*_{6,3} = [\mathbf{X}_3^* \quad \mathbf{X}_3^* \,\square\, \mathbf{P}^T \bigcirc \mathbf{K}]$$

$$\mathbf{X}^*_{6,3} = \begin{bmatrix} 1 & 1 & 1 & 1 & -1 & 1 \\ -1 & 1 & 1 & -1 & -1 & -1 \\ 1 & -1 & 1 & -1 & 1 & -1 \\ -1 & -1 & 1 & 1 & 1 & 1 \\ 1 & 1 & -1 & 1 & 1 & -1 \\ -1 & 1 & -1 & -1 & 1 & 1 \\ 1 & -1 & -1 & -1 & -1 & 1 \\ -1 & -1 & -1 & 1 & -1 & -1 \end{bmatrix}.$$

Determination of a*

At a first-power test planning it is $r_{ij}^* \in \{0, 1\}$, and by using the characteristics (14), (15), (16) it can be proved that

$$(\mathbf{X}^* \,\square\, \mathbf{R}^{*T})^T \cdot (\mathbf{X}^* \,\square\, \mathbf{R}^{*T}) = N \cdot \mathbf{E}_{m*}\,.$$

That means that Eq. (10) can be reduced to the following form:

$$\mathbf{a}^{*T} = \frac{1}{N} \cdot (\mathbf{X}^* \,\square\, \mathbf{R}^{*T})^T \cdot \mathbf{y}^T\,. \tag{20}$$

For the coefficients the followings are valid:

$$D^2(a_l^*) = \frac{D^2(y)}{N} \qquad l = 1, 2 \ldots m^* \tag{21}$$

as well as

$$\operatorname{cov}(a_l^*, a_r^*) = 0 \quad l \neq r \quad l, r = 1, 2 \ldots m^*.$$

The square of the residual scatter necessary to statistical investigations is:

$$D_{\text{res}}^2 = \frac{\mathbf{y}\mathbf{y}^T - \mathbf{a}^* \cdot (\mathbf{X}^* \,\square\, \mathbf{R}^{*T})^T \cdot \mathbf{y}^T}{N - m^*}. \tag{22}$$

Determination of a

For practical requirements it is necessary to retransform the function $\hat{\psi}^*$ into function $\hat{\psi}$, i.e. it should be valid for each $\mathbf{x}$:

$$\hat{\psi} = \hat{\psi}^*.$$

In a matrix form:

$$\mathbf{x} \,\square\, \mathbf{R}^T \cdot \mathbf{a}^T = \mathbf{x}^* \,\square\, \mathbf{R}^{*T} \cdot \mathbf{a}^{*T}. \tag{23}$$

$\mathbf{R}$ and $\mathbf{a}$ are to be determined.

From Eq. (8):

$$\mathbf{x}^* = (\mathbf{x} - \alpha) \bigcirc \beta \,\square\, (-\mathbf{E}).$$

Substituting this into the right side of Eq. (23) and using (4) and (6):

$$\mathbf{x}^* \,\square\, \mathbf{R}^{*T} \cdot \mathbf{a}^{*T} = (\mathbf{x} - \alpha) \,\square\, \mathbf{R}^{*T} \bigcirc \beta \,\square\, (-\mathbf{R}^{*T}) \cdot \mathbf{a}^{*T}. \tag{24}$$

Let us investigate in more dctails one member $(\mathbf{x} - \alpha) \,\square\, r_l^{*T}$ of the vector $(\mathbf{x} - \alpha) \,\square\, \mathbf{R}^{*T}$. It can be written:

$$\begin{aligned}(\mathbf{x} - \alpha) \,\square\, \mathbf{r}_l^{*T} &= \prod_{j=1}^{n} (x_j - \alpha_j)^{r_{lj}^*} = \prod_{j=1}^{n} \left[\sum_{r=0}^{r_{lj}^*} x_j^r \cdot \binom{r_{lj}^*}{r} (-\alpha_j)^{r_j^* - r} \right] = \\ &= \sum_{r=1}^{\prod_{j=1}^{n} (r_{lj}^* + 1)} \left[\prod_{j=1}^{n} \binom{r_{lj}^*}{r_{rj}^l} \prod_{j=1}^{n} (-\alpha_j)^{r_{lj}^* - r_{rj}} \prod_{j=1}^{n} x_j^{r_{rj}^l} \right]\end{aligned} \tag{25}$$

where

$$r^l_{rj} \in V \quad \text{and} \quad 0 \leqq r^l_{rj} \leqq r^*_{lj} \tag{26}$$

and each row of the matrix $\boldsymbol{R}_l = \{r^l_{rj}\}$ is different.

That means nothing else that we have composed all those r^*_{lj} combinations of the exponents r^l_{rj} for which Eq. (26) is valid.

Let us suppose $0 \notin \{\alpha_j\}$ what can be realized in the most of the practical cases. (If any $\alpha_j = 0$, then the approximation $\alpha_j \cong \varepsilon$ can be applied, where ε is a rather small number.)

Now by using Eqs (25, 6) it can be written:

$$(\mathbf{x} - \alpha) \square r_l^{*T} = (-\alpha) \square \mathbf{r}_l^{*T} \cdot [\mathbf{x} \square \boldsymbol{R}_l^T \bigcirc (-\alpha) \square (-\boldsymbol{R}_l^T)]\mathbf{q}_l^T \tag{27}$$

where

$$\mathbf{q}_l = \{q_{lr}\}, \quad q_{lr} = \prod_{j=1}^{n} \begin{pmatrix} r^*_{lj} \\ r^l_{rj} \end{pmatrix} .$$

Let us denote by $\boldsymbol{R} = \{r_{rj}\}$ the matrix in which each row of the matrix $\boldsymbol{R}_l$ is present, and each matrix row is different. Further let be $\mathbf{Q}$ the matrix with the element:

$$q_{lr} = \prod_{j=1}^{n} \begin{pmatrix} r^*_{lj} \\ r_{rj} \end{pmatrix} .$$

Using this, $(\mathbf{x} - \alpha) \square \mathbf{R}^{*T}$ can be written on the basis of Eq. (27) as follows:

$$(\mathbf{x} - \alpha) \square \mathbf{R}^{*T} = (-\alpha) \square \mathbf{R}^{*T} \bigcirc [\mathbf{x} \square \boldsymbol{R}^T \bigcirc (-\alpha) \square (-\boldsymbol{R}^T)]\, \mathbf{Q}^T. \tag{28}$$

Let us substitute this connection into Eq. (24), then one gets:

$$\begin{aligned}
&\mathbf{x}^* \square \mathbf{R}^{*T} \cdot \mathbf{a}^{*T} = \\
&= [(-\alpha) \square \mathbf{R}^{*T} \bigcirc [\mathbf{x} \square \boldsymbol{R}^T \bigcirc (-\alpha) \square (-\boldsymbol{R}^T)] \cdot \mathbf{Q}^T \bigcirc \beta \square (-\mathbf{R}^{*T})] \cdot \mathbf{a}^{*T} = \\
&= [\,[\mathbf{x} \square \boldsymbol{R}^T \bigcirc (-\alpha) \square (-\boldsymbol{R}^T)] \cdot \mathbf{Q}^T \bigcirc [(-\alpha) \bigcirc \beta \square (-\mathbf{E})] \square \mathbf{R}^{*T}\,] \cdot \mathbf{a}^{*T} = \\
&= [\,[\mathbf{x} \square \boldsymbol{R}^T \bigcirc (-\alpha) \square (-\boldsymbol{R}^T)] \cdot \mathbf{Q}^T] \cdot [\,[[(-\alpha) \bigcirc \beta \square (-\mathbf{E})] \square \mathbf{R}^{*T}]^T \bigcirc \mathbf{a}^{*T}] = \\
&= [\mathbf{x} \square \boldsymbol{R}^T \bigcirc (-\alpha) \square (-\boldsymbol{R}^T)] \cdot [\mathbf{Q}^T \cdot [\,[[(-\alpha) \bigcirc \beta \square (-\mathbf{E})] \square \mathbf{R}^{*T}]^T \bigcirc \mathbf{a}^{*T}]] = \\
&= \mathbf{x} \square \boldsymbol{R}^T \cdot [\,[(-\alpha) \square (-\boldsymbol{R}^T)]^T \bigcirc \mathbf{Q}^T \cdot [\,[[(-\alpha) \bigcirc \beta \square (-\mathbf{E})] \square \mathbf{R}^{*T}]^T \bigcirc \mathbf{a}^{*T}]
\end{aligned} \tag{29}$$

which follows from the associative character of the matrix multiplication and from the repeated application of connection (5).

From a comparison of Eq. (29) with Eq. (23) follows:

$$\mathbf{R} = \boldsymbol{R} \tag{30}$$

and

$$\mathbf{a}^T = [(-\alpha) \square (-\boldsymbol{R}^T)]^T \bigcirc \mathbf{Q}^T \cdot [[[(-\alpha) \bigcirc \beta \square (-\mathbf{E})] \square \mathbf{R}^{*T}]^T \bigcirc \mathbf{a}^{*T}]$$

since Eqs (23) and (29) must be fulfilled for each $\mathbf{x}$. The problem now is, how to determine $\boldsymbol{R}$ and $\mathbf{Q}$. This is very difficult in a general case, therefore let us suppose for the function $\hat{\psi}^*$ the following:

Let us denote the set of functions f_l^* by F^*. Let be further:

$$f_l^{**} = \prod_{j=1}^{n} x_j^{*r_{lj}^{**}} \quad \text{where} \quad r_{lj}^{**} \leq r_{lj}^* \quad \text{and} \quad r_{lj}^{**} \in V \tag{31}$$

then one has $f_l^{**} \in F^*$ in case of any $r_{lj}^{**} \leq r_{lj}^*$.

That means that if e.g. $x_1^* x_2^* x_3^* \in F^*$ then $1, x_1^*, x_2^*, x_3^*, x_1^* x_2^*, x_2^* x_3^*, x_1^* x_3^*$ is also element of F^*. Condition (31) does not mean a strong restriction for the function type, because in the majority of the practical cases matrix $\mathbf{R}^*$ has the form $\mathbf{R}_n^*$ and in this case it is easy to see that condition (31) is fulfilled.

By doing so, however, $\boldsymbol{R}$ can be easily determined, namely $\boldsymbol{R} = \mathbf{R}^*$, since the conditions for $\boldsymbol{R}$ and $\mathbf{R}^*$ are the same, i.e.:

$$\mathbf{R} = \mathbf{R}^* \tag{32}$$

can be received on the basis of Eq. (30).

Matrix $\mathbf{Q}$ can be composed by means of the following connection:

$$q_{lr} = \prod_{j=1}^{n} \binom{r_{lj}^*}{r_{rj}^*} = \prod_{j=1}^{r} r_{lj}^{*\,r_{rj}^*} = \mathbf{r}_l^* \square \mathbf{r}_r^{*T} \tag{33}$$

since

$$\binom{r_{lj}^*}{r_{rj}^*} = r_{lj}^{*\,r_{rj}^*} \tag{34}$$

is fulfilled, because in case of first power planning it is $r_{lj}^* \in \{0, 1\}$ and therefore the possible combinations are:

$$\binom{1}{1} = 1 = 1^1, \quad \binom{1}{0} = 1 = 1^0, \quad \binom{0}{1} = 0 = 0^1, \quad \binom{0}{0} = 1 = 0^0$$

by using the formulas of the binomial coefficients. In other words, Eq. (34) is fulfilled, and that proves the correctness of Eq. (33).

On the basis of Eq. (33) matrix $\mathbf{Q}$ is:

$$\mathbf{Q} = \mathbf{R}^* \square \mathbf{R}^{*T}. \tag{35}$$

From the foregoings function $\hat{\psi}$ is

$$\hat{\psi} = \mathbf{x} \square \mathbf{R}^{*T} \cdot \mathbf{a}^T \tag{36}$$

where

$$\mathbf{a}^T = [(-\alpha) \square (-\mathbf{R}^{*T})]^T \bigcirc (\mathbf{R}^* \square \mathbf{R}^{*T})^T \cdot [[[(-\alpha) \bigcirc \beta \square (-\mathbf{E})] \square \mathbf{R}^{*T}]^T \bigcirc \mathbf{a}^{*T}].$$

From Eq. (36) it can be seen that $\hat{\psi}$ can be determined as the function of the initial data, i.e.:

$$\hat{\psi} = \hat{\psi}\,(n, p, \mathbf{P}, \mathbf{k}, \mathbf{R}^*, \mathbf{y}, \mathbf{x}, \alpha, \beta)\,.$$

By means of this connection $\hat{\psi}$ can be generally composed, the composition process can be handled as a system, the input signals of which are

$$n, p, \mathbf{P}, \mathbf{k}, \mathbf{R}^*, \mathbf{y}, \mathbf{x}, \alpha, \beta$$

and the output signals $\mathbf{X}^*, \hat{\psi}^*, \hat{\psi}$.

For the sake of simplicity this system will be called S_F (Fig. 1). The system is a computer program carrying out the calculations for the composition of $\mathbf{X}^*, \hat{\psi}^*$ and $\hat{\psi}$ on the basis of the earlier.

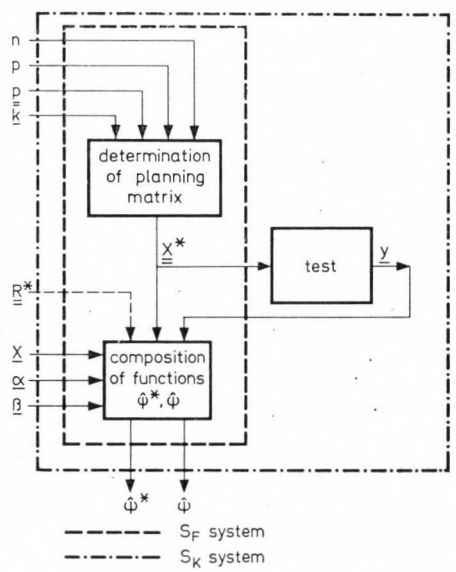

letters with simple underlining denote vectors, with double underlining matrices

Fig. 1

If $\mathbf{R}^* = \mathbf{R}_n^*$, then $\mathbf{R}^*$ can be omitted from the input signals since it is composed by the system on the basis of Eq. (11).

For the application of the described method let us see a practical example.

In gas production it is often necessary to compute the bottom pressure of the gas wells with an appropriate accuracy. In our plants, the differential equations governing the gas flow can be solved only with rough neglections due to lack of computers. Results received in this way, however, often do not fulfil the requirements. By the application of the test planning method it is possible to develop a simple computation method of suitable accuracy for the determination of the bottom pressure in wells.

The aim is to express the bottom pressure in the well as a $\hat{\psi}_n$ type function of the variables. For the determination of the function the input signals of the system must be given, in this case they will be:

$$n, p, \mathbf{P}, \mathbf{k}, \mathbf{x}, \alpha, \beta .$$

The test is carried out by a computer program, therefore this subsystem can be connected by certain commands with the system S_F when one receives the system S_K (Fig. 1), for which $\mathbf{y}$ is already no input signal and $\mathbf{X}^*$ no output signal. E.g., by taking into account the data of the gas field Szank, the $n = 10$ variables given in Table II were chosen in the given ranges. Since the function

Table II

$\mathbf{x}$	Name of variables	Range of variables	
		lowest value	highest value
x_1	q_g — gas production (m³/day)	30,000.	200,000.
x_2	R_c — ratio gas–condensatum (m³/m³)	8000.	20,000.
x_3	R_v — ratio gas–water (m³/m³)	18,000.	94,000.
x_4	p_{wh} — pressure at the casing head (bar)	80.	160.
x_5	p_{sep} — seperator pressure (bar)	3.	80.
x_6	d — diameter of pressure pipe (m)	0.062	0.076
x_7	T_n — temperature at the head of the well (K)	300.	340.
x_8	g — relative gas density	0.633	0.709
x_9	c — relative condensatum density	0.724	0.807
x_{10}	L — length of the producing pipe (m)	1750.	1850.

to be looked for is of the type $\hat{\psi}_{10}$, therefore $m = 56$, hence only planning matrices must be considered for which $N > 56$ is valid. This condition is ensured by the planning matrix $\mathbf{X}_{10,4}^*$, i.e. $p = 4$. According to à priori informations:

$$\mathbf{P} = \begin{bmatrix} 1 & 1 & 1 & 1 & 1 & 1 \\ 1 & 1 & 1 & 1 & 0 & 0 \\ 1 & 1 & 0 & 0 & 1 & 1 \\ 0 & 0 & 1 & 1 & 1 & 1 \end{bmatrix}$$

$$\mathbf{k} = \{1,\ 1,\ 1,\ 1\}$$

Vector **x** can be found in Table II, and the vectors **x** and α, β can be easily composed on the basis of Eq. (8).

$$\alpha^T = \begin{bmatrix} 115{,}000. \\ 14{,}000. \\ 56{,}000. \\ 120. \\ 41.5 \\ 0.069 \\ 320. \\ 0.671 \\ 0.766 \\ 1800. \end{bmatrix}$$

$$\beta^T = \begin{bmatrix} 85{,}000. \\ 6000. \\ 38{,}000. \\ 40. \\ 38.5 \\ 0.007 \\ 20. \\ 0.038 \\ 0.042 \\ 50. \end{bmatrix}$$

For these input signals, our system S_K delivered the following output signals:

$$\hat{\psi}_{10}^* \cong 143.36 + 4.18 \cdot x_1^* + 45.4 \cdot x_4^* - 2.06 \cdot x_6^* + 1.74 \cdot x_8^* - 1.96 \cdot x_1^* x_6^* + \\ + 1.74 \cdot x_9^* x_{10}^*$$

respectively

$$\hat{\psi}_{10} \cong 1119.21 + 2.76 \cdot 10^{-4} \cdot q_g + 1.13 \cdot p_{wh} + 84.77 \cdot d + 45.74 \cdot \gamma_g - \\ - 1507.83\ \gamma_c - 0.64 \cdot L - 3.29 \cdot 10^{-3}\, q_g d + 0.84\ \gamma_c L.$$

$\hat{\psi}_{10}$ denotes the calculated pressure p_{wf} of the well bottom.

The sign $\simeq$ means that from among the 56 coefficients several were neglected on the basis of significance investigations.

The accuracy of the formula was controlled by 17 plant measurements, we received from them that the average absolute relative error — 1.68% — is acceptable. Figure 2 gives a clear picture about the errors.

It can be said that the formula received is suitable for manual calculations, in our plants the planning calculations can be made with it quickly and with an appropriate accuracy.

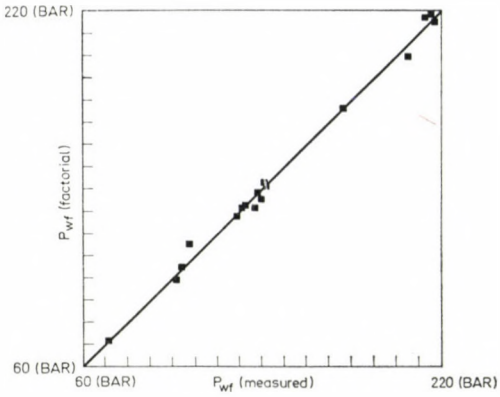

Fig. 2

Summary

The paper deals with the mathematical formalism of the 2^{n-p} type first-power factorial test planning. The calculations becoming complicated in case of more factors can be made by computers using generally developed algorithms. In this way the test planning can be handled as a system, the input signals of which are the test conditions determined on the basis of the à priori informations and the output signal is the result expected from the test.

REFERENCES

1. Davies, O. L. (Ed.): The Design and Analysis of Industrial Experiments. Hafner Publishing Co., New York, 1956.
2. НАЛИМОВ, В. В.—ЧЕРНОВА, Н. А.: Статистические методы планирования экстремальных экспериментов. Наука, Москва, 1965.
3. Nollau, V.: Statistische Analysen. VEB Fachbuchverlag, Leipzig, 1975.
4. Balla, L.—Meggyes, T.: On the weighted linearization. *Acta Geod., Geoph. Mont. Hung.*, 14 (1979), 267—287.

МАТЕМАТИЧЕСКИЙ ФОРМАЛИЗМ ПЛАНИРОВАНИЯ ЛИНЕЙНОГО ФАКТОРИАЛЬНОГО ТЕСТА ТИПА 2^{n-p}

Л. БАЛЛА

РЕЗЮМЕ

В статье рассматривается математический формализм планирования линейного факториального теста типа 2^{n-p}. Предполагается, что интуитивные решения, необходимые для планирования уже сделаны на основе априорных информаций. Дается математический формализм использованного до сих пор метода и разработан математический метод для обратного преобразования преобразованных функций. Таким образом, в случае нескольких факторов усложненные вычисления производятся с помощью ЭВМ используя алгоритмы разработанные для общих случаев.

Acta Geodaet., Geophys. et Montanist. Acad. Sci. Hung. Volume 17 (1), pp. 99—116 (1982)

ÜBER DIE ERZEUGUNG VON DOLOMIT-MAHLGUT FÜR EDELVERPUTZ

SZ. PETHŐ—E. TOMPOS

TECHNISCHE UNIVERSITÄT FÜR SCHWERINDUSTRIE, MISKOLC

[Manuscript received December 30, 1979]

Im Beschluß des Ministerrats vom 2. III. 1979 wurde neben sonstigen Rohstoffen auch die Nutzung und Verwertung der heimischen Dolomitvorräte als Aufgabe ersten Ranges bezeichnet. Hierzu soll die vorliegende Studie Beihilfe gewähren. Der Dolomit von Pilisvörösvár ist der Grundstoff zur Herstellung von Edelverputz, wofür ein Dolomitmaterial von spezieller Korngrößenverteilung erforderlich ist. Die Abhandlung erörtert die Mahltechnologie, behandelt die Frage der Optimierung und fügt den zweckmäßigsten Stammbaum für einen Betrieb mit geringsten Verlusten und maximalen Ausbringen bei.

1. Einführung und Vorgeschichte

Die Dunántúler (transdanubischen) Werke des OEAV (Landesunternehmen für Erz-, Steine- und Erdenbergbau) betreiben in Pilisvörösvár auf Grund eines österreichischen Patentes ein Werk zur Erzeugung von Dolomitgrundstoff für Edelverputz. Die Komponenten dieser in Papiersäcken in Handelsverkehr gebrachten Edelverputzmaterialien sind: Dolomit von bestimmter Kornstruktur, Zement, gebrannter Kalkstaub, sowie hydrophobe Materien und verschiedene Farbstoffe. Die Farbstoffe sind ästhetisch gewählt; die Auswahl ist reichlich und der daraus hergestellte Verputz ist sehr haltbar.

Der Grundstoff Dolomit wird als Mahlgut erzeugt. Zur Aufgabe gelangt Dolomit von 5—15 mm Korngröße, der als Fraktion durch Siebe vom Rohfördergut getrennt wird. Dieser Grundstoff wird dann einem Zweiflächen-Binder-Sieb mit zwei Siebflächen von 8 und 5 mm Lochweite aufgegeben, das mit zwei parallel laufenden glatten Walzenbrechern in geschlossenem Kreislauf arbeitet. Von hier gelangt das Mahlgut zur Trocknung, danach zur Klassierung. Durch Klassieren werden folgende Fraktionen

$$> 5,\ 3—5,\ 1—3,\ 0{,}3—1 \text{ und } < 0{,}3 \text{ mm erzeugt}$$

und in Silos abgezogen. Die Masse der dort gelagerten Siebfraktionen ist jeweils bekannt, so daß der Edelverputzgrundstoff in der gewünschten Zusammensetzung durch Einwaage hergestellt werden kann. Gewünscht ist folgende Korngrößenverteilung:

>5 mm	0%
3—5 mm	5—10%
1—3 mm	35—40%
0,3—1 mm	40—45%
<0,3 mm	5—10%

Nach der früheren Mahltechnologie erhielt man — mit Ausnahme der Kornklasse 0,3—1 mm — von jeder Kornfraktion, insbesondere aber von der Korngröße <0,3 mm einen Überschuß, so daß die Massenausbringen an brauchbarem Material für Edelverputz nur gering war. Deswegen beauftragten die OEAV-Transdanubischen Werke den Lehrstuhl für Mineralaufbereitung an der Technischen Universität für Schwerindustrie, Miskolc (NME) eine Technologie mit geringen Umänderungen zu erarbeiten, die eine Erhöhung des Nutzausbringens verspreche. Über die angestellten technologischen Versuche, den auf Grund der Ergebnisse entworfenen technologischen Stammbaum, dessen Hauptparameter und die auf das Erzielen eines maximalen Massenausbringens ausgerichteten Rechenmethoden soll nun hier wie folgt berichtet werden.

2. Technologische Grunduntersuchungen

Die technologischen Grunduntersuchungen wurden mit einem glatten Walzenpaar durchgeführt. Dieses Walzenpaar ist zur Feinzerkleinerung (d. h. 80% des Brechgutes etwa bei 5 mm Korngröße) eines härteren Materials als mittelharter Kalkstein (wie es auch der Dolomit von Pilisvörösvár ist) gut geeignet und erzeugt unter den in Frage kommenden Einrichtungen bei freier Aufgabe die möglich geringste Feinfraktion (also <0,3 mm). Durch die Spaltweite wird die Dicke des im Mahlgut vorhandenen größten Kornes bestimmt, dessen mit einem quadratisch gelochten Sieb bestimmbares Breitenmaß etwa 1,7 mal größer als der Spalt ist.

Die Funktionen des Siebrückstandes der örtlich „Mulm" benannten Dolomitaufgabe von nominell 5—15 mm Korngröße ist in Abb. 1 dargestellt. Die Proben zu den mit I/a und I/b bezeichneten Kurven wurden bei trockener Witterung genommen. In lufttrockenem Zustand entfallen 83 bzw. 87 Massen % dieser Proben auf die Kornfraktion 5—15 mm, während der Rest außerhalb dieser Grenzwerte liegt. Die mit II bezeichnete dritte Probe hatte eine große Oberflächenfeuchte von 4%. Dementsprechend waren 23,5% der Probe <5 mm; wegen Schadhaftwerden des Siebgewebes war auch der Grobkornanteil über 15 mm ziemlich beträchtlich und betrug 9%.

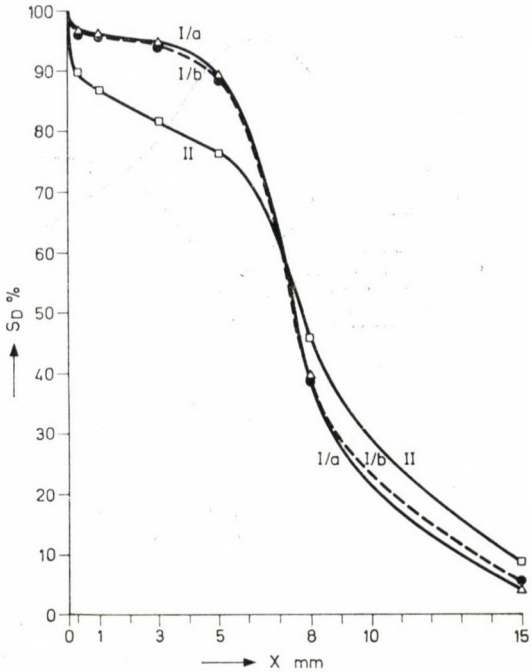

Abb. 1. **Die Korngrößenverteilung der Dolomit-Rohproben**

2.1 Einstufige Grunduntersuchungen

Als erster Schritt schien die Durchführung einstufiger Basisprüfungen notwendig zu sein. Der rohe Dolomitmulm wurde in engen Korngrößengrenzen auseinandergesiebt, die Proben bei systhematischer Änderung der Spaltweite zerkleinert, das Brechgut nach den in den Gütevorschriften angeführten Abmessungen klassiert, und dann die Verteilungsfunktionen der Korngrößen aufgenommen.

Da der Korngrößenbereich des Dolomitmulmes größer als der Nennwert war, wurde er nach folgenden Fraktionen: >15, 15—8, 8—5, 5—3, 3—1 mm ausgesiebt. Die Änderungen der größengemäßen Verteilung der aus diesen Fraktionen genommenen Proben sind als Funktionen der Spaltweite in Abb. 2, 3, 4, 5 und 6 dargestellt. Für je eine Spaltweite sind die Massenanteile der geprüften Kornfraktionen (>5, 3—5, 1—3, 0,3—1 und <0,3 mm) in den Abbildungen eingetragen (ihre Summe ist also = 100) und durch eine fortlaufende Linie miteinander verbunden, so daß mit Benützung der diskreten Werte die funktionsgemäßen Veränderungen gut verfolgt werden können. Bei den einzelnen Versuchsserien wurde die Spaltweite immer um je 0,5 mm geändert.

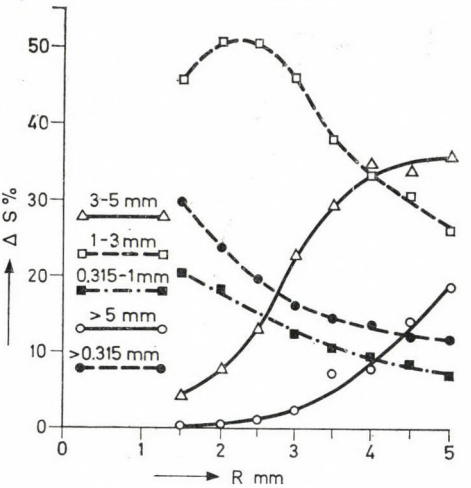

Abb. 2. Die Korngrößenverteilung des mit den Zerkleinerungswalzen erzeugten Dolomit Brechgutes > 15 mm als Funktion der Spaltweite *R*

Aus Abb. 2, 3 und 4 ist zu ersehen, daß die Brechergebnisse der drei groben Kornfraktionen, nämlich >15, 15—8 und 8—5 mm im Spaltweitenbereich zwischen 1 und 4 mm im großen und ganzen das gleiche Bild zeigen. Mit zunehmender Spaltweite nehmen die zwei feinsten Kornklassen des Brechgutes mit exponentiellem Charakter ab und der Massenanteil des Fraktion 0,3—1 mm ist im allgemeinen kleiner als jener der Fraktion <0,3 mm. Die Fraktion 1—3 mm hat mit 50—55% bei der Spaltweite 2,5 mm ein Maximum,

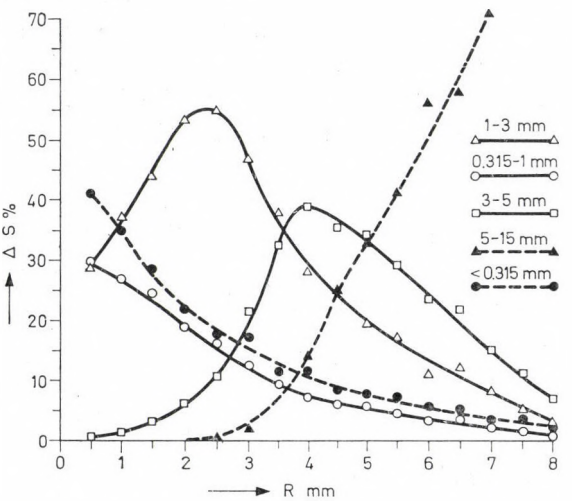

Abb. 3. Korngrößenverteilung der mit den Brechwalzen hergestellten Dolomit-Fraktion 8—15 mm als Funktion der Spaltweite R

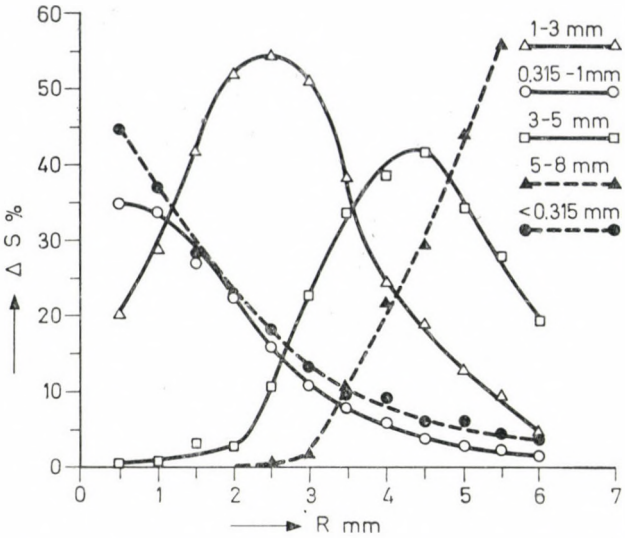

Abb. 4. Korngrößenverteilung der mit den Brechwalzen hergestellten Dolomit-Fraktion 5—8 mm als Funktion der Spaltweite *R*

und im Spaltbereich 1—3,5 mm macht diese Fraktion immer die größte Massenquote aus. Der Massenanteil der Fraktion 3—5 mm nimmt als Funktion der Spaltweite zu und erreicht ihren Höchstwert mit 35—40% bei 4 bzw. 4,5 mm Spaltweite. Bei Spaltweiten unter etwa 3 mm bildet sich kein gröberes Korn als 5 mm. — Da diese Fraktionen des Dolomitmulmes sich beim Brechen gleich verhalten, ist das gemeinsame Brechen des Produktes > 5 mm wohlbegründet.

In Abb. 5 und 6 sind die für die Kornfraktionen 3—5 und 1—3 mm des Dolomitmulmes geltenden Brechergebnisse zu sehen. Bei dem Brechen dieser Fraktionen nehmen auch hier mit der größeren Spaltweite die Massenquoten der Kornklassen <0,3 mm und 0,3—1 mm exponentiell ab; im Brechgut der Aufgabe 5—3 mm sind sie im großen und ganzen gleich, doch im Brechgut der Aufgabe 1—3 mm ist der Massenanteil der Fraktion 0,3—1 mm größer. Bei etwa 1 mm Spaltweite erreicht der Massenanteil dieser Fraktion sogar 50% (!); der Anteil der Fraktion <0,3 ist um 15% kleiner. Die durch Brechen aus dem Dolomitmulm von 3—5 mm Korngröße hergestellte Fraktion 1—3 mm hat bei etwa 2,5 mm Spaltweite ein Maximum von fast 60%, während der Massenanteil von <0,3 mm relativ niedriger ist und zwischen 10—15% liegt. Im Sinne dieser Versuchsergebnisse verhalten sich die beiden Feinkornfraktionen des Dolomitmulmes beim Brechen mit gleicher Spaltweite verschieden, so daß hier ein Brechen bei verschiedenen Spaltweiten berechtigt ist.

Da das Brechgut der drei gröberen Mulmfraktionen im großen und ganzen die gleiche Korngrößenverteilung zeigte, wurden zwecks Prüfung des gemein-

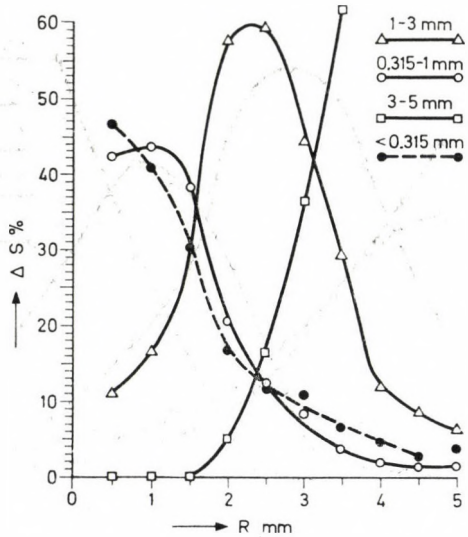

Abb. 5. Korngrößenverteilung der mit den Brechwalzen hergestellten Dolomit-Fraktion 3—5 mm als Funktion der Spaltweite *R*

samen Brechens Versuchsreihen auch mit der Korngröße >5 mm durchgeführt. Dabei wurde die Spaltweite um je 0,5 mm in den Grenzen 1,5 mm und 5,5 mm variiert. Die Korngrößenverteilung des Brechgutes und deren Änderungen wurden für die Fraktionen in Abb. 7 dargestellt. Sie bestätigten unsere frühere Annahme, da sie mit den Ergebnissen in Abb. 2, 3 und 4 eine gute Übereinstimmung zeigen.

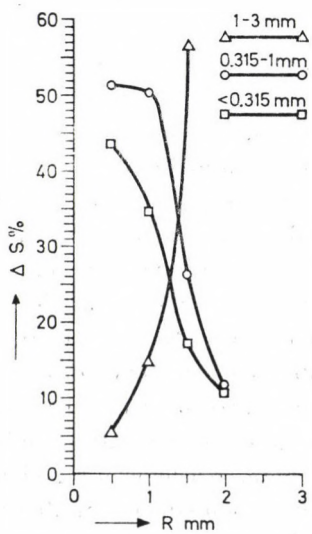

Abb. 6. Korngrößenverteilung der mit den Brechwalzen hergestellten Dolomitfraktion 1—3 mm als Funktion der Spaltweite *R*

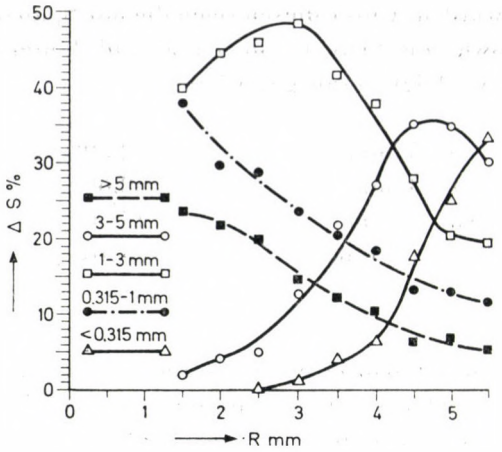

Abb. 7. Korngrößenverteilung im Dolomit-Brechgut > 5 mm der Zerkleinerungswalzen als Funktion der Spaltweite *R*

2.2 Technologische Konsequenzen der Grunduntersuchungen

Die bisherigen Ergebnisse der mit dem glatten Walzenpaar durchgeführten Grunduntersuchungen können technologisch wie folgt ausgenützt werden.

Um die Gütevorschriften mit einem je größeren Massenausbringen erfüllen zu können, ist es notwendig, die Korngrößenklasse >5, 3—5 und 1—3 mm mit verschiedener Spaltweite zu zerkleinern. Zum Zerkleinern des Grobkorns über 5 mm scheint eine Spaltweite zwischen 3 mm und 4 mm am günstigsten zu sein. Bei solchen Spaltweiten gibt es verhältnismäßig wenig Material <0,3 mm im Brechgut; zugleich entstehen auch einige Prozent Material >5 mm Korngröße, zu deren Zerkleinerung ein Kreislauf mit einem quadratisch auf 5 mm gelochten Sieb aufrecht erhalten werden muß. Bei dieser Lösung bildet sich im Siebdurchgang in großer Menge die Fraktion 3—5 mm, deren Trennung zweckmäßig gleichfalls durch Sieben gelöst werden kann. Die Spaltweite des glatten Walzenpaares für die Zerkleinerung dieser Kornfraktion muß gemäß den Grundprüfungen zwischen 2 und 3 mm eingestellt werden, um den Anteil <0,3 mm im Brechgut zu vermindern. Bei solchen Spaltweiten kann man noch erwarten, daß der Anteil der im Brechgut verbleibenden Fraktion 3—5 mm noch den Gütevorschriften genügt, aber die Masse der Fraktion 1—3 mm ist größer, die Fraktion 0,3—1 mm aber kleiner als es den Anforderungen entsprechend wäre.

Über die Kornverteilung des durch Vereinigung des Brechgutes vom zweiten glatten Walzenpaar mit dem Siebdurchgang bei 3 mm Lochweite erzielten Materials kann das gleiche wie vorher gesagt werden. Dies zeigten auch die Ergebnisse jener Zweistufen-Versuche, die mit Änderung der Spalt-

weite durchgeführt wurden. Unter diesen seien die mit Spaltweite $R_1 = 3{,}5$ mm und $R_2 = 2$ mm, sowie mit Sieben von 5 mm und 3 mm Lochweite durchgeführten Versuche wie folgt herausgegriffen:

3—5 mm	2,59%
1—3 mm	58,69%
0,3—1 mm	15,56%
<0,3 mm	23,16%
	100%

Aus dem Vergleich dieser Korngrößenverteilung mit dem vorgeschriebenen Kornanfall und den Ergebnissen der Grunduntersuchung betreffs des Produktes 1—3 mm in Abb. 6 folgt, daß durch eine Weiterzerkleinerung des verhältnismäßig reichlich anfallenden Produktes 1—3 mm die gewünschte Kornstruktur sich mit einem großen Massenausbringen verwirklichen läßt. Es empfiehlt sich, dieses Weiterzerkleinern nach der Bunkerung des getrockneten und klassierten Materials durchzuführen. Die Massen der in die Bunker geschütteten Siebfraktionen sind zufolge fortlaufender Beobachtung ihrer Schütthöhe jeweils bekannt. Fällt dann die Fraktion 1—3 mm in größeren Mengen als vorgeschrieben an, so kann je nach Bedarf der auch durch Berechnung ermittelbare, überschüssige Anteil dieser Kornfraktion einem dritten glatten Walzenpaar zugeleitet werden.

In die Bunker gelangt getrocknetes Material, deswegen führten wir an den vorgetrockneten Kornfraktionen neue Grunduntersuchungen durch.

2.3 Grunduntersuchungen an den getrockneten Kornfraktionen

Die Ergebnisse der mit der getrockneten Kornfraktion 1—3 mm durchgeführten Grunduntersuchungen sind aus Abb. 8 bzw. Tabelle I zu ersehen. Außerdem wurden auch mit der getrockneten Kornfraktion 3—5 mm Grund-

Tabelle I

Brechversuche mit einem Walzenpaar und

Korngröße x mm	$R = 0{,}5$ mm		$R = 0{,}7$ mm		$R = 1{,}0$ mm		$R = 1{,}0$ mm		$R = 1{,}2$ mm	
	ΔS %	S_D%	ΔS %	S_D %	ΔS %	S_D %	ΔS %	S_D %	ΔS %	S_D %
1—3	18,96	18,96	36,40	36,40	39,32	39,32	61,91	61,91	67,28	67,28
0,315—1,0	53,20	72,16	40,68	77,08	39,68	79,00	25,16	87,07	21,37	88,65
<0,315	27,84	100,00	22,92	100,00	21,00	100,00	12,93	100,00	11,35	100,00
	100,00		100,00		100,00		100,00		100,00	

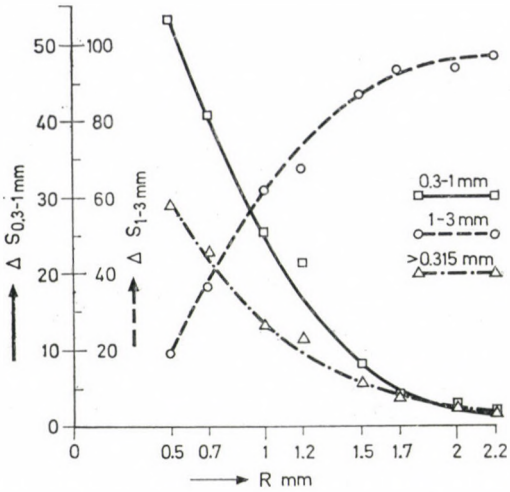

Abb. 8. Korngrößenverteilung im getrockneten Dolomit 1—3 mm des Zerkleinerungswalzen-Brechgutes als Funktion der Spaltweite ***R***

untersuchungen angestellt. Ihre Ergebnisse sind in Abb. 9 enthalten. Da die Korngrößenverteilung des Brechgutes dieser Fraktionen schon durch geringe Änderungen der Spaltweite sehr beeinflußt wird, wurden zu diesen Versuchen die Spaltweiten 0,5, 0,7, 1,0, 1,2, 1,5, 1,7, 2,0, 2,2, 2,5 und 2,7 mm gewählt. — Wird ein Material von 1—3 mm Korngröße aufgegeben, so bildet sich die Fraktion 0,3—1 mm mit dem größten Massenanteil bei der Spaltweite 0,5 mm. Dieser Massenanteil beträgt 53%. Bei einer solchen Spaltweite aber neigt das Walzenpaar schon zu Verstopfungen und zugleich fällt die Fraktion $<$0,3 mm in ziemlich großer Menge an. Mit Vergrößerung der Spaltweite sinkt die Massenquote der zwei Feinkornklassen, und die Fraktion 1—3 mm nimmt zu. Bei 1 mm Spaltweite sind die Massenanteile der im Brechgut vorhandenen Fraktionen 1—3 mm und 0,3—1 mm mit etwa 40% nahezu gleich; das Gut $<$0,3 mm wird $\sim$20%. Kommt getrockneter Dolomit von 3—5 mm Korngröße zur

getrocknetem Material von 1—3 mm Korngröße

$R = 1{,}5$ mm		$R = 1{,}7$ mm		$R = 2{,}0$ mm		$R = 2{,}2$ mm		Allgem. Form	
ΔS %	S_D %	ΔS %	S_D %	ΔS %	S_D %	ΔS %	S_D %	ΔS %	S_D %
86,67	86,67	93,04	93,04	93,77	93,77	96,73	96,73	p	p
7,92	94,59	3,53	96,57	3,36	97,13	1,47	98,20	q	$p+q$
5,41	100,00	3,43	100,00	2,87	100,00	1,80	100,00	r	$p+q+r=1$
100,00		100,00		100,00		100,00		1	

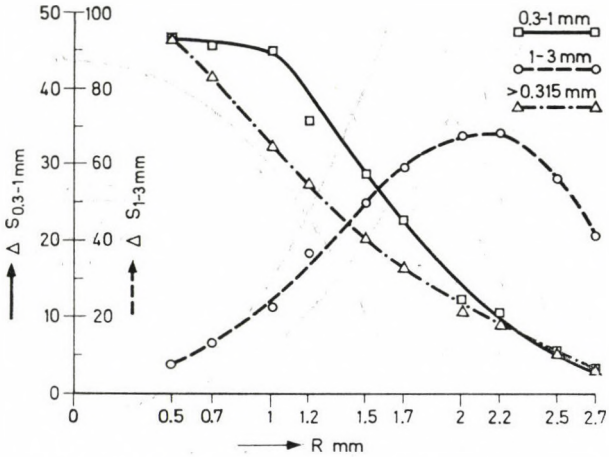

Abb. 9. Korngrößenverteilung des getrockneten Dolomites 3—5 mm aus dem Brechgut de Zerkleinerungswalzen als Funktion der Spaltweite R

Aufgabe, so bildet sich die, den engen Querschnitt darstellende Fraktion 0,3—1 mm mit dem größten Massenanteil, nämlich mit 45—48% bei einer Spaltweite von $\lesssim$ 1 mm und sinkt bei größeren Spaltweiten.

3. Die Rechentechnik der geplanten Technologie

Um ein maximales Massenausbringen zu erzielen, ist eine Rechentechnik erforderlich, die auch für die Rechenmaschine programmiert werden kann. Deswegen sollen im folgenden jene Materialgleichungen erörtert werden, die zur Bestimmung der vorgeschriebenen Korngrößenverteilung des der dritten Stufe zuzuführenden Materials, sowie des Klassierungs-Brechkreislaufes erforderlich sind.

3.1 Bestimmung der Masse des Materials für die dritte Stufe

Die in den vorherigen zwei Abbildungen und in der Tabelle I dargestellten Ergebnisse der Grunduntersuchungen können zuverlässig reproduziert werden. Auch nach dem Fachschrifttum [1, 2, 3] kann die Korngrößenverteilung des Brechgutes mit Hilfe mathematischer Funktionen vorherberechnet werden, wenn gewisse Bedingungen erfüllt sind, hauptsächlich bei einer Aufgabe von unveränderten Eigenschaften. (An dieser Stelle sei auf die Schule von Professor Hentzschel hingewiesen.)

Im folgenden soll nun die Korngrößenverteilung des Brechgutes vom glatten Walzenpaar als Funktion der Spaltweite in dem Sinne als konstant betrachtet werden, daß mit ihrer Hilfe das voraussichtliche Brechergebnis vorherberechnet wird. Auf Grund der bisherigen Prüfergebnisse fällt nach

dem zweistufigen Brechen die Fraktion 1—3 mm in relativ zu großen Mengen an, so daß ein Teil davon in der dritten Stufe weiter zerkleinert werden muß. Um die dorthin zu leitende Materialmenge genau zu bestimmen, muß auf Grund der ersten zwischentextlichen Tabelle die Zusammensetzung des Kornanfalls für den Grundstoff zu Edelverputz genau festgelegt werden:

3—5 mm	10%	10%
1—3 mm	40%	35%
0,3—1 mm	40%	45%
<0,3 mm	10%	10%
	100%	100%

Diese Tabelle im Text enthält zwei Korngrößenverteilungen. Bei beiden Verteilungen beträgt die Massenquote der Fraktionen 3—5 mm und <0,3 mm 10%. Das Verhältnis h der Massenprozente der beiden mittleren Korngrößenfraktionen beträgt im einen Fall = 1, im anderen aber (35/45) = 0,7. Es seien nun nach der zweiten Stufe die Massenanteile der Fraktionen 1—3 mm bzw. 0,3—1 mm B_2 und B_3 benannt. Vom Material der Masse B_2 soll die Menge x auf die dritte Stufe geleitet werden. Dieses Material der Masse x wird zu xq von 1—3 mm, xp von 0,3—1 mm und $xr <$ 0,3 mm. Die Summe der Werte q, p und r wird nach Tabelle I = 1. Auf Grund der bisherigen Analyse kann demnach nach der dritten Stufe das Verhältnis der Fraktionen 1—3 mm und 0,3—1 mm im Endprodukt wie folgt aufgeschrieben werden:

$$\frac{(B_2 - x) + xq}{B_3 + xp} = h\,. \tag{1}$$

Wird diese Gleichung nach x gelöst, so erhält man:

$$x = \frac{B_2 - hB_3}{1 - q + hp}\,. \tag{2}$$

3.2 Benötigte Materialgleichungen zur Erzielung der vorgeschriebenen Korngrößenverteilung

Eine Korngrößenverteilung genau nach der Vorschrift zu realisieren, ist selbst bei dreistufigem Brechen des Materials nicht möglich. Im Vergleich zur Aufgabe muß mit einem Verlust gerechnet werden. Dieser Verlust wird sich hauptsächlich bei der Fraktion <0,3 mm, eventuell bei 3—5 mm zeigen; bei den anderen beiden aber nicht, da man ja gerade mit der dritten Stufe das vorher festgelegte Verhältnis der beiden mittleren Kornklassen sicherstellen kann.

Tabelle II

Korngrössenverteilung in allgemeiner Form nach der dritten Stufe

Kornklasse mm	Massenanteil nach der dritten Stufe	Massenanteil nach der zweiten Stufe
3—5	$B_1 \quad = C_1$	B_1
1—3	$(B_2-x)+qx \quad = C_2$	B_2
0,3—1	$B_3 \quad +px \quad = C_3$	B_3
<0,3	$B_4 \quad +rx \quad = C_4$	B_4
	$+C$	$+B$

Im folgenden führen wir jene Materialgleichungen vor, die zur genauen Erzeugung der vorgeschriebenen Korngrößenverteilung erforderlich sind. Hierbei hilft Tabelle II, in welcher man im allgemeinen die Korngrößenverteilung nach der dritten Brechstufe bzw. die Daten für die zu den einzelnen Kornklassen gehörigen Massen vorfinden kann. Aus der Fraktion 3—5 mm der Masse C_1 muß ein Massenanteil y, aus der Fraktion <0,3 mm der Masse C_4 ein Massenanteil z abgeleitet werden, damit ihr Verhältnis zum Gesamtmaterial $C - y - z$ gleich a bzw. d werde. Hierfür gelten folgende Gleichungen:

$$\frac{C_1 - y}{C - y - z} = a \tag{3}$$

beziehungsweise

$$\frac{C_4 - z}{C - y - z} = d\,. \tag{4}$$

Ihre Lösung nach y bzw. z lautet

$$y = \frac{C_1(1-d) - a(C - C_4)}{1 - a - d} \tag{5}$$

und

$$z = \frac{C_4(1-a) - d(C - C_1)}{1 - a - d}\,. \tag{6}$$

Ist $a = d$, so erhält man

$$y = \frac{C_1 - a(C + C_1 - C_4)}{1 - 2a} \tag{7}$$

und

$$z = \frac{C_1 - a(C + C_4 - C_1)}{1 - 2a}\,. \tag{8}$$

Wenn jedoch der erwünschte Massenanteil für beide Siebklassen 10% betragen soll, mithin $a = d = 0{,}1$ ist, so wird

$$y = \frac{9C_1 + C_4 - C}{8} \tag{9}$$

und

$$z = \frac{9C_4 + C_1 - C}{8}. \tag{10}$$

Wenn in der Kornklasse 3—5 mm zu wenig Material vorhanden ist und hiervon nichts abgeleitet werden muß, dann ist für das Ableiten der überschüssigen Fraktion $<0{,}3$ mm die Beziehung

$$\frac{C_4 - z}{C - z} = d \tag{11}$$

nach z wie folgt zu lösen:

$$z = \frac{C_4 - Cd}{1 - d}. \tag{12}$$

3.3 Berechnung der Masse des im Kreislauf gehaltenen Materials

Da nach der geplanten Technologie das Sieb von 5 mm Lochweite mit dem ersten glatten Walzenpaar in geschlossenem Kreislauf arbeitet, ist zur Bestimmung der Hauptparameter der beiden Einrichtungen die Errechnung des im Kreislauf bewegten Materials erforderlich. Eine Hilfe bietet hier Abb. 10. Die Siebaufgabe entspricht der Masse N, und ebensoviel Material geht als Siebdurchgang aus dem System ab. Der Siebdurchgang setzt sich aus

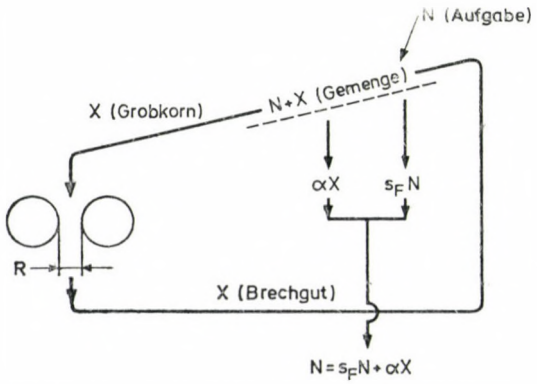

Abb. 10. Berechnung des Materialkreislaufes Klassieren-Brechen

zwei Teilen zusammen: Aus jenem $s_F N$ Teil der Aufgabe, der feiner als die Lochweite des Siebes ist, sowie aus der Fraktion $s'_F X$ des als unbekannt betrachteten Brechgutes X, die ebenfalls feiner als die Sieblochweite ist, wird laut Beziehung:

$$N = s_F N + s'_F X . \tag{13}$$

Wird diese Gleichung nach X gelöst, so erhält man:

$$X = N \frac{1 - s_F}{s'_F} = N \frac{s_D}{s'_F} . \tag{14}$$

In der obigen Gleichung ist s_D die in der Aufgabe vorhandene Massenquote, die gröber als die Lochweite des Siebes ist. Das glatte Walzenpaar muß für das Grobkorn X, das Sieb aber für das Gemenge $N + X$ (Aufgabe + Brechgut) bemessen werden.

4. Bestimmung des optimalen Massenausbringens

Dadurch, daß der Anteil $<0{,}3$ mm des Fertigproduktes mit 10% festgelegt wurde (Wahlmöglichkeit zwischen 5 und 10%), kann das Massenausbringen erhöht werden, da von den sich als Überschuß bildenden Kornfraktionen weniger abgeleitet werden muß. Der zweite Gesichtspunkt besteht darin, die Fraktion 3—5 mm auf 10% oder etwas niedrigerem Wert zu halten (Wahlmöglichkeit auch hier zwischen 5 und 10%); somit bildet sich auch aus dieser Fraktion weniger Material $<0{,}3$ mm. Das Ausbringen kann auch dadurch erhöht werden, daß die Massen der Fraktionen 1—3 mm und 0,3—1 mm gleichgroß gewählt werden, somit in der Beziehung (2) $h = 1$ wird.

Um das optimale Massenausbringen zu ermitteln, wurde von uns folgende technologische Versuchsreihe durchgeführt. Das aus dem Dolomitmulm ausgesiebte Produkt >5 mm wurde auf einem Walzenpaar bei $R_1 = 3$ mm, 3,5 mm und 4 mm Spaltweite zerkleinert, danach das Brechgut zwischen einem Sieb von 5 mm Lochweite und dem Walzenpaar mit verschiedenen Spaltweiten in Kreislauf gesetzt. Danach wurde der aus dem Produkt <5 mm abgesiebte Teil 3—5 mm ebenfalls dem Walzenpaar aufgegeben, wobei die Spaltweiten 2, 2,2 und 2,5 mm betrugen. Nach der zweiten Brechstufe erfolgte das Trocknen. Mit den bisherigen Schritten der Versuchsreihe erreichten wir, daß im Brechgut die Korngröße >5 mm verschwand; der Anteil des Kornes 3—5 mm etwa dem gewünschten Wert entsprach, die Fraktion 0,3—1 mm sich auf 12 und 18% belief, die Fraktion 1—3 mm aber 50—60% betrug. Hiernach wurde ein Teil des Produktes 1—3 mm auf ein drittes Walzenpaar geleitet, an dem die Spaltweiten 0,7, 1,0 und 1,2 mm eingestellt wurden.

Die Masse des hierhin geleiteten Produktes wurde mit der Beziehung (2) errechnet.

Dieser letzte Teil unserer experimentellen Arbeit bzw. die praktische Anwendung der Rechentechnik soll hier eingehender vorgeführt werden. In Tabelle III ist in der zweiten Kolonne die Korngrößenverteilung nach der

Tabelle III

Die Anwendung der Rechentechnik bei der dritten Brechstufe

Korngröße mm	$R_1 = 3{,}5$ mm ΔS %	$R_2 = 2$ mm ΔS %	Dritte Stufe $R_3 = 1$ mm				
			ΔS_{R1} %	ΔS_{R2} %	ΔS_1 %	ΔS_{R3} %	ΔS_2
3—5	33,39	2,59	2,59	—	2,59	2,59	3,46
1—3	37,82	58,69	8,32	24,09	32,41	32,41	43,27
0,3—1	10,45	15,56	15,56	16,85	32,41	32,41	43,27
<0,3	18,34	23,16	23,16	9,43	32,59	7,49	10,00
	100,00	100,00	49,63	50,37	100,00	74,90	100,00

ersten Stufe zu sehen, bei einer Spaltweite $R_1 = 3{,}5$ mm. Hiervon wurde das Material von 3—5 mm als 33,39% Anteil auf das mit $R_2 = 2$ mm Spaltweite laufende Walzenpaar abgezweigt, wo wir die in Kolonne 3 angegebene Korngrößenverteilung erhielten. Auf die dritte Stufe wurde ein Teil des Produktes 1—3 mm, und zwar von 58,69% ein Anteil 50,37% geleitet. Diese Massenprozente wurden mit Annahme eines Verhältnisses $h = 1$ errechnet. $R_3 = 1$ mm, deswegen werden sich nun — mit Berücksichtigung der Daten in Tabelle I nach dem Mahlen voraussichtlich die folgenden Resultate ergeben:

$$\begin{aligned} 1\text{—}3 \text{ mm: } 50{,}37 \cdot 0{,}4783 &= 24{,}09\% \\ 0{,}3\text{—}1 \text{ mm: } 50{,}37 \cdot 0{,}3346 &= 16{,}85\% \\ <0{,}3 \text{ mm: } 50{,}37 \cdot 0{,}1871 &= \underline{9{,}43\%} \\ & 50{,}37\% \end{aligned}$$

Diese Ergebnisse sind auch in Tabelle III zu finden. In der nächsten Kolonne der Tabelle erscheint — mit Δs_1 bezeichnet — die Summe je Fraktion des Materials mit den Maßen 49,63 und 50,37%. Im Sinne dieser Korngrößenverteilung ist hier mit 32,59% zuviel Material <0,3 mm vorhanden, so daß ein Teil abgeleitet werden muß. Die Berechnung erfolgte mit der Beziehung (12). Da man — um die vorgeschriebene Korngrößenverteilung zu erfüllen — aus dem Material <0,3 mm einen Anteil von 25,10% ableiten muß, wird das Massenausbringen zu 74,90%. Werden die Massenprozente der Kornfraktionen auf dieses Massenausbringen bezogen, so gelangt man zur endgültigen Korngrößenverteilung, wie sie in der letzten Kolonne der Tabelle zu sehen ist.

Dieselben Ergebnisse findet man zusammengefaßt in Tabelle IV, wenn die Spaltweiten der Stufe 2 und 3 geändert werden und $R_1 = 3{,}5$ mm ist. Bei $R_1 = 3$ und 4 mm sind die Ergebnisse schlechter, weswegen sie hier gar nicht mitgeteilt werden. In der Tabelle sind die Massenausbringen (unterstrichen), die endgültige Korngrößenverteilung, die der dritten Stufe aufgegebenen Massenanteile, schließlich auch die Verluste zu finden. Aus den Ergebnissen kann festgestellt werden, daß man das größte Massenausbringen, nämlich 75,555%, mit den Spaltweiten $R_1 = 3{,}5$ mm, $R_2 = 2{,}2$ mm und $R_3 = 1$ mm erzielen kann; in diesem Falle muß der dritten Stufe Material von 49,61 Massen % aufgegeben werden.

5. Stammbaum der Technologie von optimaler Materialbilanz

Der nach den obigen Ergebnissen optimierte Stammbaum ist in Abb. 11 dargestellt. Der Dolomitmulm gelangt auf ein zweideckiges Sieb der Bauart Binder mit den Lochweiten 5 und 3 mm. Das Produkt >5 mm gelangt auf ein Walzenpaar mit $R_1 = 3{,}5$ mm Spaltbreite, wonach das Brechgut auf die Siebeinrichtung zurückgeleitet wird. Beträgt die Aufgabe des Siebes 10 t/h, dann ist das Rücklaufprodukt 11 t/h, die Sieboberfläche muß also für 21 t/h bemessen werden. Das Produkt 3—5 mm durchläuft das im offenen Kreislauf arbeitende glatte Walzenpaar bei einer Spaltweite von $R_2 = 2{,}2$ mm. Das

Tabelle IV

Korngrößenverteilung bei Änderung

Korngröße mm		$R_2 = 2$ mm							
		$R_3 = 0{,}7$ mm		$R_3 = 1$ mm		$R_3 = 1{,}2$ mm		$R_3 = 0{,}7$ mm	
		ΔS_R%	ΔS %	ΔS_R%	ΔS %	ΔS_R%	ΔS %	ΔS_R%	ΔS %
3—5		2,59	3,48	2,59	3,45	2,59	3,46	4,14	5,52
1—3		32,16	43,26	32,413	43,27	32,358	43,27	31,68	42,24
0,3—1		32,16	43,26	32,413	43,27	32,359	43,27	31,68	42,24
<0,3		7,43	10,00	7,49	10,00	7,479	10,00	7,50	10,00
Zusammen		74,34	100,00	74,906	100,00	74,786	100,00	75,00	100,00
Der Stufe 3 aufgegebener Materialanteil		35,254		50,368		115,69		34,723	
Verluste	aus 3—5 mm	—		—		—		—	
	aus <0,3 mm	25,66		25,09		25,21		25,00	

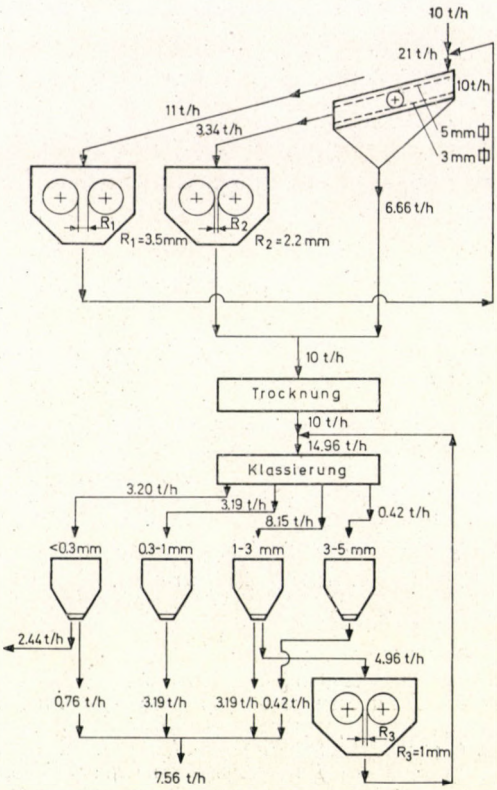

Abb. 11. Endgültiger Stammbaum der Technologie samt Materialbilanz

der Spaltweiten in Stufe 2 und 3

$R_2 = 2{,}2$ mm				$R_2 = 2{,}5$ mm					
$R_3 = 1$ mm		$R_3 = 1{,}2$ mm		$R_3 = 0{,}7$ mm		$R_3 = 1$ mm		$R_3 = 1{,}2$ mm	
ΔS_R%	ΔS %	ΔS_R%	ΔS %	ΔS_R%	ΔS %	ΔS_R%	ΔS %	ΔS_R%	ΔS %
4,14	5,48	4,14	5,48	7,295	10	7,36	10	7,34	10
31,93	42,26	31,875	42,26	29,18	40	29,43	40	29,38	40
31,93	42,26	31,875	42,26	29,18	40	29,43	40	29,38	40
7,555	10,00	7,544	10,00	7,295	10	7,36	10	7,35	10
75,555	100,00	75,434	100,00	72,950	100,00	73,58	100,00	73,45	100,00
49,609		113,95		34,412		49,165		112,93	
—		—		3,68		3,61		3,62	
24,445		24,566		23,37		22,81		22,93	

nach der Trocknung folgende Klassiersieb muß für 14,96 t/h Durchsatz ausgelegt werden, da aus dem Bunker für das Material von 1—3 mm fortlaufend 4,96 t/h auf das dritte Walzenpaar von 1 mm Spaltweite abgeleitet werden muß. Der Bunker ist für 8,15 t/h zu bemessen. Vom Material $<0,3$ mm sind aus dessen Bunker 2,44 t/h abzuleiten, während 0,76 t/h in das Fertigprodukt gehören.

SCHRIFTTUM

1. HENTZSCHEL, W.—LANGE, R.: Programmierung und Optimierung in Schotter- und Splittwerken. Baustoffindustrie, 1968, 5., Teil 1: S. 165-171, Teil 2: S. 202-205.
2. HENTZSCHEL, W.: Grundlagen des systematischen Erfassens von Aufbereitungsanlagen. *Neue Bergbautechnik*, 3 (1973), 337-340.
3. GÖLL, G.—HELFRICHT, R.—RAPSCH, S.: Zum Problem der Aufstellung von Prozeßgleichungen bei der Zerkleinerung von Hartgesteinen. *Neue Bergbautechnik*, 3 (1973), 340-347.

О ПРОИЗВОДСТВЕ ДОЛОМИТОВОГО ПРОМОЛА ДЛЯ ШТУКАТУРКИ ТЕРРАНОВЫ

С. ПЕТЁ—Е. ТОМПОШ

РЕЗЮМЕ

Постановлением Совета министров (2. III/1979) наряду с утилизацией других сырьевых источников намечается в качестве первоочередной задачи использование отечественных доломитовых ресурсов. Авторы хотят оказывать помощь к решению этого задания. Доломит, добываемый в Пилишвёрёшваре представляет собой основный материал и для производства штукатурки терранови. Для производства требуется доломит определенного гранулометрического состава. В статье изучается оптимизация и технология размола.

Acta Geodaet., Geophys. et Montanist. Acad. Sci. Hung. Volume 17 (1), pp. 117—146 (1982)

DIE SYNTHESE BERGBAULICHER TECHNOLOGIESYSTEME

J. PATVAROS

UNIVERSITÄTSPROFESSOR, KANDIDAT DER TECHN. WISS., LEHRSTUHL FÜR BERGBAUKUNDE AN DER TECHN. UNIVERSITÄT FÜR SCHWERINDUSTRIE, MISKOLC

[Eingegangen am 14. Juli 1980]

Die Arbeit gibt eine eingehende Erörterung der Grundsätze für die Anwendung kombinierter Abbausysteme, die eine wirksamere Ausbeutung der mineralischen Rohstoffvorkommen gewährleisten. In diesem Rahmen werden die grundlegenden, im Bergbau üblichen Abbauverfahren, wie der Tagebau —*K*, Tiefbau —*M*, Unterwasserabbau —*V*, Bohrlochabbau —*F* näher beschrieben, und dabei ihre kennzeichnenden Kostenfunktionen mitgeteilt. Zum Schluß enthält die Abhandlung eine Methodik zur richtigen Auswahl der zweckmäßigsten Kombination dieser Verfahren.

1. Einleitung

Der in Weltrelation ständig steigende Bedarf an mineralischen Grundstoffen einerseits, wie auch das immer schnellere Schwinden der zur Verfügung stehenden bekannten Mineralvorräte erfordern schon in unseren Tagen dringend das Schaffen und die Verwirklichung einer neuen Wirtschaftspolitik betreffs der Bodenschätze. Dies wird — wie anzunehmen ist — in Zukunft noch viel stärker erforderlich werden. Die Erfüllung dieser Kardinalaufgabe erfordert, von der Erkundung an bis zur Gewinnung, das Prinzip einer möglichst größten Komplexität.

In den verschiedenen Phasen des Suchens und Erkundens neuer Mineralvorräte bedeutet das Prinzip der Komplexität das Vordringen bis in die Tiefe des Grundgebirges, und mit allen Mitteln das Erfassen und Sammeln sämtlicher erreichbarer Informationen über die festen, tropfbar-flüssigen und gasförmigen Mineralrohstoffe in quantitativer und qualitativer Beziehung, sowie nach ihren sonstigen Merkmalen; danach die Verarbeitung und Nutzanwendung all dieser Daten.

Bei der Gewinnung bedeutet das Zurgeltungbringen des Komplexitätprinzips die kombinierte Anwendung der verschiedenen bergbautechnischen und Abbau-Verfahren, um damit die Abbauverluste und die Verdünnung zu senken.

Bei den Verarbeitungsprozessen ermöglichen aber die komplexen Verfahren, daß aus den meisten Mineralrohstoffen mehrerlei Konzentrate bzw. Endprodukte erzeugt werden können.

Ein totales Erfassen und Verfolgen des Komplexitätprinzips und seiner Lösungen durch die erwähnten großen Systeme würde, wegen der gegenseitigen

Beziehungen und Wechselwirkungen, den Rahmen dieser Abhandlung zu sehr überschreiten. Deswegen soll in den folgenden Darlegungen das Augenmerk vor allen Dingen auf die Möglichkeiten der Erhöhung der Effektivität der bergbaulichen Lösungen für Gewinnungs- bzw. -Abbautechnik gerichtet werden.

Die Hauptvorteile des Einsatzes kombinierter Bergbaubetriebs- und Abbauverfahren können wie folgt bezeichnet werden:

a) Ermöglichung des Abbaus auch solcher Teile des Mineralvorkommens, die ansonsten mit einem gegebenen Abbauverfahren aus technischen, ökonomischen oder Sicherheitsgründen nicht abgebaut werden könnten.

b) Durch die verschiedenartigen Grubenbetriebs-, und Abbaumethoden kann die Produktion mengen- und gütemäßig stabilisiert bzw. die Störungsanfälligkeit vermindert werden.

c) Durch Kombination der Gewinnungsmethoden kann die Dauer des Abbaus eines Grubenfeldes oder des ganzen Schachtbetriebes verlängert werden. Dadurch gewinnt man Zeit, neue Feldesteile eingehender zu erkunden und für den Abbau sorgfältiger vorzubereiten; ebenso auch für die Erarbeitung der zweckmäßigsten Abbautaktik und Betriebsführungsstrategie. Schließlich gewinnt man damit auch die Möglichkeiten für ein mehrfaches Einbringen der Investitionskosten.

d) Die bei den verschiedenen bergtechnischen Operationen anfallenden Abfallstoffe können auf einfache Weise in die ausgekohlten Grubenräume zurückgeführt, und damit der Schutz der natürlichen Umwelt besser gewährt werden.

e) An die zu den einzelnen bergbautechnischen Systemen gehörenden Erschließungsstrukturen (wie: Einbruchgraben bei Tagebauen, Grubenerschließungsstrecken usw.) können sich verschiedene Abbaumethoden anschließen. Dadurch kann die Wirksamkeit der bergbaulichen Investitionen wesentlich verbessert werden.

f) Bohrlöcher, die als Hilfsdienste für verschiedene Bergbauarbeiten — z. B. für den Abbau — hergestellt wurden, können auch andere Aufgaben verrichten; z. B. auf dem Gebiet der Erkundung, Wasserabsenkung, ja sogar bei der Gewinnung selbst.

g) Integrierte bergbauliche Technologiesysteme kann man beispielsweise mit Anwendung der komplexen Hydromechanisation ausgestalten. In solchen Fällen dient in den verschiedenen Grubenbetriebssystemen dasselbe Arbeitsmedium — Wasser — zum Gewinnen, Weiterbefördern, Transportieren in beliebiger Richtung, ja sogar noch zur Aufbereitung des Fördergutes. Bei dieser Lösung können die Produktionseinrichtungen großenteils typisiert werden. Außerdem läßt sich die Wirtschaftlichkeit der Produktion noch dadurch erhöhen, daß man das Arbeitsmedium rezirkulieren läßt.

2. Möglichkeiten der Kopplung von Bergbautechnologien

Bei der Gewinnung der Mineralrohstoffe besteht die Möglichkeit, die betriebs- und abbautechnischen Verfahren auf die verschiedenste Weise miteinander zu koppeln, wobei man von den einfachsten zu den kompliziertesten Strukturen fortschreitet. Selbstredend bestimmt ein erhöhter Komplexitätsgrad nicht zugleich eindeutig auch die Rangordnung der Wirtschaftlichkeit, obwohl man mit komplexeren Gewinnungsverfahren gewöhnlich auch das Effektivitätsfeld erweitern kann.

Die mit der Gewinnung der Mineralrohstoffe verbundenen und in Einklang gebrachten bergbautechnischen Lösungen können — ohne Anspruch auf Vollständigkeit — kurz wie folgt aufgezählt werden:

1. Ein gegebenes Mineralvorkommen soll ausschließlich nur mit einer Grubenbetriebs- und Abbaumethode gewonnen werden.

In diesem Fall kann der Gewinn aus folgender Beziehung berechnet werden:

$$N = Q_t(k_a - k_t) \ \ [\mathrm{Pm}].$$

Hierin sind:

Q_t gewinnbarer Mineralvorrat (in t),

k_a Verkaufspreis (Weltmarktpreis) des gegebenen Mineralrohstoffes (in Pe/t),

k_t kennzeichnende durchschn. Gewinnungskosten des gegebenen Grubenbetrieb- und Abbausystems (in Pe/t). Bei langfristiger Planung soll dieser Wert zweckmäßig mit Berücksichtigung der voraussichtlichen technologischen Veränderungen diskontiert werden.

Des weiteren soll der Verständlichkeit zuliebe die Geldmasse (Dollar, Rubel, DM oder sonst irgend ein Zahlungsmittel) mit Pm bezeichnet, als Ausdruck der Geldeinheit aber die Dimension Pe angewendet werden.

2. Das gegebene Mineralvorkommen soll ausschließlich mit einem bergtechnischen System, innerhalb dessen aber nach verschiedenen Abbauverfahren gewonnen werden (z. B. durch Tiefbau, jedoch dabei entweder mit Strebbau, Kammer-Pfeilerbau oder mit einem sonstigen Abbauverfahren kombiniert). In diesem Fall kann der erzielbare Gewinn aus folgender Beziehung errechnet werden:

$$N = \sum_{i=1}^{n} Q_{ti} \cdot (k_{ai} - k_{ti}) \ \ [\mathrm{Pm}].$$

Hierin sind:

Q_{ti} abbaubarer Mineralvorrat der einzelnen Baufelder bzw. Mineralvorratblocks (in t),

k_{ai} bei dem Abbau des Mineralvorrats der verschiedenen Baufelder erzielbarer mittlerer Verkaufspreis (in Pe/t),

k_{ti} für die einzelnen Abbaumethoden kennzeichnende mittlere Selbstkosten (in Pe/t).

Kombinationsmöglichkeiten höherer Ordnung ergeben sich dann, wenn sich — um ein Mineralvorkommen abzubauen — für die Wahl und Kopplung nicht nur der Abbaumethoden, sondern auch der Grubenbetriebsmethoden eine Möglichkeit ergibt. Hierbei sind dann die folgenden Grundfälle möglich:

3. *Einzelteile des Mineralvorkommens werden mit — räumlich getrennten — doch gleichzeitigen bergtechnischen Verfahren abgebaut* (z. B. Tagebau und Tiefbau).

Bei solchen Lösungen sind zwei Varianten möglich:

a) Jedes der beiden bergbautechnischen Systeme arbeitet mit einer bestimmten Abbaumethode.

b) Innerhalb der gegebenen bergtechnischen Systeme kommen Abbaukombinationen zum Einsatz.

4. *Die einzelnen Teile des Mineralvorkommens werden mit räumlich und zeitlich getrennten bergbautechnischen Systemen abgebaut.*

Auch hier sind zwei Varianten möglich:

a) Abbau mit einem gegebenen Abbauverfahren,

b) Abbau mit kombinierten Abbaumethoden.

5. *Die einzelnen Teile des Mineralvorkommens werden räumlich anschließend, zeitlich mit aufeinander folgenden bergtechnischen Systemen abgebaut* (z. B. zuerst Tagebau, danach Tiefbau).

Auch in diesem Falle kann die Operation wie folgt verlaufen:

a) mit einem gegebenen Abbautyp,

b) mit kombinierten Abbauverfahren.

Die Anzahl der in Frage kommenden Abbaulösungen kann noch weiter zunehmen, wenn man berücksichtigt, daß der Tagebau mit einer kontinuierlichen oder zyklisch-kontinuierlichen Lösung bzw. mit deren Kombination betrieben werden kann. Ebenso kann auch der Tiefbau durch einen Schleppschacht oder einen Seigerschacht erschlossen und betrieben werden bzw. mit kontinuierlicher oder periodischer Schachtförderung arbeiten.

6. *Einzelne Teile des Mineralrohstoff-Vorkommens werden räumlich miteinander gekoppelt gleichzeitig abgebaut oder mit zeitlich aufeinander folgenden Grubenbetriebs- bzw. Abbaumethoden gewonnen.* Eine solche Lösung ist beispielsweise ein von der Arbeitsstrosse des Tagebaus oder aus dem offenen Streckennetz hergestelltes Bohrloch und der von da ausgehende Abbau, während der Abbau auch mit den vorerwähnten Bergbaumethoden zur gleichen Zeit

läuft oder laufen kann. Auch bei dieser Variante können die einzelnen Bergbausysteme:

a) mit einer gegebenen Abbaumethode,

b) mit Abbau-Alternativen fördern.

Im Hinblick auf die Investitionen ist diese Lösung deshalb besonders günstig, da die Erschließungs- und Grubeneröffnungsbaue der einzelnen Bergbaumethoden auch zu Dienstleistungen bei anderen technologischen Systemen des Bergbaus herangezogen werden können.

Die im Schoß der Erde verborgenen Mineralrohstoffe können nach vier grundsätzlich verschiedenen Bergbausystemen (Tagebau — K, Tiefbau — M, Unterwasserabbau — V, Bohrlochabbau — F) bzw. deren Kombinationen gewonnen und zutage gefördert werden.

Der Einfachheit halber soll die Berechnung des mit kombiniertem Bergbaubetrieb erzielbaren Gewinns, des weiteren mit der Annahme eines gegebenen Abbauverfahrens durchgeführt werden. Selbstredend stößt auch dann das Aufschreiben der detaillierteren Beziehungen nicht auf besondere Schwierigkeiten, wenn innerhalb der einzelnen Bergbausysteme verschiedene Abbaulösungen zur Anwendung kommen.

Nach Vorausschicken dieser Erläuterungen sollen nun, zur Berechnung des mit den verschiedenen Abbaumethoden erzielbaren Gewinnes, die folgenden kennzeichnenden Fälle näher untersucht werden.

A) *Der gleiche Mineralrohstoff (Kohle, Bauxit) wird in den einzelnen Teilen der Lagerstätte mit verschiedenen Abbaumethoden gewonnen.*

$$N = Q_K(k_{ak} - k_{tk}) + Q_M \cdot (k_{aM} - k_{tM}) + Q_V(k_{aV} - k_{tV}) + Q_F \cdot (k_{aF} - k_{tF}) \quad \text{(in Pm)}.$$

Hierin sind:

Q_K; Q_M; Q_V; Q_F: Mineralvorratsquoten (in t), die mit Tagebau, Tiefbau, Unterwasserabbau, Bohrlochabbau-Technik gefördert werden können,

k_{aK}; k_{aM}; k_{aV} k_{aF}: Preiserlös (in Pe/t), der mit den verschiedenen Abbaumethoden erzielt werden kann,

K_{tK}; K_{tM}; K_{tV}; K_{tF}: Produktionskosten (in Pe/t), die mit den verschiedenen Abbauverfahren erwachsen (in Pe/t).

In dem Fall, wenn der Verkaufspreis der mit verschiedenen Bergbaumethoden gewonnenen nutzbaren Mineralrohstoffe praktisch übereinstimmt, kann der erzielbare Gewinn als folgende Gleichung aufgeschrieben werden:

$$N = k_a \sum_{i=1}^{n} Q_{ij} \left(1 - \frac{k_{ij}}{k_a}\right) \quad \text{(in Pm)}.$$

Hierin sind:

k_a durchschnittlicher Verkaufspreis, (in Pe/t),

Q_{ij} „i"-ter Teil jenes Mineralvorrates, der mit dem „j"-ten Bergbautechnologiesystem abgebaut wird, (in t),

k_{ij} kennzeichnende Selbstkosten (in Pe/t) für jenen Teil „i" des Mineralvorrates, der mit dem „j"-ten Bergbausystem abgebaut wird.

Selbstredend dürfen bei der Berechnung der Erlöse und Kostenausgaben nur jene Bergbaumethoden berücksichtigt werden, die im Hinblick auf Technik, Ökonomie und Grubensicherheit überhaupt in Frage kommen können.

B) *Die verschiedenen Mineralgrundstoffe (Sand, Ton, Kohle usw.) können mit einem bestimmten Bergbausystem (z. B. Tagebau) abgebaut werden.* In diesem Fall kann der erzielbare Gewinn aus folgender Beziehung errechnet werden:

$$N = Q_1 \cdot (k_{a1} - k_t) + Q_2 \cdot (k_{a2} - k_t) + \ldots + \\ + Q_n \cdot (k_{an} - k_t) = k_t \cdot \sum_{i=1}^{n} Q_i \cdot \left(\frac{k_{ai}}{k_t} - 1\right) \qquad \text{(Pm)}.$$

Hierin sind:

$Q_1 Q_2, \ldots, Q_n$ gewinnbarer Mineralvorrat aus den verschiedenen Mineralrohstoffarten (in t),

k_{ai} Verkaufspreis der verschiedenen Mineralgrundstoffe (in Pe/t),

k_t Produktions-Selbstkosten (in Pe/t), kennzeichnend für eine bestimmte Bergbaumethode.

C) *Die allgemeinste Möglichkeit liegt vor, wenn die verschiedenen Mineralrohstoffe mit kombinierten Bergbau- und Abbaumethoden gewonnen werden können.* In diesem Fall kann der erzielbare Gewinn aus folgender Gleichung berechnet werden:

$$N = \sum_{1}^{A} \sum_{1}^{N} \sum_{1}^{n} Q_{aij}(k_{aij} - k_{ait}) \qquad \text{(Pm)}.$$

Hierin sind:

$1, 2, \ldots, A$ Anzahl der gewinnbaren Nutzmineralstoffe (Lagerstätten, Flöze),

$1, 2, \ldots, N$ Anzahl der für die Gewinnung der verschiedenen Mineralrohstoffe in Frage kommenden Bergbautechnologie-Systeme,

$1, 2, \ldots, n$ Anzahl der in den verschiedenen Bergbausystemen anwendbaren Abbauverfahren,

k_{aij} kennzeichnende Produktionsselbstkosten für die kombinierten Bergbau- und Abbaumethoden bei verschiedenen Mineralrohstoffen (in Pe/t).

Bei der Gewinnung der verschiedenen Mineralrohstoffe mit kombinierten Methoden kann es vorkommen, daß ihre Gewinnungskosten in einzelnen Feldesteilen vorübergehend den Preiserlös übersteigen. In solchen Fällen muß die Bergbautaktik darauf ausgerichtet werden, daß der Mehrgewinn aus den günstigeren Revieren das Defizit übertreffe. In der Mehrzahl der Fälle ist nämlich das Ersetzen einer Draufzahlung aus einem gegebenen Mineralvorkommen viel vorteilhafter und schneller durchführbar, als neue Fundorte in Produktion zu setzen, oder eventuell eine Importlösung zu treffen.

3. Technisch-ökonomisches Modell der grundlegenden Bergbautechnologie-Systeme

Alle grundlegenden Technologiesysteme im Bergbau, die zur Gewinnung von nutzbaren Mineralgrundstoffen dienen (K — Tagebau, M — Tiefbau, V — Unterwasserbau, F — Bohrlochbau), haben eine charakteristische Kostenstruktur. In jeder von diesen aber erscheinen als Hauptparameter: die optimale Erstreckung des Schachtfeldes (im Streichen und Fallen), ferner die Förderkapazität und die Abbaugrenztiefe.

In technischer Hinsicht hat jedes Bergbausystem Grenzen seiner Leistungsfähigkeit, die sich jedoch durch die wissenschaftlich-technische Entwicklung immer stärker ausdehnen. Als Beispiel hierfür ist zu erwähnen, daß die Abbaugrenztiefe bei Großtagebauen auf Kohle heute bereits 300—400 m erreicht, während dieser Grenzwert im Erzbergbau mancher Länder bereits 500 m beträgt. Dies besagt mit anderen Worten, daß die Ausrüstung der Tagebaue mit hochleistungsfähigen und billig produzierenden Maschinen und Einrichtungen diesem technologischen Bergbausystem ermöglicht hat, selbst in solche Bereiche vorzudringen, die früher dem Anschein nach ausschließlich dem Tiefbau vorbehalten waren. Dabei ist auch jene Tendenz nicht zu verkennen, daß die rationelle Konzentration der Abbau- und Fördertätigkeit die Förderkapazität der Tiefbaugruben (bei Kohlenbergwerken 5—7 Mill. t/a, bei Erzbergwerken 10—15 Mill. t/a) in Regionen führt, die früher nur durch Tagebau für gewinnbar galten.

3.1 Tagebau

Der Hauptvorteil der mit dem Abräumen der Deckschichten verbundenen Tagebaugewinnung der Mineralvorräte besteht darin, daß man die Produktionskapazität durch den Einsatz weiterer hochleistungsfähiger Gewin-

nungsmaschinen und Ausrüstungen elastisch erhöhen und beschleunigen kann, je nach dem es der schwankende Bedarf der Verbraucher erfordert. Dabei sind die spezifischen Gewinnungskosten wegen des kleineren Bedarfes an physischer, menschlicher Arbeitskraft bedeutend niedriger als bei Tiefbau.

Die für den Abbau durch Tagebau eines Vorkommens kennzeichnenden Kosten können prinzipiell nach der Skizze in Abb. 1 aufgeschrieben werden,

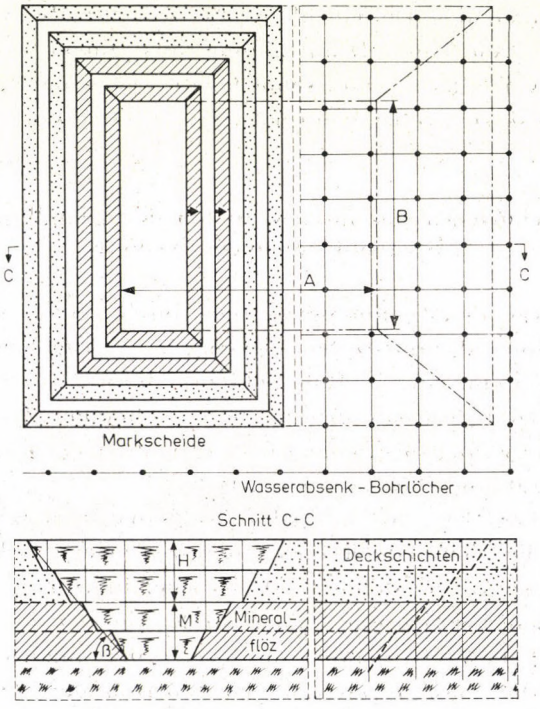

Abb. 1. Prinzipskizze eines Tagebaus

wobei die in der Praxis geforderte Genauigkeit zwar unbeeinträchtigt eingehalten ist, doch wegen wesentlicher Erleichterung der Berechnung die unregelmäßigen Konturen des Schachtfeldes durch regelmäßige Konturen ersetzt sind.

Mit Berücksichtigung des Obengesagten können die für den Tagebau kennzeichnenden Kosten wie folgt aufgeschrieben werden:

1. Herstellungskosten für Bohrlöcher zur Wasserspiegelabsenkung:

$$K_{k1} = \frac{(A + 2a \cdot l) \cdot (B + 2b \cdot l)}{l^2} \cdot H' \cdot k_{k1} \qquad \text{(in Pm)}.$$

Hierin sind:

A Erstreckung des Tagebaufeldes im Streichen in der Flözebene gemessen (in m),

B Erstreckung des Tagebaufeldes im Einfallen (in m),

l gegenseitiger Abstand der Wasserabsenkbohrlöcher (in m),

a Faktor des Übergreifens der Bohrlöcher aus Sicherheitsgründen in der Streichrichtung. Dieser Wert kann in den einzelnen Bergbaugebieten mit verschiedenen geologischen Gegebenheiten durch systematische hydrogeologische Messungen und Auswertungen bestimmt werden,

b Sicherheitsfaktor für das Übergreifen der Wasserabsenkbohrlöcher in der Einfallsrichtung,

H' Länge der Wasserabsenkungsbohrlöcher, wobei auch die obligatorische Eindringtiefe in das Liegende des Flözes oder der Flöze berücksichtigt werden muß, (in m),

k_{k1} spezifische Herstellungskosten der Wasserabsenkbohrlöcher (in Pe/m).

2. *Kosten der Wasserspiegelabsenkung:*

$$K_{k2} = (A + 2a \cdot l) \cdot (B + 2b \cdot l) \cdot H_v \cdot k_{k2} \qquad \text{(in Pm)}.$$

Hierin sind:

H_v Abstand des ruhenden Wasserspiegels vom Liegenden der zum Abbau vorgesehenen Lagerstätte (Flöz) des nutzbaren Mineralrohstoffes (in m),

k_{k2} spezifische Kosten der Wasserhebung (in Pe/m^3).

3. *Investitionskosten der Obertageobjekte:*

$$K_{k3} = q_k^v \cdot k_{k3} \qquad \text{(in Pm)}.$$

Hierin sind:

q_k Jahresförderkapazität des Tagebaus (10^6 t/Jahr),

k_{k3} spezifische Investitionskosten zur Schaffung der Einheit der Produktionskapazität

$$\left[\frac{\text{Pm} \cdot \text{Jahr}}{10^6\text{t}}\right].$$

Die Größe dieses Faktors kann so bestimmt werden, daß man die Investitionsdaten von Tagebauen ähnlicher Kapazität durch Korrelationsberechnungen auswertet.

$\nu = 0{,}5 - 1$ Faktor von solcher Größe, wobei die geologischen Gegebenheiten und der Mechanisierungsgrad zu berücksichtigen sind. Letztere können gleichfalls durch Korrelationsberechnungen ermittelt werden.

4. Auffahrungskosten des Aufschlußgrabens:

$$K_{k4} = \frac{H}{3} \cdot \{[(B + 2H \cdot \operatorname{ctg} \beta) \cdot (A' + 2H \cdot \operatorname{ctg} \beta)] +$$

$$+ \sqrt{(B + 2H \cdot \operatorname{ctg} \beta) \cdot (A' + 2H \cdot \operatorname{ctg} \beta) \cdot B \cdot A'} + B \cdot A'\} k_{k4} \quad \text{(in Pm).}$$

Hierin sind:

A' streichende Erstreckung des Aufschlußgrabens (in m),
β Generalböschungswinkel (in °),
k_{k4} spezifische Auffahrungskosten des Aufschlußgrabens (in Pe/m³).

5. Kosten für Transport des Materials aus dem Aufschlußgraben auf die Außenhalde:

$$K_{k5} = \frac{H}{3} \{[(B + 2H \cdot \operatorname{ctg} \beta) \cdot (A' + 2H \cdot \operatorname{ctg} \beta)] +$$

$$+ \sqrt{(B + 2H \cdot \operatorname{ctg} \beta) \cdot (A' + 2H \cdot \operatorname{ctg} \beta) \cdot B \cdot A'} + b \cdot A'\} \cdot \varrho \cdot l_h \cdot k_{k5}$$

(in Pm).

Hierin sind:

l_h Entfernung der Außenhalde vom Aufschlußgraben (in m),
ϱ durchschnittliche Dichte der abzuräumenden Deckschichten (in t/m³),
k_{k5} spezifische Transportkosten vom Aufschlußgraben bis zur Außenhalde (in Pm/tm).

6. Gesamtabtragungskosten der Abraumberge:

$$K_{k6} = \frac{H}{3} \{[(B + 2H \cdot \operatorname{ctg} \beta) \cdot (A - A')] + (A - A') \cdot$$

$$\cdot \sqrt{B \cdot (B + 2H \cdot \operatorname{ctg} \beta)} + B \cdot (A - A')\} k_{k6} \quad \text{(in Pm).}$$

Hierin ist

k_{k6} spezifische Abraumkosten (in Pe/m³).

7. Transportkosten für Abraumberge innerhalb des Tagebauraumes. Bei dieser Kostenposition muß die Bewegung der aus dem Aufschlußgraben

gelösten Berge nicht mehr berücksichtigt werden:

$$K_{k7} = \frac{H}{3}\{[(B + 2H \cdot \operatorname{ctg}\beta)(A - A')] + (A - A') \cdot \sqrt{B \cdot (B + 2H \cdot \operatorname{ctg}\beta)} + B \cdot (A - A')\} \cdot \left[\frac{(A - A')}{4} \cdot k_{k7c} + \frac{B}{4} \cdot k_{k7d}\right] \quad \text{(in Pm).}$$

Hierin sind:

k_{k7c} spezifische Bewegungskosten für Abraumberge in der Streichrichtung (in Pe/t · m),
k_{k7d} spezifische Bewegungskosten für Abraumberge in der Einfallsrichtung (in Pe/t · m).

8. Gesamtkosten für Bewegung des Nutzmineralrohstoffes in der Flözebene:

$$K_{k8} = A \cdot B \cdot \delta_k \cdot \left[\frac{A}{4} \cdot k_{k8c} + \frac{B}{4} \cdot k_{k8d}\right] \quad \text{(in Pm).}$$

Hierin sind:

δ_k mittlere Flözproduktivität bei Tagebaubetrieb (in t/m²),
k_{k8c} spezifische Bewegungskosten in der Streichrichtung des tagebaumäßig gewonnenen nutzbaren Mineralrohstoffes (in Pe/t · m),
k_{k8d} spezifische Bewegungskosten in der Einfallsrichtung des nutzbaren Mineralrohstoffes (in Pe/t · m).

9. Kosten der Vertikalbewegung sämtlicher tagebaumäßig gewonnenen nutzbaren Mineralrohstoffe:

$$K_{k9} = A \cdot B \cdot \delta_k \cdot H_s \cdot k_{k9} \quad \text{(in Pm).}$$

Hierin sind:

H_s Abstand des Schwerpunktes des tagebaumäßig gewonnenen Mineralvorrates von der Tagesoberfläche (in m),
k_{k9} spezifische Kosten der Vertikalbewegung (in Pe/t · m).

10. Transportkosten des geförderten Mineralvorrates zum Aufbereitungswerk oder zum Zielverbraucher:

$$K_{k10} = A \cdot B \cdot \delta_k \cdot \left(\frac{B}{2} + L\right) \cdot k_{k10} \quad \text{(in Pm).}$$

Hierin sind:

L Entfernung vom Tagebau bis zum Aufbereitungswerk oder dem Zielverbraucher (in m),

k_{k10} spezifische Kosten für Obertagsbewegung des tagebaumäßig abgebauten nutzbaren Mineralrohstoffes (in Pe/t · m).

11. Rekultivierungskosten für die abgeräumten Deckschichten:

$$K_{k11} = \{[(A - A') + 2H \cdot \operatorname{ctg} \beta] \cdot (B + 2H \cdot \operatorname{ctg} \beta)\} \cdot k_{k11} \quad \text{(in Pm)}.$$

Hierin ist:

k_{k11} spezifische Rekultivierungskosten (in Pe/m²).

Mit Hilfe der aufgeschriebenen Kostenfunktionen kann der Optimalwert der Tagebau-Hauptparameter durch Errechnung der Extremwerte mit folgenden Zielfunktionen bestimmt werden:

1. Das eine Optimierungskriterium kann das auf den ganzen abbaubaren Mineralvorrat des Tagebaus projizierte Kostenminimum sein, laut Gleichung:

$$k_k = \frac{\Sigma K_k}{Q} \rightarrow \min$$

oder bei einer Lagerstätte mit regelmäßiger Kontur:

$$k_k = \frac{\Sigma K_k}{A \cdot B \cdot \delta_k} \rightarrow \min .$$

2. Ebenso kann auch der maximal erreichbare Gewinn das Optimierungskriterium sein:

$$N = Q \cdot k_a - \Sigma K_k \rightarrow \max .$$

Hierin ist:

k_a Verkaufspreis (Weltmarktpreis) des nutzbaren Mineralgrundstoffes (in Pe/t).

Oder im Falle eines regelmäßigen Schachtfeldes:

$$N = A \cdot B \cdot \delta_k \cdot k_a - \Sigma K_k \rightarrow \max .$$

Es ist immer ratsam, die Werte der optimalen Hauptparameter mit beiden Kriterien zu bestimmen. Zuletzt müssen dann jene Bereiche der Hauptparameter festgelegt werden, welche die beiden Kriterien möglichst am besten erfüllen.

Im Falle nur einer variablen Größe können zur Berechnung der spezifischen Kosten bzw. des erzielbaren Gewinnes folgende Funktionskombinationen aufgeschrieben werden:

$$k_k = f_1(A) + C_1 \quad \text{bzw.} \quad N = g_1(A) + P_1$$

oder oder

$$k_k = f_2(B) + C_2 \qquad N = g_2(B) + P_2$$

oder oder

$$k_k = f_3(H) + C_3 \qquad N = g_3(H) + P_3$$

oder oder

$$k_k = f_4(q) + C_4 \qquad N = g_4(q) + P_4 .$$

Aus diesen Beziehungen können mit der Berechnung der einvariablen Extremwerte auch analytisch auf verhältnismäßig einfache Weise die optimalen Werte (A; B; H bzw. q) ermittelt werden.

In bivariablem Fall können folgende Funktionskombinationen untersucht werden:

$$k_k = h_1(A; B) + R_1 \quad \text{bzw.} \quad N = j_1(A; B) + S_1$$

oder oder

$$k_k = h_2(A; H) + R_2 \qquad N = j_2(A; H) + S_2$$

oder oder

$$k_k = h_3(A; q) + R_3 \qquad N = j_3(A; q) + S_3$$

oder oder

$$k_k = h_4(B; H) + R_4 \qquad N = j_4(B; H) + S_4$$

oder oder

$$k_k = h_5(B; q) + R_5 \qquad N = j_5(B; q) + S_5$$

oder oder

$$k_k = h_6(H; q) + R_6 \qquad N = j_6(H; q) + S_6 .$$

Aus diesen Funktionen können durch analytische oder Näherungslösung der durch Berechnung der Extremwerte erhaltenen algebraischen Gleichungen die Optimalwerte der Hauptparameter bestimmt werden.

Im Falle von drei Variablen können folgende Funktionskombinationen analysiert werden:

$$k_k = l_1(A; B; H) + T_1 \text{ bzw. } N = m_1(A; B; H) + V_1$$
oder oder
$$k_k = l_2(A; B; q) + T_2 \qquad N = m_2(A; B; q) + V_2$$
oder oder
$$k_k = l_3(A; H; q) + T_3 \qquad N = m_3(A; H; q) + V_3$$
oder oder
$$k_k = l_4(B; H; q) + T_4 \qquad N = m_4(B; H; q) + V_4 .$$

Auch aus diesen Funktionen kann man durch Lösung jener algebraischen Gleichungen, die man nach der Durchführung der Berechnung der Extremwerte bekommen hat, die Extremwerte der Hauptparameter bestimmen.

Schließlich können — als der allerallgemeinste Fall — die Extremwerte der folgenden Zielfunktionen untersucht werden, um die Kombinationen der optimalen Hauptparameter zu ermitteln:

$$k_k = n(A; B; H; q) + U_1 \text{ bzw. } N = p(A; B; H; q) + Z_1 .$$

In diesem Falle ist es am zweckmäßigsten, zur Bestimmung der optimalen Hauptparameterwerte entsprechende Computer-Programme abzuspielen.

Der Einsatz von EDV-Anlagen zu den weiteren Untersuchungen und zur Optimierung der Hauptparameter ist in jeder Hinsicht von Vorteil und notwendig, da man bei der Durchführung dieser Analysen noch folgendes berücksichtigen muß:

1. Wenn der Tagebau nicht als selbständige Produktionseinheit, sondern eingebettet in die Organisation des Industriezweiges analysiert werden soll, dann müssen die Optimalwerte für das ganze große System durch lineare oder dynamische Programmierung bestimmt werden.

2. Die Lebensdauer des Tagebaus muß sowohl bei dem Zinsendienst der Investitionskosten, wie auch bei der Diskontierung der Betriebsausgaben in Rechnung gestellt werden.

3. Die spezifischen Kosten (Abraumkosten, Materialbewegungskosten usw.) ändern sich oder können sich als Funktionen der Hauptparameter ändern. Sehr oft läßt sich aber dieser Zusammenhang in Form einer analytischen Funktion gar nicht auszudrücken. In solchem Falle kann man eigentlich bzw. ist es zweckmäßig die Berechnungen mit dem Produkt der fixen Werte der spezifischen Kosten durchzuführen.

4. Die spezifischen Kosten ändern sich — in Abhängigkeit von den jeweiligen technologischen Lösungen — meist mit unterbrochenem Charakter. In solchen Fällen darf man natürlich nur mit jenen spezifischen Kostenfunktionen arbeiten, die für die einzelnen Bereiche gültig sind, und bei deren Anwendung selbst der Ort der Unterbrechungspunkte bezeichnet werden muß. In der Mehrzahl der Fälle kann man den Unterbrechungscharakter dadurch

eliminieren, daß man Ausgleichfunktionen anwendet, deren Genauigkeit den Ansprüchen der Praxis entspricht.

5. Die naturgegebenen Parameter (z. B. Lagerstätten- [Flöz-]Produktivität) oder die spezifischen Kosten sind meist Wahrscheinlichkeitsvariablen, deren voraussichtlicher Wert nur angenähert bestimmt werden kann.

Die aus den erwähnten Faktoren herrührende Unsicherheit kann wesentlich dadurch eingeengt werden, wenn man — mit Berücksichtigung der möglichen technisch-wissenschaftlich-technologischen Entwicklung — mehrere Alternativen der Kosten- (Gewinn-) Funktionen aufstellt, und mit ihrer Hilfe die technisch-ökonomischen Optimalbereiche bezeichnet, innerhalb deren eine Veränderung der Hauptparameter das Kostenminimum bzw. das Gewinnmaximum um nicht mehr als ± 5—10% überschreitet.

3.2 Tiefbau

Das kennzeichnende Kostenmodell für die tiefbaumäßige Bergbautechnologie kann auf Grund von Abb. 2 aufgeschrieben werden, wobei man — um den Charakter der Einflußgrößen besser hervorzuheben — anstatt der

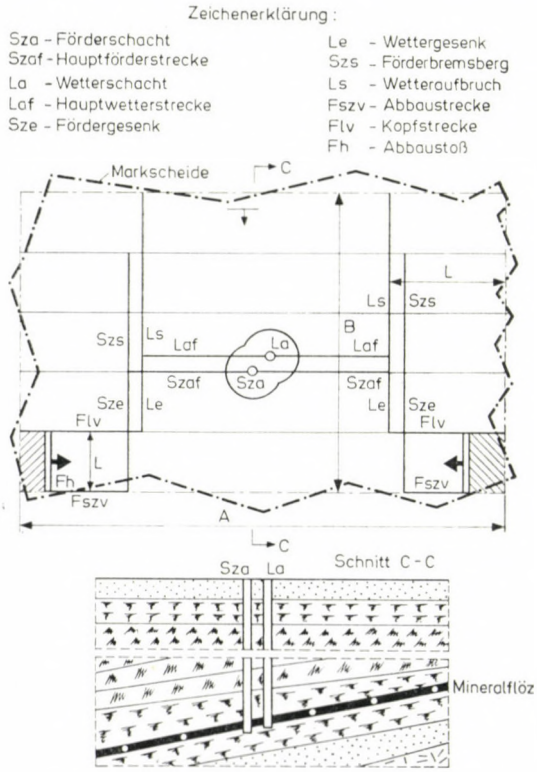

Abb. 2. Prinzipskizze einer Tiefbaugrube

unregelmäßigen wirklichen Kontur des Schachtfeldes die Untersuchungen an einem regelmäßig geformten Schachtfeld anstellt.

Das Kostenmodell des Bergbautechnologie-Systems „Tiefbau" kann aus folgenden Komponenten aufgebaut werden:

1. Investitionskosten der Obertagsobjekte:

$$K_{m1} = q_m^v \cdot k_{m1} \qquad \text{(in Pm).}$$

Hierin sind:

k_{m1} spezifische Investitionskosten $\frac{\text{Pe} \cdot \text{Jahr}}{10^6\text{t}}$, die im technologischen System „Tiefbau" zum Schaffen der Einheit der Produktionskapazität nötig sind,

q_m Jahres-Förderkapazität des Tiefbau-Bergwerks (in 10^6 t/Jahr),

v Exponent zwischen 0,5 und 1, dessen konkrete Größe sich immer nach den jeglich angewandten technologischen Lösungen gestaltet.

2. Abteufkosten der Grubenerschließungsschächte:

$$K_{m2} = n \cdot H \cdot k_{m2} \qquad \text{(in Pm).}$$

Hierin sind:

n Anzahl der Schächte, die für Grubenförderung, Bewetterung, Fahrung usw. erforderlich sind,

H mittlere Schachttiefe (in m),

k_{m2} mittlere spezifische Schachtabteufkosten (in Pe/m).

3. Auffahrungskosten der Hauptausrichtungs-Grubenräume (Schachtfüllorte, Grundstrecken):

$$K_{m3} = n'(A - 2L) \cdot k_{m3} \qquad \text{(in Pm).}$$

Hierin sind:

n' Anzahl der zur Grubenhauptausrichtung nötigen Grundstrecken, die bei flözgerechtem Aufbau $2 \div 3$ beträgt; bei Schachtsohlen-Abbau sich aber je nach der Sohlenteilung richtet,

L mittlere Streichenderstreckung der Baufelder, meist die mittlere Baulänge der Strebfelder (in m),

k_{m3} mittlere spezifische Auffahrungskosten der Grundstrecken und sonstiger Hauptausrichtungsbau (vor allem von der Größe des jeweiligen Streckenausbruch-Querschnittes abhängig) (in Pe/m).

4. Auffahrungskosten der Baufeldenschlußstrecken:

$$K_{m4} = 2 \cdot (B - l) \cdot \frac{A}{L} \cdot k_{m4} \qquad \text{(Pm)}.$$

Hierin sind:

A Schachtfelderstreckung im Streichen (in m),
B Schachtfelderstreckung im Einfallen (in m),
l mittlere Strebstoßlänge (in m),
k_{m4} spezifische Auffahrungskosten der Baufeldanschlußstrecken (in Pe/m).

5. Auffahrungskosten der Abbau-Vorrichtungsstrecken:

$$K_{m5} = \left(\frac{B}{l} + 1\right) A \cdot \frac{M}{s} \cdot k_{m5} \qquad \text{(in Pm)}.$$

Hierin sind:

M Abbauwürdige Flözmächtigkeit (in m),
s Abgebaute Scheibenmächtigkeit (in m),
k_{m5} spezifische Auffahrungskosten der Abbauvorrichtungsstrecken (in Pe/m).

6. Kosten für Ausgestaltung der Strebstöße:

$$K_{m6} = 2 \cdot B \cdot \frac{M}{s} \cdot k_{m6} \qquad \text{(in Pm)}.$$

Hierin ist:

k_{m6} spezifische Kosten für Strebstoß-Ausgestaltung, incl. spezifischer Aufwand für Auf- und Abmontage (in Pe/m).

7. Gesamtkosten für Fahrung und Materialbewegung innerhalb des Schachtfeldes:

$$K_{m7} = \frac{A^2 \cdot B \cdot \delta_m}{4} \cdot k_{m7c} + \frac{A \cdot B_s^2 \cdot \delta_m}{2} \cdot k_{m7s} + \frac{A(B - B_s)^2}{2} \cdot \delta_m \cdot k_{m7e} \qquad \text{(in Pm)}.$$

Hierin sind:

δ_m Flözproduktivität bei Anwendung der Tiefbautechnologie (in t/m²),
B_s Erstreckung des Schachtfeldflügels in der Bremsbergrichtung (in m),
k_{m7s} spezifische Gesamtkosten für Fahrung und Materialbewegung in Bremsbergrichtung (in Pe/tm),

k_{m7c} spezifische Gesamtkosten für Fahrung und Materialbewegung in der Streichrichtung (in Pe/tm),

k_{m7e} spezifische Gesamtkosten für Fahrung und Materialbewegung in Gesenk-Richtung (in Pe/tm).

8. Gesamtkosten für Fahrung und Materialbewegung in Schachtrichtung:

$$K_{m8} = A \cdot B \cdot \delta_m \cdot H \cdot k_{m8} \qquad \text{(Pm)}.$$

Hierin sind:

k_{m8} Spezifische Gesamtkosten für Fahrung und Materialbewegung zum Schacht hin (in Pe/tm).

9. Obertags-Transportkosten für den ganzen gewinnbaren Mineralvorrat:

$$K_{m9} = A \cdot B \cdot \delta_m \cdot L_k \cdot k_{m9} \qquad \text{(in Pm)}.$$

Hierin sind:

L_k Entfernung des Obertagstransportes bis zum Aufbereitungswerk oder zum Zielverbraucher (in m),

k_{m9} spezifische Gesamtkosten für obertägige Materialbewegung (in Pe/tm).

Selbstredend erweitert sich der Kreis der mit der „Tiefbau"-Technologie verbundenen Kosten weiter, wenn mit den Kosten für eine Wasserabsenkung bzw. für eine an den Grubenbetrieb anschließende Mineralaufbereitung gerechnet werden muß.

Ohne weiter auf Einzelheiten einzugehen, kann festgestellt werden, daß zur Optimierung der Hauptparameter auch bei dem technologischen Tiefbausystem ähnliche Kombinationen untersucht werden können, wie dieses oben, bei der Analysierung des tagebaumäßigen Abbaus, vorgezeigt wurde.

3.3 Unterwasser-Abbau

Das Abbausystem für die unter dem Wasserspiegel gelagerten Mineralgrundstoffe ist hinsichtlich der Struktur eine der einfachsten Lösungen. Berücksichtigt man noch, daß der größte Teil der noch gewinnbaren Mineralvorräte in den Tiefen der Meere zu finden ist, so hat dieses Bergbautechnologie-System potentiell noch eine sehr große Zukunft.

Seine wichtigsten technischen Vorzüge können wie folgt kurz skizziert werden:

a) Um Bodenschätze unter dem offenen Wasserspiegel abzubauen, ist ein Abräumen von Deckschichten nicht erforderlich.

b) Sind die Unterwassergesteine (Sand, Kies, Bauxit usw.) von Deckschichten überlagert, so kann meist der Abbau des nutzbaren Mineralrohstoffes schon nach einer minimalen Abräumarbeit beginnen.

c) Die Erschließungs- und Gewinnungsmaßnahmen können miteinander verschmolzen werden.

d) Die Bauobjekte für Gewinnung und Mineralaufbereitung haben einen einfachen Aufbau und können konzentriert angelegt werden.

e) Das Gewinnen, Fördern, ja sogar auch das Anreichern des Mineralrohstoffes kann mit Hilfe desselben Arbeitsmediums, des Wassers, verrichtet werden. Um dabei einen maximalen Effekt zu erreichen, kann das zu den verschiedensten Prozessen benützte Wasser rezirkuliert werden.

f) Die bei der Gewinnung und Verarbeitung anfallenden Berge können mit Transport über Rohrleitungen auf dem kürzesten Wege in die mit dem Abbau parallel fortschreitenden und abzuwerfenden, ausgekohlten Grubenräume gefüllt bzw. versetzt werden.

Bei dem Abbau der Unterwasser-Mineralvorkommen ist heute noch die Förderkapazität der Geräte und Einrichtungen bzw. die vertikale Tiefengrenze der Materialbewegung die Hauptschranke der Entwicklung.

Jene Kosten, die aus dem Anwenden der Unterwasser-Bergbautechnologie erwachsen, können wie folgt gekennzeichnet werden:

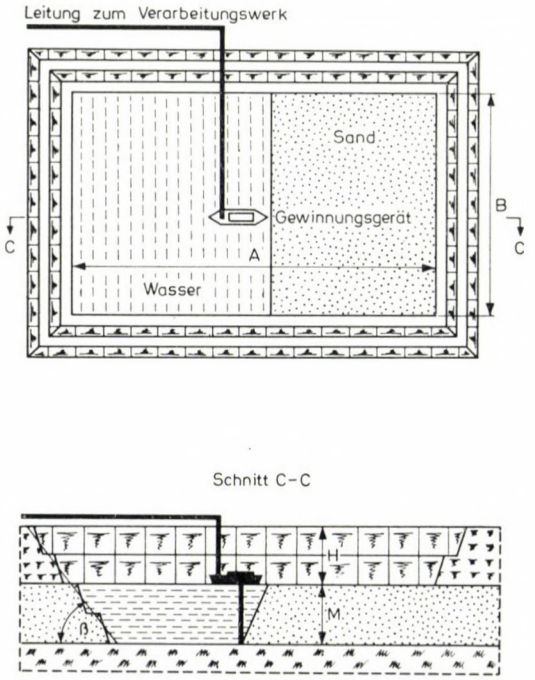

Abb. 3. **Prinzipskizze einer Unterwassergrube für feste Mineralrohstoffe**

1. Investitionskosten für die Obertags-Objekte:

$$K_{v1} = q_v^v \cdot k_{v1} \qquad \text{(Pm)}.$$

Hierin sind:

q_v Förderkapazität des Grubenbetriebes mit Unterwasserabbau (in 10^6 t/Jahr),

$v = 0{,}5 - 1$ Konstante zwischen den beiden Grenzwerten,

k_{v1} spezifische Investitionskosten zur Schaffung von 1 Produktionskapazität-Einheit bei Anwendung der Unterwasserbau-Technologie $\left(\text{in } \frac{\text{Pe} \cdot \text{Jahr}}{10^6\text{t}}\right)$.

2. Kosten für die Herstellung des Aufschlußgrabens:

$$K_{v2} = \frac{H}{3}\left[(B + 2H \cdot \operatorname{ctg}\beta) \cdot (A' + 2H \cdot \operatorname{ctg}\beta) + \right.$$
$$\left. + \sqrt{(B + 2H \cdot \operatorname{ctg}\beta)(A' + 2H \cdot \operatorname{ctg}\beta) \cdot A' \cdot B} + A' \cdot B\right] k_{v2} \qquad \text{(Pm)}.$$

Hierin sind:

A' Erstreckung des Aufschlußgrabens im Streichen (in m),

B Erstreckung des Aufschlußgrabens im Einfallen (in m),

H Durchschnittsmächtigkeit der abzuräumenden Deckschicht (in m),

β Generalböschungswinkel (in °),

k_{v2} spezifische Abraumkosten (in Pe/m^3).

3. Kosten des Bergetransports aus dem Aufschlußgraben zur Außenhalde:

$$K_{v3} = \frac{H}{3}\left[(B + 2H \cdot \operatorname{ctg}\beta) \cdot (A' + 2H \cdot \operatorname{ctg}\beta) + \right.$$
$$\left. + \sqrt{(B + 2H \cdot \operatorname{ctg}\beta) \cdot (A' + 2H \cdot \operatorname{ctg}\beta) \cdot A' \cdot B} + A' \cdot B\right] l_h \cdot k_{v3} \qquad \text{(Pm)}.$$

Hierin sind:

l_h Entfernung der Außenhalde vom Aufschlußgraben (in m),

k_{v3} spezifische Materialbewegungskosten der Berge aus dem Aufschlußgraben (in Pe/tm).

4. Gesamtkosten der Abraumberge:

$$K_{v4} = (A - A') \cdot (B + H \cdot \operatorname{ctg}\beta) \cdot H \cdot k_{v4} \qquad \text{(Pm)}.$$

Hierin sind:

k_{v4} spezifische Abraumkosten der Deckschichten (in Pm).

5. Gesamtkosten für das Bewegen der Abraumberge innerhalb der Tagebaugrube:

$$K_{v5} = \frac{(A - A')^2}{4} \cdot (B + H \cdot \operatorname{ctg} \beta) \cdot H \cdot \varrho \cdot k_{v5c} + \\ + (A - A') \cdot \frac{(B + H \cdot \operatorname{ctg} \beta)^2}{4} \cdot H \cdot \varrho \cdot k_{v5d} \quad \text{(Pm).}$$

Hierin sind:

ϱ durchschnittliche Dichte der Deckschichten (in t/m³);
k_{v5c} spezifische Gesamtkosten für Materialbewegung im Streichen innerhalb der Tagebaugrube (in Pe/tm),
k_{v5d} spezifische Gesamtkosten für Materialbewegung im Einfallen, innerhalb der Tagebaugrube (in Pe/tm).

6. Gesamtkosten für Gewinnung des nutzbaren Mineralrohstoffes in der Unterwasser-Tagebaugrube:

$$K_{v6} = (A + M \cdot \operatorname{ctg} \beta) \cdot (B + M \cdot \operatorname{ctg} \beta) \cdot \delta_v \cdot k_{v6} \quad \text{(Pm).}$$

Hierin sind:

A streichende Erstreckung der für Unterwasserabbau vorgesehenen nutzbaren Minerallagerstätte (in m),
B einfallende Erstreckung der Minerallagerstätte (in m),
M Mächtigkeit des abzubauenden Mineralflözes (in m),
δ_v mittlere Flözproduktivität des Mineralvorkommens bei Unterwasserabbau (in t/m²).

7. Gesamte Materialbewegungskosten des nutzbaren Mineralrohstoffes in der Unterwasser-Tagebaugrube:

$$K_{v7} = \left\{ \frac{(A + M \cdot \operatorname{ctg} \beta)^2}{4} \cdot (B + M \cdot \operatorname{ctg} \beta) + (A + M \cdot \operatorname{ctg} \beta) \cdot \right. \\ \left. \cdot \frac{(B + M \cdot \operatorname{ctg} \beta)^2}{4} \right\} \delta_v \cdot k_{v7} \quad \text{(Pm).}$$

Hierin sind:

k_{v7} spezifische Kosten für die gesamte Materialbewegung des nutzbaren Mineralrohstoffes in der Unterwasser-Tagebaugrube (in Pe/tm).

8. Gesamtkosten für Vertikalbewegung des abgebauten nutzbaren Mineral grundstoffes:

$$K_{v8} = (A + M \cdot \operatorname{ctg} \beta) \cdot (B + M \cdot \operatorname{ctg} \beta) \cdot \delta_v \cdot \left(H + \frac{M}{2}\right) \cdot k_{v8} \qquad \text{(Pm)}.$$

Hierin ist:

k_{v8} gesamte spezifische Gesamtkosten für Vertikalbewegung des unter Wasser abgebauten nutzbaren Materialrohstoffes (in Pe/tm).

9. Gesamtkosten für Transport des abgebauten nutzbaren Mineralrohstoffes, bis zum Verarbeitungswerk oder zum Zentrallagerplatz:

$$K_{v9} = \left\{(A + M \cdot \operatorname{ctg} \beta) \cdot (B + M \cdot \operatorname{ctg} \beta) \cdot \delta_v \cdot \left[\frac{B}{2} + (H + M) \cdot \operatorname{ctg} \beta + l_f\right]\right\} k_{v9} \qquad \text{(Pm)}.$$

Hierin sind:

l_f Entfernung vom Rand der fördernden Unterwasser-Tagebaugrube bis zum Verarbeitungswerk oder dem Zentrallagerplatz (in m),

k_{v9} spezifische Gesamtkosten für Materialbewegung bis zum Verarbeitungswerk oder dem Zentrallagerplatz (in Pe/tm).

10. Rekultivationskosten:

$$K_{v10} = (A - A') \cdot (B + H \cdot \operatorname{ctg} \beta) \cdot k_{v10} \qquad \text{(Pm)}.$$

Hierin ist:

k_{v10} Rekultivationskosten je Flächeneinheit der Berghalde (in Pe/m^2).

11. Aufbereitungskosten für den (die) unter Wasser abgebauten nutzbaren Mineralgrundstoff(e):

Mit diesem Kostenposten muß gewöhnlich dann gerechnet werden, wenn die Mineralaufbereitung direkt am Gewinnungsort angelegt ist. Wird jedoch das Aufbereitungswerk organisatorisch vom Grubenbetrieb getrennt, dann kann dieser Kostenanteil in dem Kostenaufwand für das Bergbautechnologie-System vernachläßigt werden.

Die Aufbereitungskosten für den unter Wasser abgebauten Mineralrohstoff können aus folgender Beziehung berechnet werden.

$$K_{v11} = (A + M \cdot \operatorname{ctg} \beta) \cdot (B + M \cdot \operatorname{ctg} \beta) \cdot \delta_v \cdot k_{v11} \qquad \text{(Pm)}.$$

Hierin ist:

k_{v11} gesamte spezifische Aufbereitungskosten für nutzbaren Mineralgrundstoff (oder Grundstoffe) (in Pe/t).

Auch bei der Bestimmung der optimalen Hauptparameter des Unterwasser-Abbausystems für Mineralrohstoffe kann man — gestützt auf sämtliche Kostenfunktionen — alle bereits beim technologischen System „Tagebau" vorgezeigten Kombinationen untersuchen.

3.4 Bohrloch-Abbau

Das Bergbautechnologie-System des Abbaus nutzbarer Mineralrohstoffe mit Hilfe von Bohrlöchern ist heute in der ganzen Welt am weitesten zur Gewinnung fluider Rohstoffe (wie: Erdgas, Erdöl, Wasser usw.) verbreitet. Neuerdings setzen sich aber immer mehr auch jene technologischen Systeme durch, bei denen verschiedene Mineralstoffe von festem Aggregatzustand auf diese Weise abgebaut werden.

Unter den festen Mineralrohstoffen wird vor allem die Gewinnung von Schwefel und Steinsalz in zahlreichen Ländern (Sowjetunion, USA, Mexiko, Polen usw.) mit Hilfe von Bohrlöchern seit Jahrzehnten mit Erfolg betrieben. In mehreren Bergbaurevieren laufen erfolgreiche Versuche, und ist man bemüht, die vorhandene Kohle untertägig zu vergasen. Einer Anwendung dieses Verfahrens im Großbetriebsmaßstab aber steht einstweilen noch die mindere Qualität des dabei erzeugten Gases wie auch die schwere Regulierbarkeit des Verbrennungsprozesses im Wege. Ebenso ist es der schweren Regulierbarkeit zuzuschreiben, daß die Veränderung des Aggregatzustandes von Erzlagerstätten, und ihre Ausbeutung durch gut lenkbare physikalisch-chemische Reaktionen, einstweilen nur unter Laboratoriumsbedingungen realisiert werden konnte.

Unter den heimischen Verhältnissen kann die Verbreitung der Bohrloch-Abbautechnologie zunächst bei der Gewinnung von Bauxit und sonstigen Tonmineralien erwartet werden. Es braucht nämlich bei dem Abbau dieser Mineralrohstoffe nur das einfachste Verfahren der Aggregatzustandsänderung, das Herstellen einer Arbeitstrübe, angewendet werden.

Als die hauptsächlichsten Vorzüge der Bohrloch-Abbautechnologie können die folgenden aufgezählt werden:

1. Die zum Abbau vorgesehene nutzbare Minerallagerstätte kann auf dem kürzesten und schnellsten Weg durch ein vertikales Bohrloch erreicht werden.

2. Wird die Bohrung fünding, so kann das Erkundungsbohrloch mit relativ geringem Aufwand in kürzester Zeit in eine Fördersonde umgebaut werden.

3. Die Gewinnungsstruktur ist hier am einfachsten, da sich an das Bohrloch — als Förderweg — unmittelbar der Abbaubereich anschließt.

4. Durch Fluidisierung kann das Gewinnen, Laden und Räumen, das Fördern und das Aufbereiten des nutzbaren Mineralgrundstoffes als eine einzige technologische Kette ausgebaut werden.

5. Man kann den gewonnenen Nutzmineralgrundstoff im vollen Querschnitt in der Fördersonde hochströmen lassen.

6. Im Vergleich zu anderen Bergbausystemen gewährt dieses Verfahren eine größere Betriebssicherheit, und ermöglicht auch eine größere wirtschaftliche Abbautiefe.

7. Zur Verrichtung der Abbaubarkeit müssen sich keine Menschen auf der Sohle des Bohrloches aufhalten.

8. Die sich bei dem Abbau ergebenden primären Mineralverluste können zwar größer (40—50%) sein, als sie für andere Bergbausysteme kennzeichnend sind, doch können die Verluste hier durch sekundäre bzw. tertiäre Abbauverfahren beträchtlich vermindert werden.

Die Kosten für das technologische System des Bohrloch-Abbaus können auf Grund von Abb. 4 aufgeschrieben werden. Mit Erfüllung der in der Praxis geforderten Genauigkeit, jedoch zwecks einfacherem Ausdruck der kennzeichnenden Zusammenhänge sei angenommen, daß man das Gebiet des zum

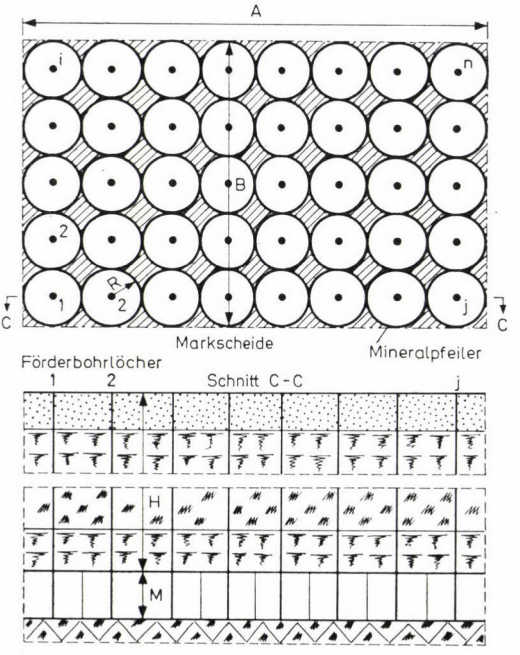

Abb. 4. Prinzipskizze einer Bohrlochabbau-Grube

Abbau vorgesehenen Mineralvorkommens in regelmäßiger Anordnung mit Bohrlochabbau-Bereichen bedecken kann.

Mit Berücksichtigung des Obigen können jene kennzeichnenden Kosten, die aus dem Bohrloch-Abbausystem auf feste Mineralrohstoffe erwachsen, mit den folgenden Funktionen ausgedrückt werden:

1. Investitionskosten der obertägigen Bauobjekte:

$$K_{f1} = q_f^v \cdot k_{f1} \qquad \text{(Pm)}.$$

Hierin sind:

q_f Förderkapazität des Grubenbetriebes mit Bohrlochabbautechnologie (in 10^6 t/Jahr),

$v = (0{,}5 - 1)$ konstanter Exponent zwischen den beiden Grenzwerten, der durch Auswertung mit Regressionsanalyse der Daten aus Bergwerken ähnlichen Typs bestimmt werden kann,

k_{f1} spezifische Investitionskosten zur Schaffung der Kapazitätseinheit bei Bohrloch-Abbautechnologie

$$\left(\text{in } \frac{\text{Pe/Jahr}}{10^6 \cdot t}\right).$$

2. Herstellungskosten der Förderbohrlöcher:

$$K_{f2} = \frac{F}{f_f} \cdot (H + M) \cdot k_{f2} \qquad \text{(in Pm)}.$$

Hierin sind:

$n = \dfrac{F}{f_f} = \dfrac{A \cdot B}{R^2 \pi}$ Anzahl der Fördersonden,

k_{f2} spezifische Abteuf- und Sondenkomplettierungskosten der Fördersonde (in Pe/m),

H Lagerungstiefe des für den Bohrlochabbau vorgesehenen Mineralmassives (in m),

M Mächtigkeit des abzubauenden Mineralmassivs (in m),

F Fläche des Schachtfeldes für Bohrlochabbau (bei regelmäßiger Kontur $A \cdot B$) (in m²),

f_f mit einem einzigen Bohrloch abbaubare Fläche ($R^2 \cdot \pi$ bei regelmäßiger Kontur) (in m²),

R Wirkungsradius des Bohrloch-Abbaus (in m).

3. Materialbewegungskosten des Produktes zur Fördersonde:

$$K_{f3} = \frac{F}{f_f} \cdot R^2 \cdot \pi \cdot \delta_f \cdot \frac{R}{2} \cdot k_{f3} \qquad \text{(in Pm)}.$$

Hierin sind:

δ_f mittlere Flözproduktivität bei Bohrloch-Abbau (in t/m²),
k_{f3} Kosten für horizontale Materialbewegung des abgebauten nutzbaren Mineralrohstoffes zum Bohrloch (in Pe/tm).

4. Kosten für Vertikalbewegung des abgebauten nutzbaren Mineralrohstoffes in den Fördersonden:

$$K_{f4} = \frac{F}{f_f} \cdot R^2 \cdot \pi \cdot \delta_f \cdot \left(H + \frac{M}{2}\right) \cdot k_{f4} \qquad \text{(in Pm).}$$

Hierin ist:

k_{f4} spezifische Kosten für Vertikalbewegung des abgebauten nutzbaren Mineralrohstoffes in den Fördersonden (in Pe/tm).

5. Gesamtbewegungskosten des abgebauten nutzbaren Mineralgrundstoffes innerhalb des Schachtfeldes:

$$K_{f5} = \frac{F}{f_f} \cdot R^2 \cdot \pi \cdot \delta_f \cdot \frac{A}{4} \cdot B \cdot k_{f5c} + \frac{F}{f_f} \cdot R^2 \cdot \pi \cdot \delta_f \cdot \frac{B}{4} \cdot A \cdot k_{f5d} \qquad \text{(in Pm).}$$

Hierin sind:

k_{f5c} Kosten für das Bewegen des abgebauten nutzbaren Mineralgrundstoffes in der Streichrichtung (in Pe/tm),
k_{f5d} spezifische Bewegungskosten für den abgebauten nutzbaren Mineralrohstoff in der Einfallrichtung (in Pe/tm).

6. Gesamtbewegungskosten des abgebauten nutzbaren Mineralgrundstoffes vom Schachtfeld bis zur Verarbeitung, bei Bohrlochabbau:

$$K_{f6} = \frac{F}{f_f} \cdot R^2 \cdot \pi \cdot \delta_f \cdot \left(\frac{B}{2} + l_f\right) \cdot k_{f6} \qquad \text{(Pm).}$$

Hierin sind:

l_f Entfernung vom Schachtfeld mit Bohrlochabbau bis zum Verarbeitungswerk (in m),
k_{f6} spezifische Gesamtkosten für Bewegung des Produkts vom Abbaufeld mit Bohrlochabbau bis zum Verarbeitungswerk (in Pe/tm).

7. Kosten für das Versetzen der durch Bohrlochabbau entstandenen Hohlräume:

$$K_{f7} = \frac{F}{f_f} \cdot R^2 \cdot \pi \cdot M \cdot \eta \cdot k_{f7} \qquad \text{(in Pm).}$$

Hierin sind:

η Versatzwirkungsgrad; bei Spülversatz 0,8—0,9,
$k_{f\eta}$ spezifische Versatzkosten (in Pe/m³).

Durch Zusammenziehen der Kostenposten können je nach den konkreten Lagerstättengegebenheiten auf verhältnismäßig einfache Weise die Teilkosten-Funktionen abgeleitet und die nötigen Optimum-Berechnungen durchgeführt werden. In multivariablen Fällen kann die Wirksamkeit der Untersuchungen durch das Abspielen von Computerprogrammen gesteigert werden.

4. Grundprinzip der Auswahl der zweckmäßigsten Kombinationen bei der Anwendung gekoppelter Bergbautechnologie-Systeme

Zur Gewinnung des Mineralvorrates eines gegebenen Vorkommens kann das Auswählen des zweckmäßigsten Bergbautechnologie-Systems durch Bestimmung des damit erzielbaren Gewinnes erfolgen. Zur Ermittlung des optimalen Bergbautechnologie-Systems sei der durch Tagebau erzielbare Gewinn mit — N_K, der durch Tiefbau erzielbare mit — N_M, der durch Unterwasserabbau erzielbare mit — N_V und der durch Bohrlochabbau erzielbare Gewinn mit — N_F bezeichnet.

In dem einfachsten Fall, wenn die Gewinnung des Rohstoffvorrates eines gegebenen Mineralvorkommens nur durch Anwendung eines oder des anderen bergbautechnologischen Systems möglich ist, können für den erreichbaren Gewinn folgende Ungleichheiten aufgeschrieben werden:

$$N_K \gtreqless N_M \qquad N_M \gtreqless N_V \qquad N_V \gtreqless N_F$$

$$N_K \gtreqless N_V \qquad N_M \gtreqless N_F$$

$$N_K \gtreqless N_F\,.$$

Auf Grund der vorgezeigten Ungleichheiten muß dann jenes bergbautechnologische System ausgewählt werden, für das sich die größte Gewinnspanne ergibt. Selbstredend muß man in der Planungsphase auch die weitere technisch-technologische Entwicklung in Betracht ziehen, wobei sich die Richtung der Ungleichheiten — auf einen Zeithorizont von 10 bis 15 Jahren projiziert — je nach den Entwicklungstendenzen sogar umkehren kann.

Bei der Anwendung von technologischen Doppelsystemen sind — wenn der gekoppelte Tagebau und Tiefbau mit anderen Abbaukombinationen verglichen werden soll — die folgenden Fälle möglich.

$$N_K + N_M \gtreqless N_M + N_K$$

$$N_K + N_M \gtreqless N_K + N_V$$

$$N_K + N_M \gtreqless N_K + N_F$$

$$N_K + N_M \gtreqless N_M + N_V$$

$$N_K + N_M \gtreqless N_M + N_F$$

$$N_K + N_M \gtreqless N_V + N_K$$

$$N_K + N_M \gtreqless N_V + N_M$$

$$N_K + N_M \gtreqless N_V + N_F$$

$$N_K + N_M \gtreqless N_F + N_K$$

$$N_K + N_M \gtreqless N_F + N_M$$

$$N_K + N_M \gtreqless N_F + N_V .$$

Wenn zur Gewinnung des Mineralvorkommens die Kombination von drei Bergbausystemen in Frage kommen kann, und dann zuerst der Tagebau angelegt wird, sind die folgenden Kombinationen möglich:

$$N_K + N_M + N_V$$

$$N_K + N_M + N_F$$

$$N_K + N_V + N_M$$

$$N_K + N_F + N_M$$

$$N_K + N_V + N_F$$

$$N_K + N_F + N_V .$$

Mit Vermeidung weiterer Detaillierung sei nur noch gesagt, daß die Anzahl sämtlicher möglicher Reihenfolgen 24 beträgt und dabei insg. 23 Ungleichheitspaare aufgeschrieben werden können.

Wenn aber zur Gewinnung des gegebenen Mineralvorkommens eine Viererkombination an Bergbautechnologie-Systemen real in Frage kommen kann, und zuerst der Tagebau angelegt wird, dann sind folgende Reihenfolgen möglich:

$$N_K + N_M + N_V + N_F$$

$$N_K + N_M + N_F + N_V$$

$$N_K + N_V + N_M + N_F$$

$$N_K + N_V + N_F + N_M$$

$$N_K + N_F + N_V + N_M$$

$$N_K + N_F + N_M + N_V .$$

Auch bei dem Vierersystem der Bergbautechnologien ist die Anzahl der möglichen Kombinationen 24, und die Anzahl der Ungleichheitspaare 23.

Aus obigem folgt, daß bei dem Vergleichen der mehr als zwei betragenden Kombinationen der Bergbautechnologie-Systeme jene Reihenfolge ausgewählt werden muß, mittels welcher die größte Gewinndifferenz erzielbar ist. Wenn dabei einige Systemkombinationen der Bergbautechnologie nahezu den gleichen Gesamtgewinn ergeben, dann soll die endgültige Reihenfolge auf Grund der technischen Durchführbarkeit, der zur Verfügung stehenden Betriebsmittel, deren Leistungsfähigkeit und Zuverläßigkeit bzw. jenes Zeitpunktes festgelegt werden, an dem sie in die Produktion eintreten.

SCHRIFTTUM

1. АГОШКОВ, М. И.: Технико-экономическая оценка полноты и качества извлечения при добыча твердых полезных ископаемых. Сборник «Проблемы рационалного использования минералных ресурсов СССР». ВИНИТИ, Москва, 1969.
2. БУРЧАКОВ, А. С.—ГРИНЬКО, Н. К.—КОВАЛЬЧУК, А. Б.: Технология подземной разработки месторождений полезных ископаемых. Изд. Недра, Москва, 1978.
3. ИМЕНИТОВ, В. Р.: Процессы подземных горных работ при разработка рудных месторождений. Изд. Недра, Москва, 1978.
4. ШЕСТАКОВ, В. Б.: Научные основы выбора и экономической оценки систем разработки рудных месторождений. Изд. Недра, Москва, 1976.
5. БЕНУНИ, А. Н.: Технико-экономическая оценка добычи и использования руд. Изд. Недра, Москва, 1978.
6. FETTWEIS, G.: Die Situation der Vorräte an Kohle und Erdöl unter Berücksichtigung von Gewinnungs- und Transportproblemen. *Berg- und Hüttenmännische Monatshefte*, 124 (1979), 353—367.
7. STOCES, E. P.: Wahl und Beurteilung von Abbauverfahren im Bergbau. Ferdinand Enke Verlag, Stuttgart. 1958.
8. WILKE, W.: Die wirtschaftliche Grenze zwischen Tagebau und Tiefbau bei Lagerstätten mit zunehmender Überlagerung. *Erzmetall*, 1959. No. 4.
9. ROBERTS, A.: Geotechnology an Introductory Text for Students and Engineers. Pergamon Press. Oxford—New York, 1969.
10. PRIETO, C.: Mining in the New World. Mc. Graw Hill. New York, 1976.
11. АРЕНС, В. Ж.: Геотехнология. Изд. «Недра» Москва, 1971.
12. АРЕНС, В. Ж.—МЕЛНЬИКОВ, Н. В.: Исползовать возможности геотехнологии для добычи полезных ископаемых. *Горный Журнал*, 1971, No. 6. Ст. 31—32.
13. MEYER, H.—HARTMANN, L.: Geotechnologische Verfahren der Rohstoffgewinnung — Wertstoffgewinnung durch Auflösen und Auslaugen. Freiberger Forschungshefte. A. 573. VEB Deutscher Verlag für Grundstoffindustrie. Leipzig, 1977.
14. PATVAROS, J.: Új típusú bányászati technológiai rendszer alkalmazási lehetőségei hazai bauxit előfordulásaink kitermelésében (Anwendungsmöglichkeiten neuer Bergbautechnologie-Systeme im heimischen Bauxit-Bergbau). *NME Közleményei, I. Sorozat. Bányászat*, 22 (1976), 237—251.
15. PATVAROS, J.: Geotechnikai (fúrólyukas) bányaművelési módszerek alkalmazási lehetőségei ércelőfordulások kitermelésére (Einsatzmöglichkeiten der geotechnischen (Bohrloch) Abbauverfahren zum Abbau von Erzvorkommen). *BKL. Bányászat*, 1976, 589—598.

16. PATVAROS, J.: A víznívó alóli fúrólyukas hidraulikus bauxittermelés összehasonlító műszaki-gazdasági vizsgálata (Technisch-ökonomische Untersuchung und Vergleich der hydraulischen Unterwasser-Bauxitgewinnung durch Bohrlöcher). *MTA X. Osztályának Közleményei, Geonómia és Bányászat*, 9 (1976), 245—252.
17. PATVAROS, J.: Geotechnikai bányaművelési módszerek alkalmazhatósága ásványi erőforrásaink hatékonyabb kiaknázására (Die Anwendbarkeit der geotechnischen Bergbauverfahren zur wirksameren Ausbeutung unserer mineralischen Kraftquellen). Preisgekrönter akademischer Wettbewerb. Miskolc, 1978.
18. ПАТВАРОШ, И.: Определение основных параметров эксплуатации скважинами линз боксита в случае конкуренции разносным карьером. *Acta Geod., Geoph. Mont. Hung.*, 14 (1979), 257—266.
19. PATVAROS, J.: Feasibility of Combined Mining Technological System in Production of Mineral Massifs. *Acta Geod., Geoph., Mont. Hung.*, 14 (1979), 437—448.
20. PATVAROS, J.: Die Anwendungsmöglichkeiten der Bohrloch-Abbautechnologie bei der Gewinnung der heimischen Bauxitvorkommen. *Acta Geod., Geoph., Mont. Hung.*, 14 (1979), 449—472.
21. PATVAROS, J.: Bányászati technológiai rendszerek szintézise (Synthese der Bergbau-Technologiesysteme). Preisgekrönter akademischer Forschungswettbewerb. 1979, Miskolc.
22. ZAMBÓ, J.—PATVAROS, J.: Geotechnikai bányaművelési módszerek alkalmazási lehetőségei hazai szilárd ásványelőfordulásaink kitermelésében (Anwendungsmöglichkeiten der geotechnischen Bergbauverfahren zur Gewinnung unserer festen Mineralvorkommen). Forschungsabschlussbericht. Techn. Universität für Schwerindustrie. Lehrstuhl für Bergbaukunde, Miskolc, 1975.

СИНТЕЗ ГОРНОЗАВОДСКИХ ТЕХНОЛОГИЧЕСКИХ СИСТЕМ

Й. ПАТВАРОШ

РЕЗЮМЕ

В статье рассматриваются основные принципы применения комбинированных разработочных систем, обеспечивающих более эффективную эксплуатацию месторождений минералов. Подробно описывается формула эксплуатационных расходов, характеризующая основные способы разработки (открытая добыча — K; разработка под землей — M; добыча под водой — V; извлечение скважинами — F). В заключение приведена методика выбора наиболее целесообразных комбинаций.

CONTENTS

Somosvári, Zs.: Investigation of the zone in front of road heads in order to determine the cause of rock and gas outbursts 1

Somosvári, Zs.: Mechanism of rock and gas outbursts 29

Somosvári, Zs.: Main parameters of the rock and gas outburst danger 51

Somosvári, Zs.: Mechanism of action of provoking explosions 67

Balla, L.: Mathematical formalism of the 2^{n-p} type first-power factorial test planning ... 81

Pethő, Sz.—Tompos, E.: Über die Erzeugung von Dolomit-Mahlgut für Edelverputz 99

Patvaros, J.: Die Synthese bergbaulicher Technologiesysteme 117

PRINTED IN HUNGARY

82.10076 Akadémiai Nyomda, Budapest

— treble underlining: bold-face italics
— red underlining: Greek letters
— green underlining: script letters.

Rules for mathematical-physical notations:

— trigonometric, logarithmic, analytic symbols, symbols for units and functions are in roman type (not underlined)
— letter symbols in mathematical and physical formulas, scalars, and subscripts of algebraic and physical quantities are in italics (underlined)
— vectors, matrices, operators in probability theory are in bold-face roman type (double underlining)
— tensors, operators and some special functions are in script letters (green underlining). These cannot be bold.
— Greek letters (red underlining) cannot be bold or extra bold type (thus they cannot be used for vectors or tensors)
— avoid upper lines e.g. for vectors
— avoid possible confusion between o (letter) and 0 (zero), l (letter) and 1 (one), ν (Greek nu) and v, u (letters) etc.
— explain ambiguous or uncommon symbols by making marginal notes in pencil
— be careful about superscripts and subscripts
— formulae must be numbered consecutively with the number in parentheses to the right of the formula. References in text to the equations may then usually be made by the number in parenthesis. When the word equation is used with a number, it is to be abbreviated, Eq. or Eqs in the plural
— the International System of Units (SI) should be used.

Authors are liable for the cost of alteration in the *proofs*. It is, therefore, the responsibility of the author to check the text for errors of facts before submitting the paper for publication.

3. *References* are accepted only in the Harvard system. Citations in the text should be as:

... (Bomford 1971) ... or Bomford (1971)

... (Brosche and Sündermann 1976) ...

... (Gibbs et al. 1976b) ...

The list of references should contain names and initials of all authors (the abbreviation et al. is not accepted here); for *journal articles* year of publication, the title of the paper, title of the journal abbreviated, volume number, first and last page.

For *books* or *chapters in books*, the title is followed by the publisher and place of publication.

All items must appear both in the text and references.

Examples:

Bomford G 1971: Geodesy. Clarendon Press, Oxford

Brosche P, Sündermann J 1976: Effects of oceanic tides on the rotation of the earth. Manuscript. Univ. of Bonn

Buntebarth G 1976: Temperature calculations on the Hungarian seismic profile-section NP-2. In: *Geoelectric and Geothermal Studies (East-Central Europe, Soviet Asia), KAPG Geophysical Monograph*. Akadémiai Kiadó, Budapest, 561—566.

Gibbs N E, Poole W G, Stockmeyer P K 1976a: An algorithm for reducing the bandwidth and profile of a sparse matrix. *SIAM J. Number. Anal.*, 13, 236—250.

Gibbs N E, Poole W G, Stockmeyer P K 1976b: A comparison of several bandwidth and profile reduction algorithms. *ACM Trans. on Math. Software*, 2, 322—330.

Szarka L 1980: Potenciáltérképezés analóg modellezéssel (Analogue modeling of potential mapping). *Magyar Geofizika*, 21, 193—200.

4. *Footnotes* should be typed on separate sheets.

5. *Legends* should be short and clear. The place of the tables and figures should be indicated in the text, on the margin.

6. *Tables* should be numbered serially with Roman numerals. Vertical lines are not used.

All the illustrations should contain the figure number and author's name in pencil on the reverse.

Figures will be redrawn. Therefore the most important point is clearness of the figures, even pencil-drawings are accepted (with a duplicate).

Photographs and *half-tone* illustrations should be sharp and well contrasted.

If a specific reduction or enlargement is required, please indicate this in blue pencil on the figure.

The editors will send information to the first author about the *arrival* and acceptance of the papers. A galley proof is also sent to the first author for *correction*. Hundred *offprints* are supplied free of charge.

These instructions are valid as from 1982.

Reviews of the Hungarian Academy of Sciences are obtainable at the following addresses:

AUSTRALIA
C.B.D. LIBRARY AND SUBSCRIPTION SERVICE, Box 4886, G.P.O., *Sydney N.S.W. 2001*
COSMOS BOOKSHOP, 135 Ackland Street, *St. Kilda (Melbourne), Victoria 3182*

AUSTRIA
GLOBUS, Höchstädtplatz 4 *1200 Wien* XX

BELGIUM
OFFICE INTERNATIONAL DE LIBRAIRIE, 30 Avenue Marnix, *1050 Bruxelles*
LIBRAIRIE DU MONDE ENTIER, 162 Rue du Midi, *1000 Bruxelles*

BULGARIA
HEMUS, Bulvar Ruszki 6, *Sofia*

CANADA
PANNONIA BOOKS, P.O. Box 1017, Postal Station "B", *Toronto, Ontario M5T 2T8*

CHINA
CNPICOR, Periodical Department, P.O. Box 50, *Peking*

CZECHOSLOVAKIA
MAD'ARSKÁ KULTURA, Národní třída 22, *115 66 Praha*
PNS DOVOZ TISKU, Vinohradská 46, *Praha 2*
PNS DOVOZ TLAČE, *Bratislava 2*

DENMARK
EJNAR MUNKSGAARD, Norregade 6, *1165 Copenhagen*

FINLAND
AKATEEMINEN KIRJAKAUPPA, P.O. Box 128, *SF-00101 Helsinki 10*

FRANCE
EUROPERIODIQUES S. A., 31 Avenue de Versailles, *78170 La Celle St.-Cloud*
LIBRAIRIE LAVOISIER, 11 rue Lavoisier, *75008 Paris*
OFFICE INTERNATIONAL DE DOCUMENTATION ET LIBRAIRIE, 38 rue Gay-Lussac, *75240 Paris Cedex 05*

GERMAN DEMOCRATIC REPUBLIC
HAUS DER UNGARISCHEN KULTUR, Karl-Liebknecht-Strasse 9, *DDR-102 Berlin*
DEUTSCHE POST ZEITUNGSVERTRIEBSAMT, Strasse der Pariser Kommüne 3—4, *DDR-104 Berlin*

FEDERAL REPUBLIC GERMANY
KUNST UND WISSEN ERICH BIEBER, Postfach 46, *7000 Stuttgart 1*

GREAT BRITAIN
BLACKWELL'S PERIODICALS DIVISION, Hythe Bridge Street, *Oxford OX1 2ET*
BUMPUS, HALDANE AND MAXWELL LTD., Cower Works, *Olney, Bucks MK46 4BN*
COLLET'S HOLDINGS LTD., Denington Estate, *Wellingborough, Northants NN8 2QT*
W.M. DAWSON AND SONS LTD., Cannon House, *Folkestone, Kent CT19 5EE*
H. K. LEWIS AND CO., 136 Gower Street, *London WC1E 6BS*

GREECE
KOSTARAKIS BROTHERS, International Booksellers, 2 Hippokratous Street, *Athens-143*

HOLLAND
MEULENHOFF-BRUNA B.V., Beulingstraat 2, *Amsterdam*
MARTINUS NIJHOFF B.V., Lange Voorhout 9—11, *Den Haag*
SWETS SUBSCRIPTION SERVICE, 347b Heereweg, *Lisse*

INDIA
ALLIED PUBLISHING PRIVATE LTD., 13/14 Asaf Ali Road, *New Delhi 110001*
150 B-6 Mount Road, *Madras 600002*
INTERNATIONAL BOOK HOUSE PVT. LTD., Madame Cama Road, *Bombay 400039*
THE STATE TRADING CORPORATION OF INDIA LTD., Books Import Division, Chandralok, 36 Janpath, *New Delhi 110001*

ITALY
EUGENIO CARLUCCI, P.O. Box 252, *70100 Bar*
INTERSCIENTIA, Via Mazzé 28, *10149 Torino*
LIBRERIA COMMISSIONARIA SANSONI, Via Lamarmora 45, *50121 Firenze*
SANTO VANASIA, Via M. Macchi 58, *20124 Milano*
D. E. A., Via Lima 28, *00198 Roma*

JAPAN
KINOKUNIYA BOOK-STORE CO. LTD., 17-7 Shinjuku-ku 3 chome, Shinjuku-ku, *Tokyo 160-91*
MARUZEN COMPANY LTD., Book Department, P.O. Box 5056 Tokyo International, *Tokyo 100-31*
NAUKA LTD., IMPORT DEPARTMENT, 2-30-19 Minami Ikebukuro, Toshima-ku, *Tokyo 171*

KOREA
CHULPANMUL, *Phenjan*

NORWAY
TANUM-CAMMERMEYER, Karl Johansgatan 41—43 *1000 Oslo*

POLAND
WĘGIERSKI INSTYTUT KULTURY, Marszałkowska 80, *Warszawa*
CKP I W ul. Towarowa 28 *00-958 Warsaw*

ROMANIA
D. E. P., *Bucureşti*
ROMLIBRI, Str. Biserica Amzei 7 *Bucureşti*

SOVIET UNION
SOJUZPETCHATJ — IMPORT, *Moscow* and the post offices in each town
MEZHDUNARODNAYA KNIGA, *Moscow G-200*

SPAIN
DIAZ DE SANTOS, Lagasca 95, *Madrid 6*

SWEDEN
ALMQVIST AND WIKSELL, Gamla Brogatan 26 *101 20 Stockholm*
GUMPERTS UNIVERSITETSBOKHANDEL AB Box 346, *401 25 Göteborg 1*

SWITZERLAND
KARGER LIBRI AG, Petersgraben 31, *4011 Basel*

USA
EBSCO SUBSCRIPTION SERVICES, P.O. Box 1943, *Birmingham, Alabama 65201*
F. W. FAXON COMPANY, INC., 15 Southwest Park, *Westwood, Mass, 02090*
THE MOORE-COTTRELL SUBSCRIPTION AGENCIES, *North Cohocton, N. Y. 14838*
READ-MORE PUBLICATIONS, INC., 140 Cedar Street, *New York, N. Y. 10003*
STECHERT-MACMILLAN, INC., 7250 Westfield Avenue, *Pennsauken* N. J. 08110

VIETNAM
XUNHASABA, 32, Hai Ba Trung, *Hanoi*

YUGOSLAVIA
JUGOSLAVENSKA KNJIGA, Terazije 27, *Beograd*
FORUM, Vojvode Mišića 1, *21000 Novi Sad*

HU ISSN 0374—1842 Index: 26.031

Acta GEODAETICA, GEOPHYSICA et MONTANISTICA

ACADEMIAE SCIENTIARUM HUNGARICAE

Editor-in-chief
A. TÁRCZY-HORNOCI

Editor
J. VERŐ

Editorial board
GY. BARTA
B. BÉLL
L. HOMORÓDI
L. KAPOLYI
F. MARTOS
J. SOMOGYI
J. ZAMBÓ

VOLUME 17
NUMBER 2
1982

AKADÉMIAI KIADÓ, BUDAPEST

ACTA GEODAETICA, GEOPHYSICA et MONTANISTICA

A Quarterly Journal of the Hungarian Academy of Sciences

Acta Geodaetica, Geophysica et Montanistica (AGGM) publishes original reports on geodesy, geophysics and minings in English.

AGGM is published in yearly volumes of four numbers by

AKADÉMIAI KIADÓ
Publishing House of the Hungarian Academy of Sciences
H-1054 Budapest, Alkotmány u. 21.

Manuscripts and editorial correspondence should be addressed to

AGGM Editorial Office
H-9401 Sopron P.O. Box 5

Subscription information

Orders should be addressed to

KULTURA Foreign Trading Company
H-1389 Budapest P.O. Box 149

INSTRUCTIONS TO AUTHORS

Manuscripts should be sent to the editors (MTA Geodéziai és Geofizikai Kutató Intézete, Sopron, Pf. 5., H-9401, HUNGARY). Only articles not submitted for publication elsewhere are accepted.

Manuscripts should be typewritten in duplicate, double-spaced, 25 lines with 50 letters each. The papers generally include the following components, which should be presented in the order listed.

1. Title, name of author(s), affiliation, dateline, abstract, keywords
2. Text, acknowledgements
3. References
4. Footnotes
5. Legends
6. Tables and illustrations

1. The *affiliation* should be as concise as possible and should include the complete mailing address of the authors. The *date of receipt* of the manuscript will be supplied by the editors. The *abstract* should not exceed 250 words and should clearly and simply summarize the most important methods and results. 5—10 significant expressions describing the content are used as *keywords*. Authors may recommend these keywords.

2. The *text* should be generally in English and as short and clear as possible. From Hungarian authors papers are also accepted in Hungarian.

The section heading should *not* be underlined or in capitals.

Please note that underlining denotes special types:

— single underlining: italics
— double underlining: bold-face roman

Acta Geodaet., Geophys. et Montanist. Acad. Sci. Hung. Volume 17 (2), pp. 147—170 (1982)

ON THE CONCEPTS OF COMBINATION OF DOPPLER SATELLITE AND TERRESTRIAL GEODETIC NETWORKS

J. ÁDÁM
SATELLITE GEODETIC OBSERVATORY, PENC

F. HALMOS †
GEODETIC AND GEOPHYSICAL RESEARCH INSTITUTE OF THE HUNGARIAN ACADEMY OF SCIENCES, SOPRON

M. VARGA
TECHNICAL UNIVERSITY, BUDAPEST

[Manuscript received January 3, 1980]

General alternative procedures can be used for combination of Doppler satellite and terrestrial geodetic networks. These procedures are shortly reviewed. Three-dimensional transformation models between Doppler satellite and terrestrial geodetic coordinate systems and networks are analysed. Their estimation procedures are also reviewed. General remarks on Doppler stallite and terrestrial geodetic networks and their coordinate systems are presented. Finally, experimental results are given.

1. Introduction

The Doppler satellite positioning is an effective method to control the systematic errors of a network and to improve even well defined terrestrial geodetic networks. Weak parts of a network can be strengthened with it.

Traditionally, the weaknesses in the triangulation network have been eliminated by measuring more lines, more distances or more azimuths in the network. These observations require much work and time, e.g. rebuilding of the observation towers. Further, strengthening a network by additional classical observations is very expensive. On the other hand, the Doppler satellite positioning techniques are versatile, economic and highly accurate means of providing local control networks. Doppler receivers are portable and ready for use in minutes. Doppler observations are not expensive and fully independent of the weather conditions.

The establishment of geodetic networks by Doppler satellite and by classical terrestrial techniques are two basically different methods. Doppler satellite techniques provide three-dimensional geocentric coordinates. Their accuracy is rather poor but independent from the distance of the Doppler points. On the other hand, the classical methods provide two-dimensional coordinates on the surface of the reference ellipsoid with considerable relative accuracies of neighbouring points. The accuracy of their location on the ellipsoid and long distance strength are rather poor. In addition to this horizontal reference system, the classical techniques require a vertical reference system to obtain the triplets of ellipsoidal coordinates. It is evident that Doppler satellite and classical (horizontal and vertical) geodetic techniques use different

data and completely different processing of these data. Consequently, the combination of Doppler satellite and classical terrestrial data is an effective means of controlling distortions in the local network and of strengthening the orientation and scale. Nowadays, the combination of these two basically different data types is an urgent scientific and practical task, see e.g. Anderle [1,2], Ashkenazi [4], Boucher et al. [13], Ehrnsperger—Hornik [16], Kouba [31], Meade [41], Moose—Henriksen [43], Mueller [47], Thompson—Krakiwsky [54, 55]. Further, the Doppler technique has an effective part in on the stellar triangulation net [48].

It should be noted that systematic errors in a local network can be isolated and determined only by external comparison with another observational system, such as a set of Doppler satellite determined coordinates. This method can indicate such errors [4].

2. General remarks on Doppler satellite and terrestrial geodetic networks and their coordinate systems

Geodetic networks are given in some reference frame, therefore, it is always necessary to define the appropriate reference frame for uniqueness of the network data. Two essentially different techniques are applied in the network determination:

1. In the first case, the network is obtained by the traditional surveying. It is then a "terrestrial network". The reference frame in which this network is given is connected generally with some reference surface, usually an ellipsoid of revolution. This frame is based on a geometrical model.

2. In the second case, the network is determined by the geodetic application of satellites and other extraterrestrial sources. It is then called "satellite network". The reference frame in the geodetic application of the satellites is not connected with any surface, it is based on a physical model, but not on a mathematical one. The principle of such a model is the dynamics of the motion of the satellites.

The reference frames of these two types of networks were different from the very beginning as their purposes were essentially different. The actual problem of the geometric and dynamic relations of terrestrial and satellite networks is the problem of the connections between reference frames used in the geodetic application of satellites. The problem of combination of the two network types can be considered as the problem of relation between appropriate reference frames.

The Doppler satellite network in which the points are given is a global three-dimensional geocentric Cartesian coordinate system. This is the most important among satellite networks. Geocentric coordinates cannot be easily obtained

as the momentaneous accurate position of the mass centre of the Earth is not known because of high-speed motions in the atmosphere, mass redistribution and other geophysical processes. If broadcast ephemeris are used in Doppler measurements, the reference frame is defined by a set of three-dimensional Cartesian coordinates of certain terrestrial points (tracking stations). This reference frame involves many uncertainties which limit the accuracy of coordinates of the given points. Some of these factors are the following:

a) This reference frame is assumed to be connected solidly with the Earth i.e. the coordinates of the tracking stations remain unchanged in respect to each other. If this is not fulfilled i.e. the coordinates assumed unchanging move due to some geophysical process, the definition of the reference frame becomes incorrect.

b) A reference frame defined in such a way depends generally on the distribution of the stations on the Earth's surface which form the basis of the frame. Moreover it depends on the frequency of observations. Repeated measurements of the stations which aim to improve the accuracy of the reference frame change the definition of this frame and consequently the coordinates of points given in this frame will be modified.

c) During Doppler measurements we have to know the position of the satellites. The position of the satellite is determined by a numerical integration of the equation of motion. This equation can be described exactly in an inertial frame only, but not in an Earth-fixed one. The celestial system defined by stars is considered as a good inertial frame. Consequently we have to know the relation between the inertial frame and the Doppler system. The transformation cannot be made directly since there is no *physical* connection between these two systems.

In the first step the celestial system is transformed into a physical frame connected somehow with the Earth. There are essentially four possible ways of defining the direction of coordinate axes: Tisserand's mean body axes, the principal axes of inertia, instantaneous rotational axes and CIO. For transformations we have to know e.g. the value of the precession constant, variation of the rotational vector of the Earth $(\mathrm{d}\bar{\omega}(t)/\mathrm{d}t)$, the polar motion, values of C_n^m, S_n^m, etc.

In the second step the appropriate reference frame is fitted to the Doppler system which is determined by the coordinates of its points.

The position of a satellite in an Earth-fixed reference frame shows what kind of errors are produced in the coordinates of network points determined by Doppler measurements.

Next we review the types of reference frames needed in Doppler measurements. Essentially two different frames are used:

A) Inertial frame.

B) Earth-fixed reference frame.

(A) is applied for the description of the motion of the satellite and in (B) are given the coordinates of the points. Problems arise in definition of both systems.

It is very simple to define (A) dynamically but in practice (A) is obtained by approximation.

a) First we use the mean-ecliptic (celestial) system which is called "quasi-intertial". In Doppler measurements this mean-ecliptic system is considered as an inertial frame. The basis of this system is the FK 4 or FK 5 catalogue in which two fundamental points determine the direction of axes:

— mean pole of the ecliptic and

— mean equinox.

Since our puspose is to find a system independent of the motion of the Earth in space, (a) is no suitable way. On the one hand a catalogue is not accurate because of

— inaccuracy of the proper motion of stars,

— inaccuracy of the constants of precession and mutation and

— possibility of the secular motion of equinox, and on the other hand this system varies with time because of

— planetary precession,

— differential rotation of the Solar System in the Galaxy, and

— proper motion of the Solar System.

The planetary precession produces a slow rotation of the ecliptic (0.''5/year) and it results in the westerly motion of the equinox by about 12.''5/century and a decrease in the obliquity of the ecliptic of about 47''/century.

This system is so inaccurate due to the above effects that it cannot be used in high precision measurements. So we should find a reference frame independent of not only the Earth but of all directions of motion or plane of Galaxy.

b) In the second step the inertial frame is defined by a catalogue of extragalactic radio sources. It is based on the momentary positions of about twenty radio sources which are presently determined with an overall internal accuracy of 0.''03—0.''08. The inertial frame is determined by three arbitrary radio sources which are not on the same straight line. As there are only a few objects which have an optical counterpart, the transformation becomes difficult. The problem can be solved by different methods applying the recent means of space geodesy. (See in details in [29]).

c) There is another possibility to define an "absolute inertial frame" independently of (a) or (b). It is based on the direction of the cosmic background radiation. This direction, however, is not known precisely and a lot of laborious astronomical measurements would be needed for the transformation, therefore we shall not discuss this possibility here.

*

After this investigation of inertial frame, we study the problems of Earth-fixed reference frames. Several models and the transformations between them are presented in the following chapters.

B) To establish a physical model of phenomena, a definition of the reference frame is needed which can be related to the deformable Earth and the different phenomena can be clearly interpreted and measured in this reference frame. The terrestrial frame should be associated with the non-rigid Earth in some well-defined way so that the rotational motions of the whole Earth are represented by the transformation parameters of the terrestrial system to the intertial system. At present there is not any reference frame having an appropriate accuracy although an attempt was made by Grafarend et al. [20] to define such a system.

In the case of an Earth-fixed reference frame we should know the following characteristics:

a) origin

b) direction of axes and

c) motion of the reference frame in the inertial frame.

a) This reference frame should have its origin (the geocentre) at the mass centre of the entire Earth. The geocentre is understood as that of the total Earth including its atmosphere. The position of geocentre is known with an accuracy ± 5 m; it varies with time and this variation causes implicit coordinate-variations [21].

b) We can choose the direction of the coordinate axes in different ways depending on the purpose we want to use it, i.e. which phenomena we intend to describe. The following possibilities emerge for z axis:

— Tisserand axes, i.e. one of the axes of the angular moment. Its advantage is that the equations of motion of the Earth in this system are formally the same as those of the motion of a rigid body. The disadvantage of this choice is its non-observability [37].

— One of the principal axes of inertia (polar axis). The inertial tensor of such a system is a diagonal. It is the only system in which the coefficients $C_2^1 = S_2^1 = 0$. Nevertheless the direction of the axes perpendicular to the z axis is not well defined.

— Rotation axis of the Earth. This system is used in laser and Doppler satellite measurements. It supposes that the coefficients $C_2^1 = S_2^1 = 0$. The use of this values with the concept of the rotation axis is not exact.

— CIO. It is a well known system in satellite dynamics. CIO does not coincide with the z axis of inertia.

The z axes are supposed to go through the geocentre in each system. This is a good approximation of reality.

c) Having defined an Earth-fixed system, the transformation between the inertial and terrestrial reference frames should be given. This transforma-

tion is the motion of the Earth in space. The two separate components of motion are the following:

— revolution around the Sun and

— rotation.

The revolution is forced by gravitational effects of the Sun and other objects of the Solar System. It is described by the Newtonian inertial theorems. If the Solar System is supposed to be a closed system and the celestial objects are considered to be points, then the equation of motion of a planet having a mass m_i and a position vector $\mathbf{r}_i$ is the following:

$$m_i \frac{\mathrm{d}^2\mathbf{r}_i}{\mathrm{d}t^2} = G \sum_{j=1}^{n} (1 - \delta_{ij})\, m_i m_j \,|\, \mathbf{r}_i - \mathbf{r}_j \,|$$

where δ_{ij} is the Kronecker-symbol; G is the gravitational constant; $|\,\mathbf{r}_i - \mathbf{r}_j|$ means the distance of points i and j; $j = 1, 2, \ldots, n$ means the number of celestial objects.

For the description of the motion of the Earth, it is necessary to define an Earth-model which is determined by astronomical and geophysical constants. This motion can be represented by the motion of a reference frame $\mathbf{e}$ which is fixed to the Earth and is given by the model. This frame is named "moving frame".

In an epoch t_0 the position of $\mathbf{e}$ in the $\mathbf{E}$ inertial frame is given by a rotational matrix:

$$\mathbf{e} = \mathbf{R}_3(\varphi)\mathbf{R}_1(\vartheta)\mathbf{R}_3(\psi)\mathbf{E} = \mathbf{R} \cdot \mathbf{E} \tag{1}$$

where φ, ϑ and ψ are the Eulerian-angles (and they correspond ω, i and Ω, respectively, which are the orbital elements in celestial mechanics) [28]. As $\mathbf{e}$ varies with time continuously, $\mathbf{e} = \mathbf{e}(t)$, the motion of $\mathbf{e}$ in $\mathbf{E}$ is obtained by differentiation of Eq. 1:

$$\frac{\mathrm{d}\mathbf{e}(t)}{\mathrm{d}t} = \frac{\mathrm{d}\mathbf{R}(t)}{\mathrm{d}t} \cdot \mathbf{E} + \mathbf{R}(t) \cdot \frac{\mathrm{d}\mathbf{E}}{\mathrm{d}t} = \omega(t)\mathbf{R}(t)\mathbf{E} \tag{2}$$

where $\mathrm{d}\mathbf{E}/\mathrm{d}t = 0$ and

$$\frac{\mathrm{d}\mathbf{R}(t)}{\mathrm{d}t} = \omega(t)\mathbf{R}(t)\,. \tag{3}$$

$\omega(t)$ is an anti-symmetric operator. Elements of this "Cartan-matrix" are non-integrable, anholonom velocity coordinates [17, 18, 19]. The moving frame $\mathbf{e}$ defined by Eqs 1 and 2 is an anholonom frame in comparison to $\mathbf{E}$. From the anholonom coordinates we can get holonom coordinates by using the Frobenius matrix (matrix of integrating factors) [18].

Motion of **e** in **E** can be given not only kinematically but also dynamically. The motion of a rigid body around a fixed point is described by the Euler-Liouville equation. For this purpose we should know the mass distribution of the whole Earth. Since the distribution is not known, an appropriate model has to be used. To describe this motion exactly, the constants of precession and nutation must be known and we have to observe the polar motion and UT 1 which characterizes the rotation of the Earth, and to measure their irregularities.

Further details can be found e.g. in [10, 11, 30, 47].

3. Comparison of Doppler satellite and terrestrial geodetic coordinate systems and networks

3.1 *The coordinate systems used*

Three coordinate systems are considered here (Fig. 1). The *Average Terrestrial* (AT) coordinate system is assumed to coincide with the system defined by the coordinates of the tracking stations as obtained from satellite

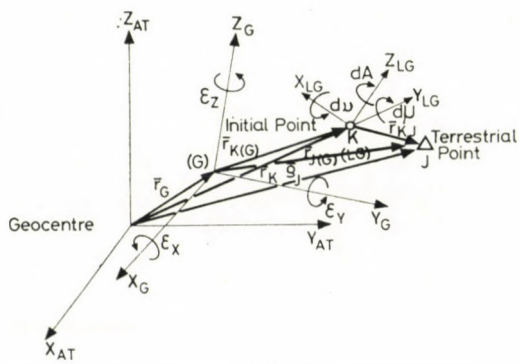

Fig. 1

geodesy. Its Z-axis is directed toward the average north terrestrial pole as defined by the International Polar Motion Service (IPMS) commonly known as the Conventional International Origin (CIO). The XZ plane is parallel to the mean Greenwich astronomic meridian as defined by the Bureau International de l'Heure (BIH). The terrain point coordinates are given by the components of the position vector $\bar{\varrho}$. The three-dimensional satellite Doppler determined coordinates of terrain points define a Satellite Doppler coordinate system (e.g. NWL-9D, WGS-72), which is assumed to be the AT-system. The Doppler system is only an estimation of this ideal coordinate system [1].

The *Geodetic* (G) coordinate system is the reference frame of the terrestrial network. The Z_G axis is coincident with the minor axis of the reference ellipsoid (horizontal datum), while the $X_G Y_G$ plane is coincident with the equatorial plane of the reference ellipsoid. The G-system is usually positioned and oriented by some specified geodetic parameters at the initial point K of the terrestrial network, see e.g. Mueller [47] and Kouba [31]. The terrestrial network must be made three-dimensional from a heterogeneous network. First, orthometric heights combined with geoid heights are used to form heights (h) above the ellipsoid. These are combined with latitudes (φ) and longitudes (λ) of the horizontal network to form triples of ellipsoidal coordinates which can be then converted along with their variance-covariance matrix into three-dimensional Cartesian coordinates:

$$\begin{aligned} X_G &= (N + h) \cos \varphi \cos \lambda \\ Y_G &= (N + h) \cos \varphi \sin \lambda \\ Z_G &= [N(1 - e^2) + h] \sin \varphi \end{aligned} \tag{5}$$

in which e denotes the first eccentricity of the ellipsoid and N is the radius of curvature in the direction of the prime vertical. This (X_G, Y_G, Z_G) coordinate system is intrinsically three-dimensional and holonom. Note that two different (horizontal and vertical) reference systems must be considered here, and the most important problem is the proper determination of the ellipsoidal heights of terrestrial triangulation network points [15].

The third coordinate system is the *Local Geodetic* (LG) system. It may be a right-handed system, located at the terrestrial initial point K. Its X_{LG} axis is tangent to the geodetic meridian with positive direction toward the south, the Y_{LG} axis is perpendicular to the meridian plane and it is positive eastward, and the Z_{LG} axis is along the ellipsoidal normal at K with its positive direction upward. The position vectors of terrestrial geodetic network points, $\mathbf{r}_{KI}$, are expressed in the system.

In the establishment of a terrestrial geodetic network, the aim is to avoid systematic errors in the network observation and computation results, and further, the axes of the G-system should be parallel to those of the (AT $\simeq$ Doppler)-system. These are difficult objectives to insure. Usually, the origin of the G-system is displaced from the geocentre with the components of the translation vector, $\mathbf{r}_G$. Further, the axis of the G- and (AT = Doppler)-systems may not be parallel. The non-parallelism is given by three rotations, ε_x, ε_y and ε_z. Because of the accumulation of the systematic errors in the terrestrial geodetic network, the axes of the LG-system at the terrestrial initial point K are rotated in the azimuth ($\mathrm{d}A$), meridian ($\mathrm{d}\mu$), and prime vertical ($\mathrm{d}\nu$) directions. Finally, there is the problem of a scale difference ($\varkappa$). This parameter can be interpreted as a difference in the scale of G- and (AT $\simeq$

Doppler)-systems (system scale difference) or as a terrestrial network scale distortion.

We note that in a general case, the transformation parameters depend on time. Dependency may be periodic (with long or short period), secular or random. So the time t will be a transformation parameter in the transformations of reference frames and consequently the resulting coordinates will be time-dependent. This field of geodesy is *called space-time geodesy* or *four-dimensional geodesy*. This term "space-time" may be misleading especially for non-geodesists. This term "space-time" is not used in the same meaning as in General Relativity, i.e. a space-time interval is not defined. In geodesy t does not depend on velocity but it is a general parameter; "the time is unique everywhere".

The question arises why we do not use the terms of General Relativity in space geodesy. It is well known from Einstein's theorems that the gravitational field is curved, i.e. it is not Euclidean. Then why do we suppose the space near the Earth to be Euclidean?

In satellite geodesy most measurements are in the region of the Solar System. Here the gravitational field is weak and the velocities are small ($v \ll c$, $v_{\max} \approx 30$ km/s). Therefore, in "first order", the Newtonian gravitational theory holds in the case of Solar System. The accuracy of second order corrections (the so-called post-Newtonian corrections) is the following:

— deflection of ligth: $\sim 10^{-6}$ second of arc.

— relativistic deformations of the Earth's orbit: ~ 10 cm.

It is clear, that these values are well under the accuracy of present measuring techniques. Therefore, there is no need in the seventies to use higher order corrections according to the post-Newtonian approximation, so we can suppose the space near the Earth to be Euclidean. The transformations are in Euclidean space and the time appears as fourth coordinate [59].

3.2 *Three-dimensional transformation models*

If the Doppler satellite $(\bar{\varrho}_J)_D$ and terrestrial $(\mathbf{r}_J)_G$ position vectors are the observables, the *Burša* or *Burša—Wolf model* [14, 62] is given by

$$\mathbf{F}_j = (\mathbf{r}_G)_D + (1 + \varkappa) \cdot \mathbf{R}_\varepsilon \cdot (\mathbf{r}_J)_G - (\bar{\varrho}_J)_D = 0 \tag{6}$$

where $\mathbf{R}_\varepsilon$ is the product of three consecutive orthogonal rotations around the axis of the G-system:

$$\mathbf{R}_\varepsilon = \mathbf{R}_x(\varepsilon_x) \cdot \mathbf{R}_y(\varepsilon_y) \cdot \mathbf{R}_z(\varepsilon_z) =$$

$$= \begin{bmatrix} 1 & 0 & 0 \\ 0 & \cos\varepsilon_x & \sin\varepsilon_x \\ 0 & -\sin\varepsilon_x & \cos\varepsilon_x \end{bmatrix} \begin{bmatrix} \cos\varepsilon_y & 0 & -\sin\varepsilon_y \\ 0 & 1 & 0 \\ \sin\varepsilon_y & 0 & \cos\varepsilon_y \end{bmatrix} \begin{bmatrix} \cos\varepsilon_z & \sin\varepsilon_z & 0 \\ -\sin\varepsilon_z & \cos\varepsilon_z & 0 \\ 0 & 0 & 1 \end{bmatrix}. \tag{7}$$

The angles ε_x, ε_y, ε_z are positive for counter-clockwise rotations about the respective X_G, Y_G, Z_G axes as viewed from the end of the positive axis. Since they are small, it is permissible to simplify Eq. 7 as

$$\mathbf{R}_\varepsilon = \mathbf{I} + \mathbf{Q}_\varepsilon = \begin{bmatrix} 1 & 0 & 0 \\ 0 & 1 & 0 \\ 0 & 0 & 1 \end{bmatrix} + \begin{bmatrix} 0 & \varepsilon_z & -\varepsilon_y \\ -\varepsilon_z & 0 & \varepsilon_x \\ \varepsilon_y & -\varepsilon_x & 0 \end{bmatrix}. \tag{8}$$

Substituting (8) into (6) and neglecting second-order terms in scale $\varkappa$ and rotations (ε_x, ε_y, ε_z) and their products, the Burša—Wolf model can be written as

$$\mathbf{F}_j = (\mathbf{r}_G)_D + (\mathbf{r}_J)_G + \varkappa \cdot (\mathbf{r}_J)_G + \mathbf{Q}_\varepsilon(\mathbf{r}_J)_G - (\bar{\varrho}_J)_D = \mathbf{0}\,. \tag{9}$$

The parameter $\varkappa$ is interpreted as a system scale difference, and the coordinates of the terrestrial initial point K are redefined (scaled and rotated).

The *Molodenskii—Badekas model* is described in [8] and is attributed to Molodenskii [42]. For describing this transformation, Molodenskii used differential transformation equations and the first vector interpretation of it is Badekas' one. Similarities and differences between the original Molodenskii formulas and Badekas' interpretation of these equations are described by Soler [53] in detail. This model can be expressed in the satellite Doppler system as follows:

$$\mathbf{F}_j = (\mathbf{r}_G)_D + (\mathbf{r}_K)_G + (1 + \varkappa)\mathbf{R}_\psi(\mathbf{r}_{KJ})_G - (\bar{\varrho}_J)_D = \mathbf{0}\,. \tag{10}$$

It is assumed that the position vector of the initial point is known in the geodetic system that is parallel to the satellite Doppler ($\simeq$AT) system. In this case, the scale difference parameter $\varkappa$ and the differentially small rotations ψ_x, ψ_y, and ψ_z [$\mathbf{R}_\psi = \mathbf{R}_x(\psi_x) \cdot \mathbf{R}_y(\psi_y) \cdot \mathbf{R}_z(\psi_z)$] are interpreted as pertaining to the terrestrial network represented by the observables $(\mathbf{r}_{KJ})_G$. All other notation is the same as in Eq. (6). After omitting second-order terms in $\varkappa$ and ψ_x, ψ_y, ψ_z and in their products, the Model (10) becomes

$$\mathbf{F}_J = (\mathbf{r}_G)_D + (\mathbf{r}_K)_G + (\mathbf{r}_{KJ})_G + \mathbf{Q}_\psi(\mathbf{r}_{KJ})_G + \varkappa(\mathbf{r}_{KJ})_G - (\bar{\varrho}_J)_D = \mathbf{0}\,. \tag{11}$$

The *Veis model* [60], in which the observables are the Doppler satellite position vectors $(\bar{\varrho}_J)_D$ and the terrestrial position vector differences $(\mathbf{r}_{KJ})_G$ is given by

$$\mathbf{F}_j = (\mathbf{r}_G)_D + (\mathbf{r}_K)_G + (1 + \varkappa)\mathbf{M}(\mathbf{r}_{KJ})_G - (\bar{\varrho}_J)_D = \mathbf{0}\,, \tag{12}$$

where the rotation matrix [8, 60]

$$\mathbf{M} = \begin{bmatrix} 1 & +\mathrm{d}A \cdot \sin\varphi_K - \mathrm{d}v \cdot \cos\varphi_K & -\mathrm{d}A \cdot \cos\varphi_K \sin\lambda_K - \mathrm{d}\mu \cdot \cos\lambda_K - \mathrm{d}v \cdot \sin\varphi_K \cdot \sin\lambda_K \\ -\mathrm{d}A \cdot \sin\varphi_K + \mathrm{d}v \cdot \cos\varphi_K & 1 & +\mathrm{d}A \cdot \cos\varphi_K \cdot \cos\lambda_K - \mathrm{d}\mu \cdot \sin\lambda_K + \mathrm{d}v \cdot \sin\varphi_K \cdot \cos\lambda_K \\ +\mathrm{d}A \cdot \cos\varphi_K \cdot \sin\lambda_K + \mathrm{d}\mu \cdot \cos\lambda_K + \mathrm{d}v \cdot \sin\varphi_K \sin\lambda_K & -\mathrm{d}A \cdot \cos\varphi_K \cdot \cos\lambda_K + \mathrm{d}\mu \cdot \sin\lambda_K - \mathrm{d}v \cdot \sin\varphi_K \cdot \cos\lambda_K & 1 \end{bmatrix} \tag{13}$$

where φ_K, λ_K are the geodetic coordinates of the initial point K of the terrestrial geodetic network. Introducing $\mathbf{M}_1 = \mathbf{M} + \mathbf{I}$ and deleting the second-order terms in scale and rotations and their products, the Model (12) becomes

$$\mathbf{F}_J = (\mathbf{r}_G)_D + (\mathbf{r}_K)_G + (1 + \varkappa)\mathbf{M}_1(\mathbf{r}_{KJ})_G - (\bar{\varrho}_J)_D = \mathbf{0}\,. \tag{14}$$

The three rotations $\mathrm{d}A, \mathrm{d}\mu, \mathrm{d}v$ are related to the rotations $\varepsilon_x, \varepsilon_y, \varepsilon_z$ of Burša—Wolf's or Molodenskii—Badekas' model as follows [38]:

$$\begin{bmatrix} \mathrm{d}A \\ \mathrm{d}\mu \\ \mathrm{d}v \end{bmatrix} = \begin{bmatrix} \sin\varphi_K & \cos\varphi_K \sin\lambda_K & \cos\varphi_K \cos\lambda_K \\ 0 & \cos\lambda_K & -\sin\lambda_K \\ -\cos\varphi_K & \sin\varphi_K \sin\lambda_K & \sin\varphi_K \cos\lambda_K \end{bmatrix} \begin{bmatrix} \varepsilon_z \\ \varepsilon_y \\ \varepsilon_x \end{bmatrix} \tag{15}$$

The main characteristic of the Burša—Wolf, Molodenskii—Badekas and Veis models is that they contain a maximum of seven unknown transformation parameters. Further details concerning the differences and similarities between these models can be found in [34, 38, 54, 55, 53, 23, 24]. When using any of these models (9), (11) or (14), one obtains identical values for the rotation parameters ($\varepsilon_x = \psi_x$, $\varepsilon_y = \psi_y$, $\varepsilon_z = \psi_z$) and scale difference. With the Burša—Wolf model (9) the geodetic position vector $(\mathbf{r}_J)_G$ of each point is scaled and rotated, while with the Molodenskii—Badekas (11) and Veis models (14) only the interstation vectors $(\mathbf{r}_{KJ})_G$ are scaled and rotated. The position vector of the initial point K is not redefined.

In the next two models, two sets of rotation parameters are introduced: one set to resolve the differences between the Doppler and Geodetic systems and another set to model the unknown systematic errors in the terrestrial network. In the *Hotine model* [26] the two sets of rotation parameters are the following: (ε_x, ε_y, ε_z) for the G-system and ($\mathrm{d}\alpha$, $\mathrm{d}\beta$) to represent the systematic errors in the terrestrial network. This model contains nine unknown parameters. It is expressed as follows [12, 55]:

$$\mathbf{F}_j = (\mathbf{r}_G)_D + \mathbf{R}_\varepsilon[(\mathbf{r}_K)_G + (1 + \varkappa)\mathbf{M}_0 \cdot \mathbf{R}_H \cdot \mathbf{M}_0^T(\mathbf{r}_{KJ})_G] - (\bar{\varrho}_J)_D = \mathbf{0}\,, \tag{16}$$

where $\mathbf{M}_0$ is a matrix of passage between the Doppler and the LG-system ($\mathbf{M}_0^T$ is transposed of $\mathbf{M}_0$), and

$$\mathbf{R}_H = \begin{bmatrix} 1 & -\mathrm{d}\alpha & \cos\alpha_{KJ}\mathrm{d}\beta \\ \mathrm{d}\alpha & 1 & \sin\alpha_{KJ}\mathrm{d}\beta \\ -\dfrac{\mathrm{d}\beta}{\cos\alpha_{KJ}} & 0 & 1 \end{bmatrix}, \tag{17}$$

where α_{KJ} is the geodetic azimuth from the initial point of the terrestrial network to an arbitrary network point j. The azimuth change, $d\alpha$, is a rotation of each interstation vector $(\mathbf{r}_{KJ})_G$ about the Z-axis of the LG-system at point K. The zenith distance parameter, $d\beta$, is a constant applied to all network difference vectors $(\mathbf{r}_{KJ})_G$. The scale difference parameter K is included to model the systematic errors in the scale in the terrestrial network.

In the *Krakiwsky—Thomson model* six parameters (3 translations, 3 rotations) are included for the G-system and four parameters (one scale difference $\varkappa$ and 3 rotations, $\mathrm{d}\nu$, $\mathrm{d}\mu$, $\mathrm{d}A$) are included to model the systematic errors in the terrestrial network. In functional form this model is as follows [34, 54, 55].

$$\mathbf{F}_J = (\mathbf{r}_G)_D + (1 + \varkappa)\mathbf{R}_\varepsilon[(\mathbf{r}_K)_G + \mathbf{R}_\psi(\mathbf{r}_{KJ})_G] - (\bar{\varrho}_J)_D = \mathbf{0}\,. \tag{18}$$

The G-system is rotated with respect to the Doppler system and the terrestrial network is rotated with respect to the G-system. This model combines the best features of the Burša—Wolf and Molodenskii—Badekas or Veis model. A system scale is used as in the Burša—Wolf model. The network rotation concept of the Molodenskii—Badekas model is applied. After assuming differentially small rotations and neglecting second-order terms in $\varkappa$, $(\varepsilon_x, \varepsilon_y, \varepsilon_z)$ and (ψ_x, ψ_y, ψ_z) and in their products the Model (18) becomes

$$\mathbf{F}_J = (\mathbf{r}_G)_D + (\mathbf{r}_K + \mathbf{r}_{KJ})_G + \mathbf{Q}_\psi(\mathbf{r}_{KJ})_G + \mathbf{Q}_\varepsilon(\mathbf{r}_K + \mathbf{r}_{KJ})_G + \varkappa(\mathbf{r}_K + \mathbf{r}_{KJ})_G - (\bar{\varrho}_J)_D = \mathbf{0}\,. \tag{19}$$

The relationships between the AT-, Doppler and G-systems are considered in the *Vaniček—Wells model*. It is assumed that the G-system is a fixed framework invariant with respect to adjustment of the geodetic network. Proceeding from this assumption and the classical definition of a G-system it is shown by Vaniček and Wells [58] that in the transformation between such a G-system and the AT-system the three rotation angles are not independent, being functions of a single rotation Δ of the G-system around the ellipsoidal normal at the initial point K. This model is as follows [55, 61]:

$$\mathbf{F}_J = (\mathbf{r}_G)_{AT} + \mathbf{R}_\Delta \cdot \varkappa(\mathbf{r}_K + \mathbf{r}_{KJ})_G - (\mathbf{r}_D)_{AT} - \mathbf{R}_\varepsilon(\bar{\varrho}_J)_D = \mathbf{0}\,, \tag{20}$$

where $(\mathbf{r}_G)_{AT}$ is the translation vector between the AT- and G-systems, $(\mathbf{r}_D)_{AT}$ is the translation vector between the AT- and Doppler systems, $\varkappa$ is the scale difference in the G system, $\mathbf{R}_\varepsilon$, $(\mathbf{r}_K + \mathbf{r}_{KJ})$ and $(\bar{\varrho}_J)_D$ are previously defined and $\mathbf{R}_\Delta$ is a rotation matrix:

$$\mathbf{R}_\Delta = \begin{bmatrix} 1 & \Delta \cdot \sin \varphi_K & -\Delta \cos \varphi_K \sin \lambda_K \\ -\Delta \sin \varphi_K & 1 & \Delta \cos \varphi_K \cos \lambda_K \\ \Delta \cos \varphi_K \sin \lambda_K & -\Delta \cos \varphi_K \cos \lambda_K & 1 \end{bmatrix}. \quad (21)$$

There are eight unknowns to be solved in this model: ε_x, ε_y, ε_z, Δ, $\varkappa$, $(\mathbf{r}_G)_D$. The last quantity is the difference vector of $(\mathbf{r}_D)_{AT}$ and $(\mathbf{r}_G)_{AT}$ since the centre of gravity (origin of the AT-system) is unknown. Introducing $\mathbf{R}_\varepsilon = \mathbf{Q}_\varepsilon + \mathbf{I}$ and $\mathbf{R}_\Delta = \mathbf{Q}_\Delta + \mathbf{I}$, the Model (20) becomes

$$\mathbf{F}_J = (\mathbf{r}_G)_D + (\mathbf{r}_K + \mathbf{r}_{KJ})_G + \varkappa(\mathbf{r}_K + \mathbf{r}_{KJ})_G + \mathbf{Q}_\Delta(\mathbf{r}_K + \mathbf{r}_{KJ})_G - \mathbf{Q}_\varepsilon(\bar{\varrho}_J)_D - (\bar{\varrho}_J)_D = \mathbf{0}. \quad (22)$$

Hence where $(\mathbf{r}_K + \mathbf{r}_{KJ})_G$ is multiplied by the small quantities $\varkappa$ and $\mathbf{Q}_\Delta$, replacing it by $(\bar{\varrho}_J)_D$ will introduce less than 1 cm error. So Eq. 22 becomes [61]

$$\mathbf{F}_J = (\mathbf{r}_G)_D + (\mathbf{r}_K + \mathbf{r}_{KJ})_G - [\mathbf{Q}_\varepsilon - \mathbf{Q}_\Delta - \varkappa] \cdot (\bar{\varrho}_J)_D - (\bar{\varrho}_J)_D = \mathbf{0}. \quad (23)$$

We have treated above six transformation models to eliminate discrepancies between a terrestrial network and the Doppler satellite network. These discrepancies are likely due partly to the differences in the coordinate systems and partly to the network distortions. The choice of the transformation model depends on the actual physical circumstances and on the assumptions one wishes to make. Concerning the circumstances given, we have to determine only those parameters which we can explain physically.

3.3 *Estimation procedures of the transformation parameters*

A solution of the Burša—Wolf, Molodenskii—Badekas and Veis models is obtained by a least-squares estimation procedure of the combined type. Eqs 9, 11 and 14 form the mathematical model [57].

$$\mathbf{F}(\mathbf{L}_a, \mathbf{X}_a) = \mathbf{0} \quad \text{or} \quad \mathbf{F}(\mathbf{L}_b + \mathbf{V}, \mathbf{X}_0 + \mathbf{X}) = \mathbf{0} \quad (24)$$

where $\mathbf{L}_a$ denotes the adjusted observations, $\mathbf{X}_a$ the adjusted parameters, $\mathbf{L}_b$ the observations, $\mathbf{X}_0$ the approximate parameters, $\mathbf{V}$ the residuals and $\mathbf{X}$ the unknown "parameters" to be solved. The usual adjustment procedure $\mathbf{V}^T\mathbf{P}\mathbf{V} = \min$, subject to the condition

$$\mathbf{BV} + \mathbf{AX} + \mathbf{W} = \mathbf{0} \tag{25}$$

applies, where

$$\mathbf{B} = \frac{\partial \mathbf{F}}{\partial \mathbf{L}_a}, \quad \mathbf{A} = \frac{\partial \mathbf{F}}{\partial \mathbf{X}_a}, \quad \mathbf{W} = \mathbf{F}(\mathbf{L}_b, \mathbf{X}_0) \tag{26}$$

and $\mathbf{P}$ is the weight matrix. Each point contributes three equations to the equation system (25), e.g., for point P_J, taking $X_0 = 0$, with the Burša—Wolf version one has

$$\overset{\mathbf{B}_J}{\begin{bmatrix} 1 & 0 & 0 & -1 & 0 & 0 \\ 0 & 1 & 0 & 0 & -1 & 0 \\ 0 & 0 & 1 & 0 & 0 & -1 \end{bmatrix}} \overset{\mathbf{V}_J}{\begin{bmatrix} V_{XG} \\ V_{YG} \\ V_{ZG} \\ V_{XD} \\ V_{YD} \\ V_{ZD} \end{bmatrix}_J} + \overset{\mathbf{A}_J}{\begin{bmatrix} 1 & 0 & 0 & X_G & Y_G & -Z_G & 0 \\ 0 & 1 & 0 & Y_G & -X_G & 0 & Z_G \\ 0 & 0 & 1 & Z_G & 0 & X_G & -Y_G \end{bmatrix}_J} \overset{\mathbf{X}}{\begin{bmatrix} \Delta X \\ \Delta Y \\ \Delta Z \\ \varkappa \\ \varepsilon_z \\ \varepsilon_y \\ \varepsilon_x \end{bmatrix}} \overset{\mathbf{W}_J}{\begin{bmatrix} X_G - X_D \\ Y_G - Y_D \\ Z_G - Z_D \end{bmatrix}_J} = \mathbf{0} \tag{27}$$

Eq. 25 leads to the well-known expressions [57]:

$$\mathbf{X} = -(\mathbf{A}^T\mathbf{M}^{-1}\mathbf{A})^{-1}\mathbf{A}^T\mathbf{M}^{-1}\mathbf{W} \tag{28}$$

$$\mathbf{V} = -\mathbf{P}^{-1}\mathbf{B}^T\mathbf{M}^{-1}(\mathbf{AX} + \mathbf{W}) \tag{29}$$

$$\sigma_0^2 = \mathbf{V}^T\mathbf{PV}/D\mathbf{F} \tag{30}$$

$$\mathbf{M} = \mathbf{BP}^{-1}\mathbf{B}^T \tag{31}$$

$$\mathbf{V}^T\mathbf{PV} = -\mathbf{K}_L^T\mathbf{W} \tag{32}$$

$$\mathbf{K}_L = -\mathbf{M}^{-1}(\mathbf{AX} + \mathbf{W}), \tag{33}$$

where $D\mathbf{F}$ is the degree of freedom. The variance-covariance matrix of unknown parameters is

$$\Sigma_x = \sigma_0^2 \cdot \mathbf{Q}_x \tag{34}$$

$$\mathbf{Q}_x = (\mathbf{A}^T\mathbf{M}^{-1}\mathbf{A})^{-1}. \tag{35}$$

For the derivation using submatrices, the partition of the matrices of Eq. 25 is as follows [38]:

$$\underset{3r,6r}{\mathbf{B}} = \begin{bmatrix} \underset{3,3}{\mathbf{I}} & \underset{3,3}{-\mathbf{I}} & 0 & 0 \;\ldots\ldots & 0 & 0 \\ 0 & 0 & \underset{3,3}{\mathbf{I}} & \underset{3,3}{-\mathbf{I}} \;\ldots\ldots & 0 & 0 \\ \vdots & \vdots & \vdots & \vdots & \vdots & \vdots \\ 0 & 0 & 0 & 0 & \underset{3,3}{\mathbf{I}} & \underset{3,3}{-\mathbf{I}} \end{bmatrix} \tag{36}$$

$$\underset{6r,1}{\mathbf{V}} = \begin{bmatrix} V_1 \\ V_2 \\ \cdot \\ \cdot \\ \cdot \\ \cdot \\ \cdot \\ \cdot \\ \cdot \\ V_r \end{bmatrix} = \begin{bmatrix} V_{1G} \\ V_{1D} \\ V_{2G} \\ V_{2D} \\ \vdots \\ \vdots \\ V_{rG} \\ V_{rD} \end{bmatrix} \quad \text{where} \quad V_{JG} = \begin{bmatrix} v_{JXG} \\ v_{JYG} \\ v_{JZG} \end{bmatrix} \quad \text{and} \quad V_{JD} = \begin{bmatrix} v_{JXD} \\ v_{JYD} \\ v_{JZD} \end{bmatrix} \tag{37}$$

$$\underset{3r,n=7}{\mathbf{A}} = \begin{bmatrix} \underset{3,3}{\mathbf{I}} & \underset{3}{\mathbf{A}_{1_4}} \\ \underset{3,3}{\mathbf{I}} & \underset{3}{\mathbf{A}_{2_4}} \\ \vdots & \vdots \\ \underset{3,3}{\mathbf{I}} & \underset{3}{\mathbf{A}_{r_4}} \end{bmatrix} \quad \text{and} \quad \underset{3r,1}{\mathbf{W}} = \begin{bmatrix} W_1 \\ W_2 \\ \vdots \\ W_r \end{bmatrix} = \begin{bmatrix} \mathbf{r}_{1G} - \bar{\varrho}_{1D} \\ \mathbf{r}_{2G} - \bar{\varrho}_{2D} \\ \vdots \\ \mathbf{r}_{rG} - \bar{\varrho}_{rD} \end{bmatrix}. \tag{38}$$

To determine the transformation parameters with Burša—Wolf model in different solutions, a computational program is written in FORTRAN language by Kumar [35].

A special estimation procedure is required to obtain a solution of the Hotine, Krakiwsky—Thomson and Vaniček—Wells models. A phased, combined case least-square estimation technique is proposed by Krakiwsky and Thomson [34], Thomson and Krakiwsky [54, 55] in which the sets of common Doppler satellite and terrestrial Cartesian coordinates are split into two zones.

Note that the collocation methods were applied for coordinate transformations by Moritz [44, 45, 46], Schwarz [51, 52], Tscherning [56], Groten and Schaab [22].

3.4 *Some experimental results*

Ashkenazi and Sykes [6] have obtained some significant discrepancies between the geocentric coordinates obtained by using the two ephemeris types. Ashkenazi [5] recommended some empirical correction parameter to transform the point positions computed with Broadcast Ephemeris into the coordinate system of Precise Ephemeris. Boucher et al. [13] improved these values. using the coordinates of 29 stations, they determined the transformation param-

eters between the coordinate systems of Broadcast and Precise Ephemeris by the Burša—Wolf transformation formula:

$$\begin{bmatrix} X_{BE} \\ Y_{BE} \\ Z_{BE} \end{bmatrix} = \begin{bmatrix} X_{PE\to BE} \\ Y_{PE\to BE} \\ Z_{PE\to BE} \end{bmatrix} + (1+\varkappa) \begin{bmatrix} 1 & -\varepsilon_z & \varepsilon_y \\ \varepsilon_z & 1 & -\varepsilon_x \\ -\varepsilon_y & \varepsilon_x & 1 \end{bmatrix} \begin{bmatrix} X_{PE} \\ Y_{PE} \\ Z_{PE} \end{bmatrix}. \tag{39}$$

From Table I, the solution 5 can be retained as transformation parameters for Europe:

$$\begin{aligned} X_{PE\to BE} &= 0.9 \pm 0.5 \text{ m} \\ Y_{PE\to BE} &= 1.9 \pm 0.6 \text{ m} \qquad \varkappa = -0.85 \pm 0.13 \text{ ppm} \\ Z_{PE\to BE} &= 8.0 \pm 0.6 \text{ m} \qquad \varepsilon_Z = -0.10'' \pm 0.03''. \end{aligned} \tag{40}$$

It is to be noted that strong correlations were experienced between some parameters using the Bursa—Wolf model. It is due to the non-global coverage of the network used. The Molodenskii—Badekas model decreased the correlation, cf. Boucher [12]. It was used as proposed in (15):

$$\begin{bmatrix} X_{BE} \\ Y_{BE} \\ Z_{BE} \end{bmatrix} = \begin{bmatrix} X_{PE} \\ Y_{PE} \\ Z_{PE} \end{bmatrix} + \begin{bmatrix} X_{PE\to BE} \\ Y_{PE\to BE} \\ Z_{PE\to BE} \end{bmatrix} + \begin{bmatrix} \varkappa & -\varepsilon_z & \varepsilon_y \\ \varepsilon_z & \varkappa & -\varepsilon_x \\ -\varepsilon_y & \varepsilon_x & \varkappa \end{bmatrix} \begin{bmatrix} X_{PE} - X_M \\ Y_{PE} - Y_M \\ Z_{PE} - Z_M \end{bmatrix}, \tag{41}$$

where $[X_M, Y_M, Z_M] = X_D^T$ is the barycentre of the network.

The transformation formula (39) was used to determine the transformation parameters between the NWL-9D (Precise Ephemeris) and the ED-50 systems. The results are in Table II where the solutions 5 is the most important. Coordinates of 23 common stations were used by Boucher [12] and Boucher et al. [13].

To determine the accuracy, orientation, and scale of the satellite Doppler system, comparisons are being made with external standards including the US Transcontinental Geodimeter Traverse and extraterrestrial geodetic systems such as mobile and fixed Very Long Baseline Interferometry (VLBI), Lunar Laser Ranging (LLR), Satellite Laser Ranging (SLR), and Deep Space Network (DSN). Hothem [25] reported the latest results that a scale decrease of 0.4 ± 0.1 ppm and a longitude rotation of $0''.80 \pm 0''.05$ eastward should be applied to the NWL-9D Doppler coordinates. The NWL-9D pole is consistent with other systems within of the $0.05''$ level. The origin of the NWL-9D system appears to be geocentric within approximately one metre [3]. These corrections which are recommended values can be taken into account to get a latest mean geocentric (Doppler) coordinate system approximating the Average Terrestrial system. E.g. similar corrections ($+0.65''$ in longitude and -0.4 ppm in scale) were considered for the Proposed Geodetic Reference System of the Canadian Test Adjustment, of [31, 32, 33].

Table I

Transformation NWL-9D → Broadcast Ephemeris

Solution	No. of parameters	$X_{PE\to BE}$ (m)	$Y_{PE\to BE}$ (m)	$Z_{PE\to BE}$ (m)	$\varkappa$ (ppm)	ε_x (″)	ε_y (″)	ε_z (″)	Unit variance σ
1	3	-2.2 ± 0.2	-0.5 ± 0.2	3.9 ± 0.2	—	—	—	—	1.2
2	4	1.2 ± 0.6	0.0 ± 0.2	8.0 ± 0.1	-0.85 ± 0.13	—	—	—	1.0
3	6	-3.3 ± 1.0	0.2 ± 1.6	4.7 ± 0.8	—	-0.04 ± 0.05	0.04 ± 0.04	-0.08 ± 0.04	1.1
4	4	-2.5 ± 0.2	1.4 ± 0.7	3.9 ± 0.2	—	—	—	-0.10 ± 0.04	1.1
5	5	0.9 ± 0.5	1.9 ± 0.6	8.0 ± 0.6	-0.85 ± 0.13	—	—	-0.10 ± 0.03	0.9
6	7	0.1 ± 0.9	0.6 ± 1.3	8.8 ± 0.9	-0.85 ± 0.12	-0.04 ± 0.04	0.04 ± 0.03	-0.08 ± 0.03	0.9

Table II

Transformation NWL-9D → European Datum ED 50

Solution	No. of parameters	$X_{PE\to ED}$ (m)	$Y_{PE\to ED}$ (m)	$Z_{PE\to ED}$ (m)	$\varkappa$ (ppm)	ε_x (″)	ε_y (″)	ε_z (″)	Unit variance σ
1	3	81.0 ± 1.2	113.5 ± 1.2	118.7 ± 1.2	—	—	—	—	5.8
2	4	96.9 ± 3.5	114.6 ± 1.1	138.2 ± 4.3	-4.04 ± 0.86	—	—	—	5.0
3	6	84.2 ± 4.6	96.0 ± 10.2	117.1 ± 4.0	—	0.21 ± 0.29	-0.07 ± 0.19	1.18 ± 0.23	4.4
4	4	82.7 ± 0.9	88.9 ± 3.5	118.7 ± 0.9	—	—	—	1.29 ± 0.18	4.3
5	5	98.6 ± 2.2	90.0 ± 2.6	138.2 ± 2.7	-4.04 ± 0.54	—	—	1.29 ± 0.13	3.2
6	7	100.1 ± 4.0	97.1 ± 7.5	136.6 ± 4.0	-4.04 ± 0.55	0.21 ± 0.21	-0.07 ± 0.14	1.18 ± 0.17	3.2

Table III

Corrected precise (Doppler 78) to Ordnance Survey of Great Britain (OSBG) 77 transformation parameters over the UK

Solution	No. of parameters	X_G (m)	Y_G (m)	Z_G (m)	$\varkappa$ (ppm)	ε_x (″)	ε_y (″)	ε_z (″)	Unit variance (σ)
1	3	-369.4 ± 0.3	$+112.1 \pm 0.8$	-430.5 ± 0.3					2.57
2	4	-354.8 ± 4.0	$+111.5 \pm 0.4$	-410.9 ± 5.4	-3.8 ± 1.1				2.18
3	5	-354.6 ± 4.1	$+116.0 \pm 4.7$	-410.9 ± 5.4	-3.8 ± 1.1			-0.2 ± 0.3	2.19
4	7	-344.6 ± 7.9	$+59.8 \pm 17.9$	-420.2 ± 7.5	-3.8 ± 1.0	$+1.6 \pm 0.5$	$+0.4 \pm 0.3$	-0.7 ± 0.4	1.93

Ashkenazi [5] has determined the transformation parameters between the mean geocentric (Doppler) coordinate system and the Ordnance Survey of Great Britain (OSGB) 77 terrestrial system. These are computed for 3, 4, 5 and 7 transformation parameters together with their mean square errors in order to determine their significance, see Table III.

The second European Doppler Observation Campaign (EDOC-2) was observed during the period from 1977 April 23 to 1977 May 07. A little later, two Doppler receivers, a JMR-1 and a CMA-722B, have been working at the Satellite Geodetic Observatory (SGO), Penc, from June 28 to July 1 of 1977. The data observed were processed by different programs, e.g. measurements of the JMR-1 by SP-2 using only Broadcast Ephemeris. The coordinates obtained are published by Ádám and Czobor [7]:

$$X_{BE} = 405\ 2449.70 \text{ m}$$
$$Y_{BE} = 141\ 7664.78 \text{ m}$$
$$Z_{BE} = 470\ 1391.00 \text{ m}.$$

Using the transformation parameters (40) and the formula (39), we can get the coordinates in NWL-9D system of the Precise Ephemeris:

$$X_{NWL-9D} = 405\ 2451.56 \text{ m}$$
$$Y_{NWL-9D} = 141\ 7666.05 \text{ m}$$
$$Z_{NWL-9D} = 470\ 1387.00 \text{ m}.$$

Using the solution 5 of Table II as the most significant values we can get the following coordinates of point 001 at the SGO in the ED-50 system:

$$X_{ED-50} = 405\ 2524.92 \text{ m}$$
$$Y_{ED-50} = 141\ 7775.66 \text{ m}$$
$$Z_{ED-50} = 470\ 1506.21 \text{ m}.$$

According to Ashkenazi [5] Doopler coordinates in the NWL-9D system should be transformed into the recent mean geocentric system (Doppler 78) by applying the corrections $+0\overset{''}{.}8$ in longitude (rotation about the Z-axis) and —0.4 ppm in scale obtained by Hothem [25]:

$$X_D = 405\ 2444.44 \text{ m}$$
$$Y_D = 141\ 7681.20 \text{ m}$$
$$Z_D = 470\ 1385.12 \text{ m}.$$

The twofold transformation (BE → NWL-9D → mean geocentric Doppler 78) equals to the following transformation parameters:

$$\begin{aligned} X_{BE\to D} &= -0.9 \text{ m} \\ Y_{BE\to D} &= -1.9 \text{ m} \qquad \varkappa = 0.45 \text{ ppm} \\ Z_{BE\to D} &= -8.0 \text{ m} \qquad \varepsilon_Z = 0''.90 \,. \end{aligned} \tag{42}$$

Subtracting the coordinates of the Broadcast Ephemeris system from those in the recent mean geocentric Doppler 78 system, we get

$$\begin{aligned} \Delta X_{D\to BE} &= -\ 5.26 \text{ m} \\ \Delta Y_{D\to BE} &= \ \ 16.42 \text{ m} \\ \Delta Z_{D\to BE} &= -\ 5.88 \text{ m} \,. \end{aligned}$$

These coordinate differences are considerable values, which must be taken into account in different geodetic problems (e.g. geoid determination, etc.).

4. Combined adjustment of Doppler satellite and terrestrial geodetic data

There are different alternative procedures for the simultaneous adjustment of Doppler satellite and terrestrial geodetic networks. If the transformation parameters between the Doppler satellite and terrestrial geodetic coordinate systems and networks are unknown, Doppler satellite derived distances may be introduced into the terrestrial horizontal network. In this case the spatial distances are approximately reduced to geodetic distances, the latter of which are treated as distance observations in the network adjustment. Thomson and Krakiwsky [54] have examined the effects of the addition of satellite determined distance data on the Atlantic Canada geodetic network. This readjustment procedure caused a significant effect on this network. A scale change of —2.3 ppm and a change in orientation of +0".1 have been found. Further it is possible to compare the satellite Doppler derived distances with those obtained from terrestrial triangulation network coordinates for determination of the scale difference parameter $\varkappa$ [27].

If the transformation parameters are known the Doppler satellite coordinates may serve as a three-dimensional framework for the triangulation network. Such a framework may be used in its inherent three-dimensional state (with X, Y, Z coordinates), or, after transformation of the rectangular coordinates, X, Y, Z into the geodetic coordinates φ, λ, h the latter coordinates may be divided into two parts. The geodetic latitude (φ) and longitude (λ) may be used in the horizontal network, see e.g. Beattie et al. [9] and Kouba [32] and the ellipsoid height (h) in the vertical network or geoid determination [36, 24, 49]. Alternatively, the Doppler satellite determined coordinates can be used to derive spatial distances, azimuths and vertical angles that are used in a terrestrial network readjustment, see e.g. Anderle [2], Meade [39, 40, 41],

Moose and Henriksen [43]. This procedure requires *a priori* knowledge of the coordinate system transformation (only translation ΔX, ΔY, ΔZ) parameters without using the accurate determination of datum-shift parameters for transforming Doppler coordinates to an other ellipsoid. However the space azimuths derived from Doppler coordinates need to be corrected before comparing them with space azimuths based on the terrestrial geodetic positions [41]. The corrections to be applied are equivalent to the Laplace and deflection corrections. The converted Doppler results obtained could be then used as observation equations in a readjustment of the triangulation network.

Some problems arise in connection with the simultaneous adjustment of Doppler satellite and terrestrial geodetic observations such as the method of *a priori* weighting of the Doppler positions and terrestrial data, the choice of datum on which to reduce all the observations before proceeding with the adjustment. According to Ashkenazi [4] there are three alternatives to choose a reference datum as a basis for carrying out the simultaneous adjustment:

a) the local (national) terrestrial datum (given ellipsoid and geodetic position of origin)

b) the Doppler geodetic reference ellipsoid (e.g. WGS-72)

c) a geodetic system of Cartesian coordinates, see e.g. Kouba [31, 33].

The first alternative is particularly convenient when the national network is relatively small, already well observed and properly adjusted and there is an adequate supply of astrogeoidal information. In this case, only the satellite derived geocentric positions have to be transformed from the WGS-72 system to the local datum. When the network to be readjusted is that of a large country or a sub-continent, one may well consider one of the two other alternatives.

Finally, on the basis of Peterson [50] and Halmos [23], we give the observation equations for the three-dimensional simultaneous adjustment of Doppler satellite and terrestrial geodetic data. The position observation equation for triangulation determinations is:

$$\begin{bmatrix} 1 & 0 & 0 \\ \dots 0 & 1 & 0 \dots \\ 0 & 0 & 1 \end{bmatrix} \begin{bmatrix} \vdots \\ \vdots \\ \Delta X_J \\ \Delta Y_J \\ \Delta Z_J \\ \vdots \end{bmatrix} = \begin{bmatrix} \bar{X}_j - X'_J \\ \bar{Y}_j - Y'_J \\ \bar{Z}_j - Z'_J \end{bmatrix} + \begin{bmatrix} V_{XJ} \\ V_{YJ} \\ V_{ZJ} \end{bmatrix} \tag{43}$$

and the position observation equation for Doppler observations:

$$\begin{bmatrix} 1 & 0 & 0 & -1 & 0 & 0 & -\bar{X}_{DJ} & -\bar{Y}_{DJ} & \bar{Z}_{DJ} & 0 \\ \dots 0 & 1 & 0 \dots & 0 & -1 & 0 & -\bar{Y}_{DJ} & \bar{X}_{DJ} & 0 & -\bar{Z}_{DJ} \\ 0 & 0 & 1 & 0 & 0 & -1 & -\bar{Z}_{DJ} & 0 & -\bar{X}_{DJ} & -\bar{Y}_{DJ} \end{bmatrix} \begin{bmatrix} \vdots \\ \Delta X_J \\ \Delta Y_J \\ \Delta Z_J \\ \vdots \\ \Delta X \\ \Delta Y \\ \Delta Z \\ \varkappa \\ \varepsilon_x \\ \varepsilon_y \\ \varepsilon_z \end{bmatrix} =$$

$$= \begin{bmatrix} \bar{X}_{DJ} - X'_J \\ Y_{DJ} - Y'_J \\ \bar{Z}_{DJ} - Z'_J \end{bmatrix} + \begin{bmatrix} V_{XJ} \\ V_{YJ} \\ V_{ZJ} \end{bmatrix} \tag{44}$$

where $\bar{X}_{DJ}, \bar{Y}_{DJ}, Z_{DJ}$ are observed Doppler coordinates,
$\bar{X}_J, \bar{Y}_J, \bar{Z}_J$ observed triangulation coordinates,
V_{XJ}, V_{YJ}, V_{ZJ} residuals on the observed coordinates,
$\Delta X_J, \Delta Y_J, \Delta Z_J$ correction to be added to approximate coordinates to give the final adjusted coordinates X_J, Y_J, Z_J
X'_J, Y'_J, Z'_J approximate coordinates and

the other symbols are mentioned earlier.

REFERENCES

1. ANDERLE, R. J.: Transformation of terrestrial survey data to Doppler satellite datum *J. Geophys. Res.*, 79 (1974), 5319—5341.
2. ANDERLE, R. J.: Simultaneous adjustment of terrestrial geodimeter and satellite Doppler observations for geodetic datum definition. Preprint of NWL Technical Report, TR-2129, Dahlgren, Virgine, 1974.
3. ANDERLE, R. J.—TANNENBAUM, M. G.: Practical realization of a reference system for Earth dynamics by satellite methods. Preprint of NWL Technical Report, TR-3166, 1974.
4. ASHKENAZI, V.: National and continental geodetic control networks. XV. FIG Congress, Vol. 5., Sweden, 1977, 15—22.
5. ASHKENAZI, V.: Recent Doppler Campaigns in the United Kingdom. Proceedings of the Second Satellite Doppler Positioning. Austin, Texas, 1979, 801—819.
6. ASHKENAZI, V.—SYSKES, R. M.: Precise and broadcast ephemerides position determination over the U.K. and Europe. 2nd Symp. on the Use of Artificial Satellites for Geodesy and Geodynamics, Athens, 1978.
7. ÁDÁM, J.—CZOBOR, Á.: Az első geodéziai pontosságú műholdas Doppler-észlelések hazánkban (Results of the first Doppler satellite measurements of geodetic accuracy in Hungary). *Geodézia és Kartográfia*, 29 (1977), 397—407.
8. BADEKAS, J.: Investigations related to the establishment of a world geodetic system. Reports of the Department of Geodetic Science, No. 124, Ohio State University, Columbus, 1969.

9. BEATTIE, D. S.—BLAIS, J. A. R.—PINCH, M. C.: Test adjustment of the Canadian primary horizontal network. Collected Papers, Geodetic Survey of Canada, 1978.
10. BLAIS, J. A. R.: Inertia, inertial reference systems and physical geodesy. Collected Papers, Geodetic Survey of Canada, 1977.
11. BLAIS, J. A. R.: Geodetic reference systems. Collected Papers, Geodetic Survey of Canada, 1978.
12. BOUCHER, C.: Investigations on geodetic applications of satellite Doppler observations for control networks. Proceedings of the Second Int. Geod. Symp. on Satellite Doppler Positioning, Austin, Texas, Vol. 2,. 1979, 1001—1027.
13. BOUCHER, C.—PAQUET, P.—WILSON, P.: The second European Doppler Observations Campaign (EDOC-2) — Results and conclusions obtained by EDOC-2 computing centers. Proceedings of the Second Int. Geod. Symp. on Satellite Doppler Positioning, Austin, Texas, Vol. 2., 1979, 819—851.
14. BURŠA, M.: The theory of the determination of the nonparallelism of the minor axis of the reference ellipsoid, polar axis of inertia of the Earth, and initial astronomical and geodetic meridians from observations of artificial earth satellites. Translation from *Geophysica et Geodaetica*, No. 6, 1976.
15. DOBACZEWSKA, W.: On comparability of terrestrial and satellite triangulation. *Artificial Satellites*, 11 (1976), 3—11.
16. EHRNSPERGER, W.—HORNIK, H.: The use of Doppler in terrestrial adjustment in the European triangulation network (RETrig). Proceedings of the Second Int. Geod. Symp. on Satellite Doppler Positioning. Austin, Texas, Vol. 2., 1979, 851—871.
17. GRAFAREND, E. W.: Attemps for a unified theory of geodesy. *Bull. Geod.*, 109 (1973), 237—260.
18. GRAFAREND, E. W.: Threedimensional geodesy I. The unholonomity problem. *ZfV*, 100 (1975) 269—281.
19. GRAFAREND, E. W.: Space-time differential geodesy. Reports of the Department of Geodetic Science. No. 250, Ohio State Univ., Columbus, 1977.
20. GRAFAREND, E. W.—MUELLER, I. I.—PAPO, H. B.—RIETER, B.: Concept for reference frames in geodesy and geophysics. American Geophysical Union Spring Meeting. Miami Beach, 1978.
21. GROTEN, E.: On variations of geocentric position with time. *Acta Geod. Geoph. Mont. Hung.*, 14 (1979), 31—58.
22. GROTEN, E.—SCHAAB, H.: Alternative determinations of geodetic datum shifts. *Veröff. Zentralinst. Physik der Erde*, 52 (1977), 333—368.
23. HALMOS, F.: Geodéziai hálózatok közötti transzformációk matematikai modelljei (Mathematical models for transformation between geodetic networks). *Geodézia és Kartográfia*, 32 (1980), 97—104.
24. HALMOS, F.: Geoid determination by satellite methods. Observations of Artificial Earth Satellites, No. 18, Warszawa—Lódz, 1979.
25. HOTHEM, L. D.: Determination of accuracy, orientation and scale of satellite Doppler point-positioning coordinates. Proceedings of the Second Int. Geod. Symp. on Satellite Doppler Positioning, Austin, Texas, Vol. 1. 1979, 609—631.
26. HOTINE, M.: Mathematical Geodesy. ESSA Monograph No. 2, U.S. Department of Commerce, Washington, D.C., 1969.
27. KAKKURI, J.: Measuring the Finnish 890 km long baseline with the Doppler receivers. Private Communication, Helsinki, 1979.
28. KAULA, W. M.: Theory of Satellite Geodesy. Blaisdell, Toronto 1966.
29. KOLACZEK, B.—WEIFFENBACH, G. (eds): On reference coordinate systems for Earth dynamics. IAU. Coll., No. 26, Torun, 1974.
30. KOUBA, J.: A proposed geodetic reference system for the Canadian adjustment. Collected Papers Geodetic Survey of Canada, 1976.
31. KOUBA, J.: Doppler satellite control in establishing geodetic control network. *Energy, Mines and Resources Canada, Publications of the Earth Physics Branch*, 45 (1976), 167—183.
32. KOUBA, J.: Geodetic satellite Doppler positioning and application to Canadian test adjustment. Collected Papers, Geodetic Survey of Canada, 1978.
33. KOUBA, J.: Datum considerations for test adjustments of Canadian primary horizontal geodetic network. Collected Papers, Geodetic Survey of Canada, 1978.
34. KRAKIWSKY, U. J.—THOMSON, D. B.: Mathematical models ofr the combination of terrestrial and satellite networks. *Canadian Surveyor*, 28 (1974), 606—615.
35. KUMAR, M.: Coordinate transformation by minimizing correlations between parameters. Reports of the Dept. of Geodetic Science, No. 184, Ohio State University, Columbus, 1972.

36. LACHAPELLE, G.: Estimation of the geoid and deflection components in Canada. Collected Papers, Geodetic Survey of Canada, 1978.
37. LEICK, A.: The observability of the celestial pole and its nutations. Reports of the Department of Geodetic Science, No. 262, Ohio State University, Columbus, 1978.
38. LEICK, A.—GELDER, B. H. W.: On similarity transformations and geodetic network distortions based on Doppler satellite observations. Reports of the Department of Geodetic Science, No. 235, Ohio State University, Columbus, 1975.
39. MEADE, B. F.: Geoceiver positions compared with results of precise surveys. XIV. Congress of FIG, Washington, 1974.
40. MEADE, B. F.: Doppler data versus results from high precision traverse. *Canadian Surveyor*, 28 (1974), 462—466.
41. MEADE, B. F.: Errors of Doppler positions obtained from results of transcontinental traverse surveys. Proceedings of the First Int. Geod. Symp. on Satellite Doppler Positioning, Las Cruces, DMA, Vol. 2., 1976, 813—831.
42. MOLODENSKII, M. S.—EREMEEV, V. F.—YURKINA, M. I.: Methods for study of the external gravitational field and figure of the Earth. Israel Program for Scientific Tranlations, Jerusalem, 1962.
43. MOOSE, R. E.—HENRIKSEN, S. W.: Effect of geoceiver observations upon the classical triangulation network. NOAA Technical Report, NOS 66 NGS 2, Rockville, 1976.
44. MORITZ, H.: Advanced least-squares estimation. Reports of the Department of Geodetic Science, No. 175, Ohio State Univ., Columbus, 1972.
45. MORITZ, H.: Eine Methode der kleinsten Quadrate zur Koordinatentransformation. V.K. Hristov septuagenario, Acad. Sci. Bulgaria, Sofia, 1973.
46. MORITZ, H.: The method of least-squares collocation in geometric geodesy. *Boll. Geod. Sci. Aff.*, 33 (1974), 193—207.
47. MUELLER, I. I.: Review of the classical methods for the determination of geodetic datums. In: On Reference Coordinate Systems for Earth Dynamics (eds: B. KOLACZEK and G. WEIFFENBACH), IAU Coll., No. 26, Torun, 1974.
48. PARM, T.: On the determination of the scale of the Finnish stellar triangulation net. Publ. of the FGI, No. 78; 1, Helsinki, 1978.
49. PERROTT, T. A.: North American datum 1927 geoid heights and coordinate shifts in Alaska from Doppler satellite data. Internal Report, DMATC, No. 00-76-07, 1976.
50. PETERSON, A. E.: Merging of the Canadian triangulation network with the 1973 Doppler satellite data. *Canadian Surveyor*, 28 (1974), 487—495.
51. SCHWARZ, K. P.: Combination and analysis of networks of different kind by generalized least-squares methods. Proceedings of the Int. Symp. "Satellite and Terrestrial Triangulation", Graz, 1972.
52. SCHWARZ, K. P.: Combination of spatial networks using an estimated covariance matrix. *Bull. Géod.*, No. 112 (1974), 171—186.
53. SOLER, T.: On differential transformations between Cartesian curvilinear (geodetic) coordinates. Reports of the Department of Geodetic Science, No. 236, Ohio State University, Columbus, 1976.
54. THOMSON, D. B.—KRAKIWSKY, E. J.: Alternative solutions to the combination of terrestrial and satellite geodetic networks. *Energy, Mines and Resources Canada, Publ. of the Earth Physics Branch*, 45 (1976), 185—197.
55. THOMSON, D. B.—KRAKIWSKY, E. J.: Concepts of the combination of geodetic networks. Proceedings of the Int. Geod. Symp. on Satellite Doppler Positioning, Las Cruces, DMA, Vol. 2., 1976. 727—745.
56. TSCHERNING, C. C.: Determination of datum-shift parameters using least squares collocation. *Boll. Geod. Sci. Aff.*, 36 (1976), 173—183.
57. UOTILA, U. A.: Introduction to adjustment computations with matrices. Lecture Notes, Dept. of Geodetic Science, Ohio State Univ., Columbus, 1967.
58. VANIČEK, P.—WELLS, D. E.: Positioning of horizontal geodetic datums. *Canadian Surveyor*, 28 (1974), 531—538.
59. VARGA, M.: Reference frames of space-time geodesy (in Hungarian), *Geodézia és Kartográfia*, 31 (1979), 397—405.
60. VEIS, G.: Geodetic uses of artificial satellites. *Smithsonian Contributions to Astrophysics*, 3 (1960), 95—161.
61. WELLS, D. E.—VANIČEK, P.: Alignement of geodetic and satellite coordinate systems to the average terrestrial system. *Bull. Géod.*, No. 117 (1974), 241—258.
62. WOLF, H.: Geometric connection and re-orientation of three-dimensional triangulation nets. *Bull. Géod.*, No. 67 (1963), 165—169.

О ПРИНЦИПЕ КОМБИНАЦИИ ДОППЛЕРОВСКИХ И НАЗЕМНЫХ ГЕОДЕЗИЧЕСКИХ СЕТЕЙ

Й. АДАМ–Ф. ХАЛМОШ–М. ВАРГА

РЕЗЮМЕ

Общие альтернативные процедуры можно использовать для комбинации допплеровских и наземных геодезических сетей. Кратко рассматривая эти процедуры исследуют трёхмерные модели преобразований между допплеровскими и наземными геодезическими системами координат и сетками. Рассматриваются также оценочные процессы. Представлены общие замечания о допплеровских и наземных геодезических сетях и их систем координат. В заключении даются экспериментальные результаты.

Acta Geodaet., Geophys. et Montanist. Acad. Sci. Hung. Volume 17 (2), pp. 171—179 (1982)

DOPPLER LOCATION EQUATIONS FOR PLATFORM LOCALIZATION USING SATELLITES

J. ÁDÁM
SATELLITE GEODETIC OBSERVATORY, PENC

GY. TARCSAI
GEOPHYSICAL DEPARTMENT, EÖTVÖS LORÁND UNIVERSITY, BUDAPEST

[Manuscript received March 18, 1980]

The paper is a continuation of the study presented in [1]. Here we give the complete derivation of the platform Doppler location equations used in our previous paper. A brief comparison with two other solutions is also given to demonstrate the equivalence of the different solutions.

1. Introduction

The different automatic platform location systems using satellites are well known. Three methods can mainly be used for platform positioning: range only, Doppler (or range rate) only and their combination. The physical quantities involved are range and Doppler shift, measured in a one- or two-way communication link between a platform and the satellite. The satellite platform location systems using these data are reviewed e.g. in [1, 2, 3]. The present study is limited to the discussion of the various equation systems for platform localization with the Doppler method. It is not intended to discuss here all of the solutions proposed or applied up to now, only to give the derivation of the equations used in certain particular mathematical models which are representative of the commonly used solutions.

Two coordinate systems are considered as it can be seen in Fig. 1: XYZ and $\xi\eta\zeta$. The rectangular coordinate system XYZ is a geocentric system. Its Z-axis is directed toward the average north terrestrial pole. The XZ-plane is parallel to the mean Greenwich astronomic meridian. The satellite positions and velocities are supposed to be known in this system, given by the coordinates X_{Si}, Y_{Si}, Z_{Si} and velocity components $\dot{X}_{Si}, \dot{Y}_{Si}, \dot{Z}_{Si}$ or direction cosines m_i, n_i, p_i of the satellite velocity vector $\mathbf{v}_{Si}$ ($i = 1, 2, 3, \ldots, t$ denotes successive moments). Values of the direction cosines m_i, n_i, p_i are:

$$m_i = \frac{\dot{X}_{Si}}{|\mathbf{v}_{Si}|}; \quad n_i = \frac{\dot{Y}_{Si}}{|\mathbf{v}_{Si}|}; \quad \text{and} \quad p_i = \frac{\dot{Z}_{Si}}{|\mathbf{v}_{Si}|}, \tag{1}$$

where

$$|\mathbf{v}_{Si}| = \sqrt{\dot{X}_{Si}^2 + \dot{Y}_{Si}^2 + \dot{Z}_{Si}^2}.$$

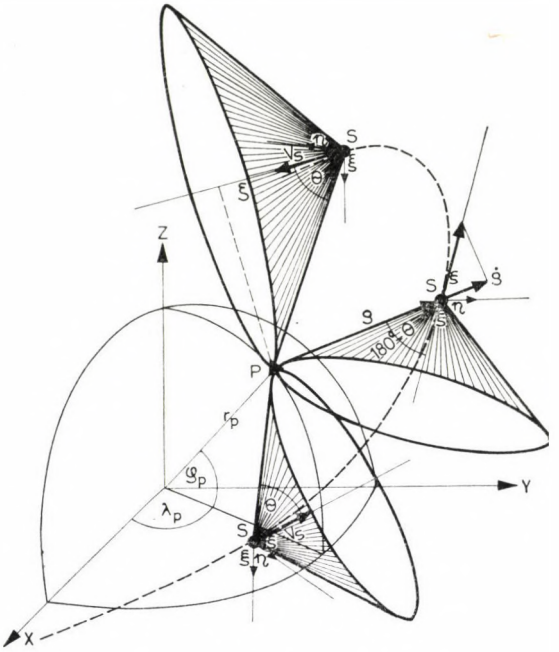

Fig. 1

After localization measurements, the position of the platform is derived in this system. The rectangular coordinates X_P, Y_P, Z_P of the platform can be expressed with the geodetic coordinates φ_G, λ_G, h_G referred to a chosen reference ellipsoid as

$$\begin{aligned} X_P &= (N + h_G) \cdot \cos \varphi_G \cdot \cos \lambda_G \\ Y_P &= (N + h_G) \cdot \cos \varphi_G \cdot \sin \lambda_G \\ Z_P &= [N(1 - e^2) + h_G] \cdot \sin \varphi_G \end{aligned} \tag{2}$$

where e denotes the first eccentricity of the ellipsoid, N is the radius of curvature in the direction of the prime vertical. Eqs (2) permit the computation of the rectangular coordinates X_P, Y_P, Z_P from the geodetic coordinates φ_G, λ_G, h_G. The inverse procedure, the computation of φ_G, λ_G, h_G from given X_P, Y_P, Z_P, is more complicated because Eqs (2) cannot be solved for φ_G, λ_G, h_G in a closed form; accordingly, the computation must be done iteratively [4]. Using an average terrestrial sphere with radius r_P (e.g. in the case of the oceans and seas), the relation between the Cartesian coordinates and the spherical coordinates r_P, φ_P, and λ_P reduces to

$$
\begin{aligned}
X_P &= r_P \cdot \cos \varphi_P \cdot \cos \lambda_P \\
Y_P &= r_P \cdot \cos \varphi_P \cdot \sin \lambda_P \\
Z_P &= r_P \cdot \sin \varphi_P .
\end{aligned} \tag{3}
$$

The other rectangular coordinate system $(\xi\eta\zeta)_i$ is centred at the instantaneous satellite positions, with its ζ-axis directed along the velocity vector $\mathbf{v}_{Si}$. The transformation formula connecting the coordinate systems XYZ and $(\xi\eta\zeta)_i$ is given by

$$\mathbf{X}_P = \mathbf{A}_i^T \cdot \xi_{Pi} + \mathbf{X}_{Si} \tag{4}$$

where $\mathbf{X}_P^T = [X_P, Y_P, Z_P]$ and $\mathbf{X}_{Si}^T = [X_{Si}, Y_{Si}, Z_{Si}]$ are the position vectors of platform P to be located and of the satellite in the XYZ-system, respectively, $\xi_{Pi}^T = [\xi_{Pi}, \eta_{Pi}, \zeta_{Pi}]$ is the position vector of platform P in the $(\xi\eta\zeta)_i$-system, and

$$\mathbf{A}_i = \begin{bmatrix} \cos(X\xi_i) & \cos(Y\xi_i) & \cos(Z\xi_i) \\ \cos(X\eta_i) & \cos(Y\eta_i) & \cos(Z\eta_i) \\ \cos(X\zeta_i) & \cos(Y\zeta_i) & \cos(Z\zeta_i) \end{bmatrix}, \tag{5}$$

is the rotation matrix between the two coordinate systems. The main properties of a rotation matrix like Eq. (5) are that the sum of squared elements of any row or column is equal to unity, and the scalar product of any two rows or any two columns is equal to zero.

2. Location equations of the Doppler only method

A single Doppler measurement Δf_i locates the platform onto a cone of angle Θ_i around the instantaneous velocity vector $\mathbf{v}_{Si}$ of the satellite (Fig. 1), according to the relation

$$\Delta f_i = f_i - f_0 = -\frac{f_0}{c} \cdot \frac{\mathrm{d}\varrho_i}{\mathrm{d}t} = -\frac{f_0}{c} \mathbf{v}_{Si} \cdot \cos \Theta_i \tag{6}$$

where f_0 and f_i are the transmitted and received frequencies, respectively, c is the velocity of light in free space, and ϱ_i is the distance between the satellite and the platform at moment t_i. It is easy to see that the equation of this cone in the satellite coordinate system $(\xi\eta\zeta)_i$ is

$$\xi_i^2 + \eta_i^2 = \zeta_i^2 \cdot \mathrm{tg}^2 \Theta_i . \tag{7}$$

On the other hand, a Doppler measurement yields the radial velocity $\mathrm{d}\varrho_i/\mathrm{d}t = \dot{\varrho}_i$ between the satellite and the observer which is also often used in formulating the location equations.

2.1 *Derivation of the location equations*

If the platform (e.g. a buoy) is located on the ocean or sea surface which can be approximated by an ellipsoid or sphere of known parameters, then having measured Δf_i for at least two successive positions of the satellite we can write a system of three equations for the intersection of the ellipsoid and the two cones:

$$X_P^2 + Y_P^2 + Z_P^2 = r_P^2 \tag{8a}$$

$$\xi_i^2 + \eta_i^2 = \zeta_i^2 \cdot \mathrm{tg}^2\, \Theta_i \qquad (i = 1, 2)\,. \tag{8b}$$

With minor alterations Eq. (8a) hold also for the case when the height of the platform above the reference ellipsoid is known.

In a general case, however, when the platform is not located on a known surface (e.g. it is borne by a floating balloon), the intersection of three cones is necessary to obtain the coordinates X_P, Y_P, Z_P.

In any case, in order to proceed with the solution, Eq. (7) has to be transformed into the XYZ system.

Adding ζ_i^2 to both sides of Eq. (7), we get

$$\xi_i^2 + \eta_i^2 + \zeta_i^2 = \zeta_i^2(1 + \mathrm{tg}^2\Theta_i)\,. \tag{9}$$

Using Eq. (4), it follows from Eq. (9) that

$$\begin{aligned}
&[(X_P - X_{Si}) \cdot \cos(X\xi_i) + (Y_P - Y_{Si}) \cdot \cos(Y\xi_i) + (Z_P - Z_{Si}) \cdot \cos(Z\xi_i)]^2 + \\
&+ [(X_P - X_{Si}) \cdot \cos(X\eta_i) + (Y_P - Y_{Si}) \cdot \cos(Y\eta_i) + (Z_P - Z_{Si}) \cdot \cos(Z\eta_i)]^2 + \\
&+ [(X_P - X_{Si}) \cdot \cos(X\zeta_i) + (Y_P - Y_{Si}) \cdot \cos(Y\zeta_i) + (Z_P - Z_{Si}) \cdot \cos(Z\zeta_i)]^2 = \\
&= [(X_P - X_{Si}) \cdot \cos(X\zeta_i) + (Y_P - Y_{Si}) \cdot \cos(Y\zeta_i) + (Z_P - Z_{Si}) \cdot \cos(Z\zeta_i)]^2 \cdot \\
&\qquad \cdot (1 + \mathrm{tg}^2\Theta_i)\,.
\end{aligned} \tag{10}$$

According to the properties of the rotation matrix (5), after squaring the left side of Eq. (10) we arrive at

$$\begin{aligned}
&(X_P - X_{Si})^2 + (Y_P - Y_{Si})^2 + (Z_P - Z_{Si})^2 = \\
&= [(X_P - X_{Si}) \cdot \cos(X\zeta_i) + (Y_P - Y_{Si}) \cdot \cos(Y\zeta_i) + (Z_P - Z_{Si}) \cdot \cos(Z\zeta_i)]^2 \cdot \\
&\qquad \cdot (1 + \mathrm{tg}^2\, \Theta_i)\,.
\end{aligned} \tag{11}$$

Note that only elements of the third row of the rotation matrix (5) are conserved in Eq. (11) by the above manipulation. This is a great advantage, because thus the knowledge of the other components of the rotation matrix (5) is not necessary at all what simplifies greatly the computations.

Let us introduce the notation

$$u_i = 1 + \mathrm{tg}^2\Theta_i \tag{12}$$

and recall that

$$\begin{aligned} m_i &= \cos(X\zeta_i) \\ n_i &= \cos(Y\zeta_i) \\ p_i &= \cos(Z\zeta_i)\,, \end{aligned} \tag{13}$$

then squaring both sides of Eq. (11) and performing some manipulations we arrive at the equation

$$a_iX_P^2 + b_iY_P^2 + c_iZ_P^2 + d_iX_PY_P + e_iY_PZ_P + f_iX_PZ_P + g_iX_P + h_iY_P + \\ + k_iZ_P + l_i = 0 \tag{14}$$

where

$$\begin{aligned} a_i &= 1 - m_i^2u_i \\ b_i &= 1 - n_i^2u_i \\ c_i &= 1 - p_i^2u_i \\ d_i &= -2m_in_iu_i \\ e_i &= -2n_ip_iu_i \\ f_i &= -2m_ip_iu_i \\ g_i &= -2a_iX_{Si} - d_iY_{Si} - f_iZ_{Si} \\ h_i &= -2b_iY_{Si} - d_iX_{Si} - e_iZ_{Si} \\ k_i &= -2c_iZ_{Si} - e_iY_{Si} - f_iX_{Si} \\ l_i &= a_iX_{Si}^2 + b_iY_{Si}^2 + c_iZ_{Si}^2 + d_iX_{Si}Y_{Si} + e_iY_{Si}Z_{Si} + f_iX_{Si}Z_{Si}\,. \end{aligned} \tag{15}$$

If the position and velocity of the satellite are known at three different moments and the corresponding Doppler shifts Δf_i $(i = 1, 2, 3)$ are also measured, we obtain a second order system of three equations by writing Eq. (14) for $i = 1, 2, 3$. From three second order equations of this type, the coordinates X_P, Y_P, Z_P of the platform can be determined by using various numerical procedures. According to our experiences [1], Powell's hybrid method [5, 6] proved to be very stable in solving Eq. (14). Of course, Eq. (14) can be used also in a least squares or maximum likelihood solution when the number of Doppler measurements is greater than three.

2.2 *Location equations of other solutions*

It is interesting to review here briefly two other solutions which differ from the one outlined above.

For a platform localization by the Doppler method, the following equation is proposed in [7]:

$$\zeta_i - \sqrt{\xi_i^2 + \eta_i^2 + \zeta_i^2} \cdot \cos \Theta_i = 0 \,, \tag{16}$$

where $\cos \Theta_i$ is known from Eq. (6). After transforming the coordinates ξ_i, η_i, ζ_i into the geocentric system XYZ, and expressing the first member of Eq. (16) as the scalar product of the topocentric vector ϱ and the normalized velocity vector $\mathbf{v}_{Si}$, one gets

$$\begin{aligned} m_i(X_P - X_{Si}) + n_i(Y_P - Y_{Si}) + p_i(Z_P - Z_{Si}) = \\ = \sqrt{(X_P - X_{Si})^2 + (Y_P - Y_{Si})^2 + (Z_P - Z_{Si})^2} \cdot \cos \Theta_i \,. \end{aligned} \tag{17}$$

After squaring both sides of Eq. (17) and performing lengthy manipulations, the following equation system can be obtained:

$$\begin{aligned} A_i X_P^2 + B_i Y_P^2 + C_i Z_P^2 + D_i X_P Y_P + E_i Y_P Z_P + F_i X_P Z_P + \\ + G_i X_P + H_i Y_P + K_i Z_P + L_i = 0 \end{aligned} \tag{18}$$

where

$$\begin{aligned} A_i &= m_i^2 - \cos^2 \Theta_i \\ B_i &= n_i^2 - \cos^2 \Theta_i \\ C_i &= p_i^2 - \cos^2 \Theta_i \\ D_i &= 2 m_i n_i \\ E_i &= 2 n_i p_i \\ F_i &= 2 m_i p_i \\ G_i &= -2 A_i X_{Si} - D_i Y_{Si} - F_i Z_{Si} \\ H_i &= -2 B_i Y_{Si} - D_i X_{Si} - E_i Z_{Si} \\ K_i &= -2 C_i Z_{Si} - E_i Y_{Si} - F_i X_{Si} \\ L_i &= A_i X_{Si}^2 + B_i Y_{Si}^2 + C_i Z_{Si}^2 + D_i X_{Si} Y_{Si} + E^i Y_{Si} Z_{Si} + F_i X_{Si} Z_{Si} \,. \end{aligned} \tag{19}$$

The basic equation for platform localization in [8] is obtained by taking the time derivative of the equation of a sphere of radius ϱ_i around the satellite position:

$$\varrho_i\dot{\varrho}_i = (X_{Si} - X_P)\cdot(\dot{X}_{Si} - \dot{X}_P) + (Y_{Si} - Y_P)\cdot(\dot{Y}_{Si} - \dot{Y}_P) + \\ + (\bar{Z}_{Si} - Z_P)\cdot(\dot{Z}_{Si} - \dot{Z}_P)\,, \tag{20}$$

where

X_{Si}, Y_{Si}, Z_{Si} coordinates of the i-th satellite position in the XYZ-system,
X_P, Y_P, Z_P coordinates of the platform to be determined,
$\dot{X}_{Si}, \dot{Y}_{Si}, \dot{Z}_{Si}$ components of the satellite velocity vector at the i-th satellite position,
$\dot{X}_P, \dot{Y}_P, \dot{Z}_P$ components of the platform velocity vector,

$$\varrho_i = \sqrt{(X_{Si} - X_P)^2 + (Y_{Si} - Y_P)^2 + (Z_{Si} - Z_P)^2} \tag{21}$$

and $\dot{\varrho}_i$ is known from Eq. (6) through the measured Δf_i.

The velocity components $\dot{X}_P, \dot{Y}_P, \dot{Z}_P$ are supposed to be known in this solution. In the first two solutions, the velocity components of the platform are not involved in the equations, they can also be taken into account as corrections to the measured data. It is to be noted that basically Eq. (20) is used also in the TWERLE mathematical model for platform location by the RAMS Doppler system [9], but the velocity components of the platform are not supposed to be known and can be determined along with X_P, Y_P, Z_P.

Substituting Eq. (21) for ϱ_i into Eq. (20) and after squaring both sides of Eq. (20) we can obtain the following equation

$$a^i_{11}X_P^2 + a^i_{22}Y_P^2 + a^i_{33}Z_P^2 + a^i_{12}X_PY_P + a^i_{23}Y_PZ_P + \\ + a^i_{13}X_PZ_P + a^i_{14}X_P + a^i_{24}Y_P + a^i_{34}Z_P + a^i_{44} = 0\,, \tag{22}$$

where

$$\begin{aligned}
a^i_{11} &= -\dot{\varrho}_i^2 + (\dot{X}_{Si} - \dot{X}_P)^2 \\
a^i_{22} &= -\dot{\varrho}_i^2 + (\dot{Y}_{Si} - \dot{Y}_P)^2 \\
a^i_{33} &= -\dot{\varrho}_i^2 + (\dot{Z}_{Si} - \dot{Z}_P)^2 \\
a^i_{12} &= 2(\dot{X}_{Si} - \dot{X}_P)\cdot(\dot{Y}_{Si} - \dot{Y}_P) \\
a^i_{23} &= 2(\dot{Y}_{Si} - \dot{Y}_P)\cdot(\dot{Z}_{Si} - \dot{Z}_P) \\
a^i_{13} &= 2(\dot{X}_{Si} - \dot{X}_P)\cdot(\dot{Z}_{Si} - \dot{Z}_P) \\
a^i_{14} &= -2(a^i_{11}X_{Si} + a^i_{12}Y_{Si} + a^i_{13}Z_{Si}) \\
a^i_{24} &= -2(a^i_{22}Y_{Si} + a^i_{12}X_{Si} + a^i_{23}Z_{Si}) \\
a^i_{34} &= -2(a^i_{33}Z_{Si} + a^i_{23}Y_{Si} + a^i_{13}X_{Si}) \\
a^i_{44} &= -\dot{\varrho}_i^2(X_{Si}^2 + Y_{Si}^2 + Z_{Si}^2) + \\
&+ [X_{Si}(\dot{X}_{Si} - \dot{X}_P) + Y_{Si}(\dot{Y}_{Si} - \dot{Y}_P) + Z_{Si}(\dot{Z}_{Si} - \dot{Z}_P)]^2.
\end{aligned} \tag{23}$$

Note that the coefficients a_{14}^{i}, a_{24}^{i} and a_{34}^{i} as written on page 94 of [8] are in error.

3. Numerical comparison of the coefficients

Here we present a brief numerical comparison of the coefficients of the above equation systems. For this we use the data of satellite position 5 and platform 3 of Fig. 1 in [1]:

$$\begin{aligned} X_P &= 400\,2609.2395 \text{ m} & & X_S &= 478\,9635.1126 \text{ m} \\ Y_P &= 88\,7289.2587 \text{ m} & \text{and} & Y_S &= 41\,9181.2332 \text{ m} \\ Z_P &= 488\,5976.0575 \text{ m} & & Z_S &= 526\,2410.2065 \text{ m,} \end{aligned}$$

furthermore

$$\begin{aligned} \dot{X}_S &= -5529.2332 \text{ m/s} & & m &= -0.735\,735\,26455 \\ \dot{Y}_S &= -483.9508 \text{ m/s} & \text{or} & n &= -0.064\,395\,84449 \\ \dot{Z}_S &= 5066.7869 \text{ m/s} & & p &= 0.674\,200\,85709 \end{aligned}$$

$$\dot{X}_P = \dot{Y}_P = Z_P = 0 \text{ m/s},$$

$$\cos \Theta = 0.298\,066\,21270 .$$

Numerical values of the coefficients (15), (19) and (23) are shown in Table I. From this Table it is clear that the three sets of coefficients are basically

Table I

Numerical values of the coefficients for the three Doppler location solutions outlined in the paper

	Coefficients of the method described in [7]	Coefficients of our solution	Coefficients of the method desribed in [8]
1	0.452 462 912	−5.092 810 162	25 554 633.58
2	−0.084 696 642	0.953 324 370	− 4 783 577.822
3	0.365 703 329	−4.116 265 835	20 654 543.29
4	0.094 756 587	−1.066 556 612	5 351 753.66
5	−0.086 831 467	0.977 353 427	− 4 904 151.148
6	−0.992 066 692	11.166 456 28	−56 030 892.68
7	846 677.1976	−9 529 988.245	4.781 94E+13
8	74099.8067	− 834 049.0198	4.18508E+12
9	939 073.7256	−10569980.62	4.30380E+13
10	−4.51406E+12	5.08092E+13	− 2.54950E+20

identical with each other, because any of them can be transformed into the other by simply multiplying all its coefficients by a constant. Therefore the three solutions lead to the same system of equations. For the first two solutions which are based on geometrical considerations, this fact is rather evident, because Eq. (16) can be easily transformed into Eq. (7). It is interesting that the third solution which after all uses the simple concept of radial velocity, results in the same second order basic equation as the other two.

REFERENCES

1. TARCSAI, GY.—ÁDÁM, J.: Accuracy of satellite platform location techniques: A study of error propagation. *Acta Geod., Geoph. Mont. Hung.* 13 (1978), 3—24.
2. TARCSAI, GY.—FERENCZ, CS.: Platform location by satellites (in Hungarian). Manuscript, 10 p., Budapest, 1974.
3. TARCSAI, GY.: Summary of platform location and data collection satellite systems. Manuscript, 15 p., Budapest, 1975.
4. HEISKANEN, W.—MORITZ, H.: Physical Geodesy. Freeman and Co., San Francisco—London, 1967.
5. POWELL, M. J. D.: A hybrid method for nonlinear equations. Numerical Methods for Nonlinear Algebraic Equations, Gordon and Breach, New York, 1970.
6. HAJNALNÉ, A.: Programs for nonlinear equation systems (in Hungarian). CDC 3300 Felhasználói Ismertetők, No. 6., MTA SzTAKI, Budapest, 1974.
7. ШЕБШАЕВИЧ, В. С.: Введение в теорию космической навигации. Издательство «Совеское радио», Москва, 1971.
8. ЧУРОВ, Е. П.: Спутниковые системы радионавигации. Издательство «Советские радио», Москва, 1977.
9. GREEN. T.: Satellite Doppler data processing for platform navigation. *IEEE Trans. on Geoscience Electronics*, GE-13 (1975), 28—38.

ДОППЛЕРОВСКИЕ ЛОКАЦИОННЫЕ УРАВНЕНИЯ ДЛЯ ОПРЕДЕЛЕНИЯ МЕСТОНАХОЖДЕНИЯ ПЛАТФОРМ ПРИ ПОМОЩИ ИСКУССТВЕННЫХ ЗЕМЛИ

Й. АДАМ—ДЬ. ТАРЧАИ

СПУТНИКОВРЕЗЮМЕ

Данная статья представляет собой продолжение исследований, приведенных в работе [I]. Задается полный вывод допплеровских локационных уравнений платформы, использованных в нашей предыдущей статье. Дается также краткое сравнение с двумя другими решениями, чтобы показывать эквивалентность разных решений.

Acta Geodaet., Geophys. et Montanist. Acad. Sci. Hung, Volume 17 (2), pp. 181—204 (1982)

AMPLIFYING RESIDUAL FILTERS

L. CSERNYÁK
COLLEGE OF FINANCE AND ACCOUNTANCY, BUDAPEST

F. STEINER
TECHNICAL UNIVERSITY OF HEAVY INDUSTRY, MISKOLC

[Manuscript received March 3, 1980]

The paper describes some residual map transformations which realize an amplification of the gravimetric indications of geological structures.

Gravimetric filters are called residual ones $t_{res}(x, y)$ if they eliminate the Bouguer-effect of deep anomalous bodies. This property means in the frequency domain that the value of the transfer of the residual filter $T_{res}(p, q)$ in the point $p = q = 0$ of the frequency plane is zero ($T_{res}(0, 0) = 0$), i.e. the sum of the matrix elements of the filter is zero.

The expression "residual" suggests that although many useful informations become visually appreciable on the residual map, the signal amplitudes can only decrease. This statement seems to be confirmed by the experience that while isolines are drawn on Bouguer-maps mostly in intervals of 1 mGal, the most common isoline-difference of residual maps is 0.1 mGal. — Clearly, if the residual value "res" is determined in a point P by subtracting from the Bouguer-anomaly value g_P of the point P a regional value "reg" computed by $t_{reg}(x, y)$ deduced on the basis of any theorem, then the residual transformation

$$t_{res}(x, y) = \delta(x, y) - t_{reg}(x, y) \tag{1}$$

has the effect of splitting the Bouguer-anomaly into two parts

$$g_P = \text{reg} + \text{res} \tag{2}$$

and this operation can hardly result in an amplification.

1. The error of the filtered values and the transformations of the type $\delta(x, y) - t_{reg}(x, y)$

For the sake of explanations following below it is worth summarizing the causes why the transformations of the type (1) cannot result practically in amplification of the signals.

Be the circularly symmetric function $t_{\mathrm{reg}}(x, y)$ used for the deduction of the regional values from the Bouguer map as

$$\mathrm{reg}\,(x, y) = g(x, y) * t_{\mathrm{reg}}(x, y) \tag{3}$$

the result of any kind of considerations, it is generally a Riemann-integrable function in its original (undigitized) form and it has very often nothing but non-negative values. As for regional filters it must be prescribed that

$$\int_{-\infty}^{\infty}\int_{-\infty}^{\infty} t_{\mathrm{reg}}(x, y)\mathrm{d}x\,\mathrm{d}y = 1 \tag{4}$$

in order to ensure that the filter of the type (1) should be really a residual one, further as it is desirable that the filter should have non-zero values in a rather big area around the reference point in order to get really regional effect from Eq. 3, — therefore it is clear that $t_{\mathrm{reg}}(x, y)$ can have only small absolute values.

In practical computations Eq. 3 is substituted by convolutional product sums. If the gravimetric measurements have been carried out in the intersection points of a quadratic grid with a side length of s, then it is advisable to compute the digital values of $t_{\mathrm{reg}}(x, y)$ also in the points of the same grid, and in that case the regional value can be computed referring to the symmetry point of $t_{\mathrm{reg}}(x, y)$, as to origin according to formula:

$$\mathrm{reg} = \sum_{i,k=-n}^{n} t_{\mathrm{reg}}(is, ks) \cdot g(is, ks)\,. \tag{5}$$

The values $t_{\mathrm{reg}}(is, ks)$ constitute the regional filter matrix whose elements are of small absolute value as explained earlier, in distances greater than $n \times s$ from the origin the values t_{reg} can already be neglected in their summation, too. — The fact that Eq. 5 is used referring to the origin means no restriction, as any grid point of the g-values can be chosen as origin, and later (after a suitable translation) the same point can be the symmetry point of the filter matrices $t_{\mathrm{reg}}(x, y)$ and $t_{\mathrm{reg}}(is, ks)$, respectively.

The "reg" regional value obtained from Eq. 5 yields already according to Eq. 2 the residual value "res". If the "res" value is to be obtained from a single filtering operation, the computations can be carried out without any problem as

$$\mathrm{res} = \sum_{i,k=-n}^{n} t_{\mathrm{res}}(is, ks) \cdot g(is, ks) \tag{6}$$

where the elements of the residual filter matrix $t_{\mathrm{res}}(is,ks)$ outside of the origin are (—1) times the elements of the regional filter matrix $t_{\mathrm{reg}}(is, ks)$, while in the symmetry point one has

$$t_{\text{res}}(0, 0) = 1 - t_{\text{reg}}(0, 0) . \tag{7}$$

The value of $t_{\text{res}}(0, 0)$ differs only slightly from the unit as the absolute values of t_{reg} are small. — As most simple example let us consider the map transformation denoted in [8] by t_0: here the average of the g-values inside of a circle with a radius of ϱ can be accepted as regional value; i.e.:

$$t_{0,\text{reg}}(x, y) = \begin{cases} \dfrac{1}{\varrho^2\pi} & \text{if } \sqrt{x^2 + y^2} < \varrho \\ 0 & \text{if } \sqrt{x^2 + y^2} \geq \varrho . \end{cases} \tag{8}$$

If e.g. $\varrho = 10/\sqrt{\pi}$, which is (according to the examples in [8]) a very small filter dimension, $t_{0,\text{reg}}(0, 0) = 0.01$, therefore from Eq. 7 one gets $t_{0,\text{reg}}(0, 0) = 0.99$; in case of greater filter sizes $t_{0,\text{res}}(0, 0)$ is even nearer to the unit.

Let us now consider the problem of the scatter of the residual value $\bar{D}$ computed from Eq. 6, if the errors of the g-values due to inaccuracies in the measurements and in the corrections can be characterized by a scatter of $\bar{D}_g$. This problem can be easily solved even for general residual filterings (that means not only for those having the form of Eq. 1), as the variance of any linear combination $\Sigma c_i \cdot \xi_i$ of the independent random variables ξ_i can be computed as $\Sigma c_i^2 \bar{D}_{\xi i}^2$ (see e.g. in [3]). Thus the variance of the residual value is

$$\bar{D}^2 = \bar{D}_g^2 \cdot \sum_{i,k=-n}^{n} t_{\text{res}}^2(i, k) \tag{9}$$

where according to the general use the length unit is the sampling distance s. — The sum of the element squares of the residual filter matrix appearing in Eq. (9) is simply equal to the value of the integral

$$\int_{-\infty}^{\infty}\int_{-\infty}^{\infty} t_{\text{res}}^2(x, y)\, \mathrm{d}x\mathrm{d}y \tag{10}$$

if $t_{\text{res}}(x, y)$ is Riemann-integrable. This again is, interpreted as a more general integral concept, equal without any restriction for any residual filter with its norm square $||t_{\text{res}}||^2$.

Let us compute the norm square of the transformation $t_{0,\text{res}}$ for $\varrho = 10/\sqrt{\pi}$, in this case as the square sum of the elements of the filter matrix. The element in the origin, as it has been shown, is equal to 0.99, its square is 0.98. The matrix contains further $\varrho^2\pi - 1 = 99$ elements of the value —0.01, their square sum is roughly equal to 0.01, therefore $||t_{0,\text{res}}||^2 = 0.99$ for the given size ϱ, i.e. $||t_{0,\text{res}}|| = 0.995$. — Equation 9 shows clearly that the scatter of the residual values is in a very good approximation equal with the scatter of

the g-values, and the same conclusion can be drawn for any residual transformation of the type (1).

Now it is clear that the scatter of the residual values is equal to the scatter of the g-values as the matrix element in the symmetry point is very great with respect to the other matrix elements. — The fact itself that the error of the residual value should be equal with the error of the Bouguer-anomalies g can be approved, moreover this can be taken as a basic requirement in order to enable an easier review of the results. This means according to Eq. 9 and to the following rows that the requirement

$$||t_{\text{res}}|| = 1 \tag{11}$$

must be fulfilled; if any transformation $\bar{t}_{\text{res}}$ does not fulfil Eq. 11, it must be normed to unit, i.e. the transformation

$$t_{\text{res}}(x, y) = \frac{\bar{t}_{\text{res}}(x, y)}{||\bar{t}_{\text{res}}||} \tag{12}$$

must be carried out in order to reach $\bar{D} = \bar{D}_g$.

If instead of the Dirac-δ appearing in the transformations of the type (1), weighted averages from several points are used in the transformation, the so constructed $\bar{t}_{\text{res}}(x, y)$ must be multiplied by a factor $1/||\bar{t}_{\text{res}}||$ being possibly much greater than 1 to get the $t_{\text{res}}(x, y)$ to be used which results in this way in an amplification of the signal with an error having the same value. — If e.g. the $t_{0,\text{res}}$ of the earlier example is modified so that the unit weight of the Dirac-δ concentrated in the symmetry point is distributed equally to the 9 central points, then one has in a good approximation $||\bar{t}_{\text{res}}||^2 \approx 9 \cdot \frac{1}{9^2} = \frac{1}{9}$, and therefore the multiplier is here $1/||\bar{t}_{\text{res}}|| \approx 3$.

It should be mentioned that such a "smearing" of the central Dirac-δ has not only the mathematical advantages described in the previous paragraphs, but it is also plausible from a physical point of view: it is quitely unjustified to consider the g-value of the reference point as the only carrier of information concerning the local structure, as it is done in the residual map transformations of the type (1).

2. The map transformation $t_{0,0}$ and the concept of the maximum amplification

Starting from the transformation $t_{0,\text{res}}(x, y)$, — which should be taken as realized in a size of ϱ — a next residual transformation can be obtained by the method described above: the unit weight of the Dirac-δ of $t_{0,\text{res}}$ should be

distributed uniformly on the surface of a circle with the radius $\bar{\varrho}(<\varrho)$. The first question is how to choose $\bar{\varrho}$ for a given ϱ?

When computing the square sum one or several too big matrix elements can srtongly increase the value of the norm by decreasing the factor $1/||\bar{t}_{\text{res}}||$. Therefore it should be demanded that the absolute value of all elements of the filter matrix inside of the circle with the radius ϱ should be equal. It follows now that the value of $\frac{1}{\bar{\varrho}^2\pi}$ (which is the part of the Dirac-δ remaining in the origin, and also the value of the weights in the other grid-points inside of the circle with the radius $\bar{\varrho}$) must be twice of $\frac{1}{\varrho^2\pi}$, thus the value of the $\bar{t}$-matrix elements is $+\frac{1}{\varrho^2\pi}$ inside of the circle with the radius $\bar{\varrho}$, and on the circular ring between the radii $\bar{\varrho}$ and ϱ it is $-\frac{1}{\varrho^2\pi}$. It is evident that in this case $\bar{\varrho}$ can only be $\varrho/\sqrt{2}$. After norming let us denote the residual transformation obtained by $t_{0,0}(x, y)$, which can be characterized with a one-variable function of $\hat{x} \equiv \sqrt{x^2 + y^2}$ due to its circular symmetry:

$$t_{0,0}(\hat{x}) = \begin{cases} +\frac{1}{\varrho\sqrt{\pi}}, & \text{if} \quad \hat{x} < \varrho/\sqrt{2} \\ -\frac{1}{\varrho\sqrt{\pi}}, & \text{if} \quad \varrho/\sqrt{2} \leq \hat{x} < \varrho \\ 0 \quad , & \text{if} \quad \hat{x} \geq \varrho\,. \end{cases} \tag{13}$$

The transformation $t_{0,0}(x, y)$ obtained its final form by multiplying with the norming factor $\varrho\sqrt{\pi}$. This value, however, cannot be considered as an amplification factor, since the signals are amplified to their $\varrho\sqrt{\pi}$-fold value only with respect to an earlier phase of the deduction (earlier denoted by $\bar{t}$), and when a filter $t_{0,0}$ with the size ϱ are used e.g. for the solution in a structural exploration problem, it is absolutely unimportant which value had this factor.

Much more important is the ratio which shows the amplitude increase in the effect of a point-like anomalous body m in a depth z (any geological structure can be substituted by the summarized effect of such bodies) in case of a residual map computed by using $t_{0,0}$ with respect to the unfiltered Bouguer-map. In the following, this ratio is called amplification a, and this means that the effect is as if the mass would be $a \cdot m$ instead of m. — It is evident that in case of $a > 1$ (and even more in case if $a \gg 1$) such gravimetrically "silent" zones may appear on the map whose gravimetric exploration would be hopeless without using amplifying filter (e.g. due to a very small $\Delta\sigma$ density contrast at the boundary surface).

The value of a depends naturally on the depth z; the next problem is therefore to determine the amplification factor for anomalous bodies in different depths z below the reference point.

It can be easily found by integration that the average of the g-values of a mass-point m in a depth z taken on the surface of a circle of radius ϱ' in epicentral position is:

$$\frac{2fm}{\varrho'^2}\left(1-\frac{1}{1+\varrho'^2/z^2}\right). \tag{14}$$

From this expression and from the definition of $t_{0,0}$ by Eq. 13 follows the effect of the mass-point m on the map filtered with $t_{0,0}$ in a point above it, which divided by the effect on a Bouguer map, i.e. by fm/z^2 yields the amplification function:

$$a_{0,0}(z)=\frac{2z^2\sqrt{\pi}}{\varrho}\left[1+\frac{1}{\sqrt{1+\varrho^2/z^2}}-\frac{2}{\sqrt{1+0.5(\varrho^2/z^2)}}\right]. \tag{15}$$

The function $a_{0,0}(z)$ is shown for some values of the parameter ϱ in Fig. 1.

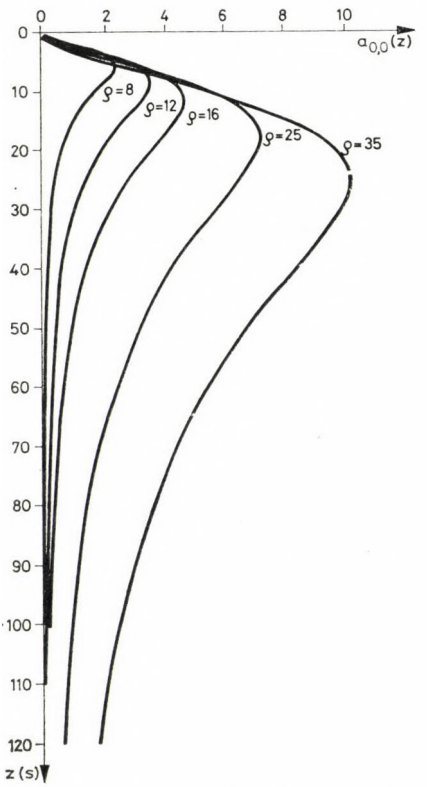

Fig. 1. The depth dependence of the amplification along the vertical line $x=y=0$ for the filters of the map transformation $t_{0,0}(x, y)$ with different sizes ϱ

— By derivation it can be easily proved that the maximum value is reached at $0.71733 \cdot \varrho$, and this value is $a_{max} = 0.289\varrho$. It is practically superfluous to give these figures with great number of digits; if the place of the maximum of Eq. 15 is denoted by z_{max}, one has:

$$a_{max} = 0.29 \cdot \varrho \tag{16}$$

and

$$z_{max} = 0.72 \cdot \varrho \,. \tag{17}$$

In Eq. 16 ϱ is expressed in units of s; it is dimensionless, as it is the ratio of $\varrho_{(km)}$ and $s_{(km)}$, both expressed in units of km-s. This can be taken similarly in Eq. 17 and now z_{max} is again dimensionless, expressed in units of s. — Here, however, z_{max} can be considered as expressed in km, too, and if ϱ is expressed in the following also dimensionless, instead of Eq. 17 the following can be written:

$$z_{max\,(km)} = 0.72 \cdot \varrho \cdot s_{(km)} \,. \tag{17a}$$

This form of z_{max} is important, because in the practice the exploration depths are the primary data, and because it is desirable to realize here the maximum amplification, i.e. this will be the value of $z_{max\,(km)}$. As next step it must be decided (in knowledge of previously known and/or supposed values) which amplification a_{max} is to be reached in that particular depth. This value yields from Eq. 16 the value of the dimensionless ϱ, and by substituting this value of $a_{max}/0.29$ into Eq. 17a one gets the sampling interval for $t_{0,0}$:

$$s_{(km)} = 0.40 \frac{z_{max(km)}}{a_{max}} \,. \tag{18}$$

If a high amplification is to be reached, the values of s to be used are considerably smaller than the values computed without taking into account the error caused by scatter only on the basis of interpolation problems (see [7]); the latter result in side lengths s of the measurement grid equal to the sixth or fourth of the exploration depth.

3. The transformation $t_{up,\,up}$ and its amplification function $a_{up,\,up}(x, y, z)$

The simplicity of the transformation $t_{0,0}$ ensures an easy manipulation. — In the following we shall use notions defined in [4]; for them and for their connection with the amplification the transformation $t_{up,\,up}$ will be a very simple example.

Let us denote by $w(x, y, z)$ the function by which the mass of the mass point m in the point (x, y, z) must be multiplied in case of a given filter matrix to get the filtered effect of the mass point in the reference point (in the point (0, 0, 0)). If the filtered map is denoted by $r(x, y)$ and the three-dimensional density distribution by σ, it is evident that

$$r(x,y) = \int_{-\infty}^{\infty}\int_{-\infty}^{\infty}\int_{0}^{\infty} \sigma(\bar{x}, \bar{y}, \bar{z}) \cdot w((x-\bar{x}), (y-\bar{y}), \bar{z}) \mathrm{d}\bar{x}\mathrm{d}\bar{y}\mathrm{d}\bar{z} \tag{19}$$

thus, the function $w(x, y, z)$ is the most important characterizing value of the connection between gravimetric anomalous bodies and filtered maps. — Its determination can be carried out mostly by numerical methods (see [9]).

It can be seen from Eq. 19 that if the $w(x, y, z_0)$ values of a certain depth level are denoted by $w(x, y)$, the filtered effect of the surface density distribution $\sigma'(x, y)$ of this level can be computed as

$$r(x, y) = \sigma'(x, y) * w(x, y) \tag{20}$$

which corresponds to the connection between the Fourier-transforms denoted by capitals:

$$R(p, q) = \Sigma'(p, q) \cdot W(p, q) \tag{21}$$

in the sense of the convolution theorem $\left(\text{here } p = \frac{2\pi}{\lambda_x/s},\ q = \frac{2\pi}{\lambda_y/s}\right)$.

The effect of the same surface density distribution $\sigma'(x, y)$ in a depth z_0 on the Bouguer-map is:

$$g(x, y) = \sigma'(x, y) * e(x, y) \tag{22}$$

where

$$e(x, y) = \frac{fz_0}{(x^2 + y^2 + z_0^2)^{3/2}}. \tag{23}$$

It is evident that

$$G(p, q) = \Sigma'(p, q) \cdot E(p, q) \tag{24}$$

and on the basis of Eq. 23 it can be seen (e.g. from [2]) that

$$E(p, q) = 2\pi f e^{-z_0\sqrt{p^2+q^2}} \tag{25a}$$

which can be written more simply when taking advantage of the circular symmetry in the frequency domain and introducing the variable $\hat{p} \equiv \sqrt{p^2 + q^2}$ with the one-variable function

$$E(\hat{p}) = 2\pi f e^{-z_0\hat{p}}. \tag{25}$$

If the unfiltered case is considered as a filtering with a unit Dirac-δ, then by comparing Eqs. 20 and 22 one gets that for that case (i.e. for the Bouguer-effect) the function $w_g(x, y)$ is identical with $e(x, y)$, therefore (see Eq. 23)

$$w_g(x, y, z) = \frac{fz}{(x^2 + y^2 + z^2)^{3/2}}. \tag{26}$$

This could have also been written directly from the definition of the w-function for the g-values. Our present aim, however, is to explain these notions in order to promote their present and future use, for which purpose it is necessary to know the connection between the w-function and the filter function $t(x, y)$. If the Bouguer-map is denoted by $g(x, y)$ and the filtered map by $r(x, y)$, then according to the basic equation of the filtering one gets

$$r(x, y) = g(x, y) * t(x, y) \tag{27}$$

and this means a connection in the form of

$$R(p, q) = G(p, q) \cdot T(p, q) \tag{28}$$

between the Fourier-transforms. By substituting in place of $G(p, q)$ the product from Eq. 24, and comparing the result with Eq. 21, one gets the important formula

$$W(p, q) = T(p, q) \cdot E(p, q). \tag{29}$$

After this introduction (which will be used in this chapter only partially) the next step will be the introduction of the transformation $t_{\mathrm{up,up}}$.

Let us consider as regional value the upward continuation to a level h. If this would be subtracted from g_P, i.e. from the Bouguer-anomaly of the reference point, one would get a known method for the determination of residual anomalies. Anyway since this filtering belongs to type (1) amplification cannot be awaited from it. Therefore let us use instead of g_P an upward continuation to a level lower than h, this is namely mathematically a weighted average which takes into account not only the value of g_P, but also the g-values in its vicinity with not negligible weights, and so it can be regarded as an effective spread of the unit Dirac-δ.

If similarly to $t_{0,0}$ the matrix element of the filter matrix referring to the reference point is expected to be twice greater for the lower level than the matrix element of the filter, referring to the same point for the upward continuation to the level h, then the lower level must lie in a height of $h/\sqrt{2}$. — The form of the transformation is before norming:

$$\bar{t}_{\mathrm{up,up}}(\hat{x}) = \frac{1}{2\pi}\left[\frac{h/\sqrt{2}}{(\hat{x}^2 + h^2/2)^{3/2}} - \frac{h}{(\hat{x}^2 + h^2)^{3/2}}\right]. \tag{30a}$$

According to Eq. 12 one gets the following normed form:

$$t_{\mathrm{up,up}}(\hat{x}) = \frac{h\sqrt{2}}{\sqrt{\pi(32\cdot\sqrt{2} - 45)}}\left[\frac{h/\sqrt{2}}{(\hat{x}^2 + h^2/2)^{3/2}} - \frac{h}{(\hat{x}^2 + h^2)^{3/2}}\right]. \tag{30}$$

One has here the advantageous situation that the function $w_{\mathrm{up,up}}$ of the map transformation $t_{\mathrm{up,up}}$ can be given in an analytical form, as only the difference of the vertically shifted (by $h/\sqrt{2}$ and by h, respectively) functions $w_g(x, y, z)$ of a known analytical form (see Eq. 26) must be multiplied with the already known norming factor:

$$w_{\mathrm{up,up}}(x, y, z) = \frac{fh\sqrt{8\pi}}{\sqrt{32\cdot\sqrt{2} - 45}}\left[\frac{h/\sqrt{2} + z}{(x^2 + y^2 + (h/\sqrt{2} + z)^2)^{3/2}} - \right.$$
$$\left. - \frac{h + z}{(x^2 + y^2 + (h + z)^2)^{3/2}}\right]. \tag{31}$$

The amplification can also be written analytically for the semi-space, as it is nothing else than the value of the actual w divided by w_g:

$$a_{\mathrm{up,up}}(x, y, z) = \frac{h\sqrt{8\pi}\,(x^2 + y^2 + z^2)^{3/2}}{z\cdot\sqrt{32\cdot\sqrt{2} - 45}}\left[\frac{h/\sqrt{2} + z}{(x^2 + y^2 + (h/\sqrt{2} + z)^2)^{3/2}} - \right.$$
$$\left. - \frac{h + z}{(x^2 + y^2 + (h + z)^2)^{3/2}}\right] \tag{32}$$

but practically this function must be known only along the vertical line $x = y = 0$ showing the greatest w-values (where the most simple notation $a(z)$ will be used instead of the exact notation $a(0, 0, z)$). — It should be mentioned that by using an amplifying transformation the filtered values in the origin can be calculated theoretically for a given density distribution $\sigma(x, y, z)$ so that the Bouguer-effect of the density distribution $a(x, y, z)\cdot\sigma(x, y, z)$ is determined.

The function $a_{\mathrm{up,up}}(z)$ has its maximum at

$$z_{\max} = \frac{\sqrt[6]{2} + 1}{\sqrt[3]{2}}\cdot h = 1.6846\cdot h. \tag{33}$$

This maximum here has the value

$$a_{\max} = 1.0164\cdot h. \tag{34}$$

Using the same sequence of ideas as at the end of Chapter 2, one gets that for a given depth level and for a prescribed amplification value one has to use a square grid with

$$s_{(\mathrm{km})} = 0.603 \frac{z_{\max(\mathrm{km})}}{a_{\max}} \tag{35}$$

for the gravimetric measurements.

4. General relations with respect to the amplification

Starting from the spatial form of Eq. 29:

$$w(x, y) = e(x, y) * t(x, y) \tag{36}$$

we shall consider at first the question, how the function w is modified if instead of the normed-to-unit $t(x, y)$ the filtering is carried out by a k-times stretched form $t^{(k)}(x, y)$ after a norming again to unit, $t^{(k;n)}(x, y)$. As the k-times stretched filter has the form:

$$t^{(k)}(x, y) = t\left(\frac{x}{k}, \frac{y}{k}\right), \tag{37}$$

it follows from the definition of the norm square and from the fact that the original t had been normed to unit that

$$\| t^{(k)} \|^2 = k^2 \cdot \| t \|^2 = k^2 \tag{38}$$

and therefore the form of the k-times stretched filter normed to unit is according to Eq. 12:

$$t^{(k;n)}(x, y) = \frac{1}{k} t\left(\frac{x}{k}, \frac{y}{k}\right). \tag{39}$$

Starting from Eq. 36 let us consider the function $w^{(k;n)}(x,y)$ of this filter referring to level z_0, i.e. the function $w^{(k;n)}(x, y, z_0)$:

$$\begin{aligned} w^{(k;n)}(x, y, z_0) &= e(x, y) * \frac{1}{k} t\left(\frac{x}{k}, \frac{y}{k}\right) = \frac{1}{k} \int_{-\infty}^{\infty} \int_{-\infty}^{\infty} e(x-u, y-v) \cdot \\ &\cdot t\left(\frac{u}{k}, \frac{v}{k}\right) \mathrm{d}u\mathrm{d}v = \frac{1}{k} \int_{-\infty}^{\infty} \int_{-\infty}^{\infty} \frac{f z_0}{((x-u)^2 + (y-v)^2 + z_0^2)^{3/2}} \cdot t\left(\frac{u}{k}, \frac{v}{k}\right) \mathrm{d}u\mathrm{d}v = \\ &= \begin{bmatrix} u/k = \bar{r} \\ v/k = \bar{s} \end{bmatrix} = \frac{1}{k} \int_{-\infty}^{\infty} \int_{-\infty}^{\infty} \frac{f z_0/k}{\left[\left(\frac{x}{k} - \bar{r}\right)^2 + \left(\frac{y}{k} - \bar{s}\right)^2 + \frac{z_0}{k}\right)^2\Bigg]^{3/2}} \cdot t(\bar{r}, \bar{s}) \mathrm{d}\bar{r}\mathrm{d}\bar{s} = \\ &= \frac{1}{k} w\left(\frac{x}{k}, \frac{y}{k}, \frac{z_0}{k}\right). \end{aligned} \tag{40}$$

This result can be described as follows: after a k-times stretching and a norming to unit of t, the isoline-system $w^{(k;n)}$ of the new filter $t^{(k;n)}$ is also stretched out in all direction k-times, only the values of the isolines decrease k-times.

Having this result, the connection between the amplification $a^{(k;n)}$ corresponding to $t^{(k;n)}$ and the amplification a corresponding to t can be easily obtained:

$$a^{(k;n)}(x,y,z) = \frac{w^{(k;n)}(x,y,z)}{w_g(x,y,z)} = \frac{\frac{1}{k} w\left(\frac{x}{k}, \frac{y}{k}, \frac{z}{k}\right)}{w_g(x,y,z)} = \\ = \frac{\frac{1}{k} w\left(\frac{x}{k}, \frac{y}{k}, \frac{z}{k}\right)}{\frac{1}{k^2} w_g\left(\frac{x}{k}, \frac{y}{k}, \frac{z}{k}\right)} = k \cdot a\left(\frac{x}{k}, \frac{y}{k}, \frac{z}{k}\right). \tag{41}$$

This result means that if one uses $t^{(k;n)}$ instead of t, the original isoline-system of amplifications is stretched out k-times, and the amplifications increase k-times. E.g. at $k = 2$, the maximum amplification along the vertical line $x = y = 0$ also increases by a factor of two, but this double maximum amplification is reached in a double depth. Therefore if one intends to remain in a given depth level, the most important content of Eq. 41 is, that the amplifications at the same point increase k-times if the sampling interval s is decreased k-times. The upper limit of the realizable amplification is set by the ratio between the value of the information surplus due to the decrease of s and the surplus expense of the densification of the measurements.

In the following the general method for the computation of the amplification $a(z)$ along the most important vertical $x = y = 0$ will be given. Here we make use of the fact that the inverse Fourier-transformation along $x = y = 0$ is nothing else as the value of the integral for the whole frequency plane multiplied by a constant, and the latter double integral is on its turn the constant-times multiplied integral after $\hat{p}$ between 0 and ∞ of the integrand multiplied by p. By taking into account Eqs 29 as well as 23, 26 and 25 one gets:

$$a(z) = \frac{w(0,0,z)}{w_g(0,0,z)} = \frac{\int_0^\infty \hat{p} \cdot W(\hat{p}) \mathrm{d}\hat{p}}{\int_0^\infty \hat{p} \cdot W_g(\hat{p}) \mathrm{d}\hat{p}} = \frac{\int_0^\infty \hat{p} \cdot T(\hat{p}) \cdot E(\hat{p}) \mathrm{d}\hat{p}}{\int_0^\infty \hat{p} \cdot E(\hat{p}) \mathrm{d}\hat{p}} = \\ = \frac{\int_0^\infty \hat{p} \cdot T(\hat{p}) \cdot e^{-z\hat{p}} \mathrm{d}\hat{p}}{\int_0^\infty \hat{p} \cdot e^{-z\hat{p}} \mathrm{d}\hat{p}} = z^2 \int_0^\infty \hat{p} \cdot T(\hat{p}) \cdot e^{-z\hat{p}} \mathrm{d}\hat{p} \tag{42}$$

which enables the computation of all important data (first of all the place of the maximum $z_{\max}$ and the maximum amplification $a_{\max}$) in dependence

of T either analytically or numerically. It is in certain cases advantageous if $z_{\max}$ is determined as the root of the equation

$$2\mathfrak{L}_z\{\hat{p} \cdot T(\hat{p})\} - z \cdot \mathfrak{L}_z\{\hat{p}^2 \cdot T(\hat{p})\} = 0 \tag{43}$$

which is deduced from Eq. 42 by derivation. ($\mathfrak{L}_z$ means the Laplace-transform containing z as variable).

5. The map transformation $t_6(x,y)$

The map transformation $t_{\mathrm{up,\,up}}(x, y)$ (as its values converge towards zero very slowly if $\hat{x} \to \infty$) results in filter matrices of great sizes. The $t_{0,0}(x, y)$ yields very practical filter matrix sizes, but its Fourier-transform:

$$T_{0,0} = \frac{2\sqrt{\pi}}{\hat{p}}\left[\sqrt{2} \cdot J_1\left(\frac{\varrho\hat{p}}{\sqrt{2}}\right) - J_1(\varrho \cdot \hat{p})\right] \tag{44}$$

has some negative values (see also Fig. 2) and this could result in reluctance for certain users. We do not want to discuss the unfoundedness of these

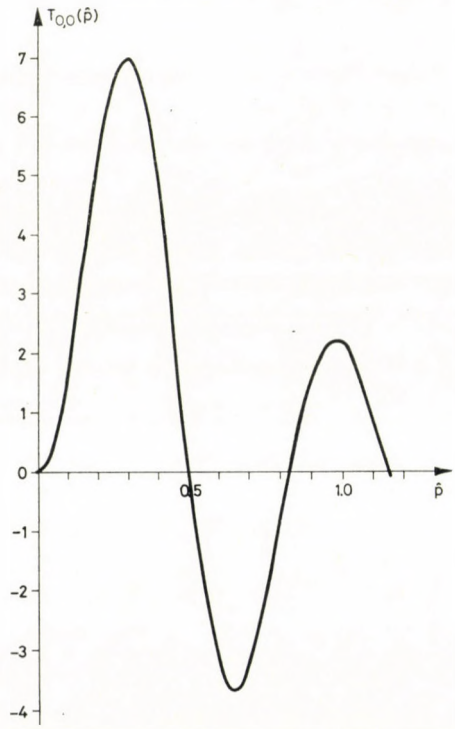

Fig. 2. The function $T_{0,0}(\hat{p})$, characterizing the transfer $T_{0,0}(p, q)$ of the map transformation $t_{0,0}(x, y)$ in case of $\varrho = 12$s

problems (or even they cannot be considered in the framework of a quantitative interpretation), — instead we should like to define an amplifying map transformation which necessitates without having negative transfers only small matrix sizes. Since already a number of numerical indices are occupied for the notation of different kinds of map transformations (see e.g. [8]), let us denote this map transformation by $t_6(x, y)$ and define it as follows:

$$t_6(\hat{x}) = \frac{1}{\sqrt{\pi\bar{\gamma}}}\left(1 - \frac{\hat{x}^2}{4\bar{\gamma}}\right) \cdot e^{-\frac{\hat{x}^2}{4\bar{\gamma}}}. \tag{45}$$

The transfer of this transformation shows that it is a residual one:

$$T_6(\hat{p}) = 4\bar{\gamma}\sqrt{\pi\bar{\gamma}} \cdot \hat{p}^2 \cdot e^{-\bar{\gamma}\hat{p}^2}. \tag{46}$$

At $p = q = 0$, T_6 is really equal to zero. (It can be shown from Eqs of [1] that the two-variable Fourier-transforms with circular symmetry can be obtained for circularly symmetric functions as Hankel-transforms (e.g. from [2])). If the integral of $t_6^2(x, y)$ is computed for the whole plane (x, y), this will be equal to unit, therefore Eq. 45 yields this map transformation already in a normed form.

On the basis of Eqs 42 and 46, the determination of $a_6(z)$ is not more than a simple integration problem:

$$a_6(z) = 2z^2\sqrt{\frac{\pi}{\bar{\gamma}}}\left[1 + \eta^2 - \sqrt{\pi} \cdot e^{\eta^2}(1 - \Phi(\eta))(\eta^3 + 1.5 \cdot \eta)\right], \tag{47}$$

where

$$\eta = \frac{z}{2\sqrt{\bar{\gamma}}} \quad \text{and} \quad \Phi(\eta) = \frac{2}{\sqrt{\pi}}\int_0^{\eta} e^{-u^2}\mathrm{d}u$$

is the Gaussian error-function.

The value of η means a depth measured in units proportional with the size of the matrix. Thus, it is advisable to choose the value $2 \cdot \sqrt{\bar{\gamma}}$ as the filter parameter P which is proportional with the matrix size (it can be directly seen from Eq. 45 that the zero place of t_6 occurs exactly at the same place $\hat{x} = 2\sqrt{\bar{\gamma}}$). Expressing by this value $a_6(z)$, its maximum will be at:

$$z_{\max} = 1.08 \cdot P \tag{48}$$

with the value:

$$a_{\max} = 0.75 \cdot P. \tag{49}$$

Consequently, if one demands in a depth of $z_{\max\,(\mathrm{km})}$ a maximum amplification $a_{\max}$, the constant s of the necessary measuring grid for the map transforma-

tion t_6 will be:

$$s_{(\mathrm{km})} = 0.69 \frac{z_{\max(\mathrm{km})}}{a_{\max}} . \tag{50}$$

6. The map transformation $t_{\bar{\gamma}, z_0}(x, y)$

The definition of the map transformation $t_{\bar{\gamma}, z_0}(x, y)$ is that it is a normed-to-unit map transformation which produces a w-function proportional to $\left(1 - \frac{\hat{x}^2}{4\bar{\gamma}}\right) \cdot e^{-\frac{\hat{x}^2}{4\bar{\gamma}}}$ at a level z_0. (In the domain of great w-values this is very

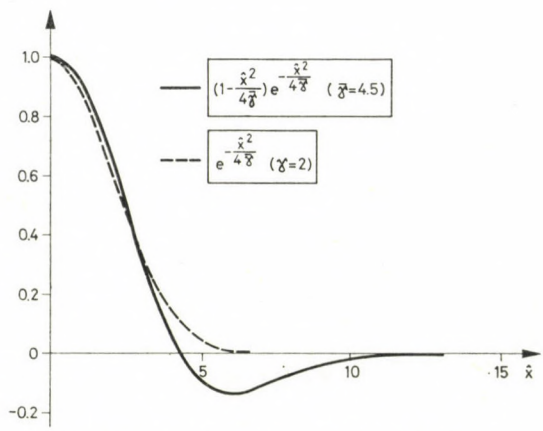

Fig. 3. A comparison of the $w(\hat{x})$ functions demanded for the transformations $t_{\bar{\gamma}, z_0}$ and t_{γ, z_0}

similar to the surface $e^{-\frac{\hat{x}^2}{4\gamma}}$ taken with $\gamma = 0.454 \cdot \bar{\gamma}$, which is realized by the transformation t_{γ, z_0} according to [5]; the value of w decreases by a factor of 2 at the same distance $\hat{x}_{1/2}$ in both cases, as seen in Fig. 3). If the norming factor referring to $t_{\bar{\gamma}, z_0}$ is denoted by c, the transfer on the basis of Eqs 29 and 46 is:

$$T_{\bar{\gamma}, z_0}(\hat{p}) = c \cdot \hat{p}^2 \cdot e^{-\bar{\gamma}\hat{p}^2 + z_0\hat{p}} , \tag{51}$$

and by using the inverse Hankel-transformation one gets:

$$t_{\bar{\gamma}, z_0}(\hat{x}) = \frac{c}{2\pi} \int_0^\infty \hat{p}^3 \cdot e^{-\bar{\gamma}\hat{p}^2 + z_0\hat{p}} \cdot J_0(\hat{x} \cdot \hat{p}) \cdot \mathrm{d}\hat{p} . \tag{52}$$

It is advisable to compute the norming factor on the basis of Eq. 51; whereby the Parseval-formula must be taken into account. The value of the norming

factor is:

$$c = 4 \cdot \sqrt{2\pi\bar{\gamma}^3}\left[\alpha^4 + 4.5\alpha^2 + 2 + e^{\alpha^2} \cdot \sqrt{\pi}\left(1 + \Phi(\alpha)\right)(\alpha^5 + 5\alpha^3 + 3.75\alpha)\right]^{-1/2} \quad (53)$$

where

$$\alpha = \frac{z_0}{\sqrt{2\bar{\gamma}}}.$$

The amplification along the z-axis is:

$$a_{\bar{\gamma}, z_0}(z) = \frac{c \cdot z^2}{2\bar{\gamma}^2}\left[1 + \beta^2 - \sqrt{\pi} \cdot e^{\beta^2}\left(1 - \Phi(\beta)\right)(\beta^3 + 1.5\beta)\right], \quad (54)$$

where

$$\beta = \frac{z - z_0}{2\sqrt{\bar{\gamma}}}.$$

If the maximum amplification should occur at the same depth, where the proportionality of w with $\left(1 - \frac{\hat{x}^2}{4\bar{\gamma}}\right) \cdot e^{-\frac{\hat{x}^2}{4\bar{\gamma}}}$ has been demanded (i.e. where maximum lateral unsensitivity has been realized farther than a certain $\hat{x}$), then the transformation has only a single parameter, z_0, as the maximum of $a_{\bar{\gamma}, z_0}(z)$ occurs at $z = z_0$ if

$$\bar{\gamma} = \frac{4}{9} z_0^2. \quad (55)$$

By choosing a $\bar{\gamma}$ according to Eq. 55, the maximum amplification at $z_{\max} = z_0$ can be computed from the value of z_0 regarded as filter parameter P:

$$a_{\max} = \frac{2}{3} z_0. \quad (56)$$

If a maximum amplification of $a_{\max}$ is to be realized in a depth of z_0 km by means of $t_{\bar{\gamma}, z_0}(x, y)$ regarded as one-parameter filter, the side length of the measurement square grid must be chosen as:

$$s_{(\mathrm{km})} = \frac{2}{3} \frac{z_{0(\mathrm{km})}}{a_{\max}}. \quad (57)$$

The $\bar{\gamma}$ can be then computed from the following formula:

$$\bar{\gamma} = \left(\frac{2}{3} \frac{z_{0(\mathrm{km})}}{s_{(\mathrm{km})}}\right)^2. \quad (55a)$$

7. Planning of a mesuring and filtering complex for the realization of a given amplification in a given depth

It follows from the general conclusions of Chapter 4 that by introducing a parameter P proportional with the filter size for the treatment of amplifying filters, the maximum value of the amplification $a(z)$ will be:

$$a_{\max} = A \cdot P \tag{58}$$

and its depth value can be computed as

$$z_{\max} = Z \cdot P \tag{59}$$

while the side length of the measurement grid can be obtained from

$$s_{(\mathrm{km})} = S \cdot \frac{z_{\max(\mathrm{km})}}{a_{\max}} \tag{60}$$

where

$$S = \frac{A}{Z}. \tag{60a}$$

The following Table presents all practically important constants for the map transformations which have been discussed in Chapters 2, 3, 5 and 6. If farther amplifying filters will be introduced, it is advisable to use for their description the same constants.

In case of the use of any one-parameter filter, their selection defines already the value of A, and Eq. 58 yields the filter parameter P in units of s in function of the necessary maximum amplification $a_{\max}$. With S known from Table I and the given depth of the maximum amplification in km, Eq. 60 yields the side length of the measurement grid, $s_{(\mathrm{km})}$.

Table I

Characteristic parameters of amplifying map transformations

Amplifying map transformation	P	A	Z	S
$t_{0,0}(x, y)$	ϱ	0.29	0.72	0.40
$t_{\mathrm{up},\,\mathrm{up}}(x, y)$	h	1.02	1.68	0.60
$t_6(x, y)$	$2\sqrt{\bar{\gamma}}$	0.75	1.08	0.69
$t_{\bar{\gamma}, z_0}(x, y)$ $\left(\bar{\gamma} = \frac{4}{9} z_0^2\right)$	z_0	$\frac{2}{3}$	1	$\frac{2}{3}$

8. Remarks to the simultaneous increase of resolving power and amplification

The authors do not know previous publication dealing with gravimetric signal amplification; the basic idea of their realization that namely the difference of two regional-type map transformations results in a certain enhancement of a depth, can already be found in [6].

Up to now, the present paper dealt with the point of view of the amplification, and from among other important characteristics only the lateral insensitivity has been mentioned in connection with the map transformation $t_{\bar{\gamma}, z_0}(x, y)$.

Residual map transformations may contribute, however, by an increase of the resolving power (or disintegrating power d) to the exploitation of important informations in the gravimetric data system. The resolving power d is defined as the reciprocal of the minimum distance in a depth z which must be surpassed by the distance between two point-like anomalous bodies in order to get two distinct maxima on the filtered map. It can be easily seen that if the maximum value at $x = y = 0$ for the level z decreases by a factor of two on a distance of $\hat{x}_{1/2}$, then

$$d = \frac{1}{2\hat{x}_{1/2}}. \tag{61}$$

Our present problem is, however, how much times greater is the resolving power of a certain filtered map for a certain depth level than the resolving power of the Bouguer-values for the same depth level? — If the latter is denoted by d_g, it can be easily seen that

$$d_g = \frac{0.6524}{z}, \tag{62}$$

since for the d_g values one has

$$\hat{x}_{1/2} = z \cdot \sqrt{\sqrt[3]{4} - 1} = 0.76642 \cdot z. \tag{62a}$$

If a quantity of D is defined as

$$d = D \cdot d_g \tag{63}$$

it is evident that the quantity D is the measure of the increase of the resolving power to be determined.

The one-parameter filter presented in Table II do not influence practically the resolving power in the depth $z_{\max}$ (i.e. for them $D \approx 1$). It would be erroneous, however, to conclude from this fact that emplifying filters cannot increase the resolving power.

Table II

The filter matrix $t_{\bar{\gamma}, z_0}(x, y)$ in case of $\bar{\gamma} = 7.11$ and $z_0 = 4$

0.26466	0.23514	0.15979	0.07020	−0.00206	−0.04051	−0.04686	−0.03450	−0.01768	−0.00498	0.00137	0.00309	0.00275	0.00172
	0.20785	0.13868	0.05664	−0.00875	−0.04239	−0.04634	−0.03347	−0.01682	−0.00446	0.00154	0.00309	0.00257	0.00172
		0.08513	0.02283	−0.02472	−0.04617	−0.04428	−0.02986	−0.01407	−0.00309	0.00206	0.00309	0.00257	0.00154
			−0.01476	−0.04051	−0.04754	−0.03913	−0.02403	−0.01013	−0.00120	0.00257	0.00309	0.00223	0.00138
				−0.04754	−0.04325	−0.03107	−0.01682	−0.00566	0.00086	0.00309	0.00291	0.00206	0.00120
					−0.03347	−0.02077	−0.00944	−0.00154	0.00223	0.00309	0.00257	0.00172	0.00086
						−0.01081	−0.00309	0.00137	0.00309	0.00291	0.00223	0.00138	0.00069
							0.00103	0.00292	0.00309	0.00240	0.00172	0.00103	0.00051
								0.00309	0.00257	0.00188	0.00120	0.00069	0.00034
									0.00188	0.00120	0.00069	0.00051	0.00017
										0.00086	0.00051	0.00034	0.00017
											0.00034	0.00017	0.00017
												0.00017	0.00000
													0.00000

The present paper does not intend the detailed discussion of this problem, but it is appropriate to make an unambiguous hint here. The first point to be mentioned is that Eq. 54 is not only valid for the one-parameter filters, and yields the amplification-values not only for the maximum case. Hence, it is possible to demand a certain increase of the resolving power in the average level of the exploration z_0. This condition can be written as

$$\hat{x}_{1/2} = \frac{1}{D} \cdot 0.76642 \cdot z_0 \tag{64a}$$

and by taking into account that for the function $\left[1 - \frac{\hat{x}^2}{4\bar{\gamma}}\right) \cdot e^{-\frac{\hat{x}^2}{4\bar{\gamma}}}$

$$\hat{x}_{1/2} = 1.122 \cdot \sqrt{\bar{\gamma}} \tag{64b}$$

thus in a depth z_0 one has to realize w with the parameter

$$\bar{\gamma} = \frac{z_0^2}{D^2} \left(\frac{0.76642}{1.122}\right)^2 = 0.4666 \frac{z_0^2}{D^2}. \tag{64}$$

The transformation $t_{\bar{\gamma}, z_0}(x, y)$ got in this way has its maximum amplification in a depth $z < z_0$ with $D > 1$, i.e. in case of a real increase of the resolving power the maximum amplification will be in the depth $z < z_0$; e.g. in case of $z_0 = 4$, $z_{\max}$ can be calculated as $\bar{\gamma}^{0,7}$. (For the shift of the level $z_{\max}$, further for the values $\hat{x}_{1/2}$ characterizing the resolving power see Figs 4 and 5; the corresponding filter matrices are shown in TablesII and III.) — If there are no important anomalous bodies above the depth domain to be explored, this causes no trouble, and the value of s can be decreased as long as the amplification required appears in a depth z_0 according to Eq. 54. Thus, amplification and resolving power can be both increased at the same time. It is, however, clear that if the values of D and $a_{\max}$ are taken irrealistically great, one finds limits set by economical considerations much earlier than if only the value of $a_{\max}$ would be prescribed.

9. A possible direction of further investigations

In the previous Chapter it has been shown that using the map transformation $t_{\bar{\gamma}, z_0}$ it is possible to increase simultaneously both the amplification and the resolving power, to which the very remarkable advantage of the lateral unsensitiveness inherent in the definition of $t_{\bar{\gamma}, z_0}$ can be added. Beside these advantages enabling an easier and more accurate geological interpretation

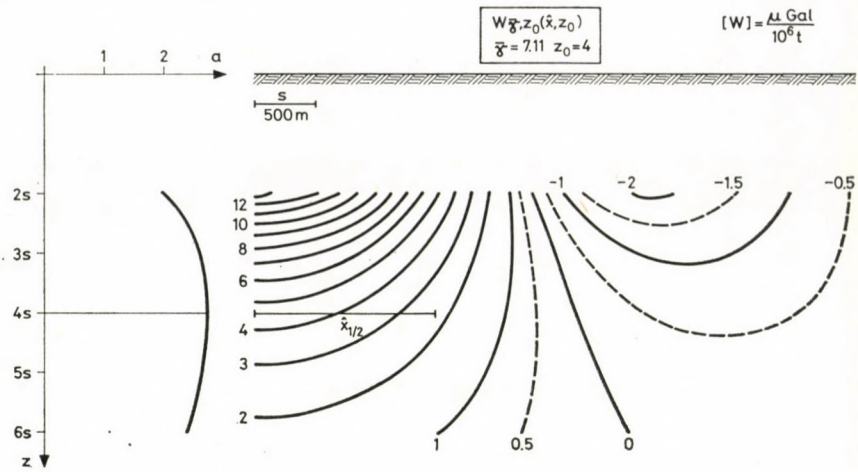

Fig. 4. The system of isolines of $w_{\bar{\gamma},z_0}(\hat{x}, z)$ and the curve $a_{\bar{\gamma},z_0}$ in case of $\bar{\gamma} = 7.11$ and $z_0 = 4$

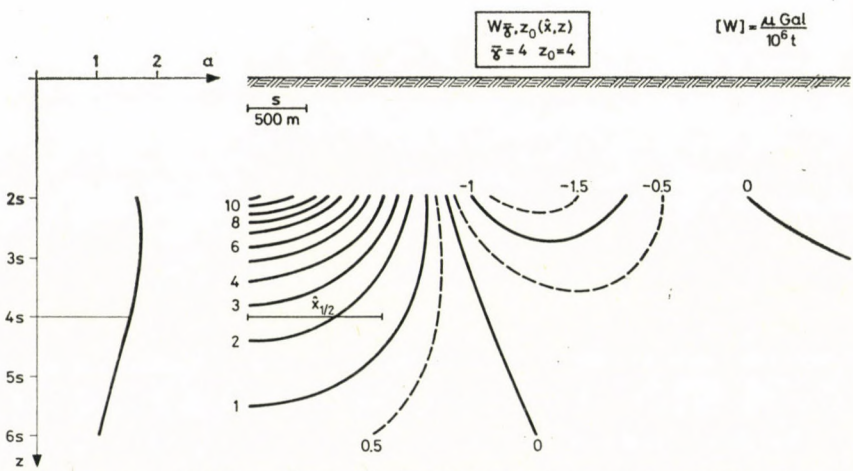

Fig. 5. The system of isolines of $w_{\bar{\gamma},z_0}(\hat{x}, z)$ and the curve $a_{\bar{\gamma},z_0}$ in case of $\bar{\gamma} = 4$ and $z_0 = 4$

the disadvantage of $t_{\bar{\gamma},z_0}$, namely that the matrix elements are to be determined by numerical integration of the type 52 looks small (in all other presented cases the matrix elements can be computed by a pocket calculator). The advantages do not mean, however, that only the use of this amplifying filter is advisable, as e.g. if only small matrix sizes can be realized, it is better to use $t_{0,0}$ (or if any advantage can be obtained from an analytical knowledge of $w(x, y, z)$, $t_{\mathrm{up,up}}$ is to be used etc.). That means that it would be too early to consider the problematics of the amplifying filters as closed, since in practical exploration problems other demands are met for the amplification, for the increase of the resolving power, for the lateral unsensitiveness, for a rapid decrease of

Table III

The filter matrix $t_{\bar{\gamma}, z_0}(x, y)$ in case of $\bar{\gamma} = 4$ and $z_0 = 4$

0.3764	0.2921	0.1107	−0.0329	−0.0739	−0.0459	−0.0100	0.0061	0.0067	0.0032	0.0010	0.0003
	0.2208	0.0691	−0.0466	−0.0728	−0.0419	−0.0078	0.0065	0.0065	0.0031	0.0009	0.0002
		−0.0152	−0.0694	−0.0652	−0.0305	−0.0024	0.0073	0.0059	0.0026	0.0008	0.0002
			−0.0709	−0.0459	−0.0148	0.0035	0.0074	0.0048	0.0019	0.0005	0.0002
				−0.0205	−0.0009	0.0071	0.0064	0.0034	0.0012	0.0004	0.0001
					0.0065	0.0071	0.0045	0.0020	0.0007	0.0002	0
						0.0049	0.0025	0.0010	0.0003	0.0001	0
							0.0010	0.0004	0.0002	0	0
								0.0001	0.0001	0	0
									0	0	0
										0	0
											0

the w-values with the depth etc., to which some other conditions, e.g. for the matrix size can be added. All these necessitate further research on these topics.

In the following a possible direction of future research is outlined.

It is advisable to look for new residual transformations in the group of the function having the form:

$$t(\hat{x}) = \sum_{i=0}^{n} c_{2i}\varphi_{2i}(\hat{x}) \tag{65}$$

because the parabolic cylindrical functions φ_k have values of practically zero beginning from a certain value $\hat{x}$ (which depends on k), what can be seen from the expression of $\varphi_k(\hat{x})$:

$$\varphi_k(\hat{x}) = \frac{e^{-\frac{\hat{x}^2}{2}} H_k(\hat{x})}{\sqrt{k!2^k\sqrt{\pi}}} \tag{66}$$

(here $H_k(\hat{x})$ means a Hermite-polynomial), thus no too great matrix sizes are to be feared.

If only a maximum amplification is desired in a depth z_0 beside a minimum prescribed value of the resolving power, the latter can be realized with a w-value being zero in a given distance $\hat{x}_0$ from the origin for a level z_0:

$$w(\hat{x}_0, 0, z_0) = 0\,. \tag{67}$$

Demanding for the origin

$$w(0, 0, z_0) = 1 \tag{68}$$

a filter $t(\hat{x})$ of the type 65 is to choose for which

$$||t||^2 = \sum_{i=0}^{n} c_{2i} = \min \tag{69}$$

is fulfilled in order to ensure a maximum increase of the w-value 1 in Eq. 68 after the norming. For the values of c_{2i} the equation expressing the residual character must also be considered, thus for the fulfilment of the minimum condition 69 (not forgetting Eqs 67 and 68) a value of at least $n = 3$ must be taken, i.e. $t(\hat{x})$ is to be looked for in form of at least 4 parabolic cylindrical functions. In the investigations the functions $\Phi_{2i}(x, z)$ introduced in [10] can be advantageously used; in the same paper a simple condition is given for the c_{2i}-s to get map transformations according to Eq. 65 which are really residual ones, i.e. $\int_{-\infty}^{\infty}\int_{-\infty}^{\infty} t(x, y)\mathrm{d}x\mathrm{d}y = 0$ is *ab ovo* fulfilled.

REFERENCES

1. BRACEWELL, R.: The Fourier Transform and its applications. McGraw-Hill, 1965.
2. ERDÉLYI, A.: Tables of Integral Transforms. McGraw-Hill, 1954.
3. RÉNYI, A.: Wahrscheinlichkeitsrechnung. Deutscher Verlag der Wissenschaften, Berlin, 1962.
4. STEINER, F.: Characterization and derivation of map transformations on the basis of the anomalous body — map relationship. *Acta Geod., Geoph. Mont. Hung.*, 8 (1973), 71—84.
5. STEINER, F.: Derivation of map-transformations with small lateral effect. *Acta Geod., Geoph. Mont. Hung.*, 9 (1974), 255—260.
6. STEINER, F.: Über einige Methoden der "sekundären" gravimetrischen Auswertung. *Geofisica Pure e Applicata*, 56 (1963), 2—16.
7. STEINER, F.: Die Rolle der Polynomdarstellungen in der Lösung geophysikalischer Probleme. *Acta Geod., Geoph. Mont. Hung.*, 6 (1971), 63—81.
8. STEINER, F.: Derivation of fully matrixed map-transformations. *Acta Geod., Geoph. Mont. Hung.*, 8 (1973), 85—102.
9. STEINER, F.—ZILAHI-SEBESS, L.: Analysis of gravitational weight-functions (in Hungarian). *Magyar Geofizika*, 18(1977), 10—17.
10. CSERNYÁK, L.— STEINER, F.: General properties of gravitational w-functions. *Acta Geod., Geoph. Mont. Hung.*, 13 (1978), 131—143.

УСИЛИВАЮШИЕ РЕЗИДУАЛЬНЫЕ ФИЛЬТРЫ

Л. ЧЕРНЯК—Ф. ШТЕЙНЕР

РЕЗЮМЕ

В статье излагаются некоторые резидуальные трансформация карт, при помощи которых осуществляется усиление гравитационных индикаций геологических структур.

Acta Geodaet., Geophys. et Montanist. Acad. Sci. Hung. Volume 17 (2), pp, 205—208 (1982)

A SHORT NOTE TO PRESCRIBED w-PROPERTIES

L. CSERNYÁK—F. STEINER
UNIVERSITY OF HEAVY INDUSTRY, MISKOLC

L. ZILAHI-SEBESS
EÖTVÖS LORÁND STATE GEOPHYSICAL INSTITUTE, BUDAPEST

[Manuscript received March 13, 1980]

The paper supplements the known characteristics of the w-function by some statements which can promote the derivation of gravimetric map transformations $t(x, y)$ characterized by prescribed $w(x, y, z)$ functions.

The weight function $w(x, y, z)$ has been introduced in [5] for the characterization of the connection between the filtered gravimetric maps $r(x, y)$ and the density distribution $\sigma(x, y, z)$ of geologic structures. It is defined by the following equation:

$$r(x,y) = \int_{-\infty}^{\infty}\int_{-\infty}^{\infty}\int_{0}^{\infty} \sigma(\bar{x}, \bar{y}, \bar{z}) \cdot w(x - \bar{x}), (y - \bar{y}, \bar{z}) \mathrm{d}\bar{x}\mathrm{d}\bar{y}\mathrm{d}\bar{z} \,. \tag{1}$$

The effective use of the theory of the Fourier-transformation is enabled by the fact that — in connection with the considerations about the w-function — the filtered effect of a surface density distribution $\sigma'(x, y)$ in a depth level z_0 is obtained by a two-variable convolution, as it can be seen from Eq. 1. The most important formulae of the filter function $t(x, y)$, its Fourier-transform $T(p, q)$, the function $e(\hat{x}) = fz_0(\hat{x}^2 + z_0^2)^{-3/2}$ characterizing the gravimetric effect and $E(\hat{p}) = 2\pi f e^{-z_0\hat{p}}$ being its transfer, as well as those of the Bouguer-map $g(x, y)$ and of $G(p, q) = \mathfrak{F}\{g(x, y)\}$ are presented in [5], therefore they are not included in this paper ($\hat{x} = \sqrt{x^2 + y^2}$, $\hat{p} = \sqrt{p^2 + q^2}$). In [7] these formulae are also summarized (see present issue).

It would be very helpful if a map transformation $t(x, y)$ could be given to any arbitrary $w(x, y, z)$ which realizes it. E.g. the interpretation would be simple if $w(x, y, z)$ would have values differing from zero only in a small domain limited from all directions; however, this requirement as others, too, cannot be fulfilled. Let us therefore quote the w-properties whose deduction and practical importance can be found in [2].

a) The integral of any $w(x, y, z_0)$ function for the whole plane (x, y) is a constant not depending on z_0.

b) The quadratic integral of any $w(x, y, z_0)$ for the plane (x, y) decreases rigorously montonically with the increase of z_0, and the function is convex everywhere.

c) The quadratic integral $||w||^2$ of $w(x, y, z_0)$ of a map transformation characterized by the transfer $T(\hat{p})$ can be easily obtained using the $u(z)$ Laplace-transform of the function $\hat{p} \cdot T^2(\hat{p})$

$$u(z) = \mathfrak{L}\{\hat{p} \cdot T^2(\hat{p})\} \tag{2}$$

in the following form:

$$||w||^2 = 2\pi f^2 \cdot u(2z) . \tag{3}$$

(For the coefficient in this equation see [3].)

d) No map transformation exists which produces at a depth level z_0 a $w(x, y, z_0)$ being equal with $\delta(x, y)$. Therefore it is an irrealizable aim to produce a filter matrix which yields an $r(x, y)$ being exactly proportional with the absolute height of a density contrast surface.

The first statement of the present paper is:

1. *The functions $w(x, y, z)$ are harmonic ones.* This statement can be proved as follows. As

$$w(x, y, z) = \int_{-\infty}^{\infty}\int_{-\infty}^{\infty} e(x - u, y - v, z) \cdot t(u, v)\mathrm{d}u\mathrm{d}v , \tag{4}$$

$$\begin{aligned} \Delta w(x, y, z) = \int_{-\infty}^{\infty}\int_{-\infty}^{\infty} [e_{xx}(x - u, y - v, z) + e_{yy}(x - u, y - v, z) + \\ + e_{zz}(x - u, y - v, z)] \cdot t(u, v)\mathrm{d}u\mathrm{d}v = \\ = \int_{-\infty}^{\infty}\int_{-\infty}^{\infty} \Delta e(x - u, y - v, z) \cdot t(u, v)\mathrm{d}u\mathrm{d}v = 0 , \end{aligned} \tag{5}$$

where Δ denotes the Laplace-operator after x, y, z, and $e(x, y, z) = fz(x^2 + y^2 + z^2)^{-3/2}$, which is clearly a harmonic function (supposing that integral 5 exists; this condition means no practical restriction for t). If the filtering is realized by a filter matrix, the statement is nearly trivial, as in that case w is the linear combination of a finite number of e-functions, and the linear combination of harmonic functions is evidently also harmonic.

Two important consequences follow from this (see e.g. [4], p. 333):

2. *Let us choose a sphere which is included in the half-space $z > 0$; the average of the w-values on the surface of this sphere is equal with the value of $w(x, y, z)$ in the centre of the sphere.*

3. *Be V an arbitrary closed domain in the half-space $z > 0$; $w(x, y, z)$ can have its maximum only at the boundary of the domain .*

These consequences mean first of all that *the maximum w-value of an upper level is always higher than the maximum w-value of a lower level* (the properties a and b are not suffice to exclude the opposite case). Consequently, as a special case, the maximum value $w_{\max}$ of w cannot be greater than the value $2\pi f \cdot t_{\max}$ referring to the level $z_0 = 0$.

The other practically very important consequence of these statements is that *it is impossible to produce high w-values in a certain exploration depth* z_0 (e.g. at $x = y = 0$) *so that the immediate and/or the farther vicinity should have only smaller w-values.*

It is also practically important to know what means the spatial harmonic property of $w(x, y, z)$ in the $(\hat{x}, z)$-quarter plane characterized by $\hat{x}, z \geq 0$ in which according to [6] the functions w are investigated (making use of the cylindrical symmetry of the $w(x, y, z)$-s corresponding to circularly symmetric $t(x, y)$-s) — and on which quarter plane the requirement for w are stated when the map transformation $t(x, y)$ fulfilling the requirements for w are looked for.

4. *A map transformation $t(x, y)$ producing a certain w can be found only if w fulfils the following differential equation on the plane $(\hat{x}, z)$:*

$$\frac{\partial^2 w(\hat{x}, z)}{\partial \hat{x}^2} + \frac{1}{\hat{x}} \frac{\partial w(\hat{x}, z)}{\partial \hat{x}} + \frac{\partial^2 w(\hat{x}, z)}{\partial z^2} = 0 . \tag{6}$$

Equation 6 follows directly from the spatial harmonic and cylindrical symmetric property of $w(x, y, z)$.

The last statement is closly connected to statement 4.:

5. *The set of functions $w(x, y, z)$ is identical with the set of the cylindrically symmetric, in the half-plane $z > 0$ harmonic functions which disappear if $z \to \infty$.*

Proof: The harmonic and cylindrically symmetric functions $f(\hat{x}, z)$ are derived as solutions of Eq. 6. Being restricted to the half-space $z > 0$ and supposing the fulfillment of

$$\lim_{z \to \infty} f(\hat{x}, z) = 0 ,$$

Equation 6 should be solved by separation of variables (see e.g. p. 31 in [1]). In this case the solution can be written in the form

$$f(\hat{x}, z) = \frac{1}{2\pi} \int_0^\infty \hat{p} C(\hat{p}) \cdot e^{-\hat{p}z} \cdot J_0(\hat{p} \cdot \check{x}) \mathrm{d}\hat{p} \tag{7}$$

which is evidently the inverse Hankel-transform of $C(\hat{p}) \cdot e^{-\hat{p}z}$ but the latter is fully identical with the general expression of $W(\hat{p})$ (if $C(\hat{p}) = 2\pi f T(\hat{p})$; see Eqs 29 and 25a in [7]).

REFERENCES

1. BARANOV, W.: Potential fields and their transformations in applied geophysics. Gebrüder Borntraeger, Berlin—Stuttgart, 1975.
2. CSERNYÁK, L.—STEINER, F.: General properties of gravitational w-functions. *Acta Geod., Geoph. Mont. Hung.*, 13 (1978), 131—143.
3. CSERNYÁK, L.—STEINER, F.: Global characterization of the depth-behaviour of gravity filters, using norms in the w-function (in Hungarian). *Nehézipari Műszaki Egyetem Közleményei, Ser. I. (Bányászat)*, 25 (1978), 3—19.
4. FICHTENHOLZ, G. M.: Differential- und Integralrechnung III. VEB Deutscher Verlag der Wissenschaften, Berlin, 1964.
5. STEINER, F.: Characterization and derivation of map transformations on the basis of the anomalous body-map relationship. *Acta Geod. Geoph. Mont. Hung.*, 8 (1973), 71—84.
6. STEINER, F.—ZILAHI-SEBESS, L.: Analysis of gravitational weight-functions (in Hungarian). *Magyar Geofizika*, 18 (1977), 10—17.
7. CSERNYÁK, L.—STEINER, F.: Amplifying residual filters. *Acta Geod., Geoph. Mont. Hung.*, 17 (1982) 181—204.

КРАТКОЕ ЗАМЕЧАНИЕ К ЗАДАННЫМ *W*-СВОЙСТВАМ

Л. ЧЕРНЯК—Ф. ШТЕЙНЕР—Л. ЗИЛАХИ-ШЕБЕШ

РЕЗЮМЕ

Содержащиеся в докладе некоторые установления позволяют дополнить для известных до сих пор свойств *w*-функций, учет которых может быть полезным при выводе преобразований гравитационных карт $t(x, y)$, характеризующихся заданной весовой функцией $w(x, y, z)$.

Acta Geodaet., Geophys. et Montanist. Acad. Sci. Hung. Volume 17 (2), pp. 209—236 (1982)

COMPARISON BETWEEN RESULTS OF THE GYRO-AZIMUTHS DETERMINED WITH OLD AND NEW GYROTHEODOLITES*

ABDELHAMID KAMAL HASSAN

BANHA UNIVERSITY, FACULTY OF ENGINEERING, CAIRO, EGYPT

[Manuscript received February 13, 1981]

The paper presents an investigation for the calibration results and the gyro-azimuth measurements with a new and an old gyrotheodolites type MOM Gi-B2. The calibration and the azimuth measurements were made in Sopron, Hungary in 1979 and 1980.

The object of the investigation is to study the accuracy of the gyro-azimuths of both the new and the old gyrotheodolites. Therefore a detailed study was made for the calibration and the gyro-north measurements of the old gyro-theodolite to evaluate its efficiency.

In this research some solutions are proposed for the calculation of the gyro-azimuth from the measurements of the old instrument to obtain results of similar accuracy as that obtained with the new instrument. This will make it possible to utilize old gyrotheodolites in higher order geodetic works similarly as the new gyrotheodolites.

The calibration results of the two gyrotheodolites as well as the gyro-north measurements of the old gyrotheodolite are tabulated. Finally a comparison is made between the azimuth results of the old gyrotheodolite obtained from the proposed solution and the azimuth results of the new gyrotheodolite, then all the results are also compared with the astro-azimuths of the same directions. The results are also tabulated together with the accuracies.

1. Introduction

The gyrotheodolites used in the investigation are of the type MOM Bi-B2. The first gyrotheodolite is an old one, it was used for the azimuth determination and for orientation purposes in geodetic works for several years, it has been used for more than 3000 azimuth determinations with independent starts, the number of reversion points observed in each azimuth determination was between 4 and 8 reversion points. The instrument has also been transported several times for long distances. The second gyrotheodolite is a new one it has not been so much used as the first, but it was only used for some measurements for its calibration and a few measurements to control its accuracy by comparing its azimuth results with the astronomical azimuth of a known direction.

The gyrotheodolites MOM Gi-B2 have special features which differentiate this type from the other types of gyrotheodolites, these features are as follows:

1. In the MOM Gi-B2 gyrotheodolite, the gyroscope unit and the theodolite unit are mounted together, but they can be moved independently of each other.

* Paper presented at the XVI th Congress of the International Federation of Surveyors (FIG) in Montreux, 9—18. August, 1981, Switzerland

2. The reversion points of the oscillations can be related with the limb (horizontal circle) of the theodolite through an autocollimation optical system (the autocollimator). The image of the autocollimator scale graduation is halved by a coincidence prism. As a facility to increase the accuracy of the readings, the two halves of the image move in opposite directions.

3. The theodolite is not used for following the swing of the gyroscope, but it is used only for measuring the amplitude of the swing on the horizontal circle.

4. The swinging gyroscope is followed by an automatic follow-up device. In this system, the mirror of the automatic follow-up device reflects light signal (controlling the follow-up action), on two photoresistors vary their resistance according to the intensity of the incident light. The right hand or the left hand resistor is exposed to light, depending on the position of the mirror of the system, this causes unbalance in the photo-resistors, as a result of this unbalance an electronic system drives a servo-motor and the automatic optical system is turned together with the upper encasing bracket of the suspension band so that it follows the swing of the gyroscope. Consequently, the difference between the band torque zero point and the scale zero point is kept to almost nil.

5. Each scale division of the scale of the gyroscope which is read in the autocollimator eyepiece represents 30 seconds of arc.

The calibration of the two gyrotheodolites was made in the Bánfalva observatory in Sopron, Hungary. The calibration of the new gyrotheodolite lasted in 1979 for three days, the old gyrotheodolite was calibrated in 1980 for nine days. The calibration of the two instruments included the determination of the instrument constant and the *C*-factor (the moment ratio; the ratio between the moment of the suspension band of the gyroscope and that of the gyroscope itself multiplied by the angular equivalent to one scale division of the autocollimator). The calibration results for both instruments are tabulated, the accuracy of the instrument constant is also shown in the tables.

The gyro-azimuth measurements were made in Sopron, too, the measuring station was the northern end of the base line of the triangulation net of the city. Five reference objects were sighted from this station.

The gyro-azimuth values of the two gyrotheodolites were compared with the astronomical azimuth values of the same reference objects. The calibration results, the gyro-north measurement, and the calculated azimuth values are shown in the Tables. The azimuth results of the new gyrotheodolite measured in different days are of an inner accuracy of ± 1 second of arc, and when compared with the astronomical azimuth values, the accuracy was also ± 1 second of arc. In the measuring result of the old gyrotheodolite a definite drift phenomenon was detected, this drift caused a clear tendency for the gyro-north values to be of smaller values than the value obtained in

the first independent determination when repeating the azimuth measurements for the same reference object. The drift is of a systematical behavior, it affected greatly the final result for the instrument constant in the calibration as well as the final values of the azimuth calculated from repeated measurements with independent starts when compared with the astronomical azimuth values.

In the paper, a study is made about the calibration results and gyro-azimuth measurements of the old gyrotheodolite. Some solutions are given to eliminate the errors due to the drift phenomenon. The accuracy obtained from these solutions is much better than the results obtained from the original measurements.

A comparison was made between the azimuth results of the old gyrotheodolite obtained from the proposed solutions and the azimuth results of the new gyrotheodolite, and finally between the results obtained with both the new and the old gyrotheodolites and the astronomical azimuths of the same directions. The results agree with the astronomical azimuth with high accuracy, the azimuth results with their accuracies are tabulated in the Tables. The following notations are used in the Tables

v = single value — mean value,
$\bar{v}$ = single value — astro value,
μ_0 = mean square error of the unit weight using $[vv]$,
$\bar{\mu}_0$ = mean square error of the unit weight using $[\bar{v}\bar{v}]$,
μ_{Am} = mean square error of the mean value using $[vv]$,
$\bar{\mu}_{Am}$ = mean square error of the mean value using $[\bar{v}\bar{v}]$.

2. The methods used in the determination of the reversion points

Two methods of observation were used for the determination of the reversion points; methods with following and without following. In the first method the reversions of the gyroscopic swingings are read on the horizontal circle of the theodolite, in the second method the reversions are read on the scale of the autocollimator. The torsion effect of the band was taken into account in the two methods.

2.1 *Determination of reversion points with following*

In this method the torsional rest position No' of the rotation axis of the gyroscope is determined from the reversion points read on the horizontal circle according to the Schuler—Fox formula as follows:

$$No' = \frac{1}{r-2}\left[\frac{1}{4}(n_i + n_r) + \frac{3}{4}(n_2 + n_3 + \ldots + n_{r-1}) + \sum_{i=3}^{r-2} n_i\right] \qquad (1)$$

where No' = the torsional rest position of the rotation axis of the gyroscope,
n_i = the reversion points (Fig. 1) and
r = the number of the reversion points.

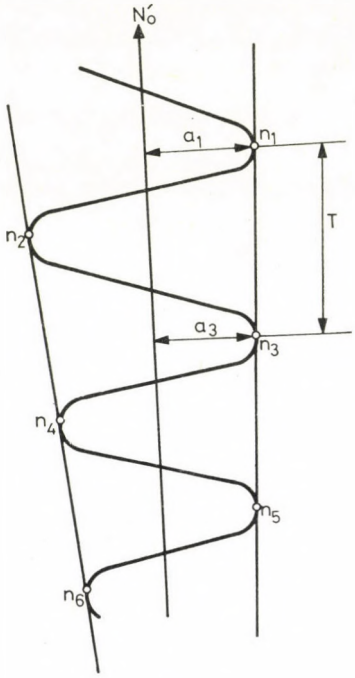

Fig. 1

This torsional rest position is identical to the direction of the resultant of the gyroscopic moment and the moment of the suspension band and of the spirals (Fig. 2), it deviates from the north direction by a small amount $\Delta No'$,

$$\Delta No' = K \frac{M_b}{M_g} u_0 \tag{2}$$

where $\Delta No'$ = the torsion correction in seconds of arc,
K = the angular equivalence to one scale division of the autocollimator ($K = 30''$),
M_b = the moment of the suspension band,
M_g = the moment of the gyroscope,
u_0 = the torsion-free position of the band (the zero point).

The torsion-free position of the band u_0 is determined by free swinging when the gyroscope is non-spinning with observing the reversion points u_i

in the autocollimator, the rest position can be calculated from the observed reversion in a similar manner as in Eq. 1.

The ratio M_b/M_g can be calculated by measuring the swinging time of a complete swing measured with following and without following which differ at different geographical latitudes [Halmos, 1966—1968].

$$\frac{M_b}{M_g} = \frac{T_f^2}{T_{wf}^2} - 1 \tag{3}$$

where T_f = swing time measured with following, and
T_{wf} = swing time measured without following.

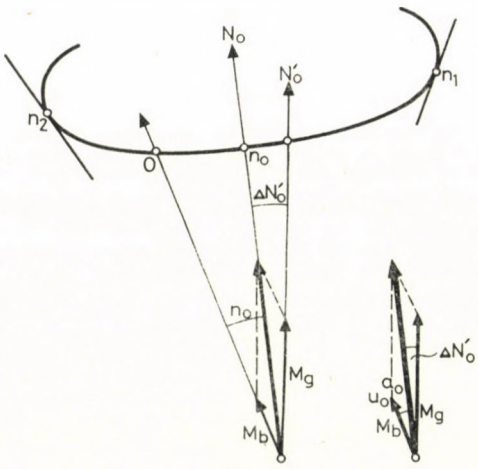

Fig. 2

In Eq. 2 the coefficient $K\dfrac{M_b}{M_g}$ is the C-factor and denoted by C. The torsion correction formula will be

$$\Delta No' = Cu_0 . \tag{4}$$

The corrected rest position can be computed from the following formula:

$$\begin{aligned} No &= No' + \Delta No' \quad \text{or} \\ No &= No' + Cu_0 . \end{aligned} \tag{5}$$

2.2 *Determination of reversion points without following*

In this method, the torsional rest position n_0' of the rotation axis of the gyroscope is calculated according to Formula 1 from the reversion points n_i read in the autocollimator.

As no following is made during the measurements, the torsion effect must be taken in the value n_0' twice. α_M (the horizontal circle reading) in this position must be read as a basic orientation. Then the rest position corrected for torsion is:

$$No = \alpha_M + Kn_0' - Cn_0' + Cu_0 . \tag{6}$$

The computational formula of the azimuth determination with the gyrotheodolite with both methods is

$$A = I - No + \Delta \tag{7}$$

where A = the azimuth to be determined,
I = the reading on the horizontal circle in case of pointing to the direction to be determined,
No = the horizontal circle reading for the corrected rest position,
Δ = the instrument constant determined by the calibration.

3. The calibration

For both the new and the old instruments, the calibration measurements were made in the Bánfalva observatory of Sopron, Hungary of latitude $\varphi = 47° 40' 55''.56$. It was constructed under a mountain of about 60 m height, it conserves humid air and keeps always fixed temperature (about 13 °C) all over the whole year due to the nature of its location. The observatory is constructed specially for the geodynamical measurements, it is in the form of two perpendicular tunnels, each about 50 m length, the center lines of the two tunnels are of known astronomical azimuths, these azimuts are controlled periodically by the geodetic department of the Geodetic and Geophysical Research Institute of the Hungarian Academy of Sciences, Sopron.

The gyrotheodolite was set up on a concrete pillar established specially for precise measuring purposes, it was mounted on a heavy steel mount to insure good stability for the instrument. The gyrotheodolite was centred underneeth a fixed point inside the main tunnel of the observatory, geodetical sights were made to the end points, the first end point was occupied with a Wild target which was centred accurately, its verticality was checked with a theodolite. The other end point was defined with plumb bob which was completly damped to insure accurate sighting.

The gyrotheodolite was left in its position during the whole period of calibration to avoid centring errors due to repeated occupation of the station. At the begining of each day measurements, the centring of the instrument and the verticality of the sighting target were checked.

The calibration of each gyrotheodolite included the determination of the C-factor and the instrument constant, for the new instrument it lasted in August, 1979 three days and for the old instrument it lasted in May, June and July, 1980 nine days.

3.1 *Determination of the C-factor*

The swinging times of $\frac{1}{2}, 1, \frac{3}{2}$ swings were measured with spinning gyroscope with the two methods (with following, and without following), and the mean value represents the swinging times of a complete swing (T_f and T_{wf}) where used in the calculation of the C-factor with the following formula [Halmos, 1968]:

$$C = K\left(\frac{T_f^2}{T_{wf}^2} - 1\right) \text{ seconds of arc/one scale division.}$$

In the above equation $K = 30$ seconds of arc. The results obtained for the C-factor are as follows: for the new gyrotheodolite: $C = -5''.10$/one scale division. For the old gyrotheodolite: $C = -5''.83$/one scale division.

The following table contains the mean value of the swing times T_f and T_{wf} and the calculated C-factor values from eight independent measurements with the old gyrotheodolite.

No.	Time of $\left(\frac{1}{2}+1+\frac{3}{2}\right)$ swings				The swing time				The calculated C-factor
	with following		without following		T_f		T_{wf}		
	m	s	m	s	m	s	m	s	$''$
1	28	35.9	26	09.8	9	31.97	8	43.27	−5.842
2	28	38.7	26	10.9	9	32.90	8	43.63	−5.885
3	28	36.7	26	11.7	9	32.23	8	43.90	−5.794
4	28	36.2	26	10.2	9	32.07	8	43.40	−5.799
The mean value of C for the old instrument									−5.830

Precautions in observations and measurements

The following important precautions were taken into considerations during the measurements for the instrument constant and for the azimuth determinations:

1. Before starting the measurements, the gyroscope was let to swing without spinning for about half an hour to eliminate smaller band torsions and deformation.

2. The gyroscope was warmed up before measurements for about one hour to reach a heat equilibrium to avoid any shift in the equilibrium position.

3. A set of at least six independent determinations was measured for the determination of the instrument constant or for the azimuth in every setting up of the instrument to increase the accuracy.

4. The zero point position of the band was regulated near to zero; it was not more than ± 1.5 scale divisions to make the disturbing effects and torsions symmetrical along the whole swinging path to the zero position, i.e. to the rest position.

5. The zero point position u_0 was determined by four observed half-swings without spinning before and after the determination of the torsional rest position of the spinning gyroscope. This is to eliminate the effect of changes of the zero point position during the measurements of the reversion points. The mean value is then used,

$$u_0 = \frac{u_0\,(\text{before}) + u_0\,(\text{after})}{2}\,. \tag{8}$$

For the new gyrotheodolite, the average value of the change in the zero point was 1″, and that for the old one was 1″.5.

6. The number of the observed reversion points was 6 to eliminate initial thermal effect, and the effect of desarrestation.

7. When the amplitude method (without following) was used, a good preliminary orientation was made to minimize as possible the effects of the reading errors in the reversion points n_i as their mean value is used twice in the azimuth calculation.

8. The pointing to the reference object was made twice before and after the gyro-measurements and the mean value was used as I in order to eliminate the warping of the horizontal circle during the gyromeasurements.

$$I = \frac{I\,(\text{before}) + I\,(\text{after})}{2} \tag{9}$$

The average difference between I (before) and I (after) was nearly 0″.5 for the new instrument and 1″.5 for the old one.

9. The instrument was always checked to ensure its horizontality.

10. The C-factor was determined in the calibration station and during the field measurements to avoid the changes in the swing time due to the change of the latitude and to the changes of the outer temperature. It was found that the difference between the C-factor determined in the calibration station and that determined in the field station is insignificant and can be neglected.

3.2 *Determination of the instrument constant Δ*

The instrument constant Δ is the angle between the axis of the telescope and the perpendicular to the swinging mirror, it is calculated from Eq. (7) as follows:

$$\Delta = A - I + No \tag{10}$$

where A = the known astronomical azimuth of the control line,
I = the reading on the horizontal circle when sighting the control line (geodetic sighting), and
No = the horizontal circle reading for the corrected rest position.

The instrument constant Δ of the new gyrotheodolite was calculated from the measurement of three days. Six measurements with independent starts were made in each day. For each independent measurement, two values for Δ were calculated because two reference objects of known astronomical azimuths (determined with an accuracy of $\pm 0''.88$) were sighted before and after the gyro-measurements, the average mean square error of sighting and reading the geodetical directions was $\pm 0''.3$ for the new instrument and $\pm 0''.5$ for the old one. The mean Δ was calculated for each independent measurement. The calculated values of Δ for the new instrument are shown in Table I, the mean values of the three days agree with high accuracy, the mean square error of a single measurement is between ± 2—3 seconds of arc and the mean square error of the mean value of the six measurements is ± 1 second of arc,

Table I

Results of the calibration

Instrument: MOM Gi-B2 No 770106 (new)

The calibration station: Sopron, Bánfalva observatory Temperature: 13 °C						
Date	14 August, 1979		15 August, 1979		16 August, 1979	
No	Δ	V	Δ	V	Δ	V
1	88°49′ 08″.19	1″.80	88°49′ 03″.67	−2″.76	88°49′ 09″.91	3″.51
2	88 49 04.32	−2.07	88 49 06.24	−0.19	88 49 08.96	2.56
3	88 49 09.54	3.15	88 49 04.83	−1.60	88 49 04.82	−1.58
4	88 49 07.41	1.02	88 49 07.18	0.75	88 49 02.59	−3.81
5	88 49 04.91	−1.48	88 49 09.43	3.00	88 49 07.42	1.02
6	88 49 03.96	−2.43	88 49 07.20	0.77	88 49 04.68	−1.72
Mean	88 49 06.39	0.00	88 49 06.43	0.00	88 49 06.40	0.00
Mean square errors	μ_0	$\pm 2.31''$	μ_0	$\pm 2.02''$	μ_0	$\pm 2.82''$
	μ_Δ	± 0.94	μ_Δ	± 0.82	μ_Δ	± 1.15
Mean value of the instrument constant (Δ)					88°49′ 06″.41	$\pm 1''.00$

Table II

Instrument constant (Δ) used in azimuth calculations

Instrument: MOM Gi-B2 No. 023119 (old)

Calibration station: Sopron, Bánfalva observatory
Date of calibration: 12 May, 1980

Temperature: 13 °C

No.	Δ from direction 2—1	Δ from direction 2—4	Mean Δ affected with syst. error	$\bar{\Delta}$ values used in azimuth calculations	
1	90°11′ 55.″27	90°11′ 53.″77	90°11′ 54.″52		mean of 1st
2	90 11 50.01	90 11 50.36	90 11 50.19	90°11′ 52.″36	(Δ_2) 2 values
3	90 11 47.41	90 11 50.16	90 11 48.79	90 11 51.17	(Δ_3) 3 values
4	90 11 45.46	90 11 45.81	90 11 45.64	90 11 49.78	(Δ_4) 4 values
5	90 11 45.26	90 11 43.66	90 11 44.46	90 11 48.72	(Δ_5) 5 values
6	90 11 42.78	90 11 43.63	90 11 43.21	90 11 47.80	(Δ_6) 6 values
7	90 11 45.45	90 11 45.20	90 11 45.33	90 11 47.44	(Δ_7) 7 values

the difference between the final value and each single value was between ± 3 seconds of arc. The mean values of Δ for each of the three days deviate from each other by $\pm 0.''04$ and from the final value by $\pm 0.''02$.

The instrument constant of the old gyrotheodolite was calculated from the measurements of nine days. In some days more than six measurements with indpendent starts were measured, also for each independent measurement there were two values for Δ, the mean value was taken as a single independent determination. Table II shows in the first three columns Δ values obtained from sighting the two control directions (2—1) and (2—4) and their means. The results shown in Table II are from the first day of the calibration. It is obvious from the calibration results that there is a clear tendency for Δ values to get smaller in a systematic way; besides the observation and random errors, this tendency is also shown in Figs 3—5, where the line representing Δ values is going downwards. Table III shows the gyro-north values of the first calibration day which seem to be affected in the same manner. The calculations showed that the mean square error of a single value of Δ in different days is between ± 4—5 seconds of arc, and for the mean value it is between ± 1.5—2 seconds of arc. On the assumption that the drift is a function of time, the first value of Δ in each day can be considered as nearly free of systematic effect. Therefore in correcting the drift, the subsequent Δ values should be reduced to the firts value, i.e., to the start, at this instant, no drift has yet occurred [Gregerson, 1970]. To evaluate the systematic effect, a linear interpolation is sufficient good estimation for the drift effect as it is caused from the heat changes due to measurements for long periods, and because these heat changes may be expressed as exponential function, which differs

Table III

Results of the calibration

Instrument: MOM Gi-B2 No. 023119

Station: Sopron, Bánfalva observatory
Date: 12 May, 1980

Temperature: 13 °C
Weather: humid air

Meas. No.	Before correcting the systematic effect: Gyro-north No	Before correcting the systematic effect: V	Syst. effect	After correcting the systematic effect: Gyro-north No	After correcting the systematic effect: V
1	82°10′ 43″.32	6″.13	0″.00	82°10′ 43″.32	0″.96
2	82 10 39.51	2.32	−2.07	82 10 41.58	−0.78
3	82 10 37.71	0.52	−4.14	82 10 41.85	−0.51
4	82 10 35.81	−1.38	−6.21	82 10 42.02	−0.34
5	82 10 34.66	−2.53	−8.28	82 10 42.94	0.58
6	82 10 32.13	−5.06	−10.35	82 10 42.48	0.12
Mean	82 10 37.19	0.00	Mean	82 10 42.36	0.00
μ_0	±3″.94 μ_{N0}	±1″.61	μ_0	±0″.67 μ_{N0}	±0″.27

Table IV

Results of the calibration

Instrument: Gi-B2 No. 023119 (old)

Station: Sopron, Bánfalva observatory
Date: 12 May, 1980

Temperature: 13 °C
Weather: humid air

Meas. No.	Before correcting the systematic effect: Instrument constant Δ	Before correcting the systematic effect: V	Syst. effect	After correcting the systematic effect: Instrument constant Δ	After correcting the systematic effect: V
1	90°11′ 54″.52	7″.07	0″.00	90°11′ 54″.52	2″.16
2	90 11 50.19	2.74	−1.64	90 11 51.83	−0.53
3	90 11 48.79	1.34	−3.28	90 11 52.07	−0.29
4	90 11 45.64	−1.81	−4.92	90 11 50.56	−1.80
5	90 11 44.46	−2.99	−6.56	90 11 51.02	−1.34
6	90 11 43.21	−4.24	−8.20	90 11 51.41	−0.95
7	90 11 45.33	−2 12	−9.84	90 11 55.17	2.81
Mean	90 11 47.45	0.00	Mean	90 11 52.36	0.00
μ_0	±3″.96 μ_Δ	±1″.50	μ_0	±1″.77 μ_Δ	±0″.67

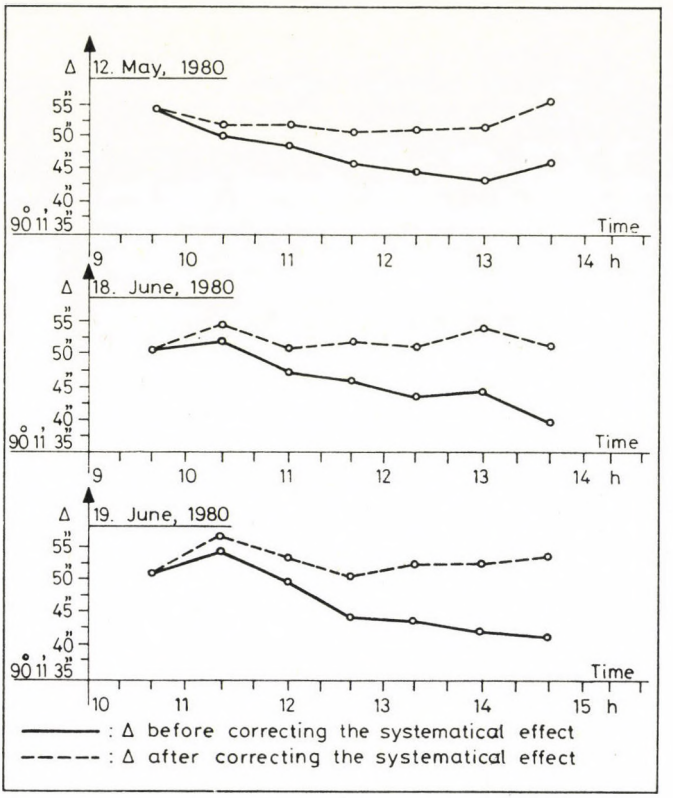

Fig. 3. The instrument constant (Δ). Instrument: MOM Gi-B2 No 023119 (old)

only slightly from a linear one. The slope of the fitted line represents the rate of the systematic effect. The linear interpolation was also calculated for the gyro-north (*No*) values of each day and a mean value of the drift rate (S) was calculated and found to be approximately 2 seconds of arc per every measurement excluding the first measurement. The instrument constant values were then calculated after eliminating the drift. The results of first day of the calibration are shown as an example in the second part of Table IV; it is clear that the results are of better accuracy. Figures 3—5 show the results after the elimination of the drift. The results obtained after the elimination of the drift are of mean square error between ± 0.5—2 seconds of arc for a single value, and for the mean value it is less than ± 1 second of arc. The summary of the calibration results of the nine days is shown in Table V. The Δ values shown are those after the elimination of the drift effect, the nine values agree with a high accuracy, they deviate from each other by (0.5—4) seconds of arc and from the final value by ± 2 seconds of arc. The

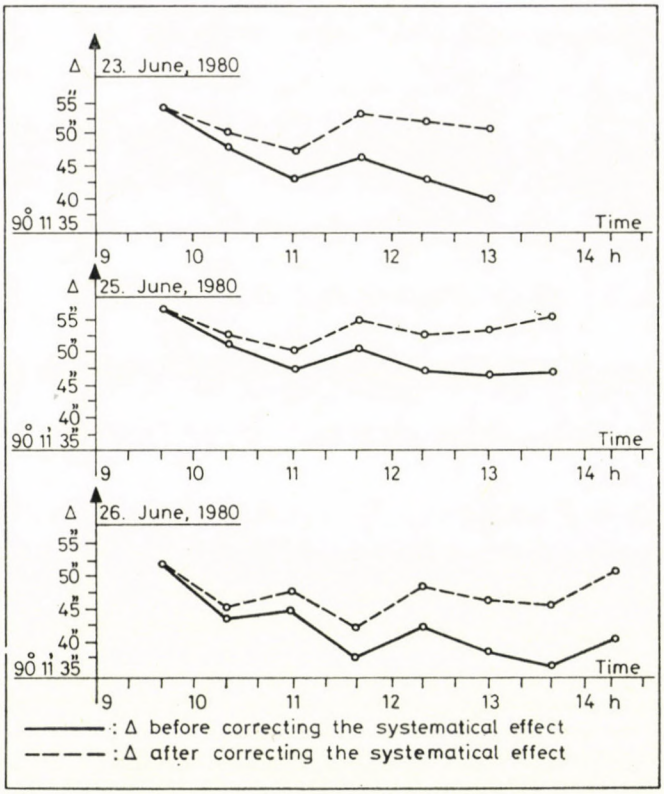

Fig. 4. **The instrument constant (Δ). Instrument: MOM Gi-B2 No 023119 (old)**

Table V

Summary of the calibration results

Instrument: MOM Gi-B2 No. 023119 (old)

Date	No. of indep. measts.	Adjusted values of Δ	V
12. May, 1980	mean of 7 measts.	90°11′ 52″.36	0″.56
18. June, 1980	mean of 7 measts.	90 11 52.10	0.30
19. June, 1980	mean of 7 measts.	90 11 53.23	1.43
23. June, 1980	mean of 6 measts.	90 11 51.76	−0.04
25. June, 1980	mean of 7 measts.	90 11 53.84	2.04
26. June, 1980	mean of 8 measts.	90 11 49.30	−2.50
27. June, 1980	mean of 7 measts.	90 11 52.21	0.41
30. June, 1980	mean of 8 measts.	90 11 50.34	−1.46
1. July, 1980	mean of 8 measts.	90 11 51.06	−0.74
Mean value of 9 days measurements		90 11 51.80	0.00
μ of the instrument constant		±0″.47	

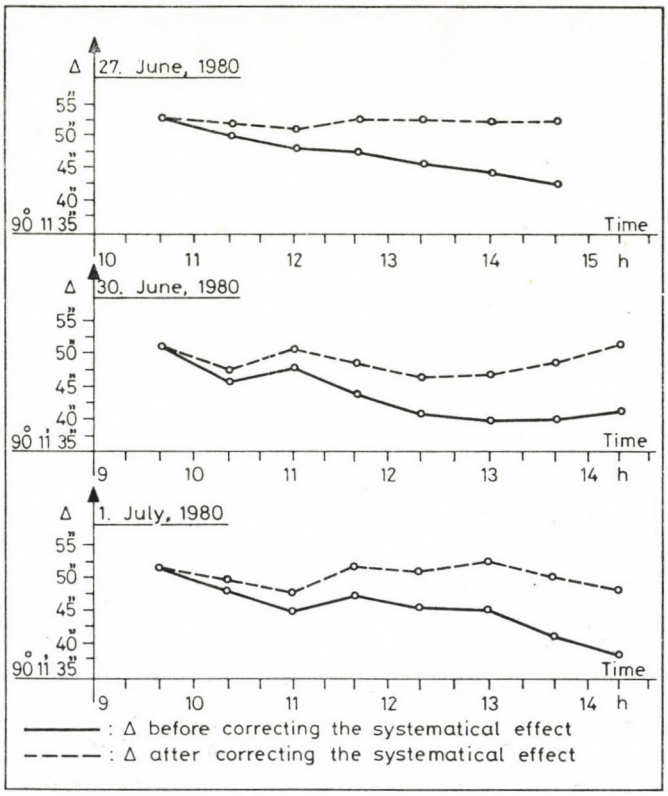

Fig. 5. The instrument constant (Δ). Instrument: MOM Gi-B2 No 023119 (old)

final value of Δ (the mean of 9 days measurements; i.e. the mean of 65 independent measurements) is of an accuracy of ± 0.47 second of arc.

4. Measurements for the azimuth determination

The measuring station was in Sopron, Hungary; it is the northern end of the base line of the triangulation net of the city of latitute $\varphi = 47° 40' 49''.47$. The instrument station is defined by the point of intersection of two perpendicular lines etched on a brass plate fixed rigidly on the top of a concrete pillar. The gyrotheodolite was mounted on a heavy steel mount placed on the concrete pillar, always, it was well protected against wind and its effect.

From the measuring stations, five directions could be sighted, the astronomical azimuths of these directions are known, they were determined with an accuracy of $\pm 0.3''$. These directions are the lines joining the measuring station and the following reference objects at the following distances from the measuring station.

1. The top of the city tower, 1160 m.
2. The star on the top of the post office, 666 m.
3. The western tower of the two-towered church, 689 m.
4. The eastern tower of the two-towered church, 692 m.
5. The Károly panoramic tower, 1750 m.

These geodetic directions were sighted and read with an average mean square error $\pm 0''.5$.

4.1 *Azimuth measurements with the new gyrotheodolite*

The measurements of azimuth with the new gyrotheodolite were made in 1979 three days, it was good horizontal visibility after little rain remained two days. More than six independent determinations were made each day, in some days the two methods of azimuth determination (with following and without following) were used to determine the *C*-factor. The mean values of the azimuth of each direction measured in different days were calculated and compared with the astronomical azimuths, some of the results are shown in Tables VI, VII. The mean square error is ± 1.5—2 seconds of arc for a single measurement and ± 0.5—1 second of arc for the mean value. When comparing with the astronomical azimuths nearly the same accuracy was obtained.

Table VI

Results of the gyro-azimuth

Instrument: MOM Gi-B2 No. 770106 (new)

Measuring station: the northern point of the base line in Sopron

Sighted station: the city tower — Astro-azimuth: 27°52′38″.80

Meas. No.	Date: 23 August, 1979 Temperature: 19 °C—26 °C			Meas. No.	Date: 3 September, 1979 Temperature: 15 °C—23 °C		
	Azimuth	V	$\bar{V}$		Azimuth	V	$\bar{V}$
1	27°52′ 38″.79	—0″.96	—0″.01	1	27°52′ 40″.50	1″.99	1″.70
2	27 52 37.70	—2.05	—1.10	2	27 52 40.62	2.11	1.80
3	27 52 38.80	—0.95	0.00	3	27 52 36.03	—2.48	—2.77
4	27 52 42.38	2.63	3.58	4	27 52 36.70	—1.81	—2.10
5	27 52 41.90	2.15	3.10	5	27 52 37.10	—1.41	—1.70
6	27 52 38.90	—0.85	0.10	6	27 52 40.10	1.59	1.30
Mean	27 52 39.75	0.00	0.95	Mean	27 52 38.51	0.00	—0.29
Mean square errors	μ_0	$\pm 1''.91$		Mean square errors	μ_0	$\pm 2''.11$	
	μ_A	± 0.78			μ_A	± 0.86	
	$\bar{\mu}_0$	± 2.17			$\bar{\mu}_0$	± 2.14	
	$\bar{\mu}_A$	± 0.89			$\bar{\mu}_A$	± 0.87	

Table VII

Results of the gyro-azimuth

Instrument: MOM Gi-B2 No. 770106 (new)

Measuring station: the northern point of the base line in Sopron

Sighted station: E. tower of the church — Astro-azimuth: 40°45′53″.00

Meas. No.	Date: 23 August, 1979 Temperature: 19 °C—26 °C			Meas. No.	Date: 3 September, 1979 Temperature: 15 °C—23 °C		
	Azimuth	V	$\bar{V}$		Azimuth	V	$\bar{V}$
1	40°45′ 55″.93	2″.09	2″.93	1	40°45′ 54″.30	1″.19	1″.30
2	40 45 54.70	0.86	1.70	2	40 45 53.78	0.67	0.78
3	40 45 55.08	1.24	2.08	3	40 45 52.43	−0.68	−0.57
4	40 45 51.90	−1.94	−1.10	4	40 45 50.97	−2.14	−2.03
5	40 45 52.30	−1.54	−0.70	5	40 45 52.10	−1.01	−0.90
6	40 45 53.10	−0.74	0.10	6	40 45 55.10	1.99	2.10
Mean	40 45 53.84	0.00	0.84	Mean	40 45 53.11	0.00	0.11
Mean square errors	μ_0	±1″.63		Mean square errors	μ_0	±1″.54	
	μ_A	±0.67			μ_A	±0.62	
	$\bar{\mu}_0$	±1.87			$\bar{\mu}_0$	±1.55	
	$\bar{\mu}_A$	±0.76			$\bar{\mu}_A$	±0.63	

4.2 *Azimuth measurements with the old gyrotheodolite*

The azimuth measurements with the old gyrotheodolite were made in 1980 at the same measuring station three days, more than six independent determinations were made in each day, the two methods of azimuth determination were also used to determine the *C*-factor. Some of the azimuth results are shown in the first column of Table VIII, the azimuths for one direction of the three days are tabulated, and compared with the astronomical azimuth. The obtained accuracy for a single measurement is ±4—6 seconds of arc and for the mean value the mean square error is ±2—2.5 seconds of arc, when the results were compared with the astronomical azimuth values, the mean square error obtained for a single measurement is between ±6—8 seconds of arc and for the mean value it is between ±2—3.5 seconds of arc. This shows that the final results of the azimuths are far from the astronomical values. It is clear also from the tabulated results that there is a systematic increase in the azimuth values due to the systematic decrease in the gyro-north (*No*) values. Also it is clear that the first azimuth value is the nearest to the astronomic value. Figures 6, 7 show the drift in some of the results, the line joining the plotted azimuths is going upwards approximatly with a linear function, the slope of the fitting line represents the rate of the systematic effect. Figure 8 shows the tendency in the *No* values for the measurements of some days.

Table VIII

Results of the gyro-azimuths

Instrument: MOM Gi-B2 No. 023119 (old)

Measuring station: the northern point of the base line in Sopron
Sighted station: the city tower — Astro-azimuth: 27°52′ 38″.80

Date: 3 July, 1980			Temperature: 17 °C—21 °C				Weather: windy
Meas. No.	Before correcting the systematic effect			Syst. effect	After correcting the systematic effect		
	Azimuth	V	$\bar{V}$		Azimuth	V	$\bar{V}$
1	27°52′ 35″.39	—6″.73	—3″.41	0″.00	27°52′ 35″.39	—0″.64	—3″.41
2	27 52 37.80	—4.32	—1.00	2.44	27 52 35.36	—0.67	—3.44
3	27 52 40.91	—1.21	2.11	4.88	27 52 36.03	0.00	—2.77
4	27 52 44.86	2.74	6.06	7.32	27 52 37.54	1.51	—1.26
5	27 52 48.56	6.44	9.76	9.76	27 52 38.80	2.77	0.00
6	27 52 45.20	3.08	6.40	12.20	27 52 33.00	—3.03	—5.80
Mean	27 52 42.12	0.00	3.32	Mean	27 52 36.03	0.00	—2.77
μ_0	±4.98″	$\bar{\mu}_0$	±6.16″	μ_0	±2.00″	$\bar{\mu}_0$	±3.64″
μ_A	±2.03″	$\bar{\mu}_A$	±2.52″	μ_A	±0.82″	$\bar{\mu}_A$	±1.49″

Date: 14 July, 1980			Temperature: 19 °C—24 °C				Weather: stable
Meas. No.	Before correcting the systematic effect			Syst. effect	After correcting the systematic effect		
	Azimuth	V	$\bar{V}$		Azimuth	V	$\bar{V}$
1	27°52′ 37″.15	—4″.67	—1″.65	0″.00	27°52′ 37″.15	0″.04	—1″.65
2	27 52 37.24	—4.58	—1.56	1.88	27 52 35.36	—1.75	—3.44
3	27 52 42.32	0.50	3.52	3.76	27 52 38.56	1.45	—0.24
4	27 52 42.89	1.07	4.09	5.64	27 52 37.25	0.14	—1.55
5	27 52 46.85	5.03	8.05	7.52	27 52 39.33	2.22	0.53
6	27 52 44.44	2.62	5.64	9.40	27 52 35.04	—2.07	—3.76
Mean	27 52 41.82	0.00	3.02	Mean	27 52 37.11	0.00	—1.69
μ_0	±3.91″	$\bar{\mu}_0$	±5.12″	μ_0	±1.70″	$\bar{\mu}_0$	±2.51″
μ_A	±1.60″	$\bar{\mu}_A$	±2.09″	μ_A	±0.69″	$\bar{\mu}_A$	±1.02″

(Continued Table VIII)

Date: 15 July, 1980				Temperature: 21 °C—28 °C			Weather: stable
Meas. No.	Before correcting the systematic effect			Syst. effect	After correcting the systematic effect		
	Azimuth	V	$\bar{V}$		Azimuth	V	$\bar{V}$
1	27°52′ 36″.64	—6″.78	—2″.16	0″.00	27°52′ 36″.64	—0″.98	—2″.16
2	27 52 41.97	—1.45	3.17	2.32	27 52 39.65	2.03	0.85
3	27 52 40.54	—2.88	1.74	4.64	27 52 35.90	—1.72	—2.90
4	27 52 46.13	2.71	7.33	6.96	27 52 39.17	1.55	0.37
5	27 52 45.76	2.34	6.96	9.28	27 52 36.48	—1.14	—2.32
6	27 52 49.48	6.06	10.68	11.60	27 52 37.88	0.26	—0.92
Mean	27 52 43.42	0.00	4.62	Mean	27 52 37.62	0.00	—1.18
μ_0	±4.60″	$\bar{\mu}_0$	±6.84″	μ_0	±1.54″	$\bar{\mu}_0$	±2.01″
μ_A	±1.88″	$\bar{\mu}_A$	±2.79″	μ_A	±0.63″	$\bar{\mu}_A$	±0.82″

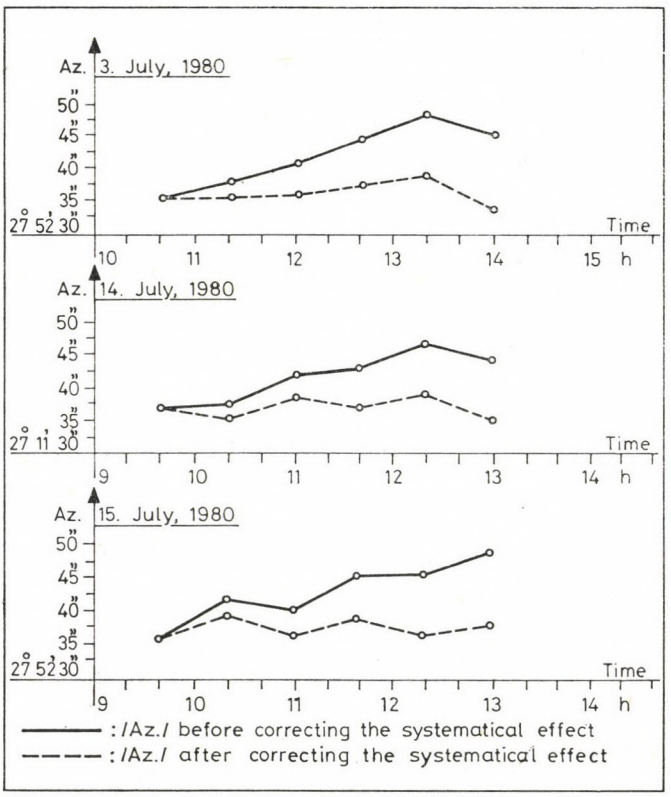

Fig. 6. The azimuth of the city tower. Instrument: MOM Gi-B2 No 023119 (old)

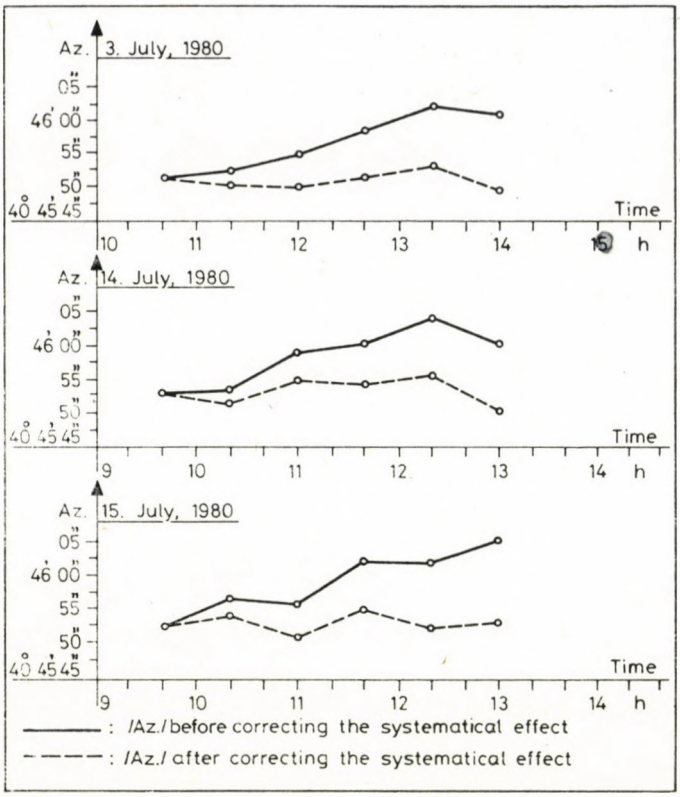

Fig. 7. The azimuth of the E. tower of the church. Instrument: MOM Gi-B2 No 023119 (old)

5. Evaluation of the error due to the drift

Linear interpolation was calculated for the different sets of the azimuth results on the assumption that the first measurement is nearly free from the systematic effect (as it is clear from the comparison with the astro-azimuths). The interpolation calculations were made for 12 sets of azimuth results, each set consisting of 6 independent determinations. The systematic effect for each independent measurement of some sets is shown as an example in the fourth column of Table VIII. The mean value of this rate is about 2 seconds of arc per each measurement, it increases systematically excluding the first measurement.

6. Methods of elimination of the systematic effect

6.1 *Drift compensation method*

In azimuth determination for the orientation purposes using the gyro-theodolite in geodetic works the least number of independent determinations is two determinations with two different starts. This number increases in higher

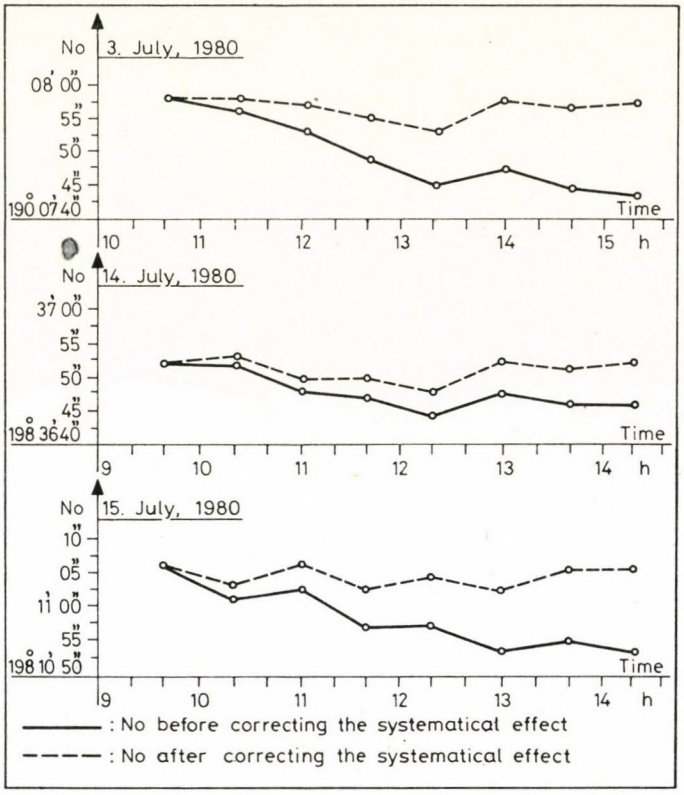

Fig. 8. The Gyro-north (*No*). Instrument: MOM Gi-B2 No 023119 (old)

order geodetic works, it may reach six or eight independent measurements.

To get better azimuth results with an old gyrotheodolite according to this method, *the number of independent measurements made in the calibration is the same as the number of independent measurements in the azimuth determination*, and the values of the instrument constant obtained from the calibration are used with the same order of the gyro-measurements for the calculation of the azimuth values, i.e. the first value of Δ, is used to calculate the azimuth (A_1) from the first gyro-north (No_1), and the second value gives the second azimuth value, and so on, or in other words one has to use the Δ values (Δ_1, $\Delta_2, \ldots, \Delta_n$) in the calculation of azimuths ($A_1, A_2, \ldots, A_n$) respectively, using the gyro-north values ($No_1, No_2, \ldots, No_n$). For example if (S) is the rate of the systematic effect, and three independent measurements for the azimuth are required, then the calibration is also repeated three times to get three values for Δ.As the first measurement in the calibration and in the azimuth are considered free from the systematic effect, then the values of Δ and *No* in the three measurements are:

$$\Delta_1,\ \Delta_2 + S,\ \Delta_3 + 2S \quad \text{and}$$

$$No_1,\ No_2 + S,\ No_3 + 2S\,.$$

Then the calculated values for the azimuth A_1, A_2 and A_3 are:

$$A_1 = I_1 - No_1 + \Delta_1$$
$$A_2 = I_2 - (No_2 + S) + (\Delta_2 + S)$$
$$A_3 = I_3 - (No_3 + 2S) + (\Delta_3 + 2S)\,.$$

The mean value A is:

$$A = \frac{[I] - [No] + [\Delta]}{3} \quad \text{or}$$

$$A = \frac{[I] - [No] + [\Delta]}{n} \tag{11}$$

where n = number of the independent measurements.

In the above equation it is clear that the systematic effect is compensated even if there exists a small drift in the first Δ and No values. The following tables shows the coefficients of (S) in both the instrument constant (Δ) and the gyro-north (No) for each measurement in sets with different number of measurements: (2, 3, 4, 5, 6) measurements. The coefficients are of the same value and of opposite sign, therefore (S) is compensated in the azimuth calculations.

No		No of measurements in the set				
		2	3	4	5	6
order of indep. meas. of the set	1st	0	0	0	0	0
	2nd	−1	−1	−1	−1	−1
	3rd		−2	−2	−2	−2
	4th			−3	−3	−3
	5th				−4	−4
	6th					−5
SUM		−1	−3	−6	−10	−15

Δ		*No* of measurements in the set				
		2	3	4	5	6
order of indep. meas. of the set	1st	0	0	0	0	0
	2nd	1	1	1	1	1
	3rd		2	2	2	2
	4th			3	3	3
	5th				4	4
	6th					5
SUM		1	3	6	10	15

It is quite inconvenient to use more than one value for the instrument constant for the same gyrotheodolite, and it is more practical to have only one Δ value for the gyrotheodolite. Therefore in this solution it is preferable

Table IX

Results of the gyro-azimuths affected with the drift

Sighted station: the city tower — Astro-azimuth: 27°52′38″80

Meas. No.	the calculated azimuth values				
	using Δ_2	using Δ_3	using Δ_4	using Δ_5	using Δ_6
Azimuth values of 3 July, 1980					
1	27°52′35″.95	27°52′34″.76	27°52′33″.37	27°52′32″.31	27°52′31″.39
2	27 52 38.36	27 52 37.17	27 52 35.78	27 52 34.72	27 52 33.80
3		27 52 40.28	27 52 38.89	27 52 37.83	27 52 36.91
4			27 52 42.84	27 52 41.78	27 52 40.86
5				27 52 45.48	27 52 44.56
6					27 52 41.20
Mean	27 52 37.16	27 52 37.40	27 52 37.72	27 52 38.42	27 52 38.12
Azimuth values of 14 July, 1980					
1	27 52 37.71	27 52 36.52	27 52 35.13	27 52 34.07	27 52 33.15
2	27 52 37.80	27 52 36.61	27 52 35.22	27 52 34.16	27 52 33.24
3		27 52 41.69	27 52 40.30	27 52 39.24	27 52 38.32
4			27 52 40.87	27 52 39.81	27 52 38.89
5				27 52 43.77	27 52 42.85
6					27 52 40.44
Mean	27 52 37.76	27 52 38.27	27 52 37.88	27 52 38.21	27 52 37.82
Azimuth values of 15 July, 1980					
1	27 52 37.20	27 52 36.01	27 52 34.62	27 52 33.56	27 52 32.64
2	27 52 42.53	27 52 41.34	27 52 39.95	27 52 38.89	27 52 37.97
3		27 52 39.91	27 52 38.52	27 52 37.46	27 52 36.54
4			27 52 44.11	27 52 43.05	27 52 42.13
5				27 52 42.68	27 52 41.76
6					27 52 45.48
Mean	27 52 39.87	27 52 39.09	27 52 39.30	27 52 39.13	27 52 39.42

to use the mean of the calibrated Δ values as the instrument constant, i.e., $\frac{[\Delta]}{n}$, to be used in the calculation of independent azimuths. In this case the drift will be compensated in the mean of the azimuths but still remains in the independent values.

Table IX shows the azimuths calculated according to this method, the tabulated results represent 5 sets of 2, 3, 4, 5 and 6 independent measurements. The calibration results of the first day shown in Table II were used in the calculation of Table IX. In Table IX the mean azimuth of each set is of high accuracy when compared with the astronomical azimuth, the difference between these mean values and the astronomical azimuth is between ± 1 second of arc, but single azimuth values are still contain the systematic effect.

To calculate the accuracy of these measurements and the mean square error for the mean values, the drift must be eliminated. The following formula gives the drift d in the independent azimuths, it is valid for azimuths of any order in observation sets having any number of independent measurements:

$$d_{ij} = \frac{i - 2j + 1}{2} \cdot S \tag{12}$$

where d_{ij} = the drift present in the azimuth number j of an observation set consisting of i independent measurements,
i = the number of independent measurements in the set,
j = the order of the independent values in the set,
S = the rate of the drift.

If S is known for any gyrotheodolite, then the drift corrections can be calculated and applied to different azimuths of any observation set consists of a given number of measurements (Eq. 12).

For the gyrotheodolite under investigation, $S = 2''$, as previously estimated, it was used in the calculation of the drift (Eq. 12) in different azimuths of the sets shown in Table IX, the following Table shows the drift distribution (in seconds of arc) in the azimuths of these sets.

Az.		No. of measurements in the set				
		2	3	4	5	6
order of indep. meas. of the set	1st	1″	2″	3″	4″	5″
	2nd	−1	0	1	2	3
	3rd		−2	−1	0	1
	4th			−3	−2	−1
	5th				−4	−3
	6th					−5
SUM		0	0	0	0	0

The azimuth values corrected for the drift can be calcultaed directly using the following formula,

$$A_{ij} = I_j - No_j + \Delta_i - \frac{i - 2j + 1}{2} \cdot S \quad \text{or}$$

$$A_{ij} = I_j - No_j + \Delta_i - d_{ij} \tag{13}$$

where i, j have the same meaning as in Eq. 12,
A = the calculated azimuth free of the drift,

I, No, Δ have the same meaning as in Eq. 7. For illustrating Eq. 12 let us calculate for example the third azimuth in a set consisting of 5 independent measurements, then, $A_{53} = I_3 - No_3 + \Delta_5 - d_{53}$, here Δ_5 means the mean of 5 independent values obtained in the calibration.

Some of the azimuth results after the elimination of the drift effect are tabulated in Tables X, XI, the mean square error for the single measurement is ± 0.5—2 seconds of arc and for the mean value ± 0.2—1 second of arc. When the results were compared with the astronomical azimuths, the accuracy was ± 1—3 seconds of arc for the single value and ± 0.5—2 seconds of arc for the mean value.

6.2 *Other correcting methods*

There are other two possibilities for calculating the gyro-azimuths free of the drift effect using the calibration and azimuth measurements. The first is to make linear interpolation for the calibration results (Table IV) to get values for the instrument constant free from drift, the same operation is to be made for the gyor-north observations of the azimuth measurements to obtain values free from drift, then the calculated azimuths, in this case are free from the drift. Using this method the obtained results agreed with good accuracy when compared with the astronomical azimuths, the mean square error obtained for a single measurement was between ± 1—4″ and for the mean, it is between ± 1—2″.

The second possibility is to use the calibration results corrected for the drift (Table IV) in the calculations of the azimuths using the measured gyro-north values then, linear interpolation is to be made for the obtained azimuths to get the drift-free values, Table VIII shows some of the obtained results. The obtained accuracy is between ± 1.5—2″ for the single value and between ± 0.7—1.0″ for the mean value, while when compared with the astronomical azimuth, it was found to be between 2—4″ for the single value and between ± 1—1.5″ for the mean value.

The above two possibilities for calculating azimuths free from the drift effect are also easy to be applied, because the linear interpolation made for the measurements can be achieved easily and quickly using a programable boket calculator.

Table XII shows a comparison between azimuth results of a given direction measured in some days with both the new and the old gyrotheodolites, after correcting the drift present in the measurements of the old one according to the proposed method. The results of both instruments were also compared with the astronomical azimuths. It is clear from this Table that the results of both the new and the old gyrotheodolites agree with a high accuracy.

Table XI

Results of the gyro-azimuths after the elimination of the systematic effect (the drift)

Instrument: MOM Gi-B2 No. 023119 (Old)

Measuring station: the northern point of the base line in Sopron

Sighted station: the city tower
Value of the astro-azimuth: 27°52′38″80
Date of the gyro-measurement: 15 July, 1980
Weather: stable. Temperature: 21—28 °C

The calibration station: Sopron, Bánfalva observatory
Date of the calibration: May, June, July, 1980
Temperature of the calibration: 13 °C
Calibrated value of instrument constant (Δ): 90°11′51″80

Meas. No.	2 measurements			3 measurements			4 measurements			5 measurements			6 measurements		
	Azimuth	V	$\bar{V}$	Azimuth	V	$\bar{V}$	Azimuth	V	$\bar{V}$	Azimuth	V	$\bar{V}$	Azimuth	V	$\bar{V}$
1	27°52′38″20	−1″67	−0″60	27°52′38″01	−1″08	−0″79	27°52′37″62	−1″68	−1″18	27°52′37″56	−1″57	−1″24	27°52′37″64	−1″78	−1″16
2	27 52 41.53	+1.66	+2.73	27 52 41.34	+2.25	+2.54	27 52 40.95	+1.65	+2.15	27 52 40.89	+1.76	+2.09	27 52 40.97	+1.55	+2.17
3				27 52 37.91	−1.18	−0.89	27 52 37.52	−1.78	−1.28	27 52 37.46	−1.67	−1.34	27 52 37.54	−1.88	−1.26
4							27 52 41.11	+1.81	+2.31	27 52 41.05	+1.92	+2.25	27 52 41.13	+1.71	+2.33
5										27 52 38.68	−0.45	−0.12	27 52 38.76	−0.66	−0.04
6													27 52 40.48	−1.06	+1.68
Mean (Am)	27°52′39″87	0.00	+1.07	27°52′39″09	0.00	+0.29	27°52′39″30	0.00	+0.50	27°52′39″13	0.00	+0.33	27°52′39″42	0.00	+0.62
Mean square errors	μ_0	±2.35		μ_0	±1.95		μ_0	±2.00		μ_0	±1.75		μ_0	±1.65	
	μ_{Am}	±1.67		μ_{Am}	±1.13		μ_{Am}	±1.00		μ_{Am}	±0.78		μ_{Am}	±0.67	
	$\bar{\mu}_0$	±2.70		$\bar{\mu}_0$	±1.98		$\bar{\mu}_0$	±2.08		$\bar{\mu}_0$	±1.79		$\bar{\mu}_0$	±1.78	
	$\bar{\mu}_{Am}$	±1.91		$\bar{\mu}_{Am}$	±1.15		$\bar{\mu}_{Am}$	±1.04		$\bar{\mu}_{Am}$	±0.80		$\bar{\mu}_{Am}$	±0.73	

Table X

Results of the gyro-azimuths after the elimination of the systematic effect (the drift)

Instrument: MOM Gi-B2 No. 023119 (Old)

Measuring station: the northern point of the base line in Sopron

Sighted station: the city tower
Value of the astro-azimuth: 27°52′38″.80
Date of the gyro-measurement: 14 July, 1980
Weather: stable. Temperature: 19—24 °C

The calibration station: Sopron, Bánfalva observatory
Date of the calibration: May, June, July, 1980
Temperature of the calibration: May, June, July, 1980
Calibrated value of instrument constant (Δ): 90°11′51″.80

Meas. No.	2 measurements			3 measurements			4 measurements			5 measurements			6 measurements		
	Azimuth	V	$\bar{V}$	Azimuth	V	$\bar{V}$	Azimuth	V	$\bar{V}$	Azimuth	V	$\bar{V}$	Azmuth	V	$\bar{V}$
1	27°52′38″.71	+0″.96	−0″.09	27°52′38″.52	+0″.25	−0″.28	27°52′38″.13	+0″.25	−0″.67	27°52′38″.07	+0″.14	−0″.73	27°52′38″.15	+0″.33	−0″.65
2	27 52 36.80	−0.96	−2.00	27 52 36.61	−1.66	−2.19	27 52 36.22	−1.66	−2.58	27 52 36.16	−2.05	−2.64	27 52 36.24	−1.58	−2.56
3				27 52 39.69	+1.42	+0.89	27 52 39.30	+1.42	+0.50	27 52 39.24	+1.03	+0.44	27 52 39.32	+1.50	+0.52
4							27 52 37.87	−0.01	−0.93	27 52 37.81	−0.40	−0.99	27 52 37.89	+0.07	−0.91
5										27 52 39.77	+1.56	+0.97	27 52 39.85	+2.03	+1.05
6													27 52 35.44	−2.38	−3.36
Mean (Am)	27°52′37″.76	0.00	−1.04	27°52′38″.27	0.00	−0.53	27°52′37″.88	0.00	−0.92	27°52′38″.21	0.00	−0.59	27°52′37″.82	0.00	−0.98
Mean square errors	μ_0	±1″.35		μ_0	±1″.55		μ_0	±1″.22		μ_0	±1″.40		μ_0	±1″.71	
	μ_{Am}	±0.96		μ_{Am}	±0.90		μ_{Am}	±0.61		μ_{Am}	±0.63		μ_{Am}	±0.70	
	$\bar{\mu}_0$	±2.00		$\bar{\mu}_0$	±1.68		$\bar{\mu}_0$	±1.66		$\bar{\mu}_0$	±1.55		$\bar{\mu}_0$	±2.02	
	$\bar{\mu}_{Am}$	±1.42		$\bar{\mu}_{Am}$	±0.97		$\bar{\mu}_{Am}$	±0.83		$\bar{\mu}_{Am}$	±0.69		$\bar{\mu}_{Am}$	±0.83	

Table XII

Final results of gyro-azimuths of the new and old gyrotheodolites

(Comparison)

Measuring station: the northern point of the base line in Sopron

Sighted station: the city tower — Astro-azimuth value: 27°52′38″.80

Meas. No.	The new gyrotheodolite						The old gyrotheodolite					
	23 August, 1979			3 September, 1979			14 July, 1980			15 July, 1980		
	Azimuth	V	$\bar{V}$	Azimuth	V	$\bar{V}$	Azimuth	V	$\bar{V}$	Azimuth	V	$\bar{V}$
1	27°52′38″.79	−0″.96	−0″.01	27°52′40″.50	1″.99	1″.70	27°52′38″.15	0″.33	−0″.65	27°52′37″.64	−1″.78	−1″.16
2	27 52 37.70	−2.05	−1.10	27 52 40.62	2.11	1.80	27 52 36.24	−1.58	−2.56	27 52 40.97	1.55	2.17
3	27 52 38.80	−0.95	0.00	27 52 36.03	−2.48	−2.77	27 52 39.32	1.50	0.52	27 52 37.54	−1.88	−1.26
4	27 52 42.38	2.63	3.58	27 52 36.70	−1.81	−2.10	27 52 37.89	0.07	−0.91	27 52 41.13	1.71	2.33
5	27 52 41.90	2.15	3.10	27 52 37.10	−1.41	−1.70	27 52 39.85	2.03	1.05	27 52 38.76	−0.66	−0.04
6	27 52 38.90	−0.85	0.10	27 52 40.10	1.59	1.30	27 52 35.44	−2.38	−3.36	27 52 40.48	−1.06	1.68
Mean (Am)	27 52 39.75	0.00	0.95	27 52 38.51	0.00	−0.29	27 52 37.82	0.00	−0.98	27 52 39.42	0.00	0.62
Mean square errors	μ_0	±1″.91		μ_0	±2″.11		μ_0	±1″.71		μ_0	±1″.65	
	μ_{Am}	±0.78		μ_{Am}	±0.86		μ_{Am}	±0.70		μ_{Am}	±0.67	
	$\bar{\mu}_0$	±2.17		$\bar{\mu}_0$	±2.14		$\bar{\mu}_0$	±2.02		$\bar{\mu}_0$	±1.78	
	$\bar{\mu}_{Am}$	±0.89		$\bar{\mu}_{Am}$	±0.87		$\bar{\mu}_{Am}$	±0.83		$\bar{\mu}_{Am}$	±0.73	

7. Conclusion

Gyrotheodolites are widely used on the surface and in the underground surveying for orientation and azimuth determination purposes. In geodetic works of higher order, azimuth measurements must be repeated with independent starts to get the accuracy needed for such geodetic works. Also in the calibration it is necessary to repeat the independent gyro-north measurements for a direction of known astronomical azimuth to get a reliable value for the instrument constant.

Using the newly manufactured gyrotheodolite of MOM, the required accuracy can be obtained by repeating the azimuth determinations. This suits the required accuracy without facing the problem of the drift. Also a reliable value for the instrument constant can be obtained from the calibration without facing this problem.

In the results of the old instrument there was a clear tendency for the gyro-north values to decrease when repeating the independent measurements, therefore the calculated azimuths are greatly affected, i.e. we get a systematic increase in the azimuths of repeated measurements, and the mean value of the azimuth is far from the astronomical azimuths. Also the value of the instrument constant obtained from the calibration will not be reliable.

When using the proposed simple methods of the elimination of the systematic effect, a reliable value of the instrument constant can be obtained and azimuth results of high accuracy can also be obtained, this accuracy is nearly the same as the accuracy obtained when using a new gyrotheodolite. According to the proposed method of the elimination of the systematic effect (the simplest method) *the number of independent measurements made in the calibration for the determination of the instrument constant must be the same as the number of independent measurements for the azimuth of the required direction.* This number of independent measurements is of course decided according to the accuracy required, i.e. according to the order of the surveying work.

The conclusion of the paper is that the old gyrotheodolites can be utilized with the same efficiency as the new gyrotheodolites, and can give azimuth results of high accuracy needed for different geodetic works.

In developing countries where great areas are unsurveyed, a great number of geodetic networks and traverses are needed to establish a system of horizontal control. The orientation of such nets and traverses need many measurements for azimuth determination. Also in the countries who are rich in mining, many underground traverses are needed in mine surveying, such traverses are also oriented by making azimuth measurements. In such cases, gyrotheodolites are widely used for the orientation purposes on the surface and in the underground, therefore they may become exhausted due to their use for a long time in numerous measurements of azimuth with independent

starts, and in the same time it may be financially difficult to get new gyrotheodolites due to their high prices.

The results of the paper may present a practical and cheap solution for this problem because the research had proved that it is possible to utilize the old gyrotheodolites with the same efficiency as the new gyrotheodolites and can give azimuth results of high accuracy.

Acknowledgements

Sincere thanks and appreciation are extended to the late Prof. Dr. F. Halmos† for his valuable advices and guidance during the period of his supervision before his death on 21 October, 1980.

The help of Dr. J. Somogyi, the director of the Geodetic and Geophysical Research Institute in Sopron, Hungary are acknowledged. Appreciation is also due to Dr. Gy. Szádeczky-Kardoss for his help in the determination of the astronomical azimuths, and to Mr. A. Orbán for his generous help.

REFERENCES

GREGERSON, L. F. 1970: An investigation of the MOM's Gi-B2 gyrotheodolite. *The Canadian Surveyor*, 1, 117—135.

GREGERSON, L. F.—VANICEK, P.—SYMONDS, G. R. 1971: Report from experiments with a gyroscope equipped with electronic registration. Paper presented at theIAG congress in Moscow.

HALMOS, F. 1966a: Untersuchungen der Kreiseltheodolite sowie deren Anwendungsmöglichkeiten. *Allgemeine Vermessungs-Nachrichten*, 73, 424—437.

HALMOS, F. 1966b: Die Schnellbestimmung der Azimuts mit Hilfe von Girotheodolitmessungen. *Acta Geod. Geoph. Mont. Hung.*, 1, 197—213.

HALMOS, F. 1966c: Ermittlung der Ruhelage der Schwingungen bei Girotheodoliten. *Acta Geod. Geoph. Mont. Hung.*, 1, 361—377.

HALMOS, F. 1968a: Theoretical and practical problems of the geodetical use of gyrotheodolites. Manuscript. Dissertation.

HALMOS, F. 1968b: Methodological and accuracy investigations of gyrotheodolite azimuth determinations. *Geodézia és Kartográfia*, 20, 7—19.

HALMOS, F. 1968c: Test of torsional suspension bands of gyrotheodolites. *Bányászati Lapok*, 101, 569—574.

HALMOS, F. 1971: Instrumentelle und methodische zeitgemässen Kreiseltheodoliten. *Allgemeine Vermessungsnachrichten*, 78, 105—111.

HALMOS, F. 1972: Systematic and random errors of direction measurements with gyrotheodolites. *MOM Review*, 4, 24—32.

HALMOS, F. 1974a: Einige Probleme der zweckmässigen Anwendung von Kreiseltheodoliten in der Ingenieurgeodäsie. *Allgemeine Vermessungsnachrichten*, 81, 179—184.

HALMOS, F. 1974b: Der mittlere Koordinatenfehler des Punktes bei mehrfach orientierten Polygonzügen. *Acta Geod. Geoph. Mont. Hung.*, 9, 153—164.

HALMOS, F.: 1976: Up-to-date methods of the determination of the rest position of gyroscopic swingings. *Acta Geod. Geoph. Mont. Hung.*, 11, 1—20.

HALMOS, F. 1977a: Theoretical and practical problems of the use of gyrotheodolites in geodesy. MTA GGKI Kiadványa, No. 6.

HALMOS, F. 1977b: High precision measurements and evaluation method for azimuth determination with gyrotheodolites. *Manuscripta Geodaetica*, 2, 213—231.

РЕЗУЛЬТАТЫ ОБРАБОТКИ ДАННЫХ И МЕТОДЫ ОПРЕДЕЛЕНИЯ АЗИМУТА С ПОМОЩЬЮ СТАРЫХ И НОВЫХ ГИРОТЕОДОЛИТОВ

АБДЕЛХАМИД КАМАЛ Х.

РЕЗЮМЕ

В статье рассматриваются результаты эталонирований гиротеодолитов старых и новых типов МОМ Gi – B2 а также результаты измерений гироазимута проведенных при помощи этих инструментов. Измерения были проведены в Шопроне в 1979 – 1980 гг.

Цель данной работы — исследование точности значений гиро-азимутов при использовании двух инструментов. Поэтому автор подробно исследовал эффективность эталонирования и определения гироскопического севера при помощи старого инструмента.

В результате исследований автором предлагаются новые методы, чтобы точность измерений гиро-азимутов, полученных с помощью старого инструмента достигали точность нового инструмента. Таким образом станет возможным применение старых гидротеодолитов в более сложных геодезических работах подобно новым гидротеодолитам.

Результаты эталонирований двух гидротеодолитов и измерений гироскопического севера проведенных с помощью старого инструмента приведены в таблице. Наконец сравниваются точности определения азимута с помощью старого инструмента и предложенного нового метода с измерениями, проведенными с помощью нового инструмента, а также оба с астрономическим азимутом одного и того же направления. Результаты и точность также приведены в таблице.

Acta Geodaet., Geophys. et Montanist. Acad. Sci. Hung. Volume 17 (2), pp. 237—253 (1982)

LASER RANGING OBSERVATIONS AT THE SATELLITE GEODETIC OBSERVATORY (SGO)

I. KARDOS—T. BORZA—T. VASS

SATELLITE GEODETIC OBSERVATORY, PENC, HUNGARY

[Manuscript received February 14, 1981]

This paper describes the installation of the laser ranging system at the SGO, Penc and presents its initial results. The system is mounted on the satellite telescope Zeiss SBG and it was developed and installed in an INTERCOSMOS cooperation during 1977 and 1978. The ranging performance is typical for a first generation instrument. During best transits 50 cm RMS values can be obtained. In 1979, 27 passes of GEOS-1 and GEOS-3 were observed. In 1980 until September 1, 44 passes with 1081 echoes have been registered.

Introduction

An SGO team has been dealing with the systematic photographic observations of satellites since 1975. We have two observing instruments to this end: one Soviet camera of type AFU-75 and one camera from the GDR (type SBG, Satellitenbeobachtungsgerät). As the Potsdam group has succesfully combined its SBG with a laser ranging equipment and INTERCOSMOS assured a first generation laser gun to the SGO, it was expedient to develop a kind of laser ranging equipment which consisted of a laser-gun, mounted on an SBG and controlled by special electronics.

Due to the INTERCOSMOS cooperation, we received in June 1977 the laser-gun, constructed at the Charles University in Prague. To enable its mounting on the SBG, we had to make previously two mechanical modifications, namely:

a) to add a holding-console for the mounting of the laser-gun and to compensate for the increased weight. Since the laser-head was relatively far positioned from the rotation-axis, this balancing was a real problem. The laser-head has a weight of 30 kg, the console of 30 kg, so a counter-weight of 350 kg had to be installed,

b) to modify the receiving-optics so that the reflected light should fall on the cathode of the PMT (Photomultiplier).

The telescope was converted for continuous photographic observations. The auxiliary mirror (see Fig. 3) reflects the light onto the PMT in the focus of the Cassegrain-system; this mirror can be pulled out by a single motion, consequently the telescope is adapted to make photographs in a Schmidt-system.

For these modifications, the electronical units were partly purchased, partly built in the workshop of the SGO.

1.
Construction of the laser ranging equipment

The laser-ranging equipment mounted on the SBG camera consists of 3 main units:

laser transmitter
laser receiver
electronics.

The block-scheme of the equipment is shown in Fig. 1.

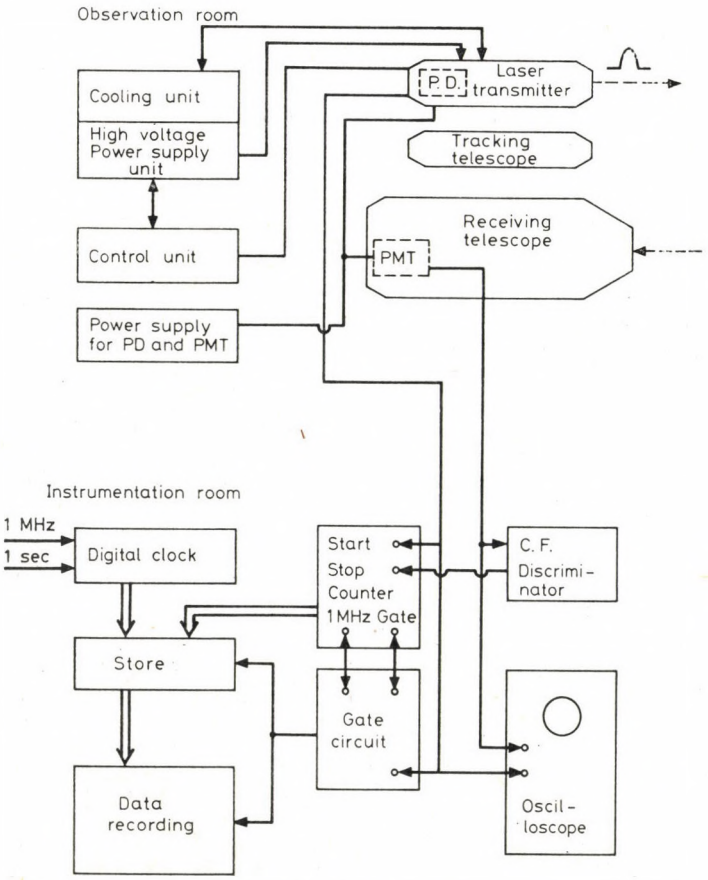

Fig. 1

Of the units shown, the transmitter and the PMT belonging to the receiver are placed in the observational room of the SBG, the rest is in the instrument room below it; the time-service is in the main building.

1.1 *Laser transmitter*

The technical data of the laser-gun, made by the Charles University (Prague) within the framework of the INTERCOSMOS cooperation are as follows:

active material	ruby rod diam. 10 mm, length 150 mm
wave length	694.3 mm
Q-switch	revolving mirror
length of one pulse	20—30 ns
energy of one pulse	1 Joule
repetition frequency	1 Hz
beam divergence with telescope	0.8—1.0 mrad
cooling	distilled water

The laser transmitter consists of 4 main units:

— laser head,
— high voltage supply unit,
— cooling system,
— control unit.

The head contains an oscillator, a photodiode (PD) and the transmitter-telescope. The latter is of the Galilei-type and it magnifies 10 times the beam diameter coming from the oscillator. The schematic diagram of this laser head is shown in Fig. 2. To minimize noise and to protect the PMT, a diaphragm

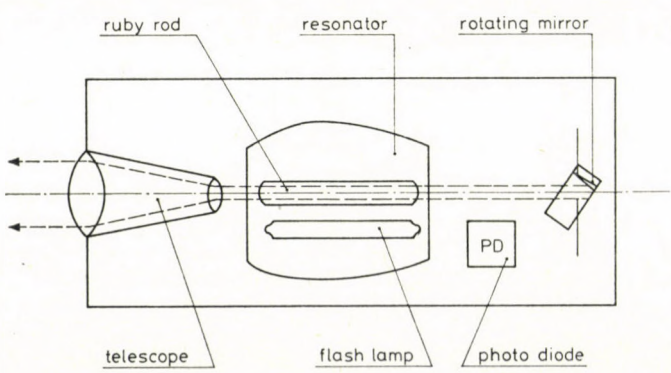

Fig. 2

and a narrow-band interference filter (0.5 nm) are used. The main mirror only for detection, tracking is carried out by the tracking telescope. Its relative illuminating power is sufficient only to observe bright objects. To track smaller, distant satellites (STARLETTE, LAGEOS) the main mirror had to be made suitable for tracking. This is possible if a mirror with special reflecting capacity (dichroic filter) is used instead of the flat mirror.

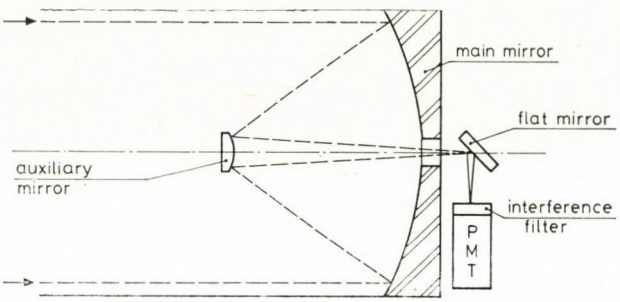

Fig. 3

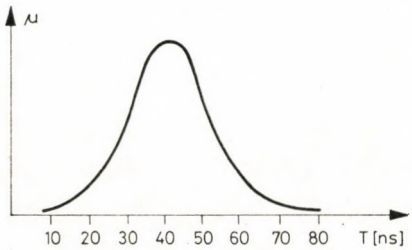

Fig. 4

1.2 *Receiving electronics*

For the measurement of the travel time of the light pulse, two different methods have been adopted. Earlier, a 100 MHz counter was used (made by EMG, Hungary) with an interval-measurement accuracy of 10 ns. This counter is started by the START signal, coming from the photodiode (PD) which detects the output signal of the laser-gun. The counter is stopped by the STOP signal coming from the PMT. The photodiode (PD) is situated between the revolving mirror and the ruby rod (Fig. 2). The shape of the pulse detected by the PD is shown in Fig. 4.

The detection of the START pulse is accomplished by the leading edge detection method, while a constant fraction discriminator is applied to detect a STOP pulse. The latter is carried out by an ORTEC type discriminator whose calibration level is 50 mV. The PMT is of Soviet manufacture (type FEU-84).

As the START pulse is detected by a leading edge detector, the amplitude fluctuation of the laser pulse would lead to timing errors. Therefore the energy of all passes is measured. A high speed 3 bit analog-digital converter (ADC) produces the digit which is proportional to the pulse energy. This digit is recorded together with the timing data.

The 100 MHz-counter is modified into an event-timer (resolution 1 ns). This can record the epochs of the START and STOP pulses with a resolution of 1 ns. In this case, there is no need to record the epoch separately, as both

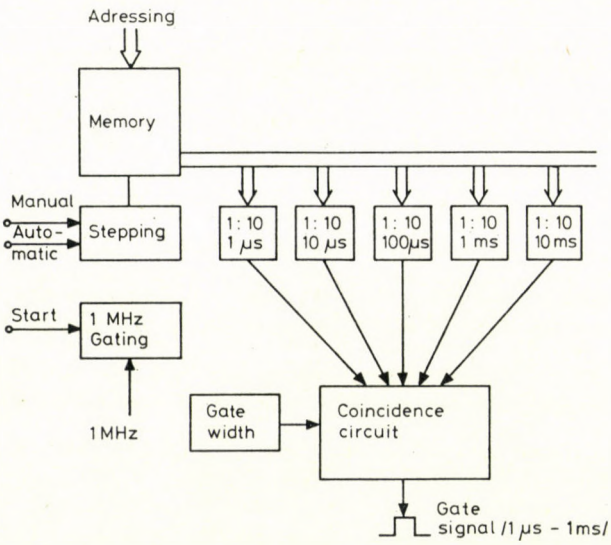

Fig. 5

the travel time and the epoch can be determined from these two epochs. The event-timer is driven by an atomic frequency standard and is started and synchronized, respectively, by the minute and second signals of the time service.

This event-timer has two different inputs, one of them is gated like the STOP input of the counter. The gating signal is produced by a gating circuit; the gating may be manual or automatic.

In the manual mode the values are set continuously during the observation by the operator. In the automatic mode, the gate values are held in a RAM in steps 5 and 10 s, respectively; it sets the desired values automatically having started the tracking. The schematic block diagram of the gating circuit is shown in Fig. 5.

The gating time is adjustable from 1 μs to 99.999 ms, in steps of 1 μs and 10 μs. The width of the gate is adjustable from 1 μs to 9.999 ms. The value

of the gating time is involved in the prediction with steps of 5 and 10 s, resp. (see Table I).

A digital clock serves for the determination of the epoch with a resolution of 100 μs. This clock is synchronized by the *s*-signal of the central time-service and is driven by the atomic frequency standard.

Travel time and epoch are recorded together so that the value of the digital clock is transferred by the START signal into a storage; when the STOP signal arrives, these two values are punched and printed. A key-board belonging to the data recording apparatus enables to store also other data on the punch-tape (pass, meteorology).

For the analysis of the START and STOP (pulses) an oscilloscope of 350 MHz (made by IWATSU) is used which is supplemented by a scopephotocamera. The event-timer data are characterized by the same recording, here the START moment is stored till the arrival of the STOP signal.

1.3 *Mounting, tracking*

The realized mounting is the camera SBG itself which is modified to fit to laser-head. This camera has 4 axes, the tracking occurs along the 3rd one. The 4th axis serves for the setting of corrections. The axes are driven by DC-motors and tracking is controlled by punched tape. The velocity tape is selected from the catalogue, or it is computed and punched for the given pass with the help of the prediction program. During tracking the velocity values and the position of the 4th axis are adjusted by a potentiometer. The equipment can track satellites only by night when they are illuminated by the Sun. For tracking the haircross of the tracking telescope is used.

1.4 *Time-service*

The epoch of the laser observation is the epoch of the output of the laser-pulse which is recorded in UTC-system. The accuracy requirements for such equipments are approximately ± 100 μs. The synchronizing pulses for the clock and for the event-timer are supplied by the time-service of the SGO. It is based on a rubidium-oscillator (type XSR-B of R/S) with stability of $\pm 5 \cdot 10^{-11}$/month. With this frequency standard a digital clock (type MIKI for Hungary) is driven having a resolution of 100 μs. For rough control an external comparison with the signals of the short-wave transmitter-station OLB-5 is applied. For very accurate UTC-comparisons the TV-synchronous signals are measured in co-operation with the Hungarian Bureau of Standards and the time-service of URE CSAV in Prague. By these means, the accuracy of the UTC-time-service amounts to ± 10 μs.

The frequency-standard is controlled by a VLF phasemeter receiving 50 kHz standard signals of the station OMA. In a measurement series during a few days, the frequency can be calibrated with a relative accuracy of about $5 \cdot 10^{-12}$.

The simplified block-diagram of the time-service is shown in Fig. 6.

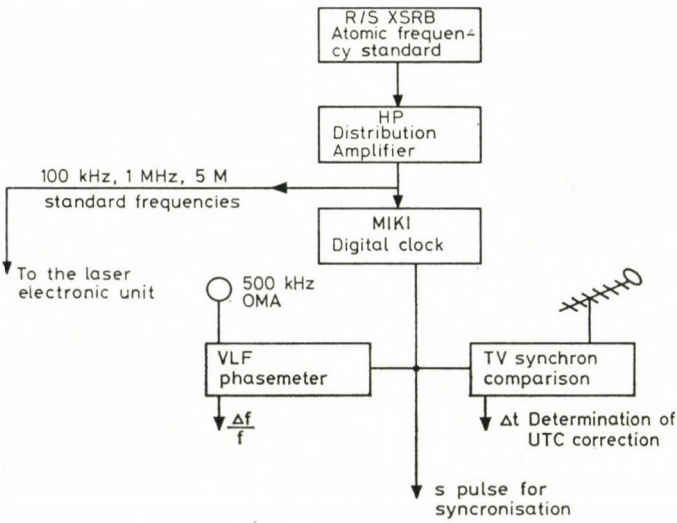

Fig. 6

1.5 *Concept for future projects*

The present first generation system is planned to be updated into a second generation one. This implies two main tasks:

— to increase the accuracy of ranging,

— to automatize the tracing.

The accuracy is influenced by the shape of the laser pulse, its stability, the detection of the START and STOP pulses and the resolution of the clock. The greatest problems are at present the shape and stability of the pulses. We plan to improve the Q-switch by substituting the revolving mirror with a Pockel's cell, later to reduce the width of the pulses by a pulse-splitting circuit. The accuracy of the detection could by increased by a faster PMT with a greater efficiency (type RCA 310034 A). Thus the range of the measurements can be increased, too.

The effectivity of the observations could be considerably increased by automatic tracking. The SBG in Potsdam was succesfully modified in the ZIPE on the same basis we also plan to develop our mount for automatic tracking.

According to experiences about the computer control of motions of the 3rd and 4th axes the automatic tracking could be realized. We plan to make these modifications partly by own development partly by purchases.

2.

2.1 *Prediction program*

Although the laser-system presently enables only the observation of visible satellites, the organization and scheduling of observation campaigns are promoted by a long-period program, the so-called *visibility prediction program.*

This program gives the visibility conditions of satellites for 400 (± 4) days and 100 (± 1) days. These informations can be obtained for the whole globe or for given stations (locations). In the first case, the program makes calculations in degrees of geographic latitude. In the latter case the program indicates of the shadow-entry and/or the shadow-exit are observable. This program is run on a CDC-3300 computer.

For every-day observations the ephemeris program is based on SAO orbital elements received weekly by telex. The inputs of this program are the elements on telex-tape, the date and the predicted duration in days. The difference between the calculated and measured slant-ranges is in general about 1 km.

The program calculates the setting data of the tracking system, gives the actual catalogue number of the velocity-controlling type, the estimated magnitude of the satellite, the input data for making a velocity-tape and the data for the gate control. The latter velocity program is used if there is no suitable tape in the catalogue.

For gate control essentially gate times are needed but the program calculates in addition the epoch belonging to the position, the position of the 3rd axis, the slant-range and the angle of elevation, too. This program is written for the desk calculator HP 9830. One example is shown in Table I.

2.2 *Preprocessing and filtering programs*

The observations, namely

— the synchronization control data of the digital clock,
— the measurements to the target,
— the measurements to the satellite,
— the synchronization control data of the digital clock are recorded on an 8-channel punch-tape in ASCII-code. The meteorological data are recorded in the observational report.

Table I

Laser		1980 7 21—22 Monday-Tuesday		Observer
	6508901			
	TK = 22 55.0 Ap = 310.4 Zp = 69.2 Del = 6.5 Tape 86	Tl = 22 53 44 = 25.3 To left	Magnitude: 7.9 7.8 8.5 Fk = 1240.4 Hk = 1122.1	

UT	Time	Sigm.	No.	G. time	Range	El.
22 53 44	0 0	23.7	0	894	1354.76	53.1
22 53 54	0 10	20.8	1	879	1328.93	55.0
22 54 4	0 20	17.8	2	866	1306.10	56.7
22 54 14	0 30	14.7	3	855	1286.42	58.3
22 54 24	0 40	11.6	4	846	1270.05	59.7
22 54 34	0 50	8.3	5	840	1257.11	60.9
22 54 44	1 0	5.0	6	836	1247.72	61.8
22 54 54	1 10	1.7	7	836	1241.95	62.4
22 55 4	1 20	—1.7	8	835	1239.86	62.5
22 55 14	1 30	— 5.0	9	836	1241.47	62.3
22 55 24	1 40	— 8.4	10	839	1246.76	61.7
22 55 34	1 50	—11.7	11	845	1255.69	60.7
22 55 44	2 0	—14.9	12	853	1268.18	59.5
22 55 54	2 10	—18.1	13	864	1284.13	58.0
22 56 4	2 20	—21.2	14	877	1303.40	56.3
22 56 14	2 30	—24.3	15	892	1325.85	54.5
22 56 24	2 40	—27.2	16	909	1351.33	52.6
22 56 34	2 50	—30.0	17	928	1379.65	50.7
22 56 44	3 0	—32.7	18	948	1410.66	48.8
22 56 54	3 10	—35.3	19	971	1444.16	46.8
22 57 4	3 20	—37.8	20	995	1480.00	44.9
22 57 14	3 30	—40.1	21	1020	1517.99	43.1
22 57 24	3 40	—42.4	22	1047	1557.98	41.2
22 57 34	3 50	—44.6	23	1075	1599.82	39.5
22 57 44	4 0	—46.6	24	1104	1643.36	37.7
22 57 54	4 10	—48.6	25	1134	1688.47	36.1

The preprocessing of the observational data is run on the desk computer HP 9830 B. The inputs of this program are the following:

— parameters and identifiers of the measuring conditions (date, number of satellite, meteorological data, etc.),

— data-tape of measurements,

— SAO orbit elements of the satellite.

Sequence of the calculations:

a) Raw filtering of measurement data (lower limit 500 km, upper limit 3000 km).

b) Computation of the reduction of the measured data (determination of the ranging epoch and topocentric distances). The corrections for the clocktime and clockrate of the digital clock, the time delay within the system, calculated from target measurements, the atmospheric corrections and the excentricity of the laser head related to the geometric reference point of the station are taken into account.

c) Fine filtering of measurement data. First the predicted range of the satellite is calculated from the SAO orbit elements for the observational epochs. Then the difference of the predicted and measured range is computed. (Observations with laser difference smaller than 5 km are neglected.) Finally, the difference ratios for seconds are calculated. The processing and analysis of these data lead to the filtered data.

d) Estimating the confidence of the measurement data. On the basis of the filtered data the coefficients of a 6th order polynomial are determined by regression analysis. According to our experience, this polynomial approximates well the topocentric distances of the satellite passing over the station. The program contains also more filtering possibilities. The estimated confidence of the measurements is calculated from the residuals. Based on extremely large residuals repeated filtering is possible if the analysis of the standard deviations makes it reasonable.

Inputs of the program (on 8-channel punch tape or magtape):

— epochs of shoots in MJD (Mean Julian Date),

— measured ranges in M meter.

The results of measurements in 1980 are shown in Table II. Figure 7 contains data for one pass (GEOS-1, August 28, 1980). This is a pass of an average point numbers; the upper part shows the measured values, the lower one the deviations from the approximating 6th order polynomial in function of time. The derived RMS-error is 0.89 m.

In 1980, we participated in the MERIT campaign. During August 1980, laser observations (7 passes, 167 points) for GEOS-3 were obtained.

2.3 *Utilisation of observation results*

Our observational data are processed by a program based on the short-arc method. In an international cooperation the data are regularly sent to the Astrosoviet coordinating centre. This cooperation provides a possibility to treat data of quasisynchronous laser ranging and photographic observations.

Table II

Total no of usebul returns 1103

GEOS-A

DATE	h	m	h	m	UR
800511	20	58	21	2	41
800512	21	1	21	6	29
800513	21	5	21	8	21
800514	21	12	21	15	3
800716	0	32	0	34	14
800721	22	53	22	55	16
800801	21	35	21	38	33
800802	21	39	21	42	38
800803	21	44	21	46	20
800807	19	55	19	59	47
800809	20	4	20	6	20
800822	23	8	23	10	14
800828	21	28	21	30	26
800903	19	49	19	52	15
800904	19	53	19	56	33
800905	19	57	20	0	25

GEOS-C

DATE	h	m	h	m	UR
800410	19	23	19	26	8
800411	19	8	19	10	16
800413	20	18	20	21	22
800414	20	3	20	6	19
800415	19	47	19	51	48
800417	19	19	19	20	17
800507	22	36	22	38	9
800511	23	16	23	18	38
800513	22	47	22	49	20
800523	23	35	23	38	14
800526	0	43	0	46	40
800624	20	40	20	42	15
800680	20	50	20	43	8
800707	22	24	22	25	16
800708	22	8	22	9	7
800710	21	39	21	41	19

(Continued Table II)

Date	h	m	h	m	UR
800711	23	2	23	6	13
800712	22	47	22	51	41
800715	22	3	22	6	27
800715	23	42	23	43	15
800717	23	12	23	15	26
800718	22	58	23	0	19
800721	23	51	23	55	45
800726	0	31	0	33	14
800727	0	16	0	19	26
800801	0	40	0	44	30
800802	0	25	0	29	29
800805	1	20	1	23	27
800806	1	4	1	8	23
800807	0	50	0	51	10
800808	0	35	0	37	32
800811	1	29	1	32	15

2.31 *Photo-laser method*

For the location of a point of the orbit the following are necessary:

a) three stations with synchronous laser observations,

b) synchronous photographic and laser observations at two different stations,

c) synchronous photographic and laser observations at one station

In Case *c*, the distance of the two different equipments is only some hundred meters, so it is easy to transform their coordinates with high accuracy into one common system and then to reduce the measured data according to the common system.

In Cases *a*, and *b*, the effect of different coordinate errors of some stations is also to be taken into account besides the problems of organisation.

It seems to be evident that Case *c*, is the best choice for us, consequently a computer program SAMULPO (Short Arc Method Using Laser and Photographic Observations) has been developed for the HP 9830 desk computer (see Fig. 8).

As in the SGO photographic as well as laser observations are possible a special short-arc method has been worked out. This method determines the observed short-arc with a relatively high accuracy. If at another station laser observations are obtained for the same short-arc the coordinates of that station

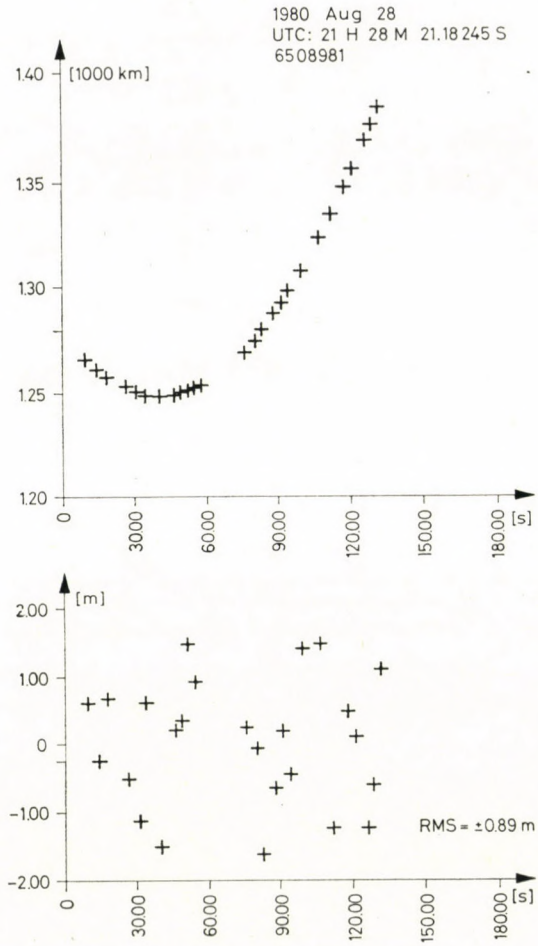

Fig. 7

can also been determined. This method is called *Photo-laser*. Referring to the block-diagram of Fig. 8 the method can be summarized as follows.

2.311 *Short-arc determination*

Using quasisynchronous photographic and laser observations for the same pass, one can determine the measured vectors pointing from the station to the satellite. By the prediction program predicted vectors are calculated for the same epochs. From these two vectors the difference vectors (measured minus calculated) are computed and decomposed into along-track, cross-track, and radial components. This decomposition separates the effects of the photographic and laser observations to the short arc (the radial component comes

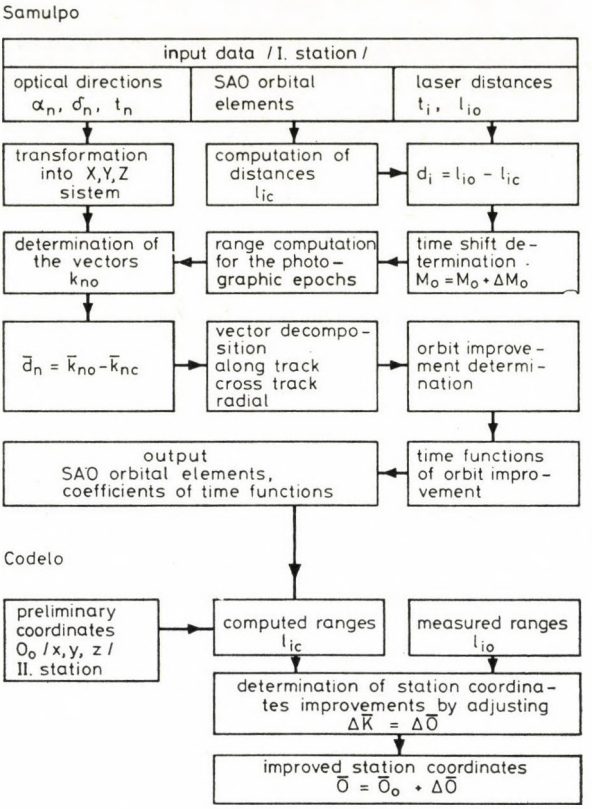

Fig. 8

from the laser, the others from the photographic observations). On the other hand the time shift which is one of the most problematic error sources is identical with the along-track component.

Having completed the procedure the components are involved into the orbit improvement process by iteration. For these series of orbit improvements (see Table III) the polynomial

$$E_{1-3} = C_1 + C_2 \cdot t + C_3 \cdot \cos A + C_4 \sin A$$

can be applied, where

t is time,

A is a function of time and of satellite velocity,

$C_1 - C_4$ are coefficients to be determined by adjustment.

The polynomial coefficients are determined by a least squares adjustment. The function of orbit improvements in radial direction (E_3) is derived

Table III

GEOS-3	21.07.1980	To = $23^h\ 52^m\ 19.0453^s$	Penc
t = UT-To (sec)	photogtaphic		laser
	E_1 (m)	E_2 (m)	E_3 (m)
0.0000	—	—	−33.4
9.9438	—	—	−42.3
29.1842	—	—	−48.8
39.6607	−19.8	−56.7	—
43.2877	−19.9	−58.8	—
49.2726	—	—	−50.2
63.3054	—	—	−52.5
82.3992	—	—	-55.8
99.0487	—	—	−55.9
112.0367	—	—	−60.6
125.7717	−85.4	−80.2	—
128.2407	—	—	−63.2
152.0110	—	—	−75.7
171.7202	—	—	−87.9
182.2927	−150.6	−107.1	—
187.7507	−148.9	−99.3	—
RMS	± 3.2	± 3.6	± 1.4

with an accuracy of In due to the laser measurements. The along-track improvements (E_1) accuracy is 10—20 m, the cross-track (E_2) is 3—5 m, due to the lower accuracy of photographic observations (see Table III).

The constant term of the orbit improvement function can be determined from the series of laser measurements (time shift see Fig. 9) with an accuracy of a few meters thus the real accuracy of the short arc is 5—10 m.

Determination of station coordinates

Having a sufficient number of determined short arcs, all synchronous observations for these arcs at other stations are examined. The coordinates of the observing station can be determined with an accuracy of 1 m from a few passes if the geometry is satisfactory. The absolute coordinates of the second station depend on the coordinates of the first one from which the short arcs were determined. The accuracy of the relative coordinates of the two stations, however, depend only on the accuracy of the laser measurements.

Let l_i be the measured distance, and $\bar{k}_i$ the predicted vector for the observation epochs.

The vectors are computed from the preliminary coordinates and the determined short arcs.

In this case the correction is

$$v_i = | k_i - \bar{\Delta k}_i | - l_i$$

where

$\bar{\Delta k}_i$ is the preliminary coordinate improvement.

$\bar{\Delta k}_i$ is determined by adjustment.

This correction is computed by the CODELO program.

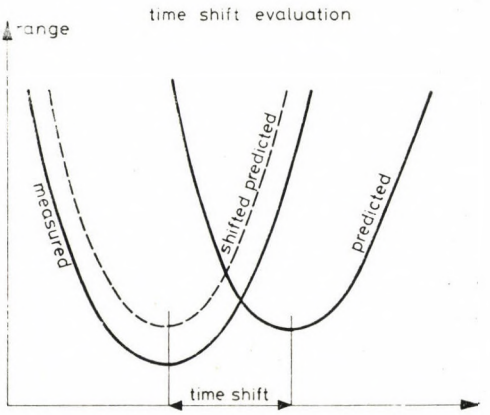

Fig. 9

2.32 *Preliminary results*

At the SGO station 16 synchronous (photographic-laser) observations of GEOS-3 have been collected in 1980. The determination of the short arc was made by the SAMULPO program. The obtained accuracy corresponds to its theoretically estimated value. A short arc determination for GEOS-3 is demonstrated in Table III.

We accumulate and process continuously all available synchronous observations at other stations for all determined short arcs. Until now three synchronous observations have been obtained from the ZIPE, Potsdam.

The coordinates of the Potsdam station have been determined by the CODELO program. The geometry of these passes was not satisfactory, thus the obtained accuracy is only 13 m, considered as a very preliminary value. The deviation from the coordinates determined by Doppler measurements is 36 m. As the effect of the photographic observations seems to be negligible, in the case of an adequate geometry of the passes the best accuracy to be obtained is estimated in about 1 m.

REFERENCES

1. Ruby Laser CVUT-FJFI Instruction Manual.
2. FISCHER, H.—NEUBERT, R.: Kombinierte Richtungs- und Entfernungsmessungen mit der weiterentwickelten Satellitenkamera SBG. *Jenaer Rundschau*, 1976/3.
3. FISCHER, H.—NEUBERT, R.: Satellite Laser Ranging Instrumentation at the Potsdam Station. Laser Workshop, Lagonissi, 1978.
4. MAREK, G.: Zur Reduktion von Laserentfernungsmessungen nach künstlichen Erdsatelliten. *VT*. 23. No. 2. pp. 57—60.
5. ÁDÁM, J.: Determination of station coordinates from laser observations. Third International Symposium, Geodesy and Physics of the Earth Weimar, 1976.
6. BORZA, T.: Predictions and orbital improvements for satellites. Dissertation, 1976.
7. KARDOS, I.—BORZA, T.—VASS, T.: Műholdakra végzett lézeres távolságmérések a penci Kozmikus Geodéziai Obszervatóriumban. *Geodézia és Kartográfia*, 5 (1980), 368—373.
8. БОРЗА, Т.: Определение Координат Станций использованием лазерных и оптиескихч наблюдений. International Scientific Conference of Section 6, Interkosmos Albena, 1980.

РЕЗУЛЬТАТЫ ЛАЗЕРНОЙ ДАЛЬНОМЕТРИИ В ОБСЕРВАТОРИИ КОСМИЧЕСКОЙ ГЕОДЕЗИИ

Т. КАРДОШ—Т. БОРЗА—Т. ВАШ

РЕЗЮМЕ

В статье описывается установка лазерного дальномера в Обсерватории космической геодезии (Пенц) и рассматриваются первые результаты. Инствумент размещается на спутниковом телескопе типа СБГ Цейс и был установлен в рамках сотрудничества Интеркосмос в 1977—78 гг. Точность дальнометра соответствует характеристикам инструментов первого поколения. При лучших прохождений достигается значение средней квадратической ошибки 50 см. В 1979 г. наблюдалось 27 прохождений спутников ГЕОС-1 и ГЕОС-3. До 1-го сентября 1980 г. наблюдалось 44 прохождений с 1081 отражениями.

Acta Geodaet., Geophys. et Montanist. Acad. Sci. Hung. Volume 17 (2), pp. 255—265 (1982)

MAGNETOTELLURIC DATA ON THE GEOELECTRIC STRUCTURE IN THE NORTH-EASTERN PART OF THE BALTIC SHIELD

A. G. KRASNOBAEVA—B. P. DIAKONOV—P. F. ASTAFIEV—O. V. BATALOVA—V. S. VISHNEV—I. E. GAVRILOVA—R. B. ZHURAVLYOVA—S. K. KIRILLOV

INSTITUTE OF GEOPHYSICS OF URAL SCIENTIFIC CENTER, SVERDLOVSK, USSR

[Manuscript received August 25, 1980]

The anomalies of the MT fields along the profile Titovka—Ponoi and D. Zelentsi—Lovozero indicate distortions in the frequency range of short-period pulsations. The results of DMTS (deep magnetotelluric soundings) along the Murmansk ledge of the ancient platform (NE-part of the Baltic Shield) are discussed.

A quantative interpretation of the ϱ_T and φ_T-curves shows the inhomogeneous structure of the upper mantle where a conductive layer at a depth 50—70 km with a longitudinal conductivity 20—270 [Ω^{-1}] was detected. The boundary of the Earth's conductive layer is found at a depth of about 600 km with a specific electric resistivity of 1 ohm · m.

Electromagnetic measurements with an electric current impulse source (1) have been carried out on the Kola Peninsula since 1976. As a result of this research large-scale blocks with different electric resistivity were settled out in the Earth's crust. The rocks with electron conductivity have a ϱ-value of 10^2—10^3 ohm · m and ϱ of nonmodified granites and granite gneisses is $\approx 10^5$ ohm · m (the Murmansk and the Central Kola blocks). The use of MHD-generators in electric surveys enables to obtain the electric conductivity at considerable depths. However this complicated experiment results in different interpretations of the received data and a more sophisticated analysis is needed. Therefore a research of this kind was carried out by the Institute of Geophysics of the Ural Scientific Center in 1978 within the large programme "Khibines" in the north-eastern part of the Baltic Shield. The geoelectric structure of the Earth's crust and upper mantle was observed using two methods of deep geoelectrics: deep magnetotelluric sounding (DMTS) and geometric sounding with a MHD-generator. These methods were supposed to increase the confidence of the parameters measured and to solve some methodical problems. In present paper the results of MTS are examined. As MTS is a rather complex method, special attention was paid to the observation area (high latitudes).

According to recent geological and geophysical surveys the Murmansk ledge of the ancient platform is considered to be most favourable for electromagnetic research. The highly resistive granite-gneissic formation enables to record the impulses at the maximum possible distance from the MHD-generator and, therefore, information from the maximum depths can be obtained. Moreover, the uniform geoelectric structure of the Earth's upper

crust improves the MTS-interpretation and makes it possible to compare the results of the artificial and natural fields. The observation points were situated along a 500 km long profile on the Murmansk block. To study the "coastal effect", observations were made between the stations Lovozero and Dalnie Zelentsi. All the stations are shown in the schematic geological map (Fig. 1).

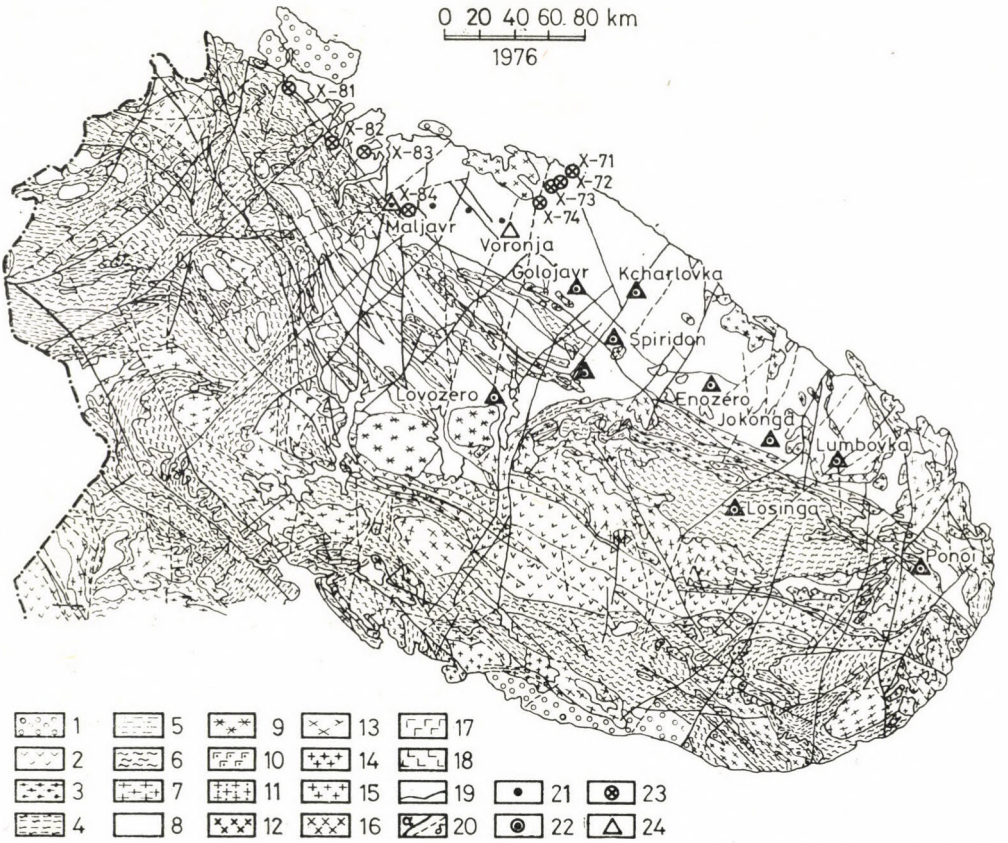

Fig. 1. Schematic geologic structure of the Kola Peninsula (after Belyaev, Zadorodny, Petrov, Voloshina [2]). Structural stratigraphical units: 1 — terrigenous rocks of the Riphean formation — PR_3; 2 — sedimentary-volcanogenic rocks of the Karelian formation — PR_2; 3 — sedimentary-volcanogenic rocks of unknown age; 4 — crystalline schists, gneisses, metavolcanics — PR_1; 5 — aluminiferous crystalline schists — PR_1; 6 — biotite and amphibolite gneisses, amphibolites — PR_1; 7 — gneisses and granite gneisses in the basement — AR — PR_1; 8 — gneisses, diorites, gneissic granodiorites and plagiogranites of the ancient basement — AR? Instrusive formations: 9 — nepheline-syenite; 10 — alkaline gabbro; 11 — laucocratic granites, alaskites — γ_2^3; 12 — post-orogenic porphyric granitoids — γ_2^2; 13 — alkaline granites — γ_2^1; 14 — charnocrites, enderbites — γ_{1-2}; 15 — plagiomicrocline granites, gneissic granites γ_1^2 — γ_2^2; 16 — diorites, quartz-diorites, granodiorites, plagiogranites — γ_{0-1}; 17 — gabbro and gabbro-anorthosites of different age; 18 — ultrabasitic blocks of different formations; 19 — geological boundaries; 20 — dislocation with a break in continuity: *a)* main, *b)* additional. Points of observation: 21 — MTP; 22 — DMTS; 23 — records of impulses from a condensator source; 24 — records of impulses from a MHD-generator

According to this map the DMTS in the points Lovozero and Losinga are situated in different structural-tectonic zones. The observation method was based on simultaneous MTS in a wide frequency range from 1 to 10^{-3} Hz. Magnetotelluric stations MTL-71, magnetovariation stations "IZMIRAN-4" and oscillographs OMS-2 as well as "MEVS-5" were used for this purpose. The point Lovozero near to the airport used for transportation of the field stations was chosen as point of reference. A continuous recording of field variations was made simultaneously at three (one basis and two field) stations. The identity of the recorders at the stations was checked at the beginning of the observations. The parties used radio communication. Time signals were given automatically from the radiostation "Majak". The 100—200 m long measuring lines were oriented along the magnetic meridian (X-axis) and the latitude (Y-axis).

We used continuous Pc1-Pc5 and irregular Pi1—Pi3 pulsations, as well as geomagnetic bays with a duration of 20 minutes to 3 hours for constructing the MTS curves. High latitudinal recordings of the magnetotelluric field are characterized by high amplitude variations and by a wide frequency range even in a short time interval which provide favourable conditions for deep magnetotelluric sounding. Thus e.g. at middle latitudes Pc1 occur only at night and in the morning, here they are observed in the daytime, too. This also concerns Pc5.

All the photorecordings of the magnetic and telluric fields with the total extension of 2.5 km could not be used. Only some parts of these records free of noises and characterized by quasi-sinusoidal variations in all the field components with an amplitude more than 10 mm were selected for further treatment. The module and argument of the input impedance were primarily determined by two methods: by the least squares method and at the stage of preliminary interpretation [3] by the method of apparent impedances. The spectral method was only used for recordings from the point Lovozero.

For the magnetotelluric and magnetovariation observations, the natural field is assumed to be homogeneous within limited regions of the Earth's surface. This supposition makes it easier to determine the inner anomalous part of the field which exists due to anomalous conductive objects (geoelectric inhomogeneities) in the Earth's crust. The detection of conductivity anomalies is based typically on profiles of intensity variations in different field components. The probability of local anomalies is here high since the profile of simultaneous observations is made on the Murmansk block where sedimentary formations shielding deep objects are absent. Figure 2 shows data on the relative anomaly (η) for different periods. This value η is given by

$$\eta_{Ex}=\frac{E_x}{E_{xb}};\quad \eta_{Ey}=\frac{E_y}{E_{yb}};\quad \eta_{Hx}=\frac{H_x}{H_{xb}};\quad \eta_{Hy}=\frac{H_y}{H_{yb}};\quad \eta_{Hz}=\frac{H_z}{H_{zb}}$$

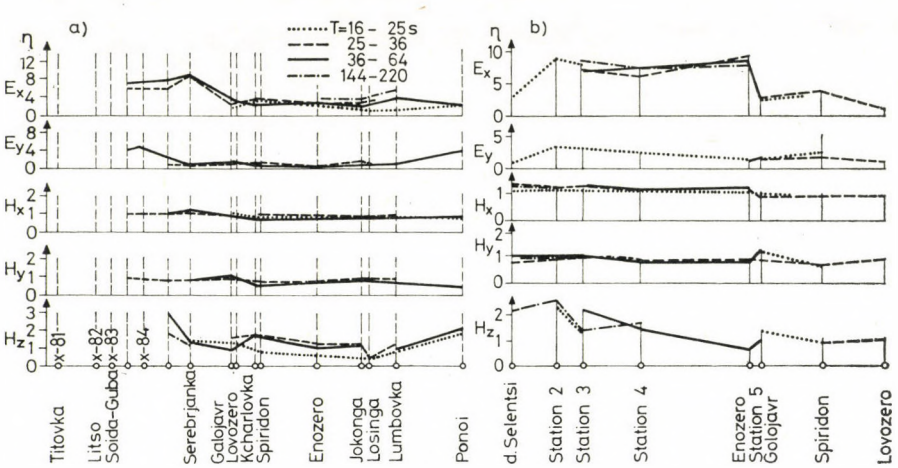

Fig. 2. The anomalous field components along the profile Titovka — Ponoi (a) and the "coastal effect" in the field components (b)

where $E_{xb}, E_{yb}, H_{xb}, H_{yb}, H_{zb}$ are the amplitudes of variations for the corresponding periods in the point Lovozero, E_x, E_y, H_x, H_y, H_z are the same values in field stations.

According to the variations of η along the profile St. Titovka—Ponoi, the horizontal magnetic field (H_x and H_y components) is normal. Slight variations are observed in the electric component in the direction of the y-axis being nearly the E-polarized field. This proves the correctness of the supposed polarization. Anomalous field variations are observed in the points Serebryanka and Lumbovka. The effect occurs in the E_x and H_z components. There is also a tendency of the conductors to strike in north-eastern direction. The maximum of the anomalous effect is in the range of 36—64 sec in Serebryanka and of 144—220 sec in Lumbovka. This period range of the variations penetrates into the asthenosphere and characterizes probably regional inhomogeneities in the Murmansk block. The narrow conductive zones may be most likely connected with faults in the Earth's crust. If it is so then two local anomalous zones are observed in the electromagnetic fields. These zones are characterized by their deep locations and correspond to a violation of horizontal layering in the geoleectric cross section.

Simultaneous MT profiling was carried out along the profile D. Zelentsi—Lovozero to display the effect of the anomalous field resulting from the contact of massive rocks in the coastal part of the Kola Peninsula and the sea ("coastal effect"). In spite of considerable resistivity contrasts reaching 5—6 orders of magnitude in the coastal zone, only a relatively weak anomalous effect occurs in the H_z and E_x components (Fig. 2b). The anomaly is absent in the components used for the construction of the DMTS curves with E-polar-

ization (E_y, H_x). This fact can be well explained by the physical model of an extended gently sloping shelf [4].

The correct interpretation of magnetotelluric data is based on impedance polar diagrams which enable to characterize the degree of inhomogeneity of the medium and to construct the ϱ_T curves with the least possible distortion. Figure 3 shows impedance diagrams of the observation points for short period variations. The main impedance diagrams are ellipses, while the secondary impedance has a quaterfoil form and hints at a two-dimensionally inhomogeneous medium. These forms are also preserved for other periods, but the azimuth of the inhomogeneity axis can change as for example in Kharlovka. The polar diagrams are oriented perpendicularly to the main strike of the basic structural elements. The azimuth of the homogeneity axis of 120° (direction of E-polarization) corresponds to this regional direction. The impedance diagrams vary in their orientation from point to point and thus reflect local inhomogeneities in the geoelectric structure of the upper horizons of the Earth's crust. So the minor axis of the main impedance diagram does not always correspond to the E-polarization. In Lovozero the major axis coincides with this direction. In the points Losinga and Panoi the measuring lines are oriented along the main axes of the impedance tensor, where the additional impedances are minimum. This means that the Z_{yx}-component can be assumed as E-polarization in these points and Z_{xy} as H-polarization. In a two-dimensionally inhomogeneous medium the longitudinal curves are least distorted by the inhomogeneity of the horizontal medium.

The curves constructed for the Kola Peninsula, corresponding to the E- and H-polarization (see Fig. 4) have typically similar forms, but at the same time they are displaced along the axis of ordinates, what hints at the galvanic distortions of the field. As there are no effective ways of the registration of distortion factors, two variants are possible in the construction of the hypothetical geoelectric cross section for the north-eastern part of the Baltic Shield.

In variant I the parameters of the cross section were obtained from the interpretation of the curves with E-polarization (Fig. 4a).

In variant II the authors suggest their own way of the registration of field galvanic distortions. Let us assume that the geoelectric parameters are at a depth of 500—600 km everywhere the same and that H-line (the descending branch) indicates the global distribution ϱ_T[5]. Thus all curves must coincide by their right-hand-side descending branches with the "normal curve".

The "normal curve" (continuous thick line in Fig. 4 and Fig. 5a) was constructed through the use of the DMTS data obtained by the authors in the eastern part of the East-European platform (pp. Arti, Nugush). Curves for Western Siberia (Salomatovo, St. Zaimka, Orlovo) are shown here for comparison. The fact that these curves coincide with the global continental

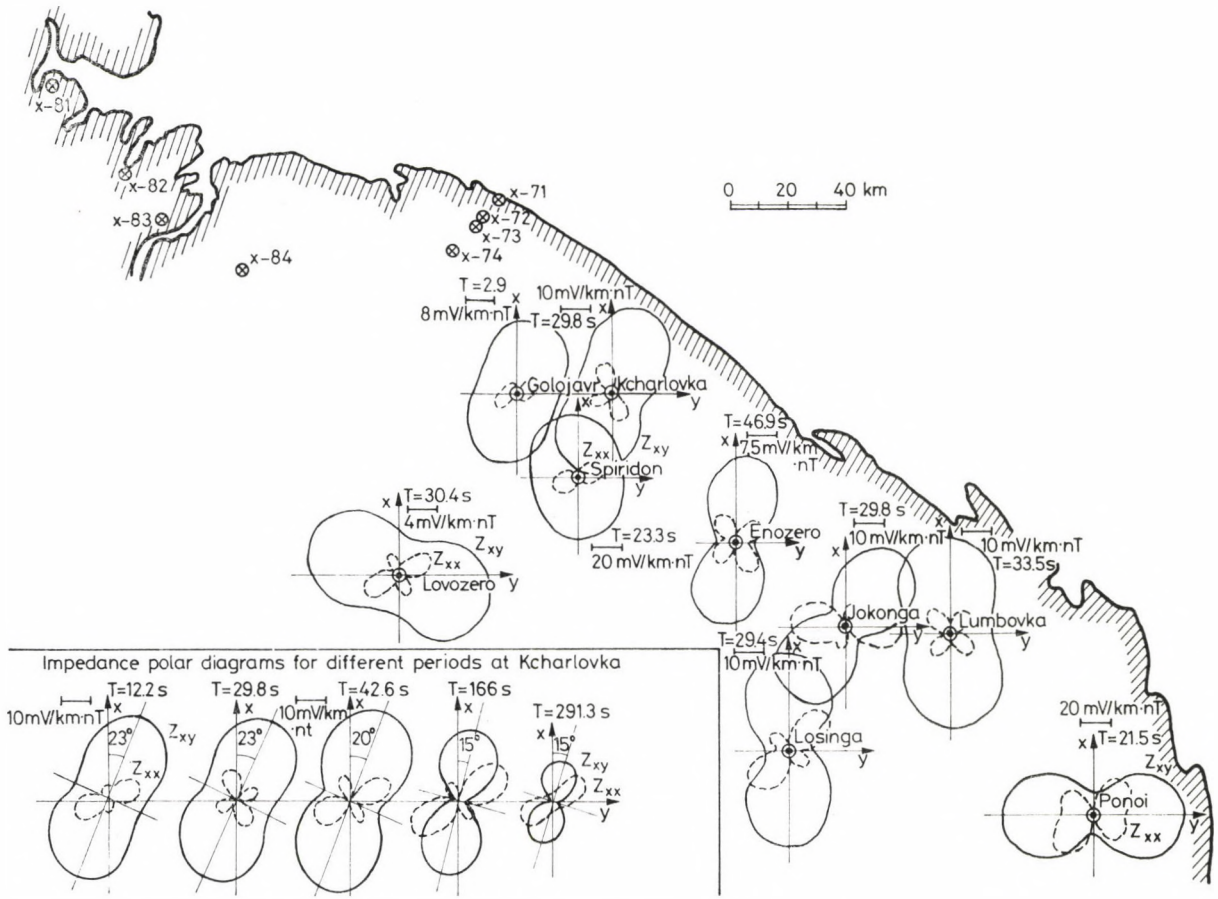

Fig. 3. Polar diagrams of the main and secondary impedances in the sites of deep MTS

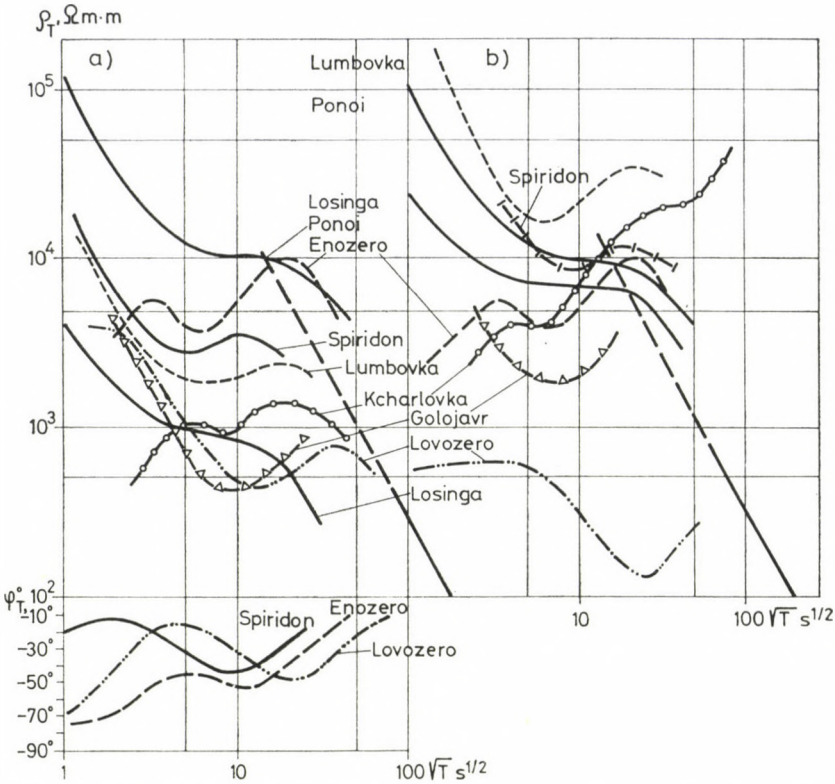

Fig. 4. Amplitude and phase DMTS-curves for E-polarization (a) and H-polarization (b

curve ϱ_T (the region of shading in Fig. 5a), within the periods of 5000—80,000 sec, can serve as the criterion for them being undistorted.

Figure 4a shows that the longitudinal curves in Lovozero, Lumbovka and Kharlovka approximate in their right-hand-side descending branches the line characterizing the normal geoelectric cross section (dashed line in Figs 4, 5a), other curves lie either higher or lower of it. If we displace now all curves ϱ_T along the axis of ordinates for their right-hand-side branches to coincide with the asymptote, we obtain a sequence of curves in Fig. 5a.

In variants I and II a quantitative interpretation of the curves was carried out by selection. The selection of the ϱ_T curves with the computer "Mir-I" ensured that the calculated curve approached the experimental one with an error less than 15—20%, while the extreme amplitude ratio and the coincidence of the extreme points in the time axis were kept unchanged. About 30 layer sequences were calculated in order to interpret a DMTS curve.

The layer sequence with a most accurate coincidence between experimental and theoretical curves was considered to be reliable (see Table I).

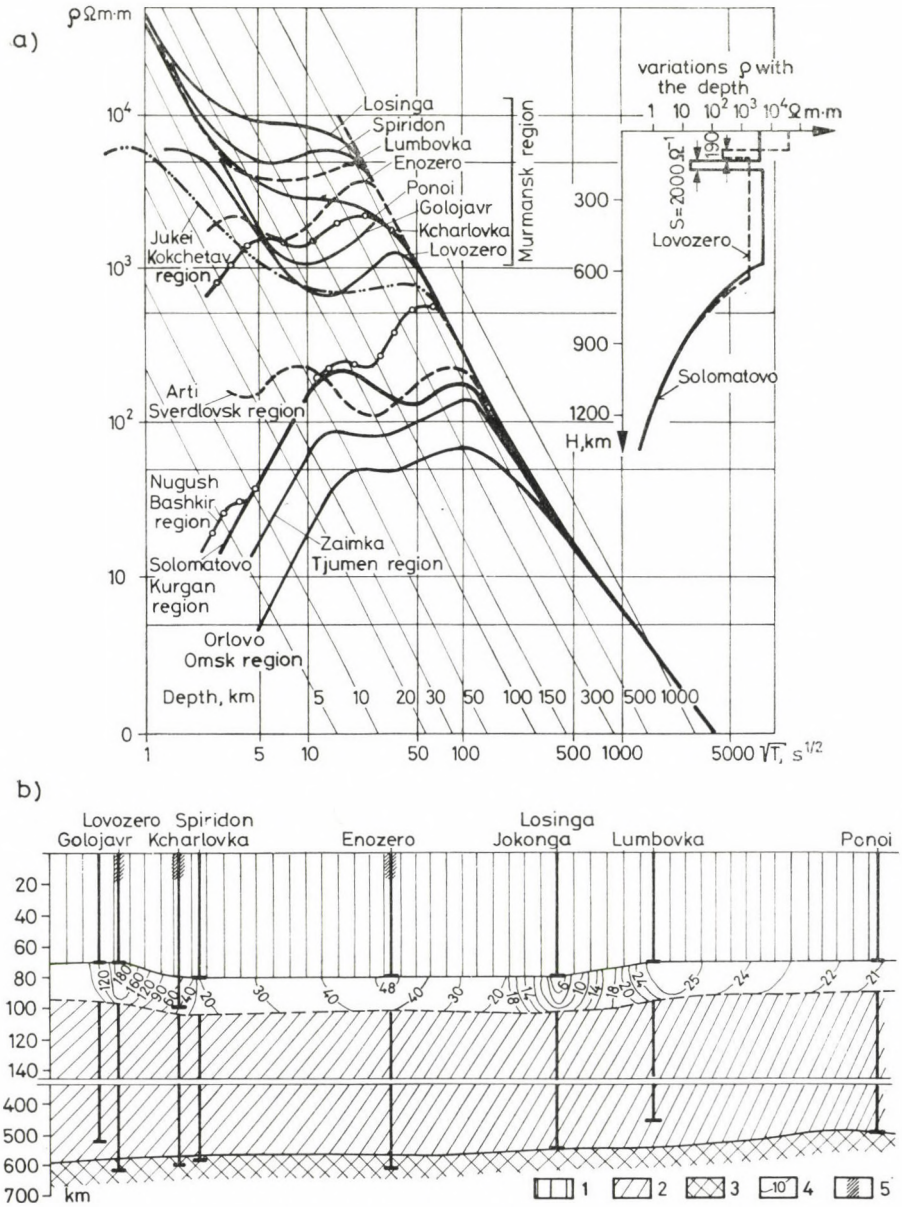

Fig. 5. Results of DMTS curves (a), schematic geoelectrical cross section of the North-Eastern Baltic Shield (b) 1 — the region within which according to MTS data the real global continental curve $\varrho_{(T)}$ is situated [5], specific electrical resistivity in ohm.m: 2 — 45 — 50 · 10³, 3 — 1.7—5 · 10³, 4 — 1, 5 — S, longitudinal conductivity in Ω^{-1}, 6 — zones with high S_1 (5.4 — 31 Ω^{-1})

Table I

Interpretation parameters of ϱ_T curves

Stations	Layers								Notes
	I	II		III	IV		V		
	S	$\varrho \cdot 10^3$	h	S	$\varrho \cdot 10^3$	h	ϱ	h	
Lovozero*	6.5	45	52	270	1.3	550	1	∞	Curves with E-polarization (variant I)
Spiridon	—	45	60	28	3.	350	1	∞	
Enozero	22.8	45	70	80	5	450	1	∞	
Lumbovka*	—	50	50	43	2.3	400	1	∞	
Goloyavr	—	50	45	240	2	300	1	∞	
Kharlovka*	38	45	75	85	2.3	400	1	∞	
Lovozero	5.4	45	70	192	1.7	550	1	∞	Displaced curves (variant II)
Spiridon	—	45	80	20	5	500	1	∞	
Enozero	16	45	70	50	5.5	550	1	∞	
Losinga	—	45	80	4	5	450	1	∞	
Lumbovka	—	50	70	26	4	500	1	∞	
Ponoi	—	50	70	21.4	2	450	1	∞	
Kharlovka	31	45	100	57	3	500	1	∞	

I, II, III, IV, V — layer numbers. Parameters of a layer sequence: ϱ — specific electric resistance in ohm. m
h = thickness in km
S — longitudinal conductivity in Ω^{-1}
* — the least distorted curves

According to Table I the interpretation parameters of the displaced curves have less scatter in depth down to intermediate layer III and the values of S are less than that in variant I.

The construction of the geoelectric cross section for the north-eastern part of the Baltic Shield is based on the data for variant II (Fig. 5b). Figure 5b shows that the Earth's crust and the upper mantle down to a depth of 70 km is highly resistive. The resistivity of the upper layers is $45—50 \cdot 10^3$ ohm·m. However, this layer is characterized by a geoelectric inhomogeneity. In the points Lovozero, Enozero and Kharlovka there are highly conductive zones the geological nature of which is not yet clear. The highly conductive layer at a depth of 50—70 km appears in a 0.4—0.5 km/sec-decrease of the elastic wave velocity [6]. According to the present notions, the high conductivity can be related to the transition of the material into an amorphous state. The S value is between 4 and 200 Ω^{-1}. The extreme values were obtained in the points Losinga and Lovozero, respectively. The longitudinal conductivity of the intermediate layer within the Murmansk block varies from 21 Ω^{-1} (Ponoi) to 85 Ω^{-1} (Kharlovka), except the point Goloyavr, where the constructed curve was less reliable due to the absence of the descending branch. The low

resistivity layer ($\varrho_T \approx 1$ ohm · m) corresponds to the global distribution and can be identified with the boundary of the C-zone (the Golitsyn layer) at a depth of 600 km.

For the determination of conductive layers, the Tikhonov—Cagniard theory supposes a stepwise change of the electric parameters at the boundary. In case of the Earth's crust and upper mantle, this suggestion is confirmed by seismic data and laboratory experiments carried out at similar temperature and pressure. However, for the interpretation of the DMTS curve it is of great interest a smooth change of the electric conductivity with depth. Here the DMTS curve in the point Salomatovo (in the Trans-Ural) is interpreted by Dmitriev and Rudneva (from the Moscow State University) on the basis to obtain the input impedance at the Earth's surface with an electric conductivity increasing exponentially with the depth. In addition to this DMTS curve, a global curve ϱ_T for long periods is also constructed (see Fig. 5).

The electric conductivity in the layer Y changes according as

$$\sigma(z) = \sigma_{n-1} \cdot e^{-a\left(\frac{1}{z} - \frac{1}{z_{n-1}}\right)}$$

where

$$z_{n-1} \leq z \leq z_n$$

$$\sigma(z) = \sigma_n(z \gg z_n), \ \sigma(z_{n-1}) = \sigma_{n-1}$$

where

$$a = \frac{z_n \cdot z_{n-1}}{z_n - z_{n-1}} \cdot \ln\left(\frac{\sigma_n}{\sigma_{n-1}}\right)$$

or

$$a = \frac{\sum_{i=1}^{n-1} \cdot h_i \cdot \sum_{i=1}^{n-2} \cdot h_i}{h_{n-1}} \cdot \ln\left(\frac{\varrho_{n-1}}{\varrho_n}\right),$$

h_i and ϱ_i are the thicknesses and resistivities of the respective layers.

The results of the joint interpretation of both the experimental and "global" curves enabled to evaluate the electric conductivity down to 1300 km.

The following conclusions can be drawn from this study:

1. The main and secondary impedance diagrams indicate that the medium in the observation points can be regarded as two-dimensionally inhomogeneous. The direction of the E-polarization ($\alpha \approx 120°$) is in good agreement with the main strike of the Kola basic formation. All points are characterized by a horizontal inhomogeneity of the medium. Due to this fact a quantitative interpretation of the DMTS curves for the longitudinal polarization of the field (minor axes of the impedance diagrams) does not totally eliminate the influence of galvanic distortions. This problem can be solved by the use of the data of the "global" sounding curve.

2. The analysis of the experimental ϱ_T-curves shows that on the Kola Peninsula variations in the frequency range of Pc5 and Pi2 pulsations can be approximated by a two-dimensional wave, while for bay-type variations this case does not hold.

3. According to simultaneous observations of the natural field, two highly conductive local zones were found within the Earth's crust. The anomalous variations of E_x and H_z-components in Serebryanka and Lumbovka indicate a north-eastern strike of the conductors.

4. A weak "coastal effect" in the natural variations can be connected with the extent shallow shelf.

5. A deep magnetotelluric survey in the north-eastern part of the Baltic Shield enabled to construct a total geoelectric layer sequence of deep horizons in the Earth's crust and upper mantle, to distinguish the intermediate conductive layer at a depth of 50—70 km and to evaluate its longitudinal conductivity as 20—270 Ω^{-1}, what enables us to study the state of the material in the upper mantle.

REFERENCES

1. ГОРБУНОВ, Г. И.—БЕЛЬКОВ, Н. В.—ПАВЛОВСКИЙ, В. И. и др.: Глубинное электромагнитное зондирование с МГД-генератором на Кольском полуострове. *ДАН*, 247 (1979), 578.
2. БЕЛЯЕВ, О А.—ЗАГОРОДНЫЙ, В. Г.—ПЕТРОВ, В. П.—ВОЛОШИНА, З. М.: Фации регионального метаморфизма Кольского полуострова. Изд-во Наука, Ленинград, 1977.
3. БЕРДИЧЕВСКИЙ, М. Н.: Электрическая разведка методом магнитотеллурического профилирования. Изд-во Недра, Москва, 1976.
4. БИЛИНСКИЙ, А. И.—КОБЗОВА, В. М.—МОРОЗ, И. П. и др.: Исследование берегового эффекта на моделях с вертикальным и наклонным контактами. В сб. «Исследование геомагнитного поля на акваториях морей и океанов», Москва, 1978 (Сборник ИЗМИРАН).
5. РОКИТЯНСКИЙ, И. И.: Исследование аномалий электропроводности методом магнитовариационного профилирования. Изд-во «Наукова Думка», Киев, 1975, стр. 254—255.
6. РЯБОЙ, В. З.: Структура верхней мантии территории СССР по сейсмическим данным. Изд-во Недра, Москва, 1979.

МАГНИТОТЕЛЛУРИЧЕСКИЕ ДАННЫЕ ОТНОСИТЕЛЬНО ГЕОЭЛЕКТРИЧЕСКОЙ СТРУКТУРЫ СЕВЕРО-ВОСТОСНОЙ ЧАСТИ БАЛТИЙСКОГО ШИТА

А. Г. КРАСНОБАЕВА—Б. П. ДЯКОНОВ—П. Ф. ОСТАФЬЕВ—О. В. БАТАЛОВА—В. Ш. ВЫШНЕВ—И. Е. ГАВРИЛОВА—Р. Б. ЖУРАВЛЕВА—С. К. КИРИЛЛОВ

РЕЗЮМЕ

В статье излагается интерпретация магнитотеллурических зондирований, проведенных на северо-восточной территории Балтийского щита. Описывается искажение электромагнитного поля в исследуемой области (влияние берега, роль хорошопроводящих дайков). Предполагая двухмерную неоднородность выбираются кривые зондирований с поляризацией Е, содержание наиболее вероятную информацию. Нисходящие ветви, появляющиеся у наибольших периодов измененных кривых зондирований, прилаживаются к «нормальным кривым», характеризующим распределение электрической проводимости кристаллических щитов и платформ.

В глубине 50—70 км выявляется промежуточных хорошопроводящий слой с горизонтальной проводимостью 20—270 Ω^{-1}.

Acta Geodaet., Geophys. et Montanist. Acad. Sci. Hung. Volume 17 (2), pp. 267—276 (1982)

LOCALIZATION OF THE Pc5-SOURCE AND OF THE AURORAL OVAL

O. M. RASPOPOV
POLAR GEOPHYSICAL INSTITUTE, APATITY, USSR

L. T. AFANASYEVA
POLAR GEOPHYSICAL INSTITUTE, MURMANSK, USSR

[Manuscript received August 25, 1980]

On the basis of material from observatories in the subauroral and auroral zones, a correlation has been found between the position of the Pc5-source and the auroral oval, whereby the Pc5-source lies near to the equatorial boundary of the oval at different levels of the geomagnetic activity. It is known from satellite data that the excitation of Pc5 is connected with the drift of plasma instabilities from the night-time region of the magnetosphere towards the daytime side during substorms. The azimuthal drift of the pulsation source could also be detected from surface observations. The drift velocity is about 0.5—1.1°/min.

The observed characteristics of the Pc5-activity are compared with theoretical predictions. The most likely generation mechanism is the drift of the instabilities which can be observed at the inner edge of the plasma layer in the morning sector of the magnetosphere during the growing phase of substorms.

Pc5 type pulsations have gained recently a quite increasing importance. This is mainly due to the fact that a study of these pulsations enables a clarification of the physical nature and of the main features of the excitation of resonant phenomena in the magnetosphere.

The periods and amplitudes of the Pc5 pulsations are great enough to allow their study by using normal magnetograms, as well as to carry out an analysis of certain phenomena connected with them, e.g. pulsations of the aurora, pulsations in the riometer absorption and radio aurora; pulsating particle currents in the magnetosphere, electric fields of the pulsations in the ionosphere etc. All these phenomena help to hypothese about the generation and propagation properties of this type of geomagnetic pulsations.

Up to now there is no generally accepted theory on the physical nature of the Pc5 type pulsations. The proposed mechanisms can explain only a part of the observed characteristics of them; they enable only a qualitative description of their parameters in terms of magnetospheric resonances or of the theory of drifting waves using quantitative estimations of certain model parameters. Thus, a number of authors suppose that the generation of Pc5 is connected with the development of the Kelvin—Helmholtz instability at the boundary of the magnetosphere and then with the propagation of these waves into the magnetosphere [Dungey, 1961; Atkinson and Watanabe, 1966, Dungey and Southwood, 1970; Samson, 1972]. In other papers the possibility of the inner-magnetospheric excitation of Pc5 is explained on the basis of the analysis of processes inside the disturbed magnetosphere [Cladic, 1971; Hasegawa, 1969; Pudovkin et al., 1976; Rostoker and Hing-Lan Lam, 1978].

In previous papers of the present authors a clear connection has been shown between the generation of Pc5 in the morning sector and the development of substorms in the night sector [Raspopov et al., 1972; Afanasyeva et al., 1973, 1974, 1977a, 1977b]. It has been found that the area of Pc5 generation is situated near the Eastern edge of the Western auroral electrojet and signalizes its transit. There is a correlation between the intensity of the substorms and the amplitudes of Pc5. It was shown by Afanasyewa et al. (1973) that the parameters of Pc5 appearing in the morning sector of the magnetosphere are in connection with the parameters of the plasma phenomena (irregular beams of electrons with energies $\geq$60 keV) drifting away from the night-side part of the magnetosphere during geomagnetically disturbed times. The results have proved the supposition that the physical nature of Pc5 in the morning sector of the magnetosphere is in connection with the development of processes in the area of plasma instabilities which are present in the disturbed magnetosphere during substorms. The generation of Pc5 can take place both near the boundary of the auroral zone and in the area of plasma instabilities drifting from the night-side part towards the morning sector of the magnetosphere.

In the paper some results of investigations are described which continued the research of the interconnection between the generation of Pc5 and the development of substorms. Further supplementary proof is given for the existence of the longitudinal drift of the Pc5 source, and a connection of the position of the equatorial boundary of the auroral zone in the morning and forenoon sectors with the areas of the excitation of Pc5 (the area of the maximum amplitudes, maximum frequency of occurrence) is also shown.

Longitudinal drift of the Pc5 source. It has been shown by Afanasyeva et al. (1973) on the basis of the data of the satellite "Elektron" that the Pc5 source has probably a longitudinal drift. An important problem is to find this longitudinal drift of the pulsation source by surface measurements. As it is known Pc5 can be recorded in an observatory during sufficiently long time intervals, which can reach in certain cases even 8—10 hours. In the case of strong Pc5 activity beginning in the morning hours it can last till noon. Pc5 pulsations have very often a modulation with an envelope period of about one hour. This characteristics of Pc5 enables an estimation of the transit of the pulsation source from the characteristic elements of synchronous records of pulsations in stations differing in their longitudinal position. In this analysis only Pc5 events have been used which were simultaneously observed at the auroral zone station pairs of Lovozero ($\lambda = 35° 05'$) — Dixon ($\lambda = 80° 34'$), and Lovozero—Chelyuskin ($\lambda = 104° 17'$) during the years 1971—1973. Only pulsations with quasisinusoidal forms and clearly visible modulation of the amplitudes were accepted. On the basis of the characteristic structural elements, the delay in the appearance of Pc5 has been estimated at the Eastern stations

Table I

Time delay of the structural elements of Pc5 at the stations Chelyuskin and Dixon with respect to the station Lovozero

Lovozero—Chelyuskin		Lovozero—Dixon	
Date	Hour	Date	Hour
January 20, 1971	2 h 01 m	December 16, 1972	0 h 42 m
March 22, 1973	1 h 15 m	May 16, 1972	0 h 40 m
March 23, 1973	1 h 12 m	March 22, 1973	0 h 54 m
April 19, 1973	1 h 36 m	March 23, 1973	0 h 40 m
July 1, 1973	2 h 08 m	April 18, 1973	0 h 40 m
July 11, 1973	2 h 00 m	August 24, 1973	1 h 30 m
August 6, 1973	1 h 43 m	June 30, 1973	2 h 00 m
	Δt=1 h 42 m	June 11, 1973	1 h 12 m
		August 24, 1973	1 h 26 m
			Δt=1 h 06 m

$LT_{Lov} = UT + 2$ h; $LT_{Dix} = UT + 5$ h; $LT_{Chel} = UT + 7$ h

with respect to the Western ones (Table I). The delay Δt of the beginning of modulated structures or of the maximum amplitudes of the pulsations in a longitudinal distance of $\Delta\lambda \sim 50$—$70°$ changes from case to case between 40 and 120 min, corresponding to drift velocities in the range of 0.5—1.1 degree/min. Supposing that this effect is due to a gradient drift, it is possible to estimate the energy of the particles [Afanasyeva et al., 1976]. The energy of the particles is thus 15—20 keV. It must be, however, mentioned that this estimations have only an approximative character as it has been supposed that the pitch-angle of the particles is nearly 90° and the drift of the particles due to convective electric fields with great dimensions, E, has been neglected.

Connection of the area of the generation of Pc5 with the position of the auroral oval in the morning-forenoon sector. It is well known that the generation of Pc5 in the morning and forenoon hours occurs at latitudes above 65—67°. Such a high-latitude position of the Pc5 source is one of the essential factors which prove that the excitation of Pc5 is not connected with inner magnetospheric processes in the auroral zone, but they are generated at the boundary of the magnetosphere. In this connection a comparison of the position of Pc5 sources (area of the maximum amplitudes and occurrence frequencies) was made with the position of the boundary of the auroral zone.

As experimental material, records of geomagnetic pulsations in an observatory network from several years were used, further results of experiments having the aim to record pulsations on station arrays synchronously. The parameters of the instruments, recording time and geomagnetic coordinates of the stations

Table II

Instrumental constants in stations used for the analysis of the time-space distribution of Pc5

Station	Code	Corrected geomagnetic coordinates		Paper speed		Scale value, γ/mm					
						1			2		
				1	2						
		Φ_M	Λ_M	mm/m	mm/h	H	D	Z	H	D	Z
1. Heiss	H	74.3°	144.1°	6	20	1.33	0.96	0.96	—	—	—
2. Cap Zhelaniya	Zh	71.1	147.5	15	20	—	—	—	9.3	4.5	10.1
3. Rybachy	R	66.2	114.9	6	20	—	—	—	12.9	11.7	16.1
4. Loparskaya	Lp	64.9	114.1	6	20	0.4	0.4	—	8.2	4.0	5.2
5. Lovozero	Lv	64.1	127.0	6	20	0.3	0.35	0.25	10.9	6.5	7.7
6. Umba	Um	62.8	114.4	—	20	—	—	—	8.3	7.6	10.4
7. Kem	Km	61.1	114.2	6	20	0.25	0.25	0.1	3.5	3.6	5.7
8. Sogra	S	56.0	132.0	6	—	0.17	0.33	—	—	—	—

can be seen in Table II. Figure 1a shows the diurnal variation of the occurrence frequency of Pc5 (Pn is the percentual ratio of hours when this type of pulsation appeared) at different observatories, Fig. 1b and 1c show the diurnal variation of the amplitudes and of the periods. The diurnal variation of the occurrence frequency can be characterized by a clear maximum in the morning and forenoon hours at latitudes 66—71°. The maximum at latitudes 66° seems to be shifted towards earlier hours in respect of stations at higher latitudes. At stations $\Phi_M \sim 64°$ a second maximum appears in the afternoon hours. Thus, at the station Lovozero ($\Phi_M \sim 64°$) these pulsations include about 20 per cent of all times when pulsation activity was present. The excitation of Pc5 pulsations in the afternoon hours takes place mainly in quiet times and in Samson et al.'s opinion (1971) in the outer magnetosphere, i.e. they have a physically different source from that of the morning Pc5.

The diurnal variation of the pulsation amplitudes at high latitude stations ($\Phi_M \sim 66$—$71°$) shows the already discussed tendency (Fig. 1b). At latitudes $\Phi_M \sim 64°$, the time variations of the amplitudes have a smooth character both in forenoon and in afternoon hours, as it has been already observed [Gupta, 1974].

Figure 1c shows the diurnal variation of Pc5 periods which has been computed similarly to that of the amplitudes using the least squares method. At high latitude stations, a relatively small shift of the periods was found from shorter periods in the morning hours towards longer ones in the daytime similarly to the variation described [Gupta, 1974b]. At lower latitudes ($\Phi_M \sim 64°$) the diurnal variation in the morning hours is either opposite or no change can

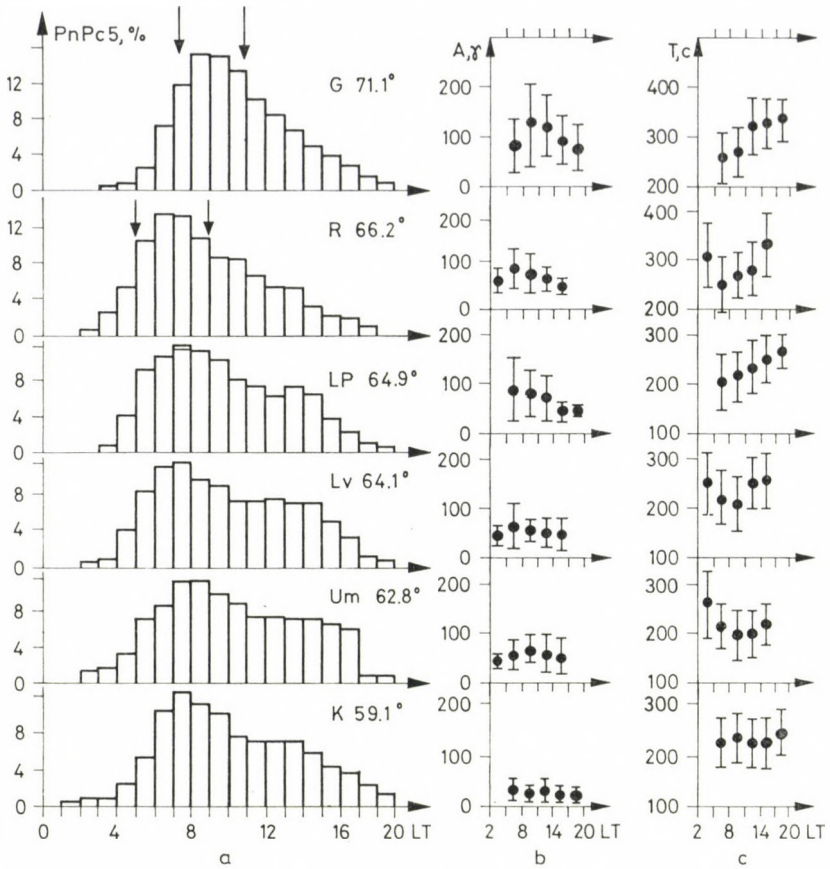

Fig. 1. Diurnal distribution of the occurrencefr equency. *a)* Number of hours with Pc5 (PnPc5, %); *b)* amplitude (A, γ); *c)* period, (T, s) on the basis of observations in a station network in 1973

be observed proving again the difference in the physical nature of high-latitude and subauroral Pc5-s.

Figure 2 represents the occurrence frequency of Pc5 (Pn Pc5 %) in function of the Kp-index along the station array. The Pn Pc5 values refer to the occurrence time of each Kp-index during the time of the experiment. In the top of the figure data are shown from the station Little America (LA, $\Phi_M = -74°$) [Hirasawa, 1970]. The following regularities have been found in the distribution of Pn Pc5 in function of the Kp-index. It can be seen that at a latitude of 74°, Pc5 can be observed practically only if Kp = 1. At a latitude of $\Phi_M \sim 71°$, however, within a wide range of Kp-indices (from 2 to 5) Pc5 appears with about the same occurrence frequency. This tendency is no more valid at even lower latitudes. Thus, at $\Phi \sim 66°$, Pc5 has a clear maximum at Kp = 4, and at $\Phi \sim 64°$, at Kp $\simeq$ 5.

Let us now discuss these results with regard to the problem of the position of the Pc5 source and of the boundary of the auroral oval.

In Fig. 3, statistical results are shown on the position of the auroral oval at different levels of the Kp-index [Starkov and Feldstejn, 1968]. The

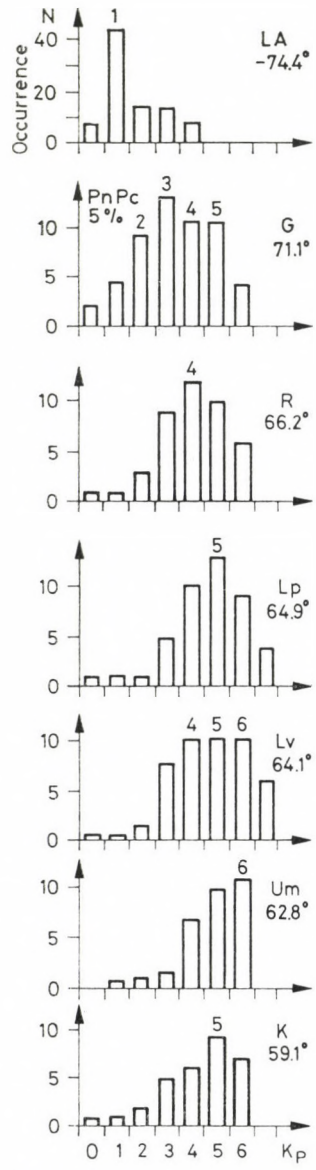

Fig. 2. Occurrence frequency of Pc5 (PnPc5, %) in the station network in function of the Kp-index. The top shows the distribution of Pc5 occurrence frequency at different Kp-indices for the year 1969 at the station Little America [Hirasawa, 1970]

Figure also shows the position of the stations where the observation of the Pc5 activity has been carried out. Vertical shading shows the area of daily occurrence maximum of the occurrence frequency of these pulsations on the basis of data from the stations Cap Zhelaniya ($\Phi_M \sim 71°$) and Rybachy ($\Phi_M \sim 66°$). Circles with dots show the maximum of the meridional distribution of the pulsation amplitudes in accordance with Gupta (1974a). It follows from this Figure that the area of the excitation of Pc5 (area of the maximum occurrence frequencies and of the maximum amplitudes) is at the equatorial boundary of the auroral zone. This fact could be confirmed and made more exact using the results presented in this paper. Thus, at a latitude of $\Phi_M \sim 74°$, the equatorial boundary of the auroral zone appears only in case of very low geomagnetic activity ($Kp \leq 1$). As a matter of fact Pc5 can be recorded at the station Little America only in such a case. In case of a greater activity ($Kp \geq 2$), this station lies always inside the auroral zone. At $\Phi_M \sim 71°$ (Cape Zhelaniya station) the equatorial boundary can be present in case of

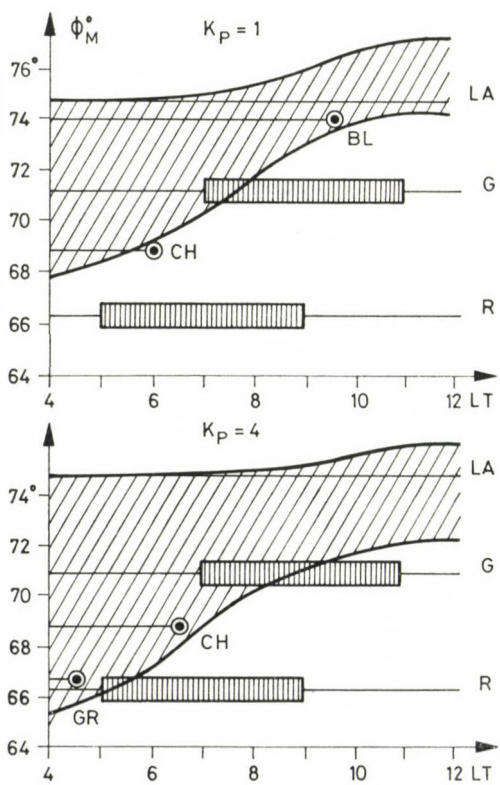

Fig. 3. Statistical position of the auroral zone at different levels of the Kp-index according to Starkov and Feldstein (1968). Thin lines show the position of the stations where Pc5 observations were made; circles with dots indicate the position of the maximum in the meridional distribution of the pulsation amplitudes according to Gupta (1974a)

both low and strong geomagnetic activities. The appearance of the Pc5 activity within a rather wide range of the Kp-index may be in connection with this situation. At stations at even lower latitudes (e.g. Rybachy, $\Phi_M \sim 66°$), the equatorial boundary of the auroral zone is near to the station only in case of higher geomagnetic activity, and this can be the reason, why excitation of Pc5 occurs only in case of higher values of the Kp-index (≥ 4).

It follows from Fig. 3 that the maximum in the diurnal variation of the occurrence frequency of Pc5 must lie in earlier hours at lower latitude stations. This is also in accordance with the experimental fact that the shift of the maximum in the daily variation is about 2 hours between the stations Rybachy and Cap Zhelaniya, whereby Cap Zhelaniya shows the later occurrences. It should be remarked that these characteristics of the Pc5 parameters are only present at stations lying at latitudes higher than 64—65°. At middle latitude stations lying at greater distances from the boundary of the auroral zone the appearence of Pc5 waves is the consequence of the propagation of MHD waves towards lower latitudes or they result from processes near the plasmapause.

Summary of results. The experimental results described in this paper are in accordance with the conclusions of the present authors in previous papers according to which the excitation of Pc5 in the morning sector is closely connected to the development of disturbances in the night time magnetosphere. This proves that the excitation of Pc5 occurs inside of the magnetosphere in the morning and forenoon hours at latitudes $\Phi_M \sim 64$—$64°$.

A review of the possible excitation mechanisms of Pc5 was given by Raspopov et al. (1978), Afanasyeva (1978) and Lam (1976), and a comparison of the consequences of different theories with the results of observations was also made. A most complete explanation of the experimental facts is yielded in our opinion by the theory of the drifting inhomogeneities which has been proposed by Mikhailovsky et al. (1963) used for the explanation of magnetospheric processes by Coroniti and Kennel (1970) and further developed by Mikhailovsky and Pokhotelov (1975). All experimental facts prove that Pc5 pulsations are excited in the magnetosphere due to drifting instabilities of the inner boundary of the plasma sheet. In accordance with the theory, the spectrum of the growing waves fulfils the resonance condition $\omega \leq \omega_D$, where $\omega_D = k_\perp V_D$ is the drift velocity, $k_\perp$ is the component of the wave vector perpendicular to the outer magnetic field B, V_D is the drift velocity of the particles. The resonance frequency which corresponds to the maximum increment is according to Mikhailovsky and Pokhotelov's estimation (1975) in the frequency range of Pc5. The increment of the growing waves is of the magnitude $\gamma/\omega \sim \beta$. Here γ is the increment, $\omega \lesssim V_D k_\perp$, $\beta = 8\pi p/B^2$ is the ratio of the plasma pressure p to the magnetic pressure. Thus, the instability grows most strongly in case of sufficiently great value of the parameter β. This corresponds to the experimental fact that Pc5 activity is most often

present in magnetically disturbed periods. The amplitude of the pulsations is also growing with the increase of the magnetic activity level. In a wide range Pc5 amplitudes are proportional with the amplitudes of magnetic bays [Afanasyeva et al., 1974]. The amplitude is the greater, the greater the increment $\gamma \sim \beta$ is. The value of β increases with increasing magnetic activity. Here also a quantitative coincidence of theory and observation can be found. The instabilities are found in the morning sector of the magnetosphere near the morning boundary of the plasma-sheet. The distribution of Pc5 at different latitudes shows a localization of its source near the equatorial boundary of the oval, to where the inner boundary of the equatorial boundary of the plasma-sheet is projected. The longitudinal distribution of Pc5 is characterized by a maximum in the early morning hours. A West–East directed azimuthal drift of the structural elements of Pc5 series has been observed.

The results of the study of Pc5 show that in a case of its excitation it can have several sources each of them having a characteristic period. The dimension of the Pc5 source in latitudinal direction is rather small and does not reach more than 1—2°. [Afanasyeva et al., 1977a], being also in accordance with the theory.

The theory describes the generation of the pulsations as excitation of Alfvén waves by high energetic particles. The high energy particles are here electrons with energies of $>$20 keV. The high correlation of Pc5 with electron fluxes drifting from the night time part of the magnetosphere towards the day-time part was shown by Afanasyeva et al. (1973).

Thus, the main characteristics of Pc5 excited in the morning sector of the magnetosphere can be sufficiently well explained by the theory of the drifting instabilities. Naturally a number of the experimental results on Pc5 needs further supplementary theoretical analysis. As a final remark to this study of Pc5 pulsations, it should be emphasized that the observed differences in the behaviour of the morning and afternoon Pc5 do not allow to reject the possibility that long period pulsations in the Pc5 period range are also excited inside the magnetosphere.

REFERENCES

АФАНАСЬЕВА, Л. Т. 1979: Магнитосферные возмущения и геомагнитные пульсации Pc5. Автореферат канд. диссертации. Москва, ИФЗ АН СССР.

АФАНАСЬЕВА, Л. Т.—РАСПОПОВ, О. М.—КУЗНЕЦОВ, С. И. 1973: О связи нерегулярных потоков электронов в магнитосфере с геомагнитными пульсациями. Исследования по геомагнитизму и аэрономии авроральной зоны. Ленинград, Наука, 3—12.

АФАНАСЬЕВА, Л. Т.—РАСПОПОВ, О. М.—КИСЕЛЕВ, Б. В.—ЛОГИНОВ, Г. А. 1974: Геомагнитные пульсации типа Pc5 как элемент суббури. Полярные сияния, Москва, Наука, 93—104.

АФАНАСЬЕВА, Л. Т.—РАСПОПОВ, О. М.—КИСЕЛЕВ, Б. В. 1977a: Пространственно-временные характеристики геомагнитных пульсаций типа Pc5. Структура магнитоионосферных и авроральных возмущений. Ленинград, Наука, 108—115.

АФАНАСЬЕВА, Л. Т.—РАСПОПОВ, О. М.—ШЕПЕТНОВ, Р. В. 1977b: О связи геомагнитных пульсаций типа Pc5 по земной поверхности с параметрами солнечного

ветра. Структура магнито-ионосферных и авроральных возмущений. Ленинград, Наука, 115—120.

ATKINSON, G.—WATANABE, T. 1966: Surface waves on the magnetospheric boundary as a possible origin of long period geomagnetic micropulsations. *Earth and Planet., Sci. Letters*, 1, 2, 89—91.

CLADIC, J. B. 1971: Multiply coupled oscillations of field lines in the magnetosphere: modulation of trapped particles and ionospheric currents. *J. Geophys. Res.*, 10, 2345—2356.

CORONITI, F. V.—KENNEL, C. F. 1970: Auroral micropulsation instability. *J. Geophys. Res.*, 75, 1863—1873.

DUNGEY, J. W.: 1958: Cosmic Electrodynamics. University Press Cambridge.

DUNGEY, J. W.—SOUTHWOOD, D. J. 1970: Ultra-low frequency waves in the magnetosphere. *Space Sci. Rev.*, 10, 672—688.

GUPTA, J. C. 1974a: Amplitude variation of Pc5 pulsation at high latitudes. *Astr. Phys. Space Sci.*, 31, 82—101.

HASEGAWA, A. 1969: Drift mirror instability in the magnetosphere. *Phys. Fluids.*, 12, 2642—2650.

HIRASAWA, T. 1970: Long-period geomagnetic pulsations (Pc5) with typical sinusoidal waveforms. *Report of Ionosphere and Space Res. in Japan*, 24, 66—79.

LAM, H-L. 1976: Generation mechanisms for the transient ultra low frequency oscillations (1—16 mHz) of the earth's magnetic field in the morning sector. Ph. D. Dissertation, University of Alberta, Edmonton, Alberta, Canada.

МИХАЙЛОВСКИЙ, А. Б.—ПОХОТЕЛОВ, О. А. 1975: Новый механизм генерации геомагнитных пульсаций быстрыми частицами. *Физика плазмы*, 1, 786—792.

МИХАЙЛОВСКИЙ, А. Б.—РУДАКОВ, Л. И. 1963: К вопросу об устойчивости пространственно-неоднородной плазмы в магнитном поле. *ЖЭТФ*, 44, 912—918.

ПУДОВКИН, М. И.—РАСПОПОВ, О. М.—КЛЕЙМЕНОВА, Н. Г. 1976: Возмущение электромагнитного поля. Ленинград, Изд-во ЛГУ.

РАСПОПОВ, О. М.—АФАНАСЬЕВА, Л. Т.—КИСЕЛЕВ, Б. В.—ЛОГИНОВ, Г. А. 1972: Динамика магнитосферы и геомагнитные пульсации типа Pc5. *Геомагнетизм и аэрономия*, 12, 150—153.

РАСПОПОВ, О. М.—ЧЕРНОУС, С. А.—РОЛДУГИН, В. К.—ПОХОТЕЛОВ, О. А. 1978: Пульсирующие потоки частиц в магнитосфере и ионосфере. Ленинград, Наука.

ROEDERER, J. G. 1970: Dynamics of Geomagnetically Trapped Radiation. Springer Verlag, Stuttgart.

ROSTOKER, G.—HING-LAN, LAM. 1978: A generation mechanism for Pc5 micropulsations in the morning sector. *Planet. Space Sci.*, 26, 393—505.

SAMSON, J. G. 1972: Three-dimensional polarization characteristics of high-latitute Pc5 geomagnetic micropulsations. *J. Geophys. Res.*, 77, 6145—6160.

SAMSON, J. G.—JACOBS, J. A.—ROSTOKER, G. 1971: Latitude dependent characteristics of long-period geomagnetic micropulsations. *J. Geophys. Res.*, 76, 3675—3683.

СТАРКОВ, Г. В.—ФЕЛЬДШТЕЙН, Я. И. 1968: Полоса полярных сияний при магнитных возмущениях. Полярные сияния, Москва, Наука, 22—33.

ЛОКАЛИЗАЦИЯ Pc5 И ОВАЛ ПОЛЯРНЫХ СИЯНИЯ

О. М. РАСПОПОВ—Л. Т. АФАНАСЬЕВА

РЕЗЮМЕ

По материалам сети наземных обсерваторий, расположенных в субавроральных широтах и авроральной зоне показана связь Pc5 с овалом полярный сияний, приуроченность области генерации Pc5 к экваториальной границе овала при различном уровне магнитной активности. По спутниковым данным известно, что возбуждение Pc5 связано с дрейфом плазменных неоднородностей из ночного региона магнитосферы на дневную ее часть во время суббури. Азимутальный дрейф источника колебаний обнаружен и по наземным данным. Скорость дрейфа $\sim$ 0,5—1,1 град/мин.

Сделано сопоставление выявленных закономерностей с имеющимися теориями возбуждения пульсаций Pc5. Наиболее вероятным механизмом генерации колебаний является дрейфовая неустойчивость, развивающаяся на внутренней границе плазменного слоя в утреннем секторе магнитосферы во время восстановительной фазы суббури.

Acta Geodaet., Geophys. et Montanist. Acad. Sci. Hung. Volume 17 (2), pp. 277—290 (1982)

ABLEITUNG VON FELDTRANSFORMATIONEN FÜR PROFILE VON POTENTIALFELDANOMALIENEN

R. RÖSLER—H. LINDNER

BERGAKADEMIE FREIBERG, SEKTION GEOWISSENSCHAFTEN WISSENSCHAFTSBEREICH ANGEWANDTE GEOPHYSIK

[Eingegangen am October 1. 1980]

Bei der Bearbeitung von Potentialfelddaten, die auf Profilen vorliegen, kann vielfach die Berechnung von Gradienten sowie der zweiten Ableitung die Interpretation erleichtern. Die Anwendung der Hilbert-Transformation und deren Realisierung durch die Fourier-Transformation erlaubt eine praktische Ableitung der gewünschten Feldtransformationen. Die Anwendung einer wellenzahlgebundenen Beschneidungsfunktion sichert eine variable Tiefpaßfilterung und damit eine Unterdrückung von Feldanteilen, welche die Interpretation beeinträchtigen. Vor allem bei hochgelegenen Störkörpern führt dieser Transformationsvorgang zu einer Extremwertverflachung bei gleichzeitiger Verminderung des Fortpflanzungsfehlers. Dieses Verhalten demonstrieren zwei praktische Beispiele. Die Anwendung der Hilbert-Transformation bietet möglicherweise auch ein Hilfsmittel bei der Ableitung von Störungen des gravimetrischen Vertikalgradienten in der Reduktion sowie bei der Dichtebestimmung über zweidimensionalen geologischen Strukturen.

1. Einleitung

Die ständig schwieriger werdenden Erkundungsaufgaben erfordern insbesondere in den Potentialmethoden eine umfassende Ausschöpfung der in den Meßdaten enthaltenen Informationen. Die Nutzung feldtransformierender Bearbeitungsverfahren nimmt daher seit längerem einen festen Platz in der Interpretation ein, wenn es darum geht, flächenhafte Potentialfeldanomalien geologisch zu deuten. Insbesondere durch die Einführung aero- und seegeophysikalischer Meßmethoden besteht jedoch hier vielfach die Aufgabe in einer Deutung profilhaft angelegter Messungen. Dies ist der Grund für zahlreiche Bestrebungen, auch unter diesen Bedingungen über die Berechnung von Gradienten die Aussagefähigkeit der Potentialmethoden zu optimieren [Nabighian, 1972; Green—Stanley, 1975; Stanley, 1977]. Da zumindest in der Gravimetrie eine ökonomisch arbeitende Messung sowohl des Horizontal- als auch des Vertikalgradienten mangels geeigneter Geräte derzeit nicht möglich ist, erscheint eine rechnerische Herleitung aus der gemessenen Feldgröße nach wie vor sinnvoll. Dies gilt auch für magnetische und geothermische Profilaufnahmen. Bei der Berechnung der Feldtransformationen erscheint insbesondere die Diskussion des Horizontalgradienten in der Gravimetrie für die Störungserkundung und die Kombination des Horizontal- und des Vertikalgradienten in der Magnetik für die Abgrenzung lateraler Blockstrukturen nützlich. Vielfach erfordern außerdem die komplizierten Erkundungsprobleme von heute eine komplexe Interpretation aller herleitbaren Feldgrößen.

2. Berechnung von Feldtransformationen

Bis Ende der 60iger Jahre erfolgte die Ableitung aller in der Interpretation benötigten Feldgrößen fast auschließlich über die Verfahren der Kreissummation, d.h. über die punktweise Berechnung sog. Funktionen des arithmetischen Kreismittels. Diese Entwicklung muß mit der umfangreichen Bereitstellung umfangreicher Formelsätze verschiedener Feldtransformationen nach diesem Prinzip durch Grosse (1967) als abgeschlossen betrachtet werden. Verschiedene Probleme, die bei dieser Methode, insbesondere bei der Realisierung größerer Eindringtiefen (z. B. durch die zwangsläufige Schaffung aufpunktsloser Zonen in der Umgebung des Ursprungs) auftraten, gaben Anlaß zu weiterführenden Entwicklungen. Früher bekanntgewordene Arbeiten von Dean (1964) und Zurflueh (1967) machten deutlich, daß auch mit den Verfahren der Fourier-Transformation die Berechnung von Feldtransformationen möglich ist. Als Vorteil dieser Bearbeitungstechnik, die u.a. zu den Verfahren der Wellenlängenfilterung [Lindner—Scheibe, 1977] und der magnetischen Reliefberechnung [Hahn, 1965] führte, muß angezogen werden, daß sämtliche Feldwerte einschließlich des Zentralpunktes in die Berechnung eingehen, ohne daß vorher aufwendige Mittelwertbildungen erfolgen. Eine konsequente Anwendung der Fourier-Transformation für die Bearbeitung von Feldtransformationen gibt Baranov (1975), der eigentlich als Vertreter der Kreissummationsverfahren Ende der 50iger Jahre international im Mittelpunkt stand.

Diese Situation erscheint auch für die Bearbeitung profilhaft vorliegender Potentialfeldanomalien richtungsweisend. Zudem verliefen frühere Versuche, hier Methoden der Kreissummation einzusetzen, als weniger erfolgversprechend (Problem der Randverluste). Angeregt durch verschiedene Arbeiten der Nutzung von Vertikalgradienten [Fajklewicz et al., 1972] und Horizontalgradienten [Hammer—Anzoleaga, 1975] in der Gravimetrie für die Interpretation wird versucht, eine Technik für die Bearbeitung von profilhaft vorliegenden Messungen zu entwickeln. Dabei wird z. T. auf ältere Arbeiten von Nabighian (1972) und Rösler—Lindner (1980) zurückgegriffen.

2.1 *Grundlagen*

Die dargestellten Entwicklungen gelten prinzipiell für alle geophysikalischen Potentialfelder, welche die Laplace-Gleichung erfüllen (z. B. Magnetik, Geothermie). Aus Gründen der Übersichtlichkeit erfolgt hier nur die Darstellung für die Belange der Gravimetrie.

Für zweidimensionale Felder definieren beide Komponenten des Gradienten des Potentials W eine komplexe Funktion

$$V(u) = W_x(u) + iW_z(u)\,, \tag{1}$$

die im Meßraum ($z < 0$) und auf der x-Achse eine reguläre Funktion der komplexen Veränderlichen $u = z + ix$ ist. Mit Hilfe der Cauchy-schen Integralformel kann man eine Beziehung für die Werte der Funktion $V(u)$ auf der x-Achse ($z = 0$) angeben [Rösler, 1976]

$$V(x) = \frac{1}{\pi i} \int_{-\infty}^{\infty} \frac{V(x')}{x' - x} \, \mathrm{d}x'. \tag{2}$$

Daraus folgt durch Zerlegung in Real- und Imaginärteil:

$$W_x(x) = \frac{1}{\pi} \int_{-\infty}^{\infty} \frac{W_z(x')}{x' - x} \, \mathrm{d}x' = \mathcal{H}\{W_z(x'), x\} \, . \tag{3}$$

Dieser Ausdruck wird als Hilbert-Transformation bezeichnet. Über eine Darstellung von (3) durch das Faltungsintegral [Rösler—Lindner, 1980] kann die Hilbert- in die Fourier-Transformation überführt werden, was zu einer Reihe von rechentechnischen Vorteilen führt. Setzt man im Wellenzahlbereich

$$\int_{-\infty}^{\infty} W_x(x) \exp(-i\omega x) \mathrm{d}x = \mathcal{F}\{W_x(x), \omega\} = f(\omega) \, , \tag{4}$$

so ergibt sich

$$W_x(x) = \mathcal{F}^{-1}\{i \operatorname{sign}(\omega) \mathcal{F}\{W_z(x'), \omega\}, x\} \tag{5}$$

d.h. $W_x(x)$ läßt sich durch eine inverse Fourier-Transformation aus dem Spektrum der gemessenen Feldgröße $W_z(x)$ darstellen. Durch Differentiation und Nutzung der Laplace-Gleichung können sämtliche zur Interpretation erforderlichen Feldgrößen aus (5) abgeleitet werden. Eine wechselseitige Bereitstellung von Horizontal- aus Vertikalgradienten und umgekehrt, wie sie z. B. Nabighian (1972) vorschlägt, erscheint daher überflüßig.

Bezeichnet man mit $Q(\omega)$ die Übertragungsfunktion, dann kann aus den an der Erdoberfläche ($z = 0$) gemessenen Feldwerten (hier W_z) nach (5) ein umfassendes System von Feldtransformationen abgeleitet werden.

$$W_{\text{transf.}}(x, z) = \mathcal{F}^{-1}\{Q(\omega) \mathcal{F}\{W_z(x', 0), \omega\}, x\} \, . \tag{6}$$

Bei Vorliegen anderer geophysikalischer Felder können die benötigten Feldtransformationen in analoger Weise mit (6) berechnet werden. An die Stelle von $W_z(x, 0)$ tritt z. B. $\delta T(x, 0)$ (Magnetik) oder $T(x, 0)$ (Geothermie) usw. Für die Belange der Gravimetrie sind in Tabelle I einige Transformationen zusammengestellt.

Tabelle I

Feldtransformationen

α	Feldgröße	Bedeutung	Übertragungsfunktion $Q^{(\alpha)}(\omega)$
1	$W_x(x, 0)$	—	i sign (ω)
2	$W_{xz}(x, 0)$	Horizontalgradient	$i\omega$
3	$W_{zz}(x, 0)$	Vertikalgradient	$\|\omega\|$
4	$W_z(x, z)$	Feldfortsetzung $z < 0$ — nach oben $z > 0$ — nach unten	$\exp(z\|\omega\|)$
5	$W_{zzz}(x, 0)$	Zweite Ableitung	ω^2
6	$\overline{W}_z(x, 0)$	Glättung (siehe 2.2)	$(\sin \omega a/\omega a)^2$
7	$\overline{W}_{zz}(x, o)$	geglätteter Vertikalgradient	$Q^{(3)}(\omega) \cdot Q^{(6)}(\omega)$
	usw.		

2.2 *Einfluß einer Glättung auf die Fehlerfortpflanzung*

Die hier beschriebene Feldtransformation kann in bestimmten Fällen von einer Verstärkung kurzperiodischer und unerwünschter Anomalienanteile begleitet werden. Die Betonung dieser Komponenten stört den Interpretationsprozeß, so daß durch die Anwendung geeigneter Glättungsoperatoren im Sinne einer Tiefpaßfilterung nur die den Interpreten interessierenden Anomalien transformiert werden.

Zweckmäßigerweise verlagert man den Glättungsvorgang in den Wellenzahlbereich. Die Übertragungsfunktion

$$Q(\omega) = \left(\frac{\sin \omega a}{\omega a}\right)^2 \tag{7}$$

bedeutet eine zweimalige gleitende Mittelung im Intervall der Länge $4a$ (Glättungsfenster) für den Ortsbereich, d. h.

$$\overline{W_z(x)} = \frac{1}{2a}\int_{u=x-a}^{x+a} \frac{1}{2a}\int_{v=u-a}^{u+a} W_z(v)\mathrm{d}v\mathrm{d}u = \int_{u=x-2a}^{x+2a} W_z(u)q(x-u)\mathrm{d}u\,. \tag{8}$$

Die für den Ortsbereich wirksame Gewichtsfunktion q lautet

$$q(x) = \begin{cases} (2a + x)/4a^2 & \text{für} \quad -2a \leq x \leq 0 \\ (2a - x)/4a^2 & \phantom{\text{für}} \quad 0 \leq x \leq 2a \\ 0 & \phantom{\text{für}} \quad 2a < |x| \end{cases} \tag{9}$$

aus der sich durch Fourier-Transformation (7) ergibt.

Diese Art der Glättung wurde in Tabelle I mit $Q^{(6)}(\omega)$ bezeichnet. Die in (7) angegebene wellenzahlgebundene Gewichtsfunktion klingt mit wachsenden Wellenzahlen schneller ab als die $\sin a\omega/a\omega$-Funktion (einfache Mittelung im Intervall $2a$). Ihre Amplitude nach der ersten Nullstelle beträgt nur etwa 4% des zentralen Maximums ($\omega = Q$) und es gilt näherungsweise

$$Q(\omega) = 0 \qquad \text{für} \qquad |\omega| > \frac{\pi}{a}. \tag{10}$$

Eine Dämpfung kurzperiodischer Anteile im Wellenzahlbereich mittels (7) nutzte auch Berezkin (1973).

Bei einem Abtastintervall s der gemessenen Anomalien liegen auf einem Abschnitt der Länge $2a$ insgesamt $k = 2a/s$ Punkte. Der "Glättungsparameter" k wird damit zu einem Maß für die Breite des Glättungsfensters. Von der Mittelbildung werden daher $2k - 1$ Abtastpunkte erfaßt. Bekanntlich ist eine Wertereihe der Länge X, bestehend aus $N = X/s$ Werten, durch die Angabe von N äquidistant im Nyquistintervall $0{,}2\pi/s$ verteilten Spektralwerten vollständig beschrieben und es gilt für die Wellenzahl

$$\omega = l\Delta\omega = l\frac{2\pi}{sN}. \tag{11}$$

Für die in die Glättung einbezogenen $2k - 1$ Anomalienpunkte ergibt sich $a = ks/2$ und es folgt aus (7) und (10)

$$Q_l = Q(l\Delta\omega) = \begin{cases} \left(\dfrac{\sin \pi kl/N}{\pi kl/N}\right)^2 & & l = 0, 1, \ldots, N/k \\ 0 & \text{für} & l = N/k + 1, \ldots, N/2 \\ Q_{N-l} & & l = N/2 + 1, \ldots, N - 1. \end{cases} \tag{12}$$

Wenn auch bei der Mittelung im Ortsbereich nur ein ganzzahliges k sinnvoll ist, so besteht dazu bei der Definition der Übertragungsfunktion (12) keine Notwendigkeit. Für den Fall $k = 0$ wird die Glättung aufgehoben. D. h. für variable k entstehen verschiedene Varianten der berechneten Feldgröße, die sich durch eine unterschiedliche Betonung der transformierten Wellenzahlbereiche auszeichnen (z. B. zur Trennung von vertikal angeordneten Störkörperensembles). Abb. 1 zeigt den Verlauf von Q_l-Funktionen für verschie-

dene Werte von $N_1 = N/k$. N_1 gibt an, das Wievielfache des halben Mittelungs fensters gleich der Profillänge X ist.

$$N_1 = N/k = X/2a \tag{13}$$

Die zugehörigen k-Werte sind für $N = 64$ und $N = 80$ Punkte in Tabelle II dargestellt.

Tabelle II

Zusammenhang von Glättunsparameter k und dem Verhältnis des halben Mittelungsfensters zur Profillänge

N_1	k	
	$N = 64$	$N = 80$
16	4	5
24	2,67	3,33
32	2	2,5
40	1,6	2

Von Rösler (1980) wurde für verschiedene Feldtransformationen der mittlere quadratische Fehler nach dem Fehlerfortpflanzungsgesetz berechnet. Für die Kombination der Berechnung des Schweregradienten mit der hier beschriebenen Glättung erhält man die in Abb. 2 dargestellte Abnahme des Fehlers mit der Vergrößerung der Breite B des Glätterungsfensters, für die der Parameter k ein Maß ist.

2.3 *Extremwertwiedergabe*

Durch Modellberechnungen konnte gezeigt werden, daß bei einer ungeglätteten Bearbeitungsvariante mit dem o.g. Algorithmus nur Extremwertbeschneidungen von etwa 1% im Vertikalgradienten auftreten [Rösler—Lindner, 1980]. Es liegt daher die Frage auf der Hand, wie diese Situation bei Nutzung der dargestellten Glättung im Wellenzahlbereich einzuschätzen ist. Dabei wird auf die sog. relative Extremwertwiedergabe

$$R(t) = W_z(0)_{\text{transf}}/W_z(0)_{\text{theoret.}} \tag{14}$$

nach Grosse (1967) zurückgegriffen. Auf Grund der geforderten Zweidimensionalität der betrachteten Potentialfelder erfolgt die Wahl des liegenden Zylinders als Modell. Den geglätteten Vertikalgradienten erhält man durch eine Faltung mit der Gewichtsfunktion

$$\overline{W_{zz}}(x, 0) = W_{zz}(x, 0) * q(x) \tag{15}$$

z. B. für den liegenden Zylinder:

$$\overline{W}_{zz}(x,0) = W_{zz}(0,0)\frac{t^2}{2a}\int_{-2a}^{+2a}\frac{t^2-(x-x')^2}{[t^2+(x-x')^2]^2}\left(1-\frac{|x'|}{2a}\right)\mathrm{d}x'. \tag{16}$$

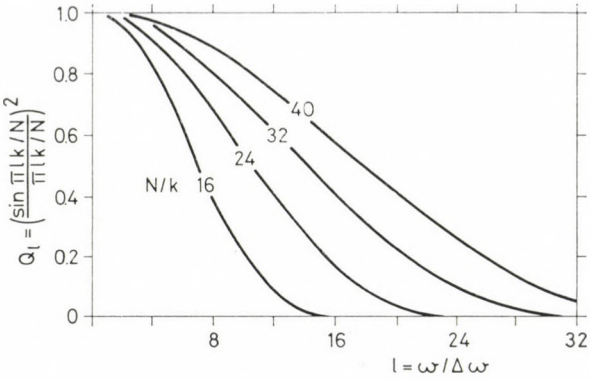

Abb. 1. Glättungsfunktionen

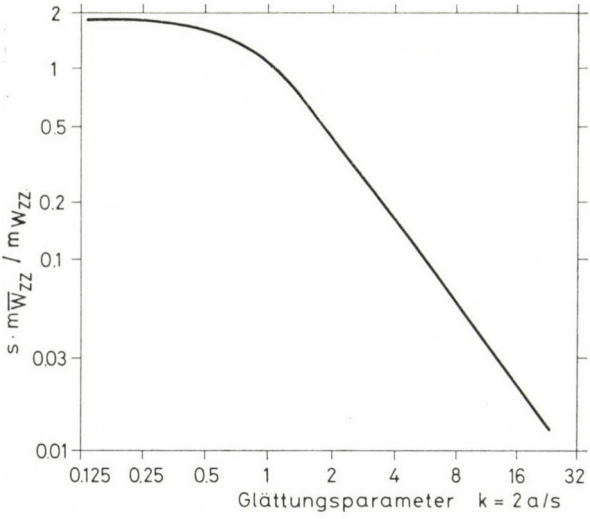

Abb. 2. Fehlerfortpflanzung des Vertikalgradienten als Funktion des Glättungsparameters

Die Beschränkung auf den Ursprung ($x = 0$) ergibt aus (16) die $R(t)$-Funktion des Vertikalgradienten

$$R(t) = \frac{\overline{W}_{zz}(0,0)}{W_{zy}(0,0)} = \frac{t^2}{4a^2}\ln\left(1+\frac{4a^2}{t^2}\right). \tag{17}$$

Abb. 3 verdeutlicht den Verlauf dieser Funktion für verschieden gewählte Glättungsparameter k und variable Teufen des Modells. Es ergibt sich das auch von anderen Feldtransformationen her gewohnte Bild:

1. Eine Erhöhung des Glättungsparameters k (entspricht im Ortsbereich einer Verbreiterung des zur Glättung verwendeten Fensters mit der Breite $4a$) führt zu einer Extremwertsbeschneidung des Nutzsignals.

2. Tiefer gelegene Störkörper folgen dieser Tendenz weniger als oberflächennahere. Dieser Effekt tendiert in Richtung der Wellenlängenfilterung, d. h. je höher der Glättungsgrad ist, umso mehr treten die kurzwelligen Anteile im transformierten Anomalienbild zurück.

3. Anwendung

Nachdem bereits früher für eine sehr glatte Schwereanomalie festgestellt werden konnte, daß die gleichzeitige Bereitstellung von Horizontal- und Vertikalgradienten mittels der Hilbert-Transformation ohne Glättung zu guten Ergebnissen führte [Rösler—Lindner, 1980], wurde zur Bearbeitung gestörter Felder übergegangen. Dabei zeigte sich sehr rasch, daß ohne eine Beschneidung kurzwelliger Anomalienteile nur schwer interpretierbare Transformationen entstehen. Ausgehend von Erfahrungen mittels der o.g. Übertragungsfunktion eine Glättung im Wellenzahlbereich für geothermische Anomalien zu erzielen [Rösler et al., 1980], erfolgte eine Anwendung des Verfahrens in der Gravimetrie.

3.1 *Bearbeitung gravimetrischer Profile*

Abb. 4 zeigt die gravimetrische Lokalanomalie einer Auskesselung im kristallinen Grundgebirge, die mit leichten neogenen Sedimenten gefüllt ist. Eine Gradientenberechnung einschl. der zweiten Ableitung zeigte eine starke Betonung des kurzwelligen Minimums bei 4,5 km. Erst die Anwendung einer wellenzahlgebundenen Glättung erbrachte die dargestellten Feldtransformationen, die einer Interpretation zugänglich sind. Bei einem Abtastintervall von 0,1 km und einem N/N_1-Verhältnis von 1 ergeben sich die in Tabelle III

Tabelle III

Fortpflanzungsfehler der in Abb. 4 und 5 dargestellten Anomalien

Anomalie	s in m	m_{W_z} in mGal	$m_{W_{xz}}, m_{W_{zz}}$ in mGal · m^{-1}	$m_{W_{zzz}}$ in mGal · m^{-2}
Abb. 4	100	0,1	$5 \cdot 10^{-4}$	$1{,}4 \cdot 10^{-6}$
Abb. 5	1,5	0,02	$66 \cdot 10^{-4}$	$2{,}2 \cdot 10^{-3}$

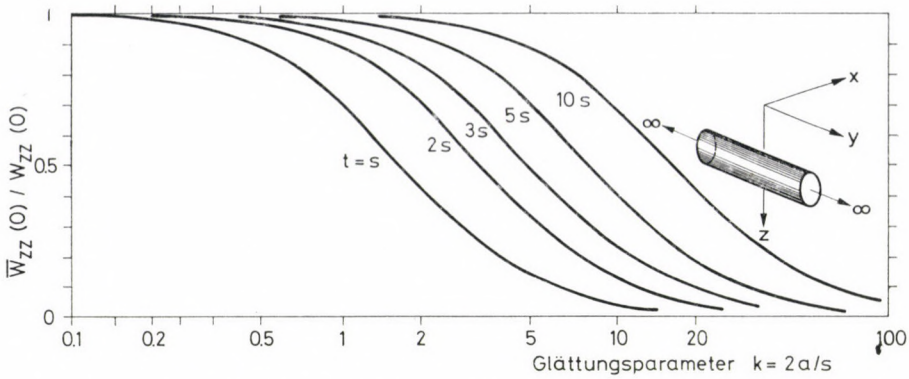

Abb. 3. Extremwertwiedergabe über dem Zylindermodell

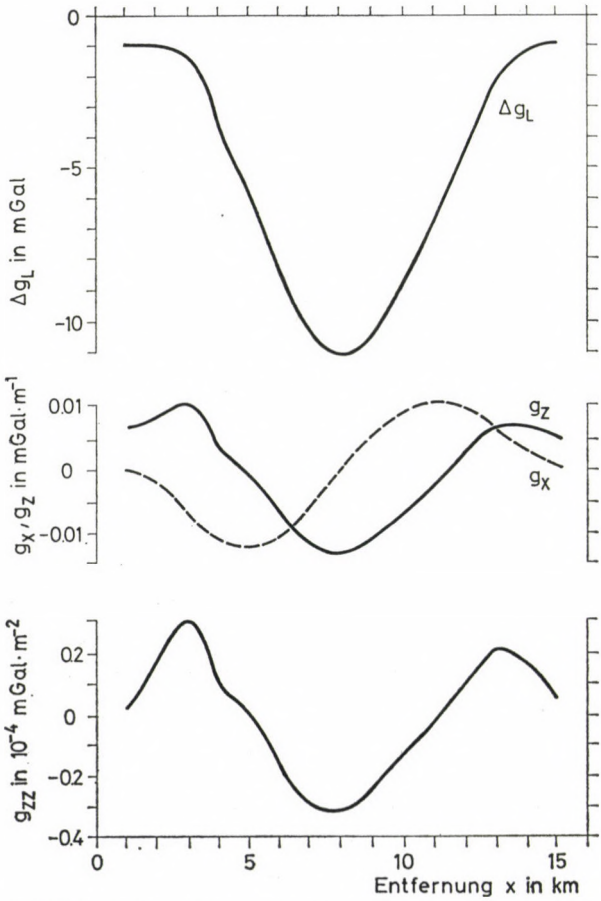

Abb. 4. Feldtransformationen über einer Auskesselung im Kristallin

dargestellten Fortpflanzungsfehler. Eine wesentlich unruhigere Anomalie aus dem Mikrobereich zeigt Abb. 5. Bei 13,5 m zeigt die Lokalanomalie ein Minimum, das die Lage eines bergmännischen Hohlraumes anzeigt. Die starke Rauhigkeit des Meßbildes erforderte bei einem Abtastintervall von 1,5 m die Wahl eines Verhältnissen $N/N_1 \approx 1{,}25$. Die berechneten Feldtransformationen bilden das Minimum deutlich ab und zeigen das über einem Hohlraum gewohnte Bild. Die entsprechenden Fortpflanzungsfehler sind in symbolischer Darstellung in Abb. 5 enthalten und gleichfalls in Tabelle III dargestellt.

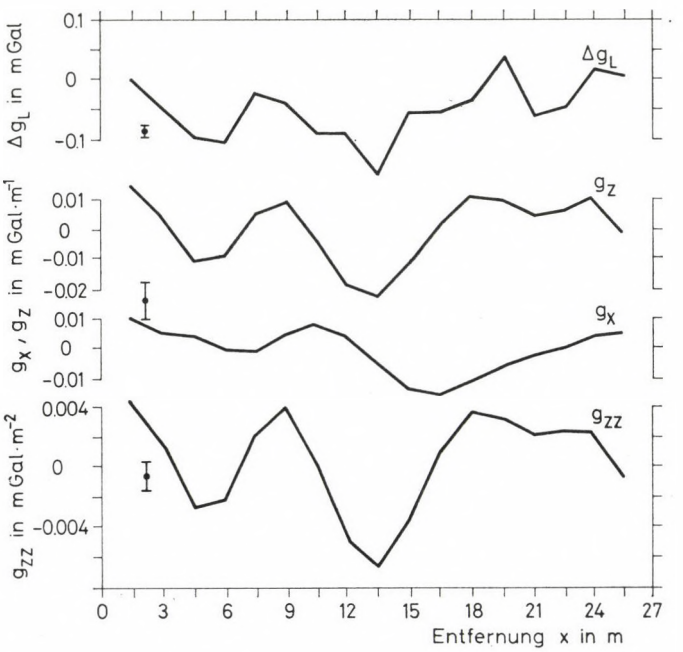

Abb. 5. Feldtransformationen über einem bergbaulichen Hohlraum

Die in Tabelle III zusammengestellten Fortpflanzungsfehler für völlig unterschiedliche Anomalien zeigen u.a. die starke Abhängigkeit der Fehler vom Abtastintervall *s*. Die angegebenen Werte liegen dabei durchwegs in der Größenordnung, wie sie auch von anderen Feldtransformationen her bekannt sind [Rösler, 1980].

3.2 *Reduktion und Dichtebestimmung*

Bei der Erhöhung der Genauigkeit gemessener Schwereanomalien gilt es, den erzielten hohen Stand der reinen Meßgenauigkeit (ca. 0,01 mGal) nicht durch den nachfolgenden Reduktionsvorgang in Frage zu stellen. Neben dem Problem der Geländereduktion kann in vielen Fälle die Unkenntnis des

Freiluftgradienten zu fehlerhaften Anomalien führen. Götze et al. (1978) errechnen unter extremen Verhältnissen alpiner Hochgebirge Fehler der Bouguer-Anomalien bis zu 20(!) mGal, die sich aus diesem Sachverhalt ableiten und bestimmen den wahren Freiluftgradienten empirisch aus Zweiniveaumessungen. Eine nachfolgende Glättung mittels Spline-Funktionen wirft daher die Frage auf, inwieweit hier der mittels der Hilbert-Transformation berechnete Gradient u. U. nicht zu einem ähnlichen Ergebnis führt. Entsprechende Anwendungsbeispiele sind in Vorbereitung. Erschwerend wirkt sich hier allerdings die Gebundenheit des Verfahrens an zweidimensionale Strukturen aus. Bei Annahme der Gleichheit von $W_z(0)$ eines zylinder- und kugelförmigen Störkörpers ergibt sich für das Verhältnis der zugehörigen Vertikalgradienten

$$W_{zz}(0_{\text{Kugel}})/W_{zz}(0)_{\text{Zylinder}} = 2$$

d. h. die Amplitude des mit der Hilbert-Transformation berechneten (Glättungsparameter $k = 0$!) besitzt im Extremfall nur die Hälfte des über einer dreidimensionalen Struktur zu erwartenden Wertes. Diesem Sachverhalt ist daher entsprechend Rechnung zu tragen.

In ähnlicher Weise tritt diese Problematik auch bei der Dichtebestimmung mittels $W_{zz}(0)$-Werten auf. Thyssen—Jacoby (1971) und Bližkovský (1979) bestimmen mittels gravimetrischer Zweiniveaumessungen die Dichteverhältnisse im Oberflächenbereich. Die Unkenntnis der normalen Freiluftgradienten bei dieser Methodik [Rösler—Lindner, 1980] kann hier durch Niveauverfälschungen Probleme aufwerfen, die mit dem o.g. Transformationsprozeß nicht gegeben ist. Allerdings gilt hinsichtlich der Konfiguration der angesprochenen Dichteinhomogenitäten das unter dem Reduktionsproblem Gesagte in gleicher Weise.

3.3 *Eine verbesserte Freiluftreduktion. Die Anwendung des Vertikalgradienten auf die Freiluftreduktion*

Zur Bestimmung der Bouguer-Anomalie gravimetrischer Messungen sind nach dem Abzug der Normalschwere γ_0 die Geländereduktion δg_{Top}, die Bouguer-Reduktion δg_B und die Freiluftreduktion anzubringen.

Wir setzen die für δg_{Top} und δg_B erforderliche Dichte als hinreichend genau bekannt voraus und untersuchen hier die Frage der genauen Bestimmung der Freiluftreduktion δg_F. Für diese wird üblicherweise der Vertikalgradient

$$F = = \frac{\partial \gamma_0}{\partial z} = 3086 \cdot 10^{-9}\,\text{s}^{-2} \text{ (für } \varphi = 50^\circ \text{ Breite)}$$

verwendet, jedoch weist schon Jung (1961) darauf hin, daß die Schwereanomalien $\Delta g''$ notwendigerweise auch mit einer Anomalie des Vertikal-

gradienten Δg_z verbunden sind. Eine exakte Reduktion sollte aber unter Verwendung des wahren Vertikalgradienten $F + \Delta g_z$ erfolgen. In den obigen Ausführungen wurde gezeigt, daß durch die beschriebenen Transformationen auch die Anomalien des Vertikalgradienten aus der Schwereanomalie, speziell aus der Bouguer-Anomalie $\Delta g''(x)$ berechnet werden können und zwar gilt nach (6) mit $Q(\omega) = |\omega|$:

$$\Delta g_z(x) = \mathfrak{F}^{-1}\{|\omega|\mathfrak{F}\{\Delta g''(x'), \omega\}, x\}\,, \tag{18}$$

so daß die exakte Freiluftreduktion für eine Höhe h des Meßpunktes über dem Reduktionsniveau

$$\delta g_F(x) = \big(F + \Delta g_z(x)\big)h \tag{19}$$

beträgt. Nun ergibt sich die Bouguer-Anomalie in folgender Weise aus den Meßwerten $g(x)$:

$$\begin{aligned} \Delta g''(x) &= g(x) - \gamma_0 + \delta g_{\mathrm{Top}} - \delta g_B + \delta g_F \\ &= \Delta g^*(x) + \delta g_F(x) \end{aligned} \tag{20}$$

wobei die ersten vier Glieder zu Δg^* zusammengefaßt worden sind. Aus (20) erhält man mit (18) und (19) eine *Integralgleichung* für die Bouguer-Anomalie

$$\begin{aligned} \Delta g''(x) &= \Delta g^*(x) + [F + \mathfrak{F}^{-1}\{|\omega|\mathfrak{F}\{\Delta g''(x'), \omega\}, x\}]h \\ &= \Delta g^*(x) + \left[F + \frac{1}{2\pi}\int_{-\infty}^{\infty} |\omega| e^{i\omega x} \int_{-\infty}^{\infty} \Delta g''(x') e^{-i\omega x'} dx' d\omega\right] h. \end{aligned} \tag{21}$$

Unter Beachtung der Tatsache, daß die Anomalie (18) des Vertikalgradienten $\Delta g_z(x)$ klein gegen den Vertikalgradienten der Normalschwere ist:

$$|\Delta g_z(x)| \ll F \tag{22}$$

kann man ein Iterationsverfahren zur Lösung der Integralgleichung (21) aufstellen. Den üblichen Ausdruck der Bouguer-Anomalie erhalten wir aus

$$\Delta g''_{k+1}(x) = \Delta g^*(x) + [F + \Delta g_{z_k}(x)]h \tag{23}$$

als erste Näherung für $k = 0$, wenn $\Delta g_{z_0}(x) = 0$ gesetzt wird. Mit

$$\Delta g_{z_k}(x) = \mathfrak{F}^{-1}\{|\omega|\mathfrak{F}\{\Delta g''_k(x'), \omega\}, x\} \tag{24}$$

kann iterativ aus (23) die Bouguer-Anomalie $\Delta g''_{k+1}(x)$ für $k = 1, 2, \ldots$ berechnet werden. Für praktische Anwendungen dürfte der erste Iterationsschritt

($k = 1$) eine ausreichende Genauigkeit des iterativen Näherungsverfahrens bieten. Es sei jedoch vermerkt, daß an dieser Stelle keine Angaben über die Konvergenz des Iterationsverfahrens gemacht werden können. Gerade bei geringen Größen von Schwereanomalien ist an lokalen Anomalien mit oberflächennahen Ursachen mit Anomalien des Vertikalgradienten zu rechnen, die bei veränderlicher Stationshöhe zu einer merklichen Beeinflussung der Anomalien führen. Es sei an dieser Stelle an Abb. 5 erinnert, in der die Anomalie von Δg_z maximal $200 \cdot 10^{-9}$ s^{-2} beträgt und an das von Rösler—Lindner (1980) gezeigte Beispiel mit $300 \cdot 10^{-9}$ s^{-2}.

SCHRIFTTUM

BARANOV, W. 1975: Potential fields and their transformations in applied geophysics. Gebr. Bornträger, Berlin—Stuttgart.

BEREZKIN, V. M. 1973: Применение гравиразведки для поиски месторождений нефти и газа. Nedra, Moskva.

BLIŽKOVSKÝ, M. 1979: Processing and applications in microgravity surveys. *Geophys. Prospecting*, 27, 848—861.

DEAN, W. C. 1958: Frequency analysis for gravity and magnetic interpretation. *Geophysics*, 23, 97—121.

FAJKLEWICZ, Z.—DUDA, W.—SLIZ, J. 1971: Pomiar gradientu pionowego sily ciekosci dla plytko lezacych struktur geologicznych i badania górotworu. *Przeglad Geol.*, 2, 101—106.

GÖTZE, H.-J.— ROSENBACH, O.—SCHÖLER, W. 1978: Gravimetrische Untersuchungen in den östlichen Zentralalpen. *Geol. Rundschau*, 68, 61—82.

GREEN, R.— STANLEY, J. M. 1975: Application of Hilbert transform method to the interpretation of surface-vehiclemagnetic data. *Geophysical Prospecting*, 23, 18—27.

GROSSE, S. 1968: Methodische Untersuchungen von Potentialfeldtransformation für die stockwerkgegliederte Interpretation von Schwerefeldern. Dissertation. Mathem. Naturwiss. Fakultät der Bergakademie Freiberg.

HAHN, A. 1965: Two applications of Fourier's analysis for the interpretation of geomagnetic anomalies. *J. Geomagnetism and Geoelectricity*, 17, 195—225.

HAMMER, S.— ANZOLEAGA, R. 1975: Exploring for stratigraphic traps with gravity gradients *Geophysics*, 40, 256—268.

JUNG, K. 1961: Schwerkraftverfahren in der angewandten Geophysik. Akadem. Verlag-Ges., Leipzig.

LINDNER, H.—SCHEIBE, R. 1977: Interpretationstechnik für gravimetrische und magnetische Felder. *Freib. Forsch. H.* C. 322.

NABIGHIAN, M. N. 1972: The analytic signal of two-dimensional magnetic bodies with polygonal cross-section: Its properties and use for automated anomaly interpretation. *Geophysics*, 37, 507—517.

RÖSLER, R. 1976: Die schnelle Hilbert-Transformation. *Nachrichtentechnik/Elektronik*, 26, 47—48.

RÖSLER, R. 1980: Über die Fehlerfortpflanzung bei Potentialfeld-Transformationen. *Gerlands-von Beiträge z. Geophysik* 90, 47—57.

RÖSLER, R.—LINDNER, H. 1980: Die Anwendung der Hilbert-Transformation bei der Deutung von Schwereprofilen. *Freib. Forsch. H.* C 359, 43—54.

RÖSLER, R.—LINDNER, H. 1982: Die Anwendung von Feldtransformationen auf Profile Schwermessungen. *Freib. Forsch. H.* C 368, 167—173.

RÖSLER, R.—LINDNER, H.—OELSNER, CHR. 1980: Die Bestimmung des vertikalen Temperaturgradienten aus horizontalen Temperaturverteilungen. *Gerlands Beiträge z. Geophysik* 89,389—398.

STANLEY, J. M. 1977: Simplified magnetic interpretation of the geological contact and thin dike. *Geophysics*, 42, 1236—1420.

THYSSEN-BORNEMISZA, St. v.—JACOBY, W. R. 1971: Vertical gradient of gravity for areal density contrast exploration. *Z. f. Geophysik*, 37, 735—741.

ZURFLUEH, E. 1967: Applications of two-dimensional linear wavelength filtering. *Geophysics*, 32, 1015—1035.

РАСЧЕТ ПРЕОБРАЗОВАНИЙ ОТ ПРОФИЛЕЙ ПОТЕНЦИАЛЬНОГО ПОЛЯ

Р. РЁЗЛЕР–Х. ЛИНДНЕР

РЕЗЮМЕ

При обработке данных потенциального поля, измеренных на профилях, расчет градиентов и второй производной может часто облегчать интерпретацию.

Применение преобразования Гильберта и его реализация через преобразование Фурье позволяет на практике получить желаемое преобразование поля. Применение множителей, связанных с волновыми числами, обеспечивает высокочастотную фильтрацию и, таким образом, подавление составляющих поля, затрудняющих интерпретацию. Особенно при неглубоко лежащих возмущающих телах этот процесс преобразования приводит к уменьшению экстремальных значений при одновременном уменьшении ошибки. Это показано на двух практических примерах. Применение преобразования Гильберта в отдельных случаях позволяет определение помех вертикального градиента силы тяжести, а также определение плотности двумерных геологических структур.

Acta Geodaet., Geophys. et Montanist. Acad. Sci. Hung. Volume 17 (2), pp. 291—306 (1982)

КОМПЛЕКСНАЯ ГЕОФИЗИЧЕСКАЯ РАЗВЕДКА В ПУСТИНЕ ГОБИ

Л. НЕМЕШИ
ВЕНГЕРСКИЙ ГЕОФИЗИЧЕСКИЙ ИНСТИТУТ ИМ. Л. ЭТВЕША

Е. БОГНАР
ВЕНГЕРСКОЕ ГИДРОТЕХНИЧЕСКОЕ ПРОЕКТНОЕ ПРЕДПРИАТИЕ „ВИЗИТЕРВ"

ЛАВДАНСУРЕН—ХОВДХАН
МОНГОЛЬСКАЯ ТОПО-ГЕОФИЗИЧЕСКАЯ ЭКСПЕДИЦИЯ

Т. МАЙКУТ—Ч. ТОТ
ВЕНГЕРСКИЙ ГЕОФИЗИЧЕСКИЙ ИНСТИТУТ ИМ. Л. ЭТВЕША

[Поступило 8 Февраля, 1981 г.]

Авторы показали методику геологической интерпретации комплексных геофизических-гидрогеологических работ, выполненных в пустынных, полупустынных областях Гоби.

Описанные приемы показывали, что применение нескольких методов геофизики может предоставлять и такие результаты, которые иногда ни один метод не может дать самостоятельно. А с другой стороны чувствуется экономическая эффективность комплексных исследований. Приемы, которые описали выше могут быть применены на решение других задач и в пределах других районов. Но так думаем, что данный прием является хорошим примером, что при поисках подземных вод в районах развития терригенных отложений, которые имеют в свою очередь частую и быструю вертикальную и горизонтальную изменчивость, как раз имеется большой необходимостью применение комплексных исследований такого характера. Так как часто имеется совпадение физических параметров водоносных толщин параметрами неперспективных — с точки зрения водоснабжения — образований (например, кажущееся сопротивление водообильных песков совпадает с ϱ неперспективных эффузивов; или скорость распространения сейсмических волн в водообильных песках и непродуктивных плотных глинах и т. д.). Но совместным применением нескольких методов интерпретации можем производить однозначно.

Правильность наших рассуждений до настоящего времени доказывалась многими буровыми скважинами.

В 1974—1975-ых годах в пределах пустыни Гоби работала комплексная геофизическая-гидрогеологическая экспедиция. Задачей экспедиции являлась поиски подземных вод, интересные геофизические результаты которых хотим описать в настоящей статье.

Площадью исследований являлась территория 4500 км^2; в пределах и в окружающей её областях за последние 90 лет на решении разнообразных задач, разной детальности, выполнили работы около 30 геологических и геофизических отрядов.

Из этих отрядов непосредственной целью работ являлись поиски подземных вод одного отряда (группа Васильева). Они занимались — главным образом поиском трещиноватых подземных вод в области выхода на поверхность гранитов, и окомляющей их в зоне коллювиальных погребных образований. Количество открытых таким образом подземных вод сказалось недостаточным. Центральные части бассейнов они изучали недостаточно, поэтому мы свои силы направили на разведку данной области. Из результатов предыдущих работ (как, например, группы Фомины и Васильева) было оче-

видно, что областью наших исследований является погруженная, осадками заполненная впадина, протяженностью 30—60 км, которая с востока открыта. На её краях простиранием восток-северо-восток, запад-юго-запад — залегают, главным образом, эффузивы, интрузии, сланцы палеозойской группы (образование которых произошло между ордовинской и пермской систем), и реже эффузивы мезозойской группы. Впадина заполнена терригенными, обломочными отложениями небольшой мощности юрской системы, но главным образом меловой и палеогеновой-неогеновой систем: конгломератами, песчаниками озерными глинами и эффузивами. Ранее проведенные работы определили, максимальную мощность как 2000—5000 метров. В конце концов эти исследования и дали хорошую основу для проектирования проводимых работ.

Для изучения внутреннего строения впадины применился комплекс геофизических методов, таких как, магниторазведка, гравиразведка, электроразведка (теллурические исследования и ВЭЗ, расположением электродов **AMNB** и ДЭЗ), и сейсморазведка методом отраженных волн. С целью определения глубины впадины и её внутреннего строения выполнялись наблюдения на 3000 гравитационных, 2000 магнитных, 650 теллурических имыстах; провели сейсмический профиль общей длиной 400 км и 500 кривых ВЕЗ. Эти измерения выполнили в вышеописанном порядке, с учетом экономики и времени необходимого для обработки. Результаты геофизических работ интерпретировались следующим образом:

Карты гравитационных (аномалии Буге) и теллурических аномалий показывали большое сходство. Из этих карт — по первичной обработке видно, что внутри площади исследований расположены друг от друга разделены разломами, гребнями и выходами фундамента на поверхность долины, балки, ложбины.

Карты магнитных (ΔZ) аномалий и карты гравитационных остаточных аномалий показывали, что в пределах долины в осадочных породах расположено чрезвычайно большое количество вулканического материала основного состава. При самостановлении данных магниторазведки и геологического опыта с нами был сделан очень интересный вывод: эффузивы основного состава образования ранних систем полеозойской группы имеют отрицательные (ΔZ) аномалии, более ранних систем полеозайской группы слабо положительные (ΔZ), а образования мезозойской группы (меловой системы) интенсивные положительные (ΔZ) аномалии, по отношению выбранного фона (по отношению нулевого ΔZ изодинама аэромагнитных аномалий). Эти данные чрезвычайно практично использовались в неоднозначных случаях определения возраста.

Качественный геофизический модель, которая была построена с помощью классических методов геофизики, старались дополнить количественным содержанием. Для этого служили ВЭЗ, сейсмические работы и в некоторых случаях бурения глубоких скважин, и выполненные в них простые

каратажные работы. С увеличением количества материала, полученного из количественных методов, стало ясным, что осадки, заполнявшие впадины (похоже на нынешнюю морфологию) были связаны реками и озерами, с диаметром в несколько километров. На это указывают и часто меняющиеся параметры как в горизонтальном, так и в вертикальном направлениях. В пределах участка исследований нам удалось различить II бассейнов, контуры которых в грубых чертах были известны по аномалиям Буге, а также по картам теллурических аномалий, и в пределах которых физические параметры относительно постоянные. Из этих II бассейнов бывают и такие, которые похожи друг на друга. Итак в конце концов в результате комплексной интерпретации геофизических измерений нам удалось разделить 7 разных геологических моделей. Эти модели показываем на 7 схематических профилях, причем в верхней половине разрезов даются результаты геофизических исследований, а под ними их геологическая интерпретация.

Первый тип (рис. 1). Толща, заполняющая среднюю, глубокую часть впадины и имеющая среднюю скорость сейсмических волн 3300 м/сек представлена конгломератом. Кровлей является граница раздела $\varrho > 60—80$ омм

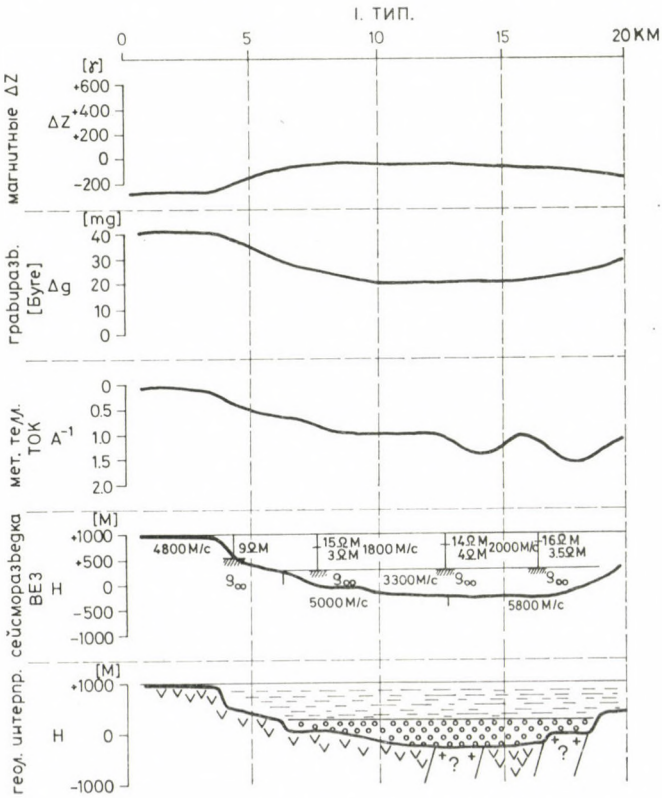

Рис. 1

по ВЭЗ. Верхняя толща, с мощностью 500—600 м; с электрическим сопротивлением ($\varrho = 2{,}5 \div 5$ омм) и со средней скоростью сейсмических волн 1800—2000 м/сек — глиной. (Эта толща вскрыта и бурением). Гравитационные аномалии имеют гладкое изменение, и хорошо прослеживаются сейсмическим уровнем волн 4800—5800 м/сек. Магнитные аномалии являются зеркальными по отношению гравитационных.

Вначале разреза андезитовый порфирий палеозойской группы имеет коренный выход на поверхность — предполагается, что данное образование является фундаментом высокой скоростью сейсмических волн. Они имеют наверняка, слабую, отрицательную намагниченность, которая при выходе на поверхность имеет интенсивность $\Delta Z = -250\ \gamma$.

Теллурические аномалии в начале разреза хорошо совпадают с морфологией фундамента. Но в центральных частях разреза бывают такие минимумы, которые различаются от глубины фундамента, определенной сейсмо- и гравиразведкой, и не могут быть объяснены границей раздела отложений, определенной с помощью ВЭЗ. Поэтому придется предпологать, что фундамент имеет неоднородное электрическое сопротивление. (Глубинность исследований использованными теллурическими импульсами > 5 км, а глубинность ВЭЗ < 2 км).

Второй тип (рис. 2). В начале разреза порфирит залегает в небольшой глубине, в середине разреза выходит на поверхность, а потом вдоль нескольких разломов сбрасывается до глубины 2000 м. Вдоль разломов по многим каналам произошло извержение эффузивов основного состава, которое отчетливо показывает карта магнитных аномалий. Базальт мезозойской группы от центров извержения покрывал осадки мощностью несколько сот метров под нынешнем уровнем в глубине примерно 500—600 м. Кровля базальта на кривых ВЭЗ разносом $AB = 1200 - 1600$ м оказалась ϱ_∞, и по сейсмической скорости являлась поверхностью граничной скорости 4000 м/сек. Не однозначно, что базальт залегает не непосредственно на фундаменте, а имеется промежуточная толща, показано сейсмическим данным и хорошо выражается и по теллурическим аномалиям, которые имеют хорошую корреляцию очертанием фундамента высокой сейсмической скоростью, доказано этим, что удельное электрическое сопротивление 2000 метров толщи небольшое, значит базальт высокого ϱ по отношению всей толщи имеет небольшое распространение и объем.

Верхняя толща, над базальтом по сейсмическим скоростям разделяется на два отложения, которые имеют сейсмическую скорость 1600—2100 м/сек и 3300 м/сек. Интересно зато и то, что обе эти толщи имеют небольшие ϱ по буровым скважинам скорости вверху более рыхлые, внизу более плотные глины, аргиллиты.

Из-за плотных глин с высокой плоскости, и базальтов, залегающие под эффузивными образованиями, независимо от больших изменений глубины

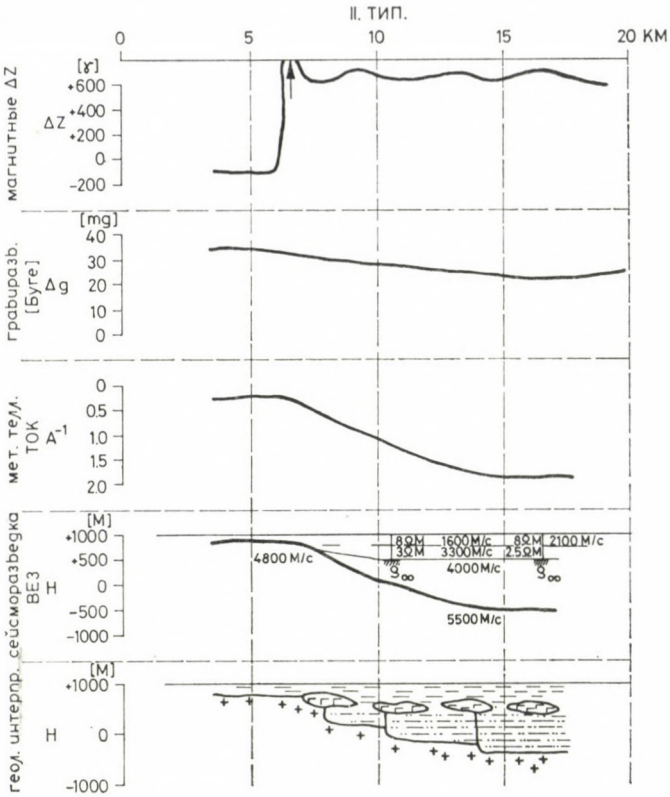

Рис. 2

фундамента Буге менее характерные, отчетливые, чем в предыдущем случае.

Третий тип (рис.3). В данный тип включаются бассейны мелкой и средней глубины залегания фундамента.

Самая характерная их черта, совпадение сейсмических и электрических границ, значит уровень высокой скорости сейсмических волн, совпадает с границей ϱ_∞. Так как вдоль разреза небольшие изменения магнитных аномалий хорошо коррелируют изменением морфологии фундамента предполагается, что фундамент состоит из слабо-основных (верхнепалеозойских) образований. В пределах осадочной толщи нет основных эффузивов, и средняя плотность, среднее ϱ вдоль разреза очень слабо меняется. Это является следствием совпадения теллурических и Буге аномалий от морфологий фундамента. Зато осадочная толща является неоднородной, главным образом, по ВЭЗ, но оправдвется эта неоднородность и по его бурениям. Сопротивление часто меняется, что соответствует чередованием слоев глин, песков, конгломератов и песчанников, но бывают пресноводные известняки. Но нам нужно заметить, что часто одинаковые параметры не означают одинаковые образования.

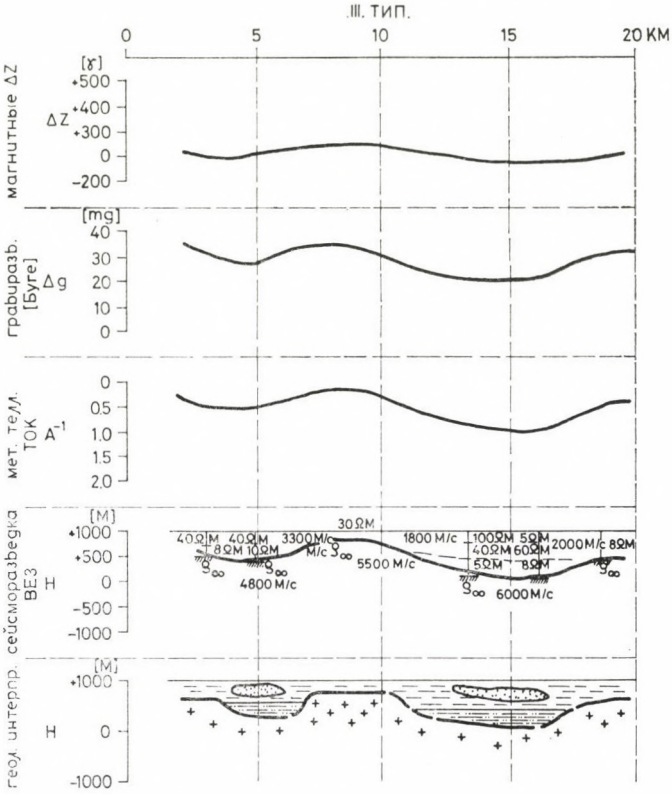

Рис. 3

Геологические исследования, бурения доказывали, что толща, с $\varrho =$ $= 60-80$ омм местами представляют эффузивы, иногда сухие глины, но могут быть и конгломераты, пески с водой, безводные песчаники. Но при III-ем типе присутствие эффузивов исключает отсутствие местных гравитационных и магнитных аномалий.

Низкое сопротивление более глубоких горизонтов указывает, главным образом, на присутствие глины. Толща глины может прерываться прослоями конгломератов, на присутствие которых можем судить на основе слабо проявляющегося отражения сейсмических волн, с поверхности горизонта скоростью от 2900 до 3300 м/сек.

Четвертый тип (рис. 4). На основе геофизических исследований наиболее трудно интерпретируется данный тип строения. Граница с ϱ_∞ отчетливо находится на 400—500 м выше, чем граница строения сейсмических волн 5500—6000 м/сек (на рисунке от 0 до 15 км). На участке мелких глубин (от 0 до 5 км) получили объяснение данного явления: здесь уже в глубине $H = 60$ м вскрыли буровыми скважинами андезит.

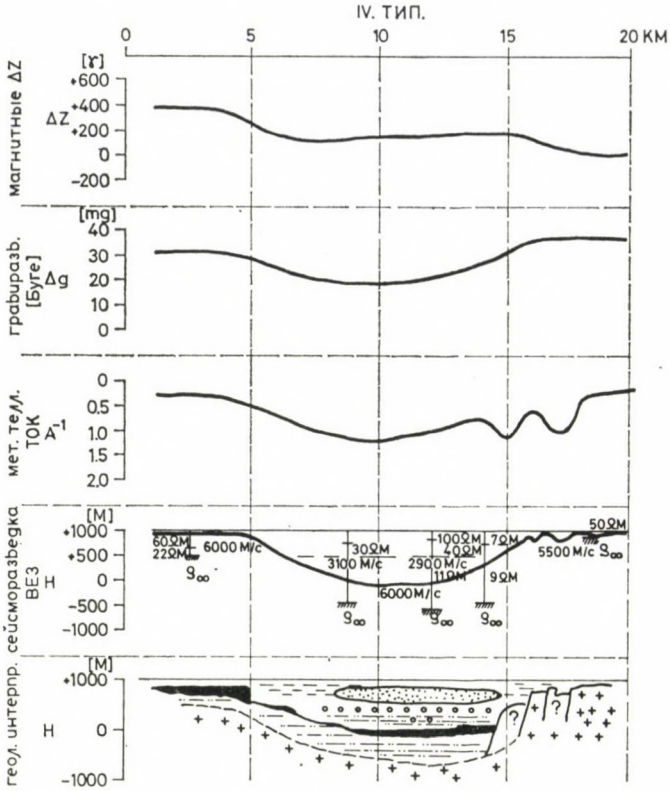

Рис. 4

Уровень высокой скорости сейсмических волн на участке 0—15 км можем сопоставить андезитом, на основе магнитных аномалий и данных бурения. Андезит является кровлей обязательно осадочных пород, таких как глины $\varrho = 8—11$ омм, аргиллиты; а кристаллический, более древний фундамент находится под этой толщи. Так как скорость распространения сейсмических волн в фундаменте меньше или равно скорости в андезитах, фундамент не определяется с помощью МОВ. Зато андезит — кроме участка профиля 7 км — не имеет большой мощности, так как для ВЭЗ данный уровень не является ϱ_∞.

На участке 14—20 км вдоль многочисленных разломов поднялся на поверхность более древний — палеозойский — фундамент, состоящий из эффузивов. Магнитные аномалии — характерно для древних палеозойских эффузивов — имеют относительно отрицательные величины. Гравитационные аномалии грубо, но совпадают с морфологией кровли фундамента, но чувствуется, что наиболее глубокие части бассейна заполнены отложениями более высокой плотности. Теллурические аномалии находятся в хорошем совпа-

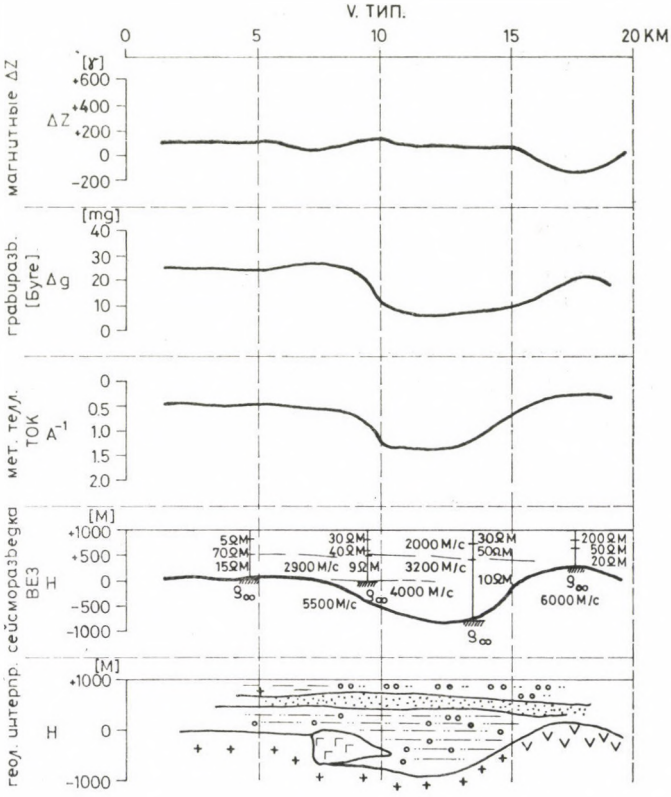

Рис. 5

дении зондированиями, но порожает участок от 14—18 км, связано с которым нужно заменить, что перпендикулярно на этот участок помешало сильное канализационное действие. Под этим имеется то, что в пределах данного участка проходит зона трещиноватости, которая хорошо определяется и сейсморазведкой, и в которой могут быть электрически хорошо проводящие (например, рудные) зоны.

Осадочные образования, покрывающие толщу высокой скорости — как и в третьем типе — представляют собой чередование слоев песка, глины, песчанника и конгломерата, и имеют консообразное строение.

Пятый тип (рис. 5). Относительное простое строение, похоже на третий тип, в этом смысле, его сейсмический уровень высокой скорости примерно совпадает с уровнем ϱ_∞. Местами появляется граница со скоростью 4000 м/сек, которая также, как во втором типе связана базальтами. Приподнимание фундамента в участке 15—20 км, гравитационный и теллурический максимум, и отрицательные магнитные аномалии как и в первом типе представляют эффузивы палеозойской группы. Новое, что в этом случае, из-за недостаточного

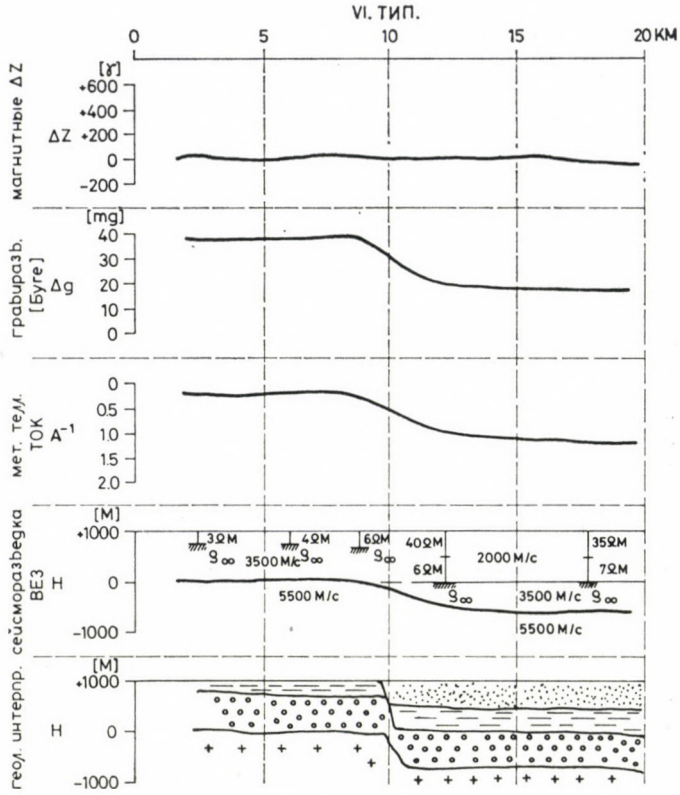

Рис. 6

количества геофизических данных, только по бурениям получили достаточную информацию о верхней 200—300 метровой толще. В этом интервале вскрыли несколько раз слои базальтов, мощностью 10—30 м, даже на тех местах, где на весь разрез характерно слабые положительные магнитные аномалии.

Скорость сейсмических волн в конгломератах местами не превышала 2000 м/сек. На многих участках разреза мощностью несколько сотен метров — вскрыли буровыми скважинами, но не добурили до подошвы — конгломераты с $\varrho = 10—11$ омм.

Шестой тип (рис. 6). Бывает на относительно небольшом участке. Характерно, что уже от поверхности до глубины примерно 1000 метров залегает толща, скоростью сейсмических волн 3500 м/сек, верхняя 150—250 метровая зона которой, вероятно, глина, аргиллит с $\varrho = 3—5$ омм. Под ними до 1000 метров предполагаем присутствие толщи конгломерата, на основе высокой средней плотности (I. Разрез Буге); высокой величины ϱ кажущегося сопротивления (ВЭЗ и теллурический профиль) и нейтральной магнитной

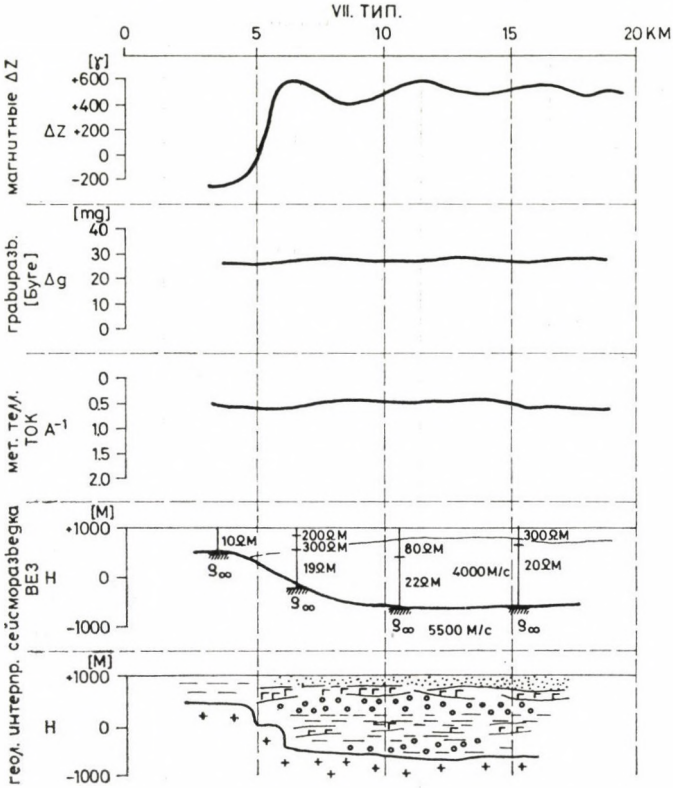

Рис. 7

величине. После сопоставлений с геологическими исследованиями, интересным совпадением является то, что при 11 км находится разлом, отчетливо выраженный и на поверхности, вдоль которого участка 0—11 км приподнят, и более молодые (менее плотные) образования подвергались выносу. На этом участке образования юрской и нижнего отдела меловой систем находятся на поверхности. Участок от 11 до 20 км по-существу совпадает с первым типом.

Седьмой тип (рис. 7). Является характерным на 20% от всей территории наших исследований. На гравитационных и теллурических картах почти полностью отсутствуют аномалии, хотя фундамент высокой скорости до начала разреза с 500 м опускается до 1500 м. На месте углубления фундамента появляется четкая положительная магнитная аномалия и сейсмическая граница (= покров базальта) со скоростью 4000 м/сек на глубине 150—300 м. Толща, мощностью больше чем 1000 м; средней скоростью 4000 м/сек, и удельным сопротивлением 19—22 омм ни в коем случае не может быть чистый базальт; нам нужно предполагать, что в нем присутствуют прослои глины — главным образом — конгломератов и песчанников. Толща обязательно

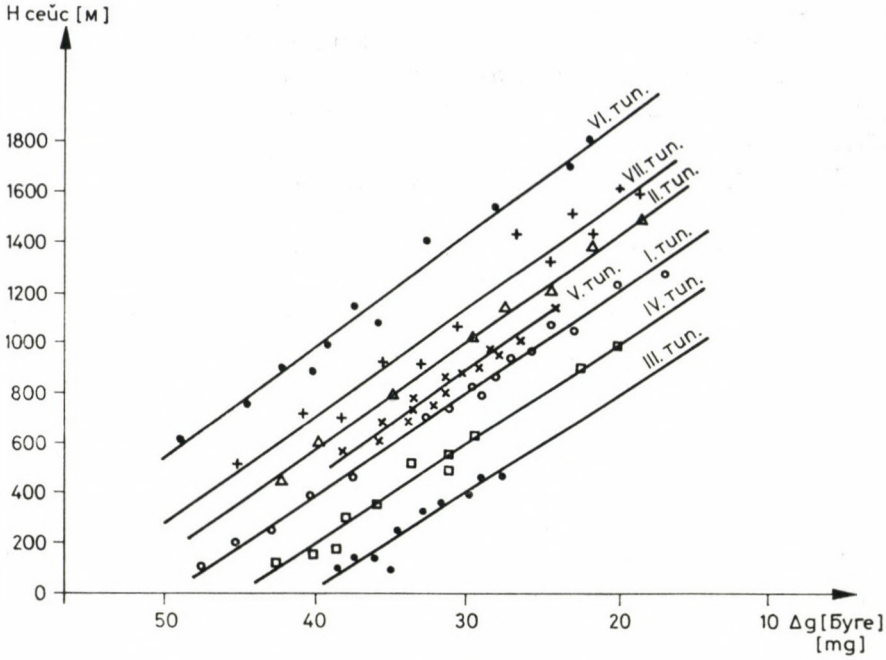

Рис. 8

должна состоять из тонких прослоев, так как ни сейсморазведка, ни ВЭЗ не могли расчленить мощную толщу на слои.

В конце концов оконтуривание 11 бассейнов и построение семи вышеописанных моделей дали возможность построения структурной карты, и оконтуриванию участков распространения эффузивов. При построении карты глубокой структуры и карты фундамента исходили из того метода, что приняли наиглубокий уровень истинным из всех глубин, полученных геодезическими методами. В геологической формулировке этот «фундамент» представляет собой такую палеозойскую поверхность, под которой рыхлые осадочные образования отсутсвуют. Данная глубина соответствует — кроме четвертого типа — скорости сейсмических волн 5500—6000 м/сек, а в четвертом типа ϱ_∞. Исследовали далее и то, что результаты разнообразных геофизических методов (главным образом, гравитационных и теллурических методов) в каких случаях можем применять для определения глубины залегания фундамента на тех местах, где не проводилась сейсморазведка, или ВЭЗ соответствующее радиусу *AB*, скрывающий фундамент. Первый раз исследовали, что какая количественная зависимость существует между сейсмическими гулбинами и аномалиями Буге. На рис. 8 отдельные точки множества получили так, что в зависимости от глубины залегания слоя высокой

сейсмической скорости изображали аномалию Буге. Этот рисунок на первый взгляд показывает на значительную неоднородность плотности осадочной толщи. Более отчетливые результаты получаем в том случае, если рассмотрим отдельно точки, соответствующие раннее описанным геологическим моделям (I—VII типы).

Точки одинаковых геологических моделей относительно небольшим разбросом определяют прямые, которые показываем на рисунках. Самая верхняя кривая соответствует бассейнам, которые заполнены осадками наибольшой плотности (VI. и VII типы). Здесь предполагали толщу из базальтов и конгломератов, мощностью выше 1000 м. Прямая, расположенная под этой прямой, характеризует II. тип, в котором замечает значительное количество базальтов, но помимо базальтов содержит плотные глины. Следующая прямая характерна для глубокого бассейна V. типа, в котором уже количество эффузивов и конгломератов по сравнению с предыдущим меньше. Следующие три прямых характерны для бассейна небольшой глубины, и из которых уже отсустствуют эффузивы.

Можно заметить, что чем меньше средняя плотность, тем больше признаков присутствия по данным сейсморазведки и электроразведки вулканического материала, конгломерата, и плотных глин. Так нижние три прямые — сверху на низ — характерны на I, IV и III тип.

Следующим шагом определили, что на различные участки исследований из прямых рис. 8. какие прямые характерны, а потом с использованием этих зависимостей определили глубины, на всех пикетах гравиразведки. Данный подход предполагает, что плотность фундамента не меняется, что выполняется только частично. Поэтому пришлось определить глубины и с помощью других методов.

ВЭЗ относительно небольшого количества непосредственно указывает на глубины залегания фундамента, а теллурический метод только в том случае, если среднее сопротивление осадочных толщ по другим методам уже определили. Условием применения электроразведки является исследование, по которой рассмотрим, что «фундамент», где дает ϱ_∞. Обязательно придется исключать и те области, где теллурические аномалии обусловлены неоднородностью фундамента, как например, на некоторых участках I и IV типов. Далее, рассмотрели, что у I, II., IV типов уровень ϱ_∞ действительно соответствует ли фундаменту, или только какая-то экранирующая поверхность, под которой еще могут быть осадочные образования низким сопротивлением, и измерения методом ВЭЗ определили уровнем «ϱ_∞», только потому, что кривые ВЭЗ, вступающие наверх под углом 45° не продолжили дальше измерять или имеется такая область, для которой характерно электрическое строение типа «*A*»; и кривая является короткой для найденной интерпретации. Для демонстрации исследований проблем такого характера служит рис. 9, на котором исследовали около 200 кривых ВЭЗ, имеющие окончание под углом 45°.

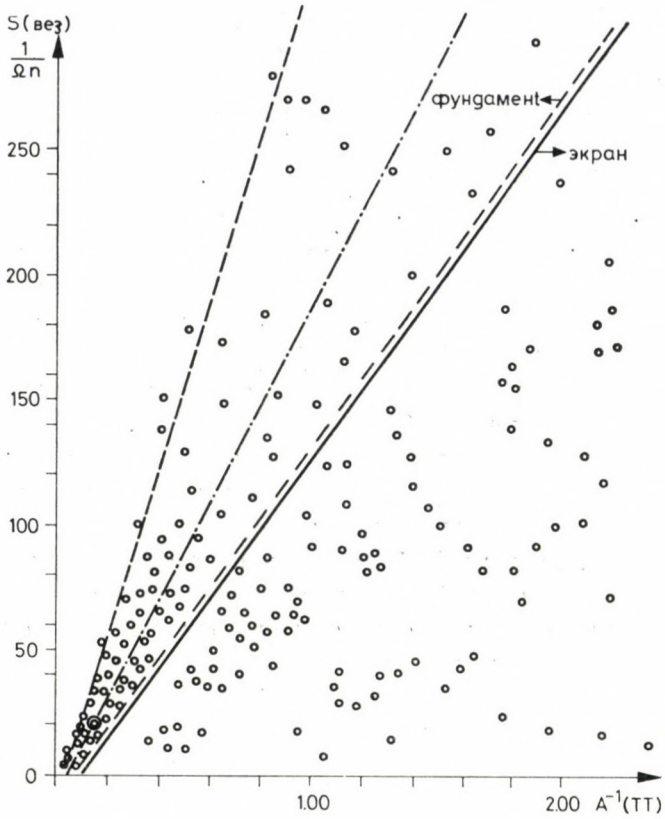

Рис. 9

Здесь изобразили значения S кривых ВЭЗ, в зависимости от значения A^{-1} теллурических наблюдений, полученных на тех же самых пикетах профилей.

При более тщательном исследовании рисунка заметили, что те точки которые соответствуют данным таких мест наблюдений, при которых уровни ϱ_∞ ВЭЗ соответствуют уровням высоких сейсмических скоростей или находятся глубже расположенные в левом верхнем квадрате рисунка. Усреднив эти точки, получились такие прямые, разброс которых не больше, чем погрешность теллурических измерений, и ВЭЗ.

Для второй половины точек в правой нижней части рисунка характерно то, что они относится без исключения участкам I и II типов. Значит, эти те точки, на месте измерений которых уровень зондирований соответствует сейсмическим уровням, скоростью 3300—4000 м/сек, значит поверхности вулканических образований, покрывающие осадочную толщу. Значит эти глубины, только кажущиеся уровни ϱ_∞. Этот вывод оправдывают и те теллурические исследования, которые имели больше глубинность исследований.

Толщи участков I и IV типов имеют чередование глинконгломератов фундамента, и строение типа «А», в соответствии с рисунком № 9, контрастность между глинами сопротивлением 3—4 омм и конгломератами сопротивлением 60—80 омм, более значительная, чем между конгломератами и фундаментом. Точки рис. 9, полученные с участков I. и IV. типов имеют незначительный разброс от выравненной прямой $S = f(A^{-1})$, с учетом погрешности измерений. Но для точек участка II. типа характерен большой разброс от выравнений прямой. Из этого можно сделать следующие выводы: между уровнями ϱ_∞ теллурических исследований и вертикальных электрических зондирований расположена толща, главным образом, характерным низким электрическим сопротивлением, значит уровень 4000 м/сек и «ϱ_∞» является только «экраном», например, покровным базальтом, под которым залегают еще образования с низким сопротивлением. Эти образования с низким сопротивлением можем охарактеризовать единственным параметром — их проводимостью (ΔS). Значения проводимости (ΔS) можем определить из следующих рассуждений: если кривую ВЭЗ продолжили бы дальше измерять до теллурического уровня ϱ_∞, тогда из кривых ВЭЗ могли бы опредедить такую величину S, которая совпадала бы с какой-то точкой A^{-1} выравненной прямой рисунка № 9. Значит, из рисунка можем определить по точкам те разности S, которые получили бы при продолжении измерения кривой ВЭЗ. Отметим, что если предполагаем совпадение сейсмического уровня высокой скорости и теллурического уровня с ϱ_∞, тогда из величины ΔS и далее из дифференции по глубине уровней 4000 м/сек и высокой скорости можем определить удельное сопротивление экранирующей толщи, которое при II. типе оказалось равным 2—5 омм. Поэтому мы предполагали здесь аргиллиты и глины, покрытые базальтами. В конце концов из зондирований, попавшие в выравненной прямой рис. 9 можем непосредственно рассчитать глубины. И при электрических методах разведки имеется еще одна возможность — можем определить среднее сопротивление осадочной толщи. Последнее можем использовать — при изображении в виде карт — для трансформации теллурических значений в величину глубин. Данная карта не распространяется на участки, на которых имеется развитие экранирующих толщин, но и для экранирующих толщин можем получить приблизительное среднее сопротивление там, где предполагается тождество уровней ϱ_∞ теллурического метода и высоких скоростей сейсморазведки.

На рис. 10 значению величины теллурического база $A^{-1} = 1{,}00$ принадлежит сейсмическая глубина — случайно — как раз 1000 м (H_c). Через данную точку и начало координат проведем прямую $\varrho'_\sigma = 1$ (значит, сопротивление отложений на теллурической базе считаем единичным). Считая величину теллурического A^{-1} относительной величине «S», для заданной глубины и заданной A^{-1} величинам разные $\varrho'_\sigma = \text{const.}$, значения которых теоретическим путем определили и начертили на рис. 10. С помощью послед-

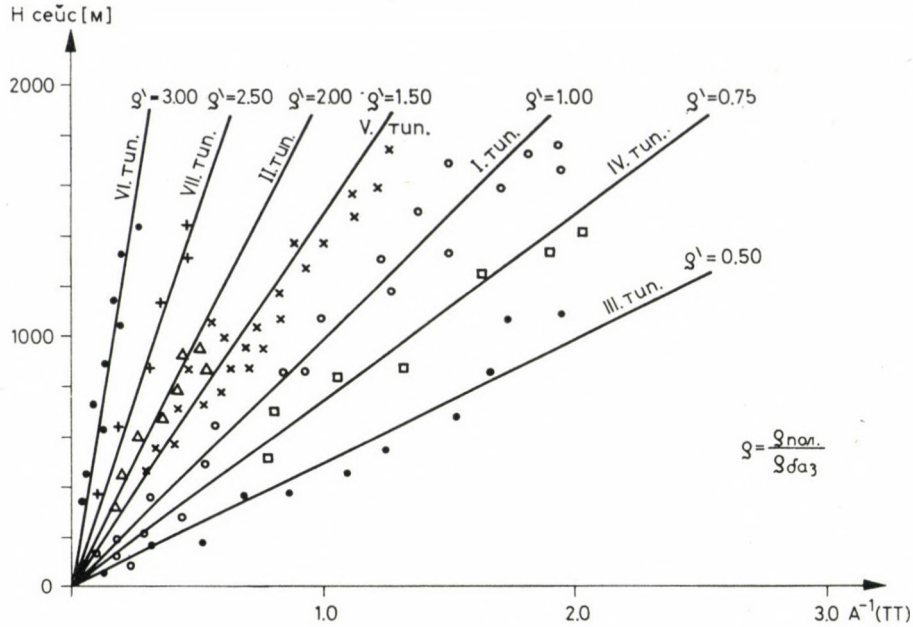

Рис. 10

них прямых можно начертить на весь участок работ характерную карту сопротивлений отложений.

В конце концов из теллурических измерений и данных средних сопротивлений следующим образом можем получать сведения о глубинах:
из значения A^{-1}, соответствующие относительным величинам S, на освове выравниваемой прямой рис. 9, можем определить действительные значения S, и далее для тех же мест наблюдений измеренные, или по рис. 10 рассчитанные значения ϱ_σ можем получать. После умножения двух данных получается глубина: $H = S \cdot \varrho_\sigma$.

При построении карты глубин опорными точками служили непосредственные точки глубин ВЭЗ и сейсморазведки.

На тех участках, где не производились ни сейсмические работы, ни ВЭЗ, там вместо интерполяции по описанным рассуждениям использовали данные гравиразведки, теллурические наблюдения и местные значения средних сопротивлений.

Интересным, но только качественным результатом комплексных исследований является контурирование и изображение на картах погребенных эффузивов. Для составления карты исходили из того, что погребенные вулканические тела, связанные с центрами извержений создают магнитные и гравитационные остаточные аномалии. Эти участки изображены на картах. С учетом расчета магнитных действий и карты выхода могли расчленить базальты и андезиты, и палеозойские и мезозойские эффузивы. Глубину их

замечания могли точно и достоверно определить из сейсморазведки и электроразведки, но довольно хорошее совпадение получили из расчета магнитных тел. Около центров извержения появились электрические экранирующие простои. Их местоположение совпадает с географическим местом правой, нижней части рис. 9. Экранирующими прослоями являлись андезит — граничной сейсмической скоростью 5500—6000 м/сек и базальты скоростью прохождения сейсмических волн 4000 м/сек.

Эти экранирующие свиты имеют значительную мощность только около центров извержения, и на этих местах для ВЭЗ появляются как слои с ϱ_∞, но обходя от центров извержения их мощность уменьшается, и только сейсморазведкой возможно их определение; а в конце концов они настолько тонкие, что ни одним геофизическим методом нельзя определить хотя бурение скрыли мощности от 8 до 20 метров.

По результатам наших исследований вычертили мощные и тонкие экранирующие прослои. Можем твердо сказать, что на тех местах, где наша карта является пустой, там экранирующая эффузивная толща может иметь крайне незначительные мощности, так как присутствие вулканического материала не может быть неважной при определении местоположений скважин. Но важно отметить, что удельное сопротивление базальтов и некоторых разновидностей андезитов как раз совпадает с величиной кажущихся сопротивлений водонасыщенных песков — 60—80 омм.

Просуммировать итоги наших исследований так чувствуем, что наши работы и результаты являются хорошим обоснованием применения комплексных геофизических методов разведки. Главным образом, в случае разведки бассейнов, заполненных терригенными образованиями — для которых характерно как и частое горизонтальное изменение физических параметров, так и совпадение величин некоторых физических параметров разнообразных образований. А в этом случае достоверные качественные и быстрые результаты можем получить только применением нескольких методов разведки.

COMPLEX GEOPHYSICAL EXPLORATION IN THE GOBI DESERT

NEMESI, L.—BOGNÁR, E.—LAVDANSUREN—HOVHDAN—MAJKUT, T.—TÓTH, CS.

SUMMARY

The paper presents the geological interpretation of the complex geophysical-hydrogeological exploration made in the arid-semiarid Gobi desert.

The results presented prove that a common use of many geophysical methods enables conclusions which could not be reached using any single method. On the other hand, the economic advantage of the complex exploration can also be seen. The tricks described here can also be used in other areas and for other purposes. The authors, however, consider it necessary to carry out similar complex explorations in basin areas with terrigenous filling of horizontally and vertically quickly changing character when looking for water. Namely, certain physical parameters of the productive layers coincide with the parameters of the unproductive ones (e.g. the electric resistivity of the productive sand in similar to that of the inproductive effusive formations, or in productive sansd the seismic velocity coincides with that in unproductive clay). Using simultaneously several methods, the interpretation can be made unambiguous, but the correctness of the interpretations presented here are also supported by many borehole data.

Acta Geodaet., Geophys. et Montanist. Acad. Sci. Hung. Volume 17 (2), pp. 307—309 (1982)

ZARATE MT SOUNDING AND UPPER MANTLE RESISTIVITY

J. C. GASCO—J. M. FEBRER—J. DEMICHELI
COMISSION NACIONAL DE INVESTIGACIONES ESPACIALES, BUENOS AIRES

H. G. FOURNIER
INSTITUTO ANTARCTICO ARGENTINO, BUENOS AIRES AND LABORATOIRE DE GEOOMAGNETISME A L'ECOLE NORMALE SUPÉRIEURE DE PARIS

[Manuscript received April 7, 1981]

The MT-sounding of Zarate was made by J. C. Gasco for implementing his master's thesis, to be presented at the Buenos Aires University, December 15th 1980 [1]. The new apparatus and the technical aspect are described in another communication [2].

The position of the site studied has the coordinates: Lat. = 34° 05′ South, Long. = 59° 10′ West. The apparatus was operated along the runways of the amateur airport of Zarate at about 90 km W—NW from Buenos Aires. Geologically, the site is over the cratonic area of Eastern Argentine; the age is approximately $2 \cdot 10^9$ years.

The provisory results are two MT-curves which perfectly coincide; one of the telluric lines is parallel to the general trend of the regional tectonics (Nm 54° Wm); the other is orthogonal to it.

The dispersion of the individual values of ϱ is very small according to the general behaviour of MT-results. A tensorial analysis is in preparation.

The sedimentary section was determined by an electric Schlumberger sounding transposed into equivalent MT by the method proposed in 1977 by Benderitter et al. [3].

Figure 1 shows the common trace for the two curves obtained for this particular sounding. We offer here two comments concerning the MT-curve considering that the sedimentary cover has a thickness of only 250 m with a low resistivity value — see the left section in Fig. 1.

1. If one intermediate conducting layer exists in the lower crust or at the top of the Upper Mantle it must be very negligible according to the left-side position and the straightness of the ascending branch of the MT-curve — 18 cagniards [4] — in the tetralogarithmic abacus (from 300 m to 300 km). This is not in favour of the presence of the asthenosphere, except if we accept the development given in [5] concerning the percentage of melted fraction in the Upper Mantle.

2. In consequence of the very thin sedimentary cover we can assume that the high resistivity layer of the Upper Mantle has a thickness of 400 km with a minimum resistivity of 10,000 ohm m in a whole.

As an inherent weakness of the MT-method, we cannot determine the true sequence of the resistivity values of the layers that one can theoretically

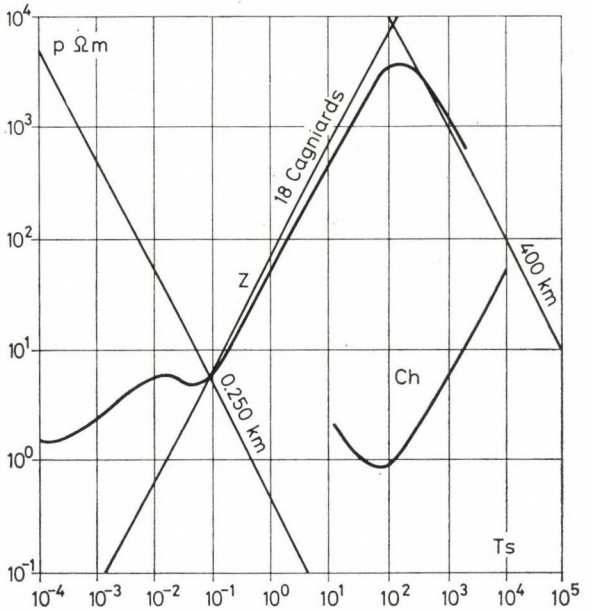

Fig. 1. Cross section given by the Zarate MT-sounding interpretation. MT curve Z = Zarate; MT curve Ch = Chivilcoy. The thicknesses and resistivities of the layers are: 1 m—10 ohmm; 8 m—1.5 ohmm; 140 m—10 ohmm; 100 m—3.3 ohmm; 400 Km—10,000 ohmm; ∞Km—9 ohmm. Note: in (4) we see that: 1 cagniard $= \dfrac{1\ \mathrm{mV/km}}{\gamma\ \text{cagniard}} = 0.0012566\ldots$ ohm; 1 ohm = 795.77488...

suppose and calculate, considering the case of increasing values of the resistivity with depth; the electrical sounding method is more appropriate for this purpose.

The 250 m thickness of the sedimentary cover stopped the increasing of the value of ϱ at the inflexion point giving a thickness of 400 km for this high resistivity layer of the Upper Mantle. We shall try, in the future, to repeat this experiment on Martin Garcia Island, 40 km NW of Buenos Aires, where the craton is uncovered, to try to find if the resistivity of this part of the Upper Mantle is yet greater than what we found at this Zarate sounding.

The interpretative curve of the MT-sounding of Chivilcoy also on the craton area (Lat. = 34° 56′ South, Long. = 70° 06′ West), is not in contradiction with the depth of what we name the ultimate conductive layer below Zarate.

REFERENCES

1. GASCO, J. C.: Deteccion de señales magnetoteúlricas en la banda de 0.1 a 10 Hz. Tesis de licenciatura en Ciencias Fisicas. Facultad de Ciencias Exactas y Naturales, Universidad de Buenos Aires. 1980.
2. GASCO, J. C.—FEBRER, J. M.—FOURNIER, H. G.: Deteccion de señales magnetotelúricas en la banda de 0.1 a 10 Hz. 11a Reunion Cientifica Argentina de Geofisica y Geodesia, San Miguel de Tucuman, 1980.
3. BENDERITTER, Y.—DUPIS, A.—FEBRER, J. M. —FOURNIER, G. H.: Comparaison de mesures de résistivits obtenues par les méthodes de sondages électrique et magnétotellurique en des sites communs situés sur terrain sédimentaire et sur des massifs de granite. Mémoire du B.R.G.M. n^0 91, Paris, 1978.
4. FOURNIER, H. G.: Concernant l'intervalle de variation du rapport E/H dans l'investigation expérimentale magnétotellurique. Garchy—Suilly-la-Tour, Nièvre, Station Géophysique en Nivernais. Bibliothèque Nationale, pièce 5361, 1963.
5. SHANKLAND, T. J.—O'CONNELL, R. J.: Electrical and elastic anomalies in the Upper Mantle. XVII General Assembly of I.U.G.G., Canberra, 1979.

МАГНИТОТЕЛЛУРИЧЕСКОЕ ЗОНДИРОВАНИЕ И УДЕЛЬНОЕ СОПРОТИВЛЕНИЕ ВЕРХНЕЙ КОРЫ В ГОРОДЕ ЗАРАТЕ

Й. Ц. ГАСКО—Й. М. ФЕБРЕР—Й. ДЕМИКЕЛИ—Х. Г. ФУРНИЕ

РЕЗЮМЕ

Магнитотеллурическое зондирование было сделано Й. Ц. Гаско для дополнения ее диссертации в университете Буенос Аирес [1] 15 декабря 1980 г. Новое оборудование и технические отношения излагаются в другой публикации [2]. Имеются некоторые предварительные замечания в отношении магнитотеллурической кривой и астеносферы.

CONTENTS

Ádám, J.—Halmos, F.—Varga, M.: On the concepts of combination of Doppler satellite and terrestrial geodetic networks 147
Ádám, J.—Tarcsai, Gy.: Doppler location equations for platform localization using satellites 171
Csernyák, L.—Steiner, F.: Amplifying residual filters 181
Csernyák, L.—Steiner, F.—Zilahi-Sebess, L.: A short note to prescribed w-properties 205
Abdelhamid Kamal Hassan: Comparison between results of the gyro-azimuths determined with old and new gyrotheodolites 209
Kardos, I.—Borza, T.—Vass, T.: Laser ranging observations at the Satellite Geodetic Observatory (SGO) 237
Krasnobaeva, A. G.—Diakonov, B. P.—Astafiev, P. F.—Batalova, O. V.—Vishnev, V. S.—Gavrilova, I. E.—Zhuravlyova, R. B.—Kirillov, S. K.: Magnetotelluric data on the geoelectric structure in the North-Eastern part of the Baltic Shield 255
Raspopov, O. M.—Afanasyeva, L. T.: Localization of the Pc5-source and of the auroral oval 267
Rösler, R.—Lindner, H.: Ableitung von Feldtransformationen für Profile von Potentialfeldanomalien 277
Немеши, Л.—Богнар, Е.—Лавдансурен—Ховдан—Майкут, Т.—Тот, Ч.: Комплексная геофизическая разведка в пустине Гоби 291
Gasco, J. C.—Febrer, J. M.—Demicheli, J.—Fournier, H. G.: Zarate MT sounding and upper mantle resistivity 307

PRINTED IN HUNGARY

Akadémiai Nyomda, Budapest

— treble underlining: bold-face italics
— red underlining: Greek letters
— green underlining: script letters.

Rules for mathematical-physical notations:

— trigonometric, logarithmic, analytic symbols, symbols for units and functions are in roman type (not underlined)
— letter symbols in mathematical and physical formulas, scalars, and subscripts of algebraic and physical quantities are in italics (underlined)
— vectors, matrices, operators in probability theory are in bold-face roman type (double underlining)
— tensors, operators and some special functions are in script letters (green underlining). These cannot be bold.
— Greek letters (red underlining) cannot be bold or extra bold type (thus they cannot be used for vectors or tensors)
— avoid upper lines e.g. for vectors
— avoid possible confusion between o (letter) and 0 (zero), l (letter) and 1 (one), ν (Greek nu) and v, u (letters) etc.
— explain ambiguous or uncommon symbols by making marginal notes in pencil
— be careful about superscripts and subscripts
— formulae must be numbered consecutively with the number in parentheses to the right of the formula. References in text to the equations may then usually be made by the number in parenthesis. When the word equation is used with a number, it is to be abbreviated, Eq. or Eqs in the plural
— the International System of Units (SI) should be used.

Authors are liable for the cost of alteration in the *proofs*. It is, therefore, the responsibility of the author to check the text for errors of facts before submitting the paper for publication.

3. *References* are accepted only in the Harvard system. Citations in the text should be as:

. . . (Bomford 1971) . . . or Bomford (1971)

. . . (Brosche and Sündermann 1976) . . .

. . . (Gibbs et al. 1976b) . . .

The list of references should contain names and initials of all authors (the abbreviation et al. is not accepted here); for *journal articles* year of publication, the title of the paper, title of the journal abbreviated, volume number, first and last page.

For *books* or *chapters in books*, the title is followed by the publisher and place of publication.

All items must appear both in the text and references.

Examples:

Bomford G 1971: Geodesy. Clarendon Press, Oxford

Brosche P, Sündermann J 1976: Effects of oceanic tides on the rotation of the earth. Manuscript. Univ. of Bonn

Buntebarth G 1976: Temperature calculations on the Hungarian seismic profile-section NP-2. In: *Geoelectric and Geothermal Studies (East-Central Europe, Soviet Asia), KAPG Geophysical Monograph.* Akadémiai Kiadó, Budapest, 561—566.

Gibbs N E, Poole W G, Stockmeyer P K 1976a: An algorithm for reducing the bandwidth and profile of a sparse matrix. *SIAM J. Number. Anal.*, 13, 236—250.

Gibbs N E, Poole W G, Stockmeyer P K 1976b: A comparison of several bandwidth and profile reduction algorithms. *ACM Trans. on Math. Software*, 2, 322—330.

Szarka L 1980: Potenciáltérképezés analóg modellezéssel (Analogue modeling of potential mapping). *Magyar Geofizika*, 21, 193—200.

4. *Footnotes* should be typed on separate sheets.

5. *Legends* should be short and clear. The place of the tables and figures should be indicated in the text, on the margin.

6. *Tables* should be numbered serially with Roman numerals. Vertical lines are not used.

All the illustrations should contain the figure number and author's name in pencil on the reverse.

Figures will be redrawn. Therefore the most important point is clearness of the figures, even pencil-drawings are accepted (with a duplicate).

Photographs and *half-tone* illustrations should be sharp and well contrasted.

If a specific reduction or enlargement is required, please indicate this in blue pencil on the figure.

The editors will send information to the first author about the *arrival* and acceptance of the papers. A galley proof is also sent to the first author for *correction*. Hundred *offprints* are supplied free of charge.

These instructions are valid as from 1982.

Periodicals of the Hungarian Academy of Sciences are obtainable at the following addresses:

AUSTRALIA
C.B.D. LIBRARY AND SUBSCRIPTION SERVICE
Box 4886, G.P.O., *Sydney N.S.W. 2001*
COSMOS BOOKSHOP, 145 Ackland Street
St. Kilda (Melbourne), Victoria 3182

AUSTRIA
GLOBUS, Höchstädtplatz 3, *1206 Wien XX*

BELGIUM
OFFICE INTERNATIONAL DE LIBRAIRIE
30 Avenue Marnix, *1050 Bruxelles*
LIBRAIRIE DU MONDE ENTIER
162 rue du Midi, *1000 Bruxelles*

BULGARIA
HEMUS, Bulvar Ruszki 6, *Sofia*

CANADA
PANNONIA BOOKS, P.O. Box 1017
Postal Station "B", *Toronto, Ontario M5T 2T8*

CHINA
CNPICOR, Periodical Department, P.O. Box 50
Peking

CZECHOSLOVAKIA
MAD'ARSKÁ KULTURA, Národní třída 22
115 66 Praha
PNS DOVOZ TISKU, Vinohradská 46, *Praha 2*
PNS DOVOZ TLAČE, *Bratislava 2*

DENMARK
EJNAR MUNKSGAARD, Norregade 6
1165 Copenhagen K

FEDERAL REPUBLIC OF GERMANY
KUNST UND WISSEN ERICH BIEBER
Postfach 46, *7000 Stuttgart 1*

FINLAND
AKATEEMINEN KIRJAKAUPPA, P.O. Box 128
SF-00101 Helsinki 10

FRANCE
DAWSON-FRANCE S. A., B. P. 40, *91121 Palaiseau*
EUROPÉRIODIQUES S. A., 31 Avenue de Versailles, *78170 La Celle St. Cloud*
OFFICE INTERNATIONAL DE DOCUMENTATION ET LIBRAIRIE, 48 rue Gay-Lussac
75240 Paris Cedex 05

GERMAN DEMOCRATIC REPUBLIC
HAUS DER UNGARISCHEN KULTUR
Karl Liebknecht-Straße 9, *DDR-102 Berlin*
DEUTSCHE POST ZEITUNGSVERTRIEBSAMT
Sraße der Pariser Kommüne 3–4, *DDR-104 Berlin*

GREAT BRITAIN
BLACKWELL'S PERIODICALS DIVISION
Hythe Bridge Street, *Oxford OX1 2ET*
BUMPUS, HALDANE AND MAXWELL LTD.
Cowper Works, *Olney, Bucks MK46 4BN*
COLLET'S HOLDINGS LTD., Denington Estate
Wellingborough, Northants NN8 2QT
WM. DAWSON AND SONS LTD., Cannon House
Folkstone, Kent CT19 5EE
H. K. LEWIS AND CO., 136 Gower Street
London WC1E 6BS

GREECE
KOSTARAKIS BROTHERS INTERNATIONAL BOOKSELLERS, 2 Hippokratous Street, *Athens-143*

HOLLAND
MEULENHOFF-BRUNA B.V., Beulingstraat 2,
Amsterdam
MARTINUS NIJHOFF B.V.
Lange Voorhout 9–11, *Den Haag*
SWETS SUBSCRIPTION SERVICE
347b Heereweg, *Lisse*

INDIA
ALLIED PUBLISHING PRIVATE LTD., 13/14
Asaf Ali Road, *New Delhi 110001*
150 B-6 Mount Road, *Madras 600002*
INTERNATIONAL BOOK HOUSE PVT. LTD.
Madame Cama Road, *Bombay 400039*
THE STATE TRADING CORPORATION OF INDIA LTD., Books Import Division, Chandralok
36 Janpath, *New Delhi 110001*

ITALY
INTERSCIENTIA, Via Mazzé 28, *10149 Torino*
LIBRERIA COMMISSIONARIA SANSONI, Via Lamarmora 45, *50121 Firenze*
SANTO VANASIA, Via M. Macchi 58
20124 Milano
D. E. A., Via Lima 28, *00198 Roma*

JAPAN
KINOKUNIYA BOOK-STORE CO. LTD.
17-7 Shinjuku 3 chome, Shinjuku-ku, *Tokyo 160-91*
MARUZEN COMPANY LTD., Book Department, P.O. Box 5050 Tokyo International, *Tokyo 100-31*
NAUKA LTD. IMPORT DEPARTMENT
2-30-19 Minami Ikebukuro, Toshima-ku, *Tokyo 171*

KOREA
CHULPANMUL, *Phenjan*

NORWAY
TANUM-TIDSKRIFT-SENTRALEN A.S., Karl Johansgatan 41–43, *1000 Oslo*

POLAND
WĘGIERSKI INSTYTUT KULTURY, Marszałkowska 80, *00-517 Warszawa*
CKP I W, ul. Towarowa 28, *00-958 Warszawa*

ROUMANIA
D. E. P., *Bucureşti*
ILEXIM, Calea Grivitei 64–66, *Bucureşti*

SOVIET UNION
SOJUZPECHAT – IMPORT, *Moscow*
and the post offices in each town
MEZHDUNARODNAYA KNIGA, *Moscow G-200*

SPAIN
DIAZ DE SANTOS, Lagasca 95, *Madrid 6*

SWEDEN
ALMQVIST AND WIKSELL, Gamla Brogatan 26
101 20 Stockholm
GUMPERTS UNIVERSITETSBOKHANDEL AB
Box 346, *401 25 Göteborg 1*

SWITZERLAND
KARGER LIBRI AG, Petersgraben 31, *4011 Basel*

USA
EBSCO SUBSCRIPTION SERVICES
P.O. Box 1943, *Birmingham, Alabama 35201*
F. W. FAXON COMPANY, INC.
15 Southwest Park, *Westwood Mass. 02090*
THE MOORE-COTTRELL SUBSCRIPTION AGENCIES, *North Cohocton, N. Y. 14868*
READ-MORE PUBLICATIONS, INC.
140 Cedar Street, *New York, N. Y. 10006*
STECHERT-MACMILLAN, INC.
7250 Westfield Avenue, *Pennsauken N. J. 08110*

YUGOSLAVIA
JUGOSLOVENSKA KNJIGA, Terazije 27, *Beograd*
FORUM, Vojvode Mišića 1, *21000 Novi Sad*

Index: 26.031

HU ISSN 0374—1842

Acta GEODAETICA, GEOPHYSICA et MONTANISTICA

ACADEMIAE SCIENTIARUM HUNGARICAE

Editor-in-chief
A. TÁRCZY-HORNOCH

Editor
J. VERŐ

Editorial board
GY. BARTA
B. BÉLL
L. HOMORÓDI
L. KAPOLYI
F. MARTOS
J. SOMOGYI
J. ZAMBÓ

VOLUME 17
NUMBERS 3—4
1982

AKADÉMIAI KIADÓ, BUDAPEST

ACTA GEODAETICA, GEOPHYSICA et MONTANISTICA

A Quarterly Journal of the Hungarian Academy of Sciences

Acta Geodaetica, Geophysica et Montanistica (AGGM) publishes original reports on geodesy, geophysics and minings in English.

AGGM is published in yearly volumes of four numbers by

AKADÉMIAI KIADÓ
Publishing House of the Hungarian Academy of Sciences
H-1054 Budapest, Alkotmány u. 21.

Manuscripts and editorial correspondence should be addressed to

AGGM Editorial Office
H-9401 Sopron P.O. Box 5

Subscription information

Orders should be addressed to

KULTURA Foreign Trading Company
H-1389 Budapest P.O. Box 149

INSTRUCTIONS TO AUTHORS

Manuscripts should be sent to the editors (MTA Geodéziai és Geofizikai Kutató Intézete, Sopron, Pf. 5., H-9401, HUNGARY). Only articles not submitted for publication elsewhere are accepted.

Manuscripts should be typewritten in duplicate, double-spaced, 25 lines with 50 letters each. The papers generally include the following components, which should be presented in the order listed.

1. Title, name of author(s), affiliation, dateline, abstract, keywords
2. Text, acknowledgements
3. References
4. Footnotes
5. Legends
6. Tables and illustrations

1. The *affiliation* should be as concise as possible and should include the complete mailing address of the authors. The *date of receipt* of the manuscript will be supplied by the editors. The *abstract* should not exceed 250 words and should clearly and simply summarize the most important methods and results. 5—10 significant expressions describing the content are used as *keywords*. Authors may recommend these keywords.

2. The *text* should be generally in English and as short and clear as possible. From Hungarian authors papers are also accepted in Hungarian.

The section heading should *not* be underlined or in capitals.

Please note that underlining denotes special types:

— single underlining: italics
— double underlining: bold-face roman

Acta Geodaet., Geophys. et Montanist. Acad. Sci. Hung. Vol. 17 (3—4), pp. 311—316 (198 2)

25 YEARS OF THE PETROLEUM ENGINEERING RESEARCH LABORATORY OF THE HUNGARIAN ACADEMY OF SCIENCES

J. TÓTH

PETROLEUM ENGINEERING RESEARCH LABORATORY OF THE HUNGARIAN ACADEMY OF SCIENCES

The decree 9/1957. MTA of the President of the Hungarian Academy of Sciences, in agreement with the Minister of Heavy Industry announced the establishment of the Petroleum Engineering Research Laboratory by declaring that

> "on 1st November 1957 a Petroleum Engineering Research Laboratory is established to organize and carry out the fundamental research and to develop practical scientific methods in petroleum engineering."

Professor Zoltán Gyulay was the initiator of the establishment of the Laboratory and had been its first director until his retirement in 1971. By defining the directions of fundamental research in petroleum engineering, he also determined the development of this field of science.

The scientific basis of petroleum engineering includes first of all a thorough and scientifically exact investigation into the basic phenomenon of the recovery process. The basic phenomenon is well known: displacement of the oil from a porous or fissured solid system (rock) by a suitable fluid. Because of the porous character of the solid system the flowing fluids interact with each other and the rock on a relatively large surface, and well-defined displacement phase-oil-rock interfaces are formed. Large interfaces possess a considerable free interfacial energy, the laboratory investigation of the fundamental phenomenon is therefore based on two strongly connected disciplines: micro fluid mechanics and surface physical chemistry.

In view of this basic research principle, the 25-year-old history and scientific progress of the Laboratory can be divided into four distinct periods.

The first period started from the foundation and ended in the early sixties. The main research directions of the Laboratory, *viz.* micro fluid mechanical research and the investigation of related basic interfacial phenomena (surface and interfacial tension, wetting etc.) took shape in this period.

The second period terminated in the early seventies. At the beginning of this stage a very important fact was realized: in order to achieve practical results for engineering purposes, the micro fluid mechanical and interfacial phenomena should be jointly investigated at formation pressures and tem-

peratures. Research carried out in this phase contributed to the introduction of a high-pressure, high-temperature measurement technique and ensured its application and further development.

The third period took start in the early seventies and in fact has been continuing even today. This phase can be characterized by the strongly intertwined fundamental and applied research and by some investigations with direct engineering purposes. These tasks are solved by the Laboratory in a wide-range co-operation with and help and control of the industry.

The fourth period started towards the end of 1976 with the completion of the new three-storeyed-building of the Laboratory that contained 11 laboratories, a terminal connected to a modern computer centre and an experimental workshop. New surroundings ensured new possibilities: the scope of research has been widened beyond the tasks of petroleum engineering and an explicitly interdisciplinary science has been created that may be called mining chemistry.

After this general overview of development of the Laboratory, we would give a more complex picture about a few characteristic tasks and results.

Even in the early sixties great efforts were focussed on determining the role of capillary forces in oil displacement. For the investigations a well-controlled and defined artificial capillary system — a solid phase manufactured of monodisperse spherical glass powder — was used. The investigations proved that the most suitable displacement velocity for oil recovery is that, which develops spontaneously according to the capillary properties of the water—oil-solid system. It was found that the value of the optimal spontaneous velocity, and recovery itself, depend to a great extent on the wetting character of the solid phase. This observation drew our attention to the necessity of a more intense investigation into wetting properties.

In the early sixties one of the most important research tasks was to determine the wetting parameters of the Nagylengyel reservoir rocks. Our investigations proved that the Nagylengyel limestone reservoir, in spite of its basically water wet properties, became oil wet after getting in contact with oil, as a result of adsorption processes. Consequently, the actual system under recovery had to be regarded oil wet and production methods chosen accordingly. This research result proved to have a direct bearing on oilfield practice.

Also, our investigations into the wetting properties of the Nagylengyel reservoir threw light upon the fact that more reliable results can be obtained if the basic interfacial parameters (interfacial tension, contact angle or other data characterizing the wetting properties) are measured under formation conditions.

First, the technique of measuring the contact angle and interfacial tension was developed. Recently, this technique was converted into a micromethod, and a measurement system unique in its measurement accuracy and versatility was developed and patented. Versatility can be demonstrated by

the fact that the interfacial tension can be measured both when the oily and aqueous phases are saturated by the same or by different gases. Further efforts made concerned the determination of the most important parameter of porous reservoir rocks, i.e. the capillary pressure curve under reservoir conditions. Two patented measurement techniques were obtained as results of this research. One of them is an improved form of the conventional "desk" method, the other enables the researcher to measure capillary pressure in the presence of a high-pressure gas (e.g. carbon dioxide). From among the several patented methods we succeeded to add to our high-pressure laboratory technique the manostatic automatic high-pressure compressor should be especially emphasized that avoided the use of mercury and ensured flow velocities needed in micro fluid mechanical investigations of reservoirs under pressures up to 100 MPa.

Our Laboratory was the first to develop and construct in the last years a displacement equipment that ensured investigations on long (1.2—1.5 m) consolidated rock samples and the determination of saturation profiles during the displacement process at experimental pressures and temperatures. The equipment is based on electronic methods, applies a microprocessor for data processing, and avoids any interference with the investigated system. The equipment is suitable to reliably carry out laboratory tests needed for modern secondary oil recovery methods (polymer, microemulsion etc. floods). The patents and know-how required for the mass production of this equipment were purchased by an Austrian firm with the intent of world-wide marketing. Our microprocessor technique is being continuously developed in co-operation with this firm to meet the rapidly increasing international standards.

While the developed measurement methods ensure an exact laboratory modelling of the recovery processes, no full physical-chemical understanding of the reservoir systems can be attained withouth a detailed chemical analysis of the formation fluids. With these aims, column chromatographic and IR spectrophotometric investigations of crude oils were also undertaken. Further developing the methods of investigation (UV spectrophotometry, CHN analysis, gaschromatography and high-pressure liquid chromatography) we joined the national organic geochemical research in the early seventies with the principal aim of compiling a hydrocarbon prognosis. Within this research programme our Laboratory determined the connections between the relative age and the genetical parameters of crude oils.

One of the important results in the last decade was the introduction in Hungary of polymers for oil displacement. Initial investigations were aimed at the determination of the structure of dilute aqueous polymer solutions. As a result of this research we could determine the influence of polymer concentration, molecular mass, degree of hydrolysis, quality and quantity of foreign ions and the temperature on the viscosity of the solution, in terms of the actual size of the molecule in the solution. It was also proved that a consider-

able fraction of the polymer is retained on the rock surface due to sorption which is essential both economically, and through its role within the displacement mechanism in oilfield practice.

After completing these essentially physical-chemical investigations, flow properties of polymer solutions and of the aqueous phases following the polymer have been studied in water wet, intermediary (natural) and oil wet consolidated porous systems. We succeeded in pointing out that even though polymer flood is an effective tool for mobility control, the physical-chemical parameters influencing the shape and size of molecules and the sorption phenomena also have a determinant role in the displacement processes. The extensive research furnished an acceptable model for the action mechanism of the polymer flood.

Having recognized the role of wettability in polymer flood, a so-called double-slug procedure was developed for the intensive recovery of crude oils from porous media. This method unifies mobility control with the beneficial effects of surfactants on the interfacial tension and wettability. This method as well as the approximative determination of the wetting character of porous rocks based on polymer adsorption, are protected by Hungarian patents.

The research on applications of polymers in our Laboratory is strongly connected with the manufacturing of these chemicals. In view of the requirement that polymer application in Hungary should be based on Hungarian chemicals, the Laboratory initiated the manufacture of a suitable scale of polyacrylamides for crude oil displacement. With the help of the Ministry of Heavy Industry a co-operation with the Nitrochemical Works has been established. This co-operation ensured that a polyacrylamide product family has become available for oil recovery purposes and for general industrial use as well (as flocculation agent in mineral and ore dressing, in the environmental technique etc.).

Another important result of the Laboratory is that we realized the applicability of various organic and inorganic gels and gel systems for oil recovery. This method is based on the fact that those parts of the porous medium already flooded by water (being barren from the production point of view) can be separated by *in situ* gelling. This method ensures a practical possibility for the modification of the pore structure of the reservoir. It has also been pointed out that the various gels offer a further possibility for mobility control and as carrier media in surfactant procedures. Based on laboratory and, to some extent, oil-field experiments, it can be said that organic and inorganic gels or complex gel systems have revealed quite new fields of application in secondary and tertiary oil recovery and in bottom hole treatment.

The need for mathematical modelling of oil displacement processes has necessarily emerged in the course of our research. Results have been achieved in determining by computer the shape of polymer fronts formed by the flow of

high-viscosity displacement phase in porous media. The calculations proved the theoretically anticipated front-equalizing effect of polymers. Starting out from simulation methods, applied for water drive in Hungary and originally developed for polymer flood abroad, the two-dimensional three-phase mathematical simulation of areal polymer flood has been developed in co-operation with the Department of Reservoir Engineering of the Mining University in Leoben, Austria. Although this mathematical model requires further development in our opinion, the results obtained to date may give a good starting point for the mathematical simulation of oil displacement processes using additives.

It is hoped that this selection of results and the studies published in this volume not only reflect the past and present of the Laboratory but also imply some of the possibilities of the future. The rapid development of interdisciplinary sciences put so much emphasis on the fundamental research, and applied research in physical chemistry and thermodynamics — besides the conventional fundamental sciences of mining — that the acquired knowledge and results have created an *independent discipline* extending over the fields of mining of fluid and solid mineral raw materials, dressing and utilization of mine products, mining safety problems and environment protection. The main topics of this science that may be called mining chemistry are:

— physical chemical and micro fluid mechanical research for establishing fluid mining technologies. The mineral raw material — independently of its original state — reaches the surface in the form of a fluid (oil, water, slurry, suspension, chemical solution, combustion product etc.);
— solution of thermodynamical, physico-chemical and analytical chemical problems concerning interactions of minerals and fluids;
— preparatory studies on the utilization of minerals as basic materials in the chemical industry and mineral processing technologies;
— numerical and physical (laboratory) modelling of fluid mining technologies;
— design, construction and application of special modern equipment for physical modelling and measurement of physical-chemical parameters.

The few topics mentioned here well illustrate the need for developing this discipline towards a scientific school. This intention is expressed by the statement of the Presidium of the Hungarian Academy of Sciences N° 32/1980:

"The Petroleum Engineering Research Laboratory of the Hungarian Academy of Sciences and its research profile seem suitable to be developed so as to establish the basis institution devoted to those physical and chemical research programmes that may lead to new and special produc-

tion and processing methods based on "in situ" change of state (solution, leaching, combustion) in the fields of mining both solid and fluid minerals."

This statement determines the future of the Laboratory whose next twenty-five years will only be filled with creative content if the problems will have been solved by a combined effort of genius and exceptional zeal. Genius and zeal. Let it be a desire and message to young scientists who are expected to carry out the greater part of this work.

Acta Geodaet., Geophys. et Montanist. Acad. Sci. Hung. Vol. 17 (3—4), pp. 317—328 (1982)

MODELLING OF FLOW PHENOMENA IN POROUS MEDIA

L. BALLA

PETROLEUM ENGINEERING RESEARCH LABORATORY OF THE HUNGARIAN ACADEMY OF SCIENCES

The modelling of flow phenomena in porous media is dealt with in the study and the knowledge acquired so far is summarized. Based on mathematical correlations of the flow, the scaling criteria are described and their suitability for practical use is analyzed.

The scaling criteria derived in the study require that the porous structure of the model and that of the prototype should be the same. Further investigations are, however, needed to reproduce the porous structure of the prototype in the model because the parameters characterizing the porous structure are theoretically not yet defined unambiguously and there is no exact measurement method available.

Further investigations are required to decide whether the permeability k and exponent n of the capillary pressure function can unambiguously characterize the porous structure from the point of view of fluid mechanics, or some further parameters have to be defined.

If the parameters characterizing the porous structure are unambiguously defined, the next task is to analyse the effect of these parameters on the relative permeability and the wettability, and to express mathematically these relationships.

Knowing the parameters characterizing the porous structure and their effect on other parameters influencing the flow, the mathematical model of the flow can be modified. Scaling criteria derived on this basis allow greater possibility in modelling the porous systems.

Symbols

a, b, c	function parameters
$\mathbf{a}$	parameter vector
f	fractional function
g	acceleration due to gravity
G	porous space
h	height
H	similarity group
k	permeability
K	relative permeability
L	macroscopic size
$\mathbf{L}$	linear matrix operator
$\mathfrak{L}$	linear operator
m	number of parameters
n	parameter of capillary pressure function
N	ratio
p, P	pressure
$\mathfrak{P}$	pore structure
S	saturation of the wetting phase
t	time
u	velocity
x, y, z	Cartesian co-ordinates
α	parameters
φ	response function
ψ	mathematical model
Φ	porosity
ϱ	density
τ	normalized time

'	differentiation with respect to S
*	normalized
[ ]	dimension
{ }	set

Subscripts

ac	average capillary
c	capillary
g	gravity
i, j	number
m	model
p	prototype
rm	relative mobility
nw	non-wetting
nwr	non-wetting residual
w	wetting
wr	wetting residual

Introduction

The modelling of flow phenomena in porous media comprises the analysis of the following four transformations:

— transformation of the macroscopic dimensions of the porous media,
— transformation of the microscopic dimensions of the porous media,
— transformation of the properties of the flowing fluids and the porous media,
— transformation of the initial and boundary conditions referring to the flowing fluids and the porous media.

Modelling is possible only if the models applied correspond to the scaling criteria derived from the mathematical model $\psi(\mathbf{a}) = 0$, $\mathbf{a} = \{\alpha_j\}$ describing the flow.

Let $N(\alpha_j)$ denote the ratio of the values of parameter α_j in the model and in the prototype, i.e.

$$N(\alpha_j) = \frac{\alpha_{jm}}{\alpha_{jp}} .$$

Let us define the linear matrix operator $\mathbf{L}$ as

$$\mathbf{L} = \{\mathfrak{L}_{ij}\} \quad \text{where} \quad \mathfrak{L}_{ij} = \begin{cases} N(\alpha_j) & \text{if} \quad i = j \\ 0 & \text{if} \quad i \neq j. \end{cases}$$

Applying the linear transformation

$$\mathbf{a}_m = \mathbf{L}\mathbf{a}_p$$

the similarity groups

$$H_i = \prod_{j=1}^{m} N(\alpha_j)^{m_{ij}} \qquad \mathbf{H} = \{H_i\}$$

can be formed so that $H_i \not\subset H_j$ holds if $i \neq j$. Here m_{ij} denotes that exponent (required by ψ) of the j-th parameter in the i-th similarity group.

The behaviour of the prototype can be analyzed by means of the model if the scaling criterion

$$\psi(\mathbf{a}_m) = c \cdot \psi(\mathbf{a}_p) \qquad c \neq 0 \tag{1}$$

is met. The values of c and $\mathbf{H}$ depend on the structure of ψ.

The modelling of two-phase laminar flow of immiscible, incompressible fluids in homogeneous, isotropic, porous media will be dealt with in the present study, because this type of flow represents the most frequently occurring phenomena in petroleum reservoirs.

Derivation of the scaling criteria

The beginning of modelling is marked by the dimensional analysis of Leverett et al. (1942) which, however, has been replaced by the equational analysis based on the mathematical model of the fluid flow because the previous one lacked the real physical background.

For our case the mathematical model of the flow in porous media can be formulated according to Rapoport (1955) as

$$1. \qquad \operatorname{div} \frac{k K_w}{\mu_w} \operatorname{grad} (p_w + \varrho_w g h) = \frac{\partial S^*}{\partial \tau}$$

$$2. \qquad \frac{\partial S^*}{\partial \tau} + \mathbf{u} f' \operatorname{grad} S^* - \operatorname{div} \left((\varrho_w - \varrho_{nw}) f g k \frac{K_{nw}}{\mu_{nw}} \operatorname{grad} h \right) - \tag{2}$$

$$- \operatorname{div} \left(f k \frac{K_{nw}}{\mu_{nw}} P_c' \operatorname{grad} S^* \right) = 0$$

where

$$\mathbf{a} = \{x, y, z, \tau, S^*, \mathbf{u}, \varrho_{nw}, \varrho_w, g, \operatorname{grad} h, \mu_{nw}, \mu_w, k, K_{nw}, K_w, P_c\}$$

$$\tau = \frac{t}{\Phi \cdot (1 - \beta \cdot S_{nwr} - S_{wr})}$$

$$f = \frac{\dfrac{K_w}{\mu_w}}{\dfrac{K_w}{\mu_w} + \dfrac{K_{nw}}{\mu_{nw}}}$$

$$S^* = \frac{S_w - S_{wr}}{1 - \beta \cdot S_{nwr} - S_{wr}} .$$

$\beta = 0$ holds for drainage, $\beta = 1$ for imbibition. It should be noted that it is beyond the scope of this paper to investigate problems of modelling material properties and initial and boundary conditions since these belong to the topics

of physics, chemistry and experimental techniques and, on the other hand, they depend on the actual system.

Applying linear transformation **L** on mathematical model (2), the criterion

$$N(x) = N(y) = N(z)$$

is obtained, save the one-dimensional case. This criterion involves the geometric similarity of the macroscopic dimension L of the prototype and that of the model, i.e.

$$G_m = N(L)G_p. \tag{3}$$

Van Daalen and van Domselaar (1972) tried to use an other transformation instead of (3) but their results can only be applied within a rather narrow range.

Further scaling criteria can be derived from the relationships

$$N\left(\frac{S^*}{\tau}\right) = N\left(\frac{uf'\,S^*}{L}\right) = N\left(\frac{(\varrho_w - \varrho_{nw})\cdot g\,|\,\mathrm{grad}\,h\,|\,fk\,K_{nw}}{\mu_{nw}\,L}\right) =$$

$$= N\left(\frac{fk\,K_{nw}\,P_c'\,S^*}{\mu_{nw}L^2}\right) \tag{4}$$

if grad h = constant. If grad $h \neq$ constant, only $N(|\mathrm{grad}\,h|) = 1$ can hold. Further, the correlation

$$N\left(\frac{\partial h}{\partial x}\right) = N\left(\frac{\partial h}{\partial y}\right) = N\left(\frac{\partial h}{\partial z}\right)$$

must be met that implies the similarity of the vector field grad h.

$$N(S^*) = 1 \qquad \text{since} \qquad 0 \leq S^*_{m,p} \leq 1.$$

On this basis, the well known similarity groups are obtained if S^* is considered to be the dependent variable and $\tau u/L$ the independent one.

The similarity groups are

$$H_{rm} = N\left(\frac{\mu_w \cdot K_{nw}}{\mu_{nw} \cdot K_w}\right) \tag{5}$$

$$H_g = N\left(\frac{(\varrho_w - \varrho_{nw})\,k \cdot K_{nw}\,|\,\mathrm{grad}\,h\,|\cdot g}{\mu_{nw} \cdot u}\right) \tag{6}$$

$$H_c = N\left(\frac{K_{nw} \cdot P_c' \cdot k}{\mu_{nw} \cdot u \cdot L}\right) \tag{7}$$

i.e.

$$\mathbf{H} = \{H_{rm}, H_g, H_c\}.$$

u denotes the velocity and

$$N(u_x) = N(u_y) = N(u_z) \tag{8}$$

must hold because of relationships (2) and (3) requiring the similarity of the velocity field.

The elements of vector **H** are

$$\mathbf{H} = \{1, 1, 1\} \tag{9}$$

because of $N(f) = 1$ since $0 \leq f_{m,p} \leq 1$.

Further, the relationship

$$\tau_m^* = \tau_p^* \qquad \text{with} \qquad \tau^* = \tau u/L \tag{10}$$

must hold.

Criterion (9) in the form (5), (6), (7) is rather difficult to meet because the similarity groups involve the relative permeability and capillary pressure functions which depend on further factors. The forms of these functions are, however, not exactly known. These factors are

— surface tension of both fluids,

— wettability,

— parameters characterizing the porous structure.

Since the two latter factors are not exactly defined for porous systems, they are very difficult to be taken into account.

Rapoport (1955) also requires the relative permeability and the capillary pressure functions and their derivatives to be identical in the model and the prototype. This restriction has been overcome by the Leverett's (1941) J-function introduced by Geerstsma et al. (1956) and by the normalized relative permeability functions suggested by Perkins and Collins (1960). The model laws of Bentsen (1976) already do not involve the derivative of the capillary pressure function, only a value characteristic of the average capillary pressure. The disadvantage of these laws however is that they only hold for drainage processes. The capillary pressure function

$$P_c = -P_{ac}(\ln S^*)^{\frac{1}{n}} \tag{11}$$

introduced by Milley and Wagner (1975) is valid for both drainage and imbibition. As shown in [Balla, 1980b]:

n characterizes the pore shape and distribution and

P_{ac} characterizes the average capillary pressure.

The value of n depends on the vector **n** determining the pore shape and distribution. Upon differentiating (11), we obtain

$$P_c' = P_{ac} \cdot P_c^{*\prime}(S^*, n) \tag{12}$$

with

$$P_c^{*\prime} = -\frac{(\ln S^*)^{\frac{1-n}{n}}}{n \cdot S^*}.$$

The normalized relative permeability functions to be used to further simplify the similarity groups, can be found in Bear's book (1972). In the present study the functions introduced by Fatt and Dykstra (1951) will be applied because they add only four parameters to the variables to be transformed and are in connection with the given system through the capillary pressure function. The normalized relative permeability curves are defined as

$$K_w = K_{wr} \frac{\int_0^{S^*} \frac{\mathrm{d}\, S^*}{P_c^{b_w}}}{\int_0^1 \frac{\mathrm{d}\, S^*}{P_c^{b_w}}} \qquad 0 < K_{wr} < 1$$

$$K_{nw} = K_{nwr} \frac{\int_{S^*}^1 \frac{\mathrm{d}\, S^*}{P_c^{b_{nw}}}}{\int_0^1 \frac{\mathrm{d}\, S^*}{P_c^{b_{nw}}}} \qquad 0 < K_{nwr} < 1. \tag{13}$$

Let us now assume that b_w and b_{nw} depend only on the pore shape and distribution, i.e. on **n**. For a capillaric model we have $b_w = b_{nw} = 2$, in practical cases some other value gives a better approximation of the normalized permeability curves. b_w and b_{nw} may be considered as constant for a given system. Any difference may be attributed to changes in pore size and distribution therefore b_w and b_{nw} will be assumed to be functions of **n** alone. Substituting capillary pressure function (11) into relationship (13), we obtain

$$K_w = K_{wr} \cdot K_w^*(S^*, \mathbf{n}) \tag{14}$$
$$K_{nw} = K_{nwr} \cdot K_{nw}^*(S^*, \mathbf{n})$$

where

$$K_w^* = \frac{\int_0^{S^*} (-\ln S^*)^{-\frac{b_w}{n}} \mathrm{d}S^*}{\int_0^1 (-\ln S^*)^{-\frac{b_w}{n}} \mathrm{d}S^*} \qquad K_{nw}^* = \frac{\int_{S^*}^1 (-\ln S^*)^{-\frac{b_{nw}}{n}} \mathrm{d}S^*}{\int_0^1 (-\ln S^*)^{-\frac{b_{nw}}{n}} \mathrm{d}S^*}.$$

In relationships (14) P_{ac} is eliminated thus the normalized relative permeability functions only depend on the pore shape and distribution and on the relative permeability of one of the phases measured and the unreducable saturation of

the other phase, characteristic of average flow condition. By making use of relationships (12) and (14) the similarity groups become

$$H_{rm} = N\left(\frac{\mu_w K_{nwr} K^*_{nw}}{\mu_{nw} K_{wr} K^*_w}\right) \tag{15}$$

$$H_g = N\left(\frac{(\varrho_w - \varrho_{nw})\, g\, |\,\mathrm{grad}\, h\,|\, k\, K_{nwr} K^*_{nw}}{\mu_{nw}\, u}\right) \tag{16}$$

$$H_c = N\left(\frac{P_{ac} k K_{nwr} K^*_{nw} P^{*\prime}_c}{\mu_{nw}\, uL}\right) . \tag{17}$$

For $N(\mathbf{n}) = 1$

$$H_{rm} = N\left(\frac{\mu_w \cdot K_{nwr}}{\mu_{nw} \cdot K_{wr}}\right) \tag{18}$$

$$H_g = N\left(\frac{(\varrho_w - \varrho_{nw})\, g\, |\,\mathrm{grad}\, h\,|\, k\, K_{nwr}}{\mu_{nw}\, u}\right) \tag{19}$$

$$H_c = N\left(\frac{P_{ac}\, k\, K_{nwr}}{\mu_{nw}\, uL}\right) \tag{20}$$

hold. Since the similarity groups obtained do not comprise functions any more, the scaling criteria have become more simple. As for K_{nwr} and K_{wr}, further investigations should be made to determine which factors do they depend on.

From the previous considerations it should become obvious that the majority of experiments, carried out on the basis of the scaling criteria used until now, could not yield valuable information about the prototype because only the permeability k characterizing the average pore size have been implied while other important microscopic properties *viz.* pore shape and distribution have been neglected, even though all these parameters play an important role in determining the microscopic structure of the porous system. Even where the application of the relative permeability and capillary pressure functions seems to indicate that the pore shape and distribution have been taken into account, the processes in the model and in the prototype are not necessarily the same in all cases, since the function has not been determined under dynamic conditions.

Until the effect of the porous system on the flow will be known, $N(k) = N(\mathbf{n}) = 1$ is an appropriate choice, i.e.

$$\mathcal{S}_m = \mathcal{S}_p. \tag{21}$$

Manufacturing a model that satisfies this requirement needs, however, further experiments.

The value of P_{ac} characterizing the average capillary pressure should be determined under dynamic conditions which increases the accuracy of modelling. A possible measurement method, that the time of the spontaneous imbibition is used to conclude somehow on the value of P_{ac}. This method, however, can only be applied after further investigations.

If S^* is regarded as dependent and τ^* as an independent variable, the scaling criteria become

$$N(S^*) = 1 \qquad N(\tau^*) = 1$$

$$G_m = N(L)\, G_p \qquad \mathcal{S}_m = \mathcal{S}_p \tag{22}$$

$$\mathbf{u}_m = N(u)\mathbf{u}_p \qquad \text{grad}\, h_m = N(|\text{grad}\, h|)\, \text{grad}\, h_p$$

$$\mathbf{H} = \{1, 1, 1\}.$$

These relationships may be completed by the initial and boundary conditions of the given case.

The model experiments based on these scaling criteria can only furnish as accurate information about the prototype as accurately ψ describes the flow, as accurately the macroscopic and microscopic characteristics of the prototype are known, and as precisely the properties required by the model can be reproduced.

Modelling fluid reservoirs

Working fluid reservoirs has always to be carried out so as to ensure an optimum for function φ characterizing the actual circumstances. Function φ is determined by the macroscopic space G of the porous system, by the mathematical model ψ describing the flow, by its initial and boundary conditions ψ_0 and the parameter vector $\mathbf{a}$, i.e.

$$\varphi = \varphi(G, \psi(\mathbf{a}), \psi_0).$$

Assume for function φ that its optimum coincides with its maximum. (If the optimum of function φ were its minimum, the optimum of $1/\varphi$ would coincide with the maximum thus the condition can be regarded as general.) The maximum of function φ shall be denoted by $\varphi_{\max}$ for the case of given G, ψ, ψ_0, i.e.

$$\varphi_{\max} = \varphi(\mathbf{a}_{\text{opt}})_{G, \psi, \psi_0}.$$

The scaling criteria (22) require the macroscopic dimensions of the model and the prototype to be geometrically similar. In the majority of practical cases,

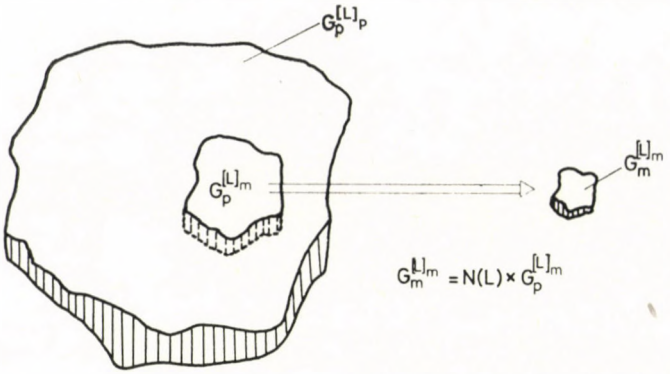

Fig. 1. Geometrically similar characteristic space

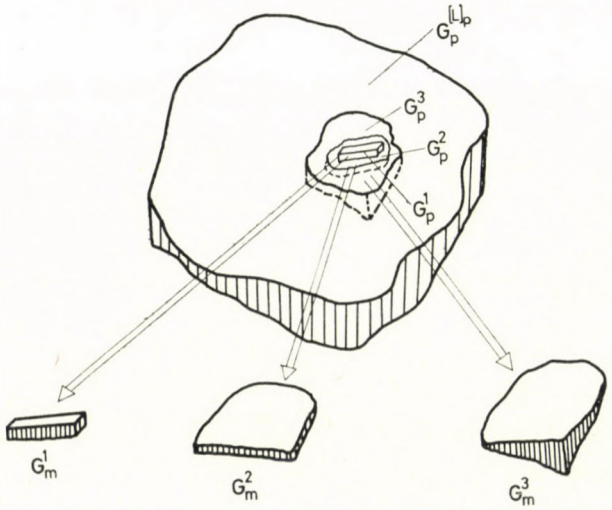

Fig. 2. Geometrically similar one-, two- and three-dimensional characteristic spaces

this condition cannot be met because of the size and complexity of the prototype. Therefore, a characteristic space of the prototype is chosen for modelling (Fig. 1).

$$G_p^{[L]_m} \subseteq G_p^{[L]_p} \qquad [L]_m \leqq [L]_p.$$

In the part $G_p^{[L]_m}$ of the reservoir we can already satisfy the criterion of geometric similarity:

$$G_m^{[L]_m} = N(L) \cdot G_p^{[L]_m}.$$

The experiments are carried out in the porous space $G_m^{[L]_m}$ meeting the scaling criteria (22). The experiments are aimed at determining

$$\varphi_{\max,m}^{[L]_m} = \varphi(\mathbf{a}_{\mathrm{opt}}^m)_{G_m^{[L]_m},\ \psi(\mathbf{a}_m),\ \psi_{0,m}}$$

and $\mathbf{a}^m_{\text{opt}}$. If $\mathbf{a}^m_{\text{opt}}$ is known, $\mathbf{a}^p_{\text{opt}}$ is determined using the similarity groups

$$\mathbf{a}^m_{\text{opt}} : \mathbf{H} : \mathbf{a}^p_{\text{opt}}$$

i.e.

$$\varphi^{[L]_m}_{\max,p} = \varphi(\mathbf{a}^p_{\text{opt}})_{G^{[L]_m}_p,\ \psi(\mathbf{a}_p),\ \psi_{0,p}}.$$

Conclusions made from $\varphi^{[L]_m}_{\max,p}$ on the value

$$\varphi^{[L]_p}_{\max} = \varphi(\mathbf{a}^p_{\text{opt}})_{G^{[L]_p}_p,\ \psi(\mathbf{a}_p),\ \psi_{0,p}}$$

of the reservoir are reliable if the ratio

$$G^{[L]_m}_p / G^{[L]_p}_p \leq 1$$

is great at given $[L]_m$ or the ratio $[L]_m/[L]_p = 1$ is great, i.e.

$$\varphi^1_{\max,p} \leq \varphi^2_{\max,p} \leq \varphi^3_{\max,p} \leq \varphi^{[L]_p}_{\max,p}$$

$$G^1_p \subseteq G^2_p \subseteq G^3_p \subseteq G^{[L]_p}_p$$

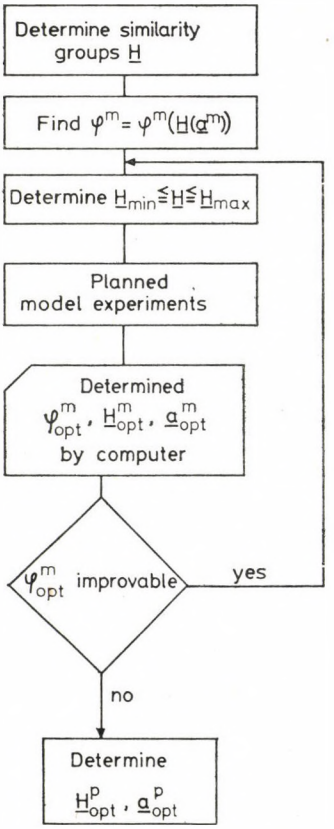

Fig. 3. Two-level factorial experiment-planning

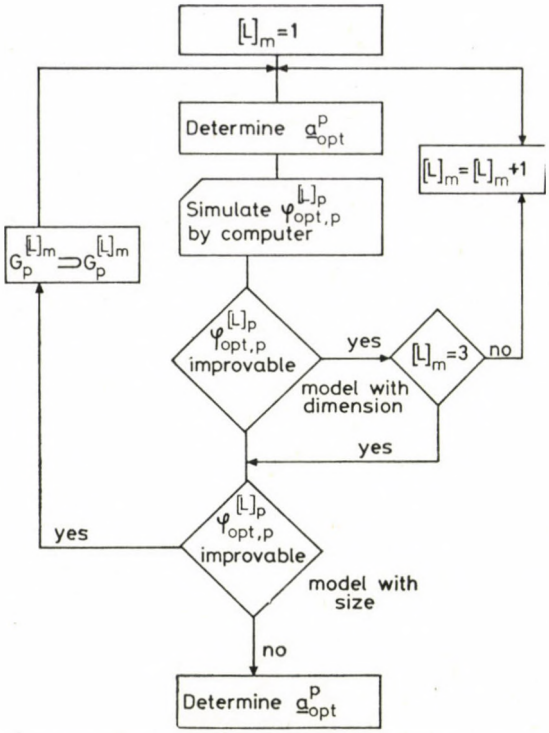

Fig. 4. Determining the optimum parameters

This statement implies that maximum characteristic space has to be selected and can be modelled so as to meet the criteria of geometric similarity (Fig. 2). The one-dimensional model yields information only about the microscopic flooding.

A two-dimensional model is required to investigate the effect of areal flooding while the gravitational segregation can only be modelled in three dimensions if all three effects have to be known.

On the basis of these statements, flow phenomena in reservoirs should possibly be modelled in several steps.

First, the optimum ranges of the parameters are determined by means of a one-dimensional model, for this requires the greatest number of experiments and the costs of one-dimensional cores are relatively low.

Narrowing the ranges of parameters and determining $\mathbf{a}^p_{opt}$ are carried out on two- or three-dimensional models depending on the nature of the problem.

The determination of the optimum parameters demands a great number of experiments. Therefore, because of the costs and time of modelling, the experiments have to be properly designed. The two-level factorial method of experiment-design [Balla, 1980a] can be used for this purpose (Fig. 3). The

necessary parameters are determined by computer from the measurement results obtained. Using these data, the behaviour of the reservoir is simulated by computer by means of the mathematical model while the accuracy of modelling can be checked by pilot plant experiments (Fig. 4).

REFERENCES

BALLA, L. 1982: Mathematical formalism of the 2^{n-p} type firstpower factorial test planning. *Acta Geod. Geoph. Mont. Hung.* 17, 81—98.

BALLA, L. 1980: Scaled fluid-flow models with normalized permeabilities and capillary functions. *Erdöl, Erdgas Zeitschrift* 17, 81—98.

BEAR, J. 1972: Dynamics of fluids in porous media. American Elsevier Publ. Co., Hew York

BENTSEN, R. G. 1976: Scaled fluid-flow models with permeabilities differing from that of the prototype. *J. Can. Petr. Tech.*, July—September, 46—52.

FATT, I.—DYKSTRA, H. 1951: Relative permeability studies. *Trans. AIME*, 192, 249—256.

GEERTSMA, J.—CROES, G. A.—SCHWARZ, N. 1956: Theory of dimensionally scaled models of petroleum reservoirs. *Trans. AIME*, 207, 118—127.

LEVERETT, M. C. 1941: Capillary behavior in porous solids. *Trans. AIME*, 142, 152—169.

LEVERETT, M. C.—LEWIS, W. B.—TRUE, M. E. 1942: Dimensional-model studies of oil-field behavior. *Trans. AIME*, 146, 175—193.

MILLEY, GY.—WAGNER, O. 1975: Theoretical and practical solution of manufacturing porous bodies made of spherical particles, and their investigation. Ph. D. Thesis, Hungarian Academy of Sciences. Budapest. (In Hungarian)

PERKINS, F. M.—COLLINS, R. E. 1960: Scaling laws for laboratory flow models of oil reservoirs *Trans. AIME*, 219, 383—385.

RAPOPORT, L. A. 1955: Scaling laws for use in design and operation of water-oil flow models. *Trans. AIME*, 204, 143—150.

VAN DAALEN, F.—VAN DOMSELAAR, H. R. 1972: Scaled fluid-flow models with geometry differing from that of the prototype. *Trans. AIME*, 253, 220—228.

Acta Geodaet., Geophys. et Montanist. Acad. Sci. Hung. Vol. 17 (3—4), pp. 329—344 (1982)

DETERMINATION OF THE DIFFUSION MASS TRANSPORT COEFFICIENT OF A CO_2—CH_4 GAS MIXTURE IN POROUS MEDIA AT RESERVOIR TEMPERATURE AND PRESSURE

K. BAUER

PETROLEUM ENGINEERING RESEARCH LABORATORY OF THE HUNGARIAN ACADEMY OF SCIENCES

The study reports experimental devices for investigation of diffusion transport processes of gas mixtures at high pressure. A measurement method is described for the determination of the molecular diffusion coefficient of a binary CO_2—CH_4 gas mixture in reservoir rock and at formation conditions, and ways for the evaluation of experimental data obtained by the gas eluation method are reported.

The results of laboratory experiments have been used for predicting gas diffusion processes in gas caps of depleted oil reservoirs worked secondarily by CO_2.

Symbols

D	average diffusivity	m^2s^{-1}
D_{AB}	diffusivity	m^2s^{-1}
G	total molar flow rate	mole s^{-1}
H	length of rock sample in vertical arrangement	m
L	length of rock sample in horizontal arrangement	m
M	molecular mass	kg
N	specific molar flow rate (density)	mole $s^{-1}m^{-2}$
p	pressure	Pa
Δp	pressure difference	Pa
t	time	s
T	temperature	K
u, v	average rate of molar volumetric change of the system	m s^{-1}
V	volume, rock pore volume	m^3
x, z	local co-ordinates	m
y	molar fraction	
ϱ	molar density of gas mixture	mole m^{-3}

First subscripts

A	CO_2 gas
B	CH_4 gas
O	intermediate point
e	state of equilibrium without natural convection
∞	state of equilibrium with natural convection

Second subscripts

O	initial state
K	final state
E	eluation space

Third subscripts

O	initial state
K	final state
E	eluation space

a, b, c, d, . . . function constants

In reservoir mechanics, one has to know the value of diffusion mass transport in gas reservoirs or in gas caps of depleted oil reservoirs worked secondarily by CO_2. Diffusivity characterising the mass transport in the space depends on pressure and temperature as well as the composition of the gas mixture.

Diffusivity of an approximately binary CO_2—CH_4 mixture can also be estimated by calculation [7, 18]. It is, however, most suitably determined experimentally on rock samples taken from the reservoir in order to take into account the dispersion effect of the rock.

For the investigation of diffusion processes of binary gas mixtures at high temperature and high pressure, porous media *viz.* sintered glass diaphragms, porous bronze etc. are generally only used to stabilize the process in the measurement cell [5—7, 11].

At the same time, there are a variety of methods to investigate free diffusion processes of gas mixtures at medium and low pressure. The unsteady-state method is the most widely used among them. The divided-cell method was first introduced by Loschmidt [3], while the gas eluation method is due to Stefan [1, 2]. The divided cell was nothing but two opposed Stefan's cells.

Many varieties of Loschmidt's method are known for high pressure and high temperature [3—9, 10—11, 13, 15] but the gas eluation method has been used for high temperatures at low pressure only because of technical difficulties in stabilizing the high pressure eluation process [12, 14].

The tasks outlined here raise requirements against the measurement method that widely differ from the atmospheric conditions and make it necessary to determine the mass transport coefficient — concentration relationship. Theoretically, varieties of the Loschmidt method for high pressure and high temperature would have furnished greater accuracy but the measurement method had to be suitable for the investigation of the diffusion mass transport in a dry rock as well as at residual fluid saturation. For this reason, a high pressure procedure of the gas eluation method has been developed in order to ensure the stabilization of the diffusion mass transport during measurements. The amount of the eluated CO_2 was measured during the experiment and the pseudo-equilibrium section of this recovery curve has been used for the evaluation. On the other hand, in order to check the measurement results obtained by the gas eluation method, a closed-cell measurement device was built according to Gavalas' suggestion [15]. During the measurement, cell pressure was recorded as a function of time and the pseudo-equilibrium section of the curve has been used for the evaluation.

Natural gas with 0.98 methane content and 0.99 purity CO_2 was used in the experiments. Measurements were carried out at 336 °K temperature and at 5 and 10 MPa pressures.

Measurement device and measurement procedure based on gas eluation principle

A schematic view of the measurement device is shown in Fig. 1. Rock sample O is placed in stainless steel sleeve N sealed by a teflon ring and fixed inside the diffusion cell. One side of the rock sample communicates with

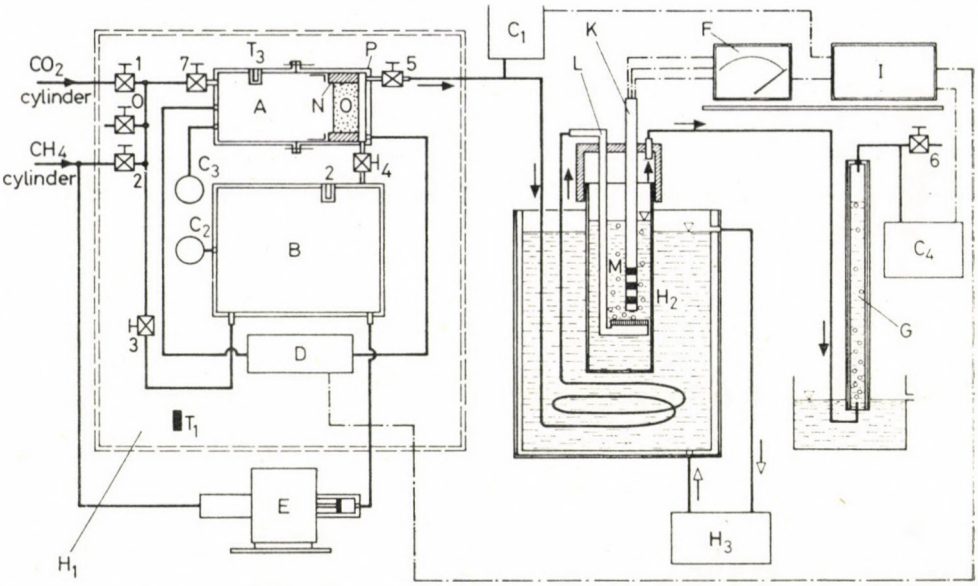

Fig. 1. Schematic diagram of the gas eluation measurement equipment. A — buffer vessel in front of the rock, B — buffer vessel connected to the eluation slit, C — pressure transducers, D — differential pressure gauge, E — microcompressor, F — conductometer, G — bubble flow meter, H — fluid thermostat, I — digital data recorder, J — conductivity electrode, K — filter pipe, L — stainless steel pipe, M — conductivity cell, N — stainless steel sleeve, P — eluation slit, T — temperature detectors

CH_4—CO_2 gas mixture while the other side faces eluation slit P. Buffer container B containing CH_4 is connected to the lower part of the eluation slit. One side of pressure differential gauge D is connected to the central part, while needle valve 5 removing the eluated gas mixture is connected to the upper part. Valves 7 and 3 conducting CO_2 and CH_4 gases lead to the upper part, while the other side of pressure differential gauge to the central part on the other side, of container A.

Pressure gauge C_2 leads to the upper part, while valve 3 conducting methane and the microcompressor transporting the eluating gas lead to the lower part of buffer-container B containing the eluating methane. Outer in- and outlet valves 1 and 2 for CO_2 and CH_4 and cell temperature measuring transistors T_1 and T_2, and temperature control transistor T_3 of the air thermostat are placed inside the thermostat.

The eluated gas mixture flows from needle valve 5 through a thin stainless steel pipe spiral and filter pipe into conductometry vessel M containing one normal KOH solution in finely dispersed state. The volumetric flow rate of the flowing gas mixture is measured and continuously recorded by electronic pressure gauge C_4.

The KOH solution fixes CO_2 in form of K_2CO_3 which results in a change of the specific electric conductivity of the solution. This is indicated by electrode K. The DC signal of the conductometer is measured and recorded as a function of time by a 0.01 millivolt accuracy digital voltmeter. The conductometry electrode and the vessel containing KOH solution are kept in the water bath at temperature 298 $\pm$ 0.1 °K. The volume of methane bubbling through the KOH solution can be determined in vessel G by measuring the pressure change by electronic pressure transducer C_4. The signal of this instrument is also continuously recorded. The microcompressor connected to container B is controlled by the signal of differential pressure gauge D. This ensures for the pressure differential between both sides of the rock sample to be kept at minimum (less than 1 kPa) during eluation.

Closed-cell device and measurement procedure

The device is illustrated in Fig. 2. The rock sample glued into stainless steel sleeve is placed into diffusion cell A. The upper end of vessel A containing CO_2 is connected through valve 1 to buffer-container B containing CH_4. Lower ends of vessels B and C are in connection with pressure differential gauge D, and through valves 2 and 3 with double-acting compressor E_1. Compressor E_1, and vessels A and B can be simultaneously filled with CO_2 of required pressure through valves 4 and 5 from blow-case vessels F_1 and F_2. Valves 4 and 5 are closed during this process. After filling up the system, valves 3 and 6 are closed. After achieving the thermal equilibrium which is indicated by thermometers T_2 and T_1, compressor E_1 is set in motion and valve 1 is opened. The compressor pumps methane of volume V into vessel B with a velocity greater by one order of magnitude than that of the diffusion mass transport, and, simultaneously, the same volume of CO_2 is extracted from vessel A. Valves 2, 8 and 3 are closed at the moment of stopping the compressor which enables pressure differential gauge D to measure pressure differential $\Delta p(t)$ between vessels B and C as a function of time. The variation of $\Delta p(t)$ characterizes the process of concentration equalization through diffusion.

The diffusion model

When real gases are mixed by diffusion, the molar density of the mixture is not constant at the various points of the cell but it changes during the process so that at the beginning a density equalization proceeds approximately with the velocity of diffusion in addition to the phenomenon of molecular diffusion of ideal gases. This process has to be taken into account as a natural convection.

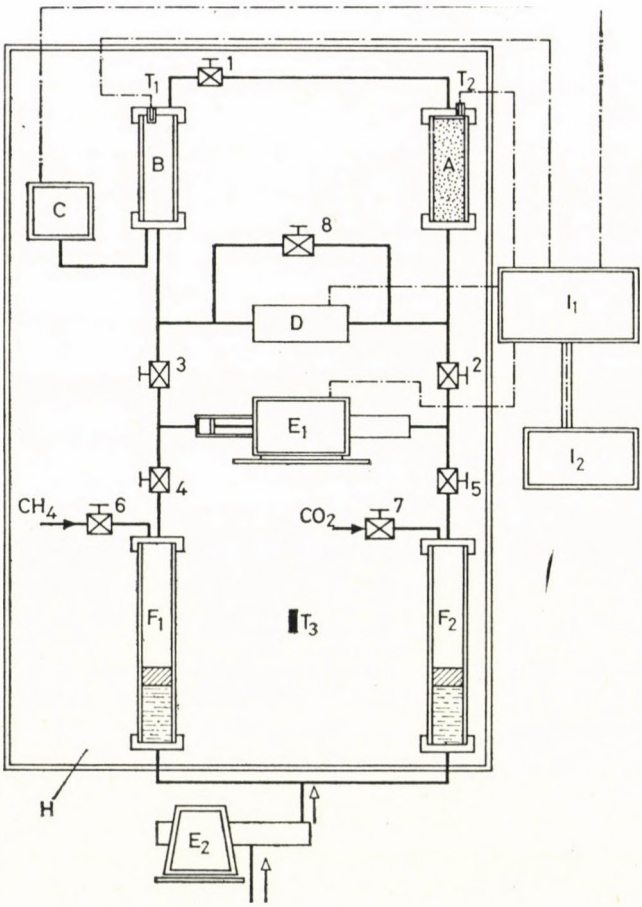

Fig. 2. Schematic diagram of the closed-cell measurement equipment. A — rock sample, B — buffer vessel, C — pressure transducer, D — differential pressure gauge

The density equalization proceeds towards the lower molar density from the higher one according to the original position of the pure components. The velocity of the molar mass transport along the length of the cell can be expressed as

$$v = \frac{N}{\varrho} \tag{1}$$

where v denotes the rate of the molar volumetric change of the mixture.

For closed-cell investigations, the average molar density calculated with respect of the length of the cell is constant thus the mixing results in changes

of pressure p and compressibility factor z in the same sense, according to the relationship

$$\varrho = \frac{P}{z\,RT}\,. \tag{2}$$

Contrary to this, the pressure of the system does not change at the gas eluation method, therefore the average of the value $z\varrho$ along the cell is constant. Thus, depending on whether the molar density of the eluating gas is smaller or greater than that of the eluated one, the molar density of the mixture decreases and the compressibility factor increases in the cell or *vice versa:* the density increases and coefficient z decreases to the same extent.

The rate of the initial natural convection in the closed cell eventually decreases to zero due to equalization of the mixture density. This ensues substantially farther than in case of the gas eluation methode where the average value of $v\varrho$ is approximately constant along the length of the cell.

Based on these considerations, the number of molecules (e.g. of component A) from among those crossing a unit surface element of an imaginary plane at some arbitrary point during unit time can be calculated for the initial stage of mixing for any of the methods by Fick's first law as

$$N_A = \varrho_A v - D_{AB}\frac{\partial \varrho_A}{\partial x}\,. \tag{3}$$

Taking into account the material balance for volume element

$$\frac{\partial \varrho}{\partial t} + \frac{\partial}{\partial x}(\varrho v) = 0. \tag{4}$$

Fick's second law can be written for component A and for the conditions of natural convection as

$$\frac{\partial \varrho_A}{\partial t} = \frac{\partial}{\partial x}\left(D_{AB}\frac{\partial \varrho_A}{\partial x}\right) - v\frac{\partial \varrho_A}{\partial x}\,. \tag{5}$$

It is useful to introduce average values

$$D(t) = \frac{1}{L}\int_0^L D_{AB}(x, t)\,\partial x \tag{6}$$

and

$$u(t) = \frac{1}{L}\int_0^L v(x, t)\,\partial x. \tag{7}$$

Making use of these expressions, equation

$$\frac{\partial \varrho_A}{\partial t} = D(t)\frac{\partial^2 \varrho_A}{\partial x^2} - u(t)\frac{\partial \varrho_A}{\partial x} \tag{8}$$

can be used for the estimation of distribution $\varrho_A(x, t)$ in the diffusion cell, instead of Eq. (5).

Since the concentration distribution in the initial stage $0 < t < t_0$ of gas mixing as estimated by Eq. (8) significantly differs from the real distribution $\varrho_A(x, t)$ in the cell, the evaluation has to be restricted to the section $t > t_0$ of the CO_2-recovery curve $M(t)$, where the change of parameters $D(t)$ and $u(t)$ can be neglected.

With the initial condition

$$\varrho_A = \varrho_{AO}; \qquad t = 0; \qquad 0 < x < L$$

and the boundary conditions

$$\begin{aligned} \varrho_A &= \varrho_{AO}; \qquad t > 0; \qquad x = 0 \\ \varrho_A &= \varrho_{AK}; \qquad t > t_0; \qquad x = L \end{aligned} \tag{9}$$

of eluation, distribution $\varrho_A(x, t)$ can be calculated by Fourier transformation

$$\varrho_A(x, t) = C(x) + e^{\left(\frac{ux}{2D} - \frac{u^2}{4D} t\right)} \sum_{n=1}^{\infty} e^{-\frac{n^2\pi^2}{L^2} Dt} \sin\frac{n\pi x}{L} \cdot$$

$$\cdot \left\{ \frac{2}{L} \cdot \int_0^L e^{-\frac{u\xi}{2D}} (\varrho_{AO} - C(x)) \sin\frac{n\xi}{L} \cdot d\xi \right\} \cdot \tag{10}$$

Thus, finally

$$\varrho_A(x, t) = \varrho_{AO} \frac{e^{\frac{ux}{D}} - e^{\frac{uL}{D}}}{1 - e^{\frac{uL}{D}}} + \varrho_{AK} \frac{1 - e^{\frac{ux}{D}}}{1 - e^{\frac{uL}{D}}} -$$

$$- \frac{\varrho_{AO} - \varrho_{AK}}{L} e^{-\left[\frac{u}{D}(L-x) + \frac{u^2}{4D} t\right]} \cdot$$

$$\cdot \left\{ \sum_{n=1}^{\infty} \frac{n\pi}{L} \cdot \frac{2(-1)^n}{\left(\frac{n^2}{L}\right)^2 \left(\frac{u}{2D}\right)^2} \cdot \sin\frac{n\pi x}{L} e^{-\frac{n^2\pi^2}{L^2} Dt} \right\}. \tag{11}$$

The total molar flow rate through the discharge cross-section of the rock facing the eluation slit can be written according to (11)

$$G_A = A\Phi \left[v\varrho_{AK} - D_{ABK} \left(\frac{\partial \varrho_A}{\partial x} \right)_K \right]. \tag{12}$$

From the material balance written up for the eluation slit

$$\varrho_{AEK} - \varrho_{AEB} = \frac{G_A}{q} \tag{13}$$

with

$$\varrho_{AEB} = 0.$$

The number of the cumulated molecules of component A eluated from the system becomes

$$M(t) = \int_0^t \varrho_{AK} q \cdot \partial t = \int_0^t G_A \cdot \partial t. \tag{14}$$

Integrating (14) under condition (13), the following relationship is obtained for $M(t)$

$$M(t) = A\Phi \left\{ v\varrho_{AK} + D_{ABK} \left[\frac{u}{D} \cdot \frac{\varrho_{AO} e^{\frac{uL}{D}} - \varrho_{AK} e^{-\frac{uL}{D}}}{1 - e^{\frac{uL}{D}}} \cdot t + \right.\right.$$

$$+ \frac{\varrho_{AO} - \varrho_{AK}}{\pi^2} \sum_{n=1}^{\infty} \frac{DL}{n^2 \left[D + \frac{1}{D} \left(\frac{L}{n\pi} \frac{u}{2} \right)^2 \right]^2} \cdot$$

$$\left.\left. \cdot \left(1 - e^{-\frac{n^2\pi^2}{L^2} \left[D + \frac{1}{D} \cdot \left(\frac{L}{n\pi} \frac{u}{2} \right)^2 \right] t} \right) \right] \right\}$$

Letting $t \to \infty$ in Eq. (15), the dynamic state of equilibrium will be characterized by the straight line

$$M(t) = A + Bt. \tag{16}$$

For $t > t_0$ the curve $M(t)$ can be fairly accurately approximated by the first term of infinite series (15), i.e. it can be described asymptotically as

$$M(t) = A + Bt - Ce^{-\frac{\pi^2}{L^2} \left[D + \frac{1}{D} \left(\frac{L}{\pi} \cdot \frac{U}{2} \right)^2 \right] t}. \tag{17}$$

If the measurements are evaluated by means of relationships (16) and (17), the logarithm of the difference of (16) and (17) taken at the same instant, starting from some $t > t_0$, can be linearized as a function of time. Doing so, equation

$$\mathrm{Ln}\, M(t) \equiv \mathrm{Ln}\, [M_\infty(t) - M(t)] = \mathrm{Ln}\, C - a_s t \tag{18}$$

of the straight line is obtained whose slope

$$a_s = \frac{\pi^2}{L^2}\left[D + \frac{1}{D}\left(\frac{L}{\pi}\cdot\frac{u}{2}\right)^2\right] \tag{19}$$

can be determined from the results of the experiments. From the quadratic equation

$$D^2 - Da_s\left(\frac{L}{\pi}\right)^2 + \frac{u^2}{4}\left(\frac{L}{\pi}\right)^2 = 0 \tag{20}$$

the value of D is calculated as the root.

$$D = \frac{a_s\pi^2}{2L^2} + \left[\frac{a_s^2 L^4}{\pi^4 4} - \left(\frac{uL}{2\pi^2}\right)^2\right]^{1/2}. \tag{21}$$

Initial and boundary conditions

$$\varrho_A = \varrho_{AO}; \qquad t = 0; \qquad 0 < z < z_0 \tag{22}$$

$$\frac{\partial \varrho_A}{\partial z} = 0; \quad t > 0; \quad z = 0; \quad z = H \tag{23}$$

are used to solve the differential equation (5) for the closed cell by Fourier transformation. Thus, assuming $v = 0$ and $D_{AB} =$ constant, the variation of $\varrho_A(z, t)$ in a rock sample in vertical position can be written as

$$\varrho_A(z, t) = \varrho_{Ae} + \frac{2\varrho_{AO}}{\pi}\sum_{n=1}^{\infty}\sin\frac{n\pi z_0}{H}\cos\frac{n\pi z}{H}\, e^{-D_{AB}\left(\frac{n\pi}{L}\right)^2 t}. \tag{24}$$

Distribution (24) can be regarded as accurate in the later phase of mixing at $t > t_0$ because if time approaches infinity, $v \to 0$ and $\varrho \to \varrho_e$ hold while D_{AB} approaches D_{ABe}. If the molar concentration $\varrho = \varrho[\varrho_A, p(t), T]$ is determined from the equilibrium value $\varrho_e = \varrho(\varrho_{Ae}, p_e, T)$ for the period $t > t_0$, the following approximate relationship can be obtained from a development into Taylor's series

$$\begin{aligned}\varrho(\varrho_A, p(t), T) = \varrho(\varrho_{Ae}, p_e, T) &+ \left(\frac{\partial \varrho}{\partial p}\right)_e (p(t) - p_e) + \\ &+ \left(\frac{\partial \varrho}{\partial_A}\right)_e \cdot (\varrho_A - \varrho_{Ae}) + \frac{1}{2}\left(\frac{\partial^2 \varrho}{\partial p^2}\right)_e (p(t) - p_e)^2 + \\ &+ \left(\frac{\partial^2 \varrho}{\partial p \partial \varrho_A}\right)_e (p(t) - p_e)(\varrho_A - \varrho_{Ae}) + \\ &+ \frac{1}{2}\left(\frac{\partial^2 \varrho}{\partial \varrho_A^2}\right)(\varrho_A - \varrho_{Ae})^2.\end{aligned} \tag{25}$$

Since the cell is closed,

$$\int_0^H (\varrho_A - \varrho_{Ae})\, \partial z = 0 \tag{26}$$

holds while

$$\int_0^H (\varrho_A - \varrho_{Ae})^2\, \partial z = \sum_{n=1}^{\infty} \frac{a_n}{2} e^{-\frac{2n^2\pi^2 D_{AB} t}{H^2}}. \tag{27}$$

Taking into account these results, we can express the pressure differential from Eq. (25) and, making use of the same neglection as in Gavalas [15], we finally get

$$p(t) - p_e = \frac{a_1^2}{4} \frac{\left(\frac{\partial^2 \varrho}{\partial \varrho_A}\right)_e}{\left(\frac{\partial \varrho}{\partial p}\right)_e} e^{-\frac{2\pi^2 D_{AB}}{H^2} t}. \tag{28}$$

The logarithm of the differences between $p(t)$ determined by the measurements and p_e can be linearized according to the relationship

$$\mathrm{Ln}(p(t) - p_e) = \mathrm{Ln}\, a - \frac{2\pi^2 D_{AB}}{H^2} t \tag{29}$$

starting from $t > t_0$. The value of D_{AB} can now be determined from the slope of the line obtained.

Analysis of the information obtained by the measurements

In order to establish the relationship between the coefficient D_{AB} and the concentration of CO_2 at constant pressure and temperature, sets of experiments have to be carried out using either the eluation or closed-cell methods.

Applying the eluation method, the conditions for the various experiments can be adjusted by changing the composition of the initial gas mixture and keeping the rate q of eluation and outlet valve opening constant. It is, however, more convenient to keep the initial gas composition constant and to have different rates of eluation and outlet valve openings.

The outlet valve opening can only be controlled, as a rule, rather coarsely at constant system pressure. Therefore, the various experiments with different rates of eluation are more conveniently carried out at the same valve opening.

In investigations of this type the value a_s is analyzed as a function of the rate q of eluation (Figs. 3 and 4). Curve a_s has a parabolic shape and crosses its minimum with increasing q.

This phenomenon is in connection with the fact that the valve opening is kept constant in the experiments with increasing q. At small values of q, a mass transport of the same sense is added to the natural convection due to a slight expansion of the diffusion cell. At great values of q, mass accumulation takes place with a direction opposite to that of the natural convection.

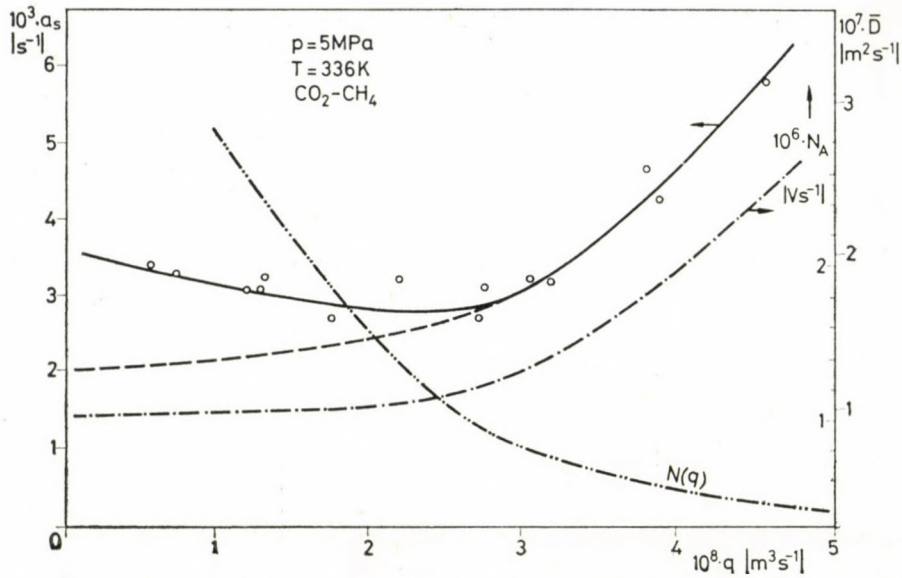

Fig. 3. Variaton of a_S (full line) and D (dash-and-dot line) as functions of volumetric flow rate of eluation in a CO_2—CH_4 system with 5 MPa pressure

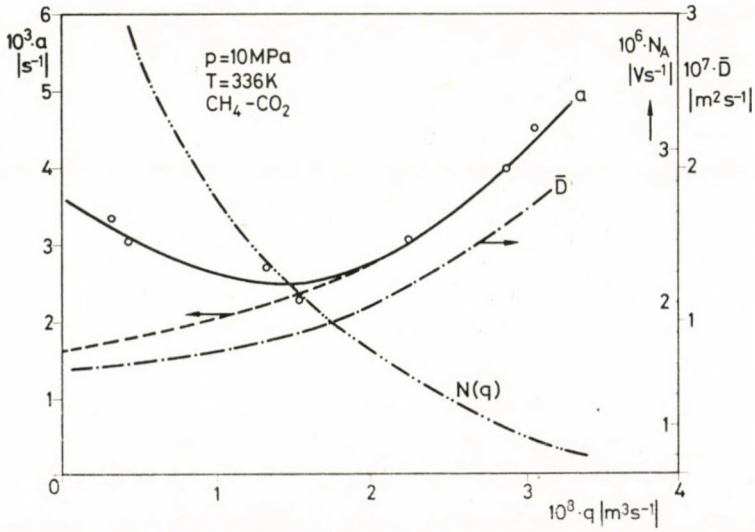

Fig. 4. Variation of a_S and D as functions of volumetric flow rate of eluation in a CO_2—CH_4 system with 10 MPa pressure

Since a gas stream rich in methane leaves now through the needle valve, the specific capacity of the valve increases due to a decrease in the viscosity of the mixture. That is why a further increase of q compensates for the effect of natural convection starting from the minimum of a_s and the change of a_s is in connection with the effect of the increase of D caused by the reduction of concentration ϱ_{AK} at the outlet end of the rock. This assumption is also justified by D_{AB} values determined by the closed-cell method.

If the effect of the artificial and natural convection is subtracted from the section before the minimum of a_s (this can be done with the help of the value N corresponding to $q = 0$), the corrected section of curve a_s increases monotonously without assuming a minimum. The corrected curve of a_s can be directly used to calculate the values of D. From the slopes of the tangents at the initial and end points of the measured curves in Figs. 5 and 6, the ratio ϱ_A/ϱ_{AO} belonging to a_s obtained from the measurement, can be determined. Consequently, the results gained by the gas eluation and the closed-cell methods, respectively, can be compared. On the other hand, certain values characterizing the concentration of CO_2 can be obtained for each D-value calculated

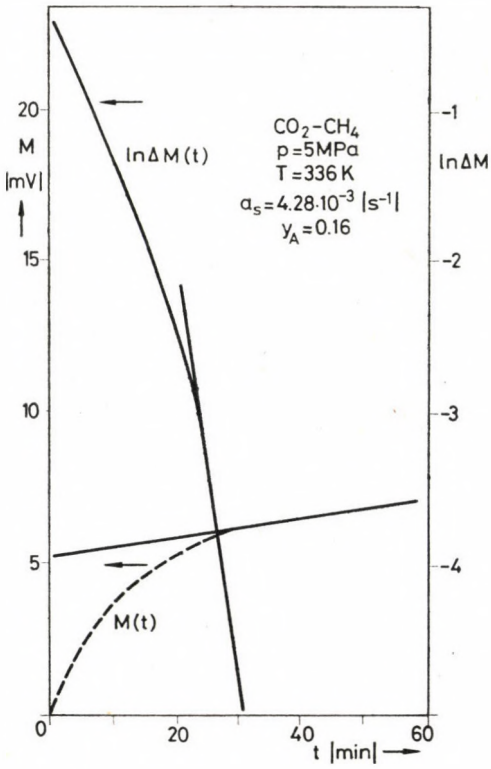

Fig. 5. Section C of the measured CO_2 recovery curve and logarithms of the values calculated by the asymptotic formula for a $CO_2 - CH^4$ mixture with 5 MPa pressure

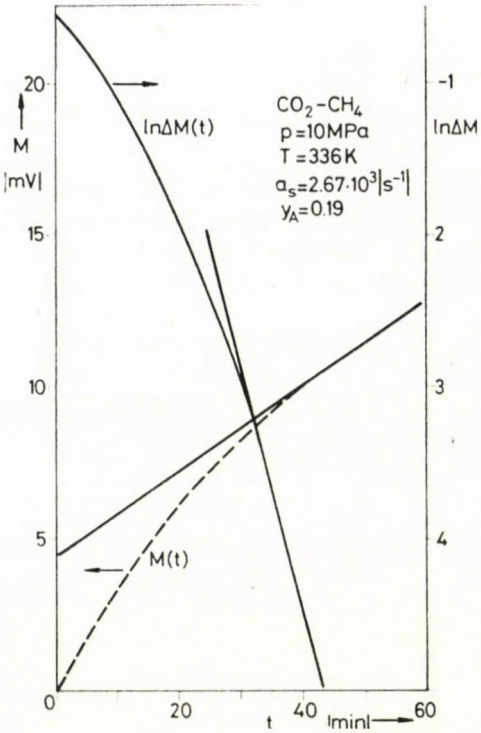

Fig. 6. Section C of the measured CO_2 recovery curve and logarithms of the values calculated by the asymptotic formula for a CO_2—CH_4 mixture with 10 MPa pressure

from a_s. Thus the variation of D can be calculated as a function of molar fraction y_A.

A full examination based on the eluation method can be divided into sections A, B and C as illustrated in Fig. 7.

In section A, the calibaration of a particular valve opening is carried out at closed valve 4 (Fig. 1) and the throughput capacity of the valve is determined. At the last section of A the dead space of the outlet part is determined by closing volumetric valve before needle valve 5.

Section B is the actual measurement section starting with opening valve 4 and volumetric valve before valve 5 and switching on compressor E. After stabilizing section B, valve 4 is closed and the compressor switched off.

Section C serves to check the measurement results in section B and the effect of the gas eluation. The area under the curve up to the stabilization of section C is proportional to the amount of CO_2 in the rock sample at the end of the measurement section.

At the end of section C the CO_2 content of the outlet dead space is determined again by closing the constant volume valve of valve 5. In this way the

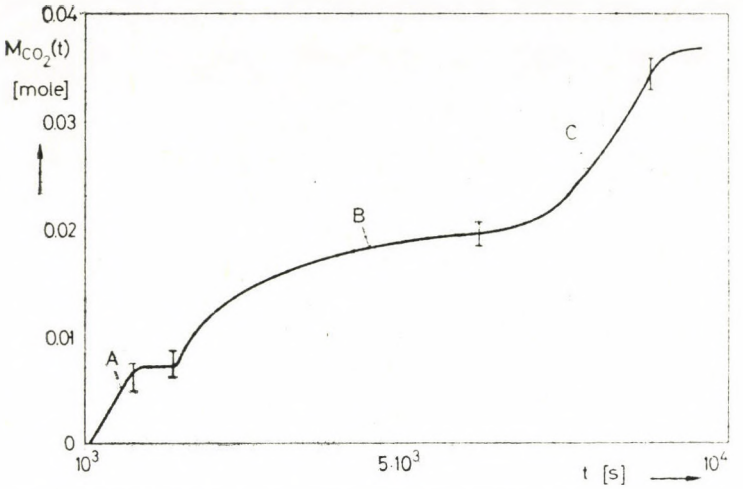

Fig. 7. Sections of the CO_2 recovery curve obtained by the gas eluation method. A — calibration section, B — measurement section, C — checking section

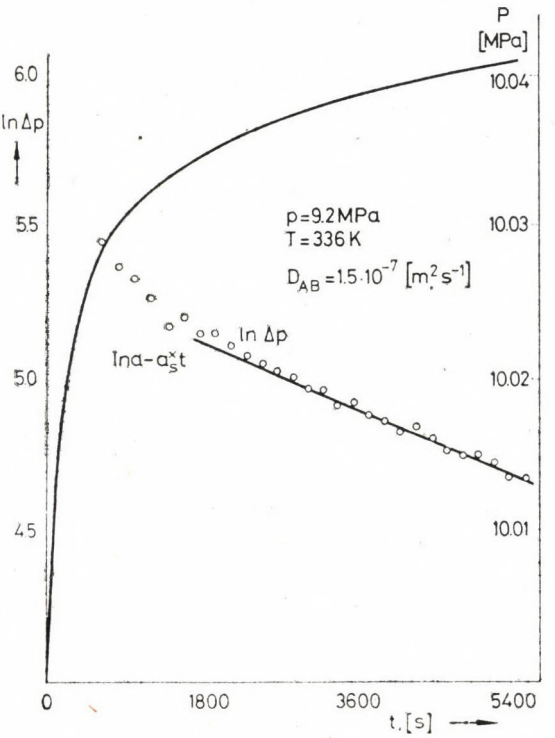

Fig. 8. Absolute pressure of the system and logarithms of the values calculated by the asymptotic formula as functions of time for closed-cell investigation

average concentration of CO_2 is obtained on the side of the rock towards vessel A at the end of section B.

The closed-cell investigation theoretically does not require additional measurements to determine coefficient D_{AB}. The concentration of CO_2 corresponding to coefficient D_{AB} calculated from the measurement, can be determined either from equations of state $\varrho_{AO}(p, T)$ and $\varrho_{BO}(p, T)$ using the volumes of vessel A, of CH_4 injected into vessel A and of CO_2 extracted parallelly from it, or from the analysis of an equilibrium gas sample taken from vessel A.

The closed-cell method is extremely sensitive to the accurate thermosting during measurement since pressure differential between vessels B and A containing gas with different molar densities in a space thermosted at temperature T can also be caused by a temperature differential between the vessels and by a temporary change of temperature of the system. The real function $p(t)$ can only be determined if the temperature correction curves $p(t)^x$ of vessels B and A are taken into account. Figure 8 illustrates the corrected function $p(t)$ and the curve fitted according to relationship (29) for a system with 10 MPa pressure. The values D_{AB} determined by the closed-cell method are illustrated in Fig. 4 beside the results of the eluation experiments. The data have been identified with the help of ratios ϱ_A/ϱ_{AO}. The results of the investigation can be regarded as real, taking into account the difference $\bar{D} - D_{AB}$.

Conclusions

a) Diffusion processes in a binary system of real gases can be described by versions of Fick's first and second laws valid for convective diffusion.

b) Our high-pressure gas eluation method stabilizes the effect of natural convection in the phase near the equilibrium of the eluation process. The effect of the natural convection has to be taken into account in calculating D from the measurement results. Therefore, additional measurements are needed to determine both D, and the concentration y_A corresponding to D.

c) If the measurement is carried out at constant valve opening at the outlet side, the resultant rate of the natural and artificial convections is zero in the section behind the minimum of curve $a_s(q)$ thus D can be directly determined from a_s.

d) Pressure $p(t)$ obtained by the measurements should be corrected by $p^x(t)$ characterizing the change of temperature because of the great temperature-sensitivity of the closed-cell method. Since the effect of natural convection can be neglected in the phase of the investigation near equilibrium, coefficient D_{AB} can be directly determined from the corrected curve $p(t)$. The concentration of the gas mixture corresponding to the diffusion coefficient can be calculated either from the compressed and extracted volumes of gas and the

equations of state of the pure components, or from the analysis of the gas samp
equations of state of the pure components, or from the analysis of the gas
sample taken from the cell after the mixing has taken place.

REFERENCE

1. STEFAN, A.: Sitzber. Akad. Wiss. Wien. 63. Abt. II. 1871.
2. STEFAN, A.: Sitzber. Akad. Wiss. Wien. 68, 1874.
3. LOSCHMIDT, J.: Sitzber. Akad. Wiss. Wien. 61, 1880.
4. ROBB, W. L.—DRICKAMER, H. G.: Diffusion in CO_2 up to 150 Atmospheres Pressure. *J. Chem. Phys.*, 19 (1951), 504.
5. TIMMERHAUS, K. D.—DRICKAMER, H. G.: *J. Chem. Phys.*, 19 (1951), 1242.
6. JEFFRIES, Q. R.—DRICKAMER, H. G.: Diffusion in the System CH_4—CH_3T to 300 atm. Pressure. *J. Chem. Phys.*, 21 (1953), 1358.
7. JEFFRIES, Q. R.—DRICKAMER, H. G.: Diffusion in CO_2—CH_4-Mixtures to 225 Atm. Pressure. *J. Chem. Phys.*, 22 (1954), 436.
8. O'HERN, H. A.—MARTIN, J. J.: Diffusion in Carbon Dioxide at Elevated Pressures. *Ind Eng. Chem.*, 47 (1955), 2081.
9. BERRY, V. J.—KOLLER, R. C.: *AICHE. J.*, 6 (1960), 274.
10. STEWART, W. E.—SUKEHIRO, G.—SØRENSEN, I. P.: Studies of the Loschmidt Diffusion Experiment II. *Ind. Eng. Chem. Fundam.*, 12 (1973), 119.
11. STEWART, E. W.: Studies of the Loschmidt Diffusion Experiment I. *Ind. Eng. Chem. Fundam.*, 12 (1973), 114.
12. REMICH, R. R.—GEANKOPLIS, G. J.: Binary Diffusion of Gases in Capillaries in the Transition Region between Knudsen and Molecular Diffusion. *Ind. Eng. Chem.*, 12 (1973), 214.
13. SIGMUND, P. M.: Prediction of Molecular Diffusion at Reservoir Conditions. *J. Can. Petr. Techn.*, 3—4 (1976), 48.
14. MING-WHE HSIEH—HUK Y. CHEH: Binary Diffusivities of Nitrogen-Methane and Nitrogen—Methyl Cloride Systems. *Ind. Eng. Chem. Fundam.*, 3 (1978), 210.
15. GAVALAS, G. R.—REAMER, H. H.—SAGE, B. H.: Diffusion Coefficients in Hydrocarbon Systems. *Ind. Eng. Chem. Fundam.*, 7 (1968), 306.
16. BENETT, Co. O.—MYERS, J. E.: Momentum, Heat and Mass Transfers. McGraw-Hill, New York, 1962.
17. STREETER, V. L.: Handbook of Fluid Dynamics. McGraw-Hill, New York, Chap. 6. 1961.
18. REID, R. C.—SHERWOOD, T. K.: The Properties of Gases and Liquids. McGraw-Hill, New York, 1966.

Acta Geodaet., Geophys. et Montanist. Acad. Sci. Hung. Vol. 17 (3—4), pp. 345—362 (1982)

STABILITY OF POLYACRYLAMIDE SOLUTIONS IN PRESENCE OF CARBON DIOXIDE

I. LAKATOS—Mrs. LAKATOS, J. SZABÓ

PETROLEUM ENGINEERING RESEARCH LABORATORY OF THE HUNGARIAN ACADEMY OF SCIENCES

The paper deals with the compatibility of systems containing polymers and carbon dioxide. The effect of the polymer type (degree of hydrolysis), the pressure of the carbon dioxide, the salinity of the aqueous phase, the presence of oil, rock and temperature on polymer degradation is discussed. Laboratory investigations have proved that the stability of polymer solutions greatly decreases with increasing degree of hydrolysis. Within the degradation process the authors distinguish on the one hand chemical degradations dependent and independent of the foreign electrolytes and on the other hand the so-called salt degradation caused by the dissolution of rock components (calcium, magnesium) due to carbon dioxide. According to experimental results, unhydrolyzed or slightly ($<10\%$) hydrolized polyacrylamides of great relative molecular mass must be applied for profile equalization and mobility control if carbon dioxide injection is used for enhanced oil recovery.

Symbols

c	concentration, g dm^{-3}, mg dm^{-3}, mole dm^{-3}
k_w	permeability, μm^2
k_{rw}	relative permeability, $\frac{k_{w\,\text{degraded}}}{k_{w\,\text{original}}}$, —
p	pressure, bar
t	time, hour
Hydr.	hydrolysis, percentage
$\overline{M}_r$	relative average molecular mass, —
RF	resistance factor
RRF	residual resistance factor
SF	screen factor
SF_r	relative screen factor, $\frac{SF_{\text{degraded}}}{SF_{\text{original}}}$, —
T	temperature, °C
α	expansion factor, —
μ	viscosity, mPas
μ_r	relative viscosity, $\frac{\mu_{\text{degraded}}}{\mu_{\text{original}}}$, —
$\Delta\mu$	salt sensitivity, mPas
$[\mu]$	intrinsic viscosity, cm^3 g^{-1}

Introduction

It is a general observation that if heterogeneous multi-layer reservoirs are flooded by carbon dioxide, the areal and vertical sweep efficiencies of flooding are rather small because of the great mobility of the displacing phase. Thus the advantageous effect of the injected carbon dioxide improving displacement efficiency is limited to a small part of the layer containing hydrocarbon. This may be a possible reason for the excess oil falling short of the expected value in certain cases. This statement leads to the conclusion that a

joint application of the conventional carbon dioxide flooding and the profile equalization by polymers as well as the subsequent flooding may improve the volumetric sweep efficiency which can result in a considerable increase of the produced excess oil.

The polymer flooding, however, cannot be effective in the presence of carbon dioxide unless there is no doubt about the stability of polymers under reservoir conditions (temperature, pressure, connate water, rock etc.). Publications investigating the stability problems of polymers, *viz.* Knight (1973), Chauveteau and Kohler (1974), Hill et al. (1974), Maerker (1974, 1976), Tinker and Bowman (1974), Bilhartz and Charlson (1975), Sparlin (1975), Vela et al. (1976), Morris and Jackson (1978), Castor and Edwards (1979), Szabó (1979) and Lakatos et al. (1980) do not or hardly deal with the compatibility of polymers against carbon dioxide. Since carbon dioxide injection can be expected to play an important role in this country, degradation phenomena in a carbon dioxide — polyacrylamide system have been thoroughly investigated. The study deals with the effect of the type of polymer (degree of hydrolysis), the pressure of the carbon dioxide, the salinity of the aqueous phase, the presence of oil, rock and temperature on the polymer degradation. Some data are presented for the influence of the degradation on the flow properties in the porous medium.

Experimental conditions

Laboratory investigations have been carried out with polymers having various average molecular mass and degree of hydrolysis (Table I). Polymer solutions with given composition were prepared at 40—50 °C under slow stirring. In some cases, in order to reduce biological and oxidative degradation, the solutions contained 0.2 g dm^{-3} formaldehyde.

The stability tests were carried out in ion-free (distilled) water, sodium chloride solution and natural brine. Thermal treatment of fluid samples was

Table I

Denomination and characteristic data of the polymers investigated

Denomination	Degree of hydrolysis %	$\overline{M}_r$ 10^6
A	0	0.7
B	5—7	1.0
C	30	2.2
D	40	3.5
E	40	9.5

performed in a high-pressure cell kept in an air thermostat. The fluid phase was saturated with gas and the cell pressure maintained by a blow case. A 99.98 per cent by volume purity gas was used for the measurements under carbon dioxide atmosphere. Mixing of the cell content during thermal treatment was carried out by periodical gas circulation. Sampling was made according to the rate of the degradation process, generally at 0—0.5—1.0—1.5—2.5—5.0—7.5—10—20—40 hours. To distinguish the effects of the oil and rock, the samples have been kept at a certain temperature in the presence of formation oil and natural clay-containing carbonaceous reservoir rock and marbel, respectively.

Degradation of polymer solutions has been characterized by measuring the change of dynamic viscosity and screen factor at 24 °C. After thermal treatment, the flow parameters of the original and degraded polymer solutions *viz.* resistant factor, residual resistant factor, apparent permeability etc. were determined. A natural sandstone model with the following parameters was used:

Diameter	30 mm
Length	30 mm
Porosity	0.21—0.23
Permeability	0.180—0.270 μm^2

Flow properties were determined with a standard device at an average reservoir flow rate of 0.5 m/day and 90 °C.

Results and discussion

Many authors have reported earlier in connection with the stability of polyacrylamide solutions that besides mechanical and biological degradation, oxidative effects and the presence of oxygen cause the most serious problems. This is the reason for adding oxygen scavangers *viz.* sodium-hydrogen-sulfite, formaldehyde etc. and preparing solutions in an inert (nitrogen) atmosphere in industrial use of water-soluble polymers. Therefore, our compatibility investigations were focussed first on the rate of degradation in presence of carbon dioxide compared with the values measured under inert and oxidative circumstances. Figure 1 illustrates the variation of viscosity of the partially hydrolized polyacrylamide solution C with a 30-percent degree of hydrolysis and 1 g dm^{-3} concentration, as a function of time. The thermal treatment was carried out at 90 °C temperature and 1 MPa cell-pressure.

From Fig. 1 the conclusion can be drawn that hydrolized polyacrylamides suffer in the presence of carbon-dioxide a significant viscosity degradation excessing the value measured in an oxidative atmosphere. The rate of

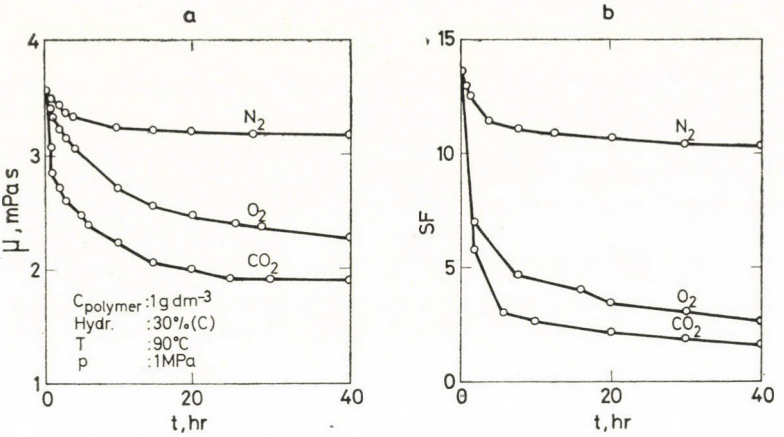

Fig. 1. Viscosity degradation (a) and screen factor (b) of a partially hydrolized polyacrylamide in various gas atmospheres

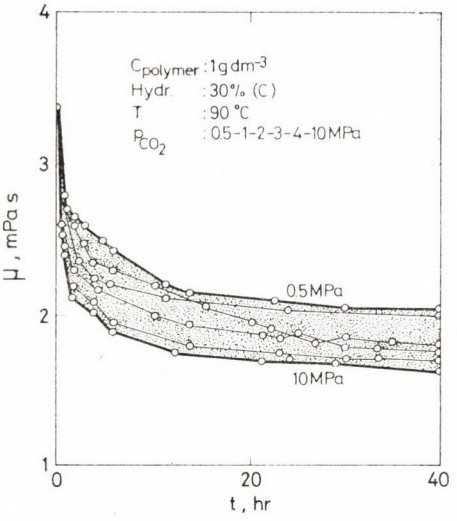

Fig. 2. Viscosity degradation of a partially hydrolized polyacrylamide at various carbon dioxide pressures

degradation is maximum in the early stage of thermal treatment, practically within 1—5 hours. Later the change remains small. Similarly to other degradation phenomena the worsening of flow parameters e.g. screen factor is greater here, too, than that expected according to the decrease of viscosity.

To determine the effect of the pressure and carbon dioxide saturation a 1 g dm^{-3} concentration solution of polymer C with a 30-percent degree of hydrolysis was used. The results of thermal treatments at 0.5—1—2—3—4—10 MPa pressures and 90 °C temperature are illustrated in Fig. 2. Though the

points scatter to some extent within the envelopes characteristic for 0.5 and 10 MPa pressures, degradation, however, shows a general tendency of slight increase with increasing pressure and saturation (dissolved) concentration. The viscosity degradation vs. pressure relationships for chemical degradation in the presence of oxygen and carbon dioxide show similarities. Therefore it can be assumed that carbon dioxide plays the role of the free radical forming agent in the chain reaction leading to degradation.

In our further investigations the effect of the polymer structure was analyzed. Figure 3 shows the variation of viscosity and screen factor as functions of time for aqueous solutions of 5 various polyacrylamides (Table I) with the same concentration after a thermal treatment at 90 °C temperature and 5 MPa carbon dioxide pressure. Screen factor SF_r is given in percents of the original value.

The curves prove that degradation drastically increases with increasing degree of hydrolysis. It seems that the degree of hydrolysis of the polymer beyond 30 percent is not likely to reduce the polymer stability any longer. This, however, has no practical importance since 70—80 percent of the viscosity-increasing effect of a polymer hydrolized to 30 percent is lost while the decrease of the screen factor is even greater. The average molecular mass of the polymer has an essentially less effect on stability than the degree of hydrolysis. Viscosity changes of polymers C and D after a 40-hour thermal treatment show a difference hardly amounting to 10 percent and the difference of screen factors is around 5 percent despite the great difference in the molec-

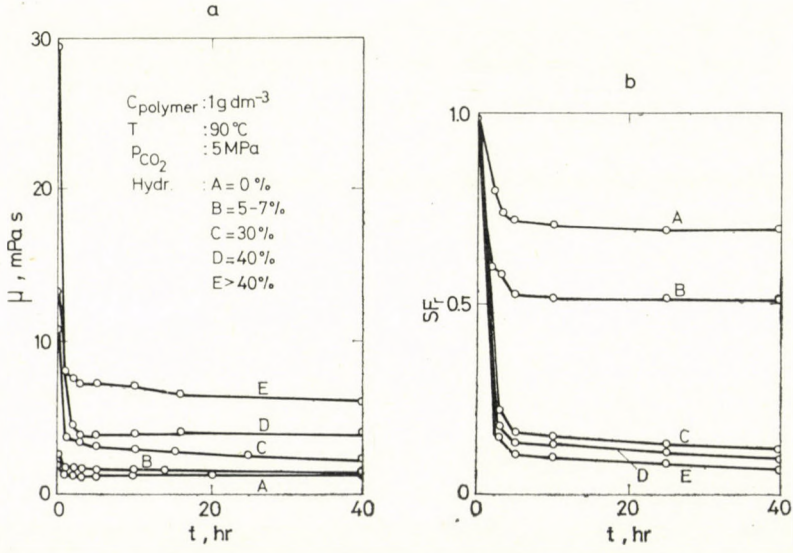

Fig. 3. Viscosity degradation (a) and screen factor (b) of polymers with various degrees of hydrolysis in carbon dioxide pressure of 5 MPa

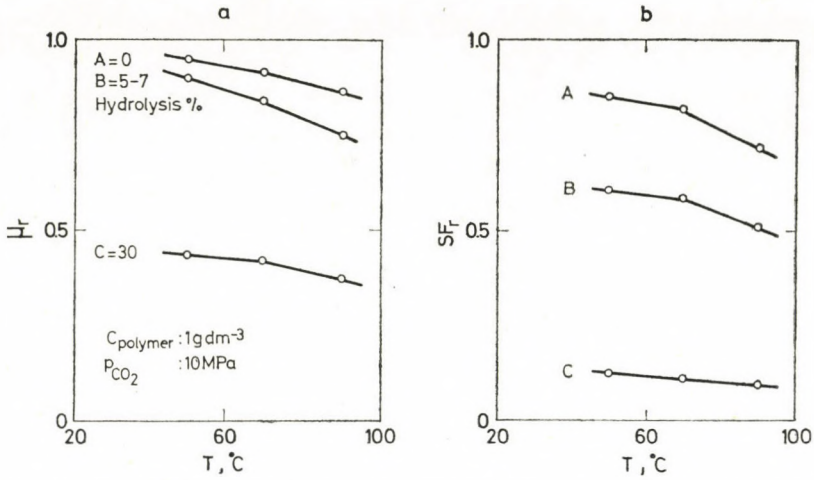

Fig. 4. Viscosity degradation (a) and screen factor (b) of polymers with various degrees of hydrolysis as a function of temperature

ular masses of these polymers. Consequently, we come to the conclusion that the compatibility of a system containing polyacrylamide and carbon dioxide is basically determined by the ionization state of the polymer and in an ion-free solution by the degree of hydrolysis.

If we assume that the degradation of polyacrylamides in presence of carbon dioxides is a consequence of a chemical reaction, then the analysis of the effect of temperature on the process cannot be neglected either. Thorough investigations have only been extended on polymers A and C, bearing in mind that only non- or slightly hydrolized polymers can be considered for industrial use. Polymer solutions free of inorganic electrolytes were thermal-treated at 10 MPa pressure and 50—70—90 °C temperatures. The results of 40-hour thermal treatments are illustrated as functions of temperature in Fig. 4.

From Fig. 4 the conclusion can be drawn that according to expectations the stability of polymers in presence of carbon dioxide deteriorates with increasing temperature. It should be added, however, that there is no significant difference in this tendency between the various polymers or the effect of temperature in the range between 50 and 90 °C.

In oil-field application of polymers the injected water and the brine contain more or less inorganic ions. It is a well-known experience that through the so-called salt effect these electrolytes significantly influence the structure of polymer solutions and their properties shown in porous systems. It seemed, therefore, of basic importance to carry out stability tests where various amounts of inorganic salt, in our case sodium-chloride, were added to the solution besides polymers, in order to model ion strength. Dynamic and relative viscosity data are illustrated in Fig. 5 for 0 degree of hydrolysis and in Fig. 6 for 30 per-

cent where polymer solutions containing sodium-nitrate conclusion can be made on the actual reduction of the average molecular mass of the polymer.

Figures 5 and 6 prove that the stability of polymers and polymer solutions improves with increasing salinity. Stability increase of hydrolyzed polyacrylamide is, of course, more significant than that of non-hydrolyzed polymers. Besides changing stability a salinity increase reduces the absolute value of the solution viscosity in the well-known manner. Thus, though stability significantly improves, solution viscosity greatly decreases because of salt

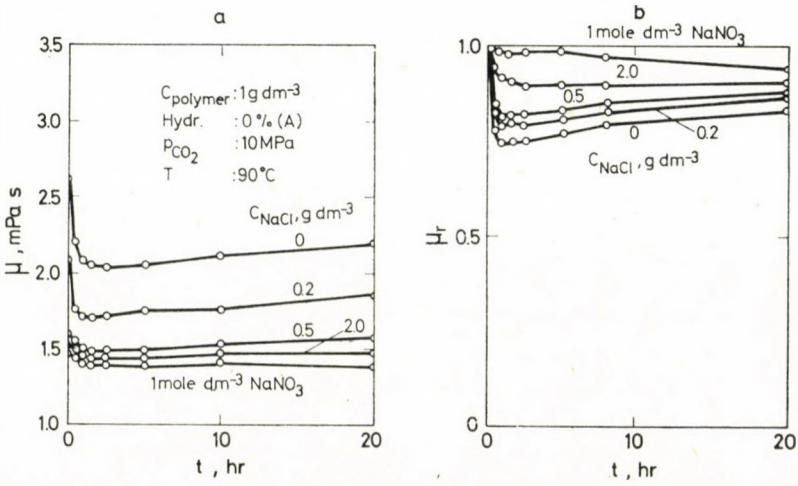

Fig. 5. Absolute (a) and relative (b) viscosity degradation of a non-hydrolized polyacrylamide at various salt concentrations

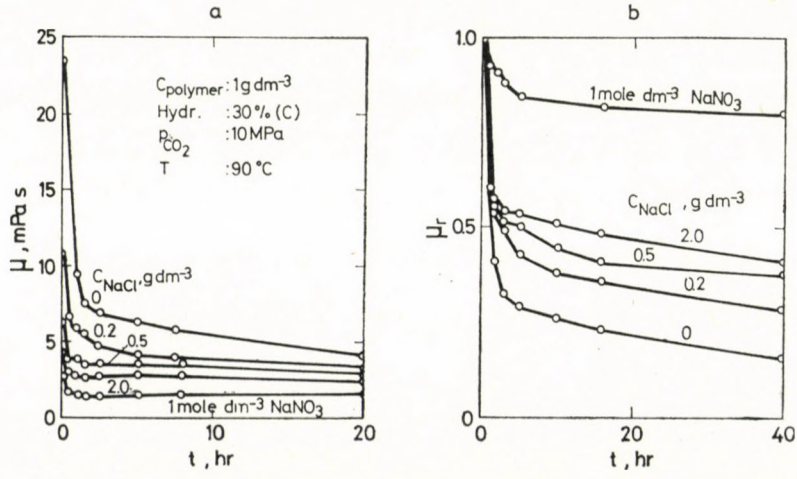

Fig. 6. Absolute (a) and relative (b) viscosity degradation of a partially hydrolized polyacrylamide at various salt concentrations

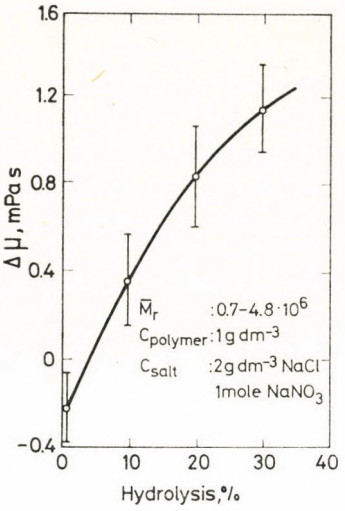

Fig. 7. Salt sensitivity of polyacrylamides as a function of hydrolysis degree

sensitivity. It is also obvious from the curve in Fig. 7 that the viscosity-reduction effect of salinity and the stability improvement due to salinity increase with the degree of hydrolysis.

The effect of the hydrolysis and salinity on polymer stability can be brought into connection with the structure and structural change of the random molecular coil. With increasing degree of hydrolysis the density of the random molecular coil decreases while its dimension increases. At low salinity or in an ion-free solution the polymer chain of ionic polyacrylamides can take an expanded or rigid state. With increasing amount of foreign electrolytes this shape has the tendency to change towards a spherical or hypsoid configuration. Meanwhile the degree of overlapping and the density of the random molecular coil also increase. This kind of structural change of the buoyant random molecular coil can be followed through the variation of the expansion factor, which is defined here according to Flory (1971) but in a basically different way as

$$\alpha = \sqrt[3]{\frac{[\mu]_{\text{solution}}}{[\mu]_{1\,\text{M}\,\text{NaNO}_3}}}\,.$$

If viscosity degradation of polymers A—E is plotted against expansion factor calculated as shown, Fig. 8 reflecting the combined effect of the degree of hydrolysis and salinity is obtained. The curves illustrated prove that besides the detrimental character of the structure the degradation of all polymers increase with increasing expansion factor. It can be, therefore, assumed that the spherical shape, similarly to mechanical degradation, encourages the in-

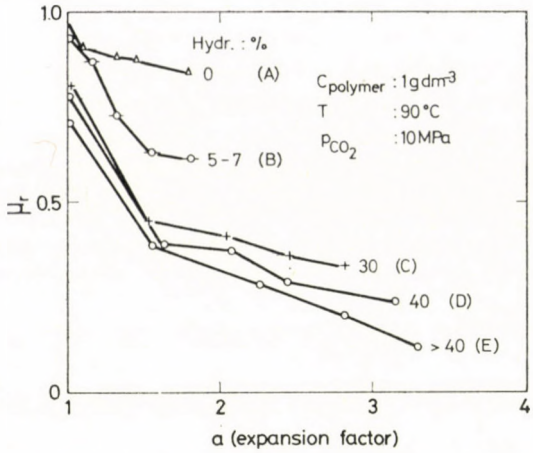

Fig. 8. Viscosity degradation of polymers with various degrees of hydrolysis as a function of expansion factor

crease of chemical stability due to the reduction of accessability of free radicals to the chain material.

Stability test in 1 mole dm^{-3} sodium-nitrate solutions provided valuable informations in two respects. Since the shape of the random molecular coil at this great ion strength approaches the spherical one and it practically does not change with further increase of salinity, on one hand degradation measured under such conditions can be considered as a minimum value which is observed in the presence of carbon dioxide in any case and on the other hand the reduction of the average molecular mass can be calculated from the viscosity decrease. Data characterizing degradation of five polymer types are summarized in Table II. It can be seen from the data that the minimum viscosity degradation of non-hydrolized polyacrylamides is only about 5 percent while that of greatly hydrolized polymers with great molecular mass exceeds even 30 percent. More unfavourable is the decrease of screen factor varying

Table II

Percentage of degradation of polymers A—C in a 1 mole dm^{-3} $NaNO_3$ solution without rock (Minimum chemical degradation)

Polymer	μ_r	SF_r	$\overline{M_r}$, %
A	4.7	9.8	12
B	6.8	17.4	20
C	19.5	55.0	62
D	30.1	64.4	76
E	35.5	71.1	78

between at least 10—60 percent. The surprisingly great change of the average molecular mass is in full accordance with that. The different extents of viscosity and molecular mass reduction are only apparently in contradiction because the viscosity of polymer solutions is less sensitive to changes of the molecular mass than e.g. screen factor or other flow properties.

If polyacrylamides are applied in the presence of carbon dioxide, the salinity of brine or thermal or surface water etc. used for preparation of solutions has two rather important effects which have to be taken into account.

a) Dynamic viscosity of the polymer solution greatly decreases with increasing salinity having unfavourable influence on flow properties.

b) With increasing salinity the random molecular coil gradually takes on a spherical or pseudo-spherical chape because of the reduction of dissociation. Spherical shape, however, increases stability of the molecule against chemical effects. In this sense, inorganic electrolytes play the role of stabilizer.

In the laboratory investigations the effects of oil and rock were also thoroughly analyzed. As for the presence of oil, it can be definitely pointed out that it does not exert significant effect on polymer stability. Investigations carried out in the presence of rock samples proved, however, that degradation is greater than that measured without rock material. Figure 9 illustrates this phenomenon by means of degradation curves of polymers A—C with and without rock samples. Further, it should be noted that it is a general tendency that the greater the molecular mass the more unfavourable the effect of rock on stability.

First we tried to explain the effect of rock by taking into account the adsorption of certain amount of polymer on the rock surface and concentra-

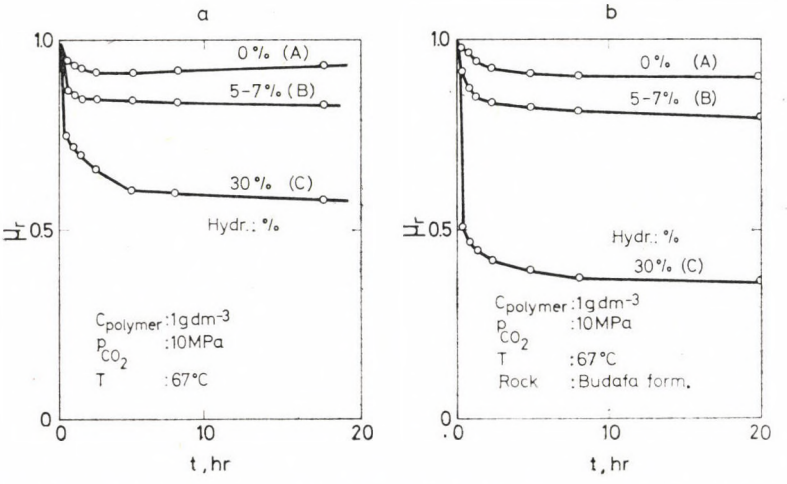

Fig. 9. Viscosity degradation of polymers with various degrees of hydrolysis without (a) and with rock (b)

tion reduction caused by it which appears as a virtual degradation. The rock sample placed into the cell adsorbs, however, only as much polymer as 0.01—0.001 g i.e. only 0.1—1.0 percent of the polymer mass in solution. Thus the hypothesis that the adsorption loss plays an important role in the degradation had to be rejected. Eventually it turned out that the decisive effect has to be

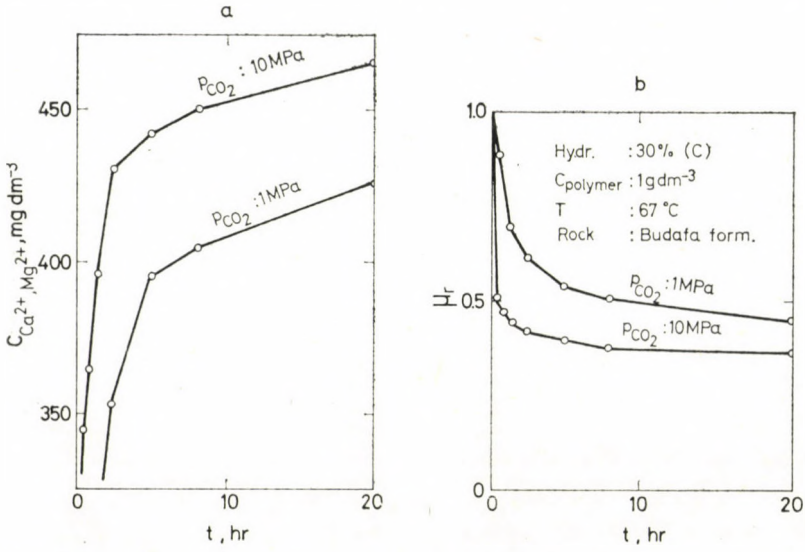

Fig. 10. Viscosity degradation of polymer C (b) and variation of calcium and magnesium content of solution (a) at 1 and 10 MPa pressures

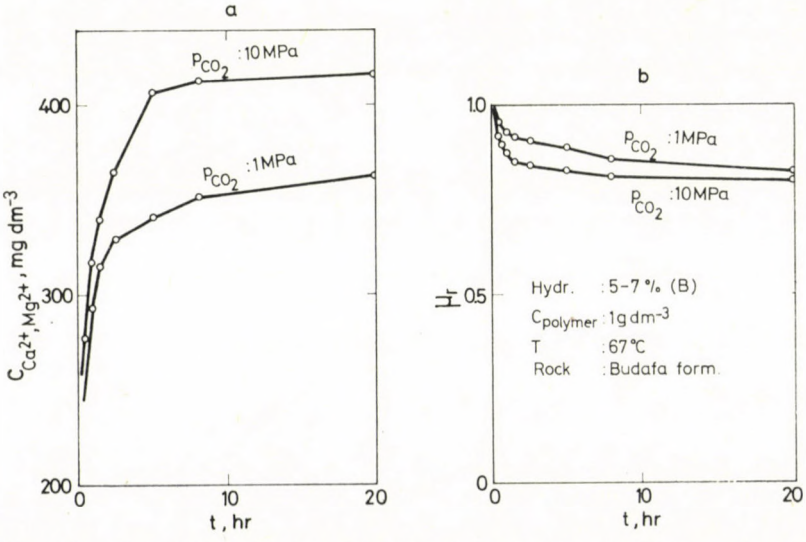

Fig. 11. Viscosity degradation of polymer B (b) and variation of calcium and magnesium content of solution (a) at 1 and 10 MPa pressures

looked for in the dissolution of calcium and magnesium ions of the rock according to the equilibrium concentration of carbon dioxide. These ions reduce the viscosity of the solution and deteriorate flow properties by their salt effect and forming cross-linkage.

The effect of the dissolution of rock components is illustrated in Figs 10—12 showing viscosity reduction and the variation of calcium and magnesium concentration as functions of time for polymers C—A at pressures 1 and 10 MPa. Figure 13 summarizes the curves of polymers A—C obtained at 10 MPa pressure in order to provide a good comparison.

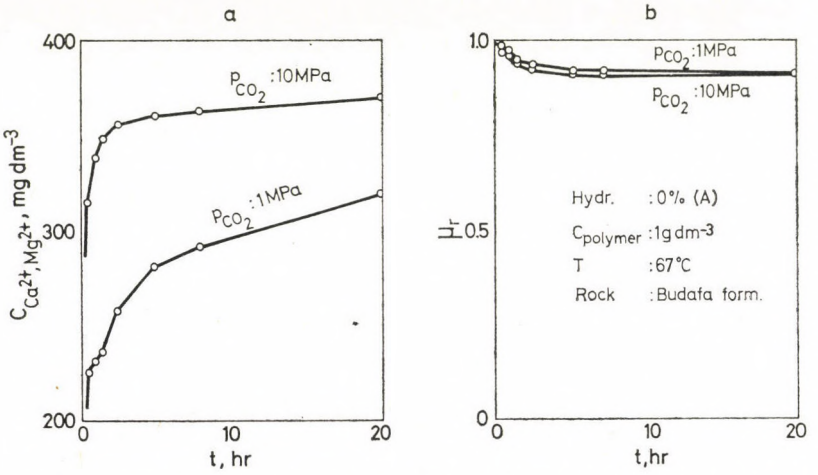

Fig. 12. Viscosity degradation of polymer A (b) and the variation of the calcium and magnesium content of the solution (a) at 1 and 10 MPa pressures

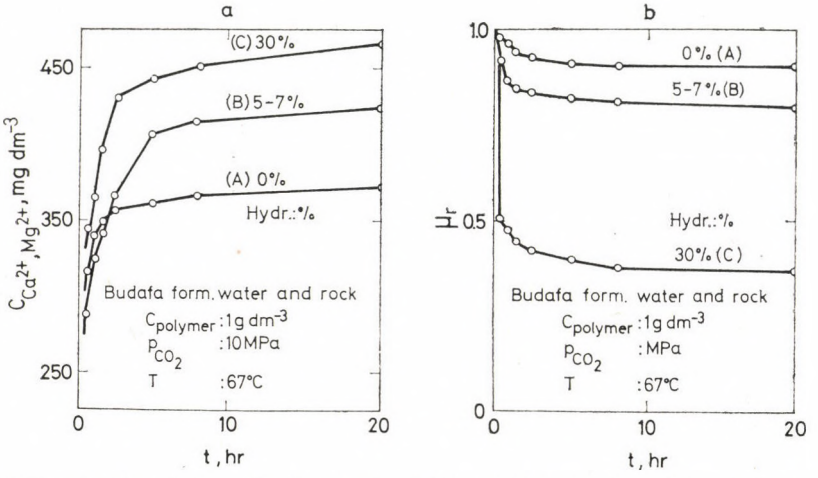

Fig. 13. Viscosity degradation of polymers A—C (b) and the variation of the calcium and magnesium content of the solution (a) at 10 MPa pressure

As shown in Fig. 10 the original calcium and magnesium content of the aqueous solution i.e. 30 mg dm^{-3} increases even above 400 mg dm^{-3} during a period of keeping it at high temperature. According to the equilibrium pressure and temperature of carbon dioxide the amount of inorganic ions is greater at 10 MPa pressure than at 1 MPa. The degradation of the polymer solution is in agreement with the change of the amount of bivalent cations i.e. at higher pressure and, correspondingly, at greater calcium and magnesium concentration the reduction of viscosity is also greater. Comparing Figs 10—12 the conclusion can be drawn that with decreasing degree of hydrolysis the effect of pressure and bivalent cations reduces. On the other hand the stability of polymers follows the same order in the presence of rocks that has been determined from experiments without rock. Finally, attention should be payed to the left-hand side of Fig. 13 because — according to the curves — the equilibrium salt concentration depends on the type of polymer in the solution, first of all on the degree of hydrolysis.

Compatibility investigations in the presence of rock have proved that besides actual degradation the change of the composition of the aqueous phase in carbon dioxide atmosphere disadvantageously influences the macroscopic properties of the polymer solution. Salt effect reduces the dissociation of the ionic groups of the polymer chain which, in turn, results in a viscosity reduction of the solution and in an unfavourable change of flow properties. From the salt sensitivity of polymers, especially from the effect of bivalent calcium and magnesium ions illustrated in Fig. 14 follows that the greater the ionization degree of the polymer the greater the salt effect which is superponed on

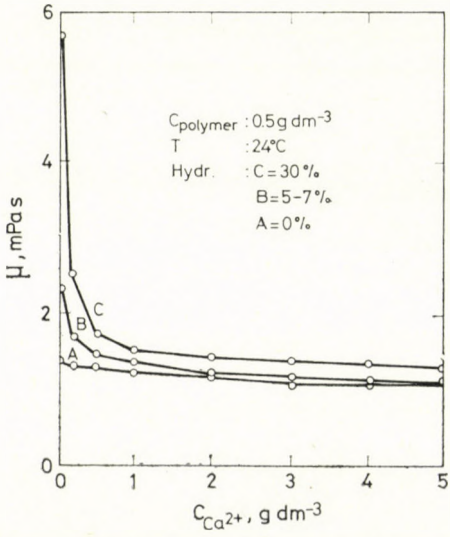

Fig. 14. Effect of the calcium content of the solution on the dynamic viscosity of the aqueous solutions of polymers A—C

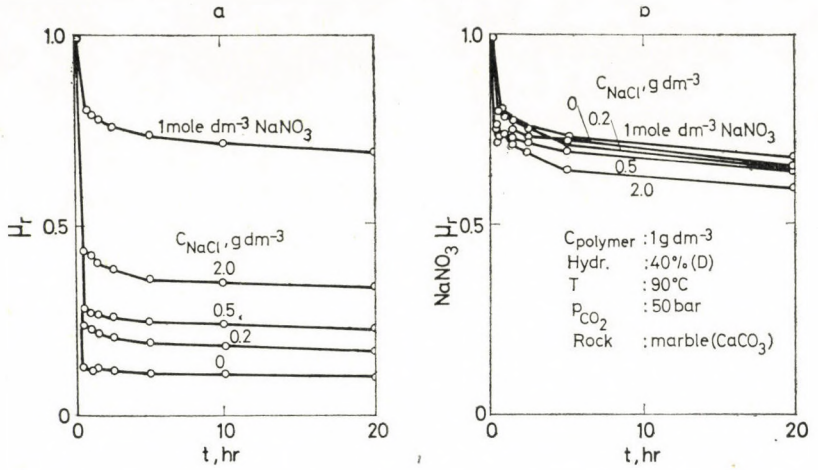

Fig. 15. Effect of salinity on the total viscosity degradation (a) and minimum viscosity degradation (b) of polymer D in the presence of rock

the chemical degradation determined by the polymer and the original brine salinity. The fact that the equilibrium calcium and magnesium concentration depends on the type of polymer can be interpreted by assuming that the value obtained for non-hydrolized polymer approximately corresponds to the equilibrium value in the solution while the excess observed for other polymers is equal to the amount of ions bound to the polymer.

Degradation in the presence of rock can be divided into the following components:

1. chemical degradation consisting of

a) minimum chemical degradation taking place in any case regardless of salinity and

b) salinity—bound chemical degradation which gradually increases with decreasing salinity of the solution starting from a minimum value;

2. salt effect which influences the properties of the solution due to the increase of solution salinity and salt sensitivity of the solution.

In order to determine and separate the effect of the parameters, a series of experiments have been performed with the strongly hydrolized polymer D. Thermal treatment in these experiments was made on solutions of various salinities in the presence of marble. After determining viscosity reduction μ_r in the usual way, as much sodium nitrate was added to the sample to be investigated as to adjust the ion strength to 1 mole. (Possible dilution is taken into account by means of correction.) Viscosity reduction ${}_{NaNO_3}\mu_r$ obtained in this way can be used to determine the percentage caused by salt effect and chemical degradation within the so-called total degradation. The experimental data are summarized in Fig. 15. The diagrams show that the smaller the orig-

inal salinity of the polymer solution the greater the viscosity reduction caused by salt effect. On the other hand, it is rather surprising that the chemical degradation amounts to the same percentage, viz. 35—40 percent, regardless of salinity. Since degradation data obtained for various salinities hardly differ from that measured in a 1 mole dm^{-3} sodium nitrate solution, the statement can be added to our previous ones that the degradation observed in the presence of rock and carbon dioxide can only be regarded as the so-called minimum chemical degradation which is independent of the electrolyte concentration and caused by the salt effect of the dissolution of inorganic ions from the rock.

Based on the laboratory experiments at various salinities and in the presence of rock, the practical conclusion can be made that the stability of polymer solutions in the presence of carbon dioxide is greatly influenced by the salinity of brine and the chemical composition of the rock. The relationships show that the degradation of partially hydrolized polymer solutions is possibly far less in the presence of rocks with low calcium and magnesium content and at low carbon dioxide saturation (equilibrium pressure and concentration) than in the case of reservoir material rich in limestone and dolomite and at high carbon dioxide saturation.

The phenomena discussed here have to be taken into account when analyzing the question of additives improving the compatibility of systems containing polymers and carbon dioxide. In this respect formaldehyde, potassium hydrogensulfite and sodium hydroxide have been investigated as stabilizers. Special attention has been payed to the absorption of carbon dioxide in the form of chemical compounds and to the use of sodium hydroxide as the only chemical with practical importance in this respect. It has been proved that other inorganic salts, mainly alkaline hydroxides used besides formaldehyde improve stability only to such an extent that could be ensured by adding other inorganic salts e.g. NaCl alone because of the unlimited carbon dioxide supply. Since the increase of ion strength in the polymer solution makes sense only until the equilibrium solution structure (approximately the spherical random molecular coil) is formed and this is usually ensured by the salinity of natural brines, addition of other stability increasing additives, besides formaldehyde, is unnecessary. Water and alkaline spacers between flooding slugs for fixing the residual carbon dioxide or purging the brine with great calcium and magnesium content cannot be excluded in certain cases, their application, however, should be decided by special analyses.

The analysis of the applicability of polymers in systems containing carbon dioxide is completed by fluid mechanical investigations. Resistance factor RF, residual resistance factor RRF and apparent permeability reduction are considered as fluid mechanical parameters. These parameters have been determined for an arbitrarily chosen natural brine — oil — rock system of the Budafa

Table III

Fluid mechanical parameters of polymers A—C in porous media
$k_w = 0.18-0.27\ \mu m^2$

	A		B		C	
	original	degraded	original	degraded	original	degraded
Degree of hydrolysis, %	0		5—7		30	
RF, —	2.2	1.8	7.4	3.9	17.0	8.0
RRF, —	1.7	1.5	3.2	1.8	8.2	3.5
Apparent permeability-reduction, %	41.6	33.3	69.0	44.5	87.7	71.5

Table IV

Fluid mechanical parameters of polymers A—B in porous media
$k_w = 0.025-0.050\ \mu m^2$

	A		B	
	original	degraded	original	degraded
Degree of hydrolysis, %	0		5—7	
RF, —	19.7	7.7	12.8	7.1
RRF, —	7.5	6.5	6.5	5.9
Apparent permeability-reduction, %	88.0	83.8	85.3	84.0

field (Hungary) using 1 g dm^{-3} concentration original and degraded polymer solutions. The investigation was extended only to polymers A—C while porous sandstones with medium (0.18—0.27 μm^2) and very low (0.025—0.040 μm^2) permeability were used as models. However, the models with very low permeability were not flooded by polymer C because of fear of strong plugging effect. Experimental data are summarized in Tables III and IV.

The results compiled in the tables suggest the following fluid mechanical properties.

a) An effective mobility control caused by polymer flooding in medium or great permeability rocks can only be expected by highly hydrolized polyacrylamides. Unfortunately these polymers are unstable in the presence of carbon dioxide. However, non- or slightly hydrolized polymers that are stable under such conditions do not cause effective mobility control if used in conventional concentrations. These polymers can exert a practically valuable effect if their concentration is increased up to 1.5—2.0 g dm^{-3} or their average relative molecular mass above $10 \cdot 10^6$.

b) In low permeability rocks in which polymer C hydrolized to 30 percent was not injected because of the plugging effect, non- or slightly hydrolized polymers A and B produce a sufficient mobility control. Since their stability is also adequate, their use may be suggested for flooding formations with

permeability less than 0.10 μm^2 without any hazard even in the presence of carbon dioxide.

Finally, our knowledge about degradation phenomena of polymers and their aqueous solutions in the presence of carbon dioxide, brine and rock can be summarized so that despite the unfavourable picture regarding hydrolized polymers, non- or slightly ($<10\%$) hydrolized polyacrylamides meet the severe requirements for their stability. The effective mobility control and profile equalization in the presence of carbon dioxide demand, however, that polymers with average molecular masses greater than normal, suitably exceeding $10 \cdot 10^6$ should be used for this purpose. Chemical experts and research workers must bear in mind that the demands of oil industry for this type of polyacrylamides should be properly reflected in the varieties of polymers offered by chemical industry.

Summary

Laboratory compatibility investigations of systems containing polymers and carbon dioxide have provided the following conclusions.

1. Degradation of polyacrylamides in the presence of carbon dioxide is greater than that measured under oxidative conditions.

2. The stability of polyacrylamides and their solutions depends to a great extent on the degree of hydrolysis and is independent of the average relative molecular mass. It holds even in the presence of carbon dioxide that the greater the hydrolysis degree of the polymer the greater the degradation.

3. In an aqueous solution, without rocks, degradation only negligibly depends on the pressure (saturation) of the carbon dioxide. It can be assumed that similarly to red-ox processes, carbon dioxide plays the role of a free radical forming agent in chemical degradation.

4. With increasing temperature the stability of polymer solutions also reduces in the presence of carbon dioxide but to a less extent than expected.

5. Salts in aqueous solutions improve the stability of polymer solutions. With increasing salt concentration the degradation decreases and approaches a limit. This limit can be regarded as a degradation minimum ensuing in the presence of carbon dioxide independently of the composition of the aqueous phase.

6. The stability of non-hydrolized polyacrylamides is independent of salt content. The stabilizing effect of the salt content also increases with increasing degree of hydrolysis in case of partially hydrolized polyacrylamides.

7. Oil content does not influence the stability of polymers in the presence of carbon dioxide.

8. Hydrolized polymer solutions show stronger degradation in the presence of rocks than without it. The apparently less stability is caused by the salt effect of calcium and magnesium ions of rock dissolved under the effect of carbon dioxide.

9. The presence of rock practically does not effect the degradation of non-hydrolized polyacrylamides. For partially hydrolized polymers, the greater the degree of hydrolysis the greater the effect of the rock.

10. Because of a partial dissolution of rock components the viscosity-reduction and deterioration of flow properties of polymer solutions depends on the pressure (saturation) of carbon dioxide.

11. Chemical degradation is the same while salt effect due to dissolution of calcium and magnesium varies within the degradation measured in solutions with various salt content in the presence of rock.

12. Because of the unlimited supply on carbon dioxide no significant improvement can be expected from the use of inhibitors e.g. alkaline hydroxides preventing the effect of carbon dioxide.

13. It is advantageous for the application of polymers in the presence of carbon dioxide if the aqueous solution contains as much and such inorganic electrolytes that ensure the equi-

librium solution structure i.e. the spherical or pseudospherical random molecular coil configuration.

Based on our investigations the final conclusion can be drawn that non-hydrolized polyacrylamides with average molecular masses greater than usual depending on reservoir permeability, are suitable for profile equalization and mobility control combined with carbon dioxide injection.

REFERENCES

BILHARTZ, H. L.—CHARLSON, G. S. 1975: Field polymer stability studies. SPE preprint 5551

CASTOR, T. P.—EDWARDS, J. 1979: Degradation of mobility control agents under mechanical, electrochemical, thermal and biological stress. 3th Int. Conf. on Surface and Colloid Sci., Stockholm

CHAUVETEAU, G.—KOHLER, N. 1974: Polymer flooding: the essential elements for laboratory evaluation. SPE preprint 4745

FLORY, P. J. 1971: Principles of Polymer Chemistry. Cornell University Press, Ithaca

HILL, H. J.—BREW, J. R.—CLARIDGE, E. L.—HITE, J. R.—POPE G. A. 1974: The behavior of polymers in porous media. SPE preprint 4748

KNIGHT, B. L. 1973: Reservoir stability of polymer solution. *J. Pet. Techn.*, 618.

LAKATOS, I.—LAKATOSNÉ-SZABÓ J.—KISSNÉ-GÁSPÁR M. 1980: Stability of polyacrylamide solutions under laboratory and field conditions. *Kőolaj és Földgáz*, 113, 166—172 (In Hungarian)

MAERKER, J. M. 1974: Shear degradation of polyacrylamide solutions. SPE preprint 5101

MAERKER, J. M. 1976: Mechanical degradation of polyacrylamide solutions in unconsolidated porous media. *Soc. Petr. Eng. J.*, 172—174.

MORRIS, C. W.—JACKSON, K. M. 1978: Mechanical degradation of polyacrylamide solutions in porous media. SPE preprint 7064

SPARLIN, D. 1975: An evaluation of polyacrylamides for reducing water production. SPE preprint 5610

SZABÓ. M. T. 1979: An evaluation of water-soluble polymers for secondary oil recovery. Part 2., *J. Pet. Techn.*, 561—570.

TINKER, G. E.—BOWMAN, R. W. 1974: Determination of in-situ mobility and wellbore impairment from polymer injectivity data. SPE preprint 4744

VELA, S.—PEACEMAN, D. W.—SANDVIK, E. J. 1976: Evaluation of polymer flooding in a layered reservoir with crossflow, retention and degradation. *Soc. Pet. Eng. J.*, 82—96.

Acta Geodaet., Geophys. et Montanist. Acad. Sci. Hung. Vol. 17 (3—4), pp. 363—381 (1982)

A COMPARATIVE LABORATORY STUDY OF WELL-TREATMENT TECHNIQUES BASED ON *IN SITU* CROSS-LINKING AND POLYMERIZATION

I. LAKATOS—MRS. LAKATOS, J. SZABÓ—MRS. KISS, M. GÁSPÁR

PETROLEUM ENGINEERING RESEARCH LABORATORY OF THE HUNGARIAN ACADEMY OF SCIENCES

The study deals with techniques based on *in situ* setting including cross-linking of polymers with multivalent cations and polymerization of monomer solutions. For the purpose of the investigation various types of polyacrylamides were used as polymers and acrylamide and N,N-methylene-bis-acrylamide as monomer. The permeability-reduction effect of the gel was determined on a linear non-consolidated porous system, and the effect on the water-oil ratio on a radial sandstone core. A comparative analysis of the methods proved that the upper limit of thermal stability of gels cross-linked by multivalent cations does not exceed 80—100 °C. The method can be greatly intensified by adding aliphatic alcohols or applying a polymer-silicate system. The method based on *in situ* polymerization is more advantageous in many respects than the first-mentioned placement technique. However, since it is more expensive, the cost factor should be taken into account when making a decision about its application.

Symbols

c	concentration, g dm^{-3}, mg dm^{-3}, mole dm^{-3}
k_w	permeability, μm^2
k_{rw}	relative permeability
t	time, min
$\overline{M}_r$	relative average molecular mass, —
T	temperature, °C
V	volume, cm^3
V_p	pore volume, cm^3
μ	viscosity, mPas
Subscripts, abbreviations	
AA	acrylamide
IPA	iso-propyl alcohol
PAA	polyacrylamide

Introduction

Various polymer well-treatment techniques have been developed to improve the water/oil ratio in producing wells, among others by Sandiford and Graham (1972), White et al. (1971—73), Sparlin (1976), Koch and McLaughlin (1970), Goddard et al. (1973, 1975), Sloat (1975), McLaughlin et al. (1975), Ford and Kelldorf (1976) and Knapp and Welbourn (1978). These procedures can be divided into three groups: simple polymer solution placement techniques, those using linear polymers gelled by cations, and methods based on *in situ* polymerization and partial cross-linking of monomer solutions. All well-treatment techniques have been thoroughly investigated in the Petroleum

Engineering Research Laboratory of the Hungarian Academy of Sciences in the last years. The motivation for this study was the understanding that the profile equalization of producing and injection wells has to be put into practice in the near future. Laboratory analyses of the simple polymer solution well-treatment techniques were completed in 1978 [Lakatos, 1978]. Regarding the fact that the effectiveness of this type of techniques is inferior to those of the other two, in the present study only the comparative laboratory investigation of polymer well-treatment techniques using *in situ* cross-linking and polymerization will be dealt with.

Experimental

Polyacrylamides of Hungarian and foreign made of average molecular masses of $1—10 \cdot 10^6$ and 10—30% degree of hydrolysis were used in the laboratory investigations. Acrylamide and N,N-methylene-bis-acrylamide were used as monomers to investigate the methods based on *in situ* polymerization. Gelling the polymer solution and catalyzing the polymerization were carried out by chemicals of analytical purity (potassium-aluminium-sulfate, aluminium-chloride, aluminium-citrate, ammonium-peroxi-disulfate). For the intensification of the processes and as chain-carrier, alcohols of analytical purity (iso-propyl alcohol, tert-butyl alcohol, glycerine) were used while the available sodium silicate to produce polymer-silicate gel was of technical quality. To model the ion strength of brines, sodium chloride was added to the aqueous polymer solutions.

The permeability-reduction effect of gels was investigated on a linear non-consolidated sand-model. The parameters of this model were:

diameter	30 mm
length	300 mm
porosity (broken)	0.38—0.44
permeability	0.76—0.88 μm^2

The model was made of silica sand of 100—200 μm grain size with a silicium dioxide content of over 99%.

For modelling the water/oil ratio as a function of time and the placement technique in general, a radial model made of consolidated natural sandstone was used with the following parameters:

diameter	80—100 mm
length	120—140 mm
porosity (broken)	0.19—0.23
permeability	0.200—0.400 μm^2

The outlet point (perforation) of the fluid in the radial model was a 2 mm dia hole at 1/3 of the length of the core. The base and top of the cylinder were impermeable thus fluids could only enter the porous model through the curved surface of the cylinder. The saturation was water-oil-water type, saturation conditions were adjusted with Alg-2 crude.

The laboratory investigations were usually carried out at 80 °C. The pressure in the cores ensured that no gaseous phase could develop. The flow rate of the fluids corresponded to the average flow rate in the reservoir (~30 cm/d). The velocity in the radial model through the curved surface was 7—19 cm/d while at the perforation point it attained ~3500 cm/d.

Results and discussion

1. *Study of polymer gels cross-linked by cations*

Cations in the aqueous solution contract the partially hydrolized polyacrylamides depending on the valency, or cross-link them through poorly dissociating salt production. In case of multivalent cations the degree of cross-linking can be partial or total depending on the concentration. Thus, if cross-linking takes place in a porous medium, the result can be a plugging effect which provides a long-lasting resistance against fluids flowing in the medium.

Methods for treating producing wells are known in the literature and they have a wide range of practical applications. Since various types of polymers (biopolymers, acrylamide derivatives) are used, and the circumstances of application also vary, several methods have been developed. The most frequently used method is based on subsequent injection into the layer of the aqueous solutions of the adequate linear polymer and then the inorganic compound used for cross-linking. This may be carried out in several cycles. Cross-linking is performed mostly by metal salt of Cr^{6+} or Mn^{7+} reduced in the reservoir by means of alkali (sodium) sulfates, hydrogen sulfide or natural gas containing hydrogen sulfide. The reducing medium is not absolutely necessary for cross-linking, in its absence however lower valency cations, e.g. Cr^{3+} or Al^{3+} of the metal should be applied.

Our investigations were concerned with the forming of polyacrylamide gels cross-linked by aluminium ions. Since this polymer is gelled quickly and the injection of polymer solutions gelled on the surface is subject to technical problems, only the placement technique based on *in situ* gelling has been investigated. The effect of gels in reducing water-permeability was determined on non-consolidated sand-models of high permeability followed by representative investigations on radial models made of natural sandstone. All laboratory measurements were carried out at 80 °C.

As the first step of the experimental program it has been studied to what extent the permeability-reduction in a non-consolidated linear porous model is affected by the type of the polymer. Figure 1 shows the results obtained by gelling polymers of approximately the same degree of hydrolysis but of significantly different average molecular mass. The figure demonstrates that with increasing average molecular mass a more massive gel is formed in the porous medium, i.e. permeability decreases to a greater extent. Though the resistance of the model starts to increase as soon as the polymer solution is injected and continues to do so as long as non-cross-linked polymers are still present, it can be stated that gel remains in the porous system for a long period.

Figure 2 summarizes the results of the *in situ* gelling of polymers with approximately the same relative molecular mass but hydrolized to 0—10—20—30%. The only difference from the previous experiments that the treatment was carried out in two cycles and the concentration of the potassium aluminium sulfate was lower.

By comparing the permeability-reduction effects of the gels obtained by cross-linking polymers with various degrees of hydrolysis it should be clear that only the strongly ionized polymer with 30% degree of hydrolysis can furnish practically useful results. The actual value of the permeability-reduction effect obviously depends on the experimental conditions. However, it can be stated that in general the greater the degree of hydrolysis of the polymer, the stronger the gelling and, consequently, the greater the decrease of water permeability.

This relationship between the permeability-reduction effect and degree of hydrolysis can be theoretically interpreted in terms of the ionic bond between the carboxyl groups and the multivalent cations. From the point of view of the structure and stability of the cross-linkage, the role of the factors determining the properties of the freely floating random molecular coil cannot be neglected. Among these parameters the effect of the cross-linking ion, the foreign electrolytes and the temperature deserve special attention. It does not require much explanation that the increase in the polymer concentration encourages gelling towards total plugging. The quality and quantity of the inorganic ions influence the properties of the gels through the dissociation equilibrium of the polyelectrolyte and, in consequence, through the configuration of the polymer molecule. At low electrolyte concentration the chain-like molecule of the ionic polymers assumes an expanded shape because of the total dissociation of the carboxyl groups. This encourages cross-linking and the lose coils form a gel of high viscosity at a low polymer concentration and small degree of cross-linking also.

The gelling of the polymer is clearly also determined by the amount of the cross-linking ion. Gelling a 1 gdm^{-3} concentration solution of polymer hydrolized to 30% was tried by using potassium aluminium sulfate in three

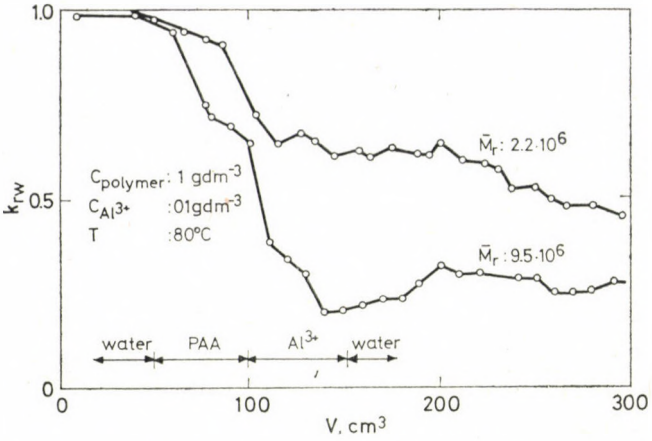

Fig. 1. Effect of molecular mass of polymers on permeability-reduction of porous systems

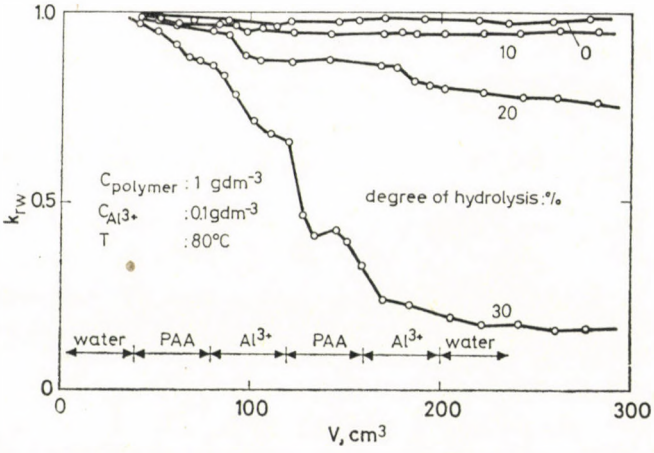

Fig. 2. Effect of hydrolysis of polymer on permeability-reduction of porous systems

different concentrations. The permeability results obtained from the experiments were rather surprising (the data are expressed as percentages of the original value):

$c_{Al^{3+}}$, gdm^{-3}	k_{rw}
1	0.43
0.25	0.28
0.1	0.15

The phenomenon presumably has a molecular explanation. On the one hand, at 0.1 gdm^{-3} concentration aluminium ions are present in an excessive amount from a molecular respect compared with the monomer concentration (segment concentration) of the acrylic acid which corresponds to 0.3 gdm^{-3}. Further, it has to be taken into consideration that potassium ions in a molecular concentration identical to that of the aluminium ions are brought into the solution. The salt effect, important in itself, brings about the contraction of the polymer molecule. This change of size can reach as much as 100 nm at a given concentration. Therefore it is reasonable that the gel cross-linked at a smaller potassium concentration would have a higher viscosity; consequently, the permeability-reduction effect would also be greater. Unfortunately, the salinity of brines is in general greater than 0.5 gdm^{-3}, thus the effect of the equivalent cation dissolved with the cross-linking ion is not apparent in practice.

The gelling, and especially its rate, are also influenced by the dissociation equilibrium of the cross-linking compound. From this point of view the gelling effect of the aluminium compounds containing various anions was investigated. Following the injection of the polymer, aluminium chloride, aluminium citrate and potassium aluminium sulfate solutions of equal aluminium content were injected into the porous medium. Ignoring normal standard deviation, the results obtained do not differ from each other and no trend could have been established. From this observation it can be concluded that the gelling is essentially independent of the quality of the anion, providing that a fully dissociating inorganic compound is used for cross-linking in aqueous solution. Thus it is logical that poorly dissociating compounds, especially organic metal complexes, have to be selected for the cross-linking on the basis of controlling the ion production.

From the ionic character of the bond between the aluminium and the carboxyl group of the polymer it follows that the stability of the cross-linkage and thus that of the gel depends a great extent on temperature. With increasing temperature the equilibrium state of the gel moves towards dissociation, i.e. gel breaking. This can be unambiguously proved; see Fig. 3 illustrating the permeability-reduction effect of systems gelled at various temperatures but otherwise under the same experimental conditions. In fact, Fig. 3 throws light on the greatest problem of gels cross linked by metal ions *viz.* they possess the required advantageous properties within only a limited temperature range of max. 80—100 °C. Smaller or greater differences in the stability of polymer gels cross-linked by different metal ions e.g. Fe^{3+}, Al^{3+}, Cr^{3+} or Ti^{3+} can exist, depending on the actual value of the degree of dissociation; their general property is, however, that they spontaneously disintegrate above 100 °C. It is fortunate if with the decrease of temperature the gel fully regains its previous structure. But this rarely occurs in practice because cross-linking can be re-

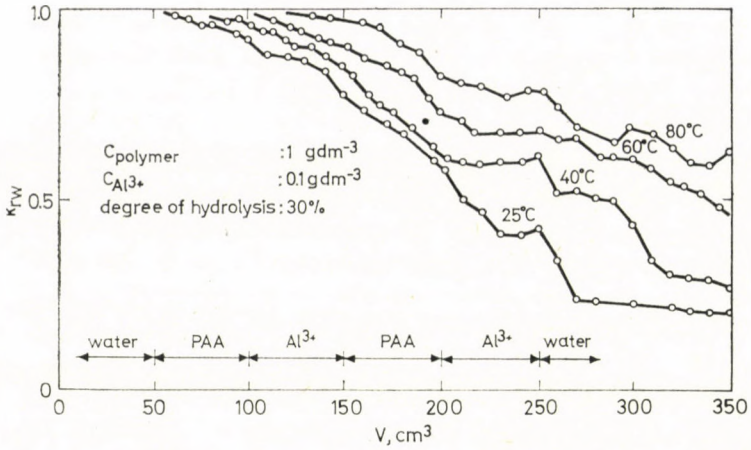

Fig. 3. Influence of temperature on permeability-reduction effect of gels cross-linked with aluminium ions

peated only with a considerable hysteresis and even so only partially, due to chemical degradation of the polymer at high temperature. While this phenomenon can be advantageous in certain operations e.g. fracturing, it is definitely disadvantageous in treating producing wells because the gel is mobilized and its effect gradually decreases and eventually disappears. Since the stability of polymer gels cross-linked by cations has been found to depend on temperature, it can be stated that the upper limit of application is 100 °C.

The necessary condition of the *in situ* cross-linking by cations is that the polymer solution and the solution containing the cross-linking material should be mixed in the porous system. Gelling is therefore influenced by all parameters that directly or indirectly relate to hydrodynamical dispersion. Experiments, e.g. Gall (1976) that tried to diminish the effect of dispersion by previous and partial cross-linking of the polymer solution can be rather considered as trials than solutions. Mixing in the porous medium is most easily influenced by the size of the slugs and the number of cycles. The results of treatments in one and in two cycles, respectively, are illustrated in Figs 1 and 2. Treatments in more cycles generally result in greater permeability-reduction effects implying that the increase in the number of cycles is only limited by considerations of cost. Our laboratory results, however, suggest that an increase in the number of cycles beyond 4—5 does not furnish any practical result.

The mixing of the injected solutions is greatly improved if the same amount of chemicals is introduced into the reservoir in a greater number of cycles but in slugs of smaller volume. Local circumstances may determine the minimum and maximum limits on the size of the slugs. In the linear high-permeability sand model experiments were carried out with polymer and alum

slugs. An estimated 15—20% increase in permeability-reduction can be achieved if the placement occurs in 5 cycles with slugs of 0.1 pore volume as instead of a single cycle and 0.5 pore volume slugs.

At identical slug size the dispersions of the two fluids are also influenced by mobility conditions. With increasing viscosity of the polymer solution the dispersion of the front reduces. At a viscosity ratio of 5 a piston-like sweeping takes place even in case of miscible fluids and, in consequence, gelling extends for only a rather narrow zone. An increase in viscosity, however, encourages dispersion of the two fluids at the back. Thus, using the cyclic injection technique, thin (front) and thick (back) gelled zones are formed in the porous system because of the symmetrical front profile of the polymer solution. However, programming the concentration or the viscosity of the polymer solution, cross-linked zones of approximately the same thickness can be produced in the reservoir.

In connection with these considerations the effect of repeated treatments was investigated. At the first treatment consisting of 10 cycles (Fig. 4) the size both of the polymer solution and of alum was 0.1 pore volume. The treatment was later repeated, using half amount of the chemicals. It can be seen that the second treatment, though it has a certain effect, does not cause as significant a permeability reduction as was caused by the first one. A repeated treatment, therefore, is only useful if the original improvement in the water/oil ratio or the reduction of water permeability diminishes because of the extraction of the polymer, or the opening of new in-flow directions. This phenomenon, however, could not be modelled by the linear porous system used in our experiments.

Besides studying the techniques described in the literature we have also

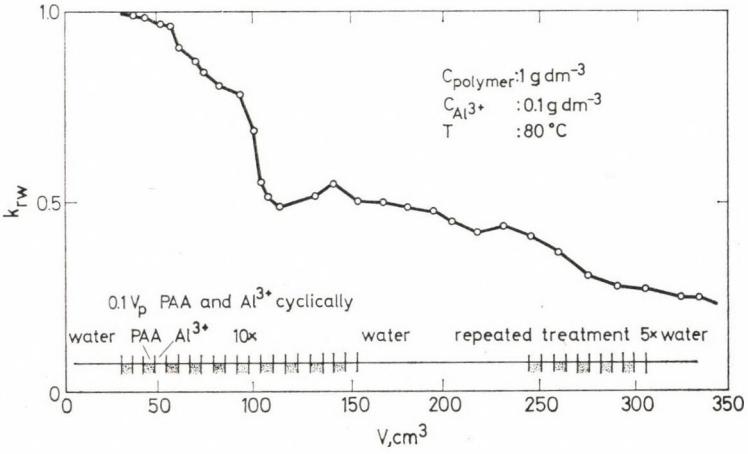

Fig. 4. Effect of repeated treatment on permeability of porous systems

succeeded in improving on the method. One task to be solved was the cross-linking of alcoholic polymer solution. The addition of alcohol or the application of water-alcohol mixtures can mainly be traced in patents: Tiner et al. (1975) and Ely et al. (1975) cross-link biopolymers and cellulose derivatives with aldehydes and titanium in mixtures with an alcohol content of less than 7%. Rhudy and Knight (1976) suggested in the case of the gelling of hydrolized polyacrylamides by chromium ion that the solid polymer be added to the water in an iso-propyl alcohol suspension. All three methods were designed to produce a fracture fluid and the application of alcohol is aimed at increasing the efficiency of the process, though the authors fail to give sufficient explanation as to what is the advantageous effect of the alcohol.

The structure, rheologic properties and flow characteristics in porous media of alcoholic polymer solutions have been investigated in our Laboratory in a detailed basic research. It has been found that aliphatic alcohols with 1—5 carbon atoms up to a concentration of 40—50% by vol. greatly increase the dynamic viscosity of polymer solutions. This viscosity value can be 5—10 times that of an aqueous polymer solution. The anomalous behaviour can be explained by the structure of the water/alcohol solution and the solvation of the polymer. Also, even without any theoretical reasons and explanations it can be expected that systems showing considerable viscosity-increase at the same polymer content, will also possess in the gelled state more favourable properties than those obtained by cross-linking pure aqueous solutions. To prove this hypothesis, solutions of polymers of 0—10—20—30% degree of hydrolysis and with varying alcohol content were gelled by potassium aluminium sulfate. These investigations have proved unambiguously that

i) with increasing alcohol content, up to about 40—50% by vol. the viscosity of the cross-linked gel increases using any kind of alcohol,

ii) the type of alcohol (the number of carbon atoms) influences the properties of the gel, the most favourable effect was found when using iso-propyl alcohol,

iii) with increasing temperature the favourable effect of the alcohol decreases but it can be positively observed at as high as 80—90 °C.

Figure 5 illustrates the results of two experiments carried out in the same system, with the same polymer at 80 °C. The difference between the two experiments is that in one of the cases the polymer solution injected into the model also contained 30% iso-propyl alcohol. The results clearly indicate that water permeability decreases more quickly and to a somewhat greater extent if the polymer solution to be gelled contains alcohol, than if it is a pure aqueous solution.

Gelled sodium silicates have been suggested for well-treatment and flooding first by Biles (1972) and Sarem (1974, 1975). The method has also been

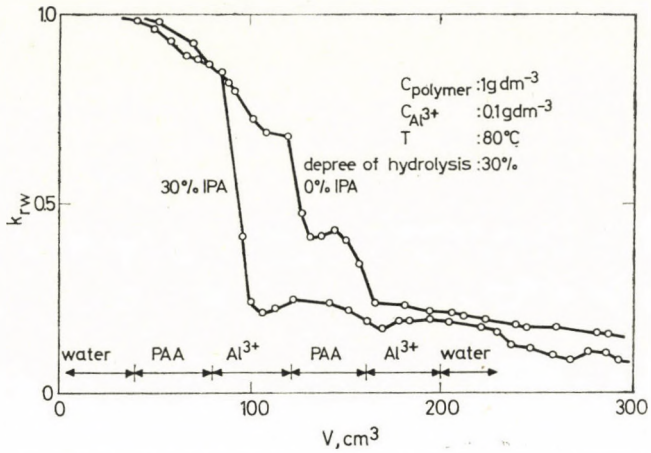

Fig. 5. Influence of alcohol on the permeability-reduction effect of polymer gels cross-linked with aluminium ions

investigated in our Laboratory [Heinemann et al., 1979]. These gels are known, apart from their effective permeability-reduction effect, mainly for their good thermal stability. The thermal stability of gels cross-linked by metal ions and the synergism of the polymer-silicate system suggested the development of a well-treatment technique based on the simultaneous gelling of combined polymers and silicates. The synergism of sodium silicate itself can be explained by solvational and associational interaction. The reason for the flexibility of the combined system of flooding and well-treatment is that gelling, and the type of gel, can be controlled within wide limits not only by the concentration but also through the polymer/silicate and Al^{3+}/Ca^{2+} ratios. By increasing the amount of the silicate and calcium for example, very massive plugs with good thermal stability can be produced.

Our flow experiments were carried out on linear models with solutions of 0.2—1.0 gdm^{-3} and 1—10% silicium dioxide content. Three different ways seemed to be available to gel these combined systems with the following results:

i) Gelling the polymer by multivalent ions, the space of cross-linkage formed by the polymer is filled by sodium silicate solution. The viscosity of the gel only slightly increases as compared with a polymer gel without silicate. (The free silicate can be spontaneously precipitated by bivalent cations in the reservoir, in this case the plugging effect naturally increases.)

ii) Gelling the sodium silicate by bivalent cations, the precipitated microcrystalline calcium silicates or silicate gels are stabilized by the polymer solution of high viscosity. The viscosity of the gel is significantly greater than that of pure silicate gels.

iii) The polymer and the sodium silicate are simultaneously cross-linked or gelled by bi- or multivalent cations. In this case an immobile phase is formed that creates a massive barrier and cannot make but extremely limited displacements.

According to our experiments on the linear model, gelled solutions containing only silicate (5% SiO_2) yield 40% permeability reduction. If the injected solution contains both polymer and silicate in the same concentration as in the previous experiment, and gelling is carried out by an Al^{3+}—Ca^{2+} system permeability is 65% less than the original value. These findings are believed to prove that the polymer-silicate system is suitable for profile equalization around producing wells or more precisely for correcting channel-forming and reducing water permeability.

The results of the laboratory investigations of *in situ* cross-linking by multivalent cations can be summarized by saying that the method is suitable for effectively changing the water/oil ratio. However, because of the factors determining the gelling of the polymer solution, many requirements have to be met. It is a disadvantageous feature that the conventional procedure can only be applied up to 90—100 °C due to the ionic character of the cross-linkage. The properties of the *in situ* formed gel are significantly improved by the presence of alcohol. The other way of intensification *viz.* applying a combined polymer-silicate system ensures a successful well-treatment even above a temperature of 100 °C in the formation.

2. *Study of methods based on in situ polymerization of monomer solutions*

In situ cross-linking by metal ions has two major disadvantages:

i) The bonds among the polymer chains are of ionic character and therefore the degree of gelling gradually decreases with increasing temperature because of the dependence of dissociation on temperature.

ii) The mixing of the polymer and the gelling material injected in separate slugs is greatly affected by the hydrodynamic dispersion in the reservoir.

The well-treatment technique developed by McLaughlin (1975) and Ford and Kelldorf (1976) based on *in situ* polymerization avoids just these disadvantages by injecting into the reservoir the monomer of a water-soluble polymer and the additives required for the polymerization. Depending on the type of the monomer it is possible to produce a blocking polymer solution of high viscosity but containing essentially a linear polymer or a partially cross-linked stable polymer gel in the reservoir. Both methods have the advantage that by using an appropriate monomer solution the viscosity of the injected fluid would hardly differ from that of water and polymerization only commences at formation temperature.

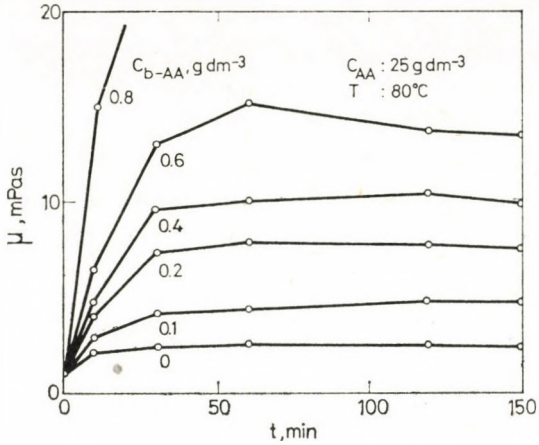

Fig. 6. Gelling of acrylamide — bis-acrylamide monomer solutions of various composition as function of time

The laboratory investigations were focussed on techniques based on *in situ* polymerization ensuring partial cross-linking. Because of economical and commercial considerations a system of acrylamide (AA) and N,N-methylene-bis-acrylamide (b-AA) was chosen. As the first step of our investigations, the mechanism and conditions of the polymerization of this pair of monomers were analyzed in detail.

The polymerization of acrylamides proceeds in form of free radical polymerization, correspondingly the aqueous monomer solution also contains free radical forming compound and chain-propagating additives. For sake of simplicity, only those results will be considered that were obtained at a constant concentration of the free radical forming compound (ammonium peroxi disulfate) and at varying type and concentration of alcohol used as chain-carrier. To model the ion strength of the brine, the solutions contained sodium chloride in a concentration of 2 g dm^{-3}. The amount of acrylamide was changed within the rang of 15—25 g dm^{-3} and that of bis-acrylamide within 0—3 g dm^{-3} to optimize the monomer composition. Figure 6 shows the results of one of the experiments carried out at 80 °C. The monomer solution contained 25 g dm^{-3} acrylamide and a varying concentration of bis-acrylamide in this experiment.

The results of the experiments to determine the monomer ratio can be summarized as follows:

i) The degree of cross-linkage increases with increasing amount of bis-acrylamide, and, as a consequence, the dynamic viscosity of the solution also steeply increases. It is further characteristic of the polymerization that the rate of gelling abruptly changes at a certain bis-acrylamide concentration.

The critical concentration of the gelling material and the monomer ratio are, for various acrylamide concentrations, as follows:

c_{AA}, g dm^{-3}	c_{b-AA}, g dm^{-3}	c_{AA}/c_{b-AA}
15	2.9—3.0	5
20	1.3—1.5	14
25	0.7—0.9	31

ii) At a constant bis-acrylamide concentration an increasing acrylamide content significantly increases the viscosity of the solution, or the greater the acrylamide concentration of the monomer solution, the smaller amount of bis-acrylamide is needed to effectively gel the system.

iii) Cross-linking at 80 °C takes about 50 minutes, the rate of the reaction depending on the monomer concentration. In dilute solutions the polymerization accelerates only after an induction period of 10—15 minutes, while in dense solutions the rate of polymerization is the highest just in this period.

To compare polymerization in systems with various monomer ratios, it was essential to determine the effect of temperature on the process. The investigation was performed on three solutions of various composition under dynamic conditions in a rheoviscosimeter. The curves of Fig. 7 were obtained by continuously increasing the temperature of the monomer solution at a shear rate of 656 s^{-1} up to 90 °C and by measuring the apparent viscosity of the solution after each 10 °C temperature increment.

It is a common feature of the three curves of Fig. 7 that, disregarding greater or smaller deviations, gelling sets in at temperature of 45—50 °C.

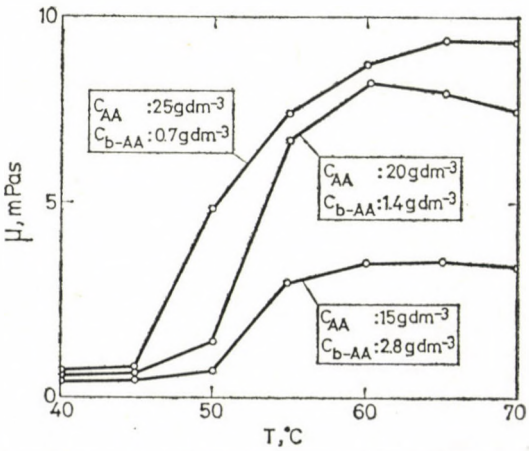

Fig. 7. Gelling of acrylamide — bis-acrylamide monomer solutions of various composition as function of temperature

This can be unambiguously explained by the fact that the formation of free radicals and the desintegration of ammonium peroxide sulfate takes place in the solution at this temperature. The figure also shows that polymerization and cross-linking is completed at 60—70 °C. Taking into account the heating rate of 0.5 °C min^{-1}, it is clear that the process takes 50—60 minutes in each cases.

It is of extraordinary importance for practice that monomer solutions of given composition are stable at a temperature not higher than 45 °C for a very long (practically unlimited) period and their viscosity does not reach even 1 mPas. The stability of gels above 60 °C, however, is very good and they resist mechanical degradation excellently, while the viscosity and mechanical degradation of gels cross-linked by cations above 60 °C depends on temperature to a much greater extent.

In the next stage of our investigations it has been studied to what extent the type and amount of alcohols used as chain-carrier influences gelling and the properties of the gel. Iso-propyl alcohol, tert-butyl alcohol and glycerine were used as models. As a characteristic example the effect of the iso-propyl alcohol is shown in Fig. 8 at two various monomer compositions. The experience about the effect of alcohols can be summarized as follows:

i) Regardless the monomer composition, alcohols generally exert an unfavourable effect on the gelling of the acrylamide—bis-acrylamide system and considerably break down the viscosity of the gel.

ii) Using iso-propyl alcohol the viscosity of the gel monotonously decreases with the concentration of the chain-carrier, while for tert-butyl alcohol a slight increase up to 2—8% by volume and then a decrease can be observed.

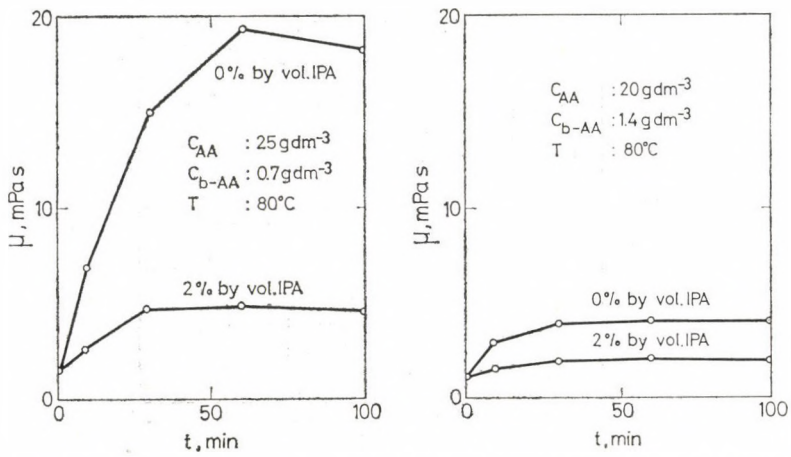

Fig. 8. Effect of iso-propyl alcohol on gelling of acrylamide — bis-acrylamide monomer solutions of various composition

The effect of the latter alcohol is, however, rather neutral than positive, as regards the extent of the change.

iii) The trivalent alcohol (glycerine) has the same effect as the iso-propyl alcohol and it reduces the viscosity of the gel very quickly (at 8% by volume to one third of the previous value).

Summarizing the results about the effect of alcohols it can be stated that their application is superfluous and even harmful because they do not encourage massive, viscouos cross-linked gels to develop.

For practical purposes *in situ* polymerized gels with various compositions can be chosen. Theoretically, there is nothing to prevent us to produce gels with approximately the same properties for small polymer concentration and high degree of cross-linkage or high polymer concentration and low degree of cross-linkage. Economical factors may determine a decision as to the application of a certain solution. It may be here taken into account that the present price of N,N-methylene-bis-acrylamide is 50—100% higher than that of the acrylamide. Regarding the fact, however, that it is beyond the scope of this paper to determine the optimum composition on this basis; the fluid mechanical experiments in porous media were carried out with the monomer solutions, the data and figures on which have already been considered. These compositions can, by no means, regarded as optimal, their only common feature is that they contain bis-acrylamide at the given acrylamide—concentration (15—20—25 g dm^{-3}) in the so-called critical quantity.

The permeability-reduction effect of the selected three acrylamide — bis-acrylamide systems was determined in a linear porous system. The permeability of the non-consolidated sand model used in the experiments was 0.85—0.95 μm^2. The conditions of investigation for the *in situ* cross-linking were slightly modified: the temperature of the model was increased gradually from 25 °C to 80 °C only after the injection of the monomer solution. Figure 9 shows the permeability-reduction effect of the three monomer solutions (in percentage of the original permeability) as a function of the injected fluid volume.

The permeability-reduction effect of the three various systems shown in the figure corresponds to the viscosity of gels and cross-linked polymers. The gel containing 15 g dm^{-3} acrylamide caused the lowest reduction not higher than 14%, while the system with 25 g dm^{-3} concentration decreased permeability below half of its original value. A common feature of the curve that the permeability starts to decrease at the beginning of heating the model. It is worth noting that even though permeability considerably varies after the rapid change during heating, the partial blocking effect prevails over a long period. This phenomenon is believed to be due to the rearrangement of the gel particles in the porous system.

The results of the procedure based on *in situ* polymerization can be compared with those of gelling with cations. The permeability-reduction effect

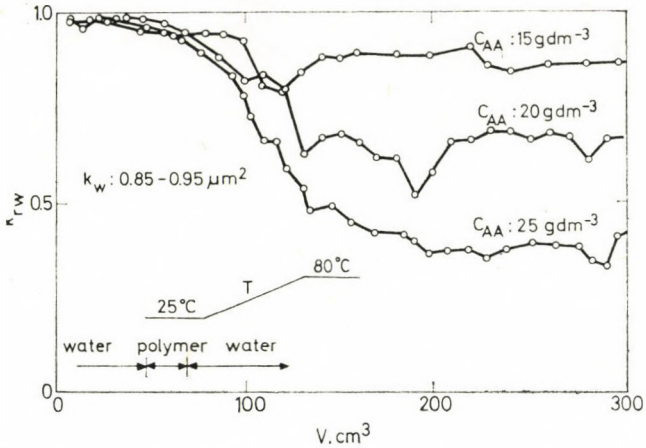

Fig. 9. Effect of acrylamide — bis-acrylamide monomer solutions of various composition on permeability of non-consolidated linear porous models as function of injected fluid volume

shown in Fig. 9 can be achieved also by gels cross-linked with alum. For example 25—40% permeability-reduction was obtained in one step with the polymer having medium molecular mass and a hydrolysis degree of 30%, as well as a placement fluid of 0.5 pore volume. On the other hand, a cyclic injection was needed to achieve the required permeability-reduction using *in situ* polymerization and 25 g dm^{-3} acrylamide concentration. The amount of monomer solution was, however, 0.2 pore volume and we tried to ensure a pseudo-mobility for the gel obtained from polymerization. Namely, in all three cases, an increase of the amount of bis-acrylamide by 0.1—0.2 g dm^{-3} would have resulted in a full plugging. This means that a very small change of the composition (i.e. of the ratio c_{AA}/c_{b-AA}) can yield extreme effect in the application of *in situ* polymerization.

The effectiveness of well-treatment techniques using monomer solutions was also investigated on radial models of natural consolidated rocks. A reliable comparison has, however, been greatly hindered by the lack of three natural models of the same structure. Eventually, core samples of the same size, with a porosity of 0.18—0.24 and permeability of 0.15—0.45 μm^2 were chosen for the experiments. Despite the differences between the rocks, saturation data shows a good agreement, within $\pm 4\%$. Figure 10 shows the effects of three gels with representative compositions. The treatment began in all of the cases at a WOR of 50 and using 30 cm^3 (approximately 0.2 pore volume) of monomer mixture. After injecting the fluid, the system was closed for 24 hours and kept at a temperature of 80 °C. Then the model was put into production and the fluid samples collected and analyzed.

The figure proves that acrylamide solutions of 20 and 25 g dm^{-3} concentration can ensure an effective improvement of WOR. It is a little surpris-

ing, however, that approximately equal efficiency was achieved with the two liquids, for the viscosity of the gel obtained from the 20 g dm^{-3} concentration solution is considerably smaller than that of the 25 g dm^{-3} solution. The explanation may be that the permeability of the model treated with the 20 g dm^{-3} polymer solution is approximately half of the other and, also, its heterogeneity is probably greater. As an effect of the treatment with the two solutions, the initial water/oil ratio of 50 temporarily decreased to 10 and 5, respectively. A decrease of this extent in industrial scale is an extremely effective treatment. It is emphasized again that in our experiments a monomer mixture was injected into the model that produced a gel of limited mobility due to polymerization and partial cross-linking. An increase of the amount of bis-acrylamide may further improve the water/oil ratio and, in consequence, the effect of the treatment.

While the change in oil saturation alone is not regarded a definite proof in comparing the various methods (the dimensions of the radial model do not allow but the modelling of a 5-m radial domain around a well in a 10-m thick layer), the values of excess output can also support the conclusions drawn from the water/oil ratio data. After the displacement of a fluid amount of 3% of the pore volume the residual oil saturation in the porous system decreased by 7% if a gel of 20 g dm^{-3} acrylamide content was used. As no polymer was found in the produced water during this period, the excess oil production was entirely due to the opening of new flow channels and directions.

From the evaluation of the *in situ* polymerized and partially cross-linked acrylamide — bis-acrylamide systems it is concluded that their efficiency is

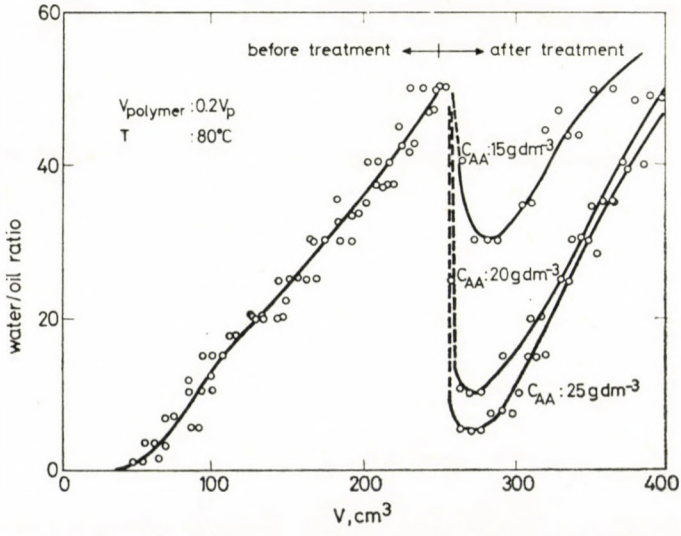

Fig. 10. Effect of acrylamid — bis-acrylamide monomer solutions of various composition on WOR in radial porous systems

higher than of the gels cross-linked by cations. Because of the different character of the bonds in the cross-linkage the following properties characterize this type of gel:

a) The gel is stable even at temperatures above 80 °C.

b) Gelling is independent of dispersion phenomena.

c) The properties of gels can be varied within a wide range.

d) The properties of gels can be adjusted at the well-site.

e) Gelling does not occur at the mixing front but it spreads over the whole volume of fluid.

f) The effect of the placement in the treated direction is more stable or permanent depending on the type of gel.

As regards economical considerations, it should be noted that though the price of monomers is only a fraction of that of polymers, the techniques based on *in situ* polymerization are more expensive, because higher monomer concentrations are required.

Summary

Comparative laboratory investigations of well-treatment techniques based on *in situ* cross-linking and polymerization proved that

i) The techniques based on *in situ* cross-linking with multivalent cations are suitable to the effective reduction of the permeability of water. Because of the parameters influencing the gelling of polymer solutions, many requirements have to be met. It is a disadvantage of conventional procedures that they can be applied only below 80–100 °C because of the ionic character of the cross-linkage. Aliphatic alcohols improve the behaviour of the *in situ* produced gel. Another possibility to improve the efficiency is a treatment with a combined polymer/silicate system. In the latter method the flexibility of the gels is combined with a high thermal stability.

ii) Main advantage of the method based on *in situ* polymerization compared with gelling with cations is that the stability of this type of gel meets the requirements even at temperatures in excess of 100 °C, gelling is independent of dispersion phenomena and extends over the whole volume of injected fluid and the parameters of gels can be varied within a wide range and adjusted at the well-site.

REFERENCES

Biles, J. W. 1972: Selective plugging method. U. S. Patent 3,658,131

Ely, J. W.—Chatterji, J.—Holtmayer, M. D.—Tinsley, J. M. 1975: Composition for fracturing high temperature well formations. U. S. Patent 3,898,165

Ford, W. O.—Kelldorf, W. F. N. 1976: Field results of a short setting time polymer placement technique. *J. Pet. Tech.*, 7, 749–756.

Gall, J. W. 1976: Partially cross-linked polymer used in correcting subterranean formation permeability. U. S. Patent 3,981,363

Goddard, J. E.—White, J. L.—Vanlandingham, J.—Carney, M. J. 1973: Use of polymers to control water production in oil wells. SPE Preprint 4407

Goddard, J. E.—White, J. L.—Vanlandingham, J. V. 1975: Improved control of water in producing wells and injection well. SPE Preprint 5402

Heinemann, Z.—Milley, Gy.—Wagner, O. 1979: Increasing the efficiency of crude oil displacement, modifying artificially the pore structure. *Oil Gas — European Magazine*, 5, 26–32.

KNAPP, R. H.—WELBOURN, M. E. 1978: An acrylic/epoxy emulsion gel system for formation plugging: Laboratory field testing for steam thief zone plugging. SPE Preprint 7083

KOCH, R. R.—MCLAUGHLIN, H. C. 1970: Field performance of new technique for control of water production or injection in oil recovery. SPE Preprint 2847

LAKATOS, I. 1978: Treatment of producing wells with water-soluble polymers. *Kőolaj és Földgáz*, 111(1), 2—6. (In Hungarian).

MCLAUGHLIN, H. C.—DILLER, J.—AYRES, H. J. 1975: Treatment of injection and producing wells with monomer solution. SPE Preprint 5364

RHUDY, J. S.—KNIGHT, B. L. 1976: Fracturing Fluid. U. S. Patent 3,938,594

SANDIFORD, B. B.—GRAHAM, G. A. 1972: Injection of polymer solution in producing wells. 71st Nat AIChe, Dallas

SAREM, S. A. M. 1974: Secondary and tertiary recovery of oil by MCCF process. SPE Preprint 4901

SAREM, S. A. M. 1975: Mobility controlled caustic flooding process for highly heterogeneous reservoir. U. S. Patent 3,871,453

SLOAT, B. 1975: Increasing oil recovery by chemical control of producing water-oil ratio. SPE Preprint 5341

SPARLIN, D. D. 1976: An evaluation of polyacrylamide for reducing water production. *J. Pet. Tech.*, 8, 906—914.

TINER, R. L.—HOLTMAYER, M. D.—KING, B. J.—GATLIN, R. A. 1975: Method and compositions for fracturing well formations. U. S. Patent 3,888,312

WHITE, J. L.—PHILLIPS, H. M. 1971: Use of polymers to control water production in oil wells. SPE Preprint 3672

WHITE, J. L.—PHILLIPS, H. M.—GODDARD, J. E.—BAKER, B. D. 1972: Use of polymers to control water production in oil wells. SPE Preprint 3783

WHITE, J. L.—GODDARD, J. E.—PHILLIPS, H. M. 1973: Use of polymer to control water production in oil wells. *J. Pet. Tech.*, 2, 143—150.

Acta Geodaet., Geophys. et Montanist. Acad. Sci. Hung. Vol. 17 (3—4), pp. 383—389 (1982)

A NEW METHOD OF MODELLING CAPILLARY PRESSURE CURVES

GY. MILLEY—O. WAGNER

PETROLEUM ENGINEERING RESEARCH LABORATORY OF THE HUNGARIAN ACADEMY OF SCIENCES

A probability distribution function is introduced in the paper to model capillary pressure curves characterizing the capillary properties of porous media. The applicability of the relationship is verified on the basis of published technical data and by experimental measurements. The suggested probability distribution function can be a useful tool both for modelling purposes and for the theoretical investigation of coarse disperse systems, because it contains only a few parameters that can be easily determined by experiments. The lognormal distribution also enabled us to simplify the experimental determination of capillary pressure curves.

Symbols

b	constant
n	constant
p_c	capillary pressure
r_p	pore radius
V_p	pore volume
ξ	$2\ \sigma \cos \theta$
σ	surface tension
θ	contact angle
Subscripts	
D	displacement
p_c	referring to capillary pressure
r_p	referring to pore radius

The pore size distribution of porous media is an important parameter from the points of view of research and of the industry, as well. Since it would be almost impossible to define exactly the terms 'pore size' and 'pore shape', they are usually referred to as indefined parameters or their theoretical definitions are used [Scheidegger 1960 or Bear 1972]. The most practical and widely used method to investigate the pore structure of a porous body is the measurement of capillary pressure being the simplest indicator of the capillary properties according to Wiggs (1958), Scheidegger (1960), Morrow et al. (1965), Morrow (1970) and Bear (1972). Adsorption methods will not be considered, since the systems investigated belong to the group of coarse disperse systems.

The pore structures, even in nearly ideal artificial porous bodies, are very complicated, their mathematical treatment is rather difficult and does not provide the expected results in many cases. Statistical methods as reported among others by Scheidegger (1960), Bear (1972) and Farrel et al. (1972) seem

very promising. In practice, however, experimental observations are unavoidable even when using these methods.

Dullien (1972, 1975), Greenkorn (1972) and Dullien et al. (1974, 1975) reported results interesting both in the theoretical and practical respects, obtained by photomicrographical techniques. This experimental technique is, however, not generally available in the laboratories for routine measurements.

The experimental approach should still be considered as the most useful method. Since the number of porous systems with specific properties is great, the empirical and semi-empirical relationships of Leverett (1941), Drake et al. (1945), Rose et al. (1949), Scheidegger (1960) and Bear (1972) are used even though these methods require a great amount of measurement data.

The authors of this paper do not intend to add one more relationship to the family of semi-empirical formulae describing capillary pressure curves but suggest a relationship that is useful in experiments, beneficial in calculations and contains only a few parameters.

Theoretical

Laboratory analysis of packed beds made of glass beads and consolidated porous bodies made of sintered glass beads has proved that the probability distribution function published by Rosin et al. (1933) and later by Herdan (1960) is suitable for the description of the grain size distribution of glass bead used for producing porous bodies.

It has been concluded that since the Rosin—Rammler's theory provides the most suitable equation for the description of the *grain* size distribution, the same should apply to the *pore* size distribution of porous bodies made of the same particles.

Let us consider the pores of a porous body as a fictive grind product. Using this hypothesis and the measurement method of capillary pressure curves, the values of capillary pressure can be regarded as members of a fictive sieve set i.e. the pore volume fraction $(V_p)_{D,\,p_c}$ saturated by the displacing phase at a given capillary pressure p_c is a fictive sieve residue.

Consequently, the pore volume distribution can be described by the probability function

$$(V_p)_{D,p_c} = \exp\left[-b \cdot p_c^n\right] \tag{1}$$

where b and n are constants characterizing the pore size and the material properties of the porous body.

Observations made by Leverett (1941), Carman (1956), Everett (1958), de Boer (1958) and Melrose (1956) suggest that the pore structure of a porous system (e.g. sandstone, sand pack) can be modelled by a capillary pipe bundle.

If so, then by Laplace's equation, we have for the pore size distribution from Eq. (1)

$$(V_p)_{D,r_p} = \exp\left[-b\left(\frac{\xi}{r_p}\right)^n\right] \tag{2}$$

where r_p ist the average radius of the pores forming the part $(V_p)_{D,r_p}$ of the pore space

$\xi = 2\sigma \cos\theta$

σ is surface tension and

θ the characteristic contact angle.

The differential distributions of pore volume and pore size can be obtained by differentiating Eqs (1) and (2)

$$\frac{\mathrm{d}(V_p)_{D,p_c}}{\mathrm{d}p_c} = [-b \cdot n \cdot p_c^{n-1} \cdot \exp(-b \cdot p_c^n)] \tag{3}$$

$$\frac{\mathrm{d}(V_p)_{D,r_p}}{\mathrm{d}r_p} = b \cdot \xi^n \cdot r_p^{-(n+1)} \cdot \exp(-b \cdot \xi^n \cdot r_p^{-n}). \tag{4}$$

Capillary pressure and capillary (pore) radius characterizing the distribution can be calculated as the second derivatives of Eqs (1) and (2).

Taking twice the logarithm of Eq. (1) and plotting log log $(V_p)_{D,p_c}$ against $\log p_c$ we obtain a straight line of slope n, wherefrom the constant b, can be determined. If one determines two pairs of quantities $(V_p)_{D,p_c}$ and p_c the pore volume distribution will be fully known. This finding is of great importance from the point of view of experimental techniques since this way the time needed for capillary pressure measurements can be considerably reduced. Also, high-pressure equipments can be constructed more simply that is especially important for the desaturation method providing the most accurate data.

If this consideration is correct, Eq. (1) can be assumed to be valid with a good approximation for the description of the capillary pressure curves of sedimentary rocks, e.g. sandstone, as well.

Verification of the theory

To verify the theory, numerous published capillary pressure curves have been investigated in view of Eq. (1). Results obtained by different authors represent measurements performed on various porous materials with various experimental techniques. Computer analysis has shown a very good agreement between calculated and measured data. Results of calculations for a few representative examples are illustrated in Fig. 1.

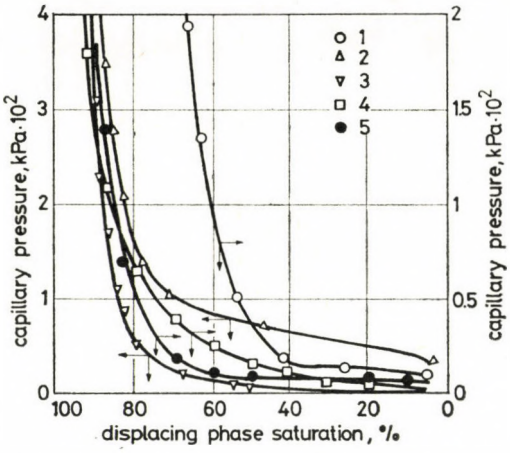

Fig. 1. Calculated capillary pressure curves (continuous line) and the measured values. Curve 1 Amyx et al. (1960). Curve 2 Roper et al. (1968). Curve 3 Hoffman (1963). Curve 4 Blair (1964). Curve 5 Wagner et al. (1766)

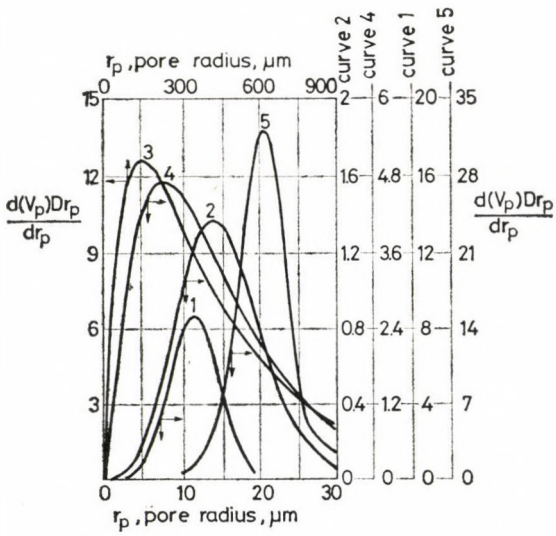

Fig. 2. Pore size distributions corresponding to the capillary pressure curves in Fig. 1, determined according to Eq. (4)

Figure 2 shows the pore size distributions calculated by Eq. (4) from the capillary pressure curves of Fig. 1.

80 capillary pressure curves published in the literature have been analyzed by the computer. The analysis of the comparatively great amount of experimental data revealed a dual character for a part of the capillary pressure curves, also indicated by Thomer's (1960) data. This dual character, however,

cannot be compared with the dual distribution curves of Dullien (1972) and Dullien et al. (1972), although a similar evaluation of experimental data seems possible.

The low-pressure section of capillary pressure curves can be accurately described by the suggested distribution function, using only two measurement

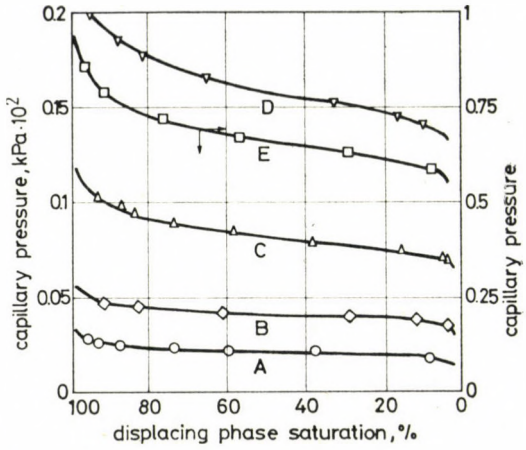

Fig. 3. Measured (dots) and calculated (continuous line) capillary pressure curves of consolidated porous media composed of glass beads of various size. Curve A particle size fraction 177—297 μm. Curve B particle size fraction 88—177 μm. Curve C particle size fraction 44—88 μm. Curve D particle size fraction 20—40 μm. Curve E particle size fraction 8—12 μm

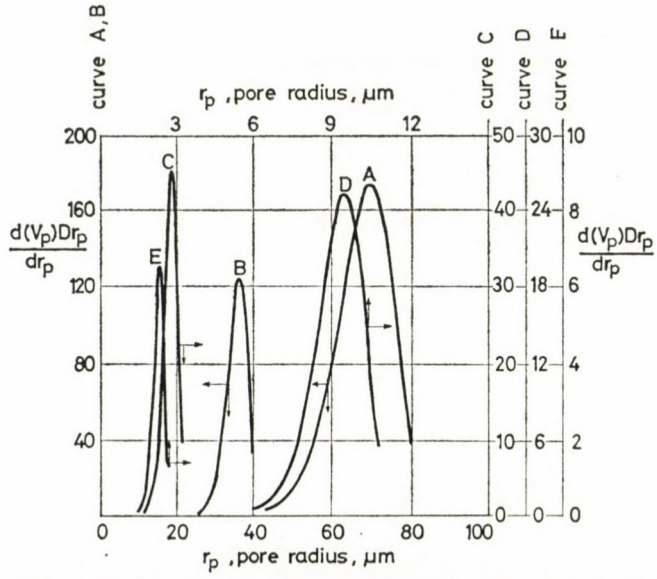

Fig. 4. Pore size distributions corresponding to the capillary curves of Fig. 3, determined according to Eq. (4)

data. To have an exact description of the high-pressure section of the curves as well, two more pairs of measurement data are required i.e. new constants b and n have to be determined the same way as before.

Taking into account Morrow's (1970) thermodynamic considerations and other experimental results, capillary pressure curves can only be described unambiguously if the fluids in the pore space of the porous body form continuous phases. This requirement is met by the low-pressure portions of the capillary pressure curves, in agreement with the observation that the flow properties are determined most of all by the pore space of greater pore channels and pores.

Figure 3 shows capillary pressure curves determined by the Bruce (1947) desaturation method on synthetic, consolidated porous bodies.

Pore size distribution curves calculated by Eq. (4) that correspond to those of Fig. 3 are illustrated in Fig. 4.

Application of Eq. (1) to natural porous rocks has proved that the exponent n is characteristic to rock quality. The conclusions are also supported by the fact that the constants in Eq. (1) have a definite physical meaning. The analysis of constants n and b is still in progress, but the results obtained already suggest that the characteristic groups of natural porous rocks (sandstones and limestones), consolidated and non-consolidated systems and synthetic porous bodies could be classified by means of the values of these constants. The exact dependence of the constants of Eq. (1) on pore structure should be cleared by further research.

Conclusions

Data obtained from experiments and results of other authors have proved the hypothesis that the pore volume distribution and pore size distribution of porous systems can be characterized by the probability distribution function Eq. (1).

To describe capillary pressure curves, two pairs of quantities $(V_p)_{D,p_c}$ and p_c have to be known for simple distributions and four pairs for dual distributions. These results can be used to reduce the time needed for the experiments and to simplify experimental techniques.

The constants b and n of Eq. (1) provide information about the material and pore structure properties so that they could be beneficial for investigating and modelling coarse disperse systems.

Equation (1) suggested for the description of capillary pressure curves (pore size distribution curves) provides essential advantages for it contains only a few parameters that can be easily determined experimentally.

REFERENCES

AMYX, J. W.—BASS, D. M.—WHITING, R. L. 1960: Petroleum Reservoir Engineering. McGraw-Hill Book Co., Inc., New York.

BEAR, J. 1972: Dynamics of Fluids in Porous Media. Elsevier Publishing Co., New York.

BLAIR, P. M. 1964: Calculation of oil displacement by countercurrent water imbibition. *Trans. AIME*, 231, 195—202.

CARMAN, P. C. 1956: Flow of Gases Through Porous Media. Academic Press, New York.

DE BOER, J. H. 1958: The Shape of Capillaries. *In:* The Structure and Properties of Porous Materials. Ed. by D. H. Everett and F. S. Stone, Butterworths, London.

DRAKE, L. C.—RITTER, H. L. 1945: Pore size distribution in porous materials. *Ind. Eng. Chem., Anal.* Ed., 17, 782—789.

DULLIEN, F. A. L. 1972: Pore Structure and Flow Properties of Porous Media. Proceedings of the Second Symposium on Fundamentals of Transport Phenomena in Porous Media, Vol. II. University of Guelph, Ontario, Canada.

DULLIEN, F. A. L. 1975: Effects of pore structure on capillary and flow phenomena in Sandstones. *The Journal of Canadian Petroleum Technology*, July—September, 48—57.

DULLIEN, F. A. L.—DHAWAN, G. K. 1974: Characterization of pore structure: a combination of quantitative photomicrography and mercury porosimetry. *J. Int. Coll. Sci.*, 47, 337—349.

DULLIEN, F. A. L.—DHAWAN, G. K. 1975: Bivariate pore size distribution of some sandstones, *J. Int. Coll. Sci.*, 52, 129—135.

EVERETT, D. H. 1958: Some Problems in the Investigation of Porosity by Adsorption Methods. *In:* The Structure and Properties of Porous Materials, Ed. by D. H. Everett and F. S. Stone, Butterworths, London.

FARREL, D. A.—LARSON, W. E. 1972: Computer Analysis of Pore Structure of Isotropic Porous Media. Proceedings of the Second Symposium on Fundamentals of Transport Phenomena in Porous Media, Vol. II., University of Guelph, Ontario, Canada.

GREENKORN, R. A. 1972: Matrix properties of porous materials. *Ibid.*

HERDAN, G. 1960: Small Particle Statistics. Butterworths, London.

HOFFMAN, R. N. 1963: Technique for the determination of capillary pressure curves using a constantly accelerated centrifuge. *Trans. AIME*, 228, 227—235.

LEVERETT, M. C. 1941: Capillary behavior in porous solids. *Trans. AIME*, 142, 152—691.

MELROSE, J. C. 1965: Wettability as related to capillary action in porous media. *Trans. AIME*, 234, 259—271.

MORROW, N. R. 1970: Physics and Thermodynamics of Capillarity. In: Flow Through *Porous* Media. American Chemical Society Publications. Washington D. C.

MORROW, N. R.—HARRIS, C. C. 1965: Capillary equilibrium in porous materials. *Soc. Petrol. Eng. J.*, 5, 15—24.

ROPER, W. A.—DOSCHER, T.—KOBAYASHI, R. 1958: Evidence of chromatographic effect during flow of gases through oilfield cores. *Trans. AIME*, 213, 359—361.

ROSE, W.—BRUCE, W. A. 1949: Evaluation of capillary characters in petroleum reservoir rocks. *Trans. AIME*, 186, 127—142.

ROSIN, P.—RAMMLER, R. 1933: The laws governing the fineness of powdered coal. *Journal of the Institute of Fuel*, 7, 29—39.

SCHEIDEGGER, A. E. 1960: The Physics of Flow Through Porous Media. University of Toronto Press, Toronto—London.

THOMER, J. H. M. 1960: Introduction of a pore geometrical factor defined by the capillary pressure curve. *Trans. AIME*, 219, 354—358.

WAGNER, O. R.—LEACH, R. O. 1966: Effect of interfacial tension on displacement efficiency. *Trans. AIME*, 237, 335—344.

WIGGS, P. K. C. 1958: The Relation Between Gas Permeability and Pore Structure of Solids. *In:* The Structure and Properties of Porous Materials. Ed. by D. H. Everett and F. S. Stone, Butterworths, London.

Acta Geodaet., Geophys. et Montanist. Acad. Sci. Hung. Vol. 17 (3—4), pp. 391—400 (1982)

APPLICATION OF MATHEMATICAL SIMULATION TO POLYMER FLOOD DESIGN

M. MUNKA

PETROLEUM ENGINEERING RESEARCH LABORATORY OF THE HUNGARIAN ACADEMY OF SCIENCES

Published mathematical models suitable for the analysis of polymer flooding are summarized. Heinemann's simulator developed in Hungary is considered in more detail. The results of five-spot experiments prove the feasibility of the method in practice. A planning method is also discussed that enables the results of modelling to be applied or extended to other fields. The examples emphasize that simulation methods cannot be omitted in the design of modern production technologies.

Symbols

A	amount of polymer adsorbed on a grid block, kg m^{-3}
B	formation volume factor
D	distance from the reference plane, m
R_s	dissolved gas content in oil
S	saturation
a	adsorptive capacity of the rock, kg m^{-3}
c	polymer concentration, kg m^{-3}
c_0	initial polymer concentration, kg m^{-3}
g	gravitational constant
h	formation thickness, m
k	absolute permeability
k_r	relative permeability
p	pressure, Pa
q	injection rate, m^3/day
t	time
u	filtration rate, ms^{-1}
Φ	porosity
μ	dynamic viscosity, mPas
ϱ	density
Subscripts	
g	gas phase
i	grid block number in the x-direction
o	oil phase
w	aqueous phase

Introduction

With the decrease of oil reserves research has begun all over the world to develop new oil production technologies to achieve a substantial increase in recovery. One of these new techniques is polymer flood giving rise to great expectation in Hungary as well.

Polymer flooding has been investigated in the Petroleum Engineering Research Laboratory of the Hungarian Academy of Sciences since the early

seventies. Research included the analysis of polymer properties and of the mechanism of flooding and design of a small-scale industrial experiment. For the design of a five spot experiment, a computer program was required to model polymer flood. This problem was all the more urgent because the design of production of actual reservoirs is no more feasible without using mathematical models. This statement especially refers to the new production methods where the role of practice is much less important than used to be with the conventional methods.

The computer simulator used for the modelling of polymer flood and the main results of design obtained by this mathematical tool will be considered in details.

Mathematical model

The first simulator capable of modelling polymer flood was developed by Jewett and Schurz (1970). This two-phase, two-dimensional model is based on Buckley—Leverett's fraction flow equations.

Further simulators developed by Patton et al. (1971), Slater and Farouq-Ali (1970), Gorbunov and Tokarev (1977), Vela et al. (1976) can be characterized by the common feature that they consider the fluid as incompressible, neglect the capillary force and are only valid for a distinct well pattern. The mobility controlling effect of the polymer is not adequately modelled by the simulators.

Bondor et al. (1972) have reached a major improvement in polymer flood modelling by taking into account all important effects in polymer displacement. Thus, their polymer flood model is of the most general validity. It is based on the differential equations of flow of three nonmiscible phases in porous media. The polymer solution is treated by the model as a separate phase so that one more equation characterizing the polymer solution is added to the system of differential equations. The so-called permeability reduction factor is introduced as a function of adsorption. Dispersion of the polymer slug is attributed to the different mobilities of the phases and it is calculated by means of the so-called mixing parameter model developed for mixing displacement.

The model developed by Bondor et al. (1972) was first to establish a simulator ensuring the analysis of polymer flood in complex reservoirs. A disadvantage of the model that it treats the polymer as a separate phase, making the comparison of the experimental and calculated results somewhat difficult. Numerical dispersion can be considerable in the calculation. This fact, because dispersion does exist in reality as well, may disturb the evaluation of the results. A beneficial feature of the model that it is capable of modelling the behaviour of the gaseous phase besides of the oil and aqueous phases. The phases

may be compressible, and the gravitational and capillary forces as well as dispersion and adsorption are also taken into account.

A two-dimensional three-phase simulator suitable for modelling of polymer flood was developed in Hungary by Heinemann (1977). It is based on the differential equations of the flow of three non-miscible phases in porous media:

$$\nabla\left[\frac{k\bar{k}_{rw}}{B_w\bar{\mu}_w}(\nabla p_w+\varrho_w g\nabla D)\right]-q_w=\frac{\partial}{\partial t}\left(\frac{\Phi S_w}{B_w}\right) \tag{1}$$

$$\nabla\left[\frac{kk_{ro}}{B_o\mu_o}(\nabla p_o+\varrho_o g\,\nabla D)\right]-q_o=\frac{\partial}{\partial t}\left(\frac{\Phi S_o}{B_o}\right) \tag{2}$$

$$\nabla\left[\frac{kk_{rg}}{B_g\mu_g}(\nabla p_g+\varrho_g g\nabla D)+R_s\frac{kk_{ro}}{B_o\mu_o}(\nabla p_o+\varrho_o g\nabla D)\right]-$$

$$-q_g=\frac{\partial}{\partial t}\left[\Phi\left(\frac{S_g}{B_g}+\frac{R_s S_o}{B_o}\right)\right]. \tag{3}$$

The equations are modified for polymer flood by replacing the viscosity of water and the relative permeability with respect to water by the logarithmic averages of the corresponding values for water and polymer:

$$\bar{\mu}_w=\mu_p^{\alpha}\,\mu_w^{1-\alpha},\quad \alpha=\frac{c_{i,j}}{c_o} \tag{4}$$

$$\bar{k}_{rw}=k_{rp}^{\varkappa}\,k_{rw}^{1-\varkappa},\quad \varkappa=\frac{A_{i,j}}{a}. \tag{5}$$

The change of adsorption in a finite element of length Δx during time Δt, assuming a perfect slug-like displacement, can be calculated as

$$\Delta A=\frac{uc_o\,a}{S_w c_o+a}\,\frac{\Delta t}{\Phi\Delta x}. \tag{6}$$

The concentration of the polymer flowing between two blocks can be given by following equation for a perfect slug

$$c_{i+1/2}=\begin{cases}0 & \text{if} \quad A_i<a \quad \text{or} \quad c_i=0\\ c_0 & \text{if} \quad A_i=a \quad \text{and} \quad c_i>0.\end{cases} \tag{7}$$

Because of dispersion, however, the outflow of polymer from a given block starts even before full adsorption saturation has been achieved. The author

of this model takes into account this dispersion effect by introducing a correction function

$$c_{i+1/2} = c_o \varphi \left(\frac{A_i}{a} \right) \psi \left(\frac{c_i}{c_o} \right), \tag{8}$$

where φ and ψ are empirical correction functions. The change of concentration is calculated by the material conservation equation of the polymer.

The essential parameters (adsorption, relative permeability reduction, mobility control effect) as regards the mechanism of action of the polymer are adequately modelled by Heinemann's (1977) polymer flood simulator. By calculating the movement of the concentration fronts within the blocks, the numerical dispersion in the simulation of slug displacement is eliminated. The correction function used for modelling physical dispersion deserves special attention. Calculations using various correction functions have proved that they can be easily fitted to all concentration profils in practice [Munka, 1978].

Modelling small-scale industrial experiments

In 1977/78 a polymer flood experiment was performed out in the Algyő Field of the Nagyalföld Oil and Gas Producing Company [Lakatos et al., 1980]. The experiment was designed by Heinemann's polymer flood model. Simulation calculations were used to predict

a) the expected amount of excess oil;

b) the effect of external factors influencing flow pattern in the experimental unit and ways of avoiding these effects;

c) place of the polymer slug in the formation after injection and the amount of polymer loss.

A normal five-spot element has been selected for experimental purposes in the Algyő-2 formation. The area selected represented the general geological features of the formation. The main geological parameters of the five-spot element are

$$\begin{aligned} \bar{h}_{\text{eff}} &= 9.75 \text{ m} \\ \bar{\Phi} &= 24.2\% \\ \bar{S}_w &= 47.5\% \\ \bar{k} &= 1.56 \cdot 10^{-3} \text{ cm}^2. \end{aligned}$$

The experimental area was 125×125 m and the modelled one 600×600 m, covered by a 15×15 m grid. Parameters of the fluid are summarized in Table I.

To answer the above questions the simulation of the experiment was calculated in three versions:

Table I

Parameters of the Algyő experiment

Parameter	Value	
Bubble point pressure	19.31	MPa
Irreducible water saturation	0.26	
Residual oil saturation	0.22	
Critical gas saturation	0.1	
Density of water	1.004	gcm^{-3}
Density of oil	0.831	gcm^{-3}
Density of gas	$9.08 \cdot 10^{-4}$	gcm^{-3}
Viscosity of water	0.28	mPas
Viscosity of oil	0.64	mPas
Viscosity of gas	0.018	mPas
Formation volume factor of water	1.0312	
Formation volume factor of oil	1.312	
Formation volume factor of gas	$5.7 \cdot 10^{-3}$	
Concentration of polymer solution	1	gdm^{-3}
Viscosity of polymer solution	1.09	mPas
Adsorptive capacity of rock	$6 \cdot 10^{-2}$	kgm^{-3}
Relative permeability reduction factor	0.6	

Version *A* The injection/production ratio calculated as well-site volumes is 1 : 1. The boundary condition assumes an open reservoir.

Version *B* The injection/production ratio is 2 : 1, the reservoir is open also in this case.

Version *C* The boundary condition differs from that of version A. Since production also extends outside the experimental area, four production wells were placed into the outmost line of grid to simulate outside production.

The results of the simulation of a 12-month period have proved that there is no significant difference between versions A and C, i.e. the assumption of an open boundary can ensure data of the required accuracy. Polymer flood simulation, therefore, was only carried out for versions A and B. The concentration of the injected polymer solution was 1 gdm^{-3} corresponding to a pore volume v of 0.23 of the five spot element.

The results of the mathematical simulation of the displacement processes can be summarized as follows.

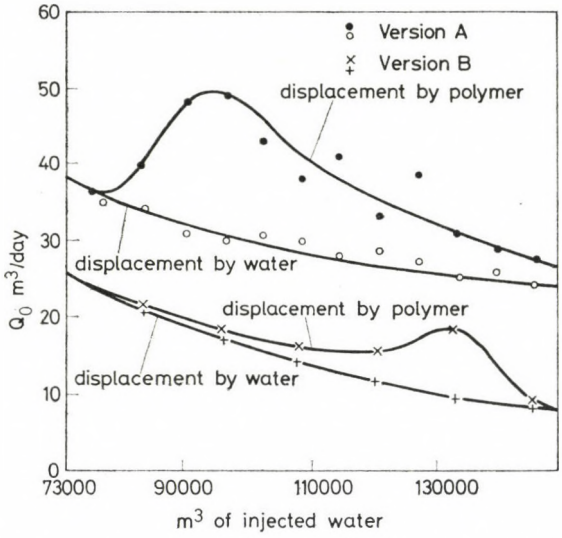

Fig. 1. Daily oil production according to simulation calculations of version *A* and *B*

1. Oil production of the producing well is illustrated as a function of the volume of injected fluids in Fig. 1. The favourable effect of polymer injection is clearly demonstrated. The amount of excess oil compared to the cumulative amount of oil produced by water displacement is 9% in version A and 3% in version B.

2. The considerable difference between the amounts of excess oil obtained in the two versions is caused by the oil flowing into the area of the experimental element. 82% of the excess oil stems from the layer outside the experimental element in version A while 33% in version B. The data suggest that an injection/production ratio of 2 : 1 has to be achieved to eliminate the effect of external factors.

3. In both versions, 66% of the injected polymer solution remains within the boundaries of the experimental element and 34% escapes. One third of the injected polymer should thus be regarded as loss. At the end of polymer injection 90% of the polymer is in solution and 10% is adsorbed on the rock of the experimental element. As regards the mechanism of action, the polymer can exert both its viscosity increasing and relative permeability decreasing effects.

Based on the data of the five-spot industrial experiment, an *a posteriori* modelling of the experiment was carried out. The results of the *a posteriori* mathematical simulation are, however, only of theoretical importance, because flooding was not performed according to the original plans due to technical reasons (polymer was injected in the other layers as well not only in the planned one). Nevertheless, *a posteriori* simulation threw light upon the fact that

an unsteady rate of injection and different injectivity of the wells significantly decreased the results of the experiment.

Modelling of the five-spot industrial experiment could not answer certain simulation questions (determining the dispersion constants, fitting concentration data etc.), but it has proved that the results of the model can be used for design purposes.

Polymer flood design in the Algyő Field

The feasibility of polymer flood in Hungarian oil field practice was scrutinized by a committee of experts. In choosing the suitable reservoir physical parameters, structure and temperature of the reservoir, fluid properties, production history and the amount of reserves played a decisive role. Oil fields were classified into three groups.

Group one, including the formation Szőreg-1, offers the most favourable conditions for polymer flooding: here the best result can be expected. In the second group the conditions and expected results are moderate, while in the third group, also in formation Algyő-1, poor and uncertain. With the assistance of the Research and Development Institute for Oil and Gas Industry simulation calculations were carried out for the formation Szőreg-1 and Algyő-1. The formation Szőreg-1 shows the effects to be illustrated more clearly. Therefore, these calculations will now be summed up.

Szőreg-1 is a multi-layer reservoir with a great gas cap, its geological features are characteristic of the Algyő field. It extends over a great area, consists of many layers separated by siltstone beds that failed to develop in all places. Production at the present time proceeds under utilization of natural energies at a reduced rate. Water injection is scheduled for the next years. It was our aim in performing simulation calculations to predict the production procedure taking into account reservoir heterogeneity, well pattern, the state of the reservoir at the beginning of polymer flood and the effect of other influencing factors.

According to our aims, the modelled procedure can be divided into two parts: fitting production history and predicting the production process on the basis of an accurate geologic model. Prediction was made in three versions: first, assuming a bilateral water flood according to the present technology in Algyő; then an areal water flood using intersecting injection wells and, finally, a polymer flood with intersecting lines of wells.

The modelled part of the Szőreg-1 reservoir can be divided into two layers communicating practically only outside the oil body, through the gas cap and the water body. The lower layer is the more important and decisive from the point of view of production parameters. Some of the producing wells penetrate both layers, but the majority produces from only one of the layers.

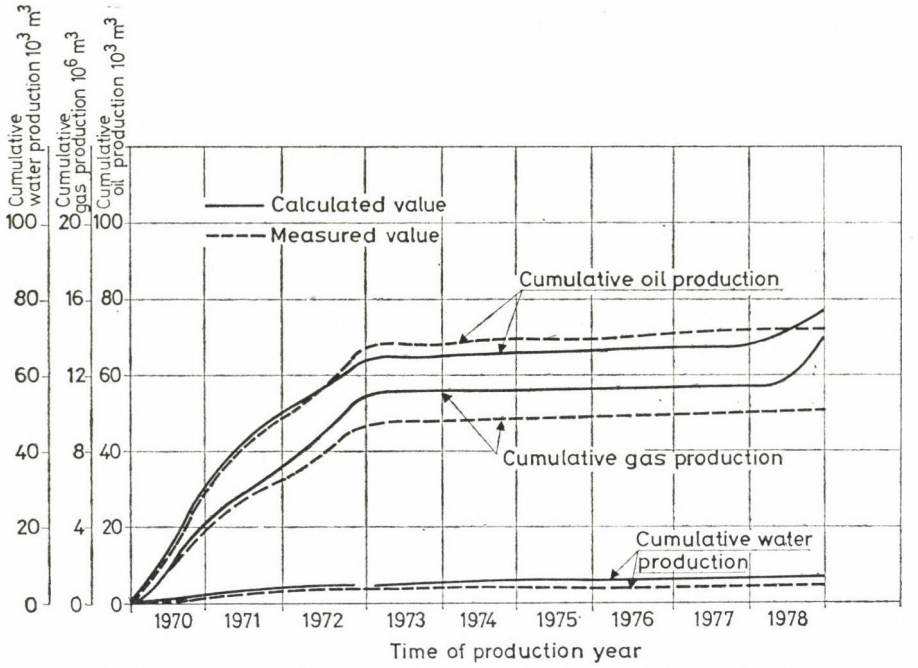

Fig. 2. Comparison of measured and calculated cumulative productions

The measured and calculated cumulative productions of the investigated part of the two layers are shown in Fig. 2. A more accurate geologic model would have further reduced the error, but the most important aim of our calculations, i.e. distinguishing the influencing factors, could also be achieved at the level of a moderate accuracy.

The results of prediction are displayed in Fig. 3, also in a summarized form for the two layers. Calculations show that reversing the flow field greatly contributed in increasing the amount of excess oil compared to that of bilateral water flood.

To compare the versions, oil recovery and cumulative water percentage curves allowing general conclusions, are illustrated as functions of the effective flood ratio in Fig. 4. The results, including the Algyő-1 formation, suggest that reversing the potential field alone can yield a 1 to 5% excess oil recovery at its optimum while injection of polymer solution results in a further 0.5 to 3% increase.

The modelling results were extended during the design for the other layers intended to be flooded by polymers. An attempt has been made to express the effects of the influencing factors in a quantitative form using the following assumptions:

1. The two modelled formation parts can be regarded as extreme cases. The parameters of the other formations were determined by assuming linear changes between those extreme ones.

2. The effect of the well pattern, formation geology and beginning of production of the amount of excess oil can be determined.

Under these assumptions, the technology of polymer injection, producing and injection well pattern and the prediction of production and injection could be designed for further 4 layers.

However, it should be noticed, that a considerable part of the results have been based on estimations. It is obvious that a prediction based on these somewhat uncertain data bears its uncertainties, too. Therefore, future in-

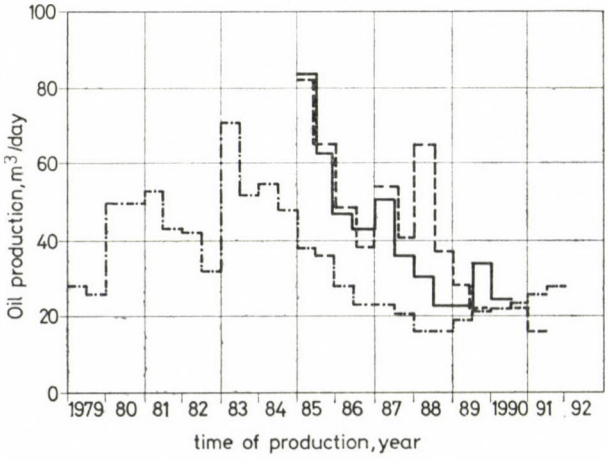

Fig. 3. Prediction of oil production

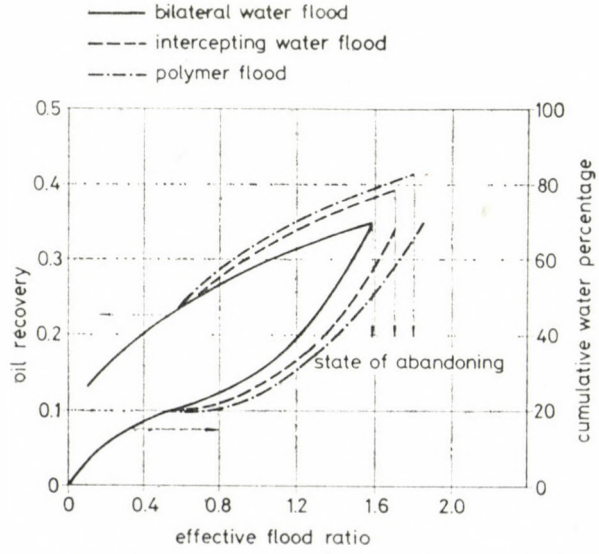

Fig. 4. Oil recovery and cumulative water percentage as functions of the effective flood ratio

dustrial-scale applications must be preceded by at least one unambiguous industrial experiment. The increase in the accuracy of the design procedure can be only gradually achieved, by using previous knowledge and results of successful industrial experiments.

Summary

Mathematical models of polymer flooding suggest that the simulators developed in the last years ensure that the simulation calculations could be used in practical design. The results of a design work carried out with Heinemann's two-dimension three-phase model can be summarized as follows.

1. Designing a five-spot scale industrial experiment enabled us to determine the injection-production ratio that eliminates the effect of external factors. Further, information was gathered about the amounts of excess oil and polymer loss.

2. A production technology was designed to investigate the feasibility of the polymer flood method in the Algyő field. The design method enabled us to extend the results of modelling for other layers.

The examples discussed in the paper prove that the simulation of oil and gas reservoirs could be a useful tool for the reservoir engineer in designing modern oil production technologies.

REFERENCE

BONDOR, P. L.—HIRASAKI, G. J.—THAM, M. J. 1972: Mathematical simulation of polymer flooding in complex reservoirs. *Soc. Petr. Eng. J.*, 12, 369—382.

GORBUNOV, A. T.—TOKAREV, M. A. 1976: Hydraulic model and calculation method of the flood process using chain polymers. Manuscript. (In Russian.)

HEINEMANN, Z. 1977: Simulation model of polymer flooding. (In Hungarian.) *Kőolaj és Földgáz*, 10, 353—359.

JEWETT, R. L.—SHURZ, G. F. 1970: Polymer Flooding — A Current Appraisal. *J. Petr. Techn.*, 675—684.

LAKATOS, I.—MUNKA, M.—TÓTH, J.—KRISTÓF, M.—TRÖMBÖCZKI, S. 1980: Five-spot polymer flood experiment at Algyő. (In Hungarian.) *Kőolaj és Földgáz*, 13, 21—28.

MUNKA, M. 1978: Analysis of Simulation Methods of Polymer Flooding. Doctor's Thesis. (In Hungarian.)

PATTON, J. T.—COATS, K. H.—COLEGROVE, G. T. 1971: Prediction of polymer flood performance. *Soc. Petr. Eng. J.*, 11, 72—84.

SLATER, G. E.—FAROUQ-ALI, S. M. 1970: Two-dimensional polymer flood simulation. SPE preprint 3003

VELA, S.—PEACEMAN, D. W.—SANDVIK, E. 1976: Evaluation of polymer flooding in a layered reservoir with cross-flow, retention and degradation. *Soc. Petr. Eng. J.*, 16, 82—96.

Acta Geodaet., Geophys. et Montanist. Acad. Sci. Hung. Vol. 17 (3—4), pp. 401—413 (1982)

MODIFICATION OF PORE STRUCTURE BY INORGANIC GELS TO INCREASE DISPLACEMENT EFFICIENCY

Z. HEINEMANN

MONTAN-UNIVERSITÄT, LEOBEN, AUSTRIA

GY. MILLEY—O. WAGNER

PETROLEUM ENGINEERING RESEARCH LABORATORY OF THE HUNGARIAN ACADEMY OF SCIENCES

The study distinguishes ideal and real porous media. In real porous media the greater part of the oil remains in the form of macroscopic spots after displacement by water. This oil fraction can not be mobilized unless the ratio of viscous to capillary forces, expressed as $u\mu/\sigma_{ow}$, is increased by at least four orders of magnitude. A real possibility for that seldom exists.

However, even a moderate decrease in surface tension can be effective, if the pore channels already filled by the displacing phase are closed and the displacing medium containing chemicals can be forced to remove the oil spots through alternative routes. Displacement efficiency can be considerably improved by modifying the pore structure at the proper place and time, i.e. in a programmed way.

Symbols

E_R	production efficiency, i.e. ratio of the produced and initial amounts of oil in the reservoir, dimensionless
ΔE_R	difference between the efficiencies of production with water and gels, dimensionless
k	permeability, μm^2
N_c	capillary number, dimensionless
Δp	differential pressure, Pa
R_{si}	initial ratio of dissolved gas-oil, m^3/m^3
S_o	oil saturation, dimensionless
S_{oR}	residual oil saturation, dimensionless
S_{oRC}	residual oil saturation after secondary displacement, dimensionless
ΔR_{oR}	change of residual oil saturation, dimensionless
S_w	water saturation, dimensionless
u	displacement velocity, m/s
μ	viscosity, Ns/m^2
Θ	contact angle, radian
σ_{ow}	water-oil interfacial tension, N/m
ϱ_o	density, kg/m^3

Introduction

Displacement of crude oil from the reservoir rocks is a complicated process not fully understood even today. It would be extremely important to have an exact knowledge about this phenomenon, since at the present level of science and technology some sixty per cent of the oil remains unrecoverable in reservoirs.

It is known that the efficiency of oil recovery can be ascribed to two factors, *viz.* to the *displacement efficiency* giving the fraction of oil that can be produced by a given medium from a homogeneous porous medium under given

circumstances and to *flooding efficiency* expressing the part of the reservoir that is flooded by the displacement medium.

The present day understanding of the parameters determining the amount of residual oil and the potential for its mobilization is summarized by Stegemeier (1977): "Trapping and release of oil in natural petroleum reservoirs occur under a wide variety of interrelated initial and applied conditions. Factors which determine the microscopic displacement mechanisms are

a) geometry of the pore network;

b) fluid-fluid properties, viz. interfacial tension, density difference, bulk viscosity ratio, and phase behaviour;

c) fluid-rock properties, including wettability, ion-exchange, and adsorption; and finally

d) applied pressure gradient and gravity.

The trapped phase can be released either by increasing the ratio of viscous to capillary forces (1.) or by changing relative phase volumes (2.)." These changes can be achieved by displacement techniques using polymers, surfactants, micellar and caustic solutions, microemulsions, carbon dioxide, alcohols and rich and high-pressure dry gas, as well as thermal methods that are widely known. Generally, these methods combine various effects and they can be assigned to groups (1) and (2) according to their determinant factors.

Moore and Slobod (1956) expressed the ratio of viscous to capillary forces by a dimensionless capillary number, $N_c = u\mu/\sigma_{ow} \cos\theta$, and they established a correlation between the reducibility of residual oil saturation and N_c. Their results have been confirmed by other authors, but as seen in Fig. 1 of Stegemeier (1977) the values of N_c plotted against S_{oRC}/S_{oR} are scattered over two orders of magnitude. This suggests that further parameters of the porous medium, other than those in N_c, also play a definite role. Dullien (1975) reported that the "structure complexity index" calculated with the average pore diameter and the average pore inlet diameter was in good correlation with S_{oRC}/S_{oR}, at a given value of N_c.

For water drive the capillary number is very low, $N_c < 10^{-7}$, and must be increased by at least two orders of magnitude to achieve a noticeable reduction in the residual oil saturation, and by two further orders of magnitude ($N_c = 10^{-3}$) to displace the greater part ($>70\%$) of residual oil.

As well known, the numerator of quotient N_c can be increased by at most one order of magnitude since the displacement velocity u in an oil reservoir is determined by the permeability and well-pattern. If the viscosity of the displacement phase is significantly increased, velocity is reduced and the product $u\mu$ scarcely increases. Consequently, surface tension σ_{ow} has to be reduced by three or four orders of magnitude to achieve a significant increase in displacement efficiency. The attendant difficulties are known from recently published studies [Reed et al., 1977]. Even if the necessary conditions are

produced in the laboratory, they usually have a very narrow range of parameters (temperature, concentration, salinity, duration time etc.) that are hardly possible to maintain in the field. At the same time, in order to meet these requirements, expensive materials and procedures, including tertiary technologies, are involved, implying high capital costs, low rate of return, and great economic risk.

Ideal and real porous media

The question arises, is it really necessary to reduce surface tension to such an extent? If a reduction of one or two orders of magnitude were sufficient, the economics of tertiary oil recovery would be considerably improved. To answer this question a working hypothesis is needed concerning the residual oil distribution in the porous medium after water displacement.

Let us first consider a regular tetrahedral arrangement of spheres of identical diameter, saturated by a non-wetting phase. If the non-wetting fluid phase is displaced by a wetting one in this porous medium, and the displacement process is absolutely stable, the displacing front will be a regular surface consisting of points moving with the same velocity. Consequently, none of the displaced phase will remain in the reservoir. This case, of course, does not exist in reality, as every significant parameter (contact angle, pore shape etc.), differs to a greater or lesser extent from pore to pore, giving rise to local perturbations. Displacement velocity in the pores is, therefore, also a random variable fluctuating around some average value. In an unfavourable case, displacement velocity in a certain pore is less than the expected value while it exceeds that in the surrounding pores. The boundary between displacing and displaced phases can thus locally remain one or even more pores (pore sizes) behind the surrounding points. Such local inequalities in the phase-boundary can then lead to discontinuities and segregation of the isolated fluid drop. Since the phenomenon is of random character, the residual oil is dispersed and shows a homogeneous distribution.

One arrives at a similar conclusion for models of more complex structure composed of capillaries or pore systems of various sizes in a random manner; see Fatt (1955), Scheidegger (1974) and Dullien (1975). While the distribution of the residual oil is homogeneous here as well, the sizes of the dispersed fluid particles scatter within a wider range. In the followings, porous media, containing residual oil saturation in the form of homogeneously distributed dispersed oil particles after a saturation with oil and displacement by water, will be called *ideal porous media*; while those lacking these properties will be called *real porous media*.

Chantenever and Calhoun (1952) observed microscopically that the residual oil saturation remained in the form of smaller and greater oil spots after

being displaced by water in a synthetic porous medium. This finding suggests that even an artifical porous body built of sphere particles cannot always be considered an ideal porous medium according to the above definition. Through the porous body small channels, a few pore-sizes wide, are formed and these channels conduct the majority of the filtrating fluid and only a very little of the displaced phase remains in them. This phenomenon cannot be explained by the heterogenity of the porous medium, since it was carefully composed of spheres of the same size.

Homogenity and heterogenity are interpreted as macro-properties of the porous media. The medium is considered homogeneous if porosity, permeability, capillary function and relative permeability functions are equal for its various parts; are they not, the medium is heterogeneous. These parameters are macro-properties because they are only defined for porous bodies whose dimensions exceed the pore size by several orders of magnitude. This way, heterogeneous ideal porous media and homogeneous real porous media can be interpreted without any difficulty. However, it should be emphasized that ideal and real porous media have only hypothetical meaning.

The essential difference between ideal and real porous bodies is that the residual saturation of the displaced phase is distributed in different ways after a non-miscible displacement process.

Let us now assume on the basis of Moore—Slobod's (1956) diagram (Fig. 1) that the interfacial tension between displacing and displaced phases is reduced by adding surfactants in a displacement process with small capillary number, $N_c < 10^{-7}$. The displacing phase containing additives will, of course, flow through the same pore channels where the flow without additives

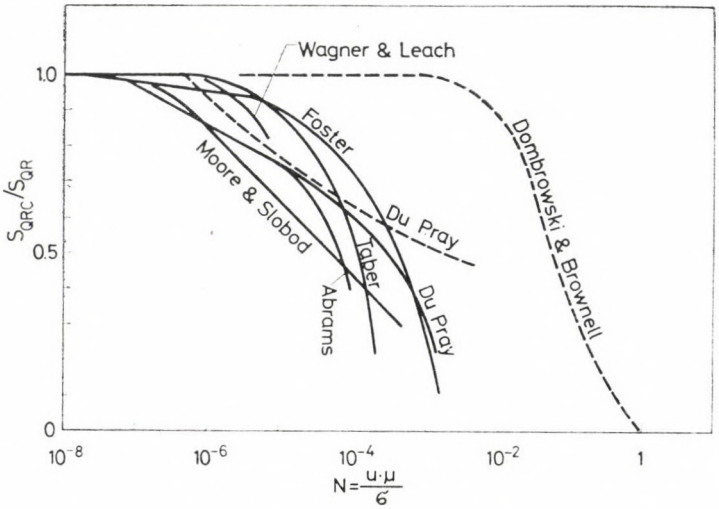

Fig. 1. Recovery of residual oil as a function of capillary number (Stegemeier)

had gone before. Surfactants will, therefore, act mainly on that part of the residual oil dispersed uniformly in the medium as small droplets. The surfactants can only reach the residual oil, retained in heterogeneously distributed spots of the size of several pores, through diffusion that substantially decreases the probability of the intended effect. Chances of increasing the efficiency through the reduction of surface tension alone are thus better in an ideal medium than in a real one.

As the viscosity of the displacing phase or the velocity of displacement is increased, greater pressure differentials act between the two ends of the oil spot. This, in turn, may remove the oil spot, creating favourable conditions for a direct contact with the flowing displacing phase and the surfactants in it. According to this model these two effects do not appear in combination in the microscopic range, or in a mutually increasing relationship, but in sequence. Viscous forces have to remove first the oil spots from their places, then disperse them so that the surfactants could reduce the capillary retaining forces.

Modification of the pore structure

If this hypothetical model even partially corresponds to reality, one has to conclude that there is no need to reduce the surface tension or to increase the viscous forces to the extent that even a weak effect of the displacing phase should sweep away the retained oil spots, but it is sufficient to direct the main flow to them. The already swept out flow channels must be closed between the retained oil spots, thus forcing the displacing phase containing additives to remove the oil spots. In other words, the pore structure of the porous body has to be changed.

The favourable effect of pore structure modification can also be observed in alternated gas-water injection and polymer and emulsion injection, as a side-effect and with a weaker force. The main problem of the known and applied versions of these methods that the chemicals needed to close selectively the pore channels have to be forwarded for great distances, and that they are required to block the relatively wide channels and leave open the narrow passages — a condition very hard to meet. The slight increase in the efficiency of oil production is a consequence of the fact that there are bottlenecks in the "wide channels" with dimensions smaller than those of the "narrow channels" which can cause statistically slight modifications in the active pore structure. Valuable results can, however, only be expected if the blocking slug is produced at the right time and place in the reservoir. The process can be realized by sodium silicate solutions, such as water glass and bivalent metal salts, such as calcium chloride. The combined use of these chemicals termed "mobility controlled caustic flood" was suggested by Sarem (1974).

Solutions of water-soluble silicates are strongly alkaline. Their properties are summarized by Weldes and Lange (1969). Sodium silicates with a SiO_2/Na_2O molar ratio of 2.4 or above have long been used as cement additives to block water break-through and high-permeability zones; see Froning (1968). Using these methods, sodium silicate reacts with the bivalent ions in the layer and the precipitates produced reduce permeability.

Sarem's (1974) method applies sodium orthosilicate with a SiO_2/Na_2O molar ratio of 0.5 and a pH approximately equal to that of a NaOH solution of the same concentration. The sodium orthosilicate reduces water-oil interfacial tension more effectively than the caustic soda. Therefore, it is highly suitable for producing *in situ* or well-site emulsions whose effects in mobility control and in increasing efficiency in areal and vertical sweeping have been shown by McAuliffe (1973).

Sodium silicate reacts with bi- or multivalent cations originally present in the layer and with the solution injected after the silicate solution. The reaction produces a silicic acid gel that can be converted into a microcrystalline precipitate depending on temperature, concentration and time. The mechanism of the process is described as by Sarem (1974), with certain additions.

1. The high pH sodium silicate solution reacts with the components of the crude oil and as a result surfactants are produced *in situ* that decrease surface tension, increase the mobility of the oil and produce a relatively stable emulsion. The emulsion reduces the speed of advance of the front and improves the volumetric sweeping efficiency. The form of the emulsion produced *in situ* depends, of course, on the chemical character of the actual crude oil.

2. The dilute calcium chloride solution injected after the silicate solution provides the multivalent cations for the reaction with the orthosilicate yielding a fine precipitate. This precipitate can pass through the high permeability channels and may reduce permeability, just as the migrating materials. After the high permeability channels have been partially closed, water can enter the previously inaccessible parts of the rock and the efficiency of volumetric flood improves. Repeating the procedure cyclically, an oil bank can be produced and the water can be prevented from forming fingerings through the oil bank.

3. The silicate solution alters the wetting character of the reservoir towards a water-wet state. This effect is caused by the caustic but even more by the "silicate" nature of the solution.

Sarem (1974, 1975) suggested the use of orthosilicate solutions with concentrations ranging between 0.01 and 0.8% by weight. Surface tension is reduced, therefore, most effectively in this concentration range, as shown by the investigations of Campbell (1977) which achieved a surface tension of 10^{-4}—10^{-6} N/m depending on the type of oil.

A subsequent injection of comparatively small slugs accumulates increasing amounts of precipitates around the injection well in the high-permeability parts, counterbalancing the unfavourable effect of heterogeneity. Various techniques based on the above principle have been patented [Sarem, 1974, 1975].

According to our working hypothesis, we proceed here with the modifications of the pore structure, this can be achieved by producing a gel precipitate in the right place. To obtain a suitable gel precipitate, a relatively concentrated sodium methasilicate solution is used instead of sodium orthosilicate. The pH of the sodium methasilicate solution is somewhat lower than that of the orthosilicate solution. It is, therefore, less effective in decreasing interfacial tension and producing emulsions but its reactions with bivalent metal ions yield more voluminous and stable gel-precipitates. The mechanism of displacement is interpreted as follows.

1. The sodium methasilicate solution reduces the water-oil surface tension and favourably alters the wettability properties of the rock; in a concentrated solution it improves the viscosity ratio and displaces that part of the residual oil that can be displaced according to the increased capillary number N_c.

2. The sodium methasilicate slug and the following $CaCl_2$ solution are dispersed in each other during displacement and produce a gel-like precipitate of great volume, partially or fully blocking the pore channels. The pressure gradient locally increases and the $CaCl_2$ solution removes the previously immovable oil spot. The methasilicate solution moves in front of the oil spot, reducing surface tension, and it is followed by the $CaCl_2$ solution. No precipitate is formed on the route of the moving oil spot. If the oil spot stops for some reason, the two solutions come into contact again, the pressure gradient locally increases and the oil spot starts to move again. This mechanism can not remove oil dispersed in the form of droplets, because blocking the surrounding "aqueous" channels only produces a further obstruction in the way of the droplets. The expression "oil spot" has been deliberately used in our previous discussions to make a distinction from dispersed droplets and the oil bank. To define quantitatively these expressions remains a problem to be solved.

If our hypothesis concerning the distribution and capacity for mobilization of the residual oil holds, a considerable amount of residual oil can be displaced by this mechanism from a homogeneous real porous body.

Displacement tests on short cores

The first set of experiments were carried out on artificially consolidated rock samples 0.25 m long with a cross-section of $0.02 \cdot 0.02$ m^2. The artificial rock was made of suitable sieve fractions of quartz sand by adding a mixture

of CaF_2, NaF, Na_2SiF_6 and glass powder to it, homogenizing and forming it under pressure and finally sintering it at a temperature of 560—810 °C in a special furnace. The rock samples were regarded as homogeneous and accepted as suitable for the tests if the porosity and permeability of 0.02 m long sections coincide within $\pm 5\%$.

The main parameters of the silicate solution applied in the experiments and the surface tension in relation to the crude oil used are summarized in Table I.

The rock samples were first saturated with water (NaCl solution of $2.0 \cdot 10^{-3}$ kg/kg) then the water was displaced by formation oil of density 823.7 kg/m³ and 3×10^{-3} Ns/m² viscosity until residual water saturation was

Table I

Characteristic parameters of silicate solutions

Concentration $SiO_2 \cdot 10^{-2}$ kg/kg	Density kg/m³ 24 °C	Viscosity $\cdot 10^{-3}$ Ns/m²		σ_{ow} N/m	
		24 °C	95 °C	24 °C	95 °C
1.0	988.7	2.15	2.03	$2.2 \cdot 10^{-3}$	$1.3 \cdot 10^{-3}$
2.5	1004.1	2.17	2.04	$1.1 \cdot 10^{-3}$	$8.3 \cdot 10^{-4}$
4.0	1018.8	2.21	2.05	$9.8 \cdot 10^{-4}$	$5.2 \cdot 10^{-4}$
5.0	1029.5	2.23	2.06	$9.1 \cdot 10^{-4}$	$3.8 \cdot 10^{-4}$
10.0	1029.5	2.41	2.14	$2.6 \cdot 10^{-4}$	$9.8 \cdot 10^{-5}$

Table II

Data of displacement experiments

N°	Displacement fluid	Parameters of rock samples			Concentration 10^{-2} kg/kg		Water		Gel	
	V_p	Φ	$\mu m^2 \cdot 10^{-3}$	S_0	SiO_2	$CaCl_2$	S_{oR}	E_R,%	ΔS_{oR}	ΔE_R, %
1.1		0.234	281	0.74	1.0	—	0.43	42	0.04	6
1.2	1.0 water	0.224	275	0.72	2.5	—	0.42	42	0.04	6
1.3	0.2 Na_2SiO_3	0.198	278	0.84	4.0	—	0.46	45	0.07	8
1.4	0.8 water	0.229	280	0.71	5.0	—	0.39	45	0.02	3
1.5		0.349	277	0.78	10.0	—	0.40	49	0.04	5
2.1	1.0 water	0.225	271	0.77	1.0	2.0	0.43	44	0.12	16
2.2	0.2 Na_2SiO_3	0.312	279	0.76	2.5	4.5	0.42	44	0.12	19
2.3	0.02 water	0.267	276	0.87	4.0	7.5	0.53	39	0.15	17
2.4	0.2 $CaCl_2$	0.257	269	0.86	5.0	9.0	0.46	46	0.27	32
2.5	0.6 water	0.244	281	0.85	10.0	18.0	0.43	49	0.20	23

achieved. This was followed by a displacement with water of 1.0 pore volume (V_p) resulting in 39—49% oil recovery.

In the first set of experiments 0.2 V_p of sodium methasilicate slug was injected after the displacement by water and then an injection of 0.8 V_p of water followed. The concentration of the silicate solutions was 1.0×; 2.5×; 4.0×; 5.0×; 10.0×10^{-2} kg/kg with respect to SiO_2.

In the second group of experiments the 0.2 V_p sodium methasilicate slug was followed by a 0.02 V_p water slug and then $CaCl_2$ was injected in the sample in stoichiometric concentration. The excess output, i.e. the difference between the efficiencies of the production methods ΔE_R was 3.4—7.9% with respect to the initial oil in place. In the second group, however, where gels were produced, the value of excess oil reached 15.9—32.2%. The results are collected in Table II.

These results do not allow definite conclusions as to the effect of the concentration of water glass solutions. It appears, however, that the caustic effect decreases recovery while the gel effect increases it within the concentration range 1× and 10×10^{-2} kg/kg SiO_2.

The second set of experiments was repeated with water slugs, separating slugs and $CaCl_2$ slugs of various dimensions as well as at concentration ratios differing from stoichiometric. The excess outputs ΔE_R varied between 16 and 40%. However, apart from a tendency of the excess outputs to relate to the quantity of the precipitate produced in the sample, no quantitative correlation could have been established between the parameters of the sample and of the displacement, and the excess output.

As a matter of fact, this kind of correlation had not been expected for the reasons discussed above, since the properties of pore structure which determine the spatial localization of the residual oil, the micro-distribution of the flow velocity of the displacement phase and the mechanism and effect of gel forming on the active pore system in the macrophysically homogeneous porous medium are not known.

The results permit the conclusion that surface tension and mobility reductions can mobilize that part of the residual oil which is in the main flow channels of the displacement phase, i.e. the dispersed fraction of the residual oil. This might be due to the fact that the surfactants cannot reach the surface of separated oil spots, and the displacing phase keeps on flowing through the swept-out channels.

Displacement tests on long cores

To determine the effect of pore structure modification, displacement tests were performed on three long cores in connection with a displacement programme using polymers and surfactants. The experimental device is discussed

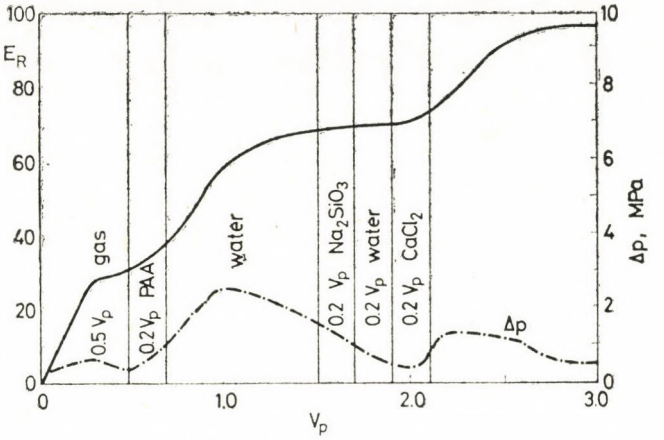

Fig. 2. First displacement experiment on long cores

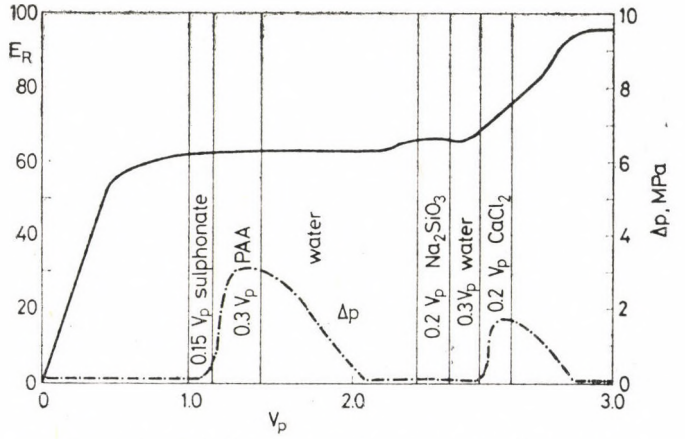

Fig. 3. Second displacement experiment on long cores

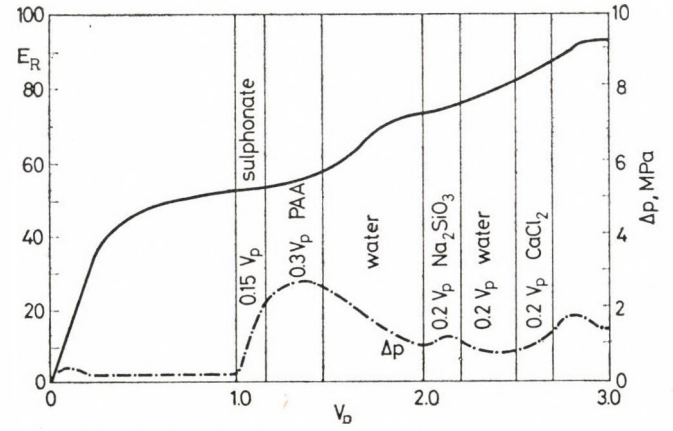

Fig. 4. Third displacement experiment on long cores

Table III

Data of displacement experiment on long cores

Length			1.2 m
Cross-section			$0.02 \cdot 0.02$ m²
Temperature			368 °K
Pressure			20.0 MPa
ϱ_0			823.7 kg/m³
μ_0			$3.3 \cdot 10^{-4}$ Ns/m²
Displacement fluids			
Gas	94% CH_4		
Water	$2.0 \cdot 10^{-3}$ kg/kg NaCl solution		
PAA 10^{-3} kg/kg PAA solution	$\sigma_{ow} = 1.2 \cdot 10^{-2}$ N/m; $N_c = 7.7 \cdot 10^{-7}$		
P-SULF $8 \cdot 10^{-2}$ kg/kg petroleumsulphonate solution;	$\sigma_{ow} = 6.0 \cdot 10^{-5}$ N/m; $N_c = 1.5 \cdot 10^{-4}$		
Na_2SiO_3 0.1 kg/kg (with respect to SiO_2);	$\sigma_{ow} = 2.0 \cdot 10^{-4}$ N/m; $N_c = 4.6 \cdot 10^{-5}$		
$CaCl_2$ stoichiometric solution			
Number of experiment	I.	II.	III.
Porosity	0.31	0.29	0.29
Permeability, $\mu m^2 \cdot 10^{-3}$	177	198	192
S_w	0.19	0.25	0.257
R_{si}, m³/m³	42	—	—

in more detail by Milley et al. (present issue). The main parameters and results of the displacement experiment are summarized in Tables III and IV.

The displacement processes are illustrated in Figs 2, 3 and 4. Apart from the recovery curves it is worth noting the shape of the depression curves. The first increase in depression follows the injection of the polyacrylamide slug (PAA), the second one comes after the $CaCl_2$, i.e. the forming of precipitate. The second increase is about half the first one.

The capillary number calculated for sodium silicate slug by Moore—Slobod's method (1956) was $4.6 \cdot 10^{-5}$ in all three experiments. In the experiment with petroleum sulphonate the capillary number amounted to $1.5 \cdot 10^{-4}$ and in that with polymer to $7.7 \cdot 10^{-7}$, using interfacial tensions and viscosities of the petroleum sulphonate and of the polymer slugs, respectively.

According to the conventional theory of oil displacement based on viscous-capillary forces, petroleum sulphonate displacement would be expected more efficient. Displacement results, however, do not support this view, indicating the need to improve the theory and the importance and feasibility of pore structure modification.

Conclusions

In homogeneous real rocks, after displacement with water, a considerable part of the residual oil is separated in the form of oil spots with dimensions several times the average pore size. The spots can be mobilized by blocking

Table IV

Displacement experiment on long cores

N°	Injected		Oil production cm³	E_R, %
	Fluid	V_p		
1.	Gas	0.5	62.5	30.6
	PAA	0.2	80.5	70.3
	Water	1.3		
	Na_2SiO_3	0.2		
	Water	0.2	49.6	94.3
	$CaCl_2$	0.2		
	Water	0.5		
2.	Water	1.0	144.5	60.8
	P-SULF	0.15		
	PAA	0.3	14.9	67.1
	Water	1.0		
	Na_2SiO_3	0.2		
	Water	0.2	78.3	96.0
	$CaCl_2$	0.2		
	Water	0.6		
3.	Water	1.0	85.9	52.1
	P-SULF	0.15		
	PAA	0.30	30.6	70.6
	Water	0.65		
	Na_2SiO_3	0.2		
	Water	0.3	36.4	92.7
	$CaCl_2$	0.2		
	Water	0.6		

the main flow channels in the porous medium and by diverting the displacement phase through these spots.

Decrease of the capillary forces and increase of the viscous forces can significantly reduce residual oil saturation only in case of an extremely high capillary number. If the pore structure is also modified, even a moderate reduction of surface tension or viscosity increase can be effective.

Precipitates produced *in situ* in the porous medium by subsequent injection of sodium silicate and calcium chloride solutions are suitable for the modification of the pore structure. At the same time, viscosity of the sodium silicate solution is greater than that of water and because of its high pH it has a caustic effect. These anorganic chemicals are not sensitive to temperature, can only be damaged by multivalent ions, they are available in great quantity at low prices; consequently they seem to be very suitable for the purposes of tertiary oil recovery.

REFERENCES

CAMPBELL, T. C. 1977: A Comparison of Sodium Orthosilicate and Sodium Hydroxide for Alcaline Waterflooding. SPE Preprint 6514

CHANTENEVER, A.—CALHOUN, I. C. IR. 1952: Visual examination of fluid behaviour in porous media. Part I. *Trans. AIME*, 195, 149—156.

DULLIEN, F. A. L. 1975a: Effects of Pore Structure on Capillary and Flow Phenomena in Sandstones. JCPT p: 48—55

DULLIEN, F. A. L. 1975b: New network permeability model of porous media. *Am. Inst. Chem. Engl. I*, 21, 299—307.

FATT, I. 1955: Network model of porous media, I.—III. *Trans. AIME*, 207, 144.

FRONING, H. R. 1968: Plugging Highly Permeable Zones of Underground Formations. US. Patent, 3,386,509.

MCAULIFFE, C. D. 1973: Crude Oil in Water Emulsions to Improve Fluid Flow in an Oil Reservoir. JPT p. 721—726.

MILLEY GY.—WAGNER O.—JÓNAP K.—BUKTA B.—LÖVEI J. (1982): Long core model apparatus for the laboratory investigation of oil recovery processes. *Acta Geod. Geoph. Mont. Hung.*,17 415—436.

MOORE, T. F.—SLOBOD, R. L. 1956: The Effect of Viscosity and Capillarity on the Displacement of Oil by Water. Prod. Monthly, 20, No. 10, 20—30.

REED, R. L.—HEALY, R. N. 1977: Some Physicochemical Aspects of Microemulsion Flooding. A Review in Improved Oil Recovery by Surfactant and Polymer Flooding. Academic Press Inc. N. Y.

SAREM, A. M. 1974: Secondary and Tertiary Recovery of Oil by MCCF Process. SPe Preprint 4901

SAREM, A. M. 1975: Mobility Controlled Caustic Flooding Process for Reservoirs Containing Dissolved Bivalent Metal Cations. US. Patent 3,971,452
Mobility Controlled Caustic Flooding Process for Highly Heterogeneous Reservoirs. US. Patent 3,871,453 (1975)

SCHEIDEGGER, A. E. 1974: The Physics of Flow throughn Porous Media. University of Toronto Press.

STEGEMEIER, G. L. 1977: Mechanisms of Entrapment and Mobilization of Oil in Porous Media in Improved Oil Recovery by Surfactant and Polymer Flooding. A Review in Improved Oil Recovery by Surfactant and Polymer Flooding. Academic Press, Inc. N. Y.

WELDES, H. H.—LANGE, R. K. 1969: Properties of Soluble Silicates. *Industrial and Eng. Chemistry*, No. 4, 29—24.

Acta Geodaet., Geophys. et Montanist. Acad. Sci. Hung. Vol. 17 (3—4), pp. 415—436 (1982)

LONG CORE MODEL APPARATUS FOR THE LABORATORY INVESTIGATION OF OIL RECOVERY PROCESSES

GY. MILLEY—O. WAGNER—K. JÓNAP—B. BUKTA—J. LÖVEI

PETROLEUM ENGINEERING RESEARCH LABORATORY OF THE HUNGARIAN ACADEMY CES

Model equipment capable of holding 120-cm-long rock samples for pressures up to 30 MPa and temperatures up to 120 °C has been developed to model underground fluid flow phenomena in oil recovery, and to provide a means to study the relevant theoretical problems. Since a great amount of data has to be recorded during long experimental periods in the model equipment, data acquisition has been solved by a microprocessor controlled data logger.

The model equipment its main operational parameters and the microprocesssor data logger are discussed in detail. This technical information will hopefully prove beneficial for research workers dealing with similar experimental problems.

Symbols

c	saturation measured by capacity measurement
k_w	permeability to water
L	length
p_1	inlet pressure
p_2	outlet pressure
p_3	pressure in the annular space of the cell
Δp	pressure drop along the rock sample
Σq_{inj}	total injected amount of fluid
q_0	flow rate of oil
q_w	flow rate of water
T	temperature
V_p	pore volume
Φ	porosity

1. Introduction

Flow phenomena in porous media are essentially physical and physicochemical processes that cannot be investigated in their original environment. Their study is essentially a scrutiny of answers of the investigated system on questions imposed by the experimental tools. The researcher has to put his questions in a strict form determined by the initial and boundary conditions, his tool of inquiry is the model equipment itself.

In developing secondary and tertiary oil recovery methods, numerous questions have to be answered apart from the information supplied by the natural system during prospecting. These investigations, naturally, are concerned with specific concrete questions, which as a rule, do not require general information about the details of the porous system and the fluids flowing in it. For this kind of investigation only a natural prototype could be used as a model. If investigating hydrodynamic phenomena in a given porous system

(petroleum reservoir), generally specific questions with narrow scope are formulated. Correspondingly, specific answers are expected with varying accuracy requirements, with the least possible investment and within as short a time as possible.

Like in all ways of scientific investigation, also in reservoir engineering modelling the researcher has to set dual aims: first he has to find the causes of the phenomena to be able to guess — at least approximately — the consequences of any of his interferences. From among the two possible research alternatives (a) the mathematical analysis appears more suitable. However, even an exact analysis can only furnish solutions for simple reservoir geometries and it cannot help to understand the effects of chemical and physico-chemical processes which continuously and rapidly gain in importance. At the same time, results obtained by purely mathematical tools do not always provide suitable solutions for engineering. Another possible method is (b) to reproduce the investigated phenomenon under experimental conditions in laboratory scale equipment, substantially differing from the natural system in its dimensions.

Without analyzing the laws of similarity in detail, it should be obvious that the geometrical, kinematic and dynamic conditions of similarity mainly apply for the macroscopic properties. Microscopic properties and chemical and physico-chemical processes playing determinant role in secondary and tertiary petroleum recovery, can only be modelled up to a limited degree if at all. This statement, naturally, reflects the limits of our present day knowledges and sets the further aims of theoretical and practical research in modelling. Apart from developing model equipments, promising efforts have been made also in this field by the Petroleum Engineering Research Laboratory of the Hungarian Academy of Sciences.

It has to be emphasized that the recently carried out model experiments serve first of all for the study of important partial problems instead of general laws. This restriction is mainly due to the inherent theoretical problems of modelling and not to the standards of our available experimentaltools.Theoretical problems of modelling are also reflected by the compromises incorporated in the laboratory models. If e. g. a displacement model is constructed on the basis of modelling laws, the fluid viscosities, front velocities and rock permeabilities must be different from those of the prototype, i.e. both the fluids and the porous medium are replaced by models. While this solution provides suitable laboratory conditions for the experiments, we have to admit the substantial deviations from the laws of similarity since the important microscopic and physico-chemical properties cannot be transferred from the prototype to the model. For example, the basic influence of the natural surfactants of crudes on the wettability character of the reservoir rock obviously cannot be successfully "fitted" by the model.

Because of these problems, those modelling methods have become more widespread for the study of certain details of production processes that applied original reservoir rocks and fluids at reservoir temperature and pressure. These considerations suggest that empirical methods should be used in drawing conclusions for the natural system from model experiments and in analyzing the processes in natural systems. Hopefully, this problem will be circumvented by continuously developing model theory and the experimental techniques.

Secondary and tertiary oil recovery methods require an analysis of the following specific phenomena and processes by laboratory model experiments:

— flow behaviour of one- and multiphase, one- and multicomponent, fluids;
— mobility and stability conditions of fluid slugs applied in flood systems;
— effect of the viscosities of the fluid phases and of the fluid-fluid interfacial tension on flow behaviour;
— fluid mobility problems, especially how to fit the mobilities of the flood systems to that of the displaced oil or brine;
— effect of chemical methods and chemical additives increasing sweeping efficiency on the oil-water-rock systems;
— development, distribution and further decrease of residual oil saturation by reducing the surface energy and optimizing the mobility conditions;
— tendencies of pressure build-up processes in various flooding systems;
— placement and mobility conditions of viscous slugs produced *in situ* or by the injection of high-viscosity fluid phases to temporarily or finally close the already watered pore channels;
— beneficial or non-beneficial effects on the displacement processes of the disperse phases produced in course of multi-phase flow.

This list of research tasks gives naturally only a general outline of the field to be investigated. Details which might be important and have not been emphasized here can be attached to one or another of the groups listed.

The paper describes a long core model equipment designed for the study of the mentioned fields individually or several of them a combined way.

2. Experimental

The block diagram in Fig. 1 illustrates the units of the technological scheme and its functions.

As seen, the model is one-dimensional (linear). The auxiliary units have been designed so as to ensure the most frequent values of reservoir pressure, temperature and fluid velocities, up to the following limits:

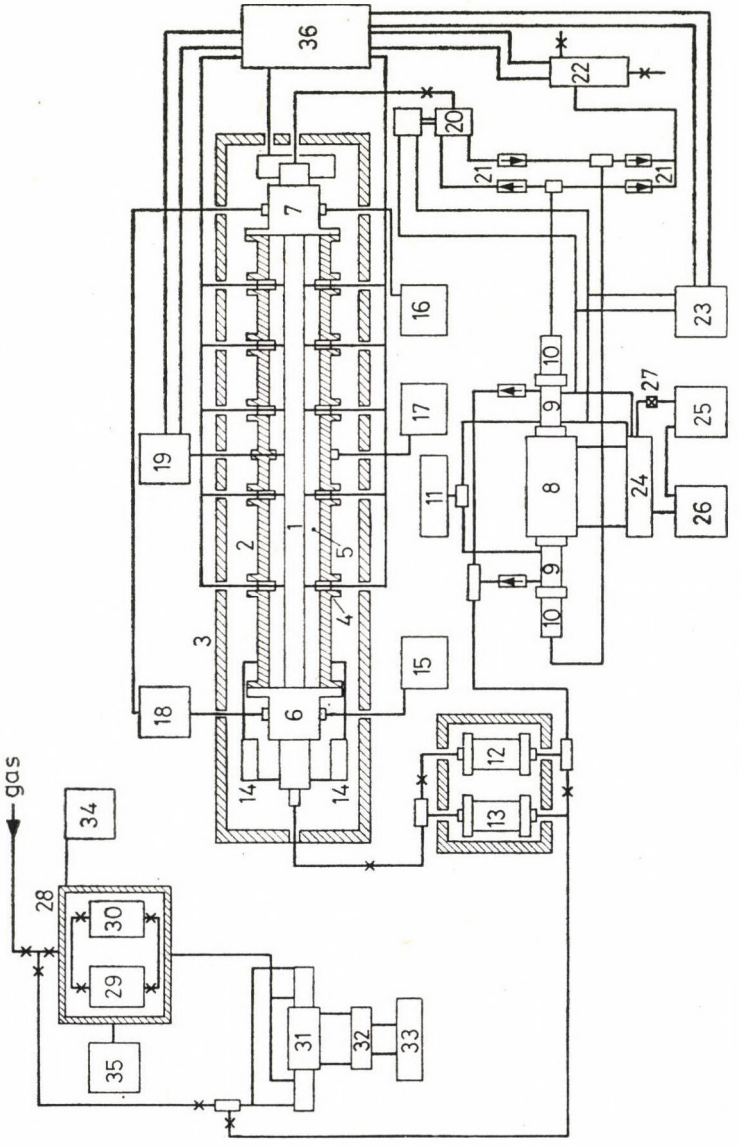

Fig. 1. Layout of the model equipment

maximum experimental pressure	30 MPa
maximum experimental temperature	120 °C
injection rate at the experimental pressure and temperature, continuously adjustable	1—100 cm^3/h.

The operation of the equipment will be explained in connection with a water drive experiment. The main steps of the experiment are

1. modelling of the oil accumulation process, and
2. modelling of the water drive.

Let us analyze a gas-free system for sake of simplicity. The modelling of oil trapping is performed as follows:

— saturation of the appropriately prepared rock sample with water;

— displacement of water by the experimental oil phase.

The aim of this process is to adjust the initial saturation state in the reservoir model, an oil drive is used to adjust the saturation of irreducible water and the initial oil saturation. Generally a water-oil saturation is required but there are cases when a low saturation of irreducible water has to be achieved (less than 30% of V_p) which is done by water-oil-oil saturation method. As an essential part of this method first the high-viscosity distillation cut (above 200 °C) is injected into the water saturated core. Injection rate is first slow, then gradually increased. When oil saturation reaches the intended initial value, the oil phase is removed by injecting original crude oil.

Without further lingering at the details of adjusting the initial state, the main steps of the experiment will be as follows (Fig. 1):

— the water and oil to be used in the experiment are fed into high-pressure power cylinders 12 and 13;

— after starting the compressor unit of the equipment, gear pump 25 pumps hydraulic fluid into the primary cylinder 8 of the compressor through hydraulic control unit 24. The pressure to be adjusted or experienced in this circuit follows the pressure adjusted or experienced on the secondary side. Its value usually does not exceed 1.2—1.4 MPa. By moving the piston of the primary cylinder into one direction, one of the high-pressure cylinders on secondary side 9 operates in discharge stroke, the other in suction stroke. Thus they pump the fluid from tank 11 to the compressor-side of the pistons in power cylinders 12 and 13. The fluid is usually brine but because it is separated, it can be any other fluid;

— from the model-side of power cylinder 12 the saturating water enters rock sample 1 through inlet head 6 of cell 2. Then it leaves the rock sample through outlet head 7 and enters separator 22 through electromagnetic valve 20 as directed by check valves 21. On its way it passes between the plates of saturation detectors 4 that give electrical

signals proportional to water saturation towards the appropriate channel of microprocessor data logger 36. The printer of the data logger (discussed in the section dealing with the electronic unit) prints out at required times the saturation values. Saturation with water is carried on until all five saturation detectors indicate non-varying values;

— in the final phase of saturation by water, we measure the model permeability to water at the flow (injection) rate that will be applied during the experiments, adjusted by control valve 27. The flow rate is generally around 0.5 m/day, it is determined from the number of strokes per unit time (counted by stroke counter 23) and from the known stroke volume. The pressure loss for the calculation of permeability is provided by pressure-differential transducer 18 for the appropriate channel of the microprocessor data logger;

— next, the temperature and the pressure of the experiments is adjusted by closing the valve between outlet head 7 and cross valve 20 and by injecting water into the model until the required pressure value is indicated by the data logger and, simultaneously, by the printer. Temperature is adjusted and controlled by air thermostat 3 whose 2 kVA electric heating unit is placed into the centre, to the axis of the cell. A dual impeller electric ventilator, operating in positive pressure system and placed under the heater, circulates hot air in the thermostat and mixes it with cold air in proper proportion. A thyristor unit controls the operation of the electric heater to compensate for heat losses. The experimental temperature is measured and fed to the microprocessor data logger by temperature transducer 19;

— in the inner annular space of cell 2 between the rock sample and the cell case, which contains rock 1 in synthetic resin and is filled with oil, the same pressure builds up than that measured by pressure transducer 16, this happens through the follow-up pressure regulators attached to the inlet head and the annular space. This ensures for the rock sample to be surrounded by a pressure identical to the actual one, that is the pressure gradient across the synthetic resin layer never exceeds the depression along the length L of the rock sample and it is directed toward the axis of the model rock so that there is no danger for the resin layer to burst;

— the experimental oil phase is injected in the next step, this starts by opening the valve at the outlet end. During oil injection the absolute value of the inlet pressure is measured by pressure transducer 15, the pressure loss along the length L by depression transducer 18, and the outlet pressure i.e. the adjusted pressure of the experiment

by pressure transducer 16. Pressure data are fed into the microprocessor data logger and printed at certain intervals. Signals sent by the saturation detectors to the microprocessor indicate the decreasing water saturation i.e. an increasing oil saturation by decreasing numerical values.

The reliable maintenance of the experimental pressure is ensured by the specially designed compressor unit. High-pressure draining pumps 10 take the fluids off from the system at precisely that flow rate q, as they are injected into the rock sample by high-pressure pumps 9. The stroke volumes of pumps 10 are equal to those of pumps 9. Isolation from the low-pressure space and separation of the discharged fluid samples and the automatic flow rate measurement is ensured by the electromagnetic servo valve (cross valve) 20, by the appropriately connected system of check valves 21, as well as by flow meter and separator 22.

Having adjusted the initial oil saturation, the reservoir model is ready for the displacement experiment. The process essentially consists of injecting a given volume of brine (expressed in terms of V_p) into the rock sample, while the microprocessor data logger records the following data:

pressure of the experiment
- outlet pressure
- inlet pressure
- depression

temperature of the experiment,
time after start (day, hour, minute),
saturation data at 5 points of the core,
flow rate data, oil-water amount,
cumulative injected fluid volume,
number of strokes.

When modelling a secondary recovery process by the displacement experiment, after the water drive the above injection operations have to be carried out with the selected displacement media, in a pre-determined order and with pre-determined slug sizes.

For experiments with gas slugs or dissolved gases, the model equipment has to be completed with supplementary units 28—35 shown in Fig. 1. The high-pressure equilibrium cells 29 and 30 in thermostat 28 are used to adjust the required gas saturation of the fluid phases. The independent high-pressure fluid compressor consisting of units 31—33 adjusts the required pressure and ensures the suitable mixing of the fluid and gas phases. The adjustment of the fluid-gas equilibrium is performed the following way: after reaching the required pressure of the water, oil and gas phases in cells 29 and 30, compressor 31 takes out the oil or water from the lower part of the equilibrium cells by switching the valves of the saturation unit to the adequate position. The fluids are then pumped back with the high-pressure side to the suitable equi-

librium cell. The upper cover of the equilibrium cells ensures for the injected fluid to enter the gas space of the cells in the form of fine spray. Thus the equilibrium can be achieved extremely quickly, approximately in 2—3 hours, depending on the saturation value, gas quality and fluid amount and on pressure and temperature. Similarly, compressor 31 pumps the phases saturated with gas into the model equipment, directly to the inlet end of the rock sample or to power cylinders 12 and 13. In this latter case compressor 8 injects the fluids to the rock.

Figure 1 shows only the most important units, some auxiliary tools and equipments have been omitted from the layout. The discussion of the whole equipment would be beyond the scope of this study, only the most important experimental units will be touched upon. They are

a) a high-pressure cell with variable length;

b) a high-pressure four-stage fluid compressor, suitable for simultaneous fluid drainage;

c) a microprocessor data-logger.

Before discussing the experimental units, a few words on the model rock, i.e. on the medium of the experiment would be in order. Core samples of natural rock exceeding 120 cm or enabling to compose this length of two pieces, are very rare to obtain. Also approximately similar rocks are never available for comparative repeated experiments. It seemed, therefore, reasonable to develop the manufacturing technique of synthetic, consolidated rock models with parameters (k_w, Φ, specific surface) close to those of natural sandstones. The thermal consolidation method of the Petroleum Research Laboratory of the Hungarian Academy of Sciences enables us to produce rock models even with clay content and adjustable wettability. The main obstacle to serial experiments has thus been removed, even though the manufacturing of model rocks still has to be improved both in quantitative and qualitative sense.

2.1 High-pressure core holder

Model experiments at high pressure and high temperature require core holders that enable the researcher to carry out many kinds of measurement, they should not be too heavy and should be easy to install. Apart from meeting the pressure and temperature conditions, the design of the cell must allow for rock samples of 1.2 m length, it also has to ensure place for samples with length different from that, usually shorter but sometimes greater. This requirement coincided with those of easy assembling. Electric connection wires also had to lead out from the high-pressure space and pressure tapping places had to be fitted to the equipment. Inlet and outlet heads were required to allow phase permeability measurements, apart from the displacement experiments.

Figure 2 illustrates the cross-section of a high-pressure core holder that meets these requirements. Rock sample 6 is bedded in synthetic resin and is connected to inlet head 1 through sleeve 7 fitted into the borehole of the inlet head. Fluid spaces are isolated by 0-rings 8. The inlet end of the core touches mixing piece 5 also fitted by a 0-ring gasket to the inlet head. 0-ring gaskets also compensate for thermal dilatations during temperature build-up. The inlet head is equipped with pressure tapping points for the manometer, depression meter, for the follow-up pressure regulators and for the inlets of the fluids used in the experiments. The mixing piece is made of high-permeability synthetic sandstone or stainless steel-sponge. The cell itself consists of separate sections 2 connected by flanges. Five connecting rings 3 ensure pressure tapping and places for the electric connection leads, they also simplify assembly. The cell body built of small units also enables the researcher to construct cells of uniform strength for rock samples of various lengths. The annular space between the cell case and the synthetic resin cover of the rock sample is filled with oil to ensure the pressure necessary on the curved surface of the sample and a uniform heat transfer. The cell sections are of different sizes, their length reduces towards outlet head 4 which allows special observations near the out-

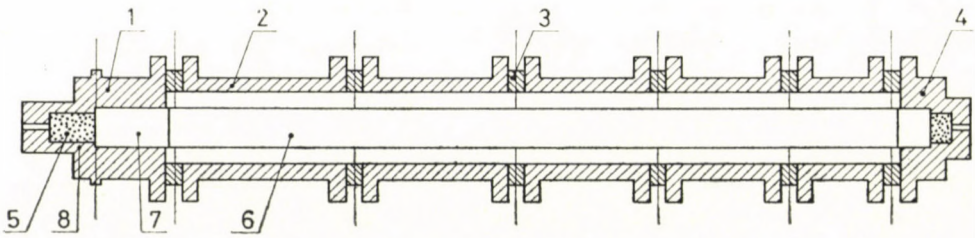

Fig. 2. High-pressure core holder

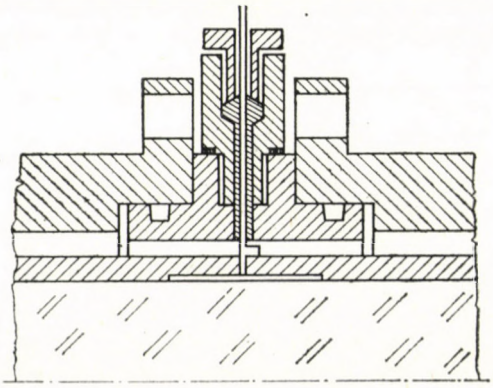

Fig. 3. Cable outlet for capacity measurement

let end (capillary end-effect investigation, measurement of local depressions during the flow of viscous slugs etc.). The connecting rings are fitted with 0-rings that provide flexible joints and leakage-proof sealing.

The connecting rings are equipped with stubs for pressure tapping pipes and electric cables as illustrated in Fig. 3.

Other stubs on the connecting rings ensure access for the cables of the thermoelement measuring cell temperature, for the cable of the cell pressure transducer and for the pipes allowing fill-up with oil and compensation for the dilatation due to pressure build-up during the heating-up period.

A special version of inlet head 1 contains a power cylinder in its front part which stores 0.1 or 0.2 V_p (20—25 and 40—50 cm^3, respectively) of the displacement fluid. This solution relieves power cylinders 12 and 13 illustrated in Fig. 1 and avoids the use of an outside thermostat.

2.2 High-pressure fluid compressor

One of the most important units of the model equipment is the fluid compressor that ensures the required pressure for the experiment and the fluid injection at the pre-determined rate. The compressor has to meet the following requirements:

— steady fluid flow rate under pressures up to 30 MPa;
— reliable stepless variation of the flow rate in the range of extremely small values (0.5—10 cm^3/h);
— it has to ensure high injection rates (10—100 cm^3/h), with stepless regulation, as often required by saturation operations;
— it has to drain fluid from the rock sample at the outlet end at the experimental pressure and to pump the fluid to the separator after selecting the sample from the high-pressure system.

Since fluid compressors meeting these requirements are not commercially available, they have been designed, developed, and manufactured by the Petroleum Engineering Research Laboratory of the Hungarian Academy of Sciences. The operational principle of the fluid compressor used in the experiments is illustrated in Fig. 4. Obviously, various industrial or laboratory compressors can be designed on the same principle, this study only discusses the laboratory scale equipment built for the pressures and temperatures of our experiments. The hydraulic motive fluid is supplied by a Sundstran (Sweden) gear pump installed in point A and equipped with a magnetic valve. The motive fluid enters hydraulic control unit consisting of magnetic valves 9—12 through regulating valve 13. Let us assume that the piston of primary cylinder 1 moves towards the right-hand side end position (cf. Fig. 4). Valves 12 and 10 are now open, from among the valves 9—12. The low-pressure (0.6—1.2 MPa)

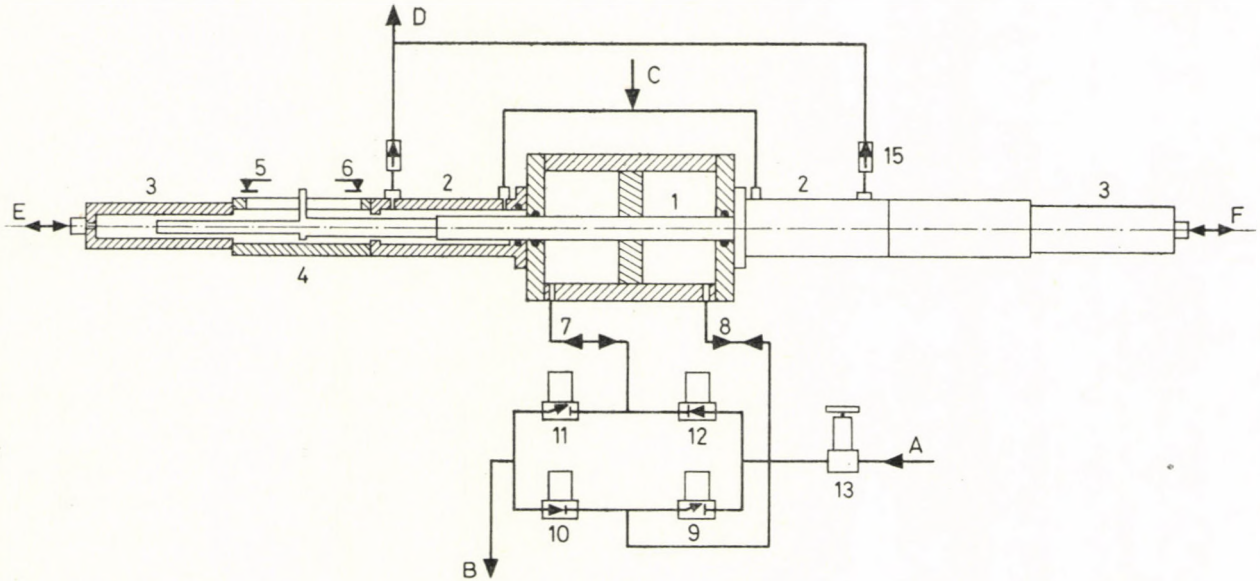

Fig. 4. Fluid compressor

motive fluid enters primary cylinder 1 behind the primary piston through valve 12 and stub 7.

The fluid in front of the piston of the primary cylinder is pushed through stub 8 to the point between valves 9 and 10 of which 9 is closed and 10 is open. The fluid flows therefore through pipe *B* to the fluid reservoir from where it enters the suction pipe of the gear pump. While the primary piston moves to the right, the fluid in the right-hand side of high-pressure cylinder 2 flows through a check valve to pipe *D* which, in turn, leads to the inlet head of the model. The pressure of the fluid leaving cylinder 2 corresponds to the ratio of the cross-sections of the primary and secondary (high-pressure) pistons. If $F_1 : F_2 = 30$, a primary pressure of 1 MPa is increased to 30 MPa. Meanwhile the piston of left-hand side cylinder 2 moves towards the suction stub and before reaching the right-hand-side end position it sucks the fluid from pipe *C*. At this direction of motion, positive pressure is maintained in the right-hand side cylinder 3 and the fluid sample taken at the end of the model in the previous cycle is pumped to the separator. Meanwhile, suction takes place in the left-hand side cylinder 3 and fluid is drained at the outlet end of the model. The stroke volumes of the plungers in high-pressure cylinders 2 and 3 are identical, consequently, cylinders 3 drain fluid amounts equalling those pumped through high-pressure side 2. The experimental device can this way be protected against extremely harmful pressure surges, harmful fluctuations of the depression and backward pressure momenta. When reaching the right-hand side end position, a signal is sent from terminal switch 6 to the electronic unit which opens valves 9 and 11 and closes valves 10 and 12 by simultaneous control commands. At the same time, a control command is sent to the electromagnetic servo valve as well which is the most important member of the draining system (cf. Fig. 1). As a result, the draining direction is transferred to right-hand side cylinder 3. The motive fluid flows now in the primary circuit through valve 9 to stub 8 and moves the plunger of the primary cylinder to the left. At the left-hand-side end position the change of direction is performed by terminal switch 5. Taking into account that the gear pump in the primary circuit pumps the driving fluid at a steady rate and a steady pressure, the change of direction does not cause pulsation in the secondary pressure, because it is performed instantly, without accelerating and decelerating sections.

As seen in Fig. 4, the compressor simultaneously operates three independent fluid circuits which are, however, in a very strong hydraulic connection. These circuits are: the low-pressure primary circuit, the high-pressure secondary circuit and the high-pressure draining circuit at the outlet end. If the power cylinder of the secondary circuit is in action, the experimental fluid flows in the fourth circuit separated even from the secondary circuit. These separation possibilities render the whole system extremely versatile, which is beneficial first of all, when aggressive fluids and gases are applied in the experiments.

One of the main advantages of this compressor type is its low energy consumption. The automatic fluid compressors applied presently are capable of producing 100 MPa final pressure with 120 VA driving power.

3. Microprocessor-based programmed data-logging system

As indicated in the previous discussions, a great number of physical parameters have to be measured and stored during the experiments with the long-core model equipment. These data are essential in evaluating the experiments, thus a data logger was required to meet the demands. In view of the parameters to be measured and the measurement tasks it was obvious that the commercially available devices are expensive and cannot be used without modifications.

The long-core model experiment can be regarded as a measurement system of medium complexity, therefore it was decided to develop and manufacture a data logger specially designed for our experimental purposes. An estimation of the requirements (communication with the system, collecting the measured data, performing calculations, providing various signals and commands and recording the results) showed that the task can be satisfactorily solved by a microprocessor (μP) device. The development of the data logger was based on the INTEL 8080 μP family being very popular in μP-technique. The circuit reserves and easy programmability of this system allows for the further development and extension of the data logger according to the accumulated experimental results.

The data logger is a purpose-oriented device of simple construction and easy accessibility. Its operation does not need special skills and knowledge in digital measurement and μP techniques. Construction and operation of the data logger and experiences acquired during its application will be discussed in the following section.

3.1 Measurement technique

As seen from the operational principles of the model equipment illustrated in Fig. 1, the following physical parameters are measured:

p_1	inlet pressure (pressure transducer),
p_2	outlet pressure (pressure transducer),
p_3	pressure in the annular space of the cell (pressure transducer),
Δp	pressure drop along the rock sample (pressure transducer),
T_1, T_2, T_3	temperature values (sensor AD 590),
c_1—c_5	saturation values measured through capacity measurement,

Σq_{inj} total injected amount of fluid determined by counting compressor strokes,

q_o and q_w flow rates (determined by flow measurement c_6 and c_7).

The electric signals of the pressure and differential pressure transducers are fed through a standard cut-off resistance to the data logger. The outlets of the temperature sensors have a sensitivity of 1 μA/K. The signals at this outlets are cut off by very accurate resistances and converted into signal changes of 1 mV/K and are fed into the input multiplexer. The schematic layouts of the analogue input channel selector and the A/D converter are illustrated in Fig. 5.

The signals of the sensors and transducers are forwarded through the two-point analogue multiplexer and buffer amplifier to the A/D converter whose outlet is connected to the μP-system.

Control signals for the multiplexer and for the A/D converter are also supplied by the μP-system. A three-point dry Reed relay was used as an analogue multiplexer, the A/D is an ADC 1100 type, 11-bit A/D converter of Analog Devices.

The greatest technical problem in capacity measurement was the fully independent measurement of the discrete capacity values. This problem has

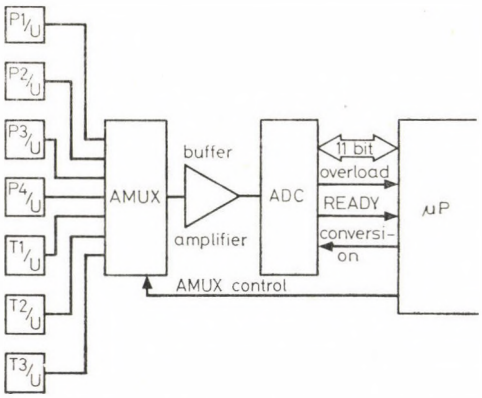

Fig. 5. Analogue input channel selector and A/D converter

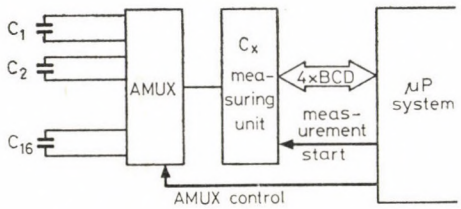

Fig. 6. Connection of capacity measuring points

been solved by a measuring point selector using a two-point Reed relay which enabled the analogue multiplexer card and the capacity measuring point selector card to have identical construction providing considerable advantages for the whole system.

The capacity measurement was reduced to time measurement. The outlet pulse width of a monostable multivibrator (MMV) with a good temperature coefficient is measured by a quartz-stabilized high-frequency signal, the signal is led to a counter circuit, and discrete values being proportional to the capacity values connected to the input to the MMV, are forwarded to the μP-unit (Fig. 6).

3.2 Digital signal processing unit (μP system)

3.21 *Hardware*

The digital signal processing unit has the following functions:

— receiving the digital values of the input parameters;
— adapting the analogue input signals to the actual physical parameters (parametrizing);
— providing measurement time during the model experiment;
— communication with a special control unit;
— comparing the measured parameters to the corresponding maxima and minima and providing alarm signal (correction command);
— automatic self-control possibility.

The μP-system has been constructed according to the layout of Fig. 7 using an INTEL 8080 CPU and the appropriate circuits.

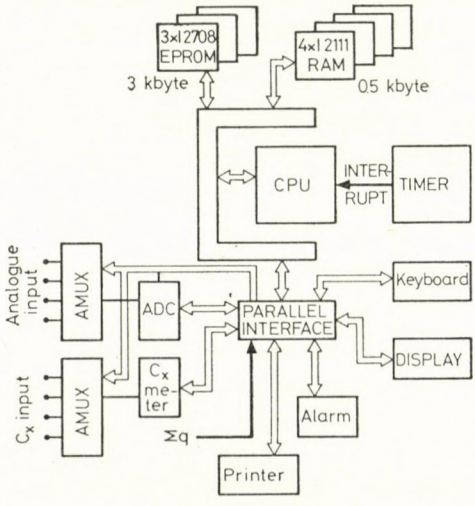

Fig. 7. Microprocessor system

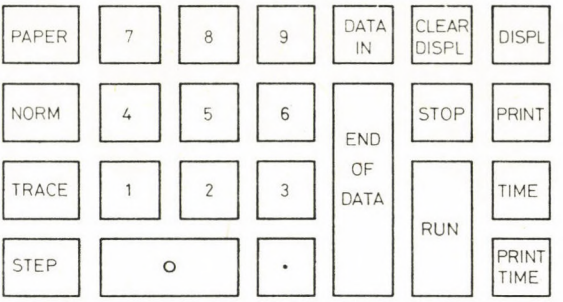

Fig. 8. Layout of the KEYBOARD. PAPER = paper forwarding; NORM = normal program running; TRACE = waiting for the NORM or STEP programs; STEP = step by step program execution; DATA IN = setting minima and maxima; END OF DATA = end of minima and maxima; DISPLAY = determining the measuring point to be displayed; CLEAR DISPL = clearing the value on the display; STOP = stopping the program; RUN = running the program; TIME=entering correct time; PRINT TIME = setting the printing interval; PRINT = entering measuring points for the measurement

The address and data supplied by the CPU unit, and the control signals provided by the system controller, are forwarded to the memory and to the parallel interface. The A/D converter and the digital capacity meter are connected to the input of the parallel interface I 8255. The digital timer counts the 1-minute time base from the signal of a quartz-stabilized oscillator. If the time base reaches the INTERRUPT of the CPU, its operation is interrupted. The INTERRUPT routine ensures that the actual time is updated by repeated additions to the correct initial time adjusted at the beginning of the measurement. Because of the relatively long time (20—40 days) and the character of the measurement, a one-minute accuracy suffices. A special easy-to-handle KEYBOARD was designed for communication purposes with the system. Servicing of the KEYBOARD built of 4×7 matrix push buttons is performed by the μP system through the interface circuit. The layout of the KEYBOARD is shown in Fig. 8.

The data entered on the KEYBOARD also appear on a 6-digit display. The display is built of 7-segment LEDs and is controlled by the interface circuit. The printer is controlled and operated by the digital signal processing unit. The printer controller, separated optoelectronically, is also connected to the interface circuit. Printing operation is performed in the following cases:

— at pre-set times;
— if the difference between the measured capacity value and that measured in the previous step exceeds $\pm 10\%$ (accelerated processes should be investigated in more details);
— if some pre-set minima or maxima are exceeded.

In the latter case printing is performed with a distinctive colour (red). An example for the printout is:

.	.
.	.
18	19 . 87 (MPa)
.	.
number of measuring point	measured value

The ALARM unit produces a warning signal (correction command) if any of the pre-set maxima or minima has been exceeded. A schematic view of the unit is illustrated in Fig. 9. In case of an ALARM signal the outlet of the interface circuit produces the digital signals. Using the four most significant bits of the 10-bit digital-analogue converter (DAC 371—10) four different levels of analogue voltage are obtained. The voltage values of the DAC are led to the voltage-frequency converter HUF 03 and signals of various pitches are produced. The loudspeaker is operated through a driving-amplifier and gives a well perceptible ALARM signal.

The digital signal processing unit, the A/D unit and the capacity measurement unit with the outlet multiplexers, and the printer with the INTERFACE are manufactured as a standard KONTASET system of cards. The system is composed of the following plug-in cards:

1. CPU card
2. Memory card
3. Four AMUX cards (each 8 AMUX)
4. A/D converter card
5. Capacity measurement card
6. ALARM card
7. TIMER card
8. Printer interface card
9. Power supply card

In view of future enlargements, free card places have been left in the instrument box.

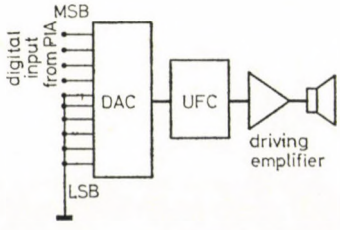

Fig. 9. Schematic layout of the ALARM unit

3.22 Software

The control program of the data logger has been stored in three 1-kbyte EPROMs (INTEL 2708). 512 byte RAM (INTEL 2111) is used for temporary data storage during measurements. The length of the program is only approximately 1.8 kbyte thus the system can be further extended. The program can be functionally divided into four main parts:

a) master program: controls the execution of the programmed measurement algorithm and the communication with the user;

b) KEYBOARD (display) printing module: contains the subroutines serving the KEYBOARD, display and printer;

c) measurement module: contains the subroutines serving the capacity meter, A/D converter, and ALARM signal and the procedure servicing the interruptions of the hardware timer;

d) utility module: contains the utilities serving the three previous groups.

KEYBOARD functions. The user communicates with the running program through the keyboard. The following functions have been defined taking into account the possibilities of the KEYBOARD:

a) running (NORMAL or STEP): enables the operator to run the program normally or step by step; the step by step operation is used for adjusting the initial parameters (pressure, temperature); thus the unnecessary printing during rapid changes can be avoided;

b) timing (TIME): the accurate time can be entered into the program and can be displayed; since the experiments take long time, day, hour and minute have to be defined;

c) printing interval (PRINT TIME): defines the time lapse between two printings (1—99 min). Generally slow processes are investigated by the experiments, therefore a more frequent printing is not necessary. However, if the limits are exceeded or the capacity abruptly changes by 10% or more, the set time interval is overdefined and immediate printing begins;

d) selecting measuring point (PRINT): the number of the measuring point to be activized can be selected. The hardware allows the measurement in 32 measuring points; all this possibility is, however, not exploited in our current measurements. To ensure simple program construction, the measuring points have been grouped as follows:

1—16 capacity (saturation, flow rate)
17—20 pressure
25 total injected fluid (number of strokes)

Only measuring points defined this way are used during running the program.

e) defining display (DISPLAY): the measuring point to be displayed can be defined. The values measured in the selected measuring point can be continuously displayed on the 6-digit display, the first two digits showing the number of the measuring point and the 3rd—6th ones the measured values. If no measuring point is selected the program displays the running time.

f) setting limits (DATA IN): lower and upper limits can be entered to the program, if they are exceeded, an ALARM signal is obtained. Six 4-digit decimal integers can be defined, the first pair define the minimum and maximum for the capacity, the second pair for the pressure, and the thrid pair for the temperature. If they are exceeded or an extreme value is measured, immediate printing and ALARM signal follows.

g) stop program (STOP): suspend the running of the program. Thereafter the operational method can be re-defined or the actual parameters modified. The program only stops when pressing the STOP botton if the running measurement cycle has been completed.

h) start program (RUN): re-start a stopped program.

i) clear display (CLEAR DISP): data on the display are cleared by this function, used during data input. Since the data are also displayed, incorrect data can be cleared and correct ones entered.

j) forwarding the paper (PAPER): the paper of the printer can be manually forwarded. The command is only functional if the program is not running; within a program the paper is controlled by printing instructions.

Testing

When starting a program, the hardware is checked by the following tests:

— DISPLAY test: checks the display digits by displaying running 8 characters;

— PRINTER test: checks the printer by printing 9999 for measuring point 1;

— analogue MULTIPLEXER test: selects each measuring point once on the analogue multiplexer cards (successful selections are indicated by flashing LEDs);

— acoustic ALARM test: sounds warning signals in the ALARM unit corresponding to each output bit combination.

Measurement

The measuring points are cyclically sampled during the experiment. An analogue multiplexing with a Reed relay in the first step, this precedes the starting of the capacity meter and the A/D converter (ADC 1100) measuring pressure and temperature. After switching the Reed relays the program com-

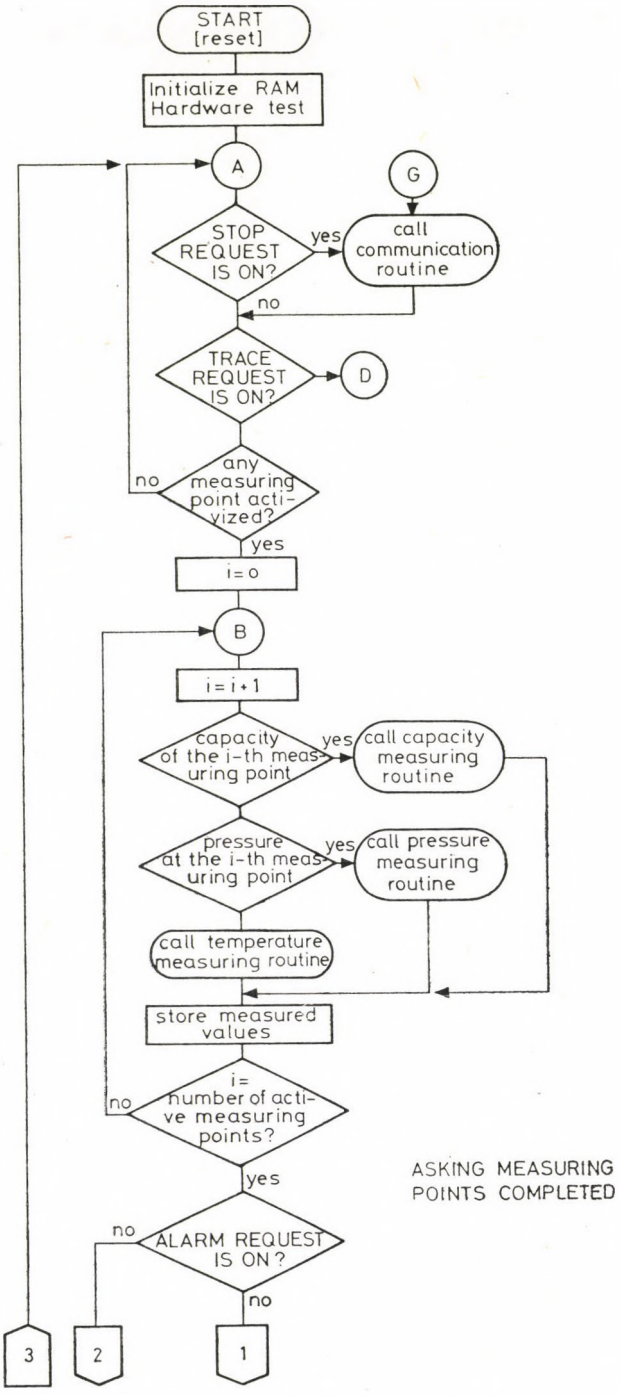

Fig. 10a. **Flow chart of the master program**

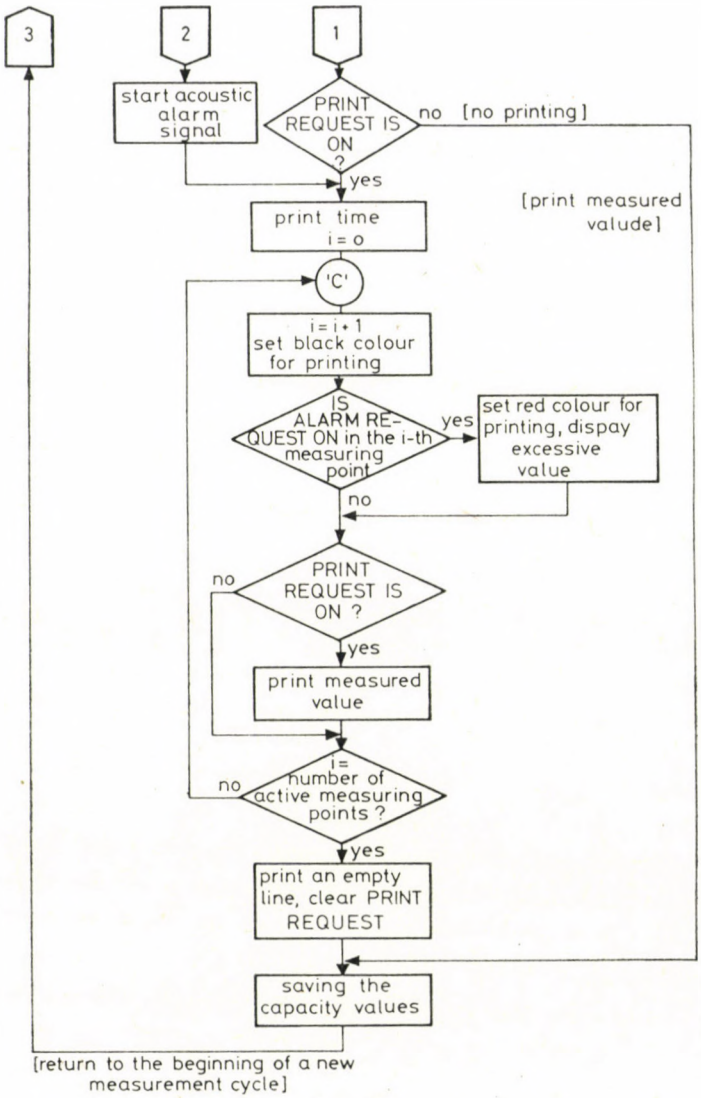

Fig. 10b

mands to start the A/D conversion or capacity measurement. After the execution of conversion, data entering commences: capacity values in 4 BCD characters, the output of A/D conversion in 11 bits binary form converted later into 4 BCD characters by the program. The resulting data are compared with the lower and upper limits. If the limits are exceeded, the measured values are printed out in red and an acoustic ALARM signal is given.

The flow chart of the master program is illustrated in Figs. 10a, 10b and 10c.

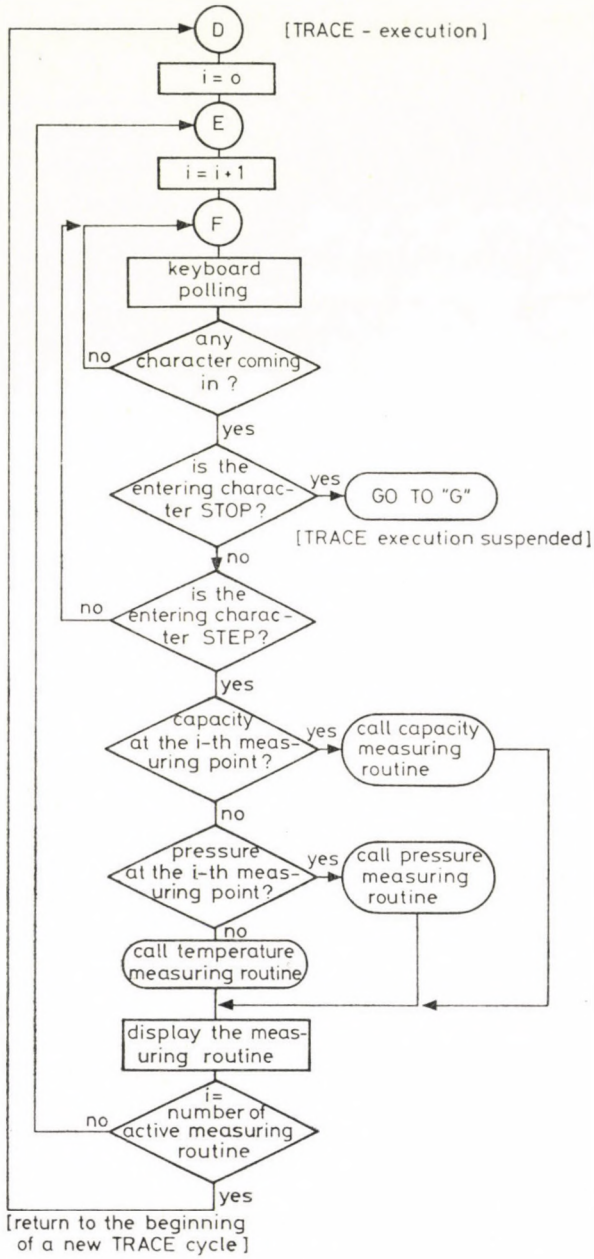
D
[TRACE - execution]
i = o
E
i = i + 1
F
keyboard polling
any character coming in ?
no
yes
is the entering charac-ter STOP ?
yes
GO TO "G"
[TRACE execution suspended]
no
is the entering charac-ter STEP?
no
yes
capacity at the i-th meas-uring point ?
yes
call capacity measuring routine
no
pressure at the i-th meas-uring point?
yes
call pressure measuring routine
no
call temperature measuring routine
display the meas-uring routine
i= number of active measuring routine
no
yes
[return to the beginning of a new TRACE cycle]

Fig. 10c

Acta Geodaet., Geophys. et Montanist. Acad. Sci. Hung. Vol. 17 (3—4), pp. 437—446 (1982)

DETERMINATION OF THE DEGREE OF CRUDE OIL METAMORPHISM WITH APPLICATION TO PROSPECTING PURPOSES

J. TÓTH—MRS. MILLEY J. TÓTH—MRS. LAKATOS J. SZABÓ

PETROLEUM ENGINEERING RESEARCH LABORATORY OF THE HUNGARIAN ACADEMY OF SCIENCES

Degree of metamorphism was determined for crude oils from the Pannonian basin and from Paleogene reservoirs in Northern Hungary. The degree of metamorphism has shown, in contradistinction with previous opinions, no direct correlation with the age of the oil or the source rock. The determination of this correlation would require a knowledge of the geothermal conditions and detailed investigations into the hydrogenation of crude oils. Y-values can only be used directly for a *relative* correlation that allows conclusions on the vertical length of oil migration.

Symbols

a_f	constant in Eq. (3)
a_T	constant in Eq. (4)
a_y	constant in Eq. (5)
A	constant in Eqs (6) and (7)
b_f	constant in Eq. (3)
b_T	constant in Eq. (4)
b_y	constant in Eq. (5)
B	constant in Eqs (6) and (8)
m_f	depth of formation
m_r	depth of the reservoir
M	ratio of the formation and reservoir depths
X	content of aromatic carbon atoms, mass %
Y	saturated hydrocarbon content, mass %

The *long-range aim* of genetical analyses is to help hydrocarbon prospecting and to answer some basic questions. At the present state of art the most important question genetical analyses have to answer: what is the age of the source rock the crude oil in the investigated area originates from? This is a complex, interdisciplinary problem that challenges both the geologist and the chemist. Genetical analyses of chemical character study the basic reactions in the formation of crude oils and determine the degree of metamorphism. To justify the latter task, recall that the degree of metamorphism of the crude oil is probably connected with the age of the source rock even if only indirectly. The clarification of these connections by chemical methods and some conclusions made on the basis of experimental results will be reported in what follows.

Determination of the degree of metamorphism of crude oils

The degree of crude oil metamorphism has to be defined with parameters that

a) are in connection with syngenetic properties of the crude oil i.e. they have developed in the source rock during genesis and have not undergone any major further change during migration, accumulation and storage,

b) are derived from common properties or components of crude oils.

These two conditions are met with good approximation in the Kisielow—Marzec (1969) method where the mass % of saturated hydrocarbons Y and aromatic carbon atoms X are determined in the asphalt-, resin- and paraffin-free fraction (called "oil") of the 200 °C destillation residue of crude oils. The scheme of analysis is illustrated in Fig. 1.

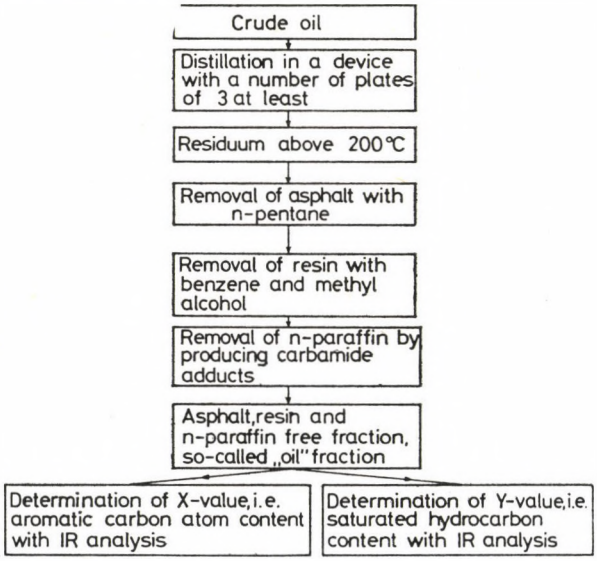

Fig. 1. Scheme of determination of the degree of metamorphism (Y) of crude oils

The authors have proved with experimental tests and theoretical considerations that there is an unambiguous correlation between the Y- and X-values. On the basis of an analysis of 99 crude oils from the Carpathian Foreland the relationship

$$Y = -2.25X + 105 \tag{1}$$

was found for X- and Y-values with a correlation coefficient of 0.885.

A theoretical interpretation to this empirical relationship has also been found, see Fig. 2. All possible chemical reactions and empirical data concerning metamorphism are plotted in a Y—X coordinate system. The diagram shows

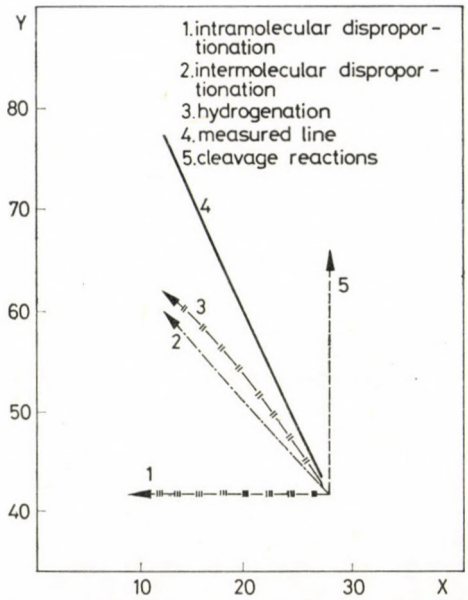

Fig. 2. Theoretically possible chemical reactions in metamorphism according to Kisielow and Marzec (1969) 1. Intramolecular disproportionation, 2. Intermolecular disproportionation, 3. Hydrogenation, 4. Measured line, 5. Cleavage reactions

that the experimentally determined line 4 can be composed as a suitable combination of reactions 1, 2, 3 and 5.

Kisielow and Marzec, however, convincingly proved with NMR, IR and UV measurements that reactions 1 and 2 did not take place. The main reaction of metamorphism is hydrogenation 3, with a minor contribution of cleavage processes 5. Experimental data also proved that oils with Y-values of 50—57 originated from Eocene and Oligocene reservoirs while those with 71—78 came from older, Mesozoic formations.

The above-mentioned authors draw two important conclusions:

a) The Y-value can be regarded as a parameter characterizing the degree of metamorphism of crude oils;

b) The Y-value can be brought into direct correlation with the age of crude oils.

Two basic questions arise from these important statements.

a) Are the parameters of the Kisielow—Marzec line, i.e. the slope —2.25 and intercept +105 of general validity or if not, how significant deviations may occur and what is their reason?

b) Is it possible to determine a correlation between the Y-value and the age of crude oils from geological conditions other than those of the Carpathian Foreland?

Comparison of the Y-values

To answer the above questions, Y- and X-values of 37 crude oils were determined and it has been found that they fit to the line

$$Y = -1.76X + 94.35 \tag{2}$$

with a correlation coefficient 0.914 (Fig. 3). Figures at the measurement points indicate serial numbers of the crude oils investigated. Oil samples were taken from the Pannonian basin, east of river Tisza and the Paleogene basin in Northern Hungary.

Figure 3 allows to draw the following conclusions.

a) Crude oils of Hungary investigated so far can be classified somewhat arbitrarily but fairly distinctly, into three groups of metamorphism:

I. low degree of metamorphism with $Y = 50—62$,

II. medium degree of metamorphism with $Y = 65—72$,

III. high degree of metamorphism with $Y = 73—80$.

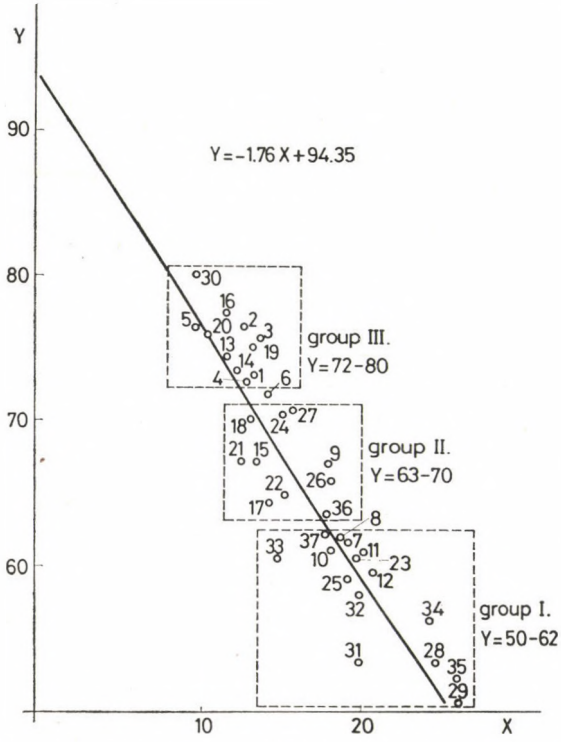

Fig. 3. Relationship $Y—X$ for Hungarian crude oils and crude oil groups according to their degrees of metamorphism

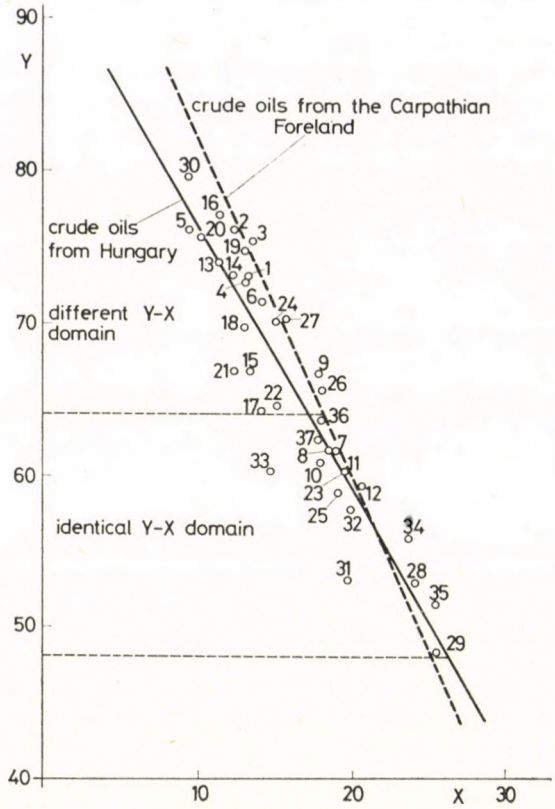

Fig. 4. Comparison of the degree of metamorphism of Paleogene-Plio-Miocene crude oils from Hungary and Paleogene-Mesozoic crude oils from the Carpathian Foreland

b) Most crude oils with low degree of metamorphism originate from reservoirs of the northern Paleogene basin with an average depth of 1280 m.

c) The majority of crude oils belonging to groups II. and III. are from young Pliocene (Lower Pannonian) and Miocene reservoirs. With increasing Y-value the reservoir depth increases. In group II. the average depth is 1639 m while it amounts to 2310 m in group III.

To interprete these data, the Kisielow—Marzec line (1) was compared with that of Paleogene and Plio-Miocene crude oils in Hungary (2). This comparison is illustrated in Fig. 4 where both the similarities and differences between the two lines can be easily observed. For Y-values less than 60—65 i.e. for oils of low degree of metamorphism, the two relationships practically coincide. In the range of high degree of metamorphism however, there is a considerable difference between the two lines, *viz.* the line representing crude oils from Hungary running somewhat below that of crudes from the Carpathian Foreland.

This difference does not contradict to the statement that the degree of metamorphism of Plio-Miocene crude oils from Hungary practically equals

that of Mesozoic oils from the Carpathian Foreland. With other words: for oils from the Carpathian Foreland the age of the reservoir rock increases with increasing Y-values along line (1) while for Hungarian crude oils there is an inverse relation. From our considerations and from Figs 3 and 4 the following conclusions can be drawn.

1. Hydrogenation and cleavage reactions were the principal factors of metamorphism for all crude oils investigated and the ratio of these reactions determined the parameters of the Y—X line.

2. The difference between Paleogene—Mesozoic oils from the Carpathian Foreland and the Paleogene-Plio-Miocene oils from Hungary is that hydrogenation reactions played a more dominant role during the metamorphism of the latter ones. This is illustrated in the diagram by the somewhat greater slope of line (2) running more closely to the pure hydrogenation curve (see Fig. 2).

3. Comparison of the degree of metamorphism of crude oils from the Carpathian Foreland and Hungary suggest that *the Y-values cannot be brought into direct correlation with the age of crude oils*. This statement follows from the approximately equal degrees of metamorphism of the Mesozoic oils from the Carpathian Foreland and of the Plio-Miocene crude oils from Hungary. Therefore, the Y-values of the Kisielow—Marzec "oil" fraction can only be directly proportional to the maximum temperature T of oil formation. This correlation possibility inevitably follows from the equilibrium laws of the chemical processes of hydrogenation.

4. The chemical composition of the "oil" fraction, i.e. the Y- and X-values as well depends predominantly on temperature and on the chemical and physical conditions of the *source rock* while migration processes do not have a considerable effect on "oil" parameters. The main reason for this is that during migration primarily the asphalt-, resin- and paraffin contents change. The "oil" fraction, however, does not contain any of these components.

Use of the Y-values for prospecting purposes

The basic question of our investigation was to decide whether the Y-values might be brought into connection with the age of the source rock. It has been found that no direct correlation exists, consequently, only indirect ways can be pursued. Let us make the following assumptions in the further discussion:

a) For crude oils formed in a basin having geologically uniform structure the depth of formation m_f is assumed to be linearly related with the depth of the reservoir m_r

$$m_f = a_f m_r + b_f \tag{3}$$

where a_f and b_f are constants.

b) The maximum temperature T_f of formation can be linearly correlated with the depth of formation i.e. no significant geothermal anomaly occurred in the verticality of the formation. Correspondingly,

$$T_f = a_T m_f + b_T \tag{4}$$

with some constants a_T and b_T.

c) On the basis of these considerations it can be assumed with a great probability that the degree of metamorphism linearly changes with the temperature of formation i.e.

$$Y = a_y T_f + b_y \tag{5}$$

a_y and b_y being constants.

On substituting Eqs (3) and (4) into Eq. (5)

$$Y = A m_r + B \tag{6}$$

with

$$A = a_y a_T a_f \tag{7}$$

and

$$B = a_y a_T b_f + a_y b_y + b_y \tag{8}$$

Equation (6) expresses that if conditions (3) to (6) are met, the Y-values of the crude oils would also change linearly with the depth of the *reservoir*.

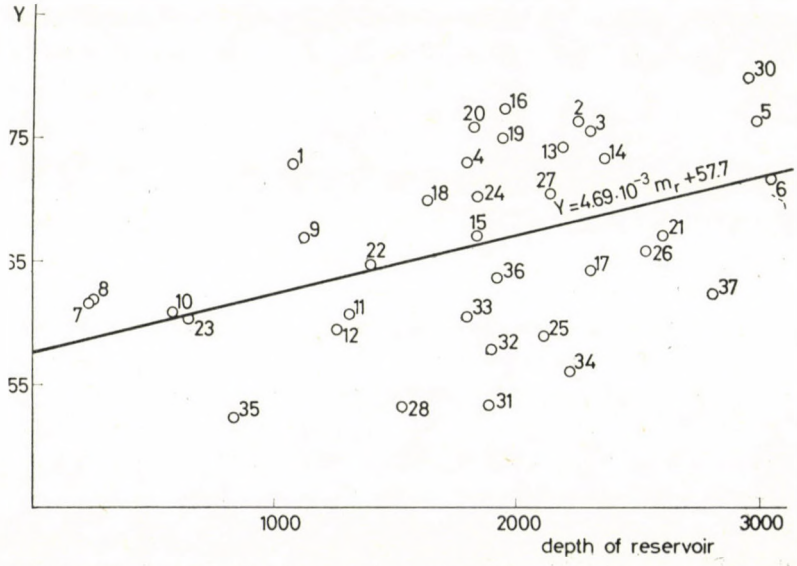

Fig. 5. Relationship between the degree of metamorphism of Hungarian crude oils and the depth of reservoir

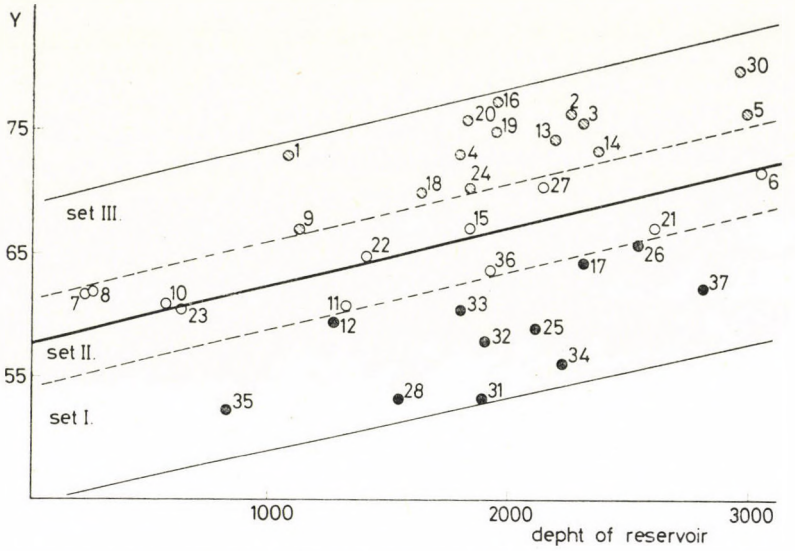

Fig. 6. Three sets of crude oils from Hungary according to the relationship between the degree of metamorphism and reservoir depth

Possibilities and extent of this correlation are illustrated in Fig. 5, where the Y-values of the discussed Hungarian crude oils are plotted against reservoir depth. The data fit the line

$$Y = 4.69 \cdot 10^{-3} m_r + 57.7 \tag{9}$$

with an accuracy characterized by a correlation coefficient of 0.45. The reason of this rather poor correlation is probably the fact that conditions (3) and (4) do not hold for all crude oils. The mere fact that there is a correlation at all, suggests that conditions (3) and (4) can be applied but with different coefficients a_f, b_f, a_T, b_T for different oils. This possibility is outlined in Fig. 6 constructed the following way. Parallel (dotted) lines have been drawn below and above the regression line (9) representing with good approximation the standard deviations of the Y-values (see also Fig. 3). This way three sets of data *viz.* sets I., II. and III. are obtained within which satisfactory correlations (0.65; 0.80 and 0.70) can be obtained by using linear relationships similar to Eq. (9). It means that three relationships of type (3), and three of type (4), having different coefficients should be assumed for the place of formation of crude oils. Of course, further artificial sets of Y-values and further relationships of type (3) and (4) could have been constructed but this would yield unreasonably better correlations than expectable on the basis of the standard deviations of the Y-values.

Conditions (3) to (5) in the three sets of Fig. 6 are thus only valid with the restriction that the respective constants in Eqs (3) and (4) are different for

the various sets. The method and possibility of construction of triple sets as illustrated in Figs 3 and 6 are also supported by the fact that at a significance level of 95% crude oils with low degrees of metamorphism lie in set I., those with medium degrees in set II. and those with high degrees in set III.

These considerations suggest that an absolute correlation between Y-values and the source rock (depth of formation) of crude oils is only possible if

i) the constants a_y and b_y are determined from chemical analyses. This problem can be solved by a further (artificial) hydrogenation of crude oils with low degree of metamorphism.

ii) the coefficients a_T and b_T characterizing the geothermal conditions are *a priori* known.

If these conditions are met, the constants of Eq. (3) can be calculated from relationships (7) and (8) as:

$$a_f = \frac{A}{a_y a_T}, \tag{10}$$

$$b_f = \frac{B - a_y b_T - b_y}{a_y a_T}. \tag{11}$$

Y-values, apart from the possibility of an absolute correlation, but in a much simpler way, can also be used for the *relative* identification of the reservoir and source rock. From relationship (3)

$$M = \frac{b_f}{m_r} + a_f \tag{12}$$

where

$$M = \frac{m_f}{m_r} \tag{13}$$

is the ratio of the depth of formation to that of the reservoir. The possibility of relative correlation is due to the fact that Eq. (12) also gives the ratio Y/m_r but with different constants. From Eq. (6), namely

$$\frac{Y}{m_r} = \frac{B}{m_r} + A. \tag{14}$$

Plotting the Y/m_r values against m_r, hyperbolae of type (14) are obtained for each of the three sets giving orientation about the *relative* values of M. Correspondingly, Fig. 7 suggests an increasing tendency of M towards low reservoir depths i.e. the length of *vertical migration increases*. The hyperbolic character of the relationship indicates that a very great value of M might correspond to

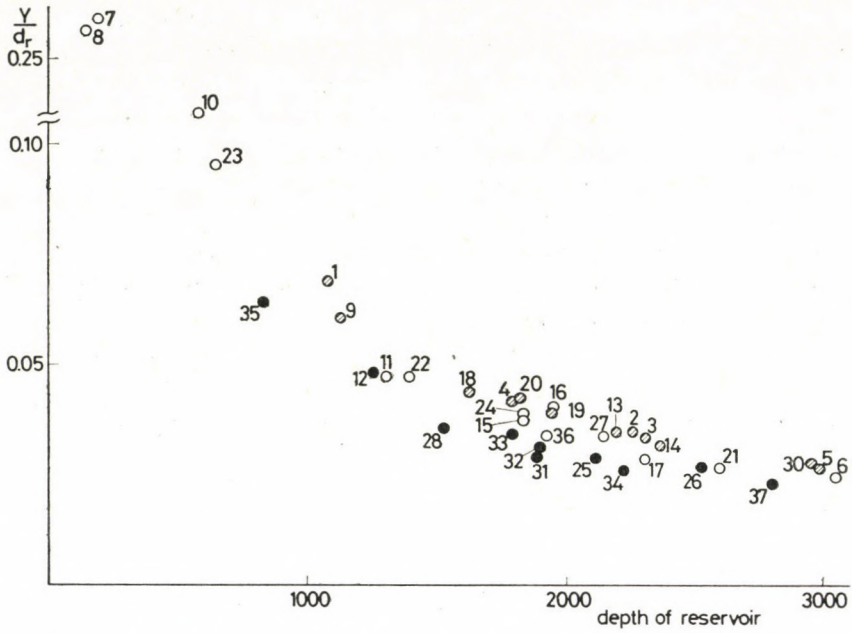

Fig. 7. Y/m_r values reflect the relative length of vertical migration

shallow reservoirs, i.e. in these reservoirs the crude oil can accumulate after a very long vertical migration. Geological investigations supported this assumption by proving that crude oils with great Y/m_r values migrated along discordance planes from several thousand metre depths to their present position.

Summarizing our considerations, it can be stated that Y-values combined with proper geologic investigations can give valuable information on the relative length of vertical migration. At the same time, with extended chemical analyses an absolute correlation of source and reservoir rocks can be obtained.

Acknowledgement

The authors wish to express their gratitude to Dr. A. Somfai, Candidate of Geological Sciences, and Mrs. I. Haáz, geologist, for their interest in this research and for their valuable geological analyses in supervising the applicability of the Y-values.

REFERENCE

KISIELOW, W.—MARZEC, A. 1969: Some Aspects of the Chemistry of Crude Oil Metamorphism. Advances in Organic Geochemistry. Pergamon Press, London. 1969.

Acta Geodaet., Geophys. et Montanist. Acad. Sci. Hung. Vol. 17 (3–4), pp. 447–454 (1982)

POSSIBLE ROLE OF MECHANICAL EFFECTS IN CRUDE OIL GENERATION AND GEOCHEMICAL INVESTIGATIONS OF HYDROCARBONS

J. TÓTH – MRS. MILLEY J. TÓTH

PETROLEUM ENGINEERING RESEARCH LABORATORY OF THE HUNGARIAN ACADEMY OF SCIENCES

Chemical reactions in various organic materials have been studied during grinding (mechanical dispersing) of pure model systems and natural sedimentary rocks.

These reactions had very likely also taken place during the generation of crude oil. It is pointed out that in the geochemical investigations of hydrocarbons the parameters of bitumen diagnosis greatly depend on the circumstances of preparatory grinding. This fact has to be taken into account in future investigations.

Symbols

BAM	benzene-acetone-methanol
$\overline{M}$	molecular mass
M	fraction of the rock non-soluble in hydrochloric acid
C_T	carbon content of the carbonate-free part of the rock
C_{org}	organic carbon content
S_K	amount of chloroform-soluble bitumen
S_B	amount of BAM-soluble bitumen
S_N	organic carbon content non-soluble in chloroform
C_R/C_T	diagenesis coefficient
β_K	coefficient of chloroform-soluble bitumen
ε	molar extinction coefficient
β_B	coefficient of BAM-soluble bitumen
β_A	coefficient of bitumen A

Chemical reactions due to specifically mechanical effects have been known since long. However, the first systematic and modern study on the topic was only published in 1962 by Peters. He introduced the term "mechanochemical reactions" for chemical processes during the grinding (mechanical dispersing) of solids. These reactions without any exception belong to the scope of the classical inorganic chemistry. Juhász (1975) pointed out that the majority of these reactions can be ascribed to secondary processes proceeding after mechanical activation.

The fact that substantial chemical changes occur in organic materials under mechanical effects (e.g. friction), is well known and investigated in tribochemistry. This has to be emphasized since outstanding representatives of tribochemistry, such as Thiessen et al. (1967) were the first to recognize the possible role of mechanical effects in the generation of crude oil and natural

gas. According to their hypothesis the mechanical energy was provided by microseismic processes.

Since laminar tectonics seems to support this hypothesis, it was reasonable to investigate by a few simple model experiments whether Peters' mechanochemical reactions were feasible in simple hydrocarbons, what was the character and direction of these processes and that they could or could not have taken place during crude oil generation.

Model experiments on pure hydrocarbon-solid systems

In selecting the model materials for the experiments, care has been taken that

— the hydrocarbon should be typical, occurring in natural crude oils, of fluid state and of comparatively simple composition, its carbon-carbon bonds be apt to cleavage due to mechanical effects;

— the solid should allow a thorough and uniform mixing with the liquid hydrocarbon, and its composition should be similar to that generating or generated crude oils could meet under natural circumstances.

According to these criteria, calcium carbonate-toluene and quartz sand-toluene systems have been chosen as the first model materials. In our further experiments, an attempt was made towards cleaving the paraffin chain for which purpose quartz sand-n-hepthane and quartz sand-n-heptadecane mixtures were used. Experimental conditions, results and conclusions will be discussed below.

Experimental

The hydrocarbons, solvents and the calcium carbonate were chemicals of analytical purity, the latter was precipitated chalk. Quartz sand of Fehérvárcsurgó was acidified, washed and extracted for 100 hours in a mixture of benzene-ethanol in the ratio of 1 : 1, then the solvents were removed and the solid dried.

A homogeneous mixture prepared from the hydrocarbon and the solid in ratio 1 : 4 (20 and 80 g) was placed into a vibration mill which had been carefully cleaned. Grinding was carried out over 100 hours without interruption using 500 pieces of 8 mm diameter high-alloy steel balls. Temperature changes were measured by built-in thermoelements, the atmosphere inside the mill could be changed through valves. After grinding, the grind product was extracted by a 1 : 1 mixture of benzene-ethanol, the extract was evaporated on water bath and the elementary composition of the solvent-free extract and the average molecular mass of the benzene-soluble part were determined. The results of the analyses are shown in Tables I and II.

Discussion

Table I summarizes the results of the experiments on calcium carbonate-toluene and quartz sand-toluene systems. The tendencies found hold, as a rule, for other systems as well. The only difference between grinding experiments 1 and 2 carried out in an air atmosphere, was the different initial temperature of the experiments. Basic changes and characteristics, however, could be distinguished even in these two experiments. The following facts and conclusions can be recognized from the data of Table I:

— compounds with average molecular masses 3—8 times greater than that of toluene are formed during grinding;

— this type of change, however, is slight, only 60—160 mg reaction product is produced from 20 g toluene;

— hidrogenation-like processes are indicated by C/H ratios of the reaction products being much lower than that of the toluene;

— it was surprising that reaction products also contained nitrogen that could have only originated from the air or in experiment 3 from the nitrogen atmosphere. The incorporation of nitrogen decreases with increasing temperature, but it still takes place even in vacuum produced by an oil pump;

— oxidative processes also take place. This is proved by E values that are high even in nitrogen atmosphere and vacuum. (E values obtained

Table I

Data of 100-h-grinding and analysis of calcium-carbonate-toluene and quartz sand-toluene systems in the ratio of 4 : 1

No	Mill atmosphere	Extracted by 1 : 1 benzene-ethanol mixture g	Benzene-soluble part vol. %	Aver. mol. mass benzene-soluble part $\bar{M}$	CHN analysis of benzene-ethanol extracts					Initial temperature °C	Temperature rise °C
					C %	H %	N %	E %	C/H		
				calcium carbonate-toluene							
1.	air	0.0860	88.4	275	22.49	3.39	1.49	67.82	6.63	30	7.4
2.	air	0.0690	26.8	323	21.72	3.43	0.29	69.16	7.91	60	4.6
3.	nitrogen	0.0620	88.2	779	45.80	6.46	2.62	45.11	7.09	30	10.8
4.	vacuum	0.0664	69.7	422	57.53	7.48	0.35	34.64	7.69	30	6.9
				quartz sand-toluene							
5.	air	0.1172	48.0	375	61.03	7.50	1.17	30.30	8.13	22	3.4
6.	air	0.4788	14.6	417	11.02	2.25	0.0	86.73	4.9	60	18.0
	data of	pure tolu	ene	92	91.30	8.70	0.00	0.00	10.49		

by elementary analysis practically indicate oxigen content besides some iron contamination.) Therefore oxigen is assumed to have been incorporated also from the calcium carbonate into the reaction product;

— infrared spectrophotometrical measurements proved that oxigen is present in the reaction product in the form of ester and other carboxyl bonds;

— when grinding quartz sand-toluene system, the amount of reaction product is increased, other tendencies and changes are essentially identical with those observed in the carbonate-toluene system.

Table I fails to illustrate an important observation *viz.* a penetrating, pungent gas (presumably formaldehyde) was noticed in all six experiments after opening the mill cover. All these observations suggest that the gross mechanochemical reaction of the solid-toluene system is essentially a disproportion where compounds with greater and smaller molecular masses than that of the toluene are formed.

In the next step of our experiments, paraffin hydrocarbons were ground in the presence of quartz sand hoping the C—C bonds might be cleaved. Results are given in Table II, the following should be noted:

— the amount of reaction products is 20—30 mg, less than in the experiments with toluene;

— nitrogen incorporation can also be observed, even more intensively than in the toluene experiments;

— oxidative processes play an important role but no ester bond was found in the reaction product;

Table II

Data of 100-h-grinding and analysis of quartz sand-n-heptane and quartz sand-n-heptadecane systems in the ratio of 4 : 1

No	Mill-atmosphere	Extracted by 1 : 1 benzene-ethanol mixture g	Benzene-soluble part vol. %	Aver. mol. mass of the benzene-soluble part M	CHN analysis of benzene-ethanol extracts					Initial temperature °C	Temperature rise °C
					C %	H %	N %	E %	C/H%		
					quartz sand-n-heptane						
7.	air	0.0252	80.0	—	41.95	7.38	4.81	45.86	5.68	22	5.5
	data of pure n-heptane				84.00	16.00	0.00	0.00	5.25		
					quartz sand-n-heptadecane						
8.	air	0.0266	90.7	—	62.21	10.17	2.36	25.27	6.12	22	5.0
	data of pure n-heptadecane				85.00	15.00	0.00	0.00	5.67		

— the gross process of the reaction is in this case very likely not a disproportion, for no compounds with molecular masses smaller than that of the initial materials were indicated with gaschromatography using flame ionization detector;
— because of the small amount of the reaction products, the molecular mass has not been determined.

These experiments with pure model materials are only regarded as of an informatory character, a more detailed analysis of the reaction mechanism was beyond the scope of this study. However, the question asked in the introduction of this paper can be answered: mechanochemical reactions observed by Peters can also be performed in liquid hydrocarbons though the rate of chemical changes is less than in solid compounds. The character and direction of the reactions allows for them having taken place in organic materials that were the sources of crude oil generation or in the crude oils themselves.

This conclusion led to the mechanochemical investigation of natural sedimentary rocks containing oil and bitumen. Measurements of bitumenology and the degree of diagenesis are well known in the geochemistry of hydrocarbons. These investigations allow local or regional forecast (prognosis) about the occurrence of hydrocarbons using the properties of organic materials in the rocks soluble or non-soluble in various solvents. When carrying out this kind of analysis, some kind of grinding always takes place in the preparatory phase, so that it seemed important to determine the changes in the best known bitumen and diagenesis parameters due to grinding.

Mechanochemical investigations in natural rocks containing bitumen and oil

Experimental

A Pliocene (Lower Pannon) sandstone sample from a depth of 1950 m was chosen for the analysis. The sample was recovered by core drilling near an oil reservoir. Three specimens were made of the sample by various methods and grinding rates (specimens A, B and C).

A) The sandstone sample was pounded to an approximate size of 0.5—1.0 cm in a braying mortar with light blows. During this process the easily weathered parts were degraded below 200 μm. This fraction with particles less than 200 μm was considered as mechanically untreated specimen.

B) One part of the material of size 0.5—1.0 cm was periodically ground in a vibration mill. That is, the mill was dismantled each hour, the sample sieved on a 200 μm sieve and the sieve residue returned for further grinding. The grinding was carried on until the total amount was ground below 200 μm. The full time of grinding was 30 hours.

C) Another part of the 0.5—1.0 cm material was continuously ground for 30 hours without dismantling the mill and removing the particles below 200 μm.

The sand specimens with grain sizes less than 200 μm obtained by treatments A, B and C were extracted by chloroform and a 70 : 15 : 15 mixture of benzene-acetone-methanol (BAM). By this method the amounts of chloroform-soluble and BAM bitumens were determined. The end point of the extraction was determined by weight measurement after evaporation of the sample taken from the upper part of the extraction device. After extraction the solvents were removed by vacuum distillation and the residue was evaporated at 40 °C in vacuum.

The basic geochemical parameters were determined both for bitumens and for the rock. To investigate the character of the chemical changes, elementary analysis and molecular mass measurements were performed and infrared spectra were taken.

Discussion

In the experiments no essential changes or tendencies were established as regards the molecular masses, elementary compositions and the parameters calculated from the infrared spectra concerning the chloroform-soluble bitumens of specimens A, B and C. The presentation of the measured data is therefore omitted.

BAM bitumens, however, showed essential and definite changes. The average molecular masses and elementary compositions of the BAM bitumens are shown in Table III, and the data calculated from the infrared measurements in Table IV.

Table III shows that with increasing degree of the mechanical treatment the average molecular mass and nitrogen content of the BAM bitumens gradually decreases while the C/H ratio increases.

Since infrared spectra were taken in a carbontetrachloride solution, peaks around 700—800 cm^{-1} wave number might not be analyzed. The values

Table III

Elementary composition of BAM bitumens

Mechanical treatment	$\bar{M}$	C %	H %	N %	E %	C/H
A	1452	47.31	5.97	1.41	45.30	7.91
B	1253	62.50	7.43	1.24	28.82	8.41
C	1160	70.75	7.93	1.12	19.93	8.62

Table IV

Data of infrared spectrophotometry of BAM bitumens

Mechanical treatment	ε^{1710}	ε^{1600}	$\frac{\varepsilon^{1710}}{\varepsilon^{1470}}$	$\frac{\varepsilon^{1600}}{\varepsilon^{1470}}$	$\frac{\varepsilon^{1380}}{\varepsilon^{1470}}$
A	184	458	0.655	1.471	0.448
B	271	133	1.210	0.665	0.426
C	277	111	1.092	0.446	0.381

ε^{1710} molar extinction coefficient of the peak at 1710 cm^{-1} wave number (characteristic of C=O bond)
ε^{1600} molar extinction coefficient of the peak at 1600 cm^{-1} wave number (generally C=C and C=N aromatic bonds)
ε^{1470} molar extinction coefficient of the peak at 1470 cm^{-1} wave number ($-CH_2$ group)
ε^{1380} molar extinction coefficient of the peak at 1380 cm^{-1} wave number ($-CH_3$ group)

calculated from the infrared spectra allow conclusions about oxidation during the mechanical treatment (the extinction coefficient of the peak at 1710 cm^{-1} wave number increases). The shift of the peak at 1600 cm^{-1} wave number suggests an intensive change of the type of nitrogen containing compounds while a rapid reduction in the extinction coefficient of the peak indicates a reduction of the nitrogen content, that is in coincidence with the change of the elementary composition. These changes can also be observed in the values of the extinction coefficients as compared to peak at 1470 cm^{-1} wave number. The slight reduction of the $\varepsilon^{1380}/\varepsilon^{1470}$ ratio indicates the cleavage of the $-CH_3$ groups.

Table V contains the basic geochemical parameters and organic geochemical parameters for bitumens and rocks, Table VI shows parameters and their changes used in bitumen diagnosis and in the determination of the degree of diagenesis, deducted from the data of the previous table. The way of calculation is also indicated below the designations.

Table V

Basic geochemical parameters of hydrocarbons

Mechanica treatment	S_K %	S_B %	M %	C_T %
A	1.0076	0.0572	74.81	0.10
B	1.0019	0.0552	72.44	0.19
C	0.9888	0.0353	72.28	0.20

S_K amount of chloroform-soluble bitumen
S_B amount of BAM-soluble bitumen
M in hydrochloric acid non-soluble part of the rock
C_T carbon content of the carbonate-free part of the rock
All data refer to mass per cuts of the rock.

Table VI

Derived organic geochemical (bitumen diagnostic) and diagenesis parameters

Mechanical treatment	S_N / $C_T \cdot \frac{M}{100}$	S'_K / $0.8 \cdot S_K$	S_B / $0.8 \cdot S_B$	C_{org} / $S'_K + S_N$	β_K / $\frac{S'_K}{C_{org}}$	β_B / $\frac{S'_B}{C_{org}}$	β_A / $\frac{S'_K + S'_B}{C_{org}}$	C_R/C_T
A	0.0748	0.8061	0.0457	0.8809	0.9151	0.0519	0.9670	0.733
B	0.1376	0.8015	0.0442	0.9391	0.8535	0.0472	0.9005	0.654
C	0.1445	0.7910	0.0283	0.9355	0.8455	0.0302	0.8758	0.586

S_N organic carbon content non-soluble in chloroform
C_{org} organic carbon content, both in mass per cent of the rock
β_K coefficient of the chloroform-soluble bitumen
β_B coefficient of the BAM-soluble bitumen
β_A coefficient of the bitumen A
C_R/C_T diagenesis coefficient, C_R indicates the residual (remanent) carbon content after a pyrolysis at 900 °C in an oxigen-free nitrogen stream

While the chloroform-soluble bitumen shows only a very limited reduction, BAM bitumen decreases sharply, especially in specimen C. The part of rock non-soluble in hydrochloric acid also shows a decreasing tendency, while the carbon content of the carbonate-free part increases. This fact allows the conclusion that besides the chemical composition of the bitumens the composition of the rock itself also changed, similarly to our assumption at the calcium-carbonate-toluene system.

Summing up, the following conclusions can be drawn from Tables III—VI:

— in the case of natural sedimentary rocks Peters' mechanochemical reaction can only be observed in a certain group of organic materials, the so-called BAM soluble bitumens;
— the basic tendency of the reactions is presumably a breakdown of oxidative character during which the organic material reacts with the inorganic components of the rock, too;
— the reactions substancially influence the diagnostic parameters based on the BAM bitumen and the values of the diagenesis coefficient. Therefore, in determining of these parameters, the changes due to grinding have to be taken into account in the future.

REFERENCES

JUHÁSZ, Z. 1975: Réz-szulfát mechanokémiai reakciói (Mechanochemical reactions of copper sulphate). *Kémiai Közlemények*, 43, 225—245.
PETERS, K. 1962: Mechanochemische Reaktionen. Symp. Zerkleinern. Düsseldorf.
THIESSEN, P. A.—MEYER, K.—HEINICHE, G. 1967: Grundlagen der Tribochemie Akad. Verlag, Berlin.

Acta Geodaet., Geophys. et Montanist. Acad. Sci. Hung. Vol. 17 (3—4), pp. 455—471 (1982)

ENERGY CONSUMPTION OF UNDERGROUND GAS STORAGE

(INDEPENDENCE OF SPECIFIC STORAGE ENERGY ON RESERVOIR STRUCTURE)

GY. ZOLTÁN

PETROLEUM ENGINEERING RESEARCH LABORATORY OF THE HUNGARIAN ACADEMY OF SCIENCES

Energy consumption of the change of state in underground gas reservoirs will be considered using the relationships between the work done by the compressing system and the state of energy of the reservoir. Components of the total energy consumption can be clearly distinguished according to their place and role, they can be compared and measured. Specific storage energy i.e. the work required to store a unit amount of energy is shown to be independent of reservoir structure. Energy consumptions of the gas storage in reservoirs of various structures may be different, but the "energy cost" to store an amount of natural gas representing unit energy does not depend on reservoir structure.

Symbols

n	mole number, number of observations
p, P	pressure
R	gas constant
S	saturation
T	temperature
V	volume
W	work, energy
Z	compressibility factor
Subscripts	
c	capillary
ck	capillary threshold
g	gas
gk	with V: gas volume, constant, in laboratory
gkt	gas volume, constant, in reservoir
gv	gas volume, varying, in laboratory
gvt	gas volume, varying, in reservoir
pk	pore volume, in laboratory rock sample
pkt	pore volume, in reservoir
mol	mole volume
norm	normal value
std	stored
stg	storing, needed to storing
w	water

Introduction

The first studies [1, 2] in this field determined the energy needed to overcome the capillary forces due to interactions between the solid and fluid phases playing important role in underground gas storage, especially in water-wet reservoir rocks. There have remained, however, two unsettled questions: first,

whether the accuracy of the applied method were satisfactory for modelling the physical phenomenon of the change of phase; and second, should the energy needed to overcome the capillary forces be regarded as great or negligible compared with the components of the total energy consumption of storage.

The first question was answered by a theoretical analysis [3] using basic laws of physical chemistry and thermodynamics to describe the change of phase in a reservoir with an idealized pore structure. It has been proved that the energy consumption of the displacement of the primary water phase by a less wetting gaseous phase can be determined with satisfactory accuracy using laboratory models built of elements of natural reservoirs, by means of theoretical considerations based on these observations. The second question has been answered by considering the change of state of a constant gas mass and comparing the energy needed to overcome capillary forces with the corresponding change in the energy factors [4]. The results obtained from the comparison have also proved that the energy needed to overcome capillary resistance cannot be neglected if it is regarded as a component of the total energy consumption in the steady operation of the reservoir. The problem is of great practical importance if the rentability of savings achieved by modifying the surface properties is investigated.

Total energy consumption of the change of state in the reservoir

Let our laboratory experimental system be composed of a rock sample of pore volume V_{pk} saturated with water, in direct contact with a constant gas volume V_{gk} where the mass of gas constantly increases (Fig. 1). The total volume

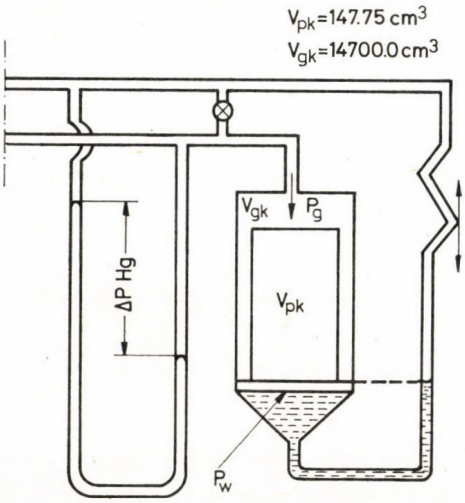

Fig. 1. Experimental reservoir model for laboratory measurements

of the gaseous phase remains constant as long as its pressure does not reach or exceed the capillary threshold of formation pressure represented by the pressure of the aqueous phase. Pressure balance in this instant can be written as

$$p_g = p_w + P_{ck},$$

and the state of the gas of n moles as

$$p_g V_g = nZRT, \tag{1}$$

where the temperature of the system is regarded as constant and equal to that of the formation.

The basic equation of the change of state in differential dimensions is

$$p_g \mathrm{d}V_g + V_g \mathrm{d}p_g = RT\,\mathrm{d}[nZ]. \tag{2}$$

If the observation of the energy content starts at the instant when

$$p_g = p_w,$$

i.e.

$$P_c = 0,$$

(see Fig. 2), the change of the energy content of the system can be calculated for an arbitrary change of state from the above differential equation as

$$\int_{V_{g0}}^{V_g} p_g \,\mathrm{d}V_g + \int_{p_{g0}}^{p_g} V_g \,\mathrm{d}p_g = RT \int_{Z_0}^{Z} n \,\mathrm{d}Z + RT \int_{n_0}^{n} Z \,\mathrm{d}n\,, \tag{3}$$

where the lower limit of the integrals denote the state parameters corresponding to $P_c = 0$. The equation expresses the change of energy accompanying the physical phenomenon as accurately as the parameters of state of the phenomenon (i.e. pressure, volume, mass and the compressibility factor of the gas — the latter depending on pressure and temperature) can be observed. For the parameters of state

$$p_g = p_w + P_c,$$

$$V_g = V_{gk} + V_{gv},$$

$$n = n_{\mathrm{I}} + n_{\mathrm{II}}$$

and

$$Z = Z_{\mathrm{I}} = Z_{\mathrm{II}}, \tag{4}$$

where subscript I denotes variables characterizing changes in the constant gas volume outside the pores while subscript II stands for the mass and compressi-

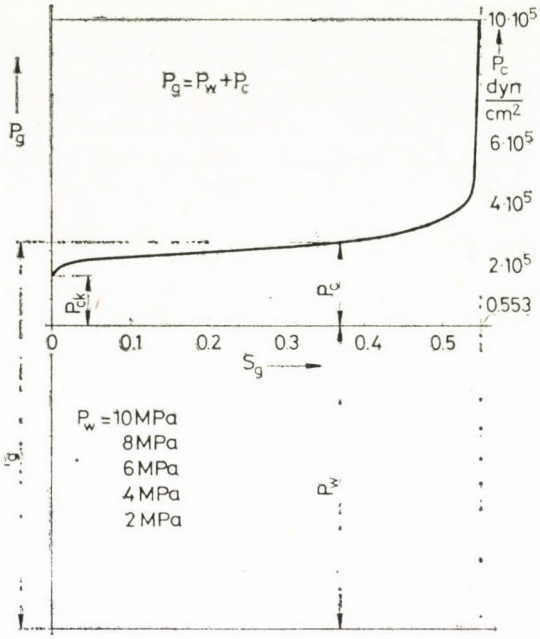

Fig. 2. Parameters of the change of state in an experimental reservoir

bility factor of the gas with changing volume in the pores. The values of Z are equal in both volumes since the pressure and temperature can be regarded equal both in the pore volume and outside it.

On substituting Eqs (4) into Eq. (3) and rewriting the limits of the integral we obtain

$$\int_{V_{g0}}^{V_g} p_w \mathrm{d}V_g + \int_{V_{g0}}^{V_g} p_c \mathrm{d}V_g + \int_{p_{g0}}^{p_g} V_{gk}\, \mathrm{d}p_g + \int_{p_{g0}}^{p_g} V_{gv} \mathrm{d}p_g =$$

$$= RT \int_{Z_0}^{Z} n_{\mathrm{I}} \mathrm{d}Z + RT \int_{Z_0}^{Z} n_{\mathrm{II}} \mathrm{d}Z + RT \int_{n_{\mathrm{I}0}}^{n_{\mathrm{I}}} Z \mathrm{d}n_{\mathrm{I}} + RT \int_{n_{\mathrm{II}0}}^{n_{\mathrm{II}}} Z \mathrm{d}n_{\mathrm{II}}. \qquad (5)$$

This equation expresses the total change of energy content due to the change of state in the reservoir as a form of several components. The terms stand for the following components of the change of energy:

— volumetric work of the expanding gas against constant water pressure i.e. formation pressure,

— volumetric work of the expanding gas against capillary pressure,

— compression work in the constant gas volume V_{gk} outside the pore volume,

— compression work in the varying gas volume V_{gv} in the pore volume,

— change of the internal energy of the gas in the pore volume,
— energy needed to increase the mass of the gas in the constant gas volume,
— energy needed to increase the mass of the gas in the varying gas volume in the pores.

Adding the two latter terms, expression

$$RT \int_{n_{I_0}}^{n_I} Z \, dn_I + RT \int_{n_{II_0}}^{n_{II}} Z dn_{II} = RT \int_{n_0}^{n} Z \, dn \,, \tag{6}$$

yields the work required from the compressing system, consequently, it has to be equal to the algebraic sum of the other terms.

Equation (5) gives the rate of change in the energy of the system under real conditions, nevertheless, its application seems to be disadvantageous. First, the engineer might find it inconvenient to use mole numbers instead of volumes and pressures, second, the number of unknown parameters is unnecessarily high, hiding the physical phenomenon behing the formulae. Equations (5) and (6) should therefore be transformed to ensure unchanged accuracy and a means to use volume and pressure data obtained from experiments.

It is obvious that

$$n_I = \frac{n_I V_{mol}}{V_{mol}}$$

and

$$n_{II} = \frac{n_{II} V_{mol}}{V_{mol}} \,.$$

These equations can be used to express gas mass in terms other than mole numbers. In what follows, products $n_I V_{mol}$ and $n_{II} V_{mol}$ will be determined.

Writing out Eq. (1) for state p_0 and T_{norm}, and expressing gas volume by mole volume, we obtain

$$p_0 n V_{mol} = n Z_0 R T_{norm} \tag{7}$$

for the new state. From Eqs (1) and (7) we have

$$n V_{mol} = \frac{Z_0 \, T_{norm}}{p_0 T} \frac{p_g}{Z} V_g \,.$$

It should be emphasized that the system has been transferred from an arbitrary state to another one while keeping gas mass constant.

Since the gas volume outside the pores is determined by

$$V_{gk},$$

and that inside the pores by

$$V_{pk} S_g,$$

the mole numbers of the gas in the two gas volumes become

$$n_{\mathrm{I}} = \frac{Z_0 T_{\mathrm{norm}}}{p_0 V_{\mathrm{mol}}} \frac{V_{gk}}{T} \frac{p_g}{Z}$$

$$n_{\mathrm{II}} = \frac{Z_0 T_{\mathrm{norm}}}{Z_0 V_{\mathrm{mol}}} \frac{V_{pk}}{T} \frac{P_g}{Z} S_g.$$

Let us now introduce the new factors

$$\frac{p_g}{Z} = J$$

and

$$\frac{p_g}{Z} S_g = K.$$

For a gas mass of one mole

$$\frac{Z_0 T_{\mathrm{norm}}}{p_0 V_{\mathrm{mol}}} = \frac{1}{R},$$

holds in the second state whereby mole numbers n_{I} and n_{II} standing for the gas masses become

$$n_{\mathrm{I}} = \frac{V_{gk}}{RT} J,$$

$$n_{\mathrm{II}} = \frac{V_{pk}}{RT} K,$$

and the changes of mole numbers

$$\mathrm{d}n_{\mathrm{I}} = \frac{V_{gk}}{RT} \mathrm{d}J$$

and

$$\mathrm{d}n_{\mathrm{II}} = \frac{V_{pk}}{RT} \mathrm{d}K.$$

Substituting the values of n and $\mathrm{d}n$ into Eqs (5) and (6), the following more convenient forms arise:

$$\int_{V_{g0}}^{V_g} p_w \mathrm{d}V_g + \int_{V_{g0}}^{V_g} p_c \mathrm{d}V_g + \int_{p_{g0}}^{p_g} V_{gk}\, \mathrm{d}p_g + \int_{p_{g0}}^{p_g} V_{gv} \mathrm{d}p_g =$$

$$= V_{gk} \int_{Z_0}^{Z} J\,\mathrm{d}Z + V_{pk} \int_{Z_0}^{Z} K\mathrm{d}Z + V_{gk} \int_{J_0}^{J} Z\,\mathrm{d}J + V_{pk} \int_{K_0}^{K} Z\mathrm{d}K\,, \tag{8}$$

and

$$RT \int_{n_0}^{n} Z\,\mathrm{d}n = V_{gk} \int_{J_0}^{J} Z\,\mathrm{d}J + V_{pk} \int_{K_0}^{K} Z\,\mathrm{d}K\,. \tag{9}$$

Equation (8) expresses the changes in the state of the underground gas storing reservoir, i.e. those of gas mass, pressure, volume and internal energy content in terms of energy. The algebraic sum of these terms equals the work done by the compressing equipment that is separately expressed by Eq. (9). These equations enable us to determine the role of the energy components, to compare them and to use their relative and absolute values to predict the energy consumption due to changes in the system. This knowledge proves to be

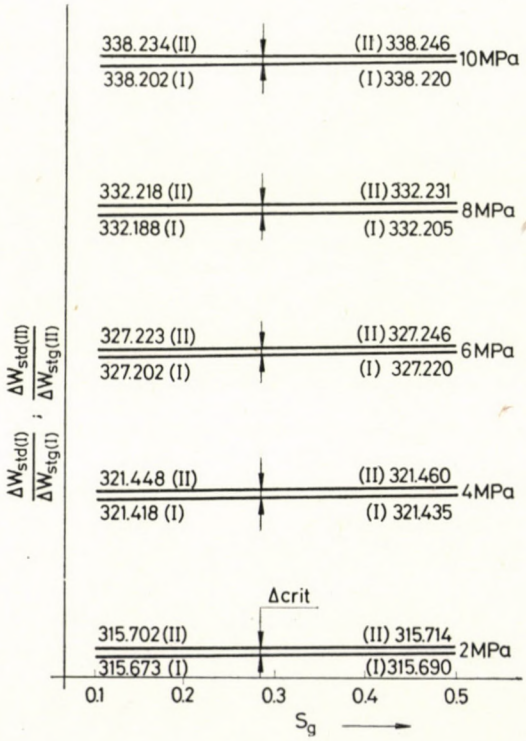

Fig. 3. Ratio of stored and storing energy as a function of gas saturation

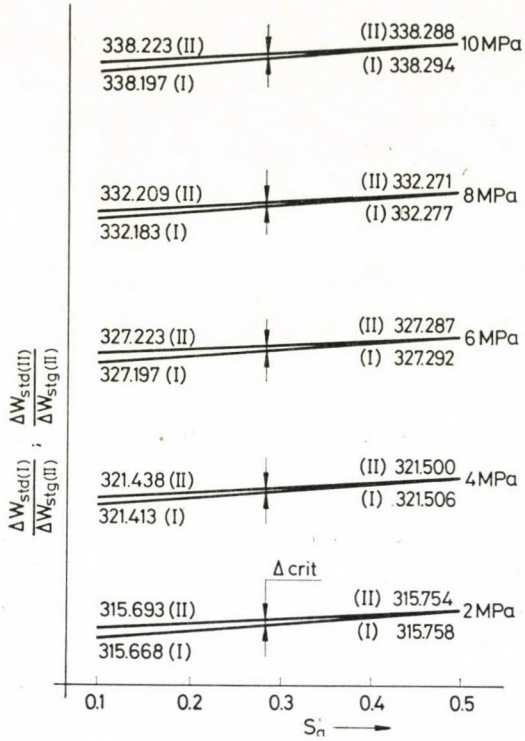

Fig. 4. Ratio of stored and storing energy as a function of gas saturation for a reservoir different from that in Fig. 3 ("high-energy pore volume")

a useful tool in technical and economical evaluation of the operation of underground gas storing reservoirs. Since the components of Eq. (8) can be exactly determined,

$$V_{gk} \int_{J_0}^{J} Z \, \mathrm{d}J = \int_{p_{g0}}^{p_g} V_{gk} \, \mathrm{d}p_g - V_{gk} \int_{Z_0}^{Z} J \, \mathrm{d}Z \tag{10}$$

and

$$V_{pk} \int_{K_0}^{K} Z \, \mathrm{d}K = \int_{V_{g0}}^{V_g} p_w \mathrm{d}V_g + \int_{V_{g0}}^{V_g} p_c \mathrm{d}V_g + \int_{p_{g0}}^{p_g} V_{gv} \, \mathrm{d}p_g - V_{pk} \int_{Z_0}^{Z} K \mathrm{d}Z \tag{11}$$

must hold. Equations (10) and (11) yield the work required from the compressing equipment in terms corresponding to the real processes, i.e. to the work done in the gas volume outside the pores and to that in the varying gas volume inside the pores.

Computer analysis of the energy components of Eq. (9), and of the total change of the energy content due to the change of state in the reservoir given by Eq. (8), suggested that the ratio of the energy contained by the varying gas mass in the reservoir to the energy needed to produce the change of the

gas mass is independent of the reservoir structure:

$$\frac{\Delta W_{\text{stored,(I)}}}{\Delta W_{\text{storing,(I)}}} \simeq \frac{\Delta W_{\text{stored,(II)}}}{\Delta W_{\text{storing,(II)}}} \tag{12}$$

where subscripts I and II denote reservoirs of entirely different structures. Figures 3 and 4 illustrate the ratio of the stored energy to that needed for storing, in various reservoirs. The results were obtained at various formation pressures and with two rock samples of different character. The diagrams show that the difference between the left- and right-hand sides of Eq. (12) is such small that it can only be observed by very exact figures.

To investigate the cause of this phenomenon, stored energy and that needed for storing were plotted against gas saturation in the next figures. The diagrams were aimed to decide whether the approximate equality expressed by relationship (12) is only due to some random coincidence or to internal properties of the system. However, neither Figs 5 and 6 nor Figs 7 and 8 (referring to two different rock types) have enabled us to establish whether an internal law was observed or the phenomenon was random. Considering Figs 5 to 8, it can be seen that the energy values ΔW_{std} and ΔW_{stg} are entirely different,

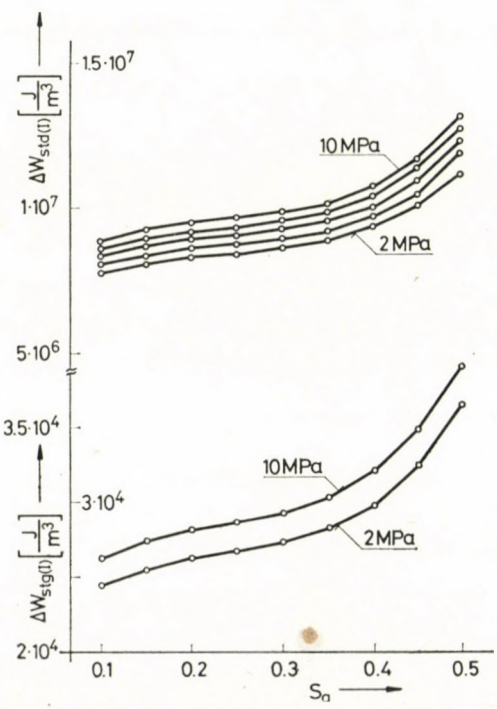

Fig. 5. Stored and storing energy as functions of gas saturation in pore volume V_{gkt} reservoir of Fig. 3

nevertheless, their quotients $\Delta W_{std}/\Delta W_{stg}$ give "equal and hardly varying ratios" illustrated in Figs 3 and 4. This observation once again emphasizes the question how is it possible for the quotients of energy change to behave as in Figs 3 and 4 in spite of the difference in rock types and in the characters of functions ΔW_{std} and ΔW_{stg}. The ratio $\Delta W_{std}/\Delta W_{stg}$ plotted against saturation S_g in Figs 3 and 4 is almost parallel to the horizontal axis. It is apparently independent of the saturation but in reality it strictly monotonously increases even though at a very moderate rate. To emphasize the slight change, the initial and closing values corresponding to $S_g = 0.1$ and $S_g = 0.5$ are indicated in the figures showing moderate changes due to regular variations.

The problem whether the finding of Eq. (12) is due to chance or is it a law, is worth-while scrutinizing for the reciprocal of expression (12) gives the specific energy of storing i.e. the storing work of a unit of stored energy which is of great economical importance in underground gas storage.

Figure 9 illustrates the reservoir used in our theoretical experiment. Gas-water contact (GWC) prior to our observation is denoted by g/w. Suppose we have

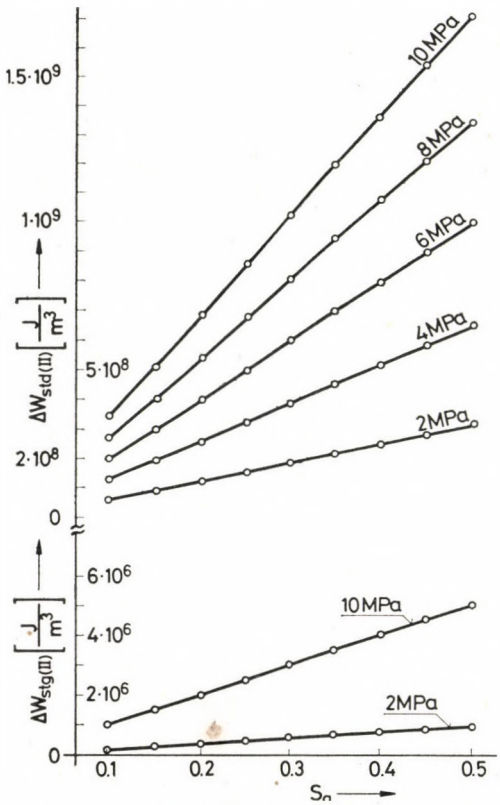

Fig. 6. Stored and storing energy as functions of gas saturation in pore volume V_{pkt} of the reservoir of Fig. 3

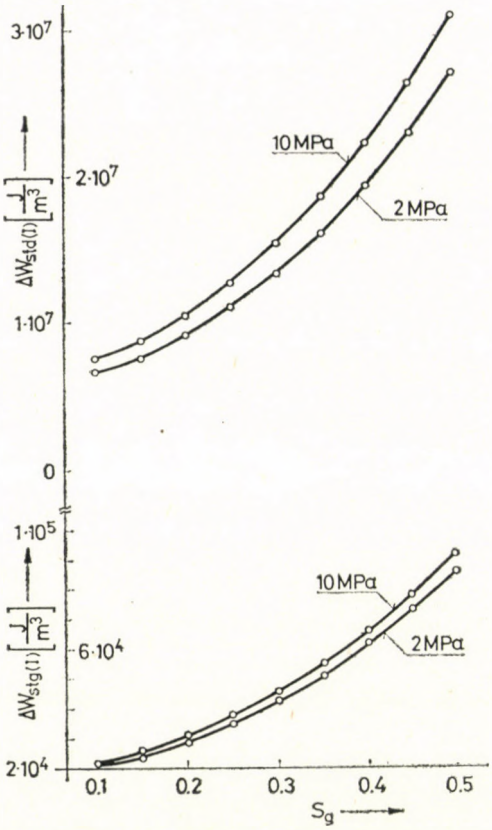

Fig. 7. Stored and storing energy as functions of gas saturation in pore volume V_{gkt} of the reservoir of Fig. 4

volume V_{gkt} in the gas space above GWC and a volume V_{pkt} below it. For these two volumes

$$V_{gkt} = V_{pkt}$$

holds, and the water saturation in the pore volume above GWC equals the residual water saturation S_{wr}. Pore volume can be calculated as

$$V_{gkt} = V_{pt}(1 - S_{wr})$$

while volume V_{pkt} is perfectly saturated with water. A more liberally thinking allows, that the volume V_{gkt} can also be regarded as a cave-like volume instead of the pore volume of a porous rock, its volume equalling pore volume V_{pkt} saturated with water. Injection of gas into the reservoir occurs continuously and we start our observation at the instant when GWC reaches pore volume V_{pkt}, or more exactly when saturation in this space starts to change.

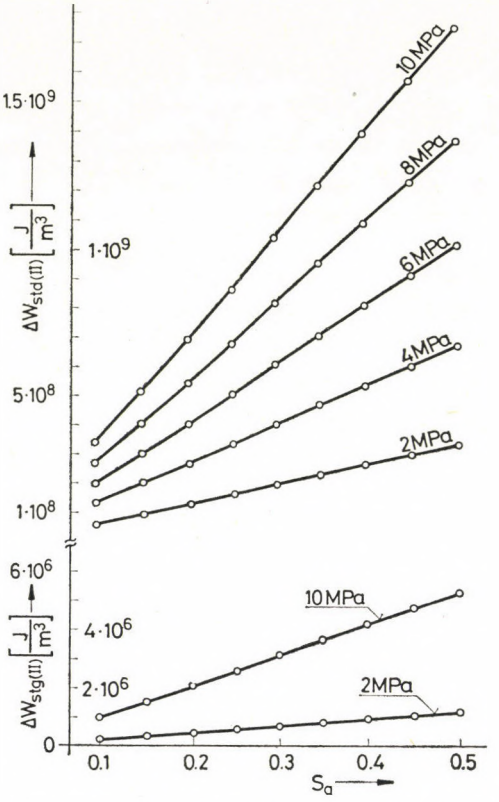

Fig. 8. Stored and storing energy as functions of gas saturation in pore volume V_{pkt} of the reservoir of Fig. 4

Gas pressure at this instant equals p_{g0}. At the final instant of an arbitrary period, observation is terminated in the i-th state of the reservoir and the pressure is now equal to p_{gi}. The changes of the normal volumes can be determined from the change of the gas mass in the investigated volume from the state $i = 0$ to the i-th state i.e. to the end of the observational period.

Equation (12) can also be formulated another way, knowing the changes of normal volumes and the change in the parameters of state. Through the possible reduction this formulation yields the following equality or inequality:

$$\frac{\dfrac{p_{gi}}{Z_i} - \dfrac{p_{g0}}{Z_0}}{\displaystyle\int_{J_0}^{J_i} Z \mathrm{d}J} \lesseqgtr \frac{\dfrac{p_{gi}}{Z_i} S_{gi} - \dfrac{p_{g0}}{Z_0} S_{g0}}{\displaystyle\int_{K_0}^{K_i} Z \, \mathrm{d}K} . \tag{13}$$

This expression corresponds to that in Eq. (12), its left-hand side referring to volume V_{gkt}, the right-hand side to V_{pkt}.

It should be noted in connection with Eqs (8) to (11) that the values of the integrals had to be computed numerically, with an approximation based on the fact that we did not have any relationships between the independent variable (gas mass) and its functions but in the measured points. Therefore, according to the procedure applied, we have in the denominators of relationship (13)

$$\int_{J_0}^{J_i} Z\mathrm{d}J \cong \bar{Z}_i(J_i - J_{i-1}) + \bar{Z}_{i-1}(J_{i-1} - J_{i-2}) + \ldots + \bar{Z}_2(J_2 - J_1) + \bar{Z}_1(J_1 - J_0),$$

where

$$\bar{Z}_i = \frac{Z_i + Z_{i-1}}{2},$$

$$\bar{Z}_{i-1} = \frac{Z_{i-1} + Z_{i-2}}{2}$$

etc.

Similarly,

$$\int_{K_0}^{K_i} Z\,\mathrm{d}K \simeq \bar{Z}_i(K_i - K_{i-1}) + \bar{Z}_{i-1}(K_{i-1} - K_{i-2}) + \ldots$$

$$\ldots + \bar{Z}_2(K_2 - K_1) + \bar{Z}_i(K_1 - K_0)$$

and in the same way as seen above.

Factors J and K are calculated as

$$\frac{p_{gi}}{Z_i} = J_i,$$

$$\frac{p_{g0}}{Z_0} = J_0$$

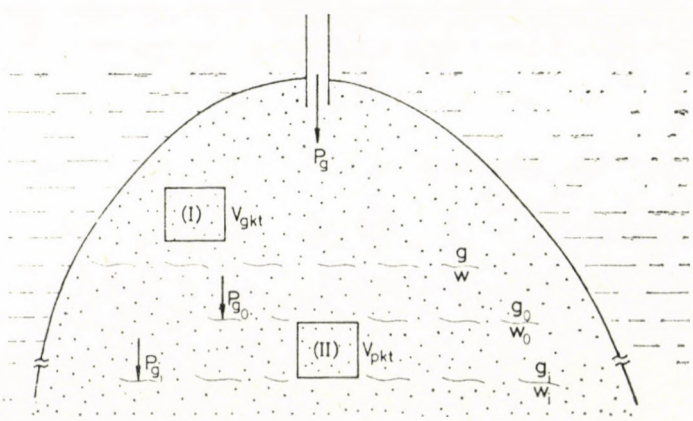

Fig. 9. Theoretical experimental reservoir with parameters of state

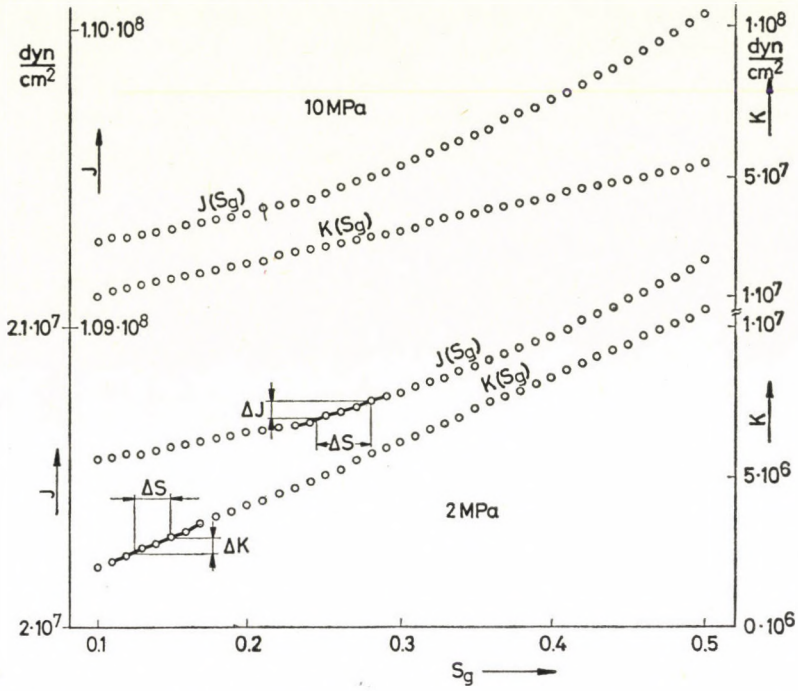

Fig. 10. Functions $J(S_g)$ and $K(S_g)$ as functions of gas saturation in the experimental reservoir

and

$$\frac{p_{gi}}{Z_i} S_{gi} = K_i ,$$

$$\frac{p_{g0}}{Z_0} S_{g0} = K_0 .$$

Substituting now the approximate values for the integrals into the denominators in Eq. (13), and the differences

$$J_i - J_0$$

and

$$K_i - K_0$$

into the numerators, the numerators can be replaced by two series of positive and negative terms each pair of them having the same absolute values:

$$J_i - J_{i-1} + J_{i-1} - J_{i-2} + J_{i-2} - J_{i-3} + J_{i-3} \cdots\cdots$$
$$\cdots\cdots - J_3 + J_3 - J_2 + J_2 - J_1 + J_1 - J_0, \qquad (14)$$

and

$$K_i - K_{i-1} + K_{i-1} - K_{i-2} + K_{i-2} - K_{i-3} + K_{i-3} - \ldots\ldots$$
$$\ldots\ldots - K_3 + K_3 - K_2 + K_2 - K_1 + K_1 - K_0. \tag{15}$$

If functions

$$J = J(S_g)$$

and

$$K = K(S_g)$$

are plotted in co-ordinate systems $J - S_g$ and $K - S_g$ (Fig. 10), it is easy to prove that one can always find such

$$\Delta S_{gi} = S_{gi} - S_{gi-1}$$

intervals for which

$$(J_i - J_{i-1}) = (J_{i-1} - J_{i-2}) = (J_{i-2} - J_{i-3}) = \ldots\ldots$$
$$\ldots\ldots = (J_3 - J_2) = (J_2 - J_1) = (J_1 - J_0),$$

and

$$(K_i - K_{i-1}) = (K_{i-1} - K_{i-2}) = (K_{i-2} - K_{i-3}) = \ldots\ldots$$
$$\ldots\ldots = (K_3 - K_2) = (K_2 - K_1) = (K_1 - K_0),$$

hold, i.e. Eq. (13) can be written in the following form:

$$\frac{n(J_i - J_{i-1})}{(J_i - J_{i-1}) \sum_{i=0}^{n} \bar{Z}_i} = \frac{n(K_i - K_{i-1})}{(K_i - K_{i-1}) \sum_{i=0}^{n} \bar{Z}_i}. \tag{16}$$

Relationship (16) does not exclude the possibility of the two sides' being equal but it does not prove it either. It is namely true that we can always find differences

$$\Delta J_i$$

and

$$\Delta K_i$$

in functions $J(S_g)$ and $K(S_g)$ which are strictly equal. However, the curves of functions $J(S_g)$ and $K(S_g)$ are not parallel, or more exactly, the derivatives of functions $J(S_g)$ and $K(S_g)$ are equal only at a single value of S_g but in no other points. Consequently, differences ΔS_{gi} determining ΔJ_i and ΔK_i are also unequal and, necessarily, they cannot have the same end points S_{gi} and S_{gi-1}.

Therefore, terms Z_i given by function

$$Z = Z[p_g(S_g);\ T]$$

in the sum of Eq. (5) are not equal, which suggests that the correct form of Eq. (16) has to be written as

$$\frac{n}{\sum_{i=0}^{n} \bar{Z}_i} = \frac{n}{\sum_{i=0}^{n} \bar{Z}'_i}\,. \tag{17}$$

If n is sufficiently high, i.e. a great number of differences ΔJ and ΔK are involved in the calculation, the sums of different compressibility factors $\bar{Z}_i$ and $\bar{Z}'_i$ may happen by chance to be equal or nearly equal. This was the case with the observation outlined in connection with Eq. (12).

However, considering equation

$$\frac{\int_{J_0}^{J_i} \mathrm{d}J}{\int_{J_0}^{J_i} Z\mathrm{d}J} = \frac{\int_{K_0}^{K_i} \mathrm{d}K}{\int_{K_0}^{K_i} Z\mathrm{d}K} \tag{18}$$

with the same physical content as that of Eq. (13) but expressed in a more exact form, the inequality will be replaced by an equality since the more the number n of the equal differences

$$J_i - J_{i-1}$$

and

$$K_i - K_{i-1}$$

increases, the more the finite differences approach the differentials, i.e.

$$\Delta J \to \mathrm{d}J$$

and

$$\Delta K \to \mathrm{d}K.$$

Differentials $\mathrm{d}J$ and $\mathrm{d}K$ in turn require also differential changes $\mathrm{d}S$, therefore, terms Z_i and Z'_i, to be summarized in Eq. (17) also differ from each other by differential amounts only, thus Eqs (12) and (13) can be written as a strict equality

$$\frac{\Delta W_{\text{stored, (I)}}}{\Delta W_{\text{storing,(I)}}} = \frac{\Delta W_{\text{stored, (II)}}}{\Delta W_{\text{storing, (II)}}}\,.$$

The fact that relationship (12) has also showed a near-equality, can be explained by the circumstance that the number of observations was chosen for the possible greatest number within the saturation interval from $S_g = 0$ to $S_g = 0.5$. Thus the differences between each pair of saturation were equal to $\Delta S_g = 0.005$. This resulted in a high accuracy of the results although at the expense of a labourous evaluation. The difference between the two sides of relationship (8) giving the total change of energy content, does not exceed 5—10 ergs at a total change of energy content of several thousand millions ergs.

Conclusions

Equations (8) and (9) give the components of the total energy balance and allow their separation according to their place and role. This enables us to define the optimum place of the compressing equipment, utilizing our knowledge of the reservoir parameters and of the volume and place of the gas spaces outside the pore volume.

Data obtained for the laboratory system can be applied to real reservoirs of any size with the help of Eq. (8). Energy consumption can be expressed in similar terms both for real reservoirs and for the laboratory system. Work and absolute and relative values of its components to be done by the compressing equipment to change the mass and state of the system, can be precisely calculated.

If energy is stored in the form of natural gas, the ratio of the stored energy to that needed for storing does not depend on the structure of the reservoir, and *vice versa*, the specific energy requirement of storage, i.e. the work needed to store a unit energy, is independent of whether the gas is stored in a steel container, underground hole, cavity or a porous medium from which the connate water having saturated the pores primarily must first be displaced by the injected gas.

Finally, it should be noted that the energy needed to store cannot be neglected if compared with the stored energy which emphasizes the economic aspects of underground gas storage.

REFERENCES

1. Zoltán, Gy. 1978: Energy requirements of the changes in phase limit surface in underground gas storage. *Kőolaj és Földgáz*, 6, 173—178. (In Hungarian.)
2. Zoltán, Gy. 1980: Der Energiebedarf der Phasengrenzenflächenänderungen bei unterirdischer Gasspeicherung. *Acta Geod. Geoph. Mont. Hung.*, 15, 143—159.
3. Zoltán, Gy. 1979: Theoretical analysis of the energy requirement of changes in phase limit surface. *Kőolaj és Földgáz*, 1, 7—9. (In Hungarian.)
4. Zoltán, Gy. 1979: Energy value of the change of state in an underground gas storing reservoir with water-wet rock. *Kőolaj és Földgáz*, 7, 207—211. (In Hungarian.)

CONTENTS

Tóth, J.: 25 years of the Petroleum Engineering Research Laboratory of the Hungarian Academy of Sciences 311

Balla, L.: Modelling of flow phenomena in porous media 317

Bauer, K.: Determination of the diffusion mass transport coefficient of a CO_2-CH_4 gas mixture in porous media at reservoir temperature and pressure 329

Lakatos, I.—Mrs. Lakatos, Szabó, J.: Stability of polyacrylamide solutions in presence of carbon dioxide 345

Lakatos, I.— Mrs. Lakatos, Szabó, J.—Mrs. Kiss, Gáspár, M.: A comparative laboratory study of well-treatment techniques based on *in situ* cross-linking and polymerization 363

Milley, Gy.— Wagner, O.: A new method of modelling capillary pressure curves 383

Munka, M.: Application of mathematical simulation to polymer flood design 391

Heinemann, Z.—Milley, Gy.— Wagner, O.: Modification of pore structure by inorganic gels to increase displacement efficiency 401

Milley, Gy.— Wagner, O.—Jónap, K.—Bukta, B.—Lövei, J.: Long core model apparatus for the laboratory investigation of oil recovery processes 415

Tóth, J.—Mrs. Milley, Tóth, J.—Mrs. Lakatos, Szabó, J.: Determination of the degree of crude oil metamorphism with application to prospecting purposes 437

Tóth, J.—Mrs. Milley, Tóth, J.: Possible role of mechanical effects in crude oil generation and geochemical investigations of hydrocarbons 447

Zoltán, Gy.: Energy consumption of underground gas storage (Independence of specific storage energy on reservoir structure) 455

PRINTED IN HUNGARY

Akadémiai Nyomda

— treble underlining: bold-face italics
— red underlining: Greek letters
— green underlining: script letters.

Rules for mathematical-physical notations:

— trigonometric, logarithmic, analytic symbols, symbols for units and functions are in roman type (not underlined)
— letter symbols in mathematical and physical formulas, scalars, and subscripts of algebraic and physical quantities are in italics (underlined)
— vectors, matrices, operators in probability theory are in bold-face roman type (double underlining)
— tensors, operators and some special functions are in script letters (green underlining). These cannot be bold.
— Greek letters (red underlining) cannot be bold or extra bold type (thus they cannot be used for vectors or tensors)
— avoid upper lines e.g. for vectors
— avoid possible confusion between o (letter) and 0 (zero), l (letter) and 1 (one), ν (Greek nu) and v, u (letters) etc.
— explain ambiguous or uncommon symbols by making marginal notes in pencil
— be careful about superscripts and subscripts
— formulae must be numbered consecutively with the number in parentheses to the right of the formula. References in text to the equations may then usually be made by the number in parenthesis. When the word equation is used with a number, it is to be abbreviated, Eq. or Eqs in the plural
— the International System of Units (SI) should be used.

Authors are liable for the cost of alteration in the *proofs*. It is, therefore, the responsibility of the author to check the text for errors of facts before submitting the paper for publication.

3. *References* are accepted only in the Harvard system. Citations in the text should be as:

. . . (Bomford 1971) . . . or Bomford (1971)

. . . (Brosche and Sündermann 1976) . . .

. . . (Gibbs et al. 1976b) . . .

The list of references should contain names and initials of all authors (the abbreviation et al. is not accepted here); for *journal articles* year of publication, the title of the paper, title of the journal abbreviated, volume number, first and last page.

For *books* or *chapters in books*, the title is followed by the publisher and place of publication.

All items must appear both in the text and references.

Examples:

Bomford G 1971: Geodesy. Clarendon Press, Oxford

Brosche P, Sündermann J 1976: Effects of oceanic tides on the rotation of the earth. Manuscript. Univ. of Bonn

Buntebarth G 1976: Temperature calculations on the Hungarian seismic profile-section NP-2. In: *Geoelectric and Geothermal Studies (East-Central Europe, Soviet Asia), KAPG Geophysical Monograph.* Akadémiai Kiadó, Budapest, 561—566.

Gibbs N E, Poole W G, Stockmeyer P K 1976a: An algorithm for reducing the bandwidth and profile of a sparse matrix. *SIAM J. Number. Anal.*, 13, 236—250.

Gibbs N E, Poole W G, Stockmeyer P K 1976b: A comparison of several bandwidth and profile reduction algorithms. *ACM Trans. on Math. Software*, 2, 322—330.

Szarka L 1980: Potenciáltérképezés analóg modellezéssel (Analogue modeling of potential mapping). *Magyar Geofizika*, 21, 193—200.

4. *Footnotes* should be typed on separate sheets.

5. *Legends* should be short and clear. The place of the tables and figures should be indicated in the text, on the margin.

6. *Tables* should be numbered serially with Roman numerals. Vertical lines are not used.

All the illustrations should contain the figure number and author's name in pencil on the reverse.

Figures will be redrawn. Therefore the most important point is clearness of the figures, even pencil-drawings are accepted (with a duplicate).

Photographs and *half-tone* illustrations should be sharp and well contrasted.

If a specific reduction or enlargement is required, please indicate this in blue pencil on the figure.

The editors will send information to the first author about the *arrival* and acceptance of the papers. A galley proof is also sent to the first author for *correction*. Hundred *offprints* are supplied free of charge.

These instructions are valid as from 1982.

Periodicals of the Hungarian Academy of Sciences are obtainable at the following addresses:

AUSTRALIA
C.B.D. LIBRARY AND SUBSCRIPTION SERVICE
Box 4886, G.P.O., *Sydney N.S.W. 2001*
COSMOS BOOKSHOP, 145 Ackland Street
St. Kilda (Melbourne), Victoria 3182

AUSTRIA
GLOBUS, Höchstädtplatz 3, *1206 Wien XX*

BELGIUM
OFFICE INTERNATIONAL DE LIBRAIRIE
30 Avenue Marnix, *1050 Bruxelles*
LIBRAIRIE DU MONDE ENTIER
162 rue du Midi, *1000 Bruxelles*

BULGARIA
HEMUS, Bulvar Ruszki 6, *Sofia*

CANADA
PANNONIA BOOKS, P.O. Box 1017
Postal Station "B", *Toronto, Ontario M5T 2T8*

CHINA
CNPICOR, Periodical Department, P.O. Box 50
Peking

CZECHOSLOVAKIA
MAD'ARSKÁ KULTURA, Národní třída 22
115 66 Praha
PNS DOVOZ TISKU, Vinohradská 46, *Praha 2*
PNS DOVOZ TLAČE, *Bratislava 2*

DENMARK
EJNAR MUNKSGAARD, Norregade 6
1165 Copenhagen K

FEDERAL REPUBLIC OF GERMANY
KUNST UND WISSEN ERICH BIEBER
Postfach 46, *7000 Stuttgart 1*

FINLAND
AKATEEMINEN KIRJAKAUPPA, P.O. Box 128
SF-00101 Helsinki 10

FRANCE
DAWSON-FRANCE S. A., B. P. 40, *91121 Palaiseau*
EUROPÉRIODIQUES S. A., 31 Avenue de Versailles, *78170 La Celle St. Cloud*
OFFICE INTERNATIONAL DE DOCUMENTATION ET LIBRAIRIE, 48 rue Gay-Lussac
75240 Paris Cedex 05

GERMAN DEMOCRATIC REPUBLIC
HAUS DER UNGARISCHEN KULTUR
Karl Liebknecht-Straße 9, *DDR-102 Berlin*
DEUTSCHE POST ZEITUNGSVERTRIEBSAMT
Sraße der Pariser Kommüne 3–4, *DDR-104 Berlin*

GREAT BRITAIN
BLACKWELL'S PERIODICALS DIVISION
Hythe Bridge Street, *Oxford OX1 2ET*
BUMPUS, HALDANE AND MAXWELL LTD.
Cowper Works, *Olney, Bucks MK46 4BN*
COLLET'S HOLDINGS LTD., Denington Estate
Wellingborough, Northants NN8 2QT
WM. DAWSON AND SONS LTD., Cannon House
Folkstone, Kent CT19 5EE
H. K. LEWIS AND CO., 136 Gower Street
London WC1E 6BS

GREECE
KOSTARAKIS BROTHERS INTERNATIONAL BOOKSELLERS, 2 Hippokratous Street, *Athens-143*

HOLLAND
MEULENHOFF-BRUNA B.V., Beulingstraat 2,
Amsterdam
MARTINUS NIJHOFF B.V.
Lange Voorhout 9–11, *Den Haag*

SWETS SUBSCRIPTION SERVICE
347b Heereweg, *Lisse*

INDIA
ALLIED PUBLISHING PRIVATE LTD., 13/14
Asaf Ali Road, *New Delhi 110001*
150 B-6 Mount Road, *Madras 600002*
INTERNATIONAL BOOK HOUSE PVT. LTD.
Madame Cama Road, *Bombay 400039*
THE STATE TRADING CORPORATION OF INDIA LTD., Books Import Division, Chandralok
36 Janpath, *New Delhi 110001*

ITALY
INTERSCIENTIA, Via Mazzé 28, *10149 Torino*
LIBRERIA COMMISSIONARIA SANSONI, Via Lamarmora 45, *50121 Firenze*
SANTO VANASIA, Via M. Macchi 58
20124 Milano
D. E. A., Via Lima 28, *00198 Roma*

JAPAN
KINOKUNIYA BOOK-STORE CO. LTD.
17-7 Shinjuku 3 chome, Shinjuku-ku, *Tokyo 160-91*
MARUZEN COMPANY LTD., Book Department, P.O. Box 5050 Tokyo International, *Tokyo 100-31*
NAUKA LTD. IMPORT DEPARTMENT
2-30-19 Minami Ikebukuro, Toshima-ku, *Tokyo 171*

KOREA
CHULPANMUL, *Phenjan*

NORWAY
TANUM-TIDSKRIFT-SENTRALEN A.S., Karl Johansgatan 41–43, *1000 Oslo*

POLAND
WĘGIERSKI INSTYTUT KULTURY, Marszałkowska 80, *00-517 Warszawa*
CKP I W, ul. Towarowa 28, *00-958 Warszawa*

ROUMANIA
D. E. P., *Bucureşti*
ILEXIM, Calea Grivitei 64–66, *Bucureşti*

SOVIET UNION
SOJUZPECHAT — IMPORT, *Moscow*
and the post offices in each town
MEZHDUNARODNAYA KNIGA, *Moscow G-200*

SPAIN
DIAZ DE SANTOS, Lagasca 95, *Madrid 6*

SWEDEN
ALMQVIST AND WIKSELL, Gamla Brogatan 26
101 20 Stockholm
GUMPERTS UNIVERSITETSBOKHANDEL AB
Box 346, *401 25 Göteborg 1*

SWITZERLAND
KARGER LIBRI AG, Petersgraben 31, *4011 Basel*

USA
EBSCO SUBSCRIPTION SERVICES
P.O. Box 1943, *Birmingham, Alabama 35201*
F. W. FAXON COMPANY, INC.
15 Southwest Park, *Westwood Mass. 02090*
THE MOORE-COTTRELL SUBSCRIPTION AGENCIES, *North Cohocton, N. Y. 14868*
READ-MORE PUBLICATIONS, INC.
140 Cedar Street, *New York, N. Y. 10006*
STECHERT-MACMILLAN, INC.
7250 Westfield Avenue, *Pennsauken N. J. 08110*

YUGOSLAVIA
JUGOSLOVENSKA KNJIGA, Terazije 27, *Beograd*
FORUM, Vojvode Mišića 1, *21000 Novi Sad*

Index: 26.031 **HU ISSN 0374—1842**